Cranfield University

S. A. Prince

The Aerodynamics of High Speed Aerial Weapons

Cranfield College of Aeronautics

Total Technology PhD Thesis

Cranfield College of
Aeronautics

The Aerodynamics of High Speed Aerial Weapons

Total Technology PhD Thesis

Simon A. Prince

Supervisors: Prof. N. Qin and Mr T. Birch

Flow Prediction and Control Group
Cranfield College of Aeronautics
Cranfield University
Bedfordshire
MK43 OAL

September 1999

Abstract

The focus of this work is the investigation of the complex compressible flow phenomena associated with high speed aerial weapons. A three dimensional multiblock finite volume flow solver was developed with the aim of studying the aerodynamics of missile configurations and their component structures.

The first component of the study involved the aerodynamic investigation of the isolated components used in the design of conventional missile configurations. The computational study of nine ogive-cylinder body experimental test cases is presented together with a new interpretation of the complex vortical flow including the windward appearance of a "vortex shock wave". In addition, a simple modification to improve the accuracy of the Baldwin-Lomax/Degani-Schiff turbulence model is put forward, and the phenomenon of "phantom vorticity" in Euler solutions and its alleviation are described. Inclined Delta Wings in supersonic flow were computed in order to study the aerodynamics of wings alone, and in particular the vortex-shock interactions which occur on their leeward surfaces.

The second component of the study was the computational and experimental investigation of a generic cruciform missile configuration. The complicated interactions between shock waves and boundary/shear layers that are seen to occur around and in the wake of the cruciform wing arrangement were studied and described.

The third component of the research involved an assessment of the prediction technologies used in the design of modern weapons. In particular the role of Computational Fluid Dynamics in the process of design.

Acknowledgements

The author is indebted to Prof. Ning Qin for his supervision and support during the course of this work. Without his expert knowledge coupled with the openness to share it, this project would have foundered on the rocks of inexperience. I would also like to thank Trevor Birch of the Defence Evaluation and Research Agency (DERA) at Bedford, who shared his considerable knowledge and experience in the aerodynamics of missiles. It was through his contacts that I was able to participate in the experimental program at NASA Langley. The contributions of Dr. Ian Wrisdal, Richard Allen, Richard Rogers and Dr. Graham Foster of DERA are also acknowledged. The assistance of Professor Bryan Richards and Laurent Dubuc of the Department of Aerospace Engineering at Glasgow University was also greatly appreciated.

I was lucky indeed to have shared my time at the College of Aeronuatics with the finest of engineers and scientists. The encouragement, advice and assistance of Dr. Kevin Garry, Professor John Stollery, and Dr. Les Oswald is warmly acknowledged. The support and comradeship of my colleagues in the Flow Control and Prediction Group, in particular, Dr. David Ludlow, Dr. Scott Shaw, Yon Han Chong, Aghis Barberopoulos, Yuping Zhu, Dr. Caroline Lowe, Dr. Steve Billett, David Perigo, Kristian Petterson and Bowen Zhong was invaluable. The tom foolery and lively debate helped enormously to maintain my sanity. In addition Dr. Sanjoy Muckherjee should also be included in this roll of honour. At the NASA Langley Research Center, Jerry Allen, Floyd Wilcox, Bill Graham, Danny Taylor, Dan Pritchard, Joseph Moore, Reggie Brown and Ricky Hall, should all be credited with performing the experiments on "Her Majesties Missile".

Finally, I would like to express my gratitude for the funding provided by the Engineering and Physical Sciences Research Council, DERA, Cranfield University and the Worshipfull Company of Coachmakers and Carriage Makers of London.

Contents

Contents ii

Nomenclature xiii

1 Introduction 1

2 Aerial Weapon Design 4
2.1 Engineering Design 4
2.2 Prediction Technologies 5
2.2.1 Empirical and Semi-Empirical Methods 6
2.2.2 Semi-Empirical Methods for Supersonic Missile Design 6
2.2.3 Computational Fluid Dynamics 8
2.2.4 Experiments 9
2.3 Computational Aerodynamics 10
2.3.1 Models for Continuum Flow 10
2.4 Complex Geometries: Multiblock Techniques 13

3 The Computational Predictive Tools 17
3.1 CRANS3D: Governing Equations And Their Discretisation . 17
3.1.1 Oshers Approximate Riemann Solver and MUSCL Variable Extrapolation 22
3.1.2 Diffusive Flux Treatment 23
3.1.3 Local Time Stepping 24
3.1.4 Boundary Conditions 25
3.2 Turbulence Closure: The Baldwin-Lomax Approach 26
3.3 CRANS3D Multiblock Implementation 30
3.4 The PNS Solver and Missile DATCOM Code 33
3.4.1 The PNS Code 33
3.4.2 USAF Missile DATCOM Code 34

4 Slender Forebody Aerodynamics 35
4.1 Slender Body Vortical Flows 35
4.1.1 The Symmetric Vortex Regime 36
4.1.2 Recent Research of Symmetric Vortical Forebody Flows 39

4.2 Analysis of Experimental Error in Surface Pressure Measurement 47
4.3 Numerical Investigation of Forebody Aerodynamics 49
4.3.1 The ONERA Experimental Test Cases: Cases 1-4 . . 49
4.3.2 The RAE Forebody: Cases 5-8 86
4.3.3 The DLR Experimental Study of the Windward Shock Phenomenon 107
4.4 Slender Forebodies and the Vortex Shock: An Aerodynamic Interpretation 110
4.5 Multiblock Validation: B1 and B2 Revisited 119

5 Euler Solutions and 'Phantom Vorticity' on Non-Uniform Grids 127
5.1 The Numerical Investigation 129
5.1.1 A New Formulation of the MUSCL Scheme for Non-Uniform Grids 133
5.2 Phantom Vorticity: An Interpretation 137

6 Delta Wings At High Speed 138
6.1 The Supersonic Flow About Delta Wings 138
6.2 Wing Alone: The NASA 75° Swept Delta Wing 144
6.2.1 The Experimental Test Case 144
6.2.2 The Computational Model 145
6.2.3 Wing Alone: Results and Discussion 148
6.2.4 NASA 75° Swept Delta Wing: Summary 162

7 Full Configuration: The Body/Wing 166
7.1 Vortical Body/Wing Flowfields: A Review 166
7.2 The Experimental Study 171
7.2.1 The Langley Unitary Plan Wind Tunnel 171
7.2.2 The B1AW20A3 Model And Instrumentation 171
7.2.3 Flow Visualisation Techniques 174
7.2.4 Experimental Procedure 177
7.3 The Numerical Study 178
7.3.1 Block Topology and Grid Generation 178
7.3.2 Turbulence Modelling Issues 181
7.4 B1AW20A3: Results and Comparisons 181
7.4.1 Body Alone Flow Visualisation 181
7.4.2 B1AW20A3 Zero Roll Investigation 186
7.4.3 B1AW20A3 45° Roll Investigation 202
7.4.4 B1AW20A3: Aerodynamic Interpretation 215
7.4.5 Force and Moment Prediction 226
7.4.6 Multiblock Efficiency Issues 233

8 General Discussion 237

9 Conclusions 243

Bibliography 245

A A Brief History of Aerial Weapons 252

B Calculation of δ^* and Local Streamwise Pressure Gradient Used in Surface Pressure Measurement Error Estimation 258

C Prediction of the Occurrence of the Embedded Crossflow Shock 261

List of Figures

1.1 *The complicated flow structure around a relatively simple missile configuration.* 2

2.1 *Approximation Levels of the Governing Equations for Continuum Flow Prediction* 11
2.2 *2D and 3D blocks bounded by ghost points* 15
2.3 *Possible Orientations for a 3D 2 Block System* 16

3.1 *Flux Balance for Cell Centred Finite Volume Technique* . . . 21
3.2 *Interface Flux Treatment* 24
3.3 *Degani-Schiff Crossflow Modification* 29
3.4 *Side Number Convention for Individual Blocks* 30
3.5 *Block Topology for T-junction of a Duct* 31
3.6 *Boundary Treatment in CRANS3D* 32
3.7 *Multiblock Interface Treatment in CRANS3D* 33

4.1 *Vortex Flow Structure Development With angle of attack* . . . 36
4.2 *Affect of Angle of Attack and Crossflow Mach Number on Vortex Structure Over A Cylindrical Body ($l/D \approx 10$ [1]* . . . 37
4.3 *Symmetric Cross Flow Vortex Structure* 37
4.4 *Movement of Separation Line Along Missile Body [35]* 38
4.5 *Comparison of Typical Viscous and Inviscid Surface Pressure Distributions for Supersonic Flow past Cylinder Afterbody* . . 38
4.6 *Evidence of an Embedded Separation Shock [9]* 40
4.7 *Shockwave Patterns Around Ogive-Cylinder In Crossflow, $M_\infty =$ 3.5 , $\alpha = 18°$.* 41
4.8 *Crossflow Streamline Patterns at x/D=8 with Increasing angle of attack [41]* 45
4.9 *Effect of Grid Refinement on Numerical Convergence of Crossflow Features [41]* 46
4.10 *ONERA-B1 Tangent-Ogive Body Geometry* 50
4.11 *ONERA-B2 Tangent-Ogive Body Geometry* 51
4.12 *B1 Computational Grid for Zero angle of attack ($61 \times 85 \times 45$)* 52

4.13 *B1 Computational Grid for* 10° *angle of attack (61 × 85 × 75)* 52
4.14 *Axial Surface Pressure Distribution: B1,* 0° *angle of attack* . 53
4.15 *Residual Convergence with Respect to Iteration Number: B1,* 0° *angle of attack, CFL=0.15* 54
4.16 *Grid Convergence Study: B1,* 10° *angle of attack* 55
4.17 *Axial Surface Pressure Distribution: B1,* 10° *angle of attack* . 56
4.18 *Circumferential Surface Pressure Distribution: B1,* 10° *angle of attack* 57
4.19 *Displacement Thickness: B1,* 10° *angle of attack, x/D=6* . . . 58
4.20 *Surface Pressure Gradient: B1,* 10° *angle of attack, x/D=6* . 59
4.21 *Estimated Expermimental* C_P *Error Distribution: B1,* 10° *angle of attack, x/D=6* 59
4.22 *Circumferential Surface Pressure, Estimated Experimental Error: B1,* 10° 60
4.23 *Surface Skin Friction Comparison, B1* 10° *angle of attack* . . 61
4.24 *Crossflow Plane Mach Number Contours, B1* 10° *angle of attack* 62
4.25 *Crossflow Plane Total Pressure Ratio Contours, B1* 10° *angle of attack* 63
4.26 *Comparison CRANS3D vs PNS, Total Pressure Ratio, B1* 10° *angle of attack* 64
4.27 *Axial Surface Pressure Distribution: B2,* 0° *angle of attack* . 66
4.28 *Residual Convergence with Respect to Iteration Number: B2,* 0° *angle of attack, CFL=0.15* 66
4.29 *Boundary Layer Mach Number Profiles, B2* 0° *angle of attack* 67
4.30 *CRANS3D, Grid Convergence: B2,* 10° *angle of attack, x/D=7* 68
4.31 *The Effect of the Degani-Sciff Cut-Off Factor Near Primary Crossflow Separation* 69
4.32 *Circumferential Surface Pressure Distribution, B2* 10° *angle of attack* 71
4.33 *Circumferential Surface Pressure, Estimated Experimental Error: B2,* 10° 72
4.34 *Surface Skin Friction Comparison, B2* 10° *angle of attack* . . 73
4.35 *Comparison of Results for Different Turbulence Models, B2* 10°, *x/D=9* 75
4.36 *Vorticity Moment Distributions at Three Circumferential Stations, x/D=6* 76
4.37 *Windward Symmetry Plane Vorticity Moment Distribution at Station I=1* 77
4.38 *Effect of Modified Degani-Schiff Parameter: Circumferential* C_P 78
4.39 *Effect of Modified Degani-Schiff Parameter: Crossflow Total Pressure Ratio* 79
4.40 *Representation of the Measurement Traverses through the Leeward Quadrant* 81

4.13 *B1 Computational Grid for* 10° *angle of attack (61 × 85 × 75)* 52
4.14 *Axial Surface Pressure Distribution: B1,* 0° *angle of attack* . 53
4.15 *Residual Convergence with Respect to Iteration Number: B1,* 0° *angle of attack, CFL=0.15* 54
4.16 *Grid Convergence Study: B1,* 10° *angle of attack* 55
4.17 *Axial Surface Pressure Distribution: B1,* 10° *angle of attack* . 56
4.18 *Circumferential Surface Pressure Distribution: B1,* 10° *angle of attack* 57
4.19 *Displacement Thickness: B1,* 10° *angle of attack, x/D=6* . . . 58
4.20 *Surface Pressure Gradient: B1,* 10° *angle of attack, x/D=6* . 59
4.21 *Estimated Expermimental* C_P *Error Distribution: B1,* 10° *angle of attack, x/D=6* 59
4.22 *Circumferential Surface Pressure, Estimated Experimental Error: B1,* 10° 60
4.23 *Surface Skin Friction Comparison, B1* 10° *angle of attack* . . 61
4.24 *Crossflow Plane Mach Number Contours, B1* 10° *angle of attack* 62
4.25 *Crossflow Plane Total Pressure Ratio Contours, B1* 10° *angle of attack* 63
4.26 *Comparison CRANS3D vs PNS, Total Pressure Ratio, B1* 10° *angle of attack* 64
4.27 *Axial Surface Pressure Distribution: B2,* 0° *angle of attack* . 66
4.28 *Residual Convergence with Respect to Iteration Number: B2,* 0° *angle of attack, CFL=0.15* 66
4.29 *Boundary Layer Mach Number Profiles, B2* 0° *angle of attack* 67
4.30 *CRANS3D, Grid Convergence: B2,* 10° *angle of attack, x/D=7* 68
4.31 *The Effect of the Degani-Sciff Cut-Off Factor Near Primary Crossflow Separation* 69
4.32 *Circumferential Surface Pressure Distribution, B2* 10° *angle of attack* 71
4.33 *Circumferential Surface Pressure, Estimated Experimental Error: B2,* 10° 72
4.34 *Surface Skin Friction Comparison, B2* 10° *angle of attack* . . 73
4.35 *Comparison of Results for Different Turbulence Models, B2* 10°, *x/D=9* 75
4.36 *Vorticity Moment Distributions at Three Circumferential Stations, x/D=6* 76
4.37 *Windward Symmetry Plane Vorticity Moment Distribution at Station I=1* 77
4.38 *Effect of Modified Degani-Schiff Parameter: Circumferential* C_P 78
4.39 *Effect of Modified Degani-Schiff Parameter: Crossflow Total Pressure Ratio* 79
4.40 *Representation of the Measurement Traverses through the Leeward Quadrant* 81

4.41 *Mach Number Profile: x/D=9* 82
4.42 *Mach Number Profile: x/D=9, Continued* 83
4.43 *Total Pressure Ratio Profile: x/D=9* 84
4.44 *Total Pressure Ratio Profile: x/D=9, Continued* 85
4.45 *B1A Supersonic NS Grid for Case 7 (89 × 89 × 119)* 86
4.46 *B1A Transonic NS Grid for Case 8 (89 × 89 × 89)* 87
4.47 *Grid Convergence, Surface C_P at x/D=5, B1A, M_∞=2.5* 14° 88
4.48 *Effect of Degani-Schiff Parameter, Surface C_P at x/D=9, B1A, M_∞=2.5* 14° 88
4.49 *Circumferential Surface Pressure Distribution, B1A, M_∞=2.5,* 14° 89
4.50 *Circumferential Surface Pressure Distribution, B1A, M_∞=2.5,* 14°, *continued* 90
4.51 *Displacement Thickness: B1A, M_∞=2.5,* 14° 91
4.52 *Pressure Gradient: B1A, M_∞=2.5,* 14° 91
4.53 *Circumferential Surface Pressure, Experimental Error: B1A, M_∞=2.5,* 14° 93
4.54 *Crossflow Pitot Pressure Contours: B1A, M_∞=2.5,* 14° . . . 94
4.55 *Symmetry Plane Density Gradient and Skin Friction Lines: B1A, M_∞=2.5,* 8° 95
4.56 *Circumferential Surface Pressure Distribution, B1A, M_∞=2.5,* 8° 96
4.57 *Effect of Degani-Schiff Parameter, Surface C_P at x/D=7, B1A, M_∞=1.8,* 14° 97
4.58 *Circumferential Surface Pressure Distribution, B1A, M_∞=1.8,* 14° 99
4.59 *Circumferential Surface Pressure Distribution, B1A, M_∞=1.8,* 14°, *continued* 100
4.60 *Schlieren Photograph: B1A, M_∞=1.8,* 14° 101
4.61 *Symmetry Plane Density Gradient: B1A, M_∞=1.8,* 14° . . . 101
4.62 *Surface Pressure Carpet Plot: B1A, M_∞=1.8,* 14° 102
4.63 *Effect of Degani-Schiff Parameter, Surface C_P at x/D=5.5, B1A, M_∞=0.7,* 14° 103
4.64 *Circumferential Surface Pressure Distribution, B1A, M_∞=0.7,* 14° 104
4.65 *Circumferential Surface Pressure Distribution, B1A, M_∞=0.7,* 14°, *continued* 105
4.66 *Effect of Modified Degani-Schiff Parameter: Crossflow Pitot Pressure Ratio* 106
4.67 *DLR Body, Computational PNS Grid for Case 9 (150 × 153 × 153)* 108
4.68 *Appearance of Windward Shock, Surface C_P at x/D=7, DLR Body, M_∞=1.4,* 16° 108
4.69 *Schlieren Photograph: DLR Body, M_∞=1.4,* 16° 109

4.70 *Symmetry Plane Density Gradient: DLR Body, M_∞=1.4, 16°* 109
4.71 *Effect of Crossflow Mach Number on Primary Separation and Surface Skin Friction Lines [19]* 111
4.72 *Computed Symmetry Plane Density Gradient and Interpretation: B2, 10° angle of attack* 112
4.73 *Computed Crossflow Density Gradient and Interpretation* . . 113
4.74 *Computed Crossflow Density Gradient and Interpretation: x/D=5, B1A, M_∞=1.8, 14°* 114
4.75 *Flow Topology for Subsonic Crossflow Over Rear of Cylinder Afterbody, $M_\infty sin\alpha < 0.44$* 117
4.76 *Flow Structure Encountered with Transonic/Supersonic Crossflow Over Whole Body Length, $M_\infty sin\alpha > 0.44$* 118
4.77 *Multiblock I-Cut test grid for Garteur B1 (33 × 33 × 33)* . . 119
4.78 *Comparison of Axial Surface Pressure Coefficient* 120
4.79 *Comparison of Multiblock I-Cut (bottom) and Single Block (top) Density Contours For Leeward Symmetry Plane* 120
4.80 *Comparison of Crossflow Density Contour Resolution for Multiblock and Single Block Computations at Plane x/D=8* 121
4.81 *Multiblock J-Cut test grid for Garteur B1 (33 × 33 × 33)* . . 122
4.82 *Comparison of Multiblock J-Cut (top) and Single Block (bottom) Density Contours For Leeward Symmetry Plane* 122
4.83 *Comparison of Multiblock J-Cut (bottom) and Single Block (top) Density Contours For Windward Symmetry Plane* . . . 123
4.84 *Multiblock K-Cut test grid for Garteur B1 (33 × 33 × 33)* . . 124
4.85 *Comparison of Vortex Density Contour Resolution for K-Cut Multiblock and Single Block Computations at Plane x/D=8* . 125
4.86 *Comparison of Circumferential Surface Pressure Coefficient, x/D=8* 125
4.87 *Comparison of Turbulent Solutions for Vortex Resolution for K-Cut Multiblock and Single Block Computations at Plane x/D=9* 126
4.88 *Comparison of Circumferential Surface Pressure Coefficient, x/D=9* 126

5.1 *Grid Convergence for Euler Solution, 3rd Order MUSCL* . . . 129
5.2 *Density Contours at x/D=8, 3rd Order MUSCL Euler Solution on Grid 1* 130
5.3 Euler Solution on Grid 5, 3rd Order MUSCL 131
5.4 B1, First Order Euler Solution on Grid 5 131
5.5 *Euler Solution on Grid 5, 1st Order vs. 3rd Order MUSCL* . 132
5.6 *Finite Volume Representation of Stretched Grid About Cell i* 133
5.7 *Euler Solution on Grid 6, x/D=8, 3rd Order Original MUSCL Scheme* 136

5.8 *Euler Solution on Grid 6, x/D=8, 3rd Order Modified MUSCL Scheme* 136

6.1 *Separation Mechanisms Identified by Stanbrook and Squire [70].* 138
6.2 *Classical Swept Leading Edge Separation Flow Structure and Surface Pressure Distribution.* 139
6.3 *The Variation with angle of attack of Mach Number for Flow Attachment on Swept Sharp Leading Edge Wings. [70].* 140
6.4 *Classification of Leeside Flow on Swept Sharp Leading Edge Delta Wings. [38] [36]* 142
6.5 *Applicability of Euler Codes to the Prediction of Supersonic Delta Wings. [36]* 143
6.6 *Model Planform, 75° Sweepback (Dimensions in Inches) [38].* 144
6.7 *Vapour Screen Photographic Apparatus [38].* 145
6.8 *Delta Wing Single Block Grid, Crossflow Plane (90 × 86× 94)* 145
6.9 *Delta Wing Multi-Block Grid, Crossflow Plane (33 × 33× 66)* 146
6.10 *Delta Wing Multi-Block Grid, Crossflow Plane (64 × 86× 148)* 147
6.11 *Demonstration of Conical Flow Past Supersonic Delta Wings, 16° angle of attack* 148
6.12 *Comparison of Grid Topologies,* $\alpha = 8°$ 150
6.13 *Delta Wing:* C_p *Distribution Comparison, M=2.8, 8° angle of attack.* 151
6.14 $P_0/P_{0\infty}$ *Contours,* $\alpha = 8°$*, 3D vs Conical NS* 153
6.15 $P_0/P_{0\infty}$ *Contours,* $\alpha = 8°$*, 3D vs Conical Euler* 154
6.16 M_C *Contours,* $\alpha = 8°$*, 3D vs Conical* 155
6.17 *Delta Wing:* C_p *Distribution Comparison, M=2.8, 16° angle of attack.* 156
6.18 $P_0/P_{0\infty}$ *Contours,* $\alpha = 16°$*, 3D vs Conical NS* 158
6.19 $P_0/P_{0\infty}$ *Contours,* $\alpha = 16°$*, 3D vs Conical Euler* 159
6.20 M_C *Contours,* $\alpha = 16°$*, 3D vs Conical* 160
6.21 *Surface Streamline Comparisons, Turbulent NS vs Euler* . . . 161
6.22 *NASA 75° Swept Delta Wing: Flow Structures at 8° and 16° Angle of Attack* 163
6.23 *Classification of Leeside Flow for the NASA and RAE W20 Delta Wing Cases* 164

7.1 *Vapour Screen Study of Longitudinal Vortex Development,* M_∞*=1.3. [2]* 167
7.2 *Single Block Mesh Around a Finned Body [56]* 168
7.3 *The B1AW20A3 Generic Missile Configuration (Dimension in Inches)* 170
7.4 *The B1AW20A3 Model Mounted in the Unitary Wind Tunnel Test Section* 172
7.5 *Tunnel Installation (Dimension in Inches) [84]* 172

7.6 *Detail of the Model Sting Mounting* 173
7.7 *Schematic of the UPWT schlieren System [42]* 174
7.8 *The Vapour Screen Flow Visualization Technique* 175
7.9 *Schematic of the UPWT Vapour Screen Setup [42]* 175
7.10 *Location of the Longitudinal Visualisation Stations (Dimension in Inches) [84]* 176
7.11 *Block Topology, Forward View* 178
7.12 *Block Topology, 0° Roll Case, xz-Plane* 179
7.13 *Comparison of Euler and Turbulent NS Grids, 0° Roll* 180
7.14 *Turbulent NS Grid, 0° Roll, xz-Plane* 180
7.15 *Body Alone: schlieren Photographs, 8° and 14° Incidence* . . 183
7.16 *Body Alone: Vapour Screen Photographs, 8° Incidence* 184
7.17 *Body Alone: Vapour Screen Photographs, 14° Incidence* . . . 185
7.18 *Total Pressure Ratio Contours Comparison, 0° Roll, x/D=11.5, 8° Incidence* 188
7.19 *Computation vs Experimental schlieren, 0° Roll, 8° Incidence* 189
7.20 *Computational Solution (xz-Plane), 0° Roll, 8° Incidence* . . 190
7.21 *Comparison of Computational and Experimental Vapour Screen Visualisation, Zero Roll, 8° Incidence* 192
7.22 *Comparison of Computational and Experimental Vapour Screen Visualisation, Zero Roll, 8° Incidence (continued)* 193
7.23 *Total Pressure Contours Comparison, 0° Roll, x/D=11.5, 14° Incidence* 196
7.24 *Computation vs Experimental schlieren, 0° Roll, 14° Incidence* 197
7.25 *Computational Solution (xz-Plane), 0° Roll, 14° Incidence* . . 198
7.26 *Comparison of Computational and Experimental Vapour Screen Visualisation, Zero Roll, 14° Incidence* 200
7.27 *Comparison of Computational and Experimental Vapour Screen Visualisation, Zero Roll, 14° Incidence (continued)* 201
7.28 *Total Pressure Contours Comparison, 45° Roll, x/D=11.5, 8° Incidence* 204
7.29 *Computation vs Experimental schlieren, 45° Roll, 8° Incidence* 205
7.30 *Comparison of Computational and Experimental Vapour Screen Visualisation, 45° Roll, 8° Incidence* 207
7.31 *Comparison of Computational and Experimental Vapour Screen Visualisation, 45° Roll, 8° Incidence (continued)* 208
7.32 *Total Pressure Contours Comparison, 45° Roll, x/D=11.5, 14° Incidence* 210
7.33 *Computation vs Experimental schlieren, 45° Roll, 14° Incidence* 211
7.34 *Comparison of Computational and Experimental Vapour Screen Visualisation, 45° Roll, 14° Incidence* 213
7.35 *Comparison of Computational and Experimental Vapour Screen Visualisation, 45° Roll, 14° Incidence (continued)* 214
7.36 *Supersonic Flow Over the RAE W20 Wing Section* 215

7.37 *Schematic of a 2D Shock Wave/Boundary Layer Interaction* . 216
7.38 *Sharp Wing-Cylindrical Body Shock-Boundary Layer Interaction* 218
7.39 *Double Vortex Formation In the Wake of Low Aspect Ratio Wings.* 219
7.40 *Shock-Shock Interaction Classifications* 221
7.41 *Interpretation of Longitudinal Flow Structure: + Configuration*223
7.42 *Interpretation of Longitudinal Flow Structure: × Configuration*225
7.43 *Force Coefficients: Plus Configuration* 228
7.44 *Force Coefficients: Plus Configuration, continued* 229
7.45 *Force Coefficients: × Configuration* 231
7.46 *Force Coefficients: × Configuration, continued* 232
7.47 *Investigation of Serial Multiblock Efficiency* 235
7.48 *B1AW20A3 Calculations: Typical Convergence History* 236

8.1 *Typical Workload, Structured 3D-NS Body-Wing Calculation* 242

A.1 *The German V-2 (A-4) Ballistic Missile* 255
A.2 *The German Wasserfall Anti-Aircraft Missile Prepared for Test Flight* 256

B.1 *Calculation of Local Streamwise Pressure Gradient* 259

C.1 *Calculation of Critical Conditions* 262

List of Tables

4.1 Experimental Test Cases 49
4.2 Experimental Accuracy 86
4.3 Experimental Accuracy 107
4.4 Testcase Summary 116

6.1 Flow Conditions Normal to Delta Wing Leading Edge 164

7.1 B1AW20A3 Experiments: Freestream Flow Conditions 171

8.1 Cost Analysis: B1AW20A3 Investigation 238

Nomenclature

A	Cross sectional area (m^2)
A^+	van Driest constant
C_A	Axial force coefficient
C_D	Drag coefficient
C_L	Lift coefficient
C_M	Pitching moment coefficient based on centre of gravity
C_N	Normal force coefficient
C_{cp}	Constant in Baldwin-Lomax model
C_{kl}	Constant in Baldwin-Lomax model
$\mathbf{E}, \mathbf{F}, \mathbf{G}$	Cartesian flux vextors
E	Specific energy (J/kg)
e	Specific internal energy (J/kg)
F_{wake}	Baldwin-Lomax wake function
F_{kleb}	Klebannoff inermittency function
$\mathbf{H}$	Flux tensor
i, j, k	Computational indices
$\mathbf{i}, \mathbf{j}, \mathbf{k}$	Cartesian unit vectors corresponding to i, k, k
k	von Karman constant
K	Klauser constant
l	Turbulent length scale (m)
M	Mach number
r	Local body radius (m)
$\mathbf{r}$	Position vector
R	Specific gas constant (J/kg.K)
Re	Reynolds number
p	Pressure (N/m^2)
Pr	Prandtl number
q	Dynamic pressure (N/m^2)
q	Heat conduction flux (W/m^2)
$\mathbf{S}$	Area vector
s	Slope Limiting parameter used in MUSCL
T	Temperature (K)
u, v, w	velocity components (m/s)

U	Vector of conserved variables
U	Tangential velocity component (m/s)
V	Cell volume
v^*	Friction velocity (m/s)
x	Axial distance along body from nose apex (m)
y	Local distance normal to wall (m)
y^+	Friction height
α	Angle of attack (deg)
δ^*	Displacement thickness (m)
δ	Boundary layer thickness (m)
ϕ	Circumferential angle from windward symmetry plane (deg)
γ	Ratio of specific heats c_p/c_v
κ	Spatial accuracy parameter
μ	Viscosity (Ns/m^2)
ω	Vorticity
φ	Allens 3D proportionality factor
ρ	Density (kg/m^3)
τ	Shear stress (N/m^2)
θ	Thermal energy flux (W/m^2)
ϑ	SOSE pressure gradient parameter
ξ, η, ζ	Transformed coordinates

Subscripts

0	Stagnation Condition
∞	Freestream Conditions
C	Crossflow Conditions
L, R	Conditions to Left and Right of Interface
w	Wall Conditions

Chapter 1

Introduction

This section presents the motivating factors behind the work and introduces some of the aerodynamic phenomena which affect the design and operation of modern guided and unguided weapons. The focus and content of each chapter of the thesis is then outlined.

Modern guided weapon configurations typically incorporate complicated control surfaces representing significant challenges for aerothermodynamic prediction. Due to very high operating speeds, however, the margin of error in vehicle performance is very small, requiring accurate knowledge of the surrounding viscous flowfield. The flowfields around such geometries are extremely complicated, especially since they are expected to perform at high angles of attack, α, and Reynolds numbers with turbulent boundary layers and separated flows. Figure 1.1 illustrates the flow features encountered during such operations, and highlights some of the issues which the aerodynamicist must consider.

The configuration shown is actually relatively simple since many designs incorporate forward lifting surfaces, instrumentation protuberances or even inlet manifolds for air breathing engines. Of critical importance to the flight dynamic performance is the aerodynamic design of the lifting and control surfaces.

One or even more of the fins will be oriented in the leeward quadrants and, hence, will be immersed in the vortical wake generated by the forebody. The interaction of these vortices with the control surfaces will therefore have a considerable impact on the aerodynamic performance of the missile. In order to accurately predict the vortex/boundary layer and the vortex/shock wave interactions, a numerical model must first be able to accurately simulate the physics of the forming vortices alone. This task, however, is not trivial, especially when the flow field is turbulent, and much effort is still expended in the goal of accurate prediction technologies for slender body configurations in supersonic flow.

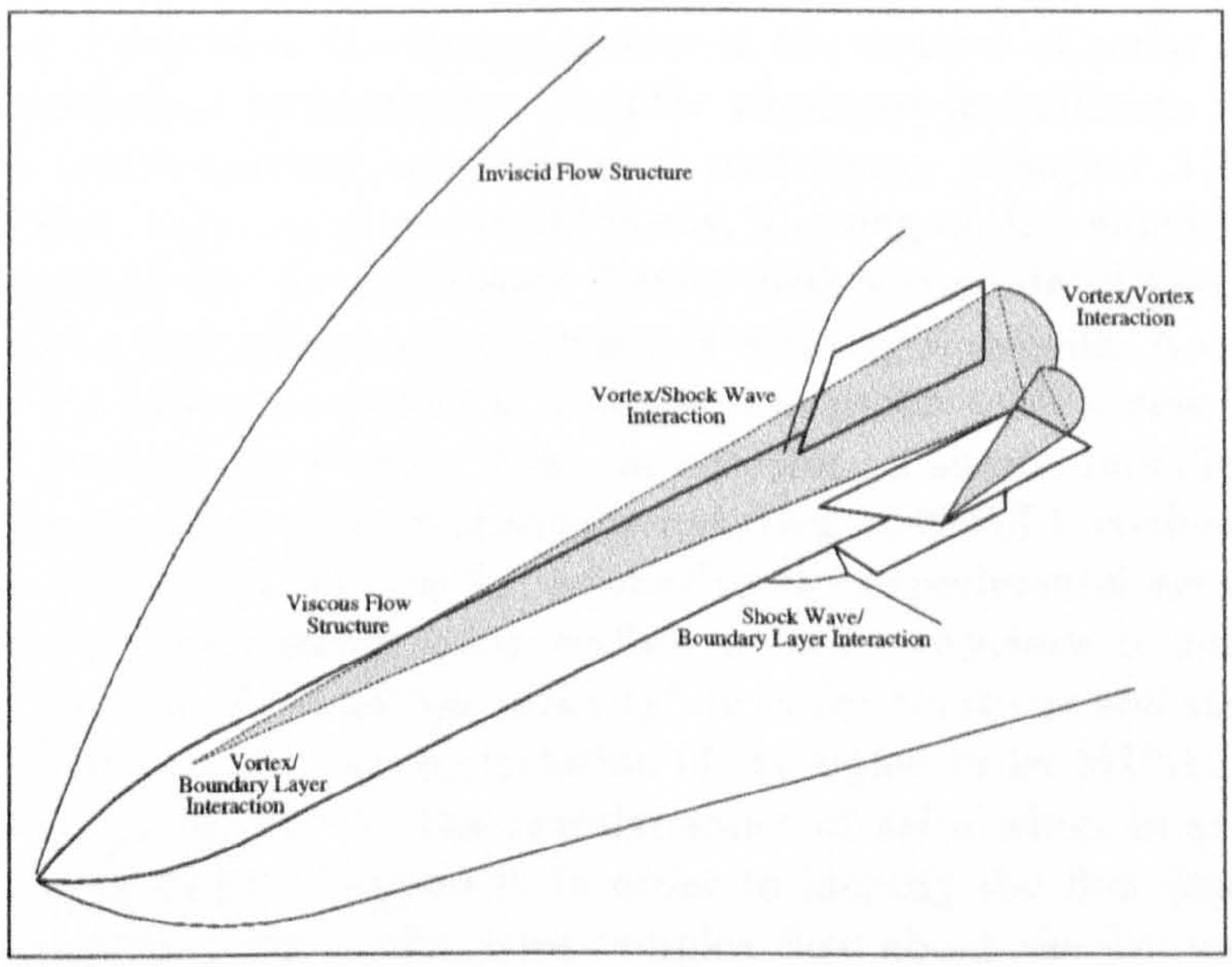

Figure 1.1: *The complicated flow structure around a relatively simple missile configuration.*

The aim of the present work was the investigation and classification of the compressible, viscous flow features typically encountered in the flight envelope of modern aerial weapons, in particular, an AIM-9 sparrow type cruciform wing missile configuration, and the assessment of the prediction methods used in their design.

Considerable progress has been made in understanding and controlling vortical flows by experimental and computational studies of the flow over geometrically simple components such as isolated bodies and wings. Although the geometries are simple, the flow fields may be extremely rich and complex. It was, therefore, decided to analyse the complex aerodynamic interactions occurring in the flowfield of the missile configuration by first studying the aerodynamics of its isolated components.

A three-dimensional, high resolution, multiblock Navier-Stokes solver was developed, validated and employed, together with a pre-existing PNS solver, on the investigation of the vortical flows about isolated slender bodies and delta wings. The solvers were then applied on the prediction of the flow about a winged missile configuration, and together with an experimental investigation, the complex flow physics was resolved and explained.

The historical development of aerial weapons over 5000 years is charted in Appendix A. It is clear that the trend in this development has always been for more accuracy in delivery, regardless of size, speed or killing power. This motivation is as relevant today as when man first developed the bow. Improved design practices and more accurate prediction technologies will allow future weapons engineers to better meet this goal.

Chapter 2 describes the design process in the context of aerial weapons, and the prediction technologies currently employed in industry, including empirical, semi-empirical and numerical techniques. Chapter 3 describes the prediction codes employed in the study, focusing on the numerical techniques employed in the multiblock Navier-Stokes code developed for this investigation. The computational study of nine ogive-cylinder body experimental test cases is presented in Chapter 4 together with a new interpretation of the complex vortical flow. In addition, a simple modification to improve the accuracy of the Baldwin-Lomax/Degani-Schiff turbulence model is put forward, and a method for estimating the experimental error in surface pressure measurement using surface pressure tappings is introduced. The phenomenon of "phantom vorticity" in Euler solutions and its alleviation by application of a new formulation of the higher order MUSCL scheme is described in Chapter 5. The aerodynamics of delta wings in supersonic flow is investigated in Chapter 6, in order to identify the flow features associated with the wing in the more complex flow about the full wing-body configuration. The aerodynamics the generic missile configuration is studied in Chapter 7. Both the experimental study and the corresponding numerical investigation is presented together with an interpretation of the shock-wave/shear-layer/vortex interactions occurring around and downstream of the cruciform wing arrangement. Chapter 8 then discusses the applicability of the various prediction methods employed in the study, to the cost effective design of aerial weapons, and Chapter 9 presents a list of the conclusions derived from the research.

Chapter 2

Aerial Weapon Design

The process of design and its component stages are introduced in this section. The prediction methods currently employed in the design of aerial weapons, are then reviewed, together with an assessment of their applicability and their relative cost effectiveness.

2.1 Engineering Design

The design of high speed aerospace vehicles and weapons to efficiently meet both performance and economic constraints is no trivial task. A modern launch vehicle or air-to-air missile represents state of the art technology, many years work and millions of tax payers pounds to develop. Considerable efforts are being expended in all fields of engineering and manufacturing to develop more efficient design techniques in order to more accurately match performance to specification, to increase quality, and to reduce development costs and thus increase profit margins.

Engineering design is the solution to a technical problem, and the optimisation of that solution, within the given material, technological and economic constraints. The design process must take into account the function of the design, its end user, the manufacturing process and its organisation, and not least the manufacturing cost, the operation cost, and the cost of design and development itself.

The design process of an aeronautical vehicle can be said to go through three different phases, the boundaries of which are not precisely fixed, and vary depending on the nature of that vehicle:

Conceptual Design: Conceptual design usually begins with either a specific set of design requirements from a prospective customer, or a company derived guess as to what future customers may need. The concept definition stage generates some initial solutions which are analysed

before a particular design concept is chosen. It is here that the general configuration, sizing and weights are developed, the engine type and thrust level, and the arrangement of the aerodynamic control surfaces. The entire configuration will be developed through an iterative process of design drawing, analysis, and optimization, until the finished conceptual design is complete.

Preliminary Design: Preliminary design can be said to begin when the concept has been decided, the general configuration design has been developed, and all component technologies decided on. The configuration can be expected to remain as depicted on the conceptual design drawing, although minor revisions may occur. Here, the specialists in such areas as aerodynamics, structures, control systems and flight dynamics, will design and analyse their portion of the vehicle, and testing is initiated in areas such as aerodynamics, propulsion, structures and stability and control. The principal objective of preliminary design is to prepare for the detail design stage where prototypes will be manufactured, and all components must be fabricated. It is therefore important at this stage to include inputs from the manufacturing departments in order to effectively match the component design with efficient manufacture and production.

Detail Design: This starts with the individual components being designed for manufacture along with the machine tools etc. to perform this task. During this stage all full scale systems are exhaustively tested before the full scale configuration is assembled. Finally, the complete system will be tested - for aerospace vehicles this is called flight testing.

The specific prediction methods employed, and where in the design process they take place are critical factors which influence how accurately the design requirements are met, and also the financial costs of design and subsequent manufacture. The following section introduces the prediction technologies specific to high speed aerodynamics.

2.2 Prediction Technologies

There are a number of prediction methods available in the missile aerodynamicist's toolkit. The flow about a configuration can be analysed by manufacturing a scale model and testing it under the appropriate conditions in a wind tunnel. The designer can also estimate aerodynamic characteristics by employing simple mathematical theories coupled with experimental data from similar configurations or conditions that can be extrapolated or interpolated. In addition to these experimental and empirical methodologies, the aerodynamicist can now employ digital computers to simulate the flow over complex geometries. Each of analysis technique has its own advantages and

disadvantages, and incorporates inherent inaccuracies in its representation of actual flight conditions. The following sections briefly outline the three main analysis methods and present the issues which have to be addressed when analysing an aerodynamic design.

2.2.1 Empirical and Semi-Empirical Methods

These methods employ existing experimental databases for similar configurations and conditions and use interpolation or extrapolation together with simple theoretical models such as slender body theory and second order shock-expansion theory. Semi-empirical methods are the most widely employed tools in aeronautical design. They require very small computational resources and time to calculate the aerodynamic characteristics of different configurations for systematic design studies.

Most semi-empirical codes, such as Missile DATCOM [10] and the Engineering Sciences Data Unit (ESDU) code, are based on component build-up methods. The aerodynamic characteristics of the individual components of a configuration, such as forebodies, wings and tails, are estimated using simple theory or data sheets. The individual component characteristics are then combined by a suitable treatment of the way each component affects each of the others, introducing mutual interference factors.

The theories employed in empirically based methods rely on numerous simplifying assumptions, and the experimental data bases will be valid only for a limited set of configurations and conditions. Inaccuracies in empirical predictions will, therefore, occur for configurations or for operating conditions which are very much different from those in the existing data bases. Semi-empirical methods become invalid when the aerodynamic coefficients are small compared with the interference effects. In addition, these techniques furnish only a limited number of aerodynamic characteristics such as forces and pressure coefficients on the surface, and are unable to provide predictions over the whole flow field.

2.2.2 Semi-Empirical Methods for Supersonic Missile Design

The following semi-empirical methods are those most commonly employed in the design analysis of supersonic missiles and are incorporated into Missile DATCOM and ESDU design codes.

Slender Body Theory

Developed by Munk (1932) from small perturbation theory and later refined by Ward (1949), slender body theory for slender bodies of revolution at supersonic speeds assumes that the angle of attack α is small and that the gradient of the velocity potential in the streamwise direction is negligible. The inviscid component of the normal force per unit length is given by:

$$f_I = q_\infty sin2\alpha cos\left(\frac{\alpha}{2}\right)\frac{dA}{dx} \tag{2.1}$$

where dA/dx is the gradient of the cross-section area at the given axial station along the body.

Further development by Allen (1949) introduced the non-linear effect of viscous crossflow to the theory. Allen assumed that the total force on the slender body is equal to the inviscid force f_I per unit length plus a viscous crossflow force per unit length given by:

$$f_V = 2q_\infty r\varphi C_{D_n} sin^2\alpha \tag{2.2}$$

where r is the local body radius at the desired axial station, C_{D_n} is the 2D crossflow drag coefficient found from simple theory (such as Newtonian Impact Theory) or an empirical database at the specific crossflow values of Reynolds number and Mach number, and φ is a 3D proportionality factor which accounts for the longitudinal development of the leeside vortices in 3D.

Second Order Shock-Expansion Method

Eggers derived first order shock expansion theory for bodies of revolution at supersonic speeds in 1951 by an approximation to the method of characteristics. The body shape is modelled as a series of conical elements and the pressure on each element is estimated as $p = p_c - p_e$ where p_c is the pressure on a cone of half angle equivalent to the slope of the local element, obtained from oblique shock relations, and p_e is the pressure due to expansion over the next element obtained from a Prandtl-Meyer expansion solution. This method assumes that the expansion waves created by the change of curvature of body surface are totally absorbed by the shock with no reflections back to the surface, such that the pressure along a conical element is constant.

Syverson et al (1953),(1957) extended the theory to second order by defining the pressure on each element in the form:

$$p = p_c - (p_c - p_e)\, e^{-\vartheta} \tag{2.3}$$

where ϑ is a parameter based on the local pressure gradient.

Second Order Shock Expansion Theory is an inviscid theory and viscous crossflow effects can be introduced by use of Allen's crossflow method previously discussed.

Methods for Thin Wings at Supersonic Speed

Various methods can be employed in the estimation of the force characteristics of isolated wings at supersonic speeds, depending on factors such as sweepback (ie: whether the leading edge is supersonic or subsonic), thickness, planform shape, etc. Pitts, Nielsen and Kattari (1957) applied the concepts of slender body theory to the estimation of overall forces and moment characteristics but their methods cannot yield detailed pressure and load distributions.

Modern codes such as Missile DATCOM employ Three Dimensional Thin Wing Theory which is the supersonic version of Lifting Surface Theory which solves the three dimensional perturbation equation. This method calculates inviscid lift and pitching moment and pressure distributions. Wave drag can be estimated using Shock Expansion Theory while non-linear vortical characteristics can be estimated empirically or by Allens crossflow technique with the appropriate crossflow drag coefficient.

Component Build-Up Methods for Complete Configurations

Once the aerodynamic characteristics of the individual components are evaluated, the aerodynamic characteristics of the entire missile configuration can be estimated by taking into account the aerodynamic interference produced when the components are brought together and combining the interfered characteristics in an appropriate manner. The most universal method for calculation of the interference between various missile components into aeroprediction codes is that developed by Pitts, Nielsen and Kattari. This method identifies three forms of interference; i) the interference due to the presence of the wing on the body, ii) the effect of the body on the wing and iii) the effect of upstream vortices on wings or fins. Methods have also been developed to model the effects of wing-wing and shockwave interference.

Modern Aeroprediction codes such as Missile DATCOM, ESDU and the US Navy Aeroprediction 93 code [39], extensively employ the theoretical methods briefly outlined here but use many empirical databases which are hard coded into the software and which differentiate one from the other. Experience has shown that these semi-empirical codes applied within the applicability of their constituent methods, can predict the force and moment characteristics, at low to moderate angle of attack, with an accuracy to within about 10-20 percent.

2.2.3 Computational Fluid Dynamics

Numerical solution of a discretised set of governing equations will provide a complete flowfield definition with fewer limitations and restrictive assumptions than empirical techniques. Computational Fluid Dynamic methods

are therefore essential to compute the aerodynamics of unconventional configurations such as air-breathing missiles, to determine load distributions for structural calculations, local flow properties and to provide the designer with the fundamental information on the physical effects taking place in complex flow fields.

There are many problems with CFD, however. The discretisation of the governing equations introduces inaccuracy due to numerical error. The accurate resolution of compressible flows requires the use of complex numerical techniques which need high levels of computational power. The accurate modelling of transition and subsequent turbulent flow is a problem which still eludes the scientific community.

2.2.4 Experiments

Wind Tunnel Testing

With wind tunnel experiments the designer can test a scale model of a real complex configuration such as a combat aircraft loaded with its full complement of fuel tanks and weaponry in as much detail as costs will allow. The wind tunnel permits the observation of, and acquisition of aerodynamic data from, physical flow phenomena. Wind tunnel experiments, however, are relatively expensive because of the costs of design, manufacture and construction of the model and because of the high wind-tunnel costs of energy, personnel, maintenance and measurement instrumentation. Furthermore, the wind tunnel flow field is an artificial environment which may not strictly represent flight conditions. Problems can arise with the effects of scaling, where the flow properties must be scaled in relation to the dimensions of the experimental and full size configurations. Other sources of inaccuracies include the effects of tunnel wall boundary layers, blockage, and non-uniformity of the test section flow conditions.

Flight Testing

More costly still are the experiments performed on full size prototypes in actual flight - flight testing. Here there are no problems with scale effects or with tunnel blockage, and the affects of actual atmospheric conditions such as turbulence intensity are included in the aerodynamic data. The costs of such experiments, however, usually relegate flight testing to the very end of the design process.

Both forms of experimental analysis, however, suffer from the limitations of the measurement instrumentation. All instruments exhibit varying levels of inaccuracy to measure actual conditions. In addition flow conditions can, in general, only be measured at discrete points on the surface of the configuration, or within the flow field in its vicinity. This means that important

flow features can be poorly resolved, or even missed completely. Section 4.2 presents an analysis of the experimental error in static pressure measurement arising from the disturbance of the flowfield due to pressure tappings, and is relevant to the error analysis in subsequent sections.

2.3 Computational Aerodynamics

The most comprehensive mathematical description of continuum fluid flow are the Navier-Stokes equations, developed independently by C. Navier and G. Stokes between 1820 and 1845. Different forms of these governing equations can be derived based on the level that they approximate the physical fluid flow. The engineer can decide how much to reduce the Navier-Stokes equations and still predict the aerodynamic characteristics to acceptable levels of accuracy. The following chart presents the various approximations that can be applied to the Navier-Stokes equations, starting from the most comprehensive solutions by direct numerical simulation, down to the linearized form of the potential equation.

The following section discusses the applicability of the different models used for missile aerodynamic prediction.

2.3.1 Models for Continuum Flow

Linearized Potential Methods

The most common techniques to solve the linearized potential equation are the surface singularity techniques. For the analysis of subcritical flows, these "panel methods" are very effective tools for engineering purposes. The extension of panel methods to supersonic flows, however, require special treatment of Mach wave reflections in the interior of bodies and also of discontinuities of singularity distributions across panels [22]. Panel methods are not capable of handling detached shock waves adequately, but when they are applicable they can estimate aerodynamic characteristics with good accuracy and with reasonable computational cost. They are, however, linearized methods which means that they are limited to slender bodies at very small angles of attack. This is a very severe restriction for missile aerodynamic applications, and so extensions have been developed to include the non-linear effects due to vortices.

Full Potential Methods

The full potential equation in integral form can be solved iteratively and vortex models may be introduced in a similar fashion as employed in panel methods. Full potential methods are normally field-based finite difference

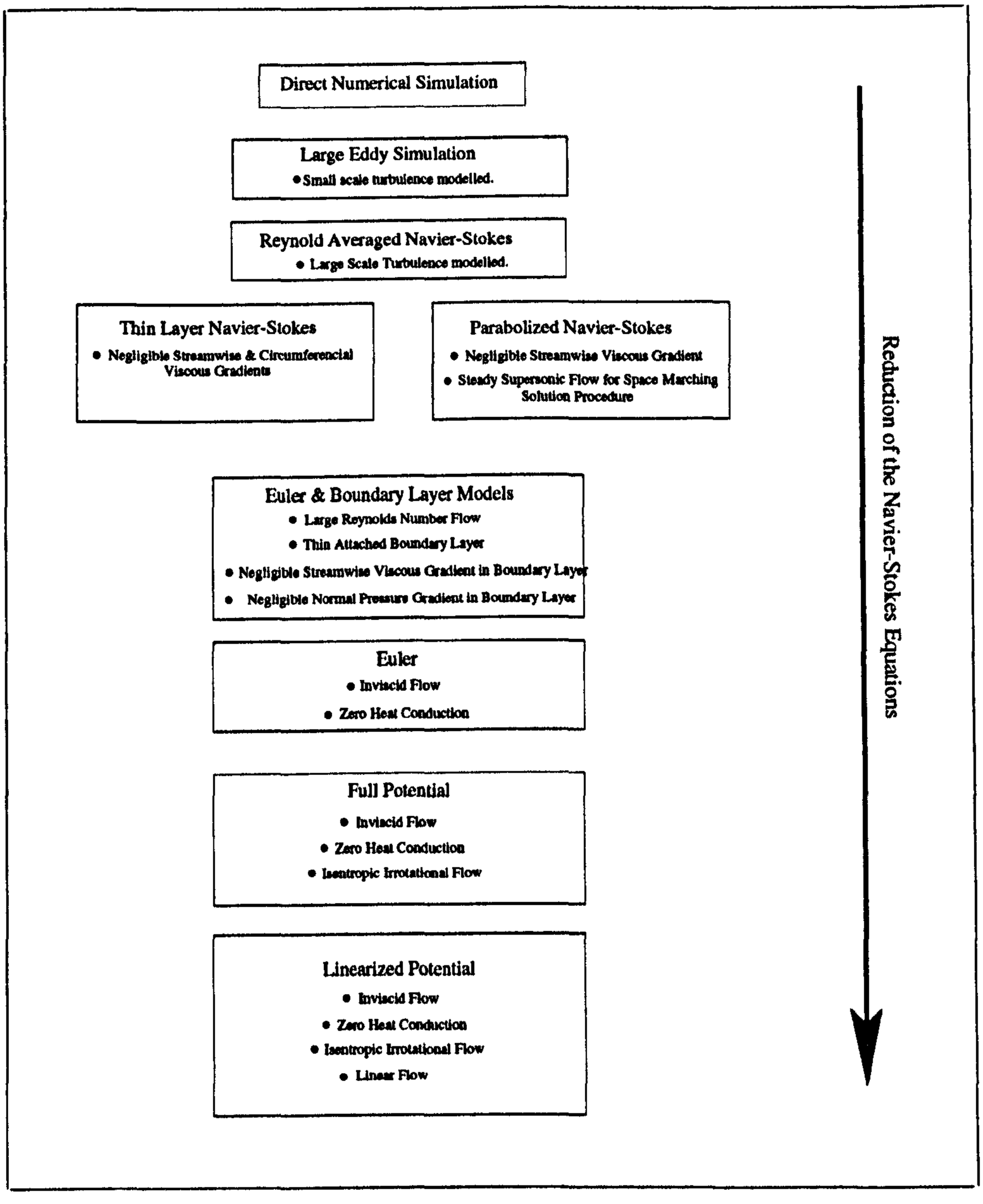

Figure 2.1: *Approximation Levels of the Governing Equations for Continuum Flow Prediction*

schemes, need finer grids than linearized schemes which are surface-based and are more numerically sensitive.

Euler Equations

The Euler equations represent the full set of conservation equations for continuous, inviscid media. They allow "weak" solutions and can therefore predict physical discontinuities such as shock waves. Unlike potential meth-

ods, the Euler equations allow rotational flow and thus convect vorticity without the necessity of introducing point vortices to the flow field. Vorticity generation due to physical viscosity, however, is not described by the Euler equations except by a curved shock or by numerical dissipation caused by a coarse grid. In addition, the Euler equations cannot model the physical diffusion of vorticity which can only take place by numerical dissipation.

The Euler equations can be solved in three dimensions by two techniques. Time marching schemes advance all the flow variables in the field in time until a steady solution is obtained. These methods can be used for any speed range, but the computational cost is far greater than for surface element techniques and the 3D grid generation required represents considerable effort.

If the flow is purely supersonic such that the Euler equations are hyperbolic in space in the streamwise direction, a space marching approach may be used. This technique involves streamwise plane by plane iteration using only upstream information for each step. At any one station, only two streamwise planes need to be stored and so space marching codes require much less computational memory and time to obtain a solution.

Boundary Layer Methods

Viscous effects can be introduced within an Euler code without the addition of viscous terms to form the Navier-Stokes equations. This is achieved by solving the boundary layer equations which assume that the the boundary layer is attached and very thin. The boundary layer equations are parabolic and can therefore be solved using a space marching technique. For slender missile body flows where considerable portions of the flow field contain viscous features, boundary layer methods are invalid.

Navier-Stokes Equations

Until very recently, the Navier-Stokes code is a tool which has rarely been used in missile design due to the great effort required. The Navier-Stokes equations represent the full set of conservation equations for a viscous continuum media and will predict all physical flow features. Given a sufficient grid resolution in the boundary layer, Navier-Stokes codes are capable of predicting skin friction and heat transfer at body surfaces.

For turbulent flows the equations can be solved by Direct Numerical Simulation, but because this technique would require huge computational resources which are beyond the capabilities of modern computing, simplifying assumptions must be made. The most widely employed simplification is that attributed to Reynolds which involves the time averaging of rapidly fluctuating flow variables. The "Reynolds-Averaged" Navier-Stokes (RANS) equations then require a turbulence model for the prescription of

turbulent length and time scales to complete the set of governing equations. Turbulence modelling still presents one of the main problems for practical aerodynamic simulation and, is such, a research field in itself.

A further approximation neglects the viscous terms in the non-surface-normal directions and leads to the "Thin Layer" Navier-Stokes equations. The "Parabolized" Navier-Stokes (PNS) equations are obtained by neglecting the streamwise viscous term and assuming the flow is steady and supersonic outside the boundary layer. The PNS equations, by their mathematical nature, are restricted to the solution of steady supersonic flows with no localized, reverse flow in the streamwise direction. Steady supersonic flows over slender bodies at low to moderate angle of attack, which are important cases in the design of high speed weapons, are ideally suited for prediction by PNS solvers. In addition, the PNS equations can be solved using the space marching approach and therefore require much less time and computational effort to obtain solutions than the full Navier-Stokes equations. For these reasons PNS codes are now widely employed within the missile design community.

The work described in this thesis focuses on the application and accuracy of RANS, PNS and Euler methods to describe the flows commonly experienced by high speed missiles operating up to moderate angle of attack.

2.4 Complex Geometries: Multiblock Techniques

The accurate prediction of the flow around complex three dimensional configurations relies on both the capability of the solver to resolve the desired flow features, and the quality of the computational mesh on which it solves the governing equations.

The task of generating a three dimensional mesh on which to perform a computational simulation is not a straightforward process, and represents the major contribution to the total process to gain an engineering solution. The quality of a computational solution around a complex geometry such as a finned missile, or a complete aircraft configuration depends very highly on the resolution and smoothness of the computational grid. The grid must be sufficiently dense that the numerical approximation converges to a physically accurate solution resolving features such as boundary layers and shock waves. On the other hand, the grid must not be so dense that the memory or the CPU time required renders the solution impractical.

Analysis and experience have shown that orthogonality, smoothness and a suitable point distribution in regions of expected high gradients in the flow variables are beneficial. The accuracy of solution algorithms are often highly degraded on grids that are too skewed. The accuracy of a numerical approximation may also be degraded if there is discontinuous cell stretching. A body conforming grid is also desirable since it lends itself better for

the application of boundary conditions, and allows for the use of various approximate equations such as the boundary layer equations.

The way in which a point in a grid is related to other points has been used to define the different types of grid which have been employed. These usually fall into two categories [83]; i) structured grids usually use quadrilateral cells in 2D and hexahedral cells in 3D and can be body conforming or non-conforming (cartesian), and ii) unstructured grids which are distinguished by their lack of geometric regularity and usually employ triangular cells in 2D and tetrahedral cells in 3D. Recently hybrid techniques such as the CHIMERA and semi-structured methods, have been developed which employ both types of grids in different regions of the domain in order to make use of the flexibility of the unstructured approach while maintaining the structure in regions of the flow where it is beneficial. For the purpose of the current investigation it was decided to employ the structured multiblock grid philosophy.

Two major problems must be addressed when designing a multiblock solver. Firstly it must be ensured that the solution algorithm is conservative across block interfaces. Secondly, a consistent method for the management of block topology and interconnectivity must be developed. Conservation of mass is achieved by the condition that neighbouring blocks meet exactly at the interface and is aided by the further requirement that the grid must be completely continuous across block interfaces. Complete continuity at the interfaces, that is, continuity of slope and curvature of grid lines, is not trivial and implies that the grid lines are as differentiably smooth as lines interior to the blocks. This requirement leads to the use of ghost cells.

Consider the 2D block shown in Figure 2.2. Any block of size $i = 1, ...imax, j = 1, ...jmax$ is increased to a size $i = 1, ...imax + 4, j = 1...jmax + 4$. This *ghosted* block is thus enclosed within a set of points representing the boundary points of adjacent blocks. During the iterative solution procedure, the ghost points are updated with values from adjacent blocks, after each iteration. The obvious disadvantage with this technique is the resulting increase in memory requirement when several blocks are stored at once.

For three dimensional blocks two layers of ghost cells are usually added to maintain second order accuracy in space. Such ghost points then maintain the required boundary conditions. Another difficulty, frequently encountered with multi-blocked grids is that of the singular point. This is the point where a number of blocks intersect, and several families of curves coincide. The usual finite difference formulations for partial derivatives cannot be defined at singular points, and so a different formulation must be derived for these cases.

Each block has its own curvilinear coordinate system which is independent of those in adjacent blocks. The local coordinates within each block

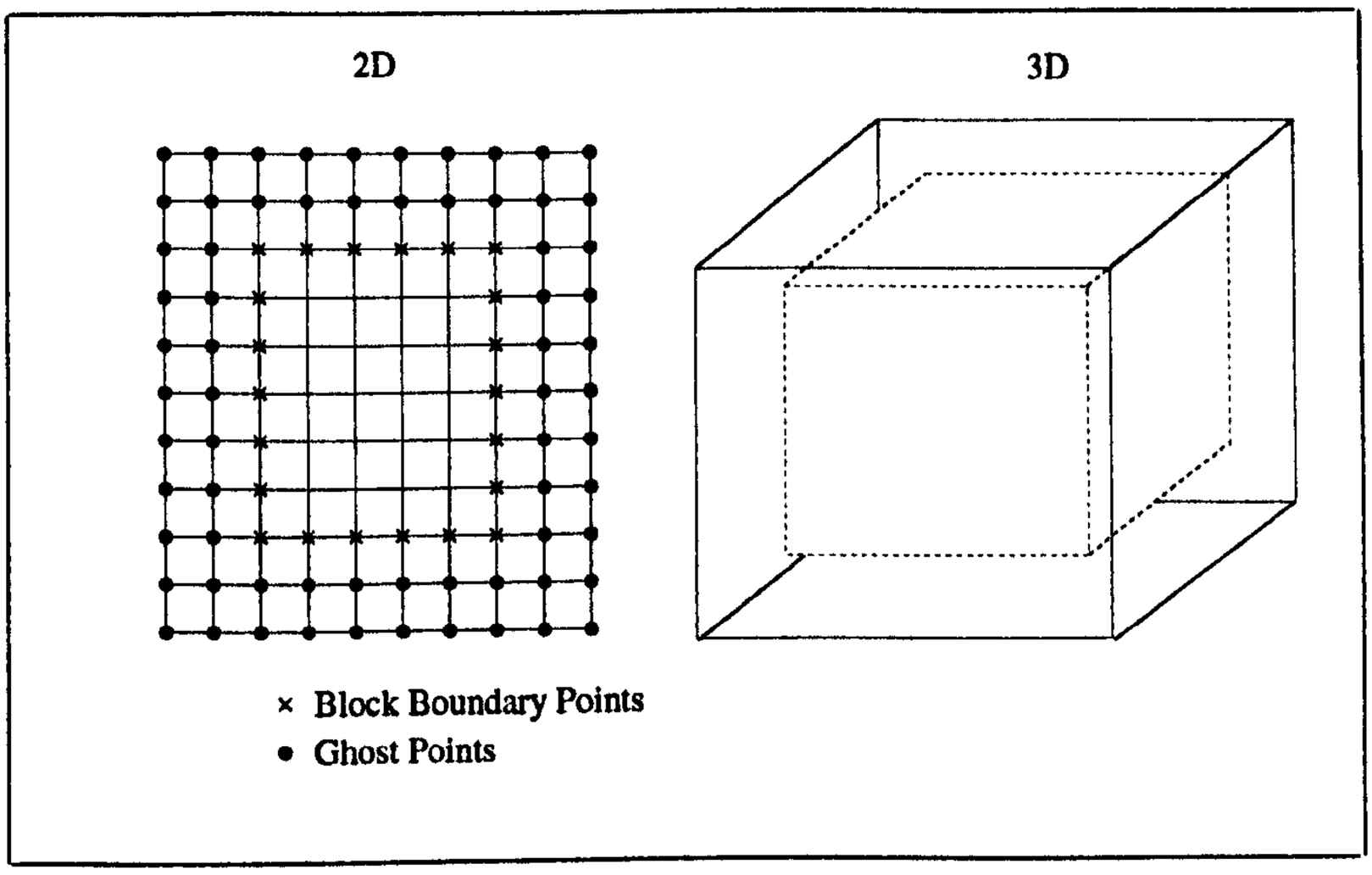

Figure 2.2: *2D and 3D blocks bounded by ghost points*

may not be aligned in the same sense, and a situation could arise where the η = constant lines in one block correspond to lines of constant ξ in another. Thompson and Weatherill [73] showed that for a three dimensional block having a local right handed set of axes (I,J,K) there are 24 possible orientations leading to 24 possible ways in which one block may be oriented with respect to another, as illustrated in Figure 2.3.

In a multiblock environment it is therefore necessary to define a way of describing the relative position of one block with respect to the others. This is done by defining a block connectivity matrix. It is not necessary to define a list of point coordinates and connectivities, as required with unstructured meshes. It is essential, only to define how each block and its coordinate system correspond to its neighbours and to implement a suitable technique to pass information between them. A number of papers have been published on this subject [73] [58].

The multiblock concept is not restricted to any particular mesh generation technique. In addition, from a mathematical and numerical point of view, there is no difference between a single block and a multiblock solver. The difference lies in the incorporation of an interface boundary condition. In fact a different equation system may be solved within each block in order to cut down on computational cost. For instance, within blocks containing wall boundaries, the Navier-Stokes equations may be solved, whereas inside blocks away from walls, the Euler equations may be solved with the appropriate shock capturing scheme.

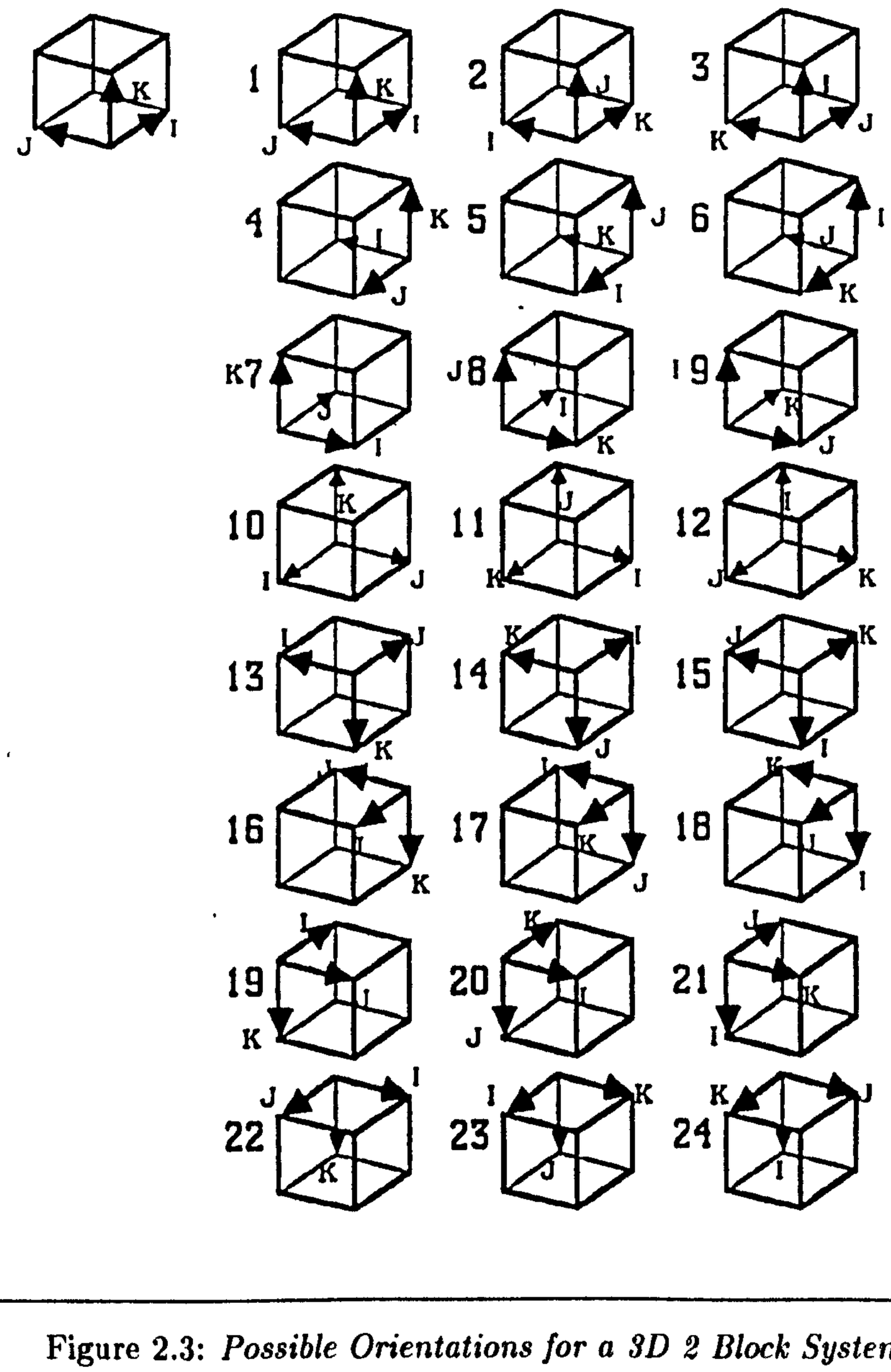

Figure 2.3: *Possible Orientations for a 3D 2 Block System*

Chapter 3

The Computational Predictive Tools

The mathematical and numerical basis of the CRANS3D solver, used in the aerodynamic analysis, is described in this section together with descriptions of the other predictive tools employed.

For the computational investigation of the aerodynamics of aerial weapon components and configurations presented in this thesis, a multiblock three-dimensional time marching Navier-Stokes solver (CRANS3D) was developed using the Fortran 77 programming language. The software was designed as an engineering and scientific tool for the solution of the governing equations of fluid flow and can solve both the steady Navier-Stokes and Euler equations by the finite volume technique within a structured domain.

In addition, the Parabolized Navier-Stokes solver developed by Qin, Ludlow and Shaw [61] [53] was employed on the same cases in order to assess the accuracy and efficiency of both approaches with reference to the design of aerial weapons. The USAF Missile DATCOM code was also employed to predict the force and moment characteristics of a number of configurations.

3.1 CRANS3D: Governing Equations And Their Discretisation

The Reynolds Averaged Navier-Stokes equations can be integrated within the finite volume framework. The conservative laws of mass, momentum and energy can then be written in the integral form. Thus, within a control volume V bounded by surface S:

$$\frac{\partial}{\partial t}\int_V \boldsymbol{U}\,dV + \int_S (\boldsymbol{H}\cdot\boldsymbol{n})\,dS = 0 \tag{3.1}$$

where **n** is the outward unit vector normal to the surface and **U** the vector of conservative variables.

$$\mathbf{U} = \begin{pmatrix} \rho \\ \rho u \\ \rho v \\ \rho w \\ \rho E \end{pmatrix}$$

The flux tensor H is expressed as:

$$\begin{aligned} \mathbf{H} = &\left(\mathbf{E}^I - \mathbf{E}^V\right)\mathbf{i} + \left(\mathbf{F}^I - \mathbf{F}^V\right)\mathbf{j} \\ &+ \left(\mathbf{G}^I - \mathbf{G}^V\right)\mathbf{k} \end{aligned} \tag{3.2}$$

Here, **i** , **j** and **k** are the Cartesian unit vectors, and the corresponding Cartesian flux vectors are given below, where superscripts I and V correspond to the convective and diffusive contributions respectively.

$$\mathbf{E}^I = \begin{pmatrix} \rho u \\ \rho u^2 + p \\ \rho uv \\ \rho uw \\ \rho u\left(E + p/\rho\right) \end{pmatrix}$$

$$\mathbf{F}^I = \begin{pmatrix} \rho v \\ \rho uv \\ \rho v^2 + p \\ \rho vw \\ \rho v\left(E + p/\rho\right) \end{pmatrix}$$

$$\mathbf{G}^I = \begin{pmatrix} \rho w \\ \rho uw \\ \rho vw \\ \rho w^2 + p \\ \rho w\left(E + p/\rho\right) \end{pmatrix}$$

and;

$$\mathbf{E}^V = \begin{pmatrix} 0 \\ \tau_{xx} \\ \tau_{xy} \\ \tau_{xz} \\ \theta_x \end{pmatrix}, \mathbf{F}^V = \begin{pmatrix} 0 \\ \tau_{yx} \\ \tau_{yy} \\ \tau_{yz} \\ \theta_y \end{pmatrix}$$

$$\mathbf{G}^V = \begin{pmatrix} 0 \\ \tau_{zx} \\ \tau_{zy} \\ \tau_{zz} \\ \theta_z \end{pmatrix}$$

The components of the viscous shear stress tensor τ, the thermal energy flux θ and heat conduction flux q are given by:

$$\begin{aligned} \theta_x &= u\tau_{xx} + v\tau_{xy} + w\tau_{xz} - q_x \\ \theta_y &= u\tau_{xy} + v\tau_{yy} + w\tau_{yz} - q_y \\ \theta_z &= u\tau_{xz} + v\tau_{zy} + w\tau_{zz} - q_z \end{aligned} \tag{3.3}$$

$$\begin{aligned} \tau_{xx} &= \frac{2\mu}{3Re}\left(2\frac{\partial u}{\partial x} - \frac{\partial v}{\partial y} - \frac{\partial w}{\partial z}\right) \\ \tau_{yy} &= \frac{2\mu}{3Re}\left(2\frac{\partial v}{\partial y} - \frac{\partial u}{\partial x} - \frac{\partial w}{\partial z}\right) \\ \tau_{zz} &= \frac{2\mu}{3Re}\left(2\frac{\partial w}{\partial z} - \frac{\partial u}{\partial x} - \frac{\partial v}{\partial y}\right) \\ \tau_{xy} = \tau_{yx} &= \frac{\mu}{Re}\left(\frac{\partial u}{\partial y} + \frac{\partial v}{\partial x}\right) \\ \tau_{yz} = \tau_{zy} &= \frac{\mu}{Re}\left(\frac{\partial v}{\partial z} + \frac{\partial w}{\partial y}\right) \\ \tau_{zx} = \tau_{xz} &= \frac{\mu}{Re}\left(\frac{\partial u}{\partial z} + \frac{\partial w}{\partial x}\right) \\ q_x &= -\frac{\mu}{(\gamma-1)M_\infty^2 RePr}\left(\frac{\partial T}{\partial x}\right) \\ q_y &= -\frac{\mu}{(\gamma-1)M_\infty^2 RePr}\left(\frac{\partial T}{\partial y}\right) \\ q_z &= -\frac{\mu}{(\gamma-1)M_\infty^2 RePr}\left(\frac{\partial T}{\partial z}\right) \end{aligned} \tag{3.4}$$

In the above equations ρ, u, v, w, p and E denote density, the three Cartesian velocity components, the pressure and the specific energy respectively. The code, however, is written in non-dimensional form, which accounts for the appearance of Mach number M, the Reynolds number Re and the Prandtl number Pr. The dimensionless flow variables are defined as:

$$\begin{aligned} x &= x^*/L \\ u &= u^*/U_\infty \\ v &= v^*/U_\infty \\ w &= w^*/U_\infty \\ p &= p^*/\rho_\infty U_\infty^2 \\ \rho &= \rho^*/\rho_\infty \\ \mu &= \mu^*/\mu_\infty \\ T &= T^*/T_\infty \\ E_t &= E_t^*/\rho_\infty U_\infty^2 \end{aligned} \tag{3.5}$$

where the non-dimensional variables are related to the local physical variables (denoted with an asterix *) and their physical freestream values.

The total specific energy E_t (ie: per unit mass) is related to the specific internal energy e by:

$$E_t = \rho\left(e + \frac{\left(u^2 + v^2 + w^2\right)}{2}\right) \tag{3.6}$$

In non-dimensional form, the perfect gas equation of state can be given as:

$$p = (\gamma - 1)\,\rho e \tag{3.7}$$

or for non-dimensional temperature as:

$$T = \gamma M_\infty^2 \frac{p}{\rho} \tag{3.8}$$

To complete the set of equations, the molecular viscosity coefficient μ is simply give by Sutherlands law as:

$$\mu = T^{1.5}\frac{\left(1 + \frac{110.4}{T_\infty}\right)}{\left(T + \frac{110.4}{T_\infty}\right)} \tag{3.9}$$

The inviscid form of the governing equations, the Euler equations, are obtained simply by neglecting the viscous fluxes, $\mathbf{E}^V, \mathbf{F}^V, \mathbf{G}^V$.

A convenient way of solving Equation (3.1) is to treat each hexahedral cell as a control volume (i,j,k) as illustrated in Figure 3.1 with the cell averaged flow properties stored at the cell centres. The conservative fluxes passing through each cell interface are computed using the flow properties on either side. Equation (3.1) then becomes:

$$\begin{aligned}
&\frac{\partial}{\partial t}\left(V_{i,j,k}U_{i,j,k}\right) + \boldsymbol{H}_{i+\frac{1}{2},j,k}\cdot d\boldsymbol{S}_{i+\frac{1}{2},j,k} \\
&- \boldsymbol{H}_{i-\frac{1}{2},j,k}\cdot d\boldsymbol{S}_{i-\frac{1}{2},j,k} + \boldsymbol{H}_{i,j+\frac{1}{2},k}\cdot d\boldsymbol{S}_{i,j+\frac{1}{2},k} \\
&- \boldsymbol{H}_{i,j-\frac{1}{2},k}\cdot d\boldsymbol{S}_{i,j-\frac{1}{2},k} + \boldsymbol{H}_{i,j,k+\frac{1}{2}}\cdot d\boldsymbol{S}_{i,j,k+\frac{1}{2}} \\
&- \boldsymbol{H}_{i,j,k-\frac{1}{2}}\cdot d\boldsymbol{S}_{i,j,k-\frac{1}{2}} = 0
\end{aligned} \tag{3.10}$$

The three forward surface vectors are evaluated as:

$$
\begin{aligned}
d\boldsymbol{S}_{i+\frac{1}{2},j,k} &= \frac{1}{2}\left(\boldsymbol{r}_{i+\frac{1}{2},j+\frac{1}{2},k+\frac{1}{2}} - \boldsymbol{r}_{i+\frac{1}{2},j-\frac{1}{2},k-\frac{1}{2}}\right) \times \\
&\left(\boldsymbol{r}_{i+\frac{1}{2},j+\frac{1}{2},k-\frac{1}{2}} - \boldsymbol{r}_{i+\frac{1}{2},j-\frac{1}{2},k+\frac{1}{2}}\right) \\
d\boldsymbol{S}_{i,j+\frac{1}{2},k} &= \frac{1}{2}\left(\boldsymbol{r}_{i+\frac{1}{2},j+\frac{1}{2},k+\frac{1}{2}} - \boldsymbol{r}_{i-\frac{1}{2},j+\frac{1}{2},k-\frac{1}{2}}\right) \times \\
&\left(\boldsymbol{r}_{i-\frac{1}{2},j+\frac{1}{2},k+\frac{1}{2}} - \boldsymbol{r}_{i+\frac{1}{2},j+\frac{1}{2},k-\frac{1}{2}}\right) \\
d\boldsymbol{S}_{i,j,k+\frac{1}{2}} &= \frac{1}{2}\left(\boldsymbol{r}_{i+\frac{1}{2},j+\frac{1}{2},k+\frac{1}{2}} - \boldsymbol{r}_{i-\frac{1}{2},j-\frac{1}{2},k+\frac{1}{2}}\right) \times \\
&\left(\boldsymbol{r}_{i-\frac{1}{2},j+\frac{1}{2},k+\frac{1}{2}} - \boldsymbol{r}_{i+\frac{1}{2},j-\frac{1}{2},k+\frac{1}{2}}\right)
\end{aligned}
\tag{3.11}
$$

where the vector **r** denotes the position vector of the grid points.

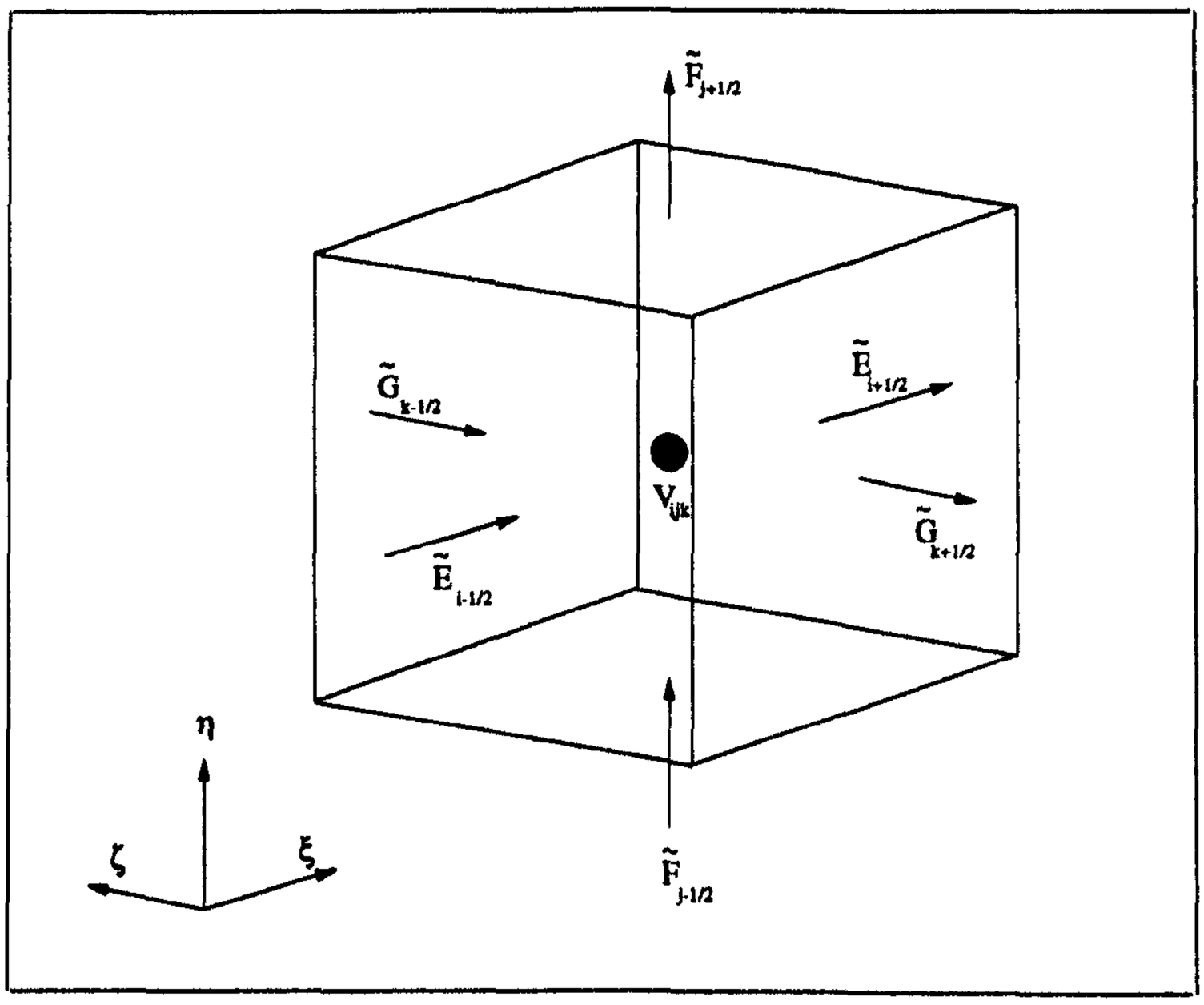

Figure 3.1: *Flux Balance for Cell Centred Finite Volume Technique*

The remaining backward surface vectors are evaluated in a similar fashion. The cell volume is then evaluated using the expression:

$$
\begin{aligned}
V_{i,j,k} &= \frac{1}{3}\left(d\boldsymbol{S}_{i+\frac{1}{2},j,k} + d\boldsymbol{S}_{i,j+\frac{1}{2},k} + d\boldsymbol{S}_{i,j,k+\frac{1}{2}}\right) \cdot \\
&\left(\boldsymbol{r}_{i+\frac{1}{2},j+\frac{1}{2},k+\frac{1}{2}} - \boldsymbol{r}_{i-\frac{1}{2},j-\frac{1}{2},k-\frac{1}{2}}\right)
\end{aligned}
\tag{3.12}
$$

Equation (3.10) can be rewritten in a curvilinear coordinate system thus:

$$\frac{\partial}{\partial t}\left(V_{i,j,k}\boldsymbol{U}_{i,j,k}\right)+\tilde{\boldsymbol{E}}_{i+\frac{1}{2},j,k}-\tilde{\boldsymbol{E}}_{i-\frac{1}{2},j,k}+\tilde{\boldsymbol{F}}_{i,j+\frac{1}{2},k}-\tilde{\boldsymbol{F}}_{i,j-\frac{1}{2},k}+\tilde{\boldsymbol{G}}_{i,j,k+\frac{1}{2}}-\tilde{\boldsymbol{G}}_{i,j,k-\frac{1}{2}}=0 \tag{3.13}$$

where $\sim$ denotes that the flux has been evaluated by the addition of the convective contribution, computed using Oshers Approximate Riemann Solver, and the numerical diffusive terms.

3.1.1 Oshers Approximate Riemann Solver and MUSCL Variable Extrapolation

The convective fluxes are evaluated using Oshers approximate Riemann Solver [44] which has been extensively tested for high speed viscous applications by Qin et al [8], [61], [54]. Qin demonstrated that the scheme is extremely effective in capturing shock waves and shear flows without the necessity of the entropy fix used with the Roe scheme [59] in order to prevent non-physical expansion shocks. Osher's scheme is given as:

$$\tilde{\boldsymbol{E}}_{i+\frac{1}{2},j,k}=\frac{1}{2}\left[\bar{\boldsymbol{E}}\left(\boldsymbol{U}^{L},d\boldsymbol{S}_{i+\frac{1}{2},j,k}\right)+\bar{\boldsymbol{E}}\left(\boldsymbol{U}^{R},d\boldsymbol{S}_{i+\frac{1}{2},j,k}\right)\right]-\frac{1}{2}\int_{U^{L}}^{U^{R}}\left|\frac{\partial\bar{\boldsymbol{E}}}{\partial\boldsymbol{U}}\right|d\boldsymbol{U} \tag{3.14}$$

where:

$$\bar{\boldsymbol{E}}\left(\boldsymbol{U}^{L},d\boldsymbol{S}_{i+\frac{1}{2},j,k}\right)=\left(\boldsymbol{i}\cdot d\boldsymbol{S}_{i+\frac{1}{2},j,k}\right)\boldsymbol{E}+\left(\boldsymbol{j}\cdot d\boldsymbol{S}_{i+\frac{1}{2},j,k}\right)\boldsymbol{F}+\left(\boldsymbol{k}\cdot d\boldsymbol{S}_{i+\frac{1}{2},j,k}\right)\boldsymbol{G} \tag{3.15}$$

The integration of Equation (3.14), given the variables U^L on the left of the interface and U^R on the right, is carried out along a path piecewise, parallel to the eigenvectors of the Jacobian. The P-variant ordering of the Osher fluxes has been utilized in the present investigation. The left and right states, U^L and U^R, are determined using the MUSCL scheme of van Leer [29] and an appropriate limiter in order to obtain higher order spatial accuracy. Qin [52] found that the use of primitive variables in the variable extrapolation was more robust, such that negative pressure errors were more easily avoided. The MUSCL scheme is therefore employed using the primitive variable vector **u** as:

$$
\begin{aligned}
\boldsymbol{u}^{L}_{j+\frac{1}{2},k} &= \boldsymbol{u}_{j,k} \\
&+ \left[\left(\frac{s}{4}\right)\left[(1-\kappa s)\,\Delta^{-} + (1+\kappa s)\,\Delta^{+}\right]\boldsymbol{u}\right]_{j,k} \\
\boldsymbol{u}^{R}_{j+\frac{1}{2},k} &= \boldsymbol{u}_{j+1,k} \\
&- \left[\left(\frac{s}{4}\right)\left[(1+\kappa s)\,\Delta^{-} + (1-\kappa s)\,\Delta^{+}\right]\boldsymbol{u}\right]_{j+1,k}
\end{aligned}
\tag{3.16}
$$

where the parameter κ determines the spatial accuracy of the extrapolation scheme, and the parameter s limits the high order terms in the extrapolation, which cause oscillations at discontinuities. For the present study κ is set to $\frac{1}{3}$ which corresponds to a nominally third order upwind scheme, and s is implemented using the formulation of Anderson et al [3] which is written as:

$$
s = \frac{2\Delta^{+}u\Delta^{-}u + \epsilon}{(\Delta^{+}u)^2 + (\Delta^{-}u)^2 + \epsilon} \tag{3.17}
$$

where ϵ is a small number to prevent division by zero in regions of negligible gradients.

3.1.2 Diffusive Flux Treatment

The diffusive, or viscous, terms are computed at the cell interfaces by use of Gauss's theorem within a secondary control volume surrounding the centre of the given cell interface as shown in Figure 3.2. The required area vectors and derivatives can then be evaluated by interpolation from surrounding values. For the derivatives on the cell interface between the cells (i,j,k) and (i+1,j,k), the following approximation was used:

$$
\begin{aligned}
\left(\frac{\partial u}{\partial x}\right)_{i+\frac{1}{2},j,k} &= \left(u^{F}dS^{F} - u^{B}dS^{B} + u^{R}dS^{R}\right. \\
&\left. -u^{L}dS^{L} + u^{U}dS^{U} - u^{D}dS^{D}\right)/V_{i+\frac{1}{2},j,k}
\end{aligned}
\tag{3.18}
$$

where $V_{i+\frac{1}{2},j,k}$ is the average volume of the cells (i,j,k) and (i+1,j,k) and:

$$
\begin{aligned}
u^{F} &= u_{i+1,j,k} \\
u^{B} &= u_{i,j,k} \\
u^{R} &= \left(u_{i,j+1,k} + u_{i+1,j+1,k} + u_{i,j,k} + u_{i+1,j,k}\right)/4 \\
u^{L} &= \left(u_{i,j-1,k} + u_{i+1,j-1,k} + u_{i,j,k} + u_{i+1,j,k}\right)/4 \\
u^{U} &= \left(u_{i,j,k+1} + u_{i+1,j,k+1} + u_{i,j,k} + u_{i+1,j,k}\right)/4 \\
u^{D} &= \left(u_{i,j,k-1} + u_{i+1,j,k-1} + u_{i,j,k} + u_{i+1,j,k}\right)/4
\end{aligned}
$$

$$
\begin{aligned}
dS^F &= \left(idS^{i,j,k} + idS^{i+1,j,k}\right)/2 \\
dS^B &= \left(idS^{i,j,k} + idS^{i-1,j,k}\right)/2 \\
dS^R &= \left(idS^{i,j,k} + idS^{i+1,j,k}\right)/2 \\
dS^L &= \left(idS^{i,j-1,k} + idS^{i,j-1,k}\right)/2 \\
dS^U &= \left(idS^{i,j,k} + idS^{i+1,j,k}\right)/2 \\
dS^D &= \left(idS^{i,j,k-1} + idS^{i+1,j,k-1}\right)/2
\end{aligned}
$$

Similar expressions are employed for the other gradients and cell interfaces.

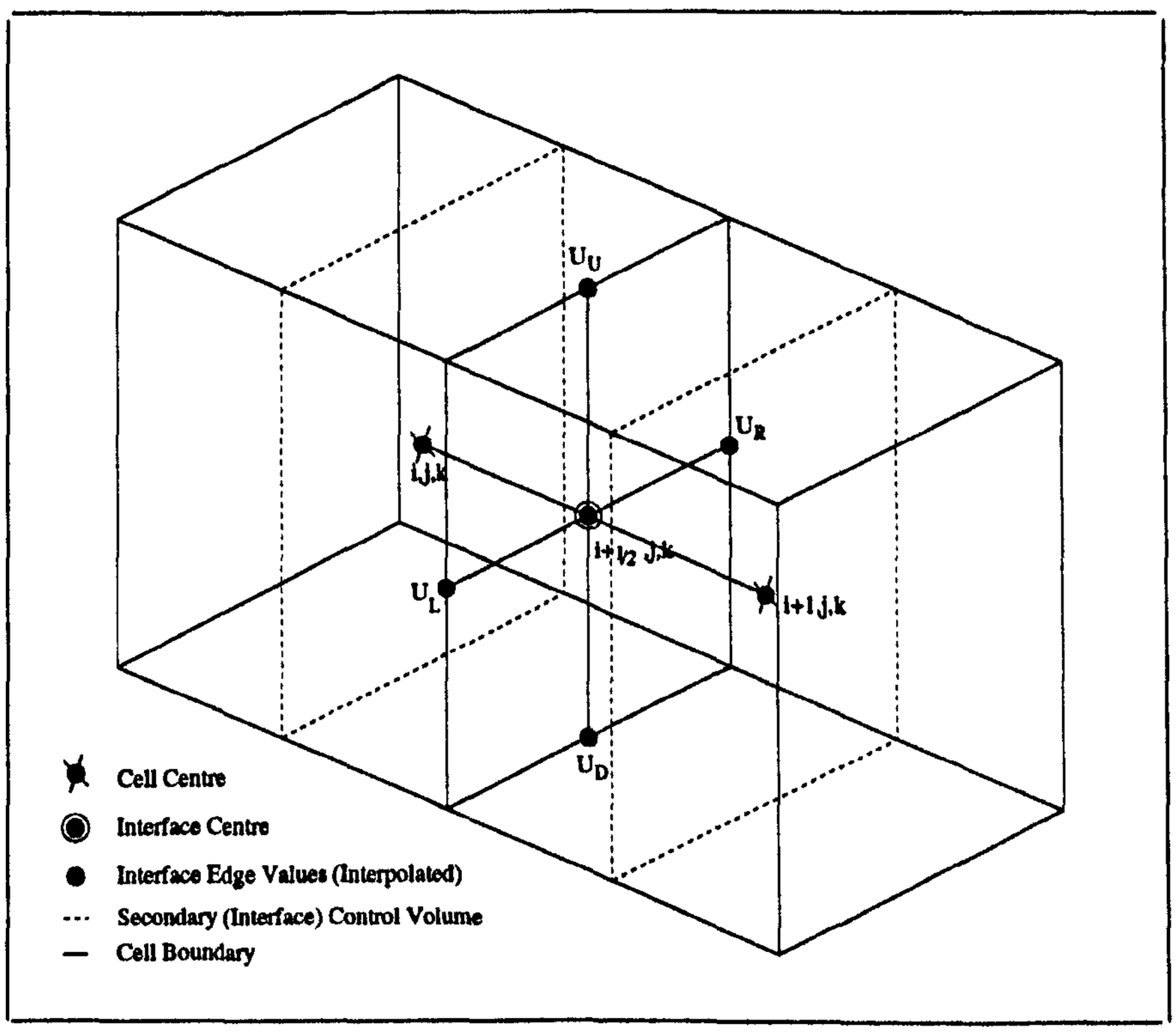

Figure 3.2: *Interface Flux Treatment*

3.1.3 Local Time Stepping

Since the time dependent approach is used to solve the steady-state equations, the local time stepping approach is employed. This allows a greater time step to be applied in areas of coarse grid resolution. The time step is calculated as follows:

$$\begin{aligned}\Delta t \leq CFL/\,&(|u\cdot d\xi| + |u\cdot d\eta| + |u\cdot d\zeta| \\ &+ a\,(|d\xi| + |d\eta| + |d\zeta|) \\ &+ b\left(|d\xi|^2 + |d\eta|^2 + |d\zeta|^2\right)\end{aligned} \tag{3.19}$$

where a is the local sound speed, CFL is the Courant-Friedrichs-Lewy number and:

$$b = \frac{2\gamma\mu}{\rho PrRe}$$

Convergence is measured by calculating the root-mean square of the ratio of the current to the initial residual. In each block the square of the residual in each cell is summed up, and then the values for each block are summed up to give the square of the residual for the whole domain. The square root of this global value is then calculated.

$$||R|| = \sqrt{\frac{\sum_{nblocks}\left(\sum_{ijk} R^2\right)}{\sum_{nblocks}\left(\sum_{ijk} R^2\right)_{initial}}} \tag{3.20}$$

Convergence is deemed to have been achieved after $||R||$ drops to 10^{-4}, that is, four orders of reduction.

3.1.4 Boundary Conditions

CRANS3D employs a number of boundary conditions. Each boundary condition can be applied on any of the six sides of the given block. A transmissive boundary condition has been implemented based on the approximate solution of the Riemann boundary problem on the local cell face. The velocity normal to the local cell face is determined together with the speed of sound on either side. The cell face can then be treated using either i) a supersonic inflow, ii) supersonic outflow, iii) subsonic inflow or iv) a subsonic outflow Reimann boundary solution. An approximate solution of the Riemann boundary problem is also used in the prescription of the Euler wall boundary condition where the velocity normal to the boundary is set to zero leaving only the tangential components for a slip boundary treatment. For the viscous case, the no-slip condition is applied and an adiabatic or isothermal boundary condition can be applied depending on the input wall temperature. The solver also includes a symmetry boundary condition, a singular line and singular point boundary condition and an extrapolation boundary condition for supersonic outflow, each of which can be applied on any of the six sides of a block. For a detailed discussion of the approximate solution of the Riemann boundary problem refer to Spekreijse [68].

3.2 Turbulence Closure: The Baldwin-Lomax Approach

The turbulent eddy viscosity was computed by the use of the Baldwin-Lomax algebraic turbulence model [4] with the Degani-Schiff modification [14] for highly separated crossflows. The approach has been successfully used before for the prediction of slender body, vortex dominated flows. The model is still very popular due to its ease of implementation and simplicity, combined with the relative accuracy compared to more complex models for this application.

The Standard Model (1978) Baldwin and Lomax modified the Cebeci-Smith algebraic turbulence model [11] by substituting new conditions at the outer edge of the shear flow. Their method was more efficient since it eliminated the need to define the edge of the boundary layer. The standard Baldwin-Lomax turbulence model [4] is quoted as follows. The effective viscosity is written in the conventional form, with the laminar (molecular) and turbulent components.

$$\mu = \mu_{laminar} + \mu_{turbulent} \tag{3.21}$$

where:

$$\mu_{turbulent} = \begin{cases} (\mu_{tur})_{inner}, y \leq y_{crossover} \\ (\mu_{tur})_{outer}, y > y_{crossover} \end{cases} \tag{3.22}$$

and y is the local distance normal to the wall, and $y_{crossover}$ is the smallest value of y at which the turbulent viscosities calculated by both inner and outer formulas are equal.

The mixing length formulation and eddy viscosity concept applies in the fully turbulent region of the boundary layer, excluding the buffer layer and laminar sublayer close to the wall. They can be modified, in order to make them applicable over the entire boundary layer by using various empirical expressions such as the Van-Driest (1956) damping factor, applied to the mixing length model as:

$$L = l\left(1 - e^{-y/A}\right) \tag{3.23}$$

where A is a damping length constant defined as $26v(\tau_w/\rho)^{-1/2}$. This expression provides continuous velocity and shear distributions for turbulent flow through the non-turbulent to the inner turbulent region. However, by Van-Driest's definition of A, it is restricted to flows of negligible pressure gradient.

The viscosity in the inner layer in the Baldwin-Lomax model is calculated by the Prandtl-Van Driest formulation.

$$(\mu_{tur})_{inner} = \rho l^2 |\omega| \tag{3.24}$$

where:

$$l = ky(1 - e^{-y^+/A^+}) \tag{3.25}$$

with k being the Karman constant, and $|\omega|$ is the magnitude of the local vorticity vector given by:

$$|\omega| = \sqrt{\left(\frac{\delta u}{\delta y} - \frac{\delta v}{\delta x}\right)^2 + \left(\frac{\delta v}{\delta z} - \frac{\delta w}{\delta y}\right)^2 + \left(\frac{\delta w}{\delta x} - \frac{\delta u}{\delta z}\right)^2} \tag{3.26}$$

and the friction height, y^+ is expressed as:

$$y^+ = y\sqrt{\frac{\rho_w}{\mu_w}\frac{\delta u}{\delta y}} = y\sqrt{\frac{\rho \tau_w}{\mu_w^2}} \tag{3.27}$$

In the outer region, for attached boundary layers the Cebeci-Smith model gives the turbulent viscosity coefficient as:

$$(\mu_{tur})_{outer} = KU\delta^*(1 + 5.5(y/\delta)^6)^{-1} \tag{3.28}$$

where δ is the boundary layer thickness, δ^* is the displacement thickness and K is the Clauser constant. This relationship was based on the Clauser Relation for the outer region of the boundary layer, which states:

$$(\mu_{tur})_{outer} = \alpha \rho U_e \delta^* \tag{3.29}$$

Baldwin and Lomax modified the Cebeci-Smith formulation using the assumption that the maximum of the moment of vorticity is related to the boundary layer thickness. Their formulation is given as follows:

$$(\mu_{tur})_{outer} = KC_{cp}\rho F_{wake} F_{kleb} \tag{3.30}$$

where C_{cp} is an additional constant, and:

$$F_{wake} = min \begin{cases} y_{max} F_{max} \\ C_{wk} y_{max} U_{dif}^2 / F_{max} \end{cases} \tag{3.31}$$

Here the quantity U_{dif} represents a velocity scale and expresses the difference between maximum and minimum total velocity along the same line. The second term is taken to be zero for wall bounded flows.

$$U_{dif} = (u^2 + v^2 + w^2)^{1/2}_{max} - (u^2 + v^2 + w^2)^{1/2}_{min} \tag{3.32}$$

and F_{max} and y_{max} are the maximum value (and corresponding y value) in a line perpendicular to the wall, of the function:

$$F(y) = y|\omega|(1 - e^{-y^+/A^+}) \tag{3.33}$$

The Klebanoff intermittency function is defined as:

$$F_{kleb}(y) = \left(1 + 5.5\left(\frac{yC_{kl}}{y_{max}}\right)^6\right)^{-1} \tag{3.34}$$

The thickness of the boundary layer is then equal to $\delta = y_{max}/C_{kl}$. The constants are given by Baldwin and Lomax as:

$A^+ = 26$	$C_{cp} = 1.6$
$C_{kl} = 0.3$	$C_{wk} = 0.25$
$k = 0.41$	$K = 0.0168$

The present formulation of the turbulence model employs a smoothing factor, such that in the inner region of the turbulent boundary layer the value of $\mu_{turbulent}$ is taken as $(\mu_{tur})_{inner}$, while within the outer region, the following formulation is employed:

$$\mu_{tur} = (\mu_{tur})_{outer} tanh\left(\frac{(\mu_{tur})_{inner}}{(\mu_{tur})_{outer}}\right) \tag{3.35}$$

The Degani-Schiff Modification (1986)

Vortical flows over slender bodies is another application on which the standard Baldwin-Lomax model exhibits shortcomings. The large crossflow separations cause a difficulty in the determination of physically realistic length and velocity scales for the outer eddy viscosity model in the vortical region on the leeside of the body. In this region the moment of vorticity $F(y)$ typically exhibits two local maxima along the outward body normal rays. The first maxima occurs within the boundary layer, while the second occurs due to the effect of the overlying vortex structure, as shown in Figure 3.3.

The basic Baldwin-Lomax turbulence model searches outward along each ray y to determine $F(y)_{max}$, and in the leeside vortical region (along y_3), may select the second maximum,$F(y_3)^*_{max}$, resulting in a $(\mu_{tur})_{outer}$ which is much too high. This will cause the primary vortices to be smaller than those observed experimentally and the primary separation point will be located closer to the leeward symmetry plane. Also, the secondary vortices may not appear in the computed flow.

To prevent the selection of the wrong peak of the moment of vorticity, Degani and Schiff [14] chose an $F(y)_{max}$ when the value of $F(y)$ drops to 90 percent of the first maximum. Choice of $F(y)_{max}$ this way will prevent the selection of the second maximum.

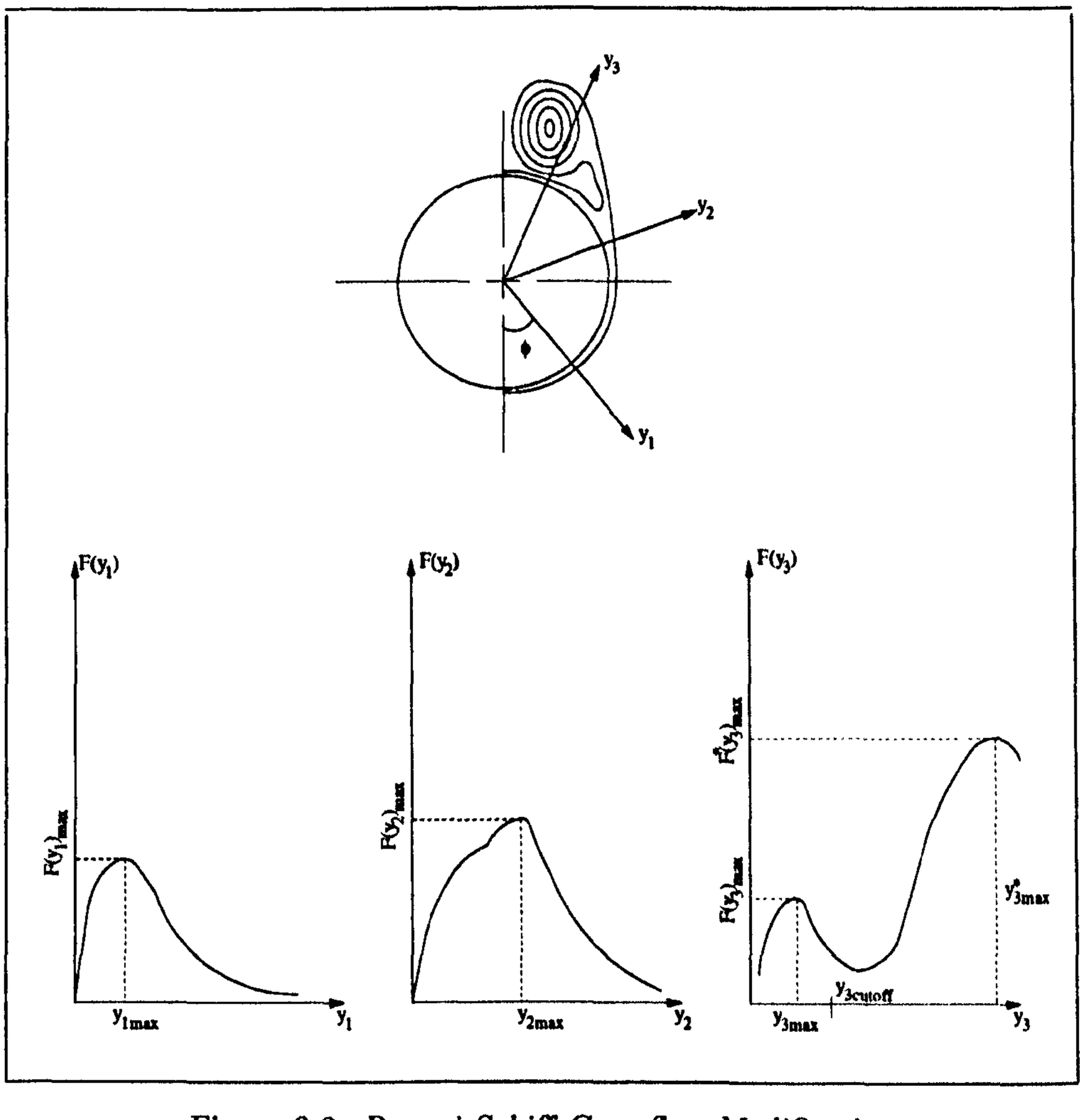

Figure 3.3: *Degani-Schiff Crossflow Modification*

For most rays the distance between the two local maximum is large enough for the minimum to drop below the prescribed 90 percent of the first maximum. However, close to the point of crossflow separation, the vor-

tex feeding sheets lie close to the outer edge of the attached boundary layer, and the peaks in $F(y)$ merge, as shown along y_2 in Figure 3.3. Consequently a further test must be applied. Degani and Schiff specified a cutoff distance on each ray (except the ray on the windward plane of symmetry) in terms of y_{max} from the previous ray. Thus:

$$y_{cutoff}(\phi) = cy_{max}(\phi - \Delta\phi) \tag{3.36}$$

where c is a constant taken as 1.5, and ϕ is the angle subtended by a ray from the windward symmetry plane [14]. This means that if a peak in the moment of vorticity cannot be detected within a cut-off distance from the wall defined at 150% of the peak position on the previous ray, the length scale used for previous ray is taken again.

3.3 CRANS3D Multiblock Implementation

It was decided that, since no large parallel computing facility was available at Cranfield at the start of the research program, and no plans were then made for obtaining one, a serial multiblock strategy would be developed. In order to design a multiblock three-dimensional structured flow solver, one must first design a strategy for describing block connectivity. This can then be used to develop an interface treatment for passing information correctly from one block to another. In CRANS3D, a side numbering convention was adopted as shown in Figure 3.4 where the sides of each block are numbered according to their positions relative to the coordinate axes.

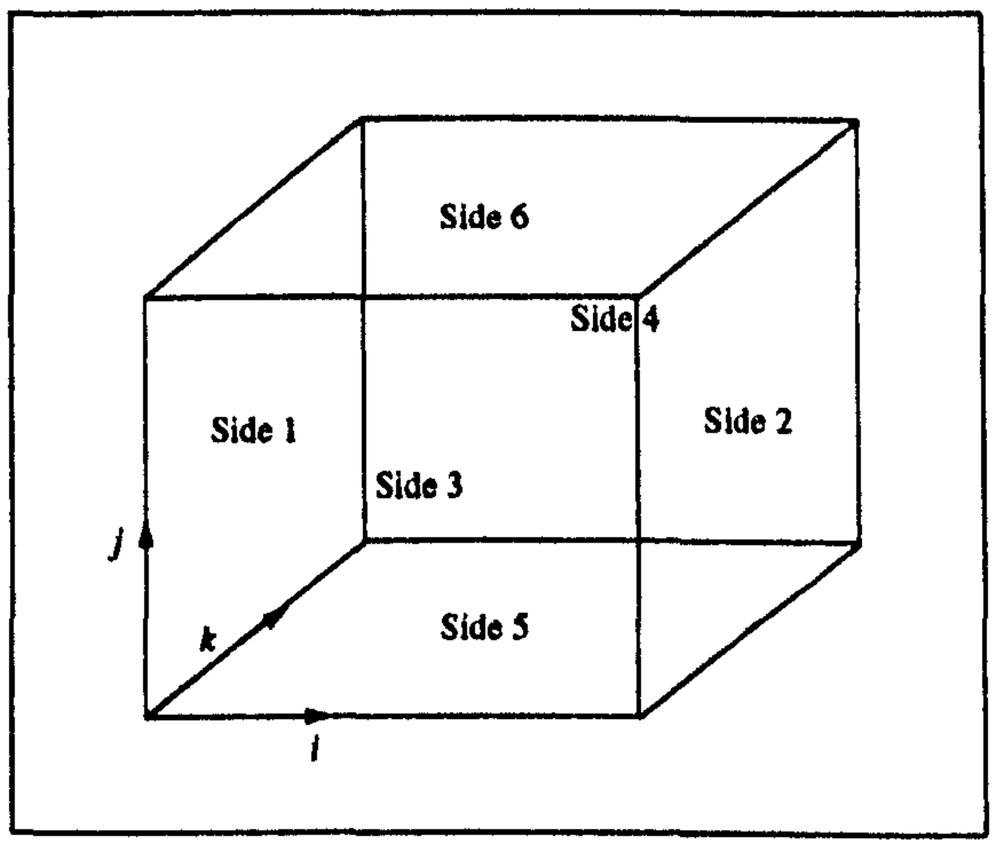

Figure 3.4: *Side Number Convention for Individual Blocks*

Each block in the overall domain is then ascribed a (2×6) matrix where the upper row contains the adjacent block numbers and the lower row the adjacent side numbers, as follows:

Adjacent Block No →	IBLK1	IBLK2	IBLK3	IBLK4	IBLK5	IBLK6
Adjacent Side No →	ISD1	ISD2	ISD3	ISD4	ISD5	ISD6

The adjacent block number tells the code which block is adjacent to which side of the local block. The adjacent side number defines which side of the adjacent block interfaces with which side of the local block. If the local side has no adjacent block, both its corresponding adjacent block number and side number are set to zero, and the appropriate boundary condition is applied.

Consider the case of a flow through a T-junction of a duct as illustrated in Figure 3.5

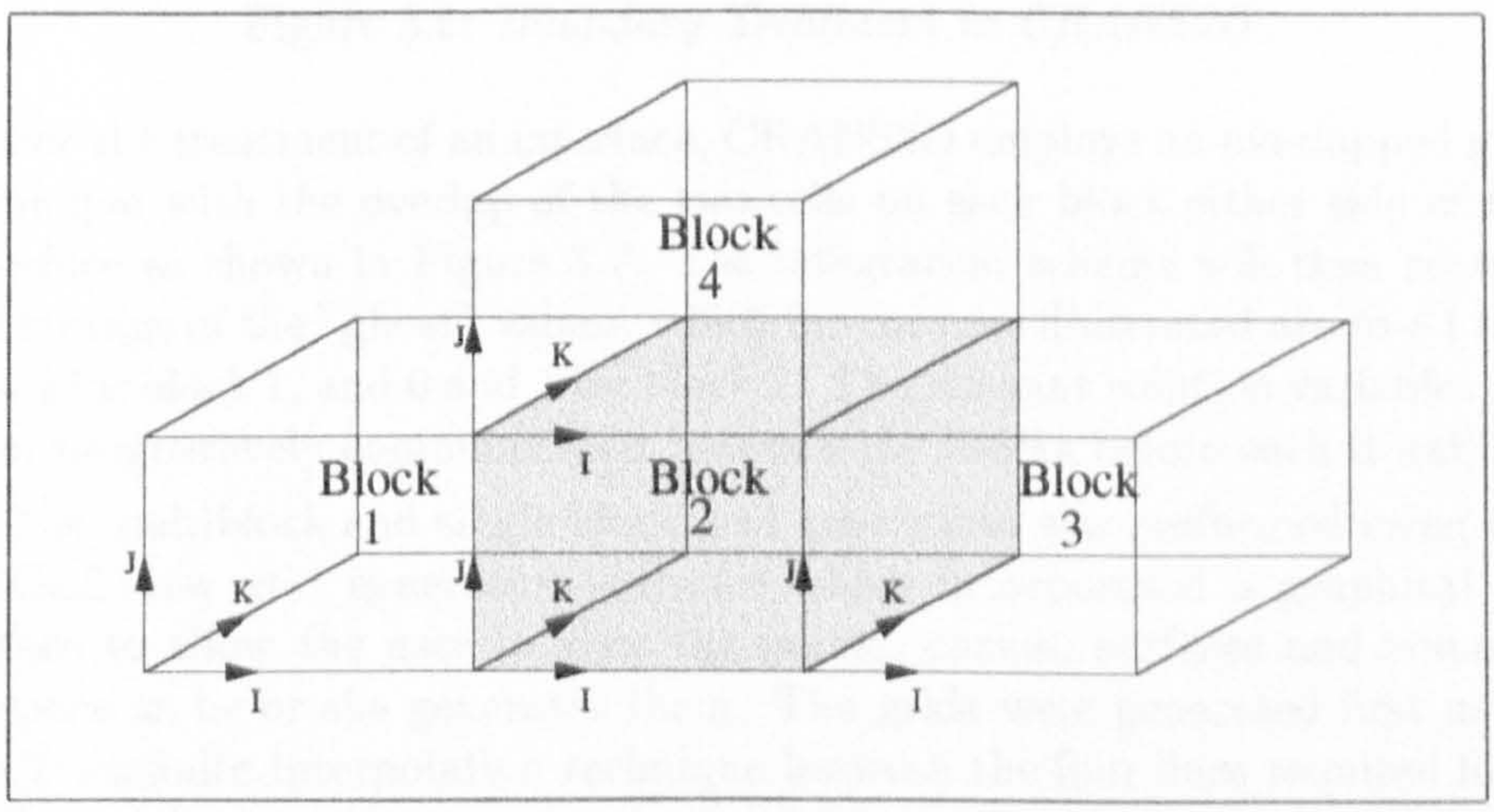

Figure 3.5: *Block Topology for T-junction of a Duct*

Block 2 has three different neighbouring blocks, and its connectivity matrix would appear as:

$$\begin{pmatrix} 1 & 3 & 0 & 0 & 0 & 4 \\ 2 & 1 & 0 & 0 & 0 & 5 \end{pmatrix}$$

The block connectivity matrix for each block in the domain is read in as part of the input data file.

After the solver reads in the block connectivity matrices, it then generates the appropriate secondary or solution grid. For a block boundary with no

interface, the secondary grid will be set up for boundary treatment, that is, for the implementation of a boundary condition as shown in Figure 3.6. A boundary value is placed at the end grid point, in the case illustrated at $in+1$, with the ghost value at $in+2$ which does not require storage.

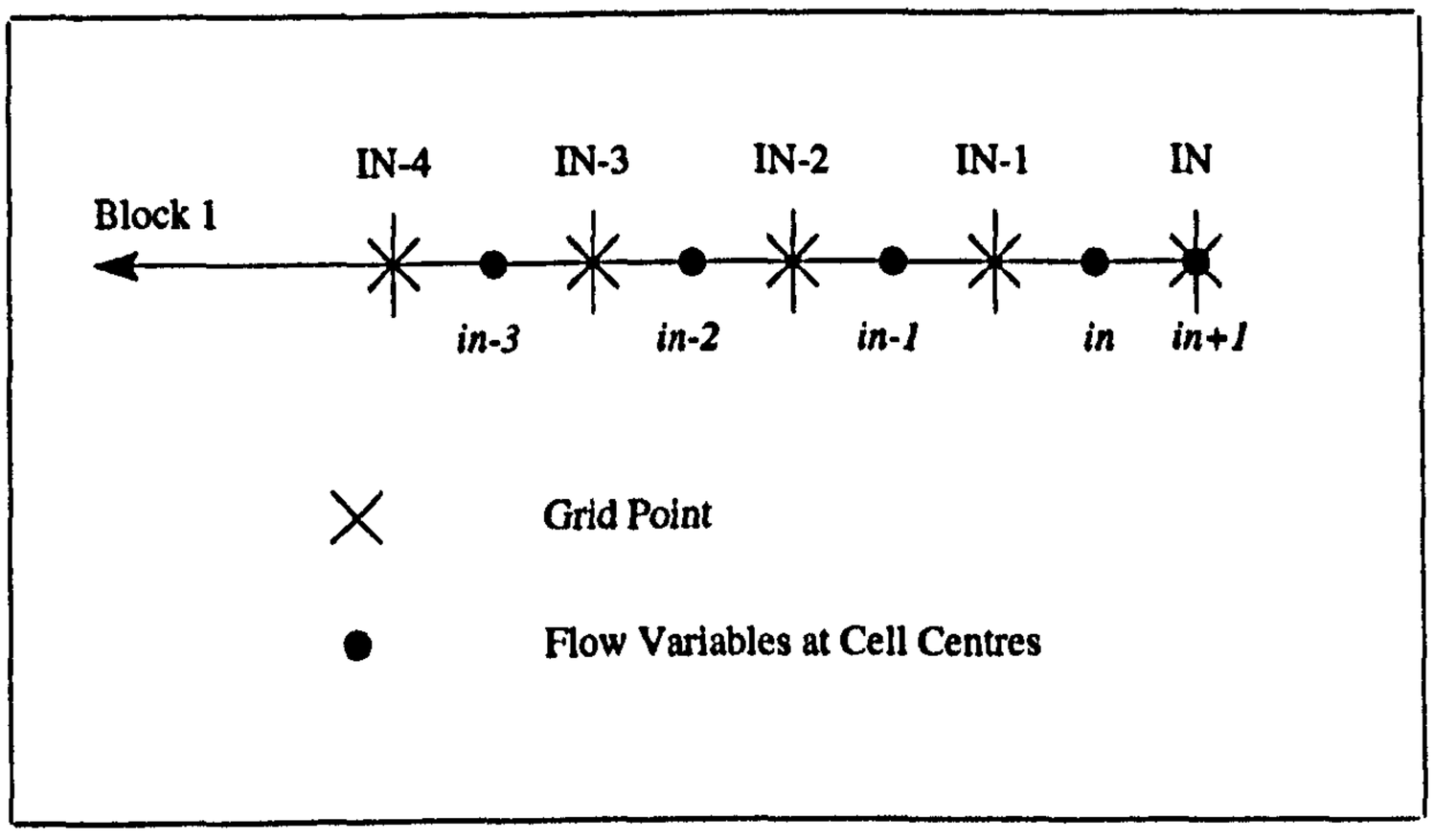

Figure 3.6: *Boundary Treatment in CRANS3D*

For the treatment of an interface, CRANS3D employs an overlapped grid technique with the overlap of the two cells on each block either side of the interface as shown in Figure 3.7. The integration scheme will then require the storage of the "ghost" values, which for the case illustrated are $in+1$ and $in+2$ for block 1, and 0 and 1 for block 2. The relevant solution variables are then progressively communicated between the blocks before each iteration.

The multiblock and single block grid generation was performed using the EAGLEView grid generation software which incorporated a graphical interface to allow the user to view the points, curves, surfaces and volumes in space as he or she generates them. The grids were generated first using the Transfinite Interpolation technique between the four lines required for a surface and six surfaces required to generate a volume. Axisymmetric grids, such as those used for the forebody grids, were generated by rotating the windward or leeward symmetry surface grid by 180°. Cell clustering was achieved using one of the clustering functions provided, and by setting the thickness of the near wall cell according to the desired resolution of the grid. The end cell thickness could also be specified in the same manner. EAGLEView also provided the facility of both elliptic and hyperbolic smoothing algorithms in order to produce smoother better quality grids for complex configurations. In this study only the elliptic smoothing algorithm was implemented in the study of the delta wing and of the full missile configuration.

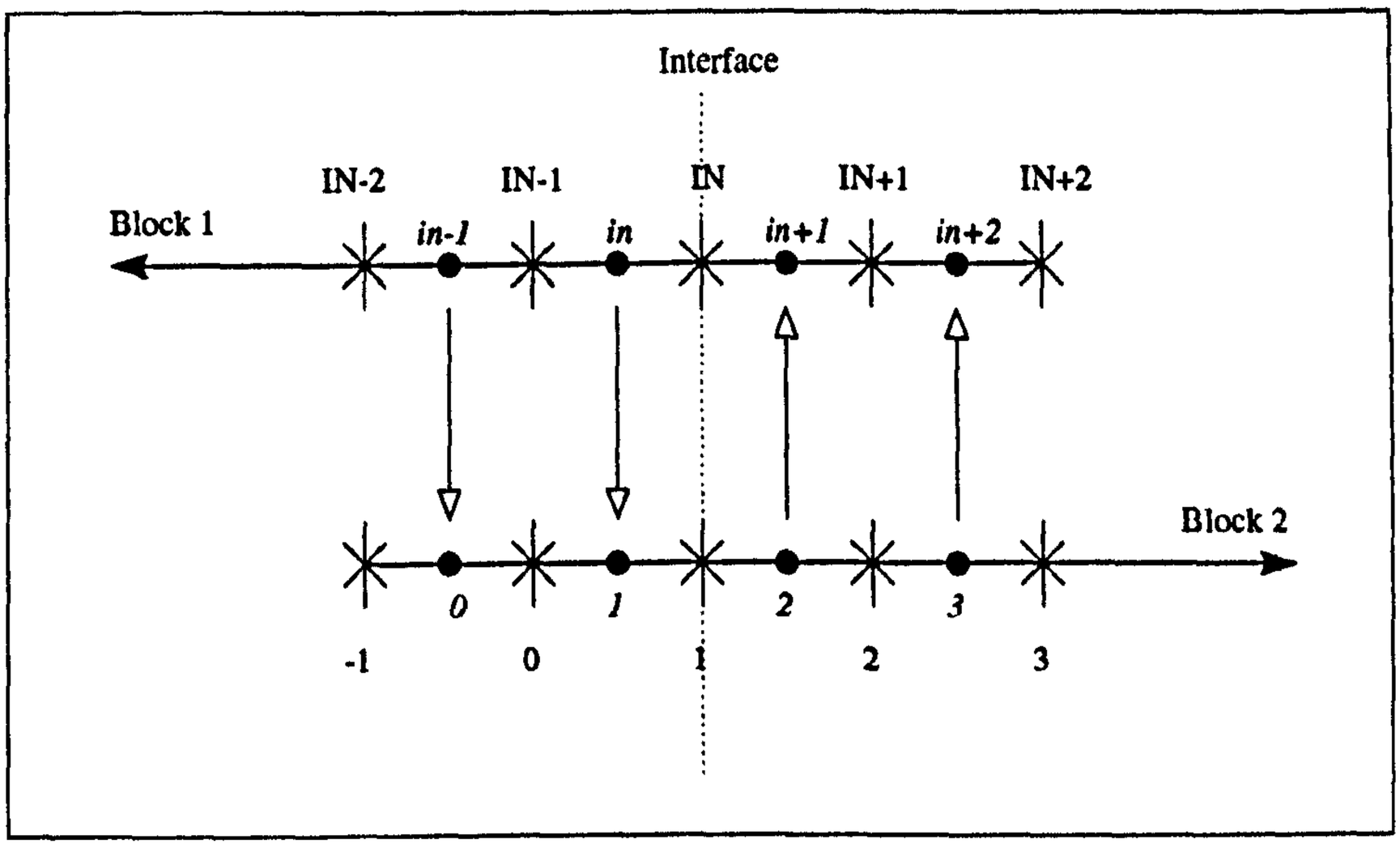

Figure 3.7: *Multiblock Interface Treatment in CRANS3D*

3.4 The PNS Solver and Missile DATCOM Code

3.4.1 The PNS Code

The finite volume PNS solver employed in the study was that developed by Qin, Ludlow and Shaw [61] [53], the multiblock version of which was due to Ludlow. The solver computes the flow in 2D crossflow planes successively marched downstream and employs the same shock capturing and high order schemes as employed in CRANS3D. The requirement for time as a fourth dimension is therefore removed, and the speed of the simulation increased to a level similar to a 2D computation.

The solver employs the approximation proposed by Vigneron et al [76] for the treatment of upstream pressure gradients within subsonic portions of supersonic boundary layers. This approach involves the splitting of the streamwise flux vector and the introduction of an extra term. The PNS solver is fully implicit in the space marching (streamwise) direction. A pseudo-time term, similar to that incorporated into the dual time stepping technique, is added to the governing equations and the solution is advanced in pseudo-time until a converged solution is attained at each streamwise station. The sparse linear system is solved at each pseudo-time step by an unfactored AF Preconditioned Krylov-subspace method [61]. The spatial accuracy in the space marching direction can be chosen as first or second order.

3.4.2 USAF Missile DATCOM Code

Missile DATCOM was run at the computing laboratory of the DERA Bedford Research Centre and was first developed in 1984 by the U.S. Airforce. The program was written for the prediction of the aerodynamic stability and control characteristics of missile configurations. For the estimation of the aerodynamics of the body alone, slender body theory is employed at subsonic speeds and embedded Newtonian theory at hypersonic speeds. In the supersonic range, slender body theory together with Newtonian theory can be applied, as can Second Order Shock Expansion Theory for the calculation of surface pressure coefficient. The body crossflow effects are estimated using Allen's crossflow method with the appropriate value of the crossflow drag coefficient, at the design crossflow Mach and Reynolds number, taken from an experimental database. Similar methods are used for the estimation of wing alone characteristics, and the aerodynamics of the full configuration is obtained using experimental data and the component build-up method of the Pitts, Nielsen and Kattari type. A detailed description of the code and its constituent methods is given in the Missile DATCOM User's Manual [10].

Chapter 4

Slender Forebody Aerodynamics

The aerodynamics of sharp nosed, slender bodies of revolution is investigated in this section. The computational study of nine ogive-cylinder body experimental test cases is presented together with a new interpretation of the complex vortical flow. In addition, a simple modification to improve the accuracy of the Baldwin-Lomax/Degani-Schiff turbulence model is put forward, and a new method for the estimation of the measurement error from pressure tappings is introduced.

4.1 Slender Body Vortical Flows

As a sharp nosed-slender cylindrical forebody encounters flow at increasing angle of attack, the leeward flow pattern goes through several distinct regimes. At angle of attacks above about 5° the boundary layer separates from the body. The reason for this is the inability of the boundary layer to remain attached in the region of strong adverse pressure gradient. The separated boundary layer sheet possesses a rotational characteristic or vorticity due to the higher velocities outward than near the surface. These separated vortical layers curl up to form well defined vortices in the leeward quadrants. The onset of separation and subsequent development of these vortices cause a significant increase in the aerodynamic loads and extreme loading non-linearities.

At an angle of attack above a few degrees the boundary layer on the leeward side of a body rolls up to form symmetric vortices as illustrates in Figure 4.1a. When the angle of attack is increased above around 20°, the symmetrical pattern gives way to an asymmetric flow field as shown in Figure

4.1b, which may be characterised by the appearance of more vortices. Both of these flow regimes are nominally steady. As the angle of attack approaches $45 - 90^o$ the vortex pattern becomes unsteady as shown in Figure 4.1c, the shed vortices move off periodically away from the body surface.

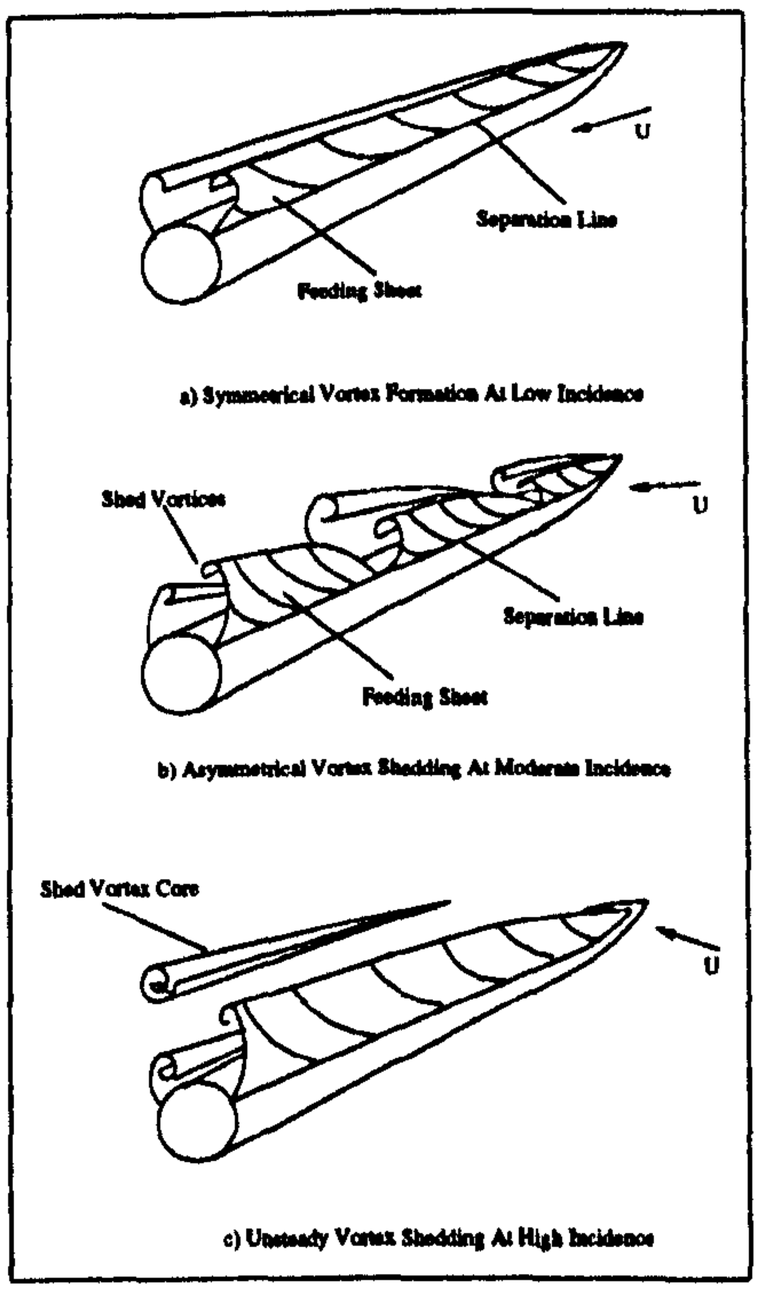

Figure 4.1: *Vortex Flow Structure Development With angle of attack*

The vortex structure in supersonic flow changes as the crossflow Mach number approaches unity. Vortices become more elliptic (elongated) in shape as they pass further downstream, and with increasing crossflow Mach numbers, degenerate into free shear layers.

At supersonic speeds the vortex structure has very little influence on total body loads since the leeside pressures become very low. A qualitative outline of Mach number-angle of attack bounds of the various high angle of attack flow regimes is shown in Figure 4.2.

4.1.1 The Symmetric Vortex Regime

The focus of the present investigation is the understanding and prediction of the missile aerodynamics within the symmetric vortex state. The symmetric vortex pattern illustrated in Figure 4.3, occurs at angle of attacks above a few degrees and below around 20 degrees.

The general crossflow pattern is relatively insensitive to Mach number when crossflow Mach number M_c is less than unity, and is insensitive to

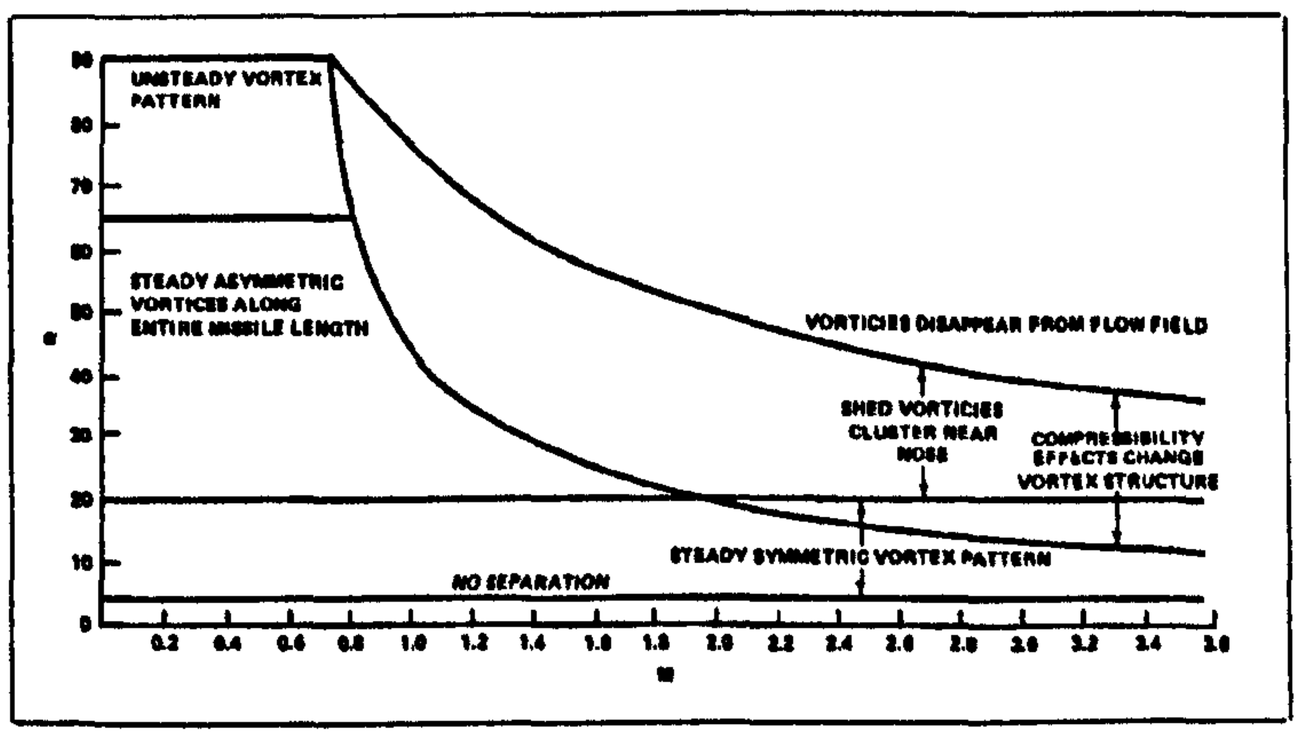

Figure 4.2: *Affect of Angle of Attack and Crossflow Mach Number on Vortex Structure Over A Cylindrical Body ($l/D \approx 10$ [1]*

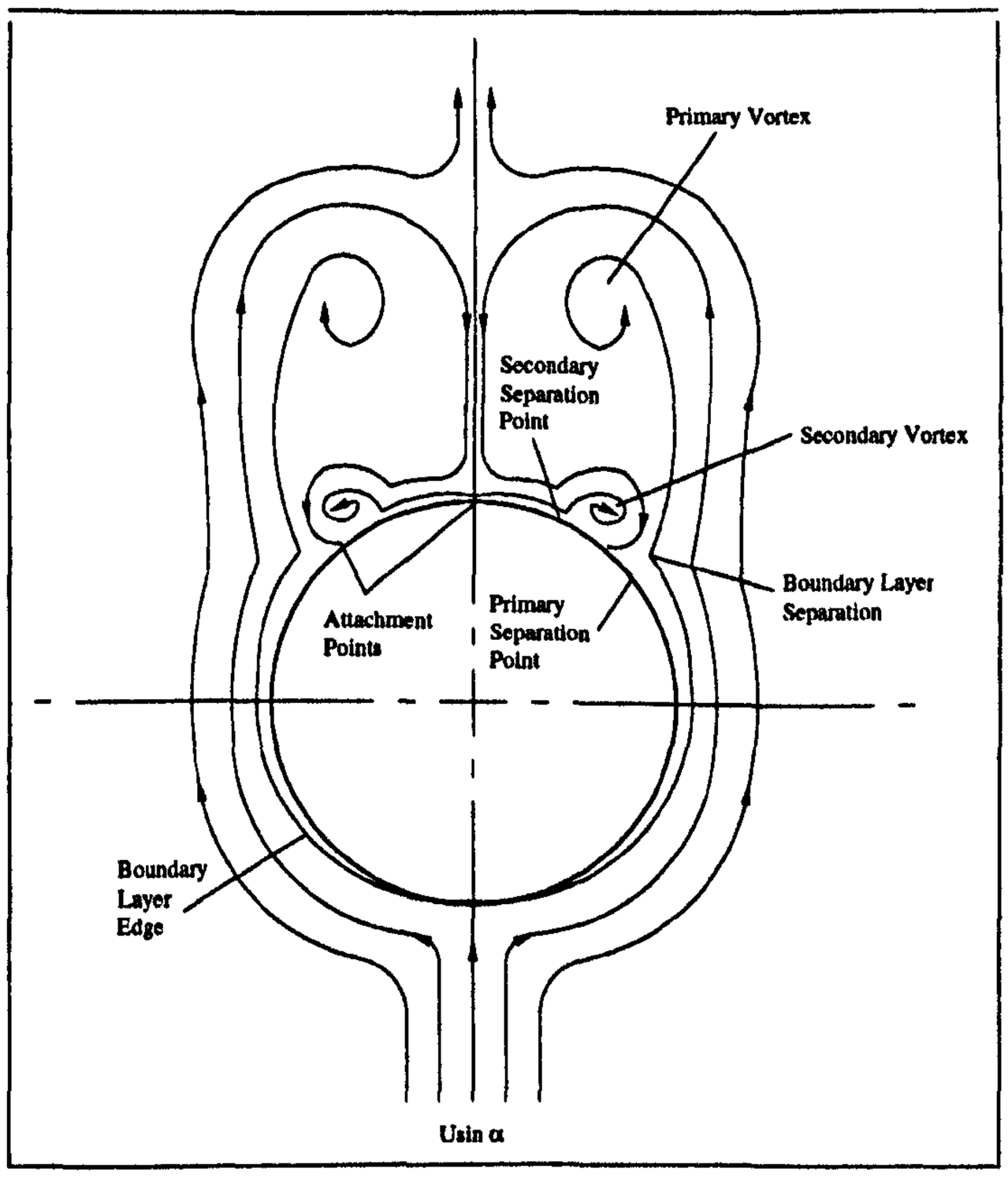

Figure 4.3: *Symmetric Cross Flow Vortex Structure*

Reynolds number when M_c is greater than 0.8. With increasing M_c, the vortices become more elliptic as they progress downstream, eventually degenerating into free shear layers far downstream. The fully developed symmetric vortex pattern shown in Figure 4.3 is characterised by primary and small

secondary vortices and associated separation and reattachment points. The primary separation point has been found to yield much information about the flow, particularly the state of the windward boundary layer and subsequent vortex physics. Three distinct trends have been identified [80] in the separation point data. Firstly, the separation point moves windward with increasing axial distance from the nose, as illustrated in Figure 4.4.

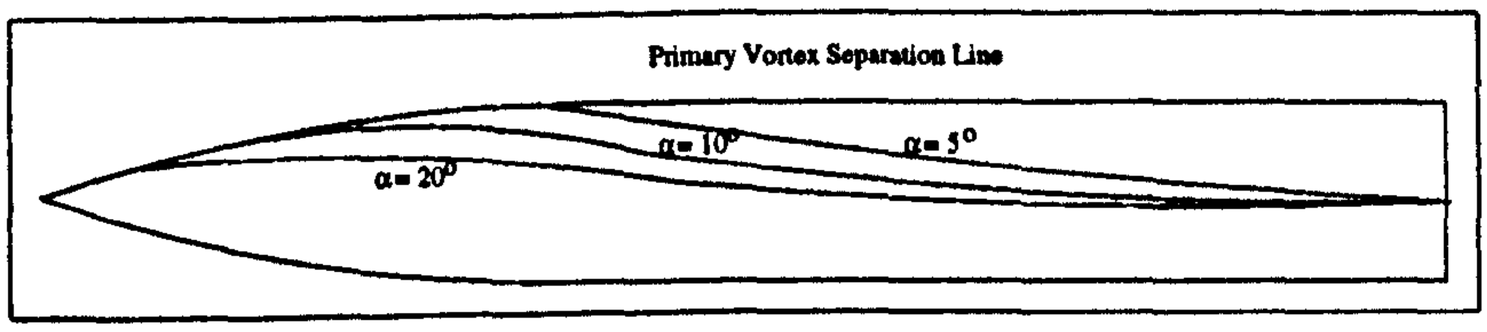

Figure 4.4: *Movement of Separation Line Along Missile Body [35]*

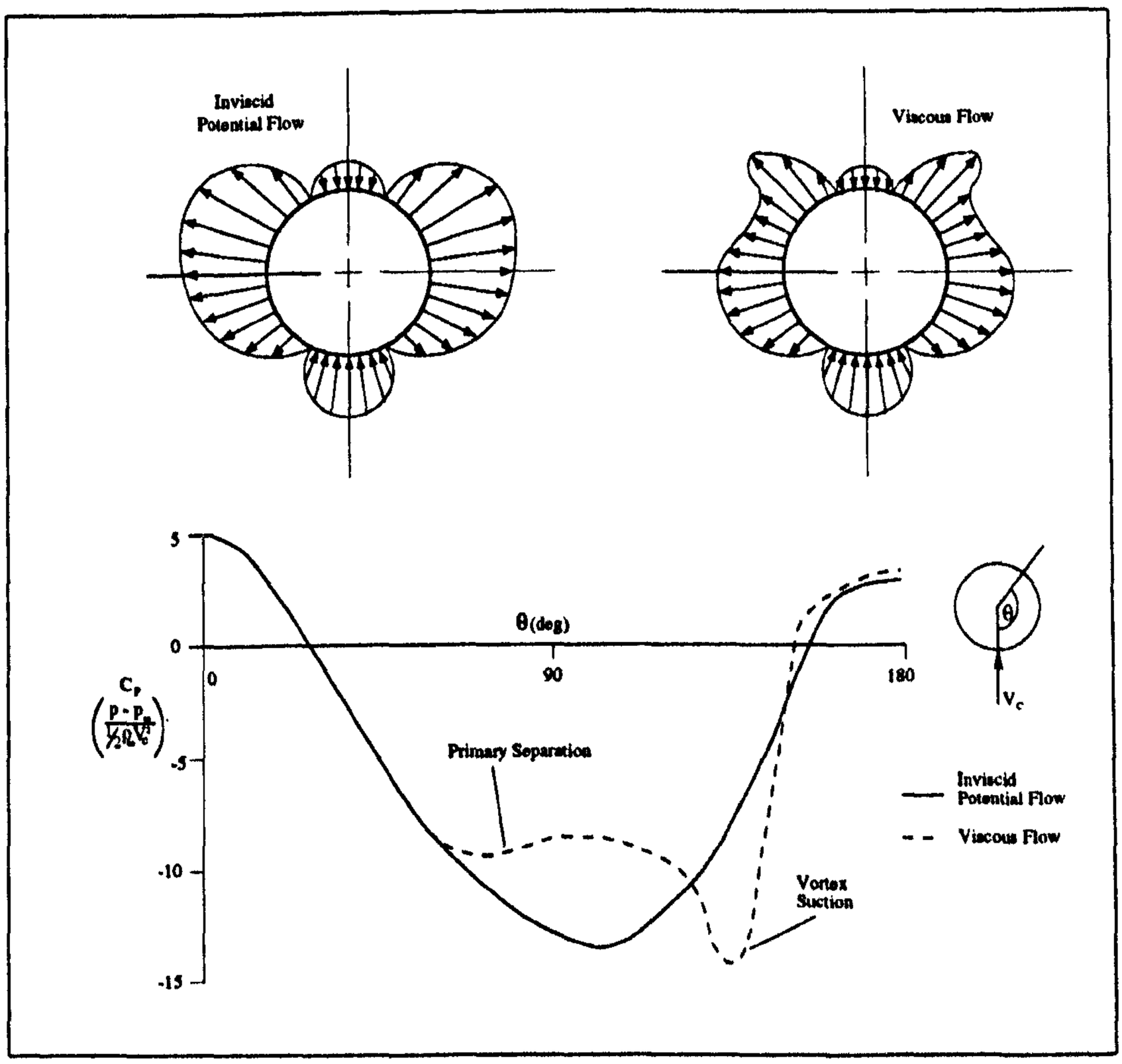

Figure 4.5: *Comparison of Typical Viscous and Inviscid Surface Pressure Distributions for Supersonic Flow past Cylinder Afterbody*

Secondly, the separation point at a given axial station moves progressively more windward as the angle of attack is increased. This is due to increased

skin friction and corresponding adverse pressure gradient associated with a higher crossflow velocity. Finally, at crossflow Mach numbers greater than 0.8, the separation point moves in the leeward direction as M_c is increased, thus narrowing the wake. This phenomena is associated with the appearance of transonic shockwaves around the horizontal symmetry axis where local flow velocity is maximum. If the boundary layer is laminar, a similar affect can be observed with transition to a turbulent boundary layer. Mendenhall and Nielsen [37] suggested an equation to predict the separation point for sharp nosed bodies depending on the nose semi-apex angle θ_N , as:

$$\frac{x_s}{r_N} = 32\left(1 - \sqrt{\frac{\alpha - 4}{\theta_N - 4}}\right) \tag{4.1}$$

where x_s is the axial distance from the nose of the position of separation and r_N is the radius of the body at the base of the nose. For angles of angle of attack less than 4^o no vortex generation is assumed. This equation takes no account of the effects of either Mach number or Reynolds number.

A typical circumferential surface pressure distribution [28] for a viscous separated flow is shown in Figure 4.5 together with that for an inviscid flow. The two distributions diverge at primary separation and the viscous curve develops a distinct peak due to suction from the leeside vortex system.

4.1.2 Recent Research of Symmetric Vortical Forebody Flows

Over recent years many researchers have investigated the aerodynamics of slender bodies both experimentally and numerically. Experiments have been performed on different bodies at a range of angle of attacks and Mach number and at different freestream Reynolds number. The Royal Aerospace Establishment (RAE), lately the Defense Evaluation and Research Agency (DERA), has performed extensive wind tunnel tests on generic forebody shapes in order to develop a database of experimental results to increase the understanding of such flows, and for the evaluation of aerodynamic prediction technologies. Ward et al [78] [23] [79] performed experiments on a number of tangent-ogive bodies over the Mach number range 0.7 to 4.5, at angle of attacks up to 26^o and at Reynolds numbers of 0.5 to 10 million per foot.

A similar set of experiments have been performed by Barberis [5] and Champigny [12] at ONERA and by Esch [19] at DLR. The results from these investigations have been compared with the results of a number of CFD codes.

Sturek *etal.* [71] performed a study of Navier-Stokes computational techniques applied to complex highly separated missile body flows to evaluate the predictive technologies under the auspices of the Technical Cooperation Program of Canada, the U.S., and the U.K. Nine Navier-Stokes codes were

applied to predict the flow about a three calibre ogive-cylinder configuration at various Mach numbers at 8° and 14° angle of attack. The computational results were compared with experimental measurements for surface pressure, pitot surveys of the flow field, and strain gauge force measurements from DERA Bedford. Computational results were obtained for seven turbulence models: Baldwin-Lomax; Baldwin-Lomax-Degani-Schiff; k-epsilon; k-omega; Spallart-Allmaras; Smagorinsky; and Baldwin-Barth.

Each code was tested for like conditions of grid density and turbulence model, and all performed consistently well. For the conditions of this study, however, no best turbulence model could be identified when compared to experiment. The conclusion was that there was no consistent benefit obtained from utilisation of a two equation model over the algebraic models even though substantial separated flows were present on the leeside.

Both experimental and computational results provided evidence of an embedded separation shock emanating from the separation line for some supersonic cases, as demonstrated in the experimental pitot pressure ratio crossflow contours measured in a Mach 2.5 flow at 14°, shown in Figure 4.6.

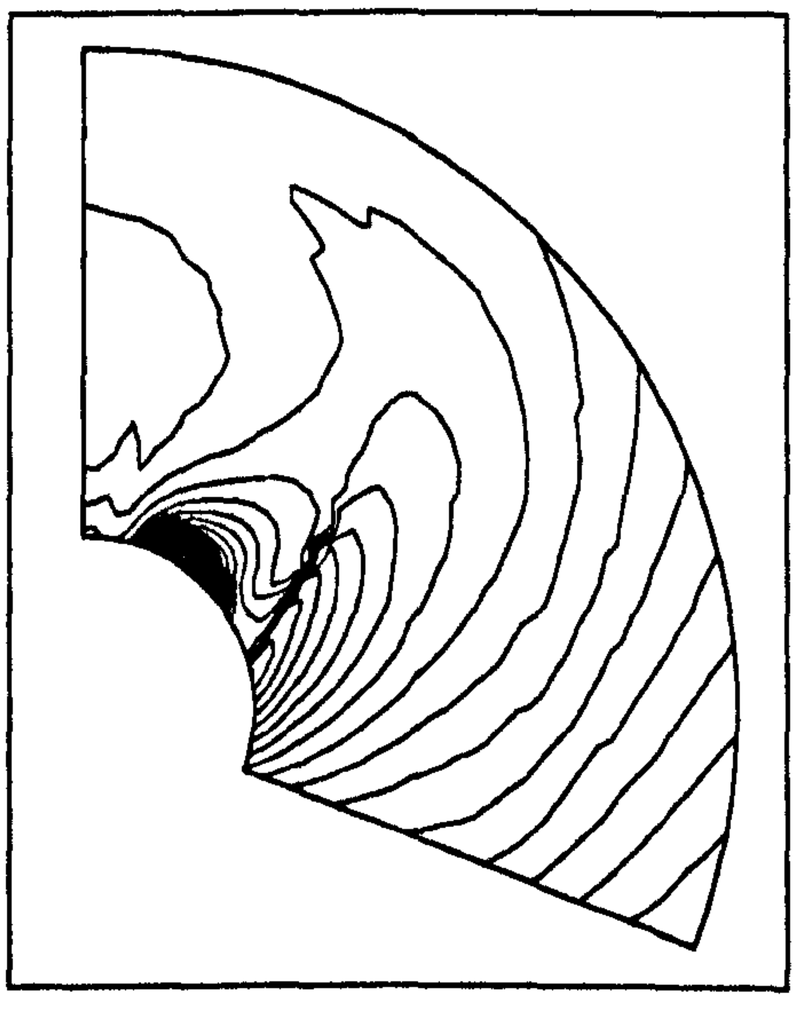

Figure 4.6: *Evidence of an Embedded Separation Shock [9]*
[1]

Hsieh et al [24] performed a computational analysis of the vortical flow for the Mach 3.5, $\alpha = 18°$ RAE ogive-cylinder. The experimental surveys of crossflow plane pitot pressure carried out at stations 5.5 and 11.5 calibres from the nose indicated the presence of a weak separation shock, and additionally showed evidence for the development of a shockwave above the

[1]Pitot measurement plane did not extend to body surface and so did not capture the entire primary vortex structure or its feeding sheet.

vortex at the 11.5 calibre station, which was much stronger than the separation shock. As the vortex moved away from the surface and became more elliptic in shape, it appeared as if a lambda shockwave pattern developed with the weak separation shock coalescing with the stronger "leeside" crossflow shockwave as illustrated in Figure 4.7

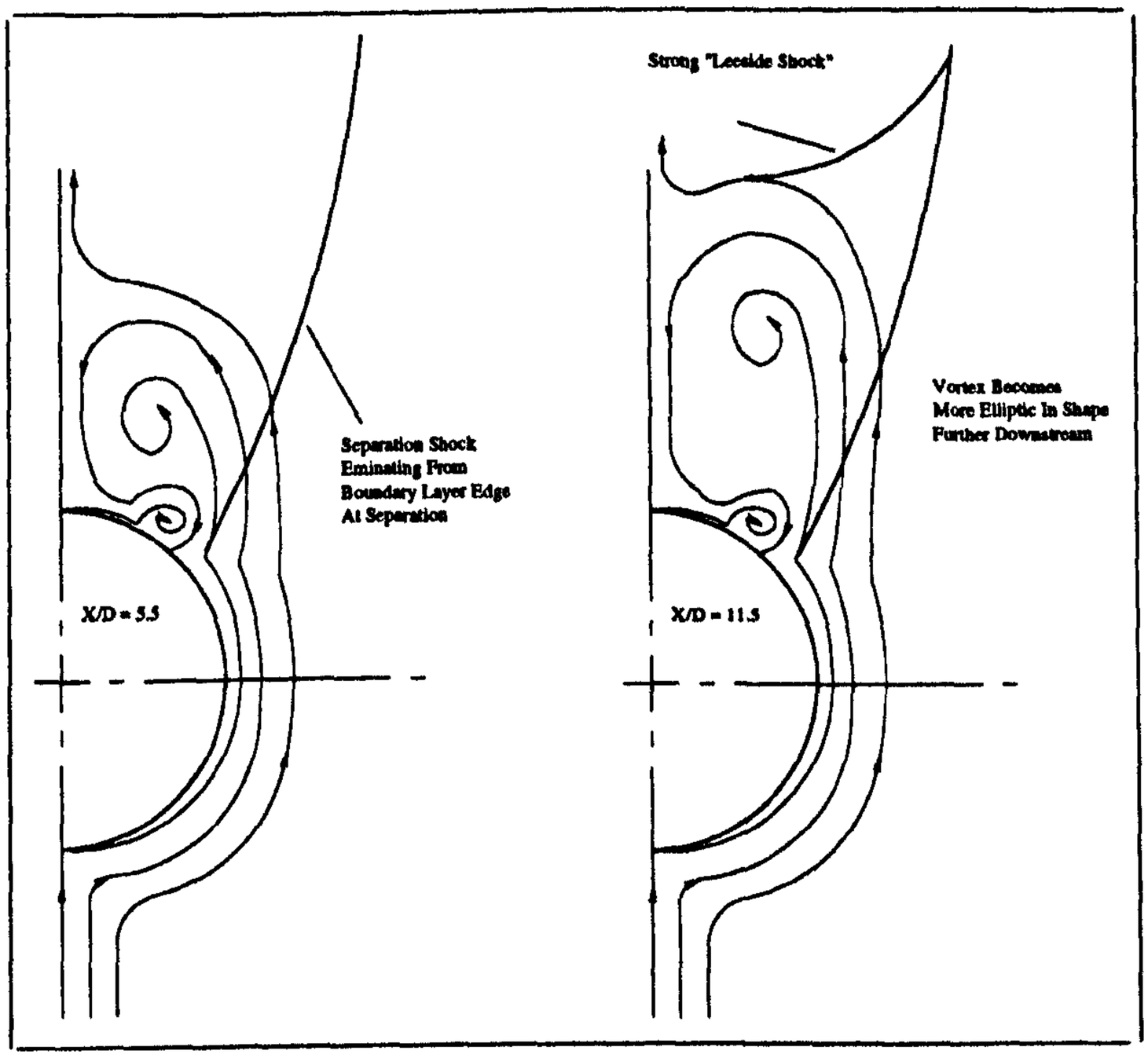

Figure 4.7: *Shockwave Patterns Around Ogive-Cylinder In Crossflow,* $M_\infty = 3.5$, $\alpha = 18^o$.

The CFL3D flow solver was used to compute the case for both laminar and turbulent conditions. Turbulence was modelled using the Baldwin-Lomax Turbulence model with Degani-Schiff modification.

The laminar Navier-Stokes solutions obtained appeared closer to experiment than the corresponding turbulent solutions at x/D=5.5. Boundary layer/Vortex traverses were carried out at stations 5.5 and 11.5 calibres. The corresponding Navier-Stokes calculations showed that in general the laminar computations provided the best comparison with experiment, and indeed resolved the weak crossflow shocks within surface pressure data whereas the turbulent data gave no evidence. The laminar results also resolved the shock above the vortex much more accurately.

Josyula [27] who also participated on the TTCP program, published his own paper on the ability of the three dimensional Navier-Stokes equations to predict flowfields about high length to diameter bodies at moderate angles

of attack ($8^o - 14^o$) for supersonic Mach numbers. Five of the DERA test cases were studied as follows: Mach 1.45 at $\alpha = 14^o$, Mach 1.8 at $\alpha = 14^o$, Mach 2.5 at $\alpha = 14^o$, Mach 3.5 at $\alpha = 8^o$, and Mach 3.5 at $\alpha = 14^o$. The upwind and central difference FDL3DI computations were compared with experimental data and showed that the surface pressure and pitot pressure predictions matched experiment reasonably well. Very little variation was found in the comparison between the central and the upwind calculations for both laminar and turbulent cases. The surface pressure comparisons using the turbulence model were found to match the experiment better than those for the laminar computations. The $k - \epsilon$ turbulence model, however, was found to be highly dissipative for capturing vortical flows, with the vortex core pitot pressure loss being more accurately modelled by the laminar solution. The pitot pressure comparisons showed that the crossflow shock waves evident in the experimental flow fields were captured in the turbulent calculations, but were not resolved in the laminar solution. Josyula regarded local grid refinement as a necessary tool for the accurate prediction of supersonic vortical flow physics.

Thornburg and Soni [74] developed an adaptive grid system based on a weight function algorithm for the detection of the desired flow features. The weight functions were then used to construct forcing functions to attract or repel points in an elliptic system. The algorithm was applied to the tangent-ogive cylinder test case of Pagan and Molton [45]. In particular the case of a Mach number of 2.5, an angle of attack of 14^o and a Reynolds number of 4 million per foot was studied in detail using an $81 \times 69 \times 101$ grid.

It was found that solutions on unadapted grids adequately represented all of the supersonic vortical flow features apart from the feeding shear layer as it rolled up to form the vortex. The authors stated that this was due in part to the poor grid resolution in the unadapted calculation. When these weight functions were then employed within the grid adaption algorithm, the solver was able to more accurately resolve a greater portion of the feeding shear layer.

Pagan et al [45] performed an experimental study of the flowfield around a 3 calibre tangent-ogive body at a Mach number of 2.0 with freestream Reynolds number based on body diameter of 0.16×10^6 for an α range of 0^o to 20^o for both laminar and turbulent flows.

At low to moderate angle of attack (up to 10^o) the flow structure included both primary and secondary vortices. At higher angle of attacks, a complex substructure was also seen with a third separation and associated tertiary vortex situated underneath the secondary structure, very close to the surface.

The largest differences between the laminar boundary layer flow and the turbulent case were seen to exist at $\alpha = 5^o$ when the turbulent flow remained attached compared with the separated laminar case. At $\alpha = 10^o$ it was confirmed that the primary separation line is further leeward in the

turbulent case since the turbulence tends to delay boundary layer separation. At higher angle of attacks, results were very similar in both cases and downstream primary vortices were seen to develop more elliptic structures.

Pagan, Moltan, and Delery [46] later performed corresponding numerical investigations in order to test the experimental evidence. The computations were executed for both laminar and turbulent boundary layer development. The results confirmed that below about 10°, the flow structure includes only primary and secondary vortices, whereas at higher angle of attacks up to 20°, these two vortices occur in addition to a more complex substructure.

Deniau *etal.* [15] presented work done on the development and validation of turbulence models for the computation of 3D supersonic flows with crossflow separation. They analysed various different models ranging from algebraic to two equation $k-\epsilon$ models. The various turbulence models were implemented in their parabolized Navier-Stokes solver - *TORPEDO*. Results for an ogive-cylinder at angle of attack were compared with detailed experimental data. Their preliminary results showed that the application of $k-\epsilon$ type two equation models proved to be significantly more accurate than the algebraic Baldwin-Lomax model for the computation of three dimensional flowfields with large separated regions. In particular they found slightly better performance with a $k-\epsilon$ model using a two layer approach for the near wall treatment as compared to the low Reynolds $k-\epsilon$ models provided the matching line between the two layers is appropriately defined. For the case of an ogive-cylinder flow, best results were obtained when the matching line was defined by the position from the wall of the first maximum of the Reynolds Stress uv.

Moschetta *etal.* [41] performed a numerical investigation to study the physics of laminar crossflow separation and resulting vortices for an ogive-cylinder at angle of attack with an oncoming flow of Mach 2. The PNS version of the French TORPEDO code was used and the results compared with corresponding wind-tunnel measurements performed by Pagan et al [46].

Comparison of experimental and computed surface pressure distributions showed very good agreement for each angle of attack although experimental pressure levels were found to be slightly higher. The loss of total pressure within the vortex core, which must be correctly predicted for the efficient design of downstream air intakes or control surfaces, was also computed very accurately. The authors also performed a topological analysis of the vortical structures at angle of attacks of 5° , 10° , 15° and 20° and their results are summarized in Figure 4.8. The topological patterns for $\alpha = 5°$ and 10° were seen to be equivalent, agreeing with the experimental findings. The primary separation is indicated by S_1 and the associated attachment point by A_2 . secondary separation was seen to occur at S_2 while a secondary attachment point A_3 was clearly visible between S_1 and S_2.

For the higher angles of attack at 15° and 20°, the flowfield takes a much

more complex form. The primary and secondary vortices are still clearly visible, but at least a further four small vortices have also developed, which were not observed experimentally. The topological analysis of crossflow vortical flows based on the critical point theory of Visbal and Gordnier [77] was used to confirm numerical findings. Here, topological laws specify relationships between the number of nodes, N, or half nodes, N', and the number of saddle points, S, or half saddle points (surface separation or attachment points), S', present in the crossflow plane. The relationship of Shen *etal*. [62] was used which states that for streamlines in the crossflow plane:

$$\left(\Sigma N + \Sigma\frac{N'}{2}\right) - \left(\Sigma S + \Sigma\frac{S'}{2}\right) = -1 \tag{4.2}$$

The validity of this relation was further strengthened by the numerical results.

In addition a comparison of the computed crossflow streamlines for different grids was made. Figure 4.9 shows the effect of transverse grid refinement on the converged solutions. The results clearly demonstrate the importance of mesh sensitivity on the accuracy of the converged results.

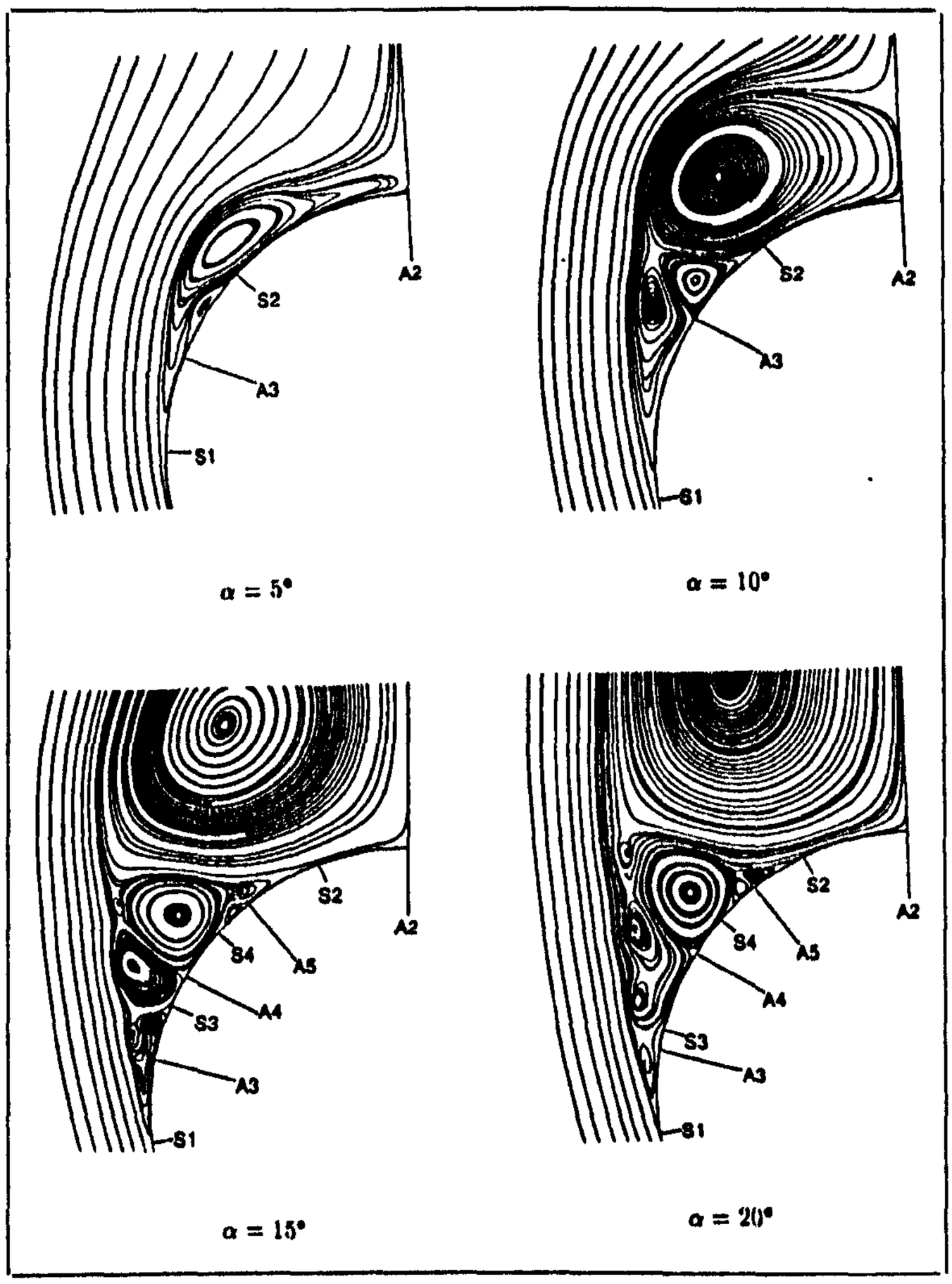

Figure 4.8: *Crossflow Streamline Patterns at x/D=8 with Increasing angle of attack [41]*

Birch, Qin and Jin [8] investigated the supersonic vortical flow around a slender body at angle of attack using a Parabolised Navier-Stokes (PNS) code. The effects of the parabolising assumptions, which allow the use of an efficient space marching approach, were found to have little impact on the predicted vortex flowfield when compared with a time marching Navier-Stokes results. The quality of the solution was found to be strongly influenced by the choice of computational grid, particularly the radial and circumferential grid spacings which effect the resolution of the position of crossflow separation. Good agreement with measured flowfields was obtained for turbulent test cases using the modified Baldwin-Lomax turbulence model proposed by Degani and Schiff.

In spite of all the work done on slender cylindrical body aerodynamics,

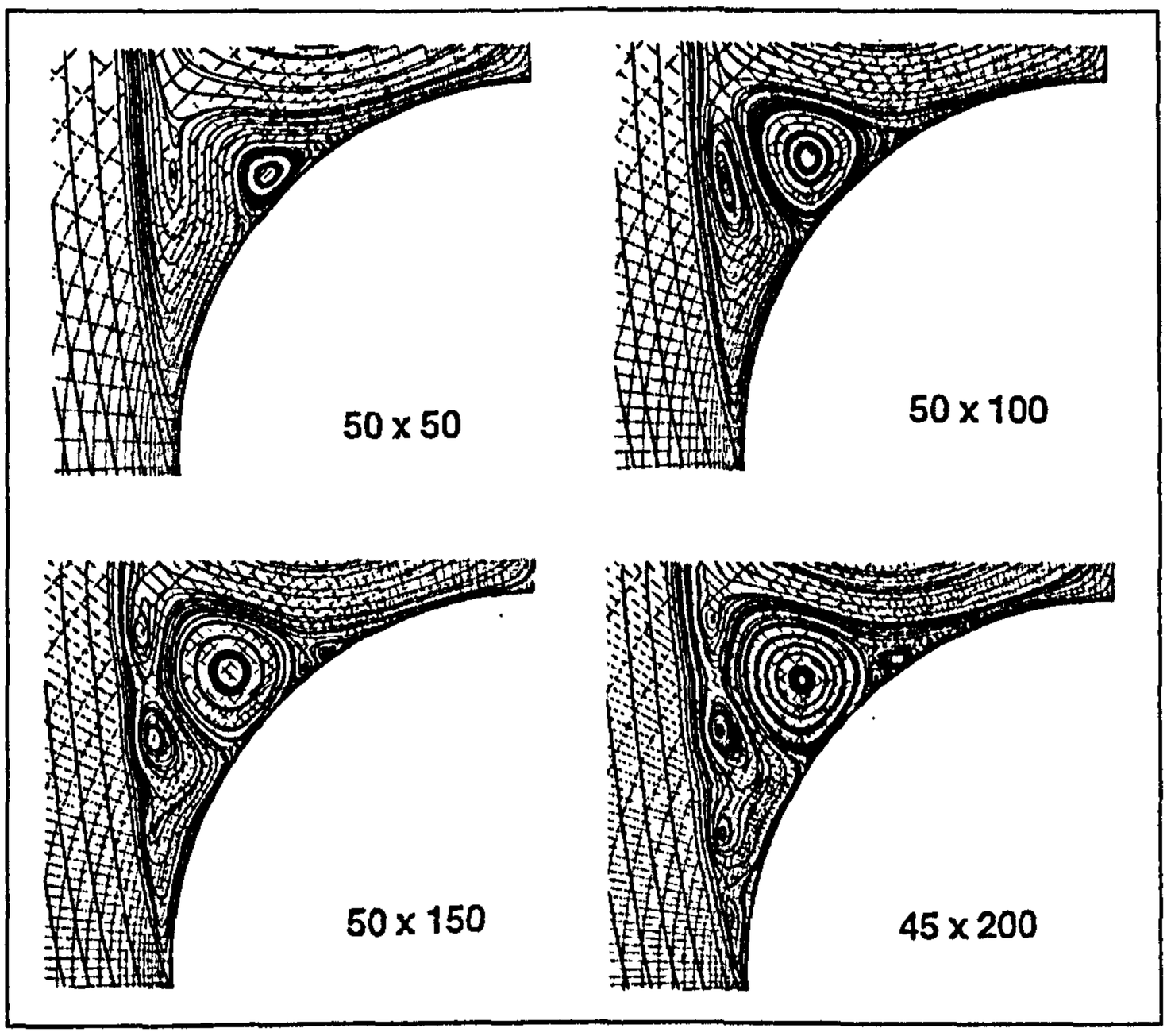

Figure 4.9: *Effect of Grid Refinement on Numerical Convergence of Cross-flow Features [41]*

however, the prediction of turbulent flow separation and the resulting leeside vortex structure is still a remaining problem. Although it has been shown that the boundary layer separation, vortex formation and embedded shock development can be resolved in Navier-Stokes solutions, there are still problems in accurately capturing both their strength and location for turbulent flows. In addition, the origin and conditions required for the appearance of certain shock wave features, in particular an additional windward shock wave which has been seen to occur in several experimental studies, are not fully understood. A detailed investigation of nine slender body test cases was, therefore, performed in order to investigate these issues.

4.2 Analysis of Experimental Error in Surface Pressure Measurement

In order to assess the accuracy of a given solver, it is usual to compare its solutions of a given flow problem with experimental measurements. This is only useful, however, if the level of experimental accuracy is known. The following technique has been derived for the assessment of the accuracy in the measurement of surface pressure by means of pressure tappings.

The measurement of static pressure of a moving fluid, involving the use of pressure tappings - small holes on the surface of the wind tunnel model or the working section wall - will be inherently erroneous. The hole in the surface will act as a cavity and disturb the local flow conditions resulting in an error in the measured pressure. The degree of disturbance, and the corresponding error in measured pressure, will depend on the hole size and geometry and on the local flow conditions. A larger hole will result in a larger disturbance and therefore a higher degree of measurement error. For a given size of static hole a thinner boundary layer will also result in a greater disturbance as will a pressure gradient outside the boundary layer.

For supersonic speeds, Morrison *etal.* [40] correlated a relationship for the effect of static hole size on the pressure gradient on a hemispherical body:

$$\frac{1}{p}\frac{\partial p}{\partial \eta} + 0.37\frac{1}{p}\frac{\partial p}{\partial \phi} + 0.19\left(M^2 - 1\right) = 0 \tag{4.3}$$

Peto *etal.* [48] applied Equation (4.3) for the case of a supersonic flow past a sharp cone model. They demonstrated that the static pressure error due to a large pressure gradient, $dC_{p_{\Delta p}}$, in the vicinity of a static hole of diameter d is equivalent to the change in pressure due to an upstream displacement of the hole by $0.37d$, as follows:

$$dC_{p_{\Delta p}} = -0.37d\left(\frac{\partial p}{\partial s}\right) \tag{4.4}$$

Peto and Pugh [49] employed the technique of multiple regression analysis to investigate the effect of static hole size on the experimental error in measured pressure. In particular the effect of the hole size relative to the local thickness of the boundary layer was investigated together with the effects of surface burrs, of size h, around the edge of the holes, and also manufacturing errors in the machining of the cone semi-apex angle, ϵ. Experiments were performed at Mach 3.08 with different operating pressures (Reynolds Numbers), cone angle models and variations in the hole diameter and the distance between the cone apex and the hole. Equation (4.5) is the regression equation for the effects of the boundary layer, correlated from the experimental results and from measurements from other investigations.

Peto and Pugh estimated that the equation predicts the measurement error ,dC_p, for a given static hole to within 1.2% of the true cone surface pressure.

$$dC_{p_\delta}\sqrt{M_L^2-1} = B\left(\frac{d}{\delta^*}\right) + C\left(\frac{d}{x}tan\epsilon\right) + D\,(h) + E\,(\Delta\epsilon) \tag{4.5}$$

Where:

$$B = 2.07\times10^{-3} - 4.06\times10^{-4}\left(\frac{l}{d}\right)$$

$$C = -2.9\times10^{-4} - 0.146tan\epsilon$$

$$D = 6.01, \qquad E \approx 2$$

And M_L is the local Mach number, ϵ is the semi-apex angle of the cone and $\Delta\epsilon$ is the manufacturing error in semi-apex angle of the cone.

For the case of the tangent-ogive wind tunnel models investigated, the pressure tappings were spaced far enough apart for the factor d/x to be small enough for the whole of the second term in equation (4.5) to be neglected. The models were also manufactured to such a standard that the errors due to roughness at the edge of the tappings and those due to manufacturing inaccuracy can also be assumed negligible. Equation (4.5) can then be reduced to the following relation:

$$dC_{p_\delta} = \frac{B}{\sqrt{M_L^2-1}}\left(\frac{d}{\delta^*}\right) \tag{4.6}$$

The total error in static pressure due an individual pressure tapping's interference on the external flow can be assumed to be the addition of the contribution due to the boundary layer and that due to the local pressure gradient. The equation for the magnitude of the maximum total error is thus:

$$dC_p = 0.37d\left(\frac{\partial p}{\partial s}\right) + \frac{B}{\sqrt{M_L^2-1}}\left(\frac{d}{\delta^*}\right) \tag{4.7}$$

This technique can now be employed in the investigation of the supersonic vortical aerodynamics about inclined slender bodies, and the assessment of the flow solvers employed.

4.3 Numerical Investigation of Forebody Aerodynamics

In this section a systematic numercial study of high speed flows past slender ogive-cylinder bodies is presented. Nine nine experimental test cases were computed, spanning Mach numbers from 0.7-2.5, angle of attacks from 0^o to 16^o and Reynolds numbers from 0.16×10^6 to 8.0×10^6 based on body diameter. The following table lists the nine cases and the corresponding geometric and aerodynamic properties.

Table 4.1: Experimental Test Cases

Case	Ogive l/d	M_∞	Re/D	α^o	Flow Condition
1	3.0 (B1)	2.0	0.16×10^6	0	Laminar
2	3.0 (B1)	2.0	0.16×10^6	10	Laminar
3	3.0 (B2)	2.0	1.2×10^6	0	Turbulent
4	3.0 (B2)	2.0	1.2×10^6	10	Turbulent
5	3.0 (B1A)	2.5	1.123×10^6	14	Turbulent
6	3.0 (B1A)	2.5	1.123×10^6	8	Turbulent
7	3.0 (B1A)	1.8	0.667×10^6	14	Turbulent
8	3.0 (B1A)	0.7	0.667×10^6	14	Turbulent
9	3.5	1.4	8.0×10^6	16	Turbulent

Flow physics are discussed along with comparisons with experimental data and an estimation of the error in measurement of surface pressure in order to give a better indication of the performance of a given solver or turbulence model. In particular the appearance of additional windward shocks for certain flow conditions will be investigated leading to a new interpretation of the supersonic flow past ogive-cylinder bodies. The following sections present the details of the experimental data, the numerical studies and the results and comparisons.

4.3.1 The ONERA Experimental Test Cases: Cases 1-4

The following test cases were those studied as the first stage of the European GARTEUR Action Group 24 exercise which correspond to the series of wind tunnel experiments performed for tangent-ogive forebodies at ONERA.

The laminar and turbulent flow fields were computed using the Cranfield Reynolds Averaged Navier-Stokes Three Dimensional solver ($CRANS3D$) and the PNS solver developed by Qin, Ludlow and Shaw [61] [53]. The results were compared with the experimental flow field and surface pressures, and the boundary layer traverse measurements.

The experimental database [5] was provided by Patrick Champigny of the Office National d'Études et de Recherches Aérospatiales (ONERA).The laminar B1 test case was performed on the B1 geometry (Figure 4.10) at a freestream Mach number of 2.0 and a Reynolds number, based on body diameter, of 0.16×10^6. An adiabatic wall boundary condition was assumed, which is consistent with the run time of the experiment. Surface pressures were measured for angle of attacks of both 0 and 10^o. In addition, crossflow total pressure ratio, Mach number and velocity components were measured for 10^o angle of attack, at crossflow planes $x/D = 6, 7$ and 8.

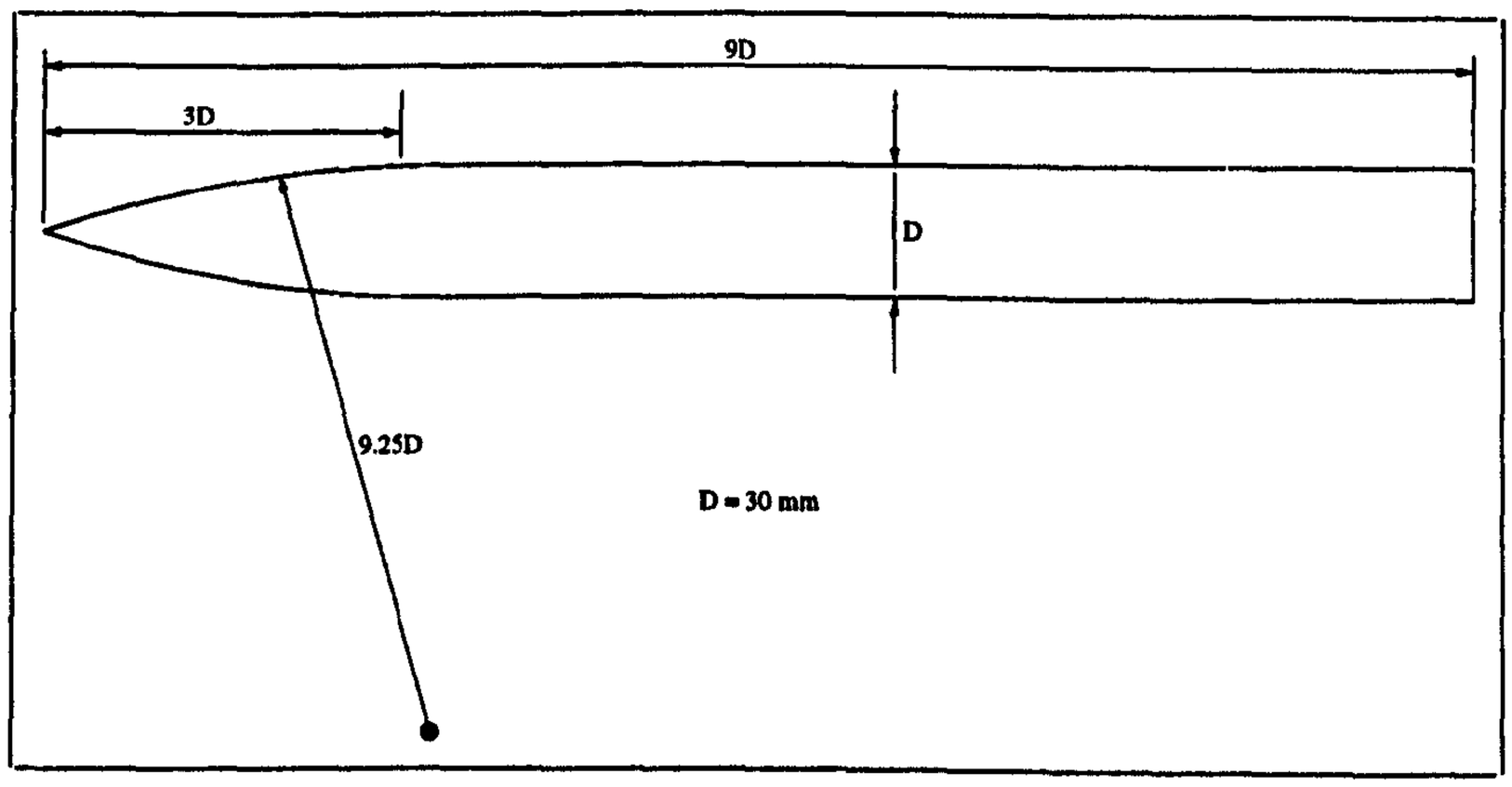

Figure 4.10: *ONERA-B1 Tangent-Ogive Body Geometry*

The B2 geometry (Figure 4.11) was tested at a freestream Mach number of 2.0 and a Reynolds number, based on body diameter, of 1.2×10^6. The freestream stagnation pressure and temperature were 120 kPa and 300K respectively. The wall temperature was measured as approximately 285K, but as with the laminar case, the simulations were performed with an adiabatic wall boundary condition. The turbulent flow in these 0 and 10^o angle of attack test cases was achieved by fixing transition at $x/D = 0.15$. Measurements were made of surface pressures for both angle of attacks. For zero angle of attack the Mach number and total pressure ratio was measured within the boundary layer at stations $x/D = 3, 5, 7, 9$ and 12. For the 10^o angle of attack case, surface pressures were measured axially for ϕ of $0, 90$ and 180^o, and circumferentially at $x/D = 5, 7$ and 9. Crossflow total pressure ratio, Mach number and local angle of attack were also measured at the same axial stations together with the corresponding Mach number and total pressure ratio profiles within the separated shear layer and boundary layer for $\phi = 90, 120, 135, 152.5$ and 180^o.

The experimental accuracy for the B1 study was determined from a repeatability assessment. The freestream conditions are quoted with the following accuracy. $\Delta M = \pm 0.01$, $\Delta P = \pm 30Pa$ within the range 2-$50kPa$

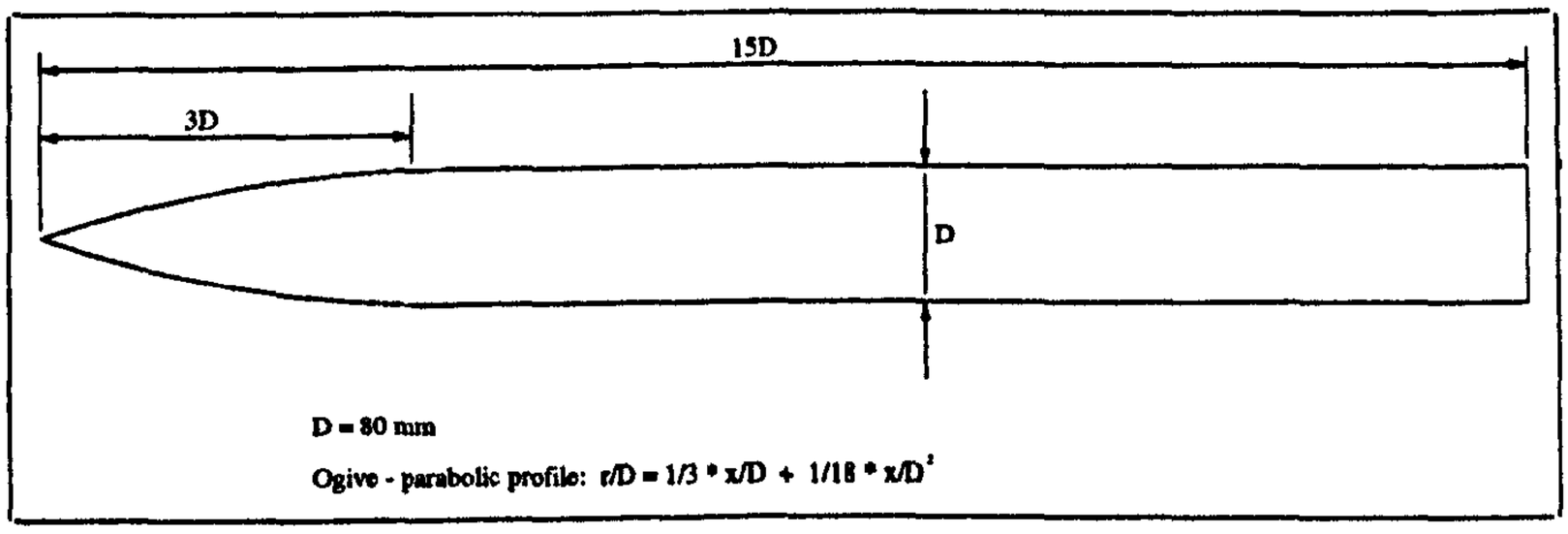

Figure 4.11: *ONERA-B2 Tangent-Ogive Body Geometry*

and $\Delta\alpha = \pm 0.1^o$. The five hole pressure probe used for the flow field measurements was calibrated with the following accuracy: $\Delta M = \pm 0.02$, $\Delta P = \pm 30Pa$ within the range 2-$50kPa$, $\Delta\alpha = \pm 0.2^o$. The accuracy of the traverse mechanism was quoted as $\Delta x, \Delta y, \Delta z = 0.2$ mm. Barberis [5] states that the various properties were measured with an accuracy of 2-3 % in regions where gradients were moderate, but at 5-10 % in the core of the more intense vortices where the gradients are much higher. Similar experimental accuracy can be expected for the turbulent B2 study

The four test cases were computed with the time marching approach of the *CRANS3D* code and the space marching approach utilized by the PNS code. Both codes were run using the same computational grids in order to assess the accuracy and efficiency of the respective formulations. Various grids were employed in the study, from the coarsest ($33 \times 33 \times 33$) to the finest ($89 \times 89 \times 119$) grid. Figure 4.12 presents the ($61 \times 85 \times 45$) grid used for the laminar B1 zero angle of attack test case, while Figure 4.13 shows the finer ($61 \times 85 \times 73$) grid used for the B1 10° case. The grids for the B1 test cases were designed with the near wall cell size in the radial direction set to $2 \times 10^{-4} D$ such that the value of y^+ was of the order of 1.0. Similarly the B2 grids were designed for y^+ of around 1.0, which required a near wall cell of $0.5 \times 10^{-5} D$ radial thickness in order to resolve the laminar sublayer. The radial clustering was achieved using a *tanh* function which placed between 20-40 points in the boundary layer on the finest grid.

The Navier-Stokes solutions were used in the estimation of the flow gradients required in the calculation of the magnitude of the error in the measured C_p presented in Section 4.2. The following sections present the numerical results for the Garteur test cases together with the analysis of the error in the measured C_p

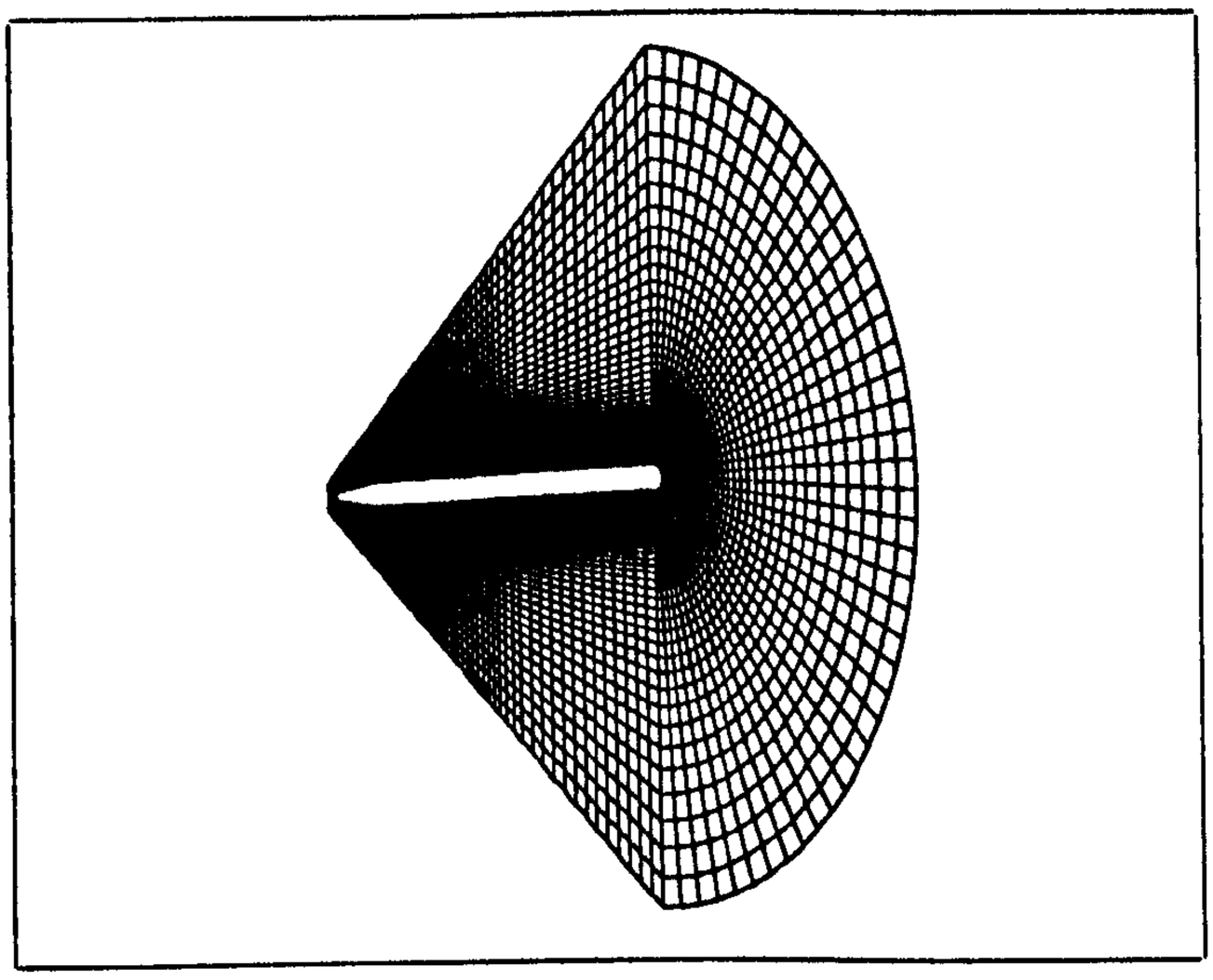

Figure 4.12: *B1 Computational Grid for Zero angle of attack (61 × 85 × 45)*

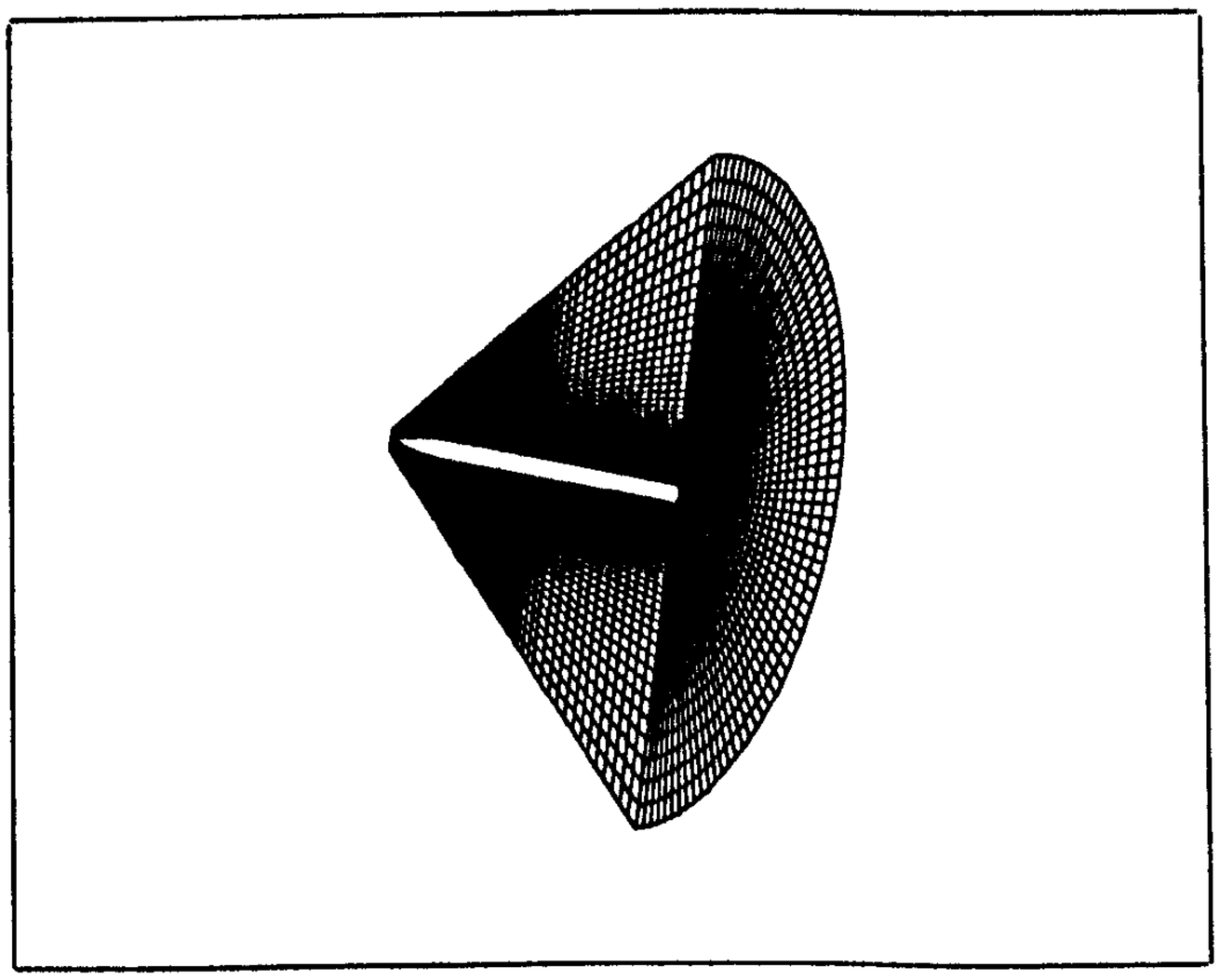

Figure 4.13: *B1 Computational Grid for* 10^{o} *angle of attack (61 × 85 × 75)*

Case 1: B1 Forebody, Mach 2, Zero Angle of Attack

Both Navier-Stokes and Euler Solutions for this case were obtained on a viscous grid (61 × 85 × 45) and an Euler grid (61 × 54 × 45). For both this case and case 2, only laminar solutions were computed as the experiments were performed under laminar conditions. The comparison between the CRANS3D Navier-Stokes solution for the axial surface pressure distribution, on the viscous grid, and the corresponding experimental measurements is shown in Figure 4.14 together with the estimated experimental static pressure error. Little difference was observed between the surface pressure distribution of the four solutions. The residual convergence for the finest grid calculation is presented in Figures 4.15, the solutions eventually converging to almost 4 orders after 8000 iterations.

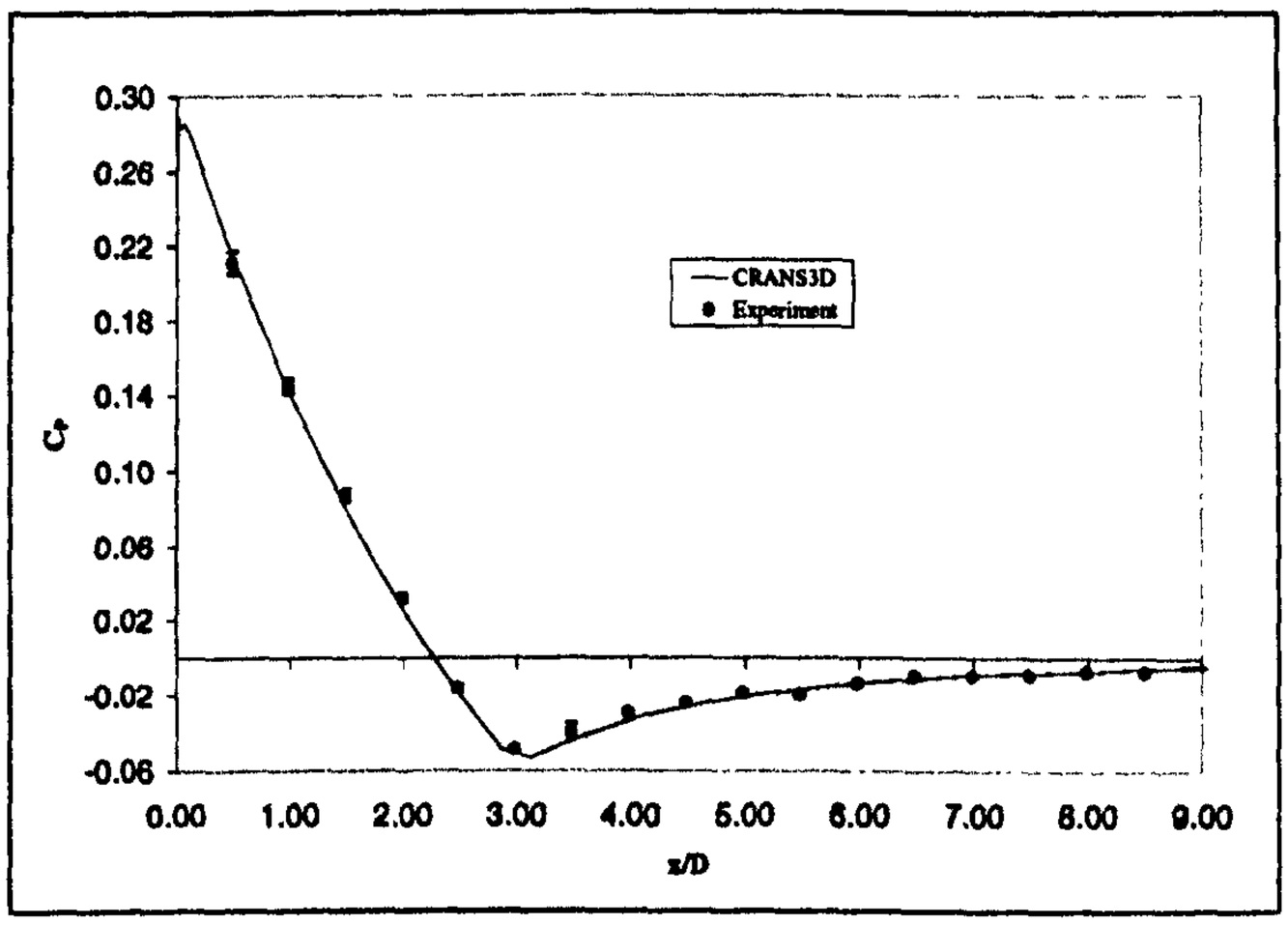

Figure 4.14: *Axial Surface Pressure Distribution: B1, 0° angle of attack*

The inviscid surface pressure distribution matched the viscous distribution exactly. From Figure 4.14 it can be seen that the experimental measurement error in surface C_p is larger on the ogive nose than on the cylinder afterbody further downstream. This is because the boundary layer displacement thickness is smaller over the nose and the local streamwise pressure gradients are larger. Both factors contribute to the measurement error associated with surface pressure holes.

Both the Euler and Navier-Stokes (NS) solutions for the surface pressure were consistently within the bounds of the estimated experimental error. The NS solution will provide accurate predictions of the axial force distribution and drag coefficient, while the Euler solution will provide only the components due to pressure alone. PNS computations performed by Shaw and Qin [61] produced solutions equivalent to the NS results but with far greater efficiency.

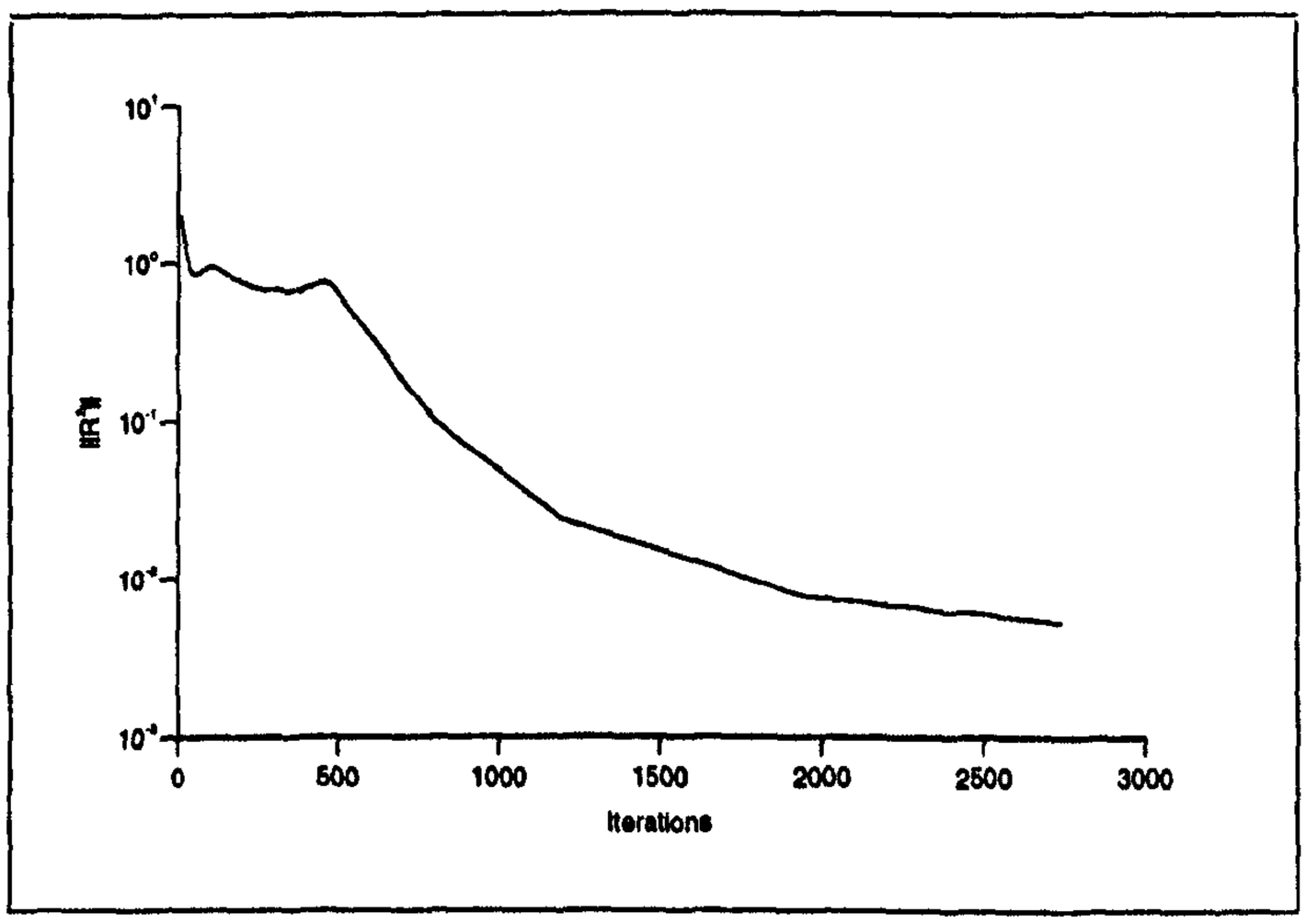

Figure 4.15: *Residual Convergence with Respect to Iteration Number: B1, 0° angle of attack, CFL=0.15*

Case 2: B1 Forebody, Mach 2, 10° Angle of Attack

Six grid sizes were used for the study of testcase 2, the coarsest being $(33 \times 33 \times 33)$ and the finest $(89 \times 89 \times 119)$. Figure 4.16 presents the circumferential surface pressure distributions at $x/D = 8$ on five successively coarser grids. The windward surface pressure distribution changes little on grids finer than $(60 \times 70 \times 73)$, but the leeside surface pressure distributions, affected strongly by the resolution of primary separation and the leeside vortical flow structure, continued to differ until the solutions on the two finest grids $(60 \times 85 \times 119)$ and $(89 \times 89 \times 119)$ were practically the same. Grid converged results could then be said to be achieved on the second finest grid, and that the solution accuracy is sensitive to the resolution of the crossflow. All following solutions are those on the finest grid.

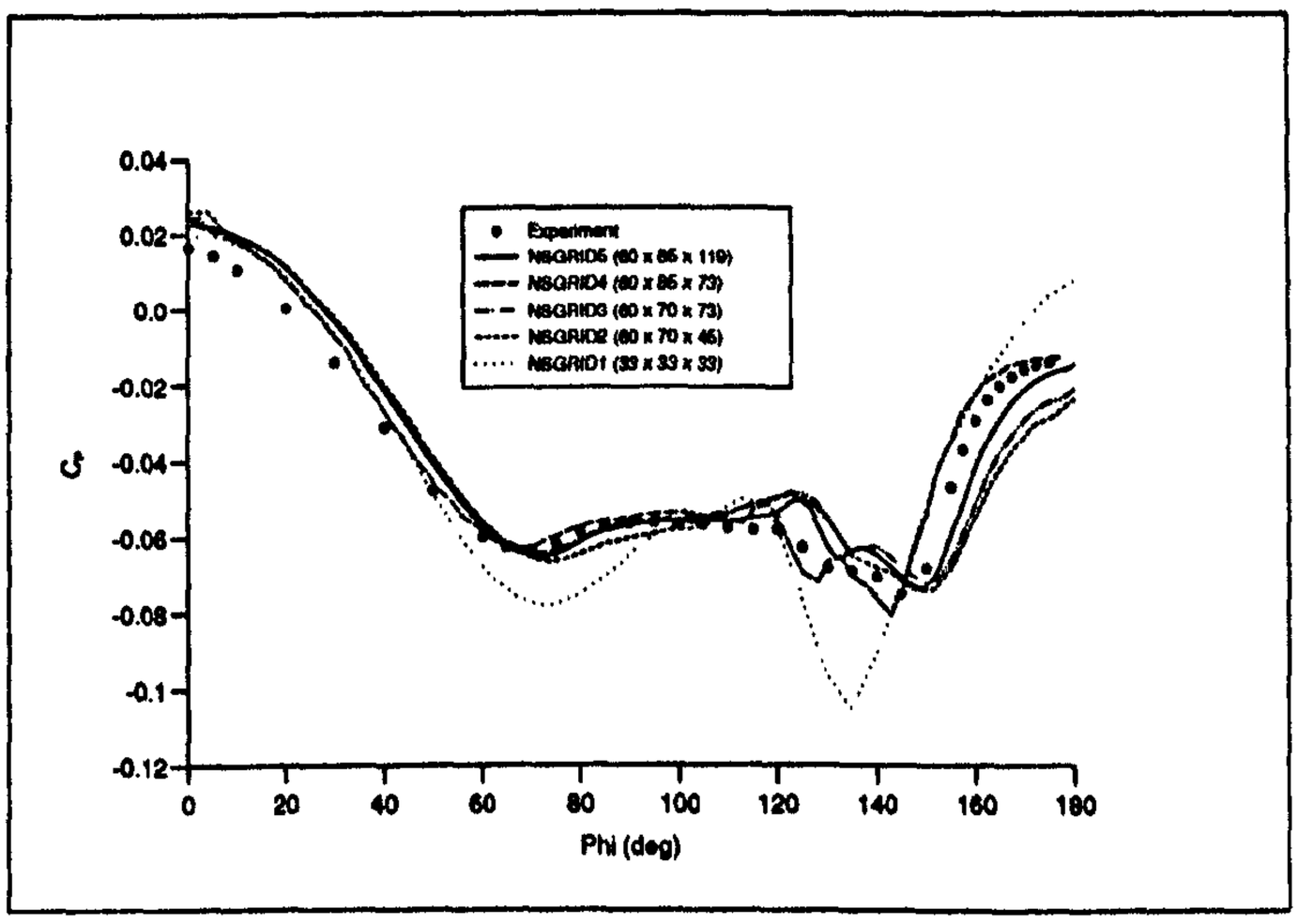

Figure 4.16: *Grid Convergence Study: B1, 10° angle of attack*

The axial pressure distribution comparisons between CRANS3D and experiment are presented in Figure 4.17 for $\phi = 0, 90$ and $180°$. The predicted pressure distributions are seen to agree well with experiment.

A more rigorous test of physical accuracy is comparison of computed and experimental circumferential surface pressure distribution. Figure 4.18 presents the circumferential surface pressure comparisons between experiment, PNS and NS solutions at stations $x/D = 6, 7$ and 8.

Both CRANS3D and the PNS solver successfully predicted the general trends in the surface pressure including primary separation at around $\phi = 70°$ followed by the pressure plateau indicative of separated flow, the primary and secondary vortex suction peaks between $\phi = 130 - 150°$ and the subsequent recompression associated with leeward reattachment at $\phi = 180°$. Significant differences between NS and PNS solutions exist in the

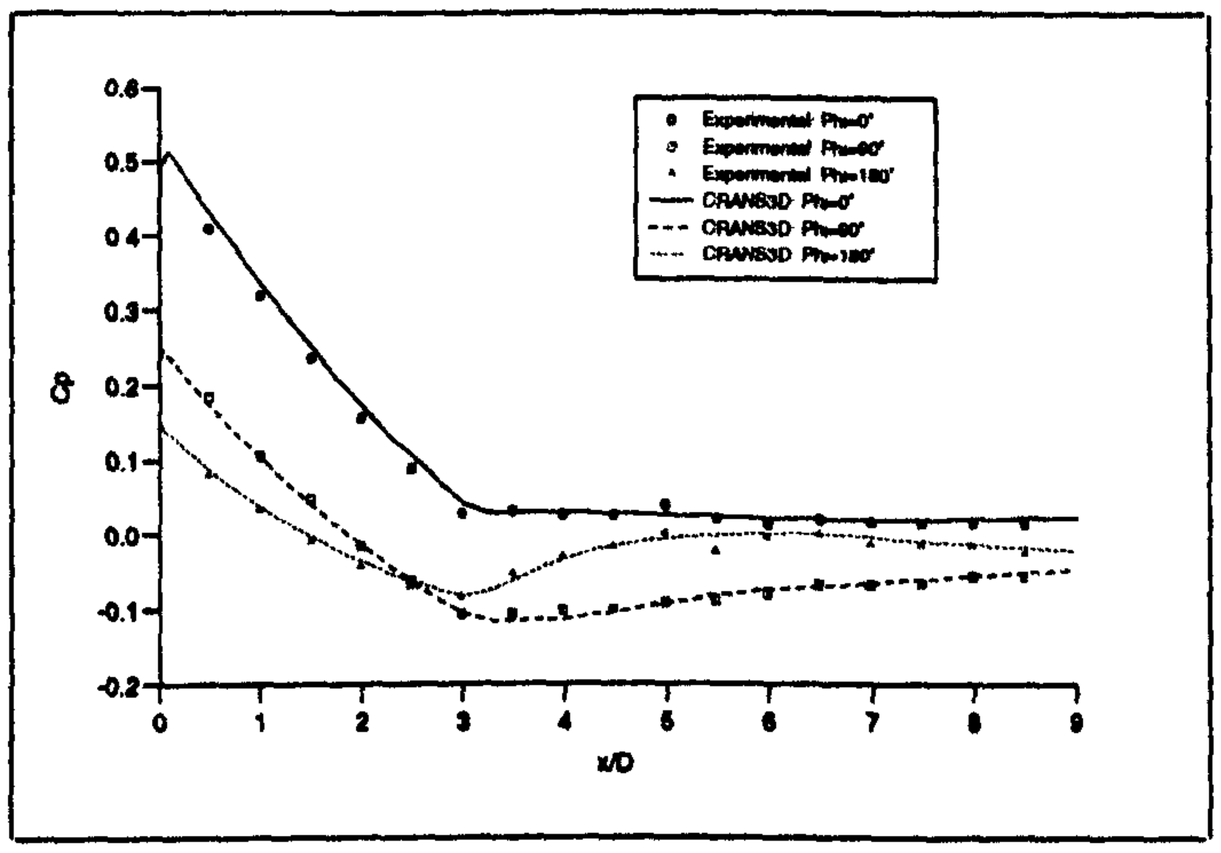

Figure 4.17: *Axial Surface Pressure Distribution: B1,* 10° *angle of attack*

resolution of the magnitude of the pressure at primary separation and across the pressure plateau where the PNS curve is higher by around $\Delta C_p \approx 0.01$. The solutions agree much better on the windward surface and in the resolution of the vortex suctions and leeward recompression.

Comparison between the experimental measurements and the numerical solution shows that the NS solver performs only marginally better than the PNS solver, specifically with the prediction of the pressure plateau between $\phi = 70 - 120°$. In order to assess the accuracy of the CFD solvers properly, however, one must have an appreciation of the magnitude of the error in the experimental measurements. The error in the measurement of surface pressure by the use of pressure tappings was assessed using the technique presented in Section 4.2. The boundary layer displacement thickness was obtained from the CRANS3D solution since no experimental information was available. The local surface streamwise pressure gradient (ie: the surface pressure gradient aligned with the local surface skin friction vector) was also computed from the CRANS3D solution. The details of the methods used to calculate these parameters from the NS solution are presented in Appendix B. Figure 4.19 and 4.20 present the circumferential distributions of the computed displacement thickness and local surface streamwise pressure gradient at $x/D = 6$. Figure 4.21 then shows the resulting estimate of the circumferential distribution of the measurement error in surface C_p at the same axial station. The estimated contribution to the measurement error due to the effect of the local streamwise pressure gradient across the pressure hole was found to be much smaller than that due to the local size of the boundary layer. The estimated error is largest close to secondary separation where the displacement thickness is smallest and the local surface streamwise pressure gradient is greatest.

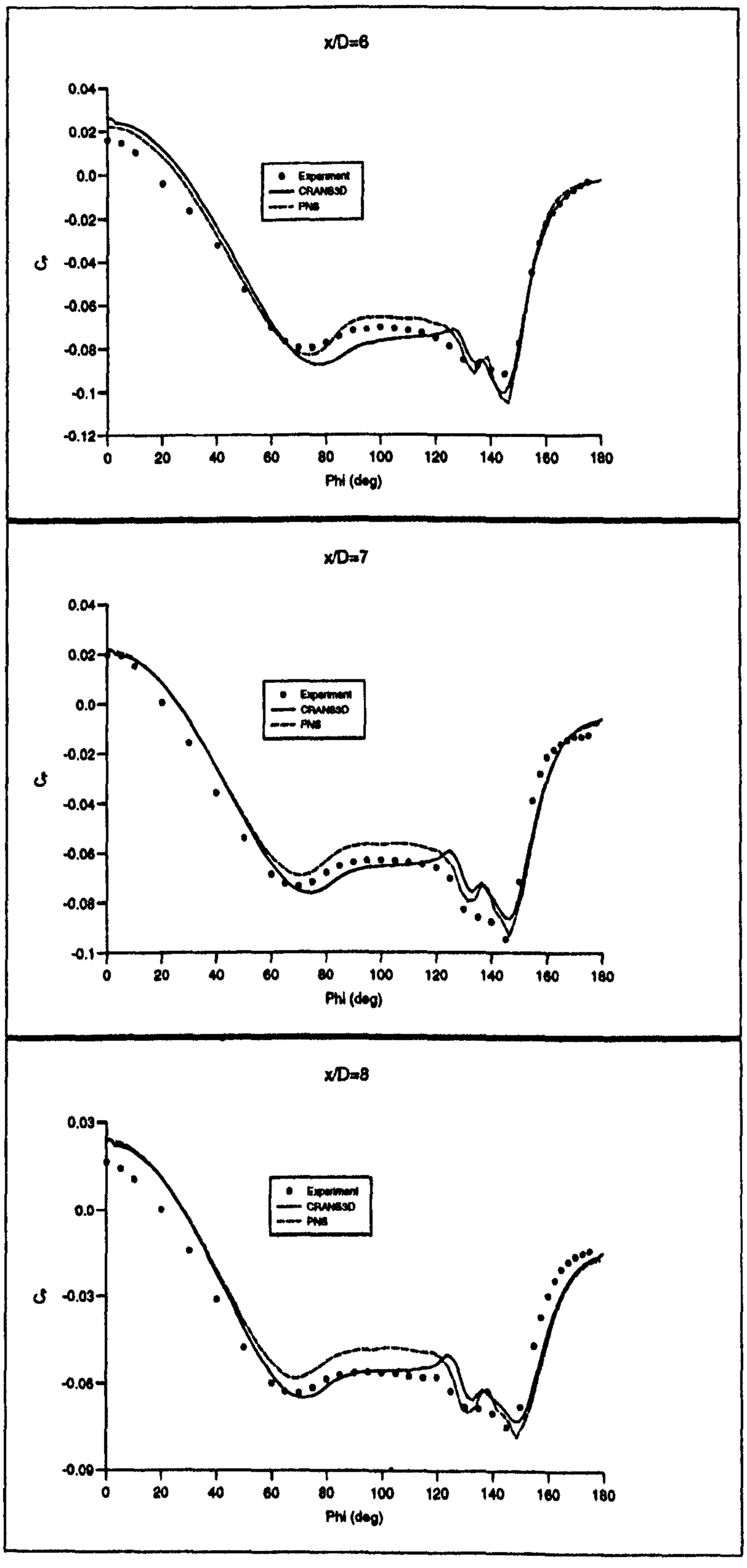

Figure 4.18: *Circumferential Surface Pressure Distribution: B1,* 10° *angle of attack*

Figure 4.22 shows the comparison of the CRANS3D pressure distributions at the three axial stations with the corresponding experimental measurements together with the estimated error bars. Over the length of the forebody from $x/D = 6 - 8$ it can be said that the size of the estimated C_p measurement error is smaller than expected, with significant regions of the computed C_p curves lying outside the experimental error boundaries. Two further computations were performed at angle of attacks of 9.9° and 10.1°. It was found that the small changes in angle of attack significantly changed the computed surface pressures such that the agreement with experiment in the leeward regions was much worse than for the 10° result. From this it can be concluded that it is unlikely that there was significant error in the angle of attack measurement influencing the data.

One source of experimental error that might contribute to this anomaly was the slight mismeasurement of the circumferential angle ϕ which appeared to have occured during the experiments. Exactly how much the measurement of ϕ was in error, is not known, but a correction to the data was applied when comparing with the computational results by simply moving the data points back by $\phi = -2°$. It is suggested that this source of inaccuracy is a major contributing factor to the observed discrepancy. Another effect which will contribute to the mismatch between computation and experiment is that of transition. Even without the nose grit used to trip a turbulent boundary layer, the Reynolds number of 0.16 million per D is high enough, and the model long enough, for the possibility of transition to occur far down the afterbody, in the region of the three measurement stations. With the lack of any boundary layer measurements for this case, however, no judgements can be made as to whether transition did occur during the experiments.

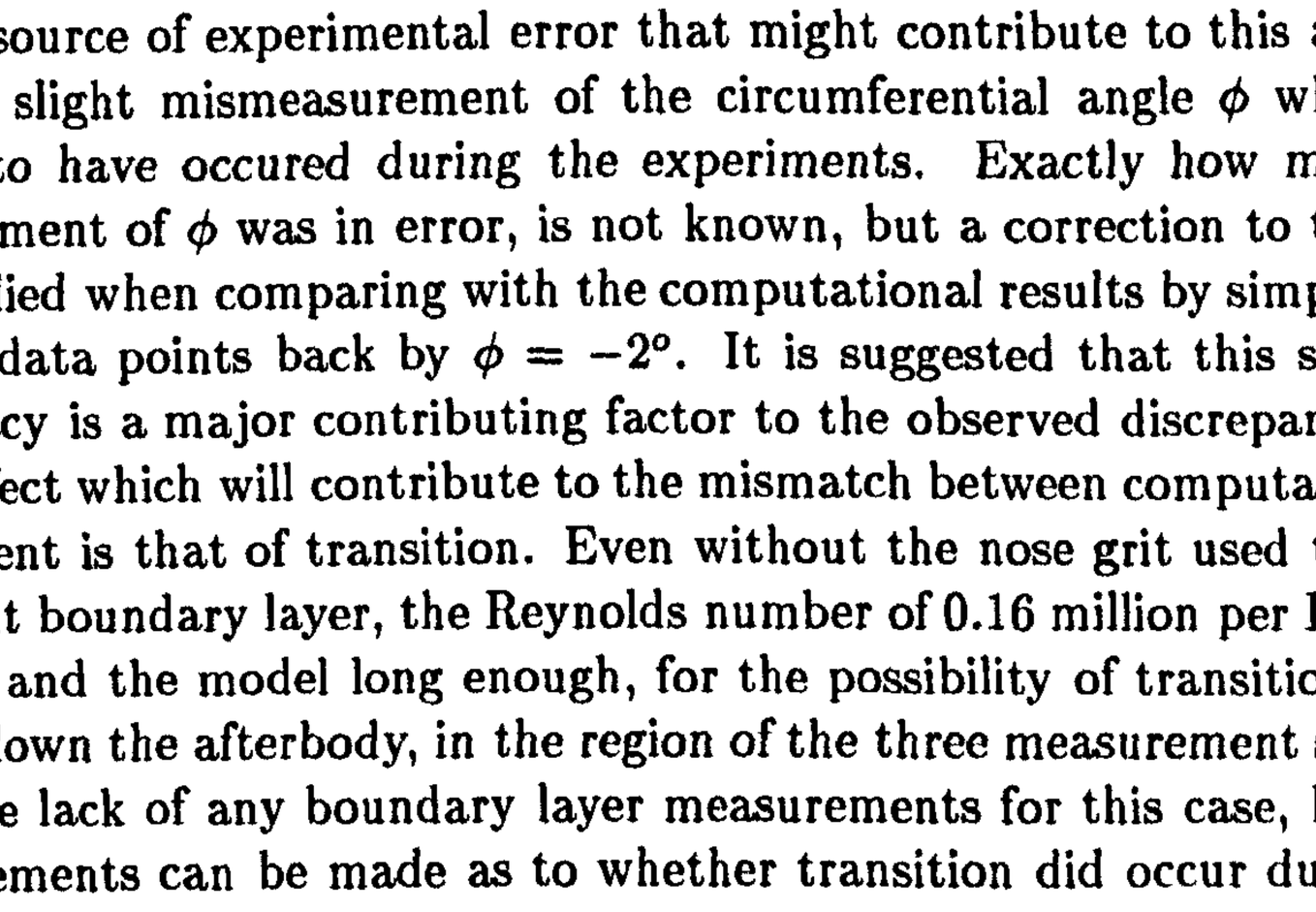

Figure 4.19: *Displacement Thickness: B1,* 10° *angle of attack, x/D=6*

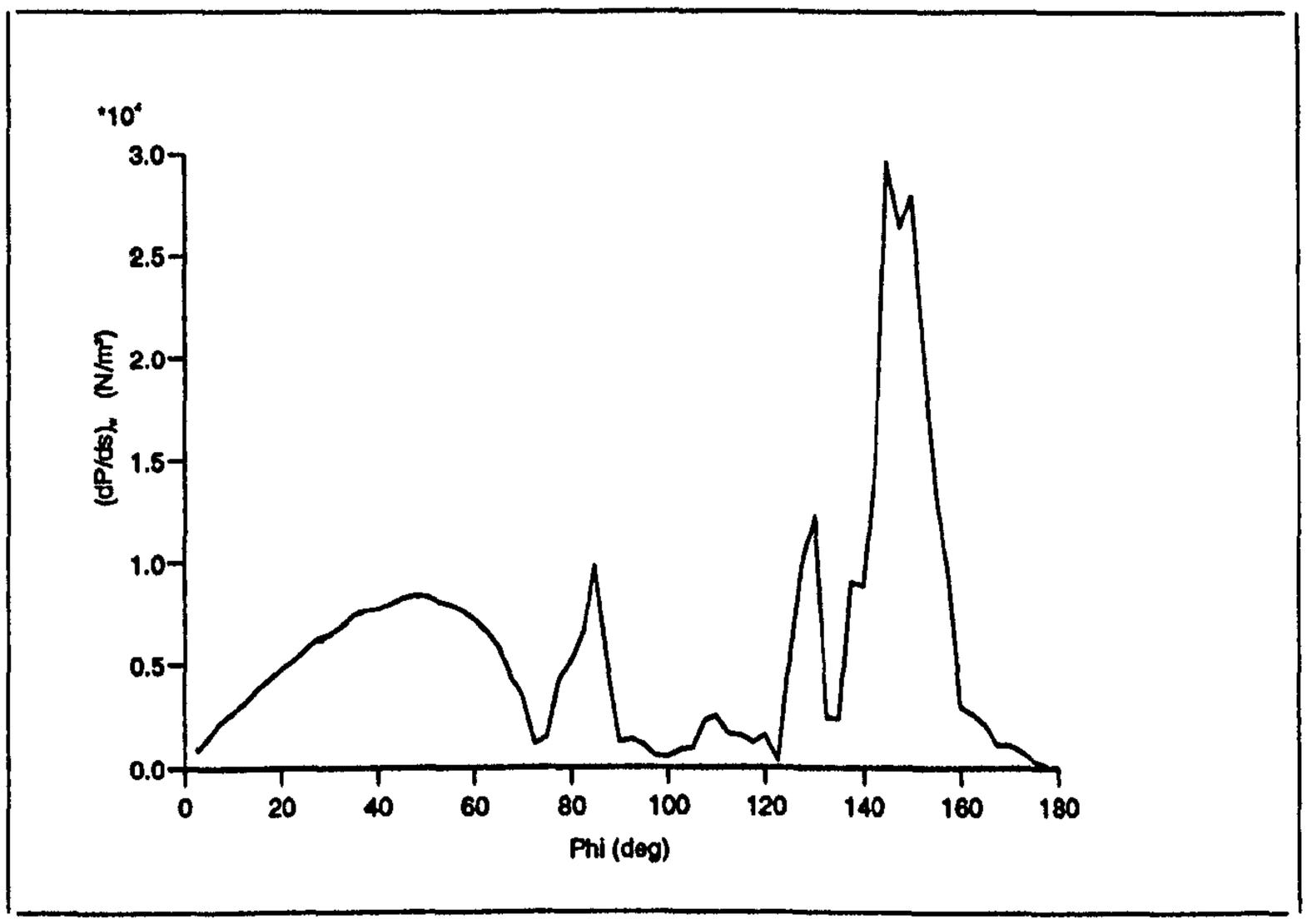

Figure 4.20: *Surface Pressure Gradient: B1,* 10° *angle of attack, x/D=6*

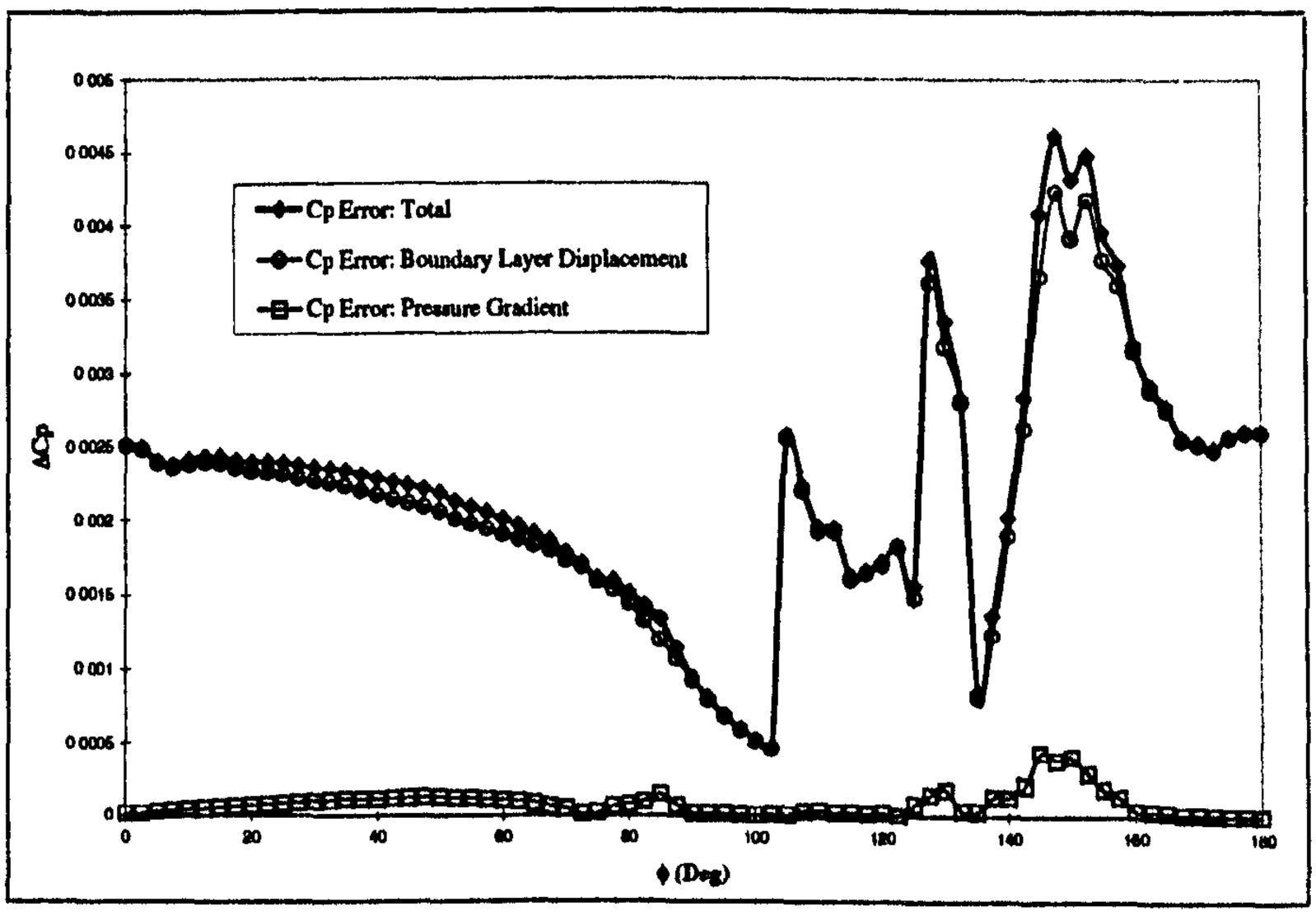

Figure 4.21: *Estimated Expermimental C_P Error Distribution: B1,* 10° *angle of attack, x/D=6*

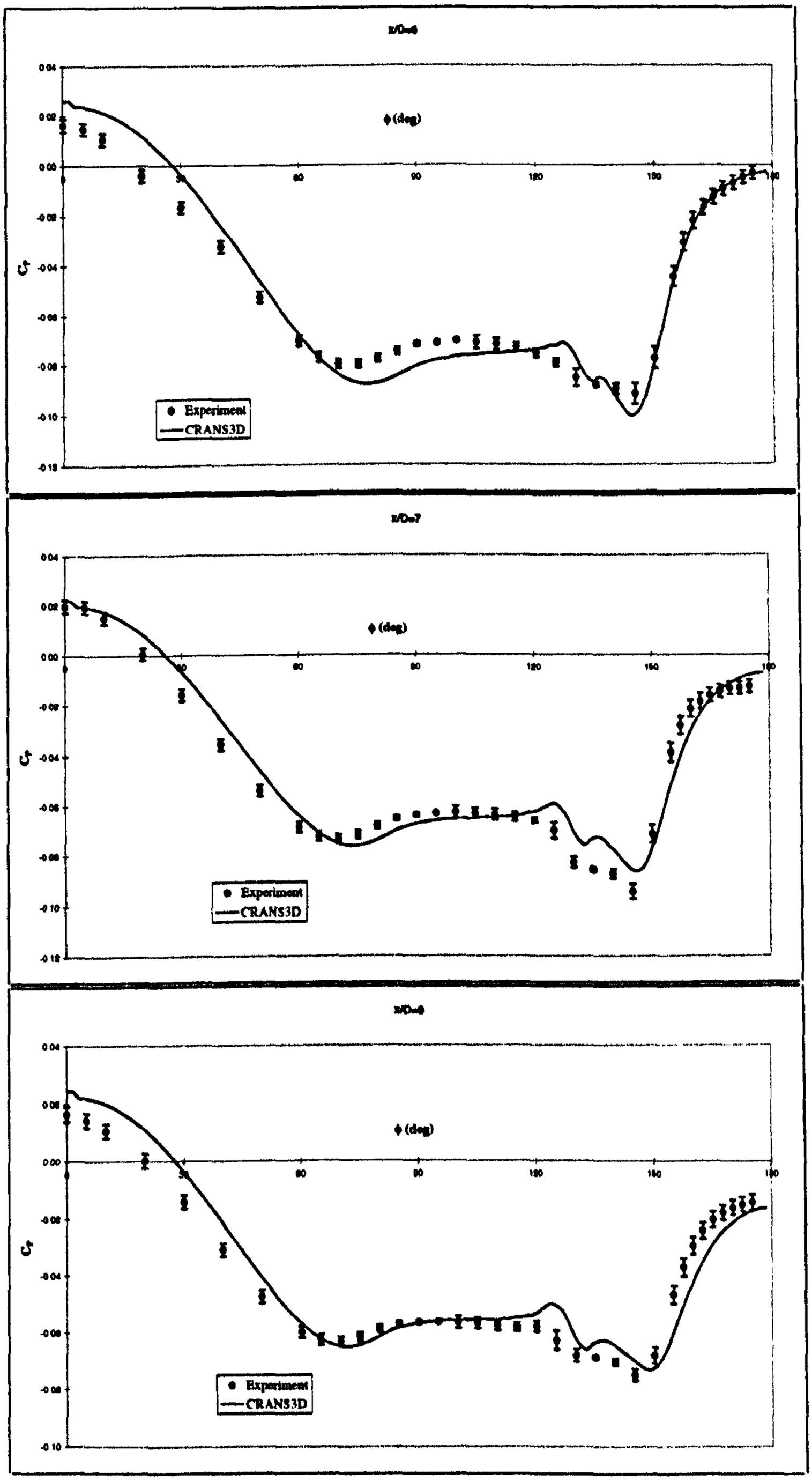

Figure 4.22: *Circumferential Surface Pressure, Estimated Experimental Error: B1,* 10°

Questions must also be asked concerning the validity of the procedure derived in Section 2.4 for estimating the experimental error associated with pressure tappings, when applied to slender bodies at angle of attack. Peto and Pugh [49] developed the relationship between d/δ^* (the ratio of the hole diameter with the boundary layer displacement thickness) used in the present analysis, based on experiments performed under laminar conditions. Comparisons were made between their data and that of other studies spanning Reynolds numbers from 1.7×10^4 [40] up to 77×10^6 [57]. Although the correlation did not appear to perform well when compared with Rainbird's turbulent experimental data, it was pointed out that the Reynolds number of Rainbirds test (77×10^6 based on cone length) was extremely large, and that because of the fairly strong dependence of laminar boundary layer skin friction coefficient on Reynolds number, the importance of boundary-layer state will usually not be large. The authors stated that the presence of a turbulent boundary layer increases the effect of a finite hole diameter, but even so, the errors are not large. If this is correct then the technique should be applicable for both laminar and turbulent boundary layers if the object is to identify a maximum possible error in the measurement of surface static pressure using pressure tappings.

Skin friction lines for both the NS and PNS solutions are presented in Figure 4.23. Little difference can be discerned between the two solutions, and both illustrate the primary and secondary separation lines on the cylindrical afterbody.

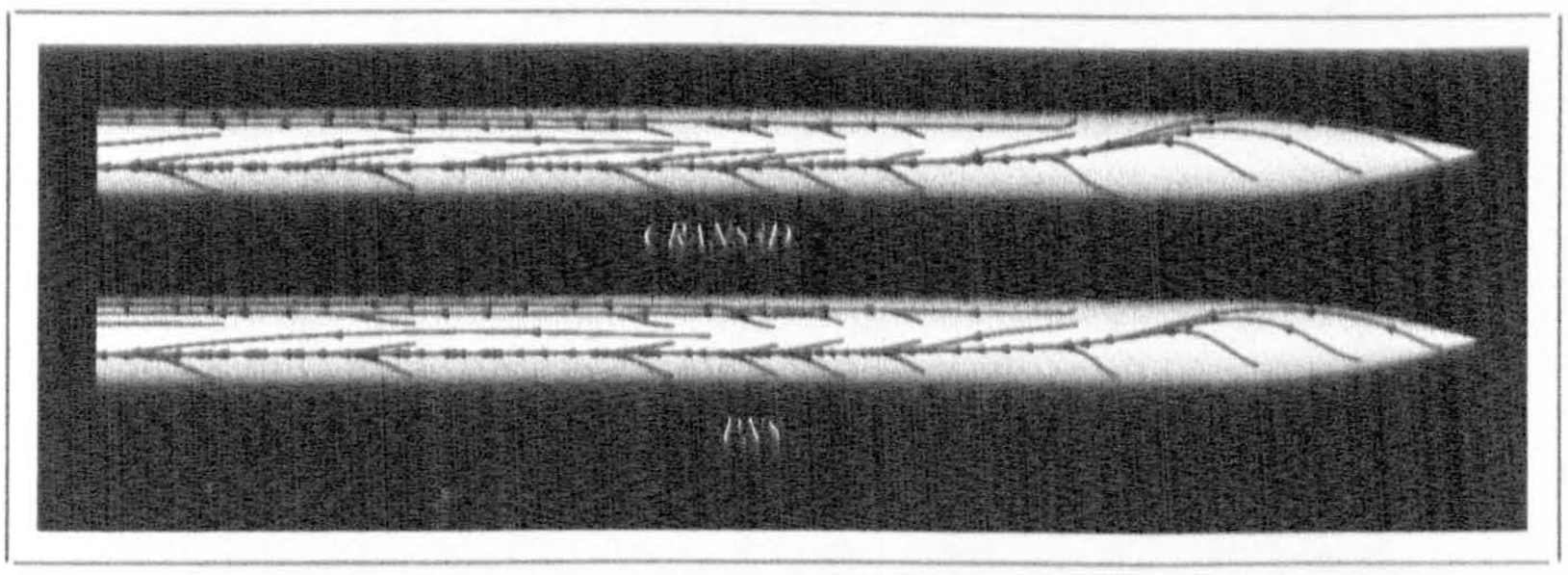

Figure 4.23: *Surface Skin Friction Comparison, B1* 10° *angle of attack*

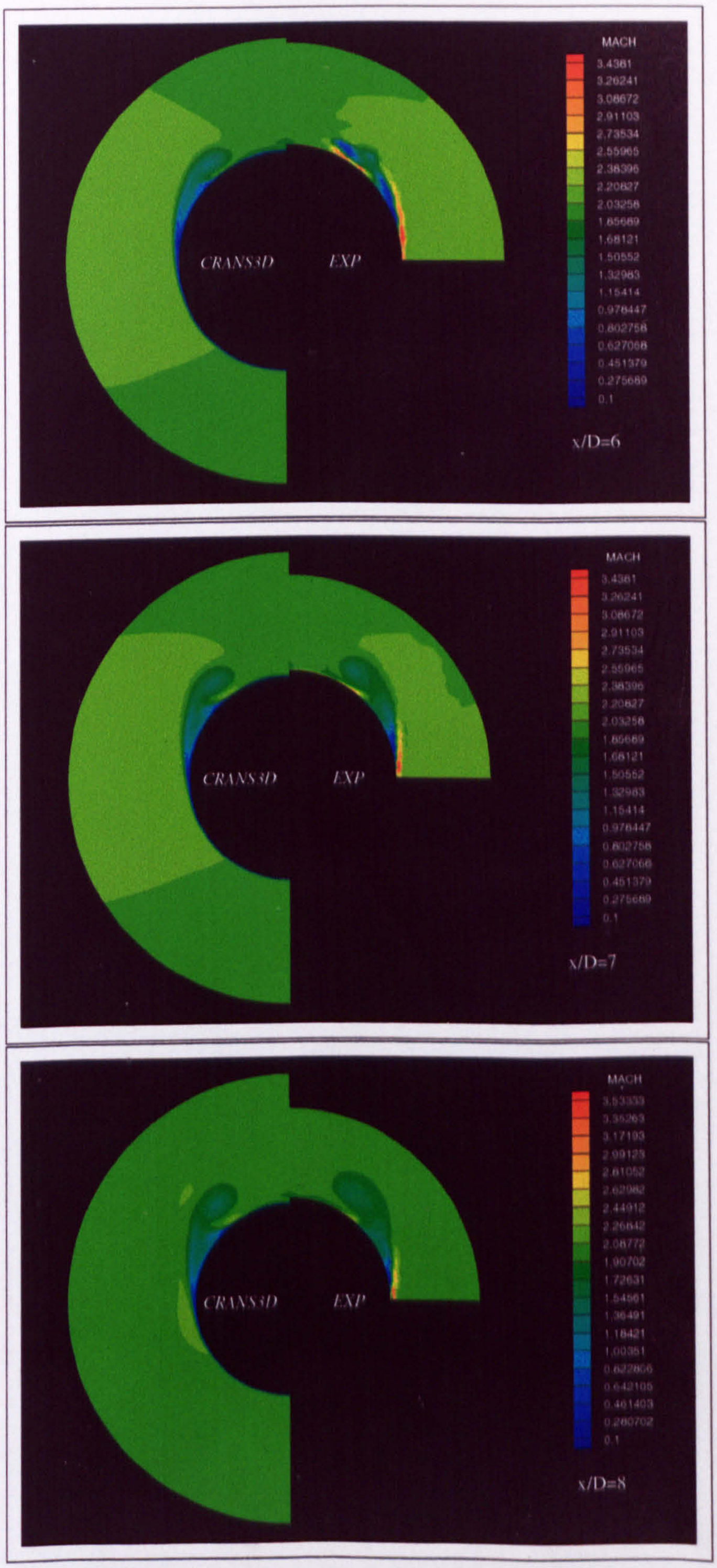

Figure 4.24: *Crossflow Plane Mach Number Contours, B1* 10° *angle of attack*

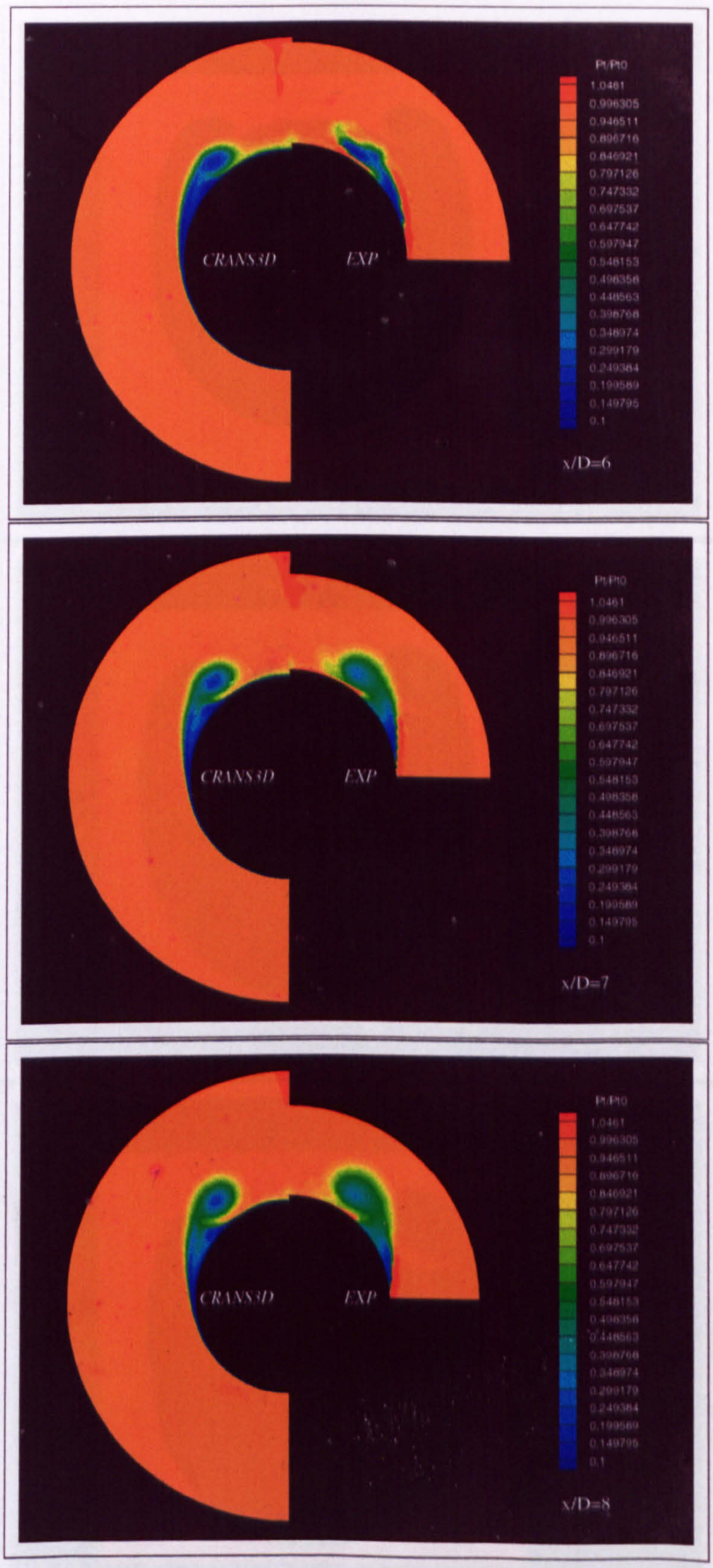

Figure 4.25: *Crossflow Plane Total Pressure Ratio Contours, B1* 10° *angle of attack*

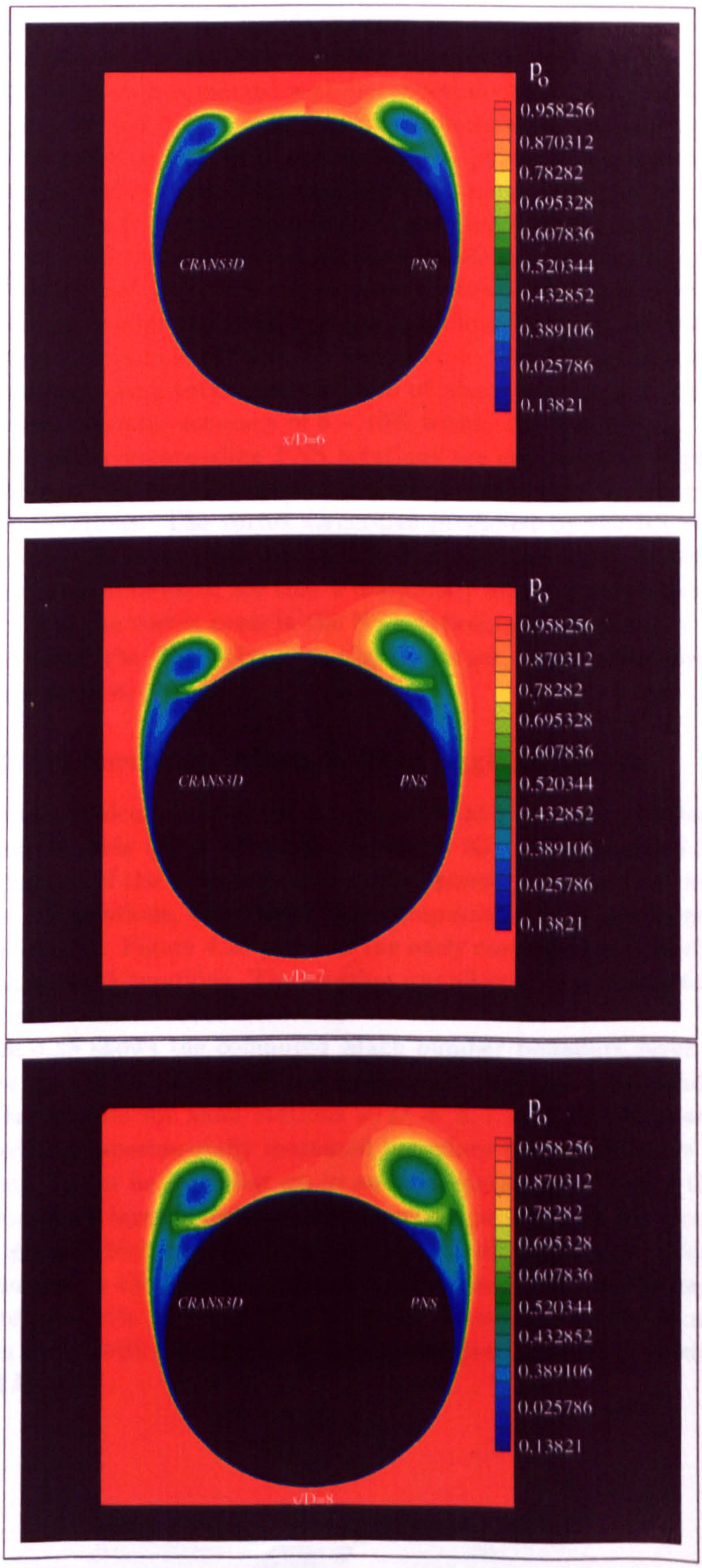

Figure 4.26: *Comparison CRANS3D vs PNS, Total Pressure Ratio, B1* 10^o *angle of attack*

The development of the leeside vortices are examined in Figures 4.24 - 4.26 which present the crossflow structure at stations $x/D = 6, 7$ and 8. The CRANS3D solution is compared with the experimentally measured crossflow in Figures 4.24 and 4.25. Note that the experimental measurements did not extend down to the body surface due to physical constraints of the pitot traverse mechanism. The crossflow plots comparing the NS and the experimental Mach number contours are presented in Figure 4.24 and show that the NS predicted primary vortex matches the experimentally measured primary vortex very well. The comparisons for the total pressure ratio given in Figure 4.25 exhibit the same agreement although the NS results resolve slightly lower suctions in the primary vortex core. The difference in this core suction amounts to a total pressure ratio of about 0.1 which is consistent with the experimental accuracy of $5 - 10\%$ within the vortex core.

The NS and corresponding PNS solutions are compared in Figure 4.26 which presents the crossflow plots for total pressure ratio contours at the three axial stations. The vortex structures predicted by the NS and PNS solvers, using the same grid, compare well at all three axial stations. The only discernible differences are that a marginally higher total pressure ratio is predicted in the vortex cores in the NS solution, and the primary vortices predicted using the PNS solver are slightly larger, and further away from the leeside surface.

Case 3: B2 Forebody, Mach 2, Zero angle of attack

The turbulent calculations of the B2 geometry at zero angle of attack were performed on grids ($61 \times 85 \times 45$) and ($61 \times 85 \times 73$). Figure 4.27 gives the comparison of the measured axial surface pressure distribution with that from the NS solutions, and shows that computation is in good agreement with experiment. Figure 4.28 presents the early convergence characteristics up to almost 3000 iterations. The solution was allowed to converge to almost 4 orders after almost 10000 iterations.

Figure 4.29 shows the computed Mach number boundary layer profiles predicted by CRANS3D which are contrasted with the corresponding experimental profiles for axial stations $x/D = 3, 7$ and 12. In general the computed and experimentally measured boundary layer profiles are in good agreement. It can be seen that up to an axial station of $x/D = 7$ the computed boundary layer follows the experimental profile with an accuracy of $\Delta M \approx \pm 0.05$ which equates to about $2 - 3\%$ of freestream. This figure corresponds with the experimental accuracy quoted at $2 - 3\%$ in regions of moderate gradients in the flow properties. At station 12 the comparison is not as good, with the Mach number is overpredicted by a maximum of about $\Delta M \approx 0.1$.

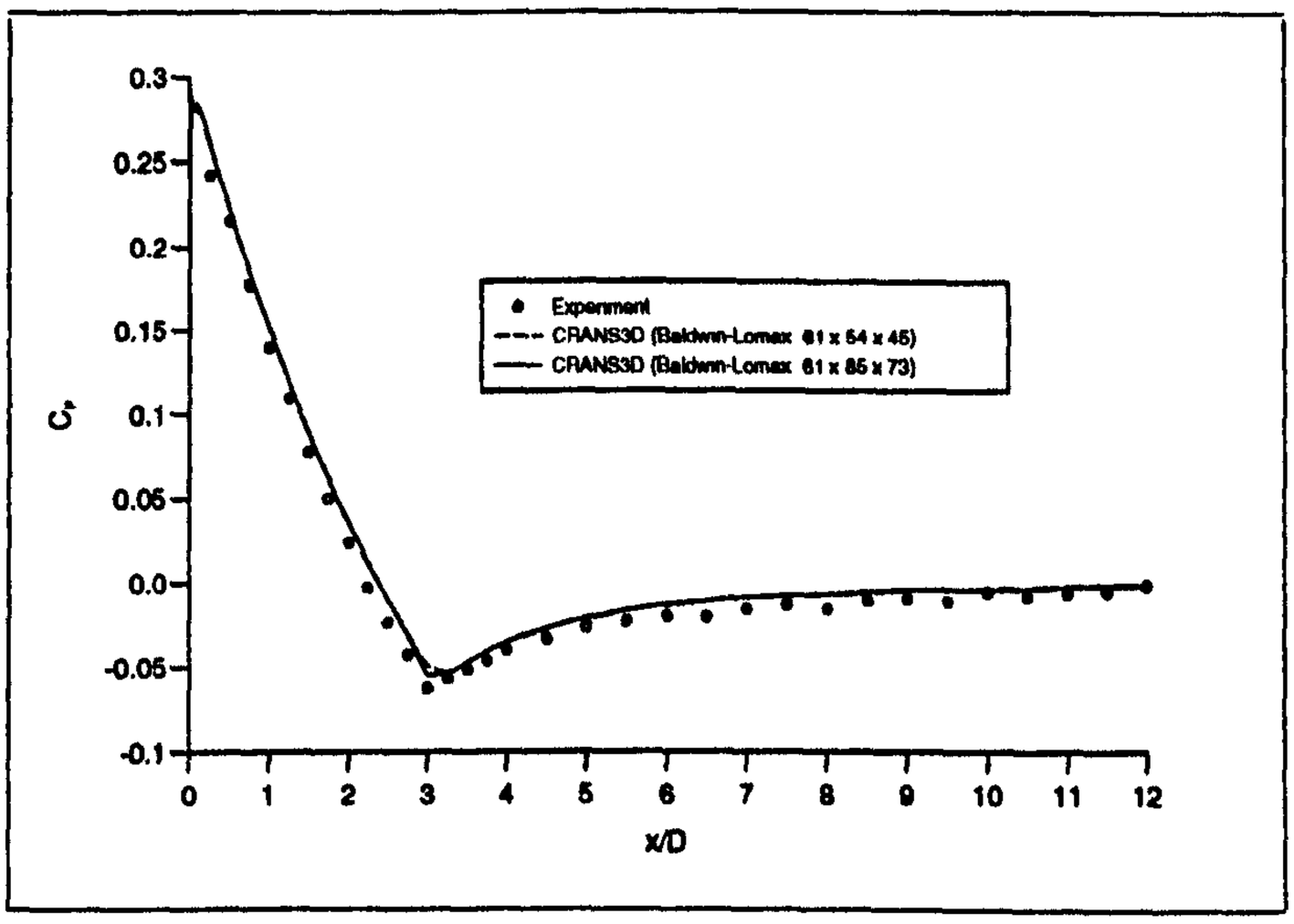

Figure 4.27: *Axial Surface Pressure Distribution: B2, 0° angle of attack*

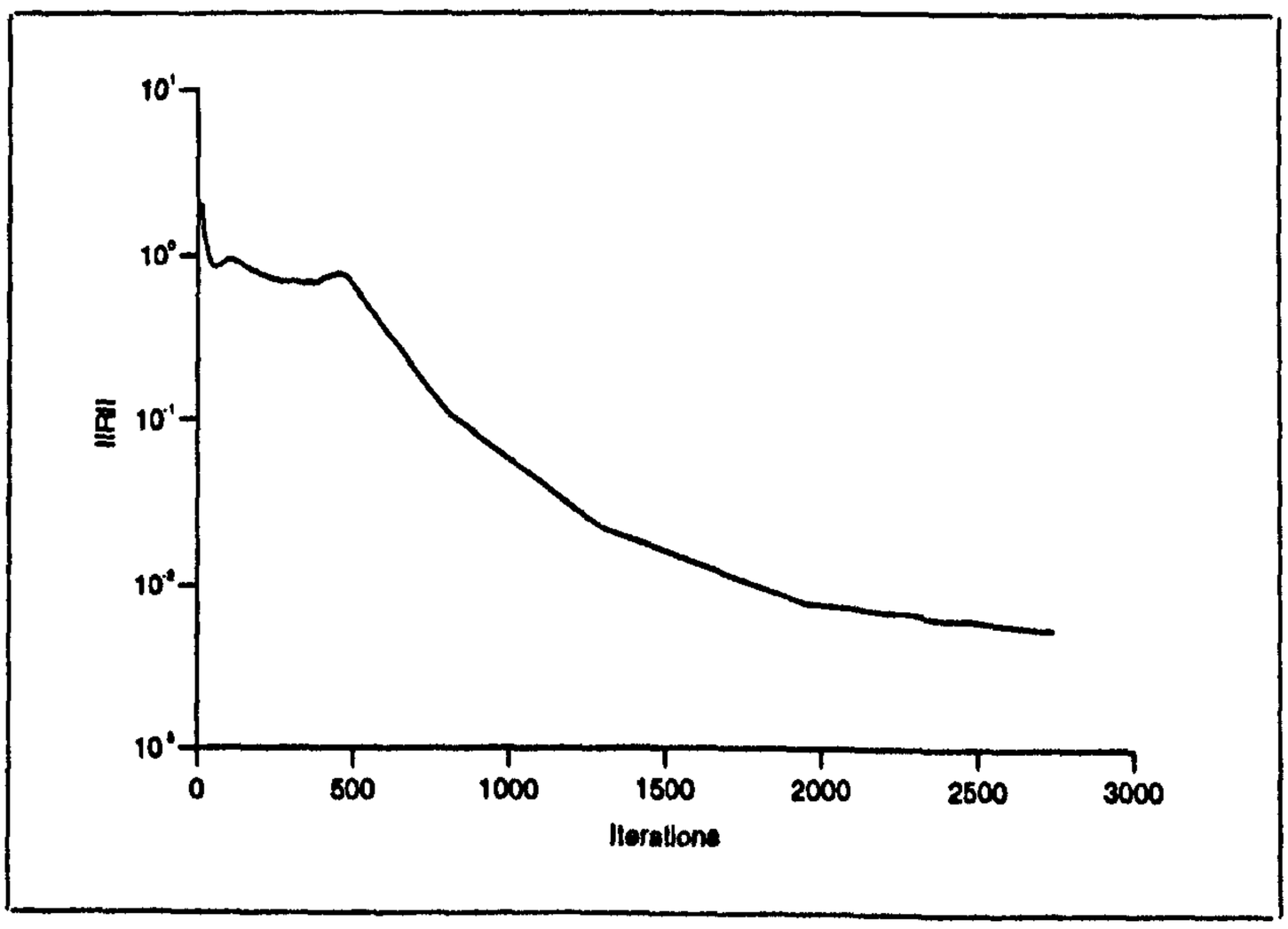

Figure 4.28: *Residual Convergence with Respect to Iteration Number: B2, 0° angle of attack, CFL=0.15*

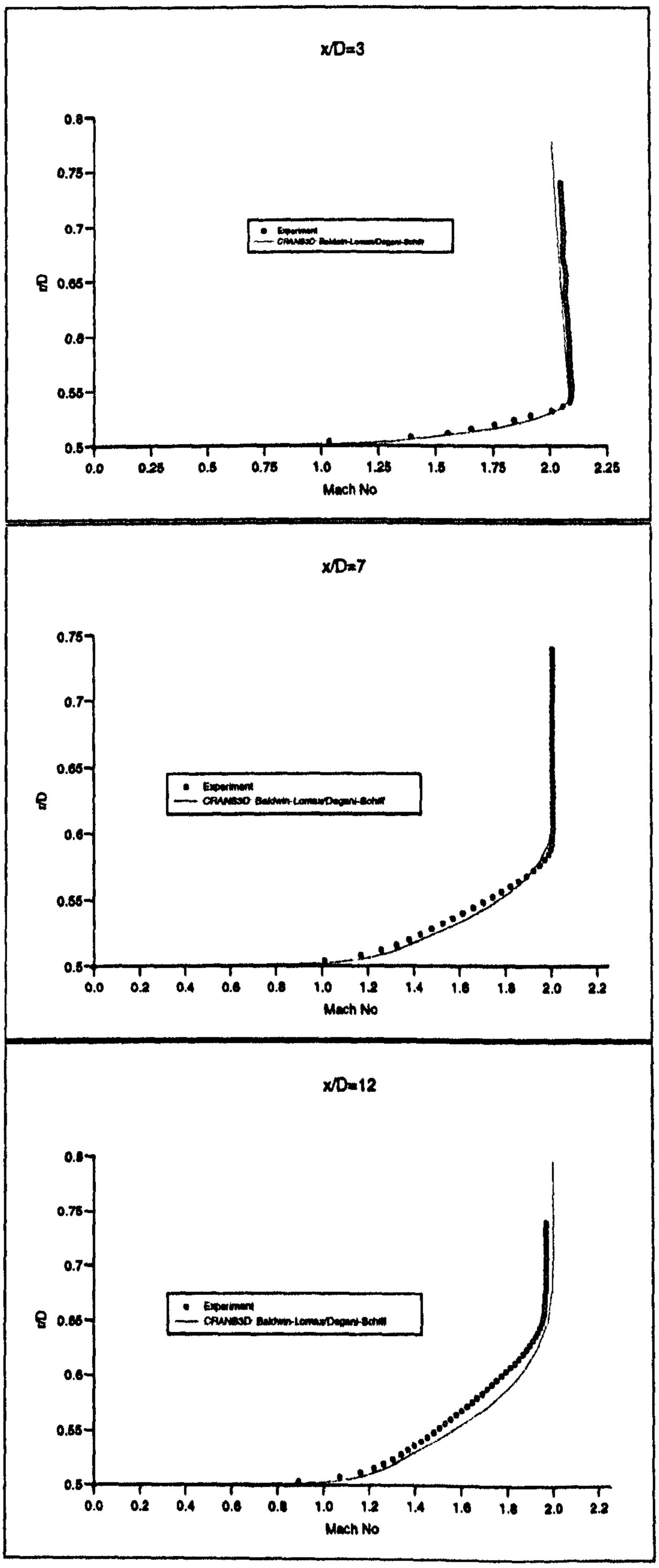

Figure 4.29: *Boundary Layer Mach Number Profiles, B2 0° angle of attack*

Case 4: B2 Forebody, Mach 2, 10° Angle of Attack and an Analysis of the Degani-Schiff Modification

This case was computed using both CRANS3D and the PNS solver on a number of grids. The coarsest grid was of size (33 × 33 × 33) while the finest was (89 × 89 × 119). Figure 4.30 presents the circumferential surface pressure distribution at $x/D = 7$ obtained on a number of these grids and is representative of the grid convergence for this case. The result on the finest grid, which will be presented as the grid converged result for this case, was found to be equivalent to the (60 × 89 × 119) result, indicating that a grid converged result was achieved. This suggests that the grid convergence is very sensitive to the grid resolution in the crossflow plane, in particular in the circumferential direction.

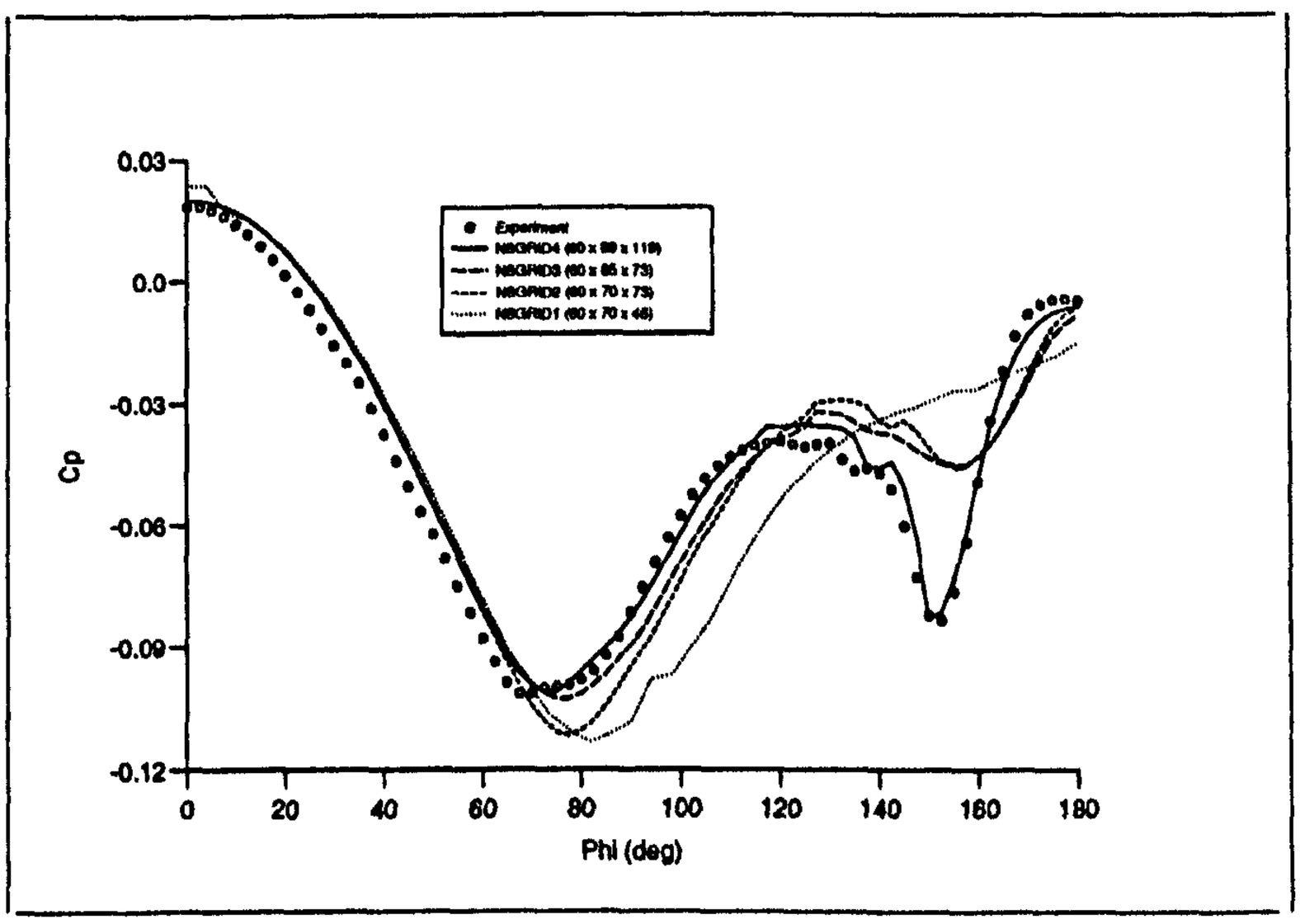

Figure 4.30: *CRANS3D, Grid Convergence: B2, 10° angle of attack, x/D=7*

The sudden change in resolution of the primary vortex suction between the grids having 73 and 119 circumferential points is suggested to be indicative of a problem with the Baldwin-Lomax/Degani-Schiff turbulence models ability to correctly resolve primary separation until a sufficiently fine circumferential resolution is used. Close examination of the way the Degani-Schiff modification works to resolve primary separation focuses on the calculation of a radial cut-off distance imposed to ensure that the correct peak in vorticity moment is chosen close to primary separation. Equation (3.36) gave this cut-off distance as:

$$y_{cut-off}(\phi) = C y_{max}(\phi - \Delta\phi)$$

and works to prevent large discontinuous changes in $F(y)_{max}$ due to the erroneous selection of the peak in vorticity moment. Degani and Schiff stated that the value C should be 1.5, which means that between two circumferential stations y_{max} can change by as much as 1.5 times, leading to a large difference in the corresponding values of $F(y)_{max}$ and an overestimation of the turbulent viscosity near crossflow separation [55]. A reduction in the value of the cut-off factor C would act to prevent large changes in, and a smoother distribution of y_{max} in the circumferencial direction.

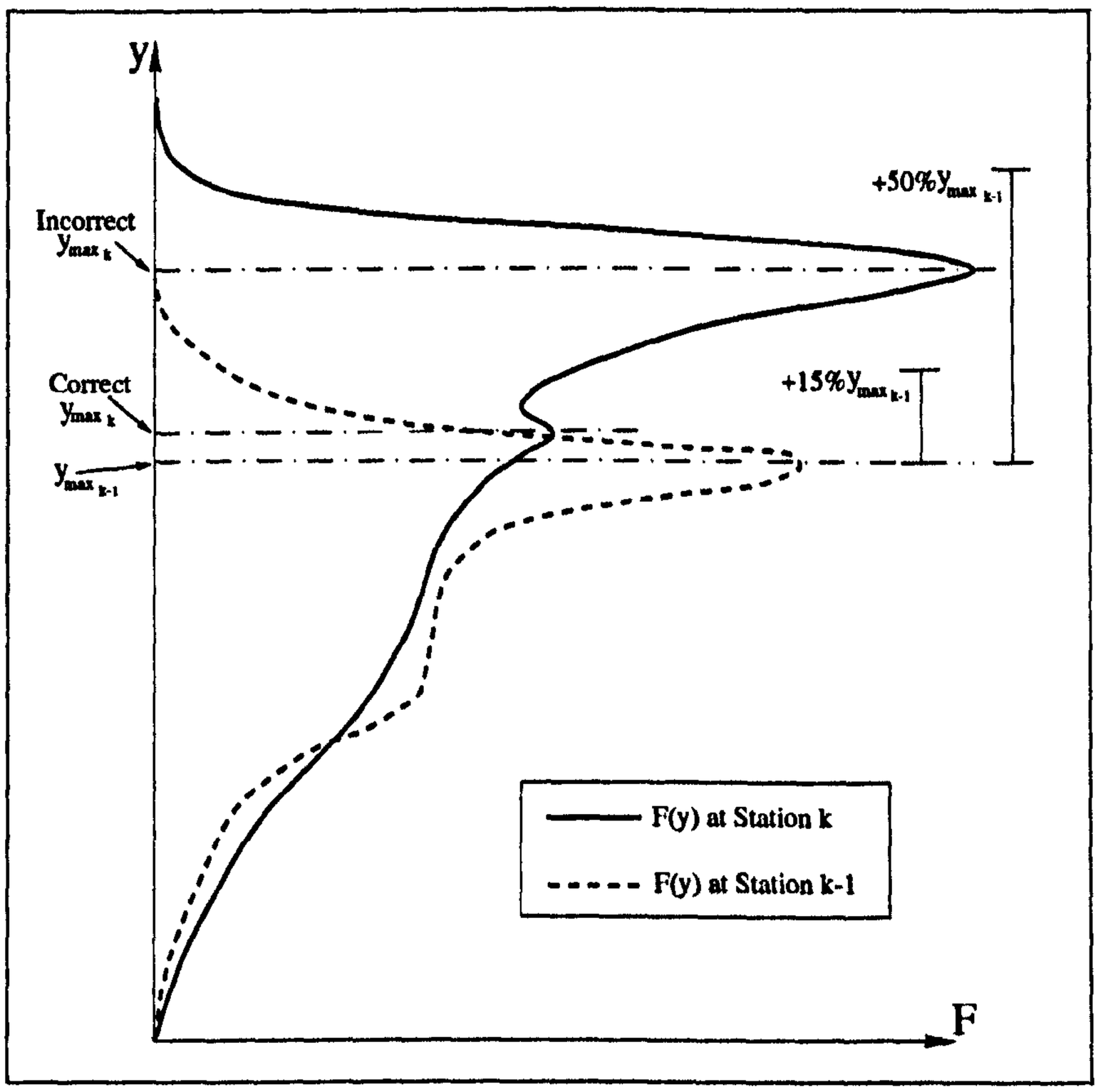

Figure 4.31: *The Effect of the Degani-Sciff Cut-Off Factor Near Primary Crossflow Separation*

Consider Figure 4.31 which depicts a typical situation in the vicinity of primary crossflow separation (occuring at station $k-1$). At station k the separated boundary layer, which forms the primary feeding sheet, corresponds to the second large peak in the moment of vorticity while a much smaller peak forms closer to the surface due to the transverse component of the velocity profile (corresponding to the attached boundary layer beneath the feeding sheet) which is that used for the correct definition of the turbulent length scale. Investgation during the present study, and by Qin and

Jayatunga [55], has shown that at the first peak the moment of vorticity may not fall back below 90 % of its peak value and may, therefore, not be detected by the Degani-Schiff algorithm. If, in addition, the second peak, associated with the separated shear layer, is within $y_{max_{k-1}} < y < 1.5y_{max_{k-1}}$, it will be selected in preference to the first peak value. A reduction of the cut-off factor will, therefore, reduce the risk that if the first peak value is not detected, the second peak lying much further away from the surface is erroneously selected. If the cut-off factor is reduced too much, however, there is a danger that the length scale will become "frozen" over a considerable circumferential region [55].

It was, therefore, decided to test the effect of reducing the value of the Degani-Schiff cut-off parameter, C, on the accuracy of the solution on a given grid. Initially, however, the standard Baldwin-Lomax/Degani-Schiff turbulence model was employed to compute the flow.

Figure 4.32 compares the NS and PNS solutions at three axial stations, $x/D = 5, 7$ and 9, with experiment. At the first station, $x/D = 5$, the NS solution is clearly superior to the PNS solution in the prediction of the suction due to the developing primary vortex on the leeward side. At $x/D = 7$ the PNS solver overpredicts both the position of primary separation and the corresponding value of the minimum C_p. The NS solution captures primary separation very accurately at about $\phi = 75^o$, and the correspondence between the NS and experimentally resolved primary vortex suction is almost exact. The PNS solver, however, overpredicts the minimum C_p at primary separation by as much as $\Delta C_p \approx 0.02$, and though it successfully resolved the appearance of suction due to the primary vortex, it failed to resolve the pressure plateau between $\phi = 110^o - 150^o$, and underpredicted the suction by over $\Delta C_p \approx 0.03$.

The comparison of the surface pressure distributions clearly reveal that the PNS solver performs poorly when compared with the corresponding NS solver on the (89 × 89 × 119) grid. The primary separation is poorly captured, and the subsequent pressure plateau and the secondary vortex suction are consistently unresolved. The only difference between the two solvers is that all streamwise viscous gradients are neglected in the PNS approach, though upstream pressure effects are modelled and second order spatial accuracy is maintained in the freestream direction. The difference in the two solutions can be explained by the lower spatial accuracy and the different treatment of upstream influence, especially in the subsonic portions of the turbulent boundary / shear layers, which can be quite substantial in the leeward region. For the laminar case 2, the NS and PNS solutions agreed better perhaps because the subsonic regions of the boundary layer and shear layers, where disturbances can feed upstream, are much smaller for laminar flow.

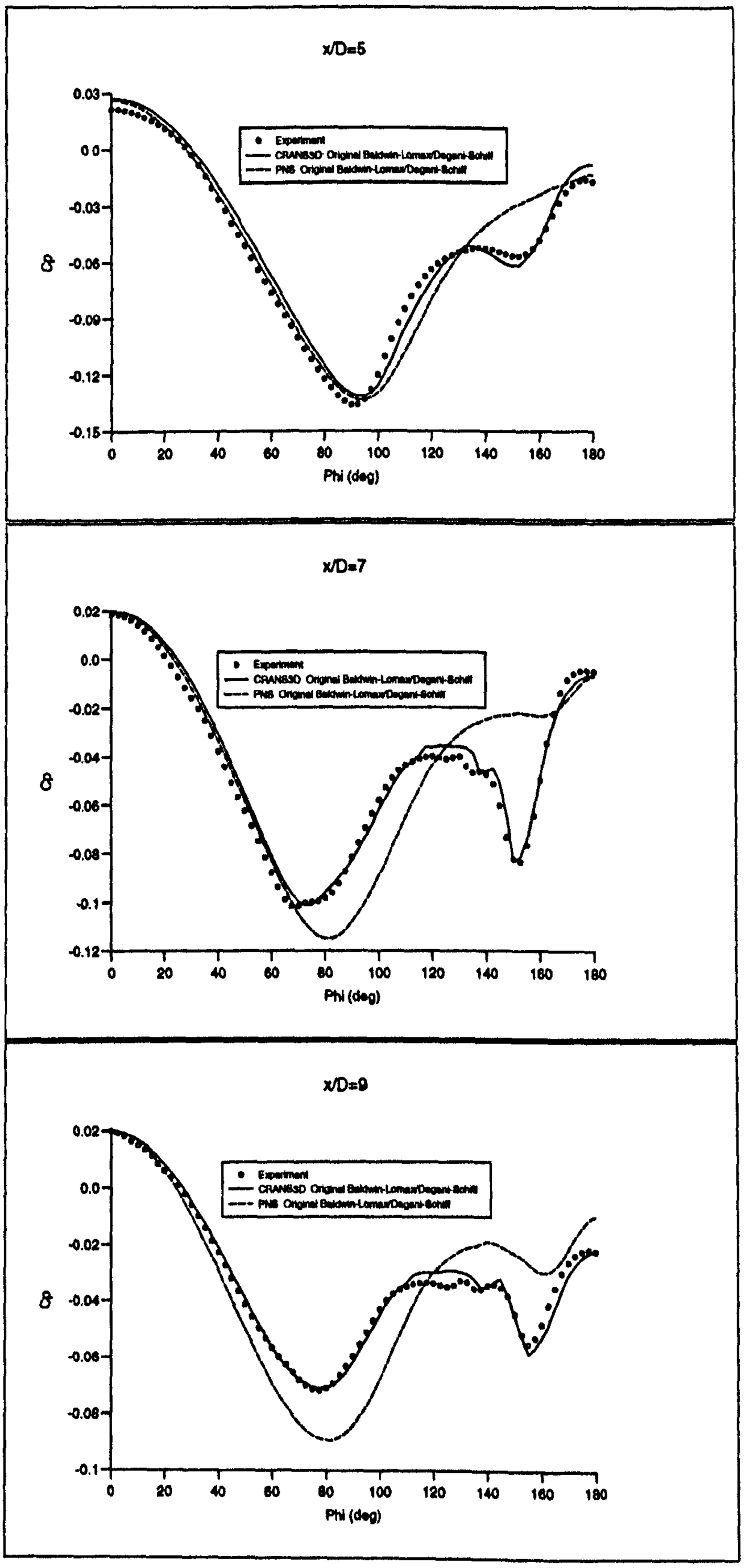

Figure 4.32: *Circumferential Surface Pressure Distribution, B2* 10° *angle of attack*

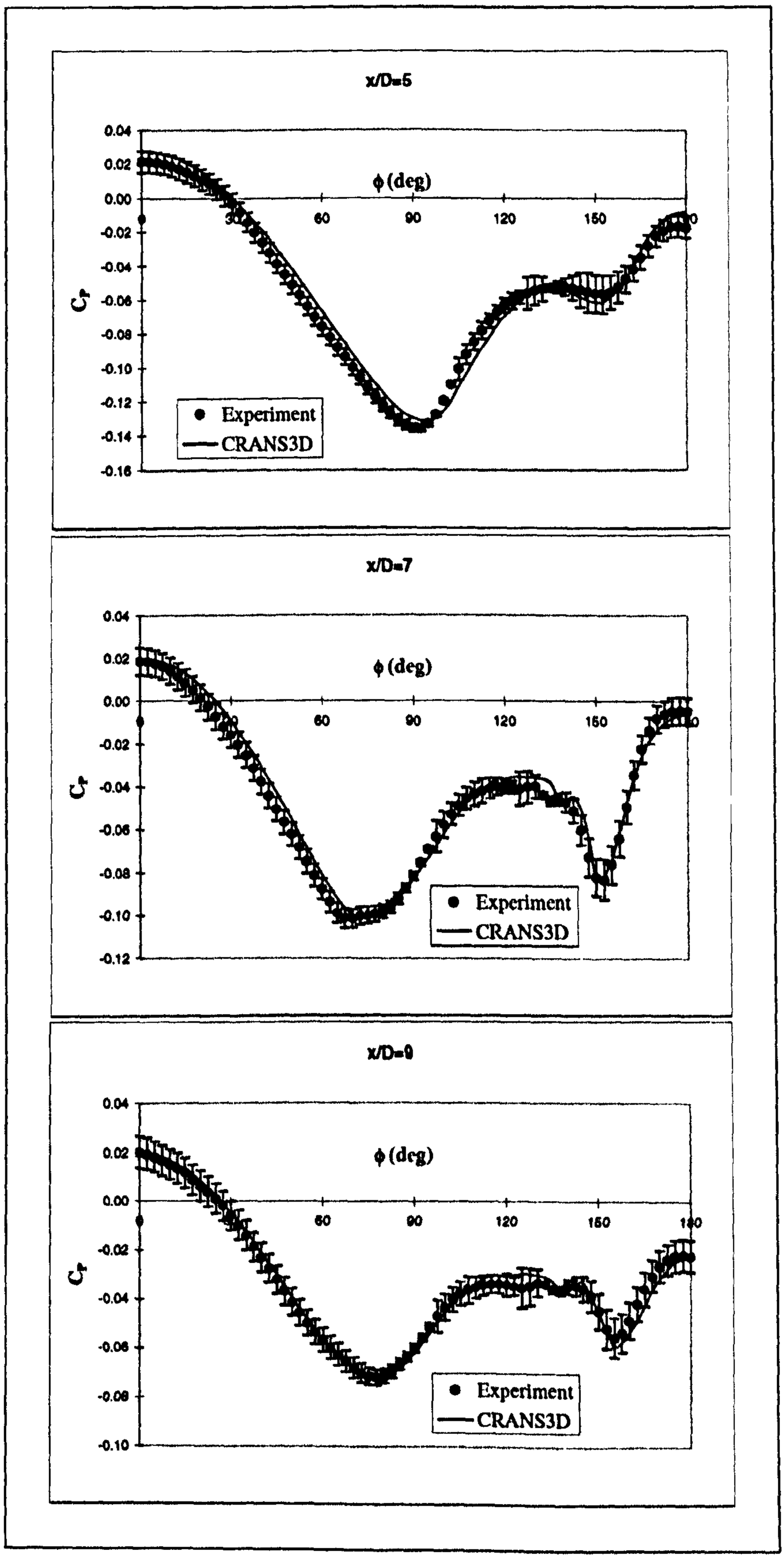

Figure 4.33: *Circumferential Surface Pressure, Estimated Experimental Error: B2,* 10°

An estimation of the error in the measurement of surface C_p was made in the same manner as was done for case 2, using the technique presented in Section 2.4 and the fine grid NS solution. Figure 4.33 shows the comparison of the CRANS3D pressure distributions at the three axial stations with the corresponding experimental measurements together with the estimated error bars. The estimated errors are seen to be generally 2-3 times larger than those calculated for the laminar case 2. This can be explained by the fact that the error in measured C_p is proportional to the ratio of the hole diameter to the local displacement thickness. Since the freestream Reynolds number is 7.5 times larger than that for case 2, leading to a displacement thickness generally 2-3 times thinner, the error will be about 2-3 times greater. It is shown that the NS predicted surface pressure curves generally lie within the estimated error bounds. This result provides more confidence in the agreement between computation and experiment, and therefore in the ability of NS solvers employing the Baldwin-Lomax/Degani-Schiff approach for inclined slender bodies in supersonic flow.

Surface streamline plots for both the NS and PNS solvers are compared in Figure 4.34. The only discernible differences are seen in the primary and secondary separation streamlines. The CRANS3D primary separation streamline develops sooner and is noticeably more windward than the corresponding PNS result. In addition the secondary separation streamline is evident at the back of the body in the NS solution, but is not noticeable in the corresponding PNS case.

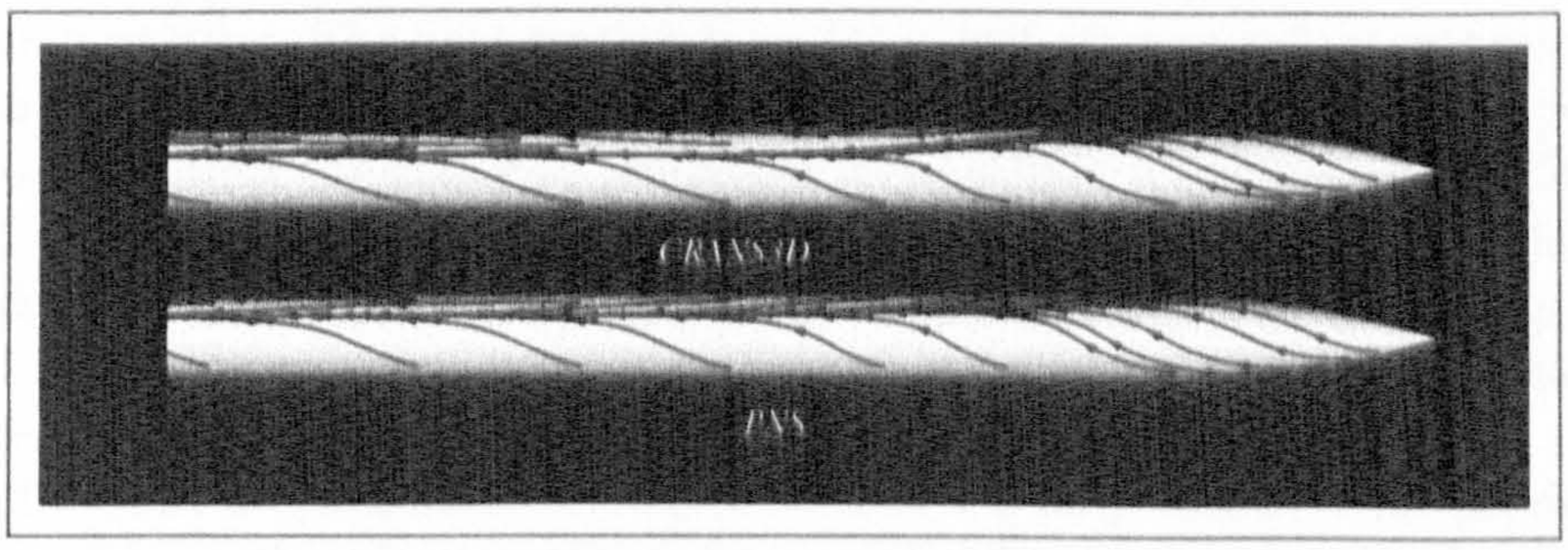

Figure 4.34: *Surface Skin Friction Comparison, B2* 10^o *angle of attack*

The PNS solver was used in the study of the Degani-Schiff cut-off factor, C, which was successively reduced in order to see if the solutions on the coarser grids could be improved thus improving grid convergence. Values for the cut-off factor at infinity (ie: with no cut-off at all) 1.5, 1.4, 1.3, 1.2, 1.18, 1.16, 1.15, 1.14, 1.12, 1.1 and 1.05 were tested, and the solution run to five orders of convergence. In addition to the Degani-Schiff tests, a standard Baldwin-Lomax turbulence model result was obtained. Figure 4.35 presents the crossflow plots of the turbulent viscosity ratio $\mu_t/\mu_{t\infty}$, the Mach number and the total pressure ratio at station $x/D = 9$ for the standard Baldwin-

Lomax model together with the corresponding Degani-Schiff results for the cut-off factors set at infinity, 1.5 and 1.15. The solutions for a cut-off factor set at infinity, 1.5, 1.4 and 1.3 were almost identical. Reducing the factor from 1.3 to 1.2 caused a dramatic improvement. The solutions for C=1.18 and 1.16 were found to be identical to the improved solution for C=1.2. The solution for cut-off factors of 1.15 and 1.14 were different again, and were so improved that they were almost identical with the NS results presented in Figure 4.32.

These results show that, for this case, there is no benefit in employing the cut-off routine with C greater than 1.3. The crossflow plots of turbulent viscosity ratio shown in Figure 4.35 a) are also very revealing. For $C = 1.15$ the solver successfully captures the peak in vorticity moment associated with the edge of the thin attached primary and secondary boundary layers. The standard algorithm with $C = 1.5$, however, fails to detect the peak from the inner secondary boundary layer until much further leeward resulting in large turbulent viscosity within the separated shear layer. This can be explained by looking at how the Degani-Schiff cut-off algorithm works at primary separation.

A plot of the radial vorticity moment distribution at three successive k stations just after primary crossflow separation at station x/D=6 for the original Degani-Schiff formulation is reproduced in Figure 4.36. This graph demonstrates how the original formulation can select the wrong peak in vorticity moment. At the first circumferential station ($k = 40$) just before crossflow separation the vorticity moment profile is typical of an attached boundary layer. The next station ($k = 41$) is just after crossflow separation, with a large peak associated with the separated shear layer. The peak associated with the attached boundary layer is only just beginning to form and will not be detected by the Degani-Schiff algorithm. The shear layer peak lies within the 50% cut-off distance from the previous value of y_{max} and so will be erroneously selected for the definition of the boundary layer edge.

If the cut-off parameter is lowered so that it is only 15% over the previous value of y_{max}, the selection of the wrong peak will not occur, as the algorithm will select the previous y_{max}. At the third circumferential station ($k = 42$) both algorithms will correctly select the peak due to the attached boundary layer, which is now fully developed and distinct from the larger peak further away. This is because the vorticity moment is seen to drop back below 90% of the first peak value before the shear layer begins to take affect. If this did not happen then the original algorithm would incorrectly select the second peak, while an algorithm with the cut-off factor set to 1.15 would reselect the y_{max} from station $k = 40$ which, though wrong, is much closer to the correct distance than that for the second peak.

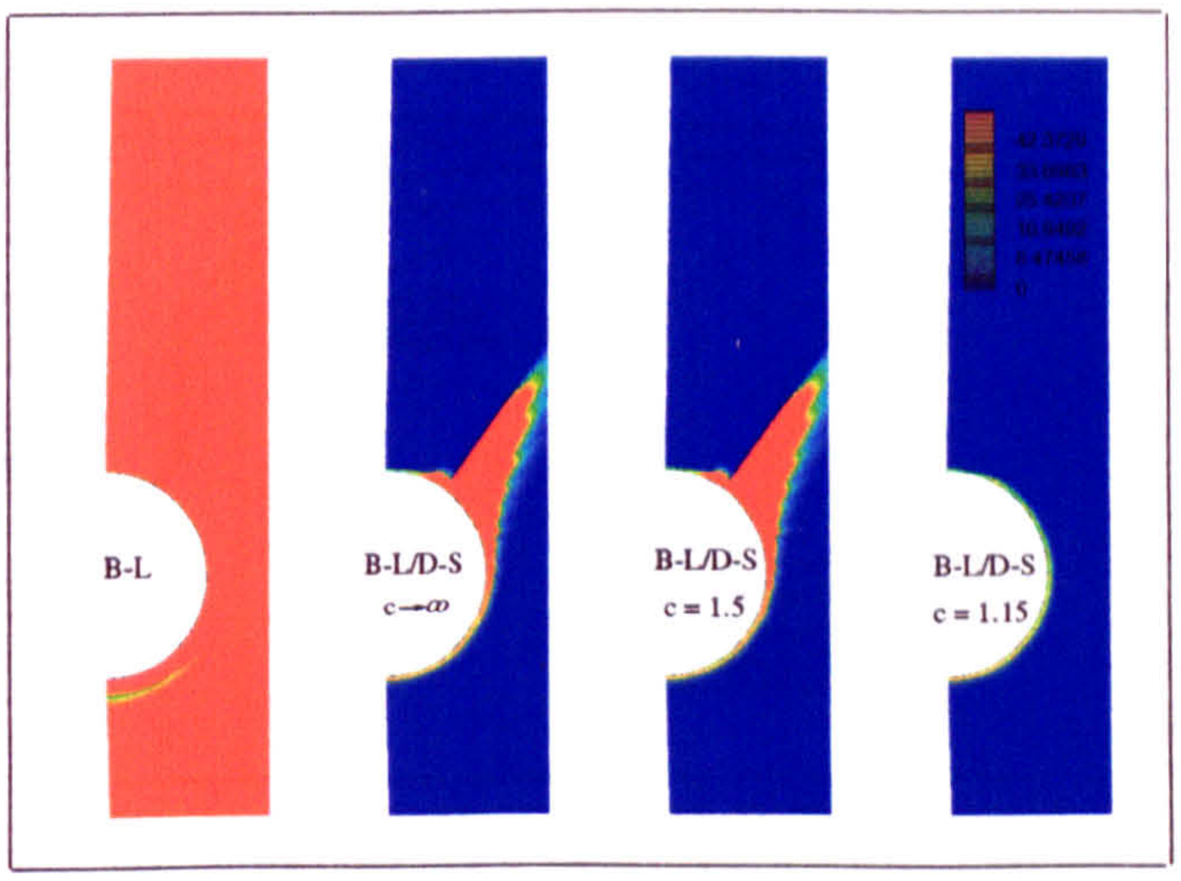

(a) Turbulent Viscosity Ratio $\mu_t/\mu_{t\infty}$

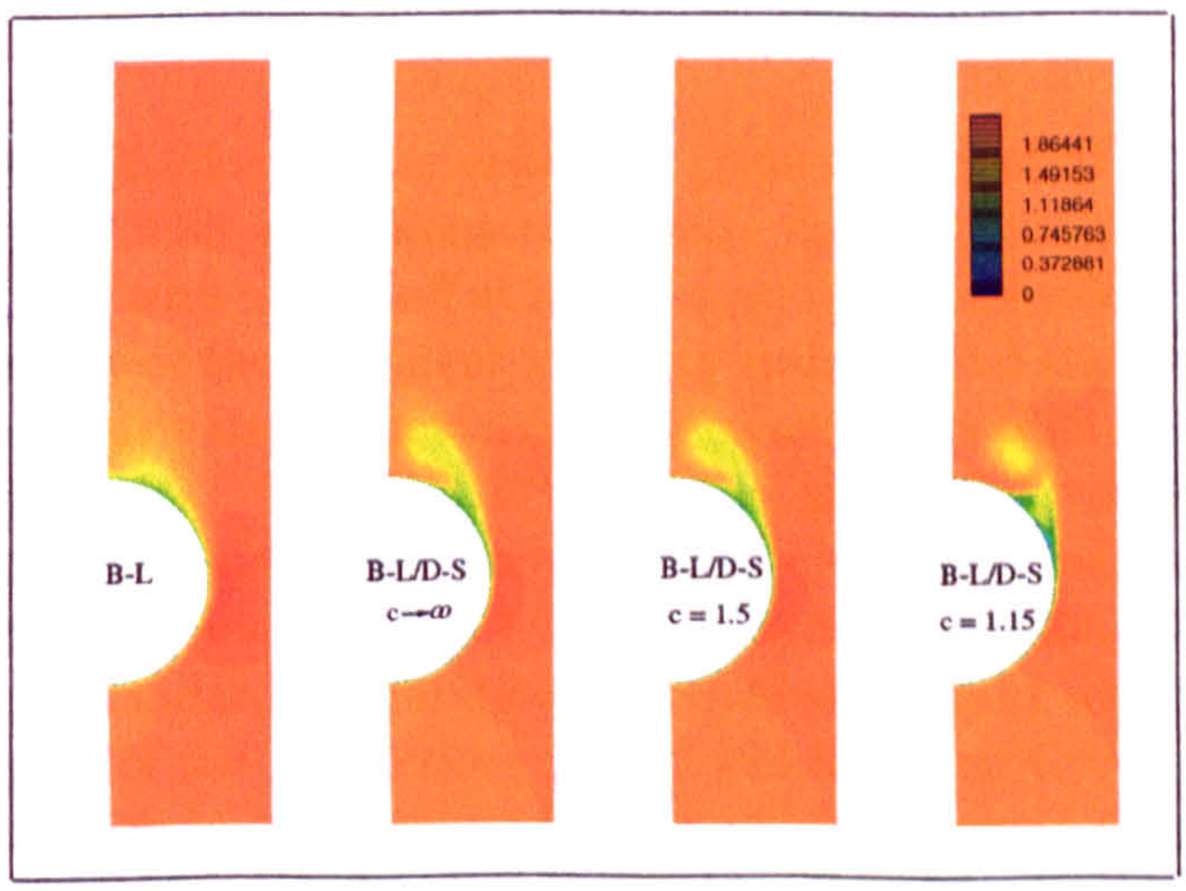

(b) Mach Number

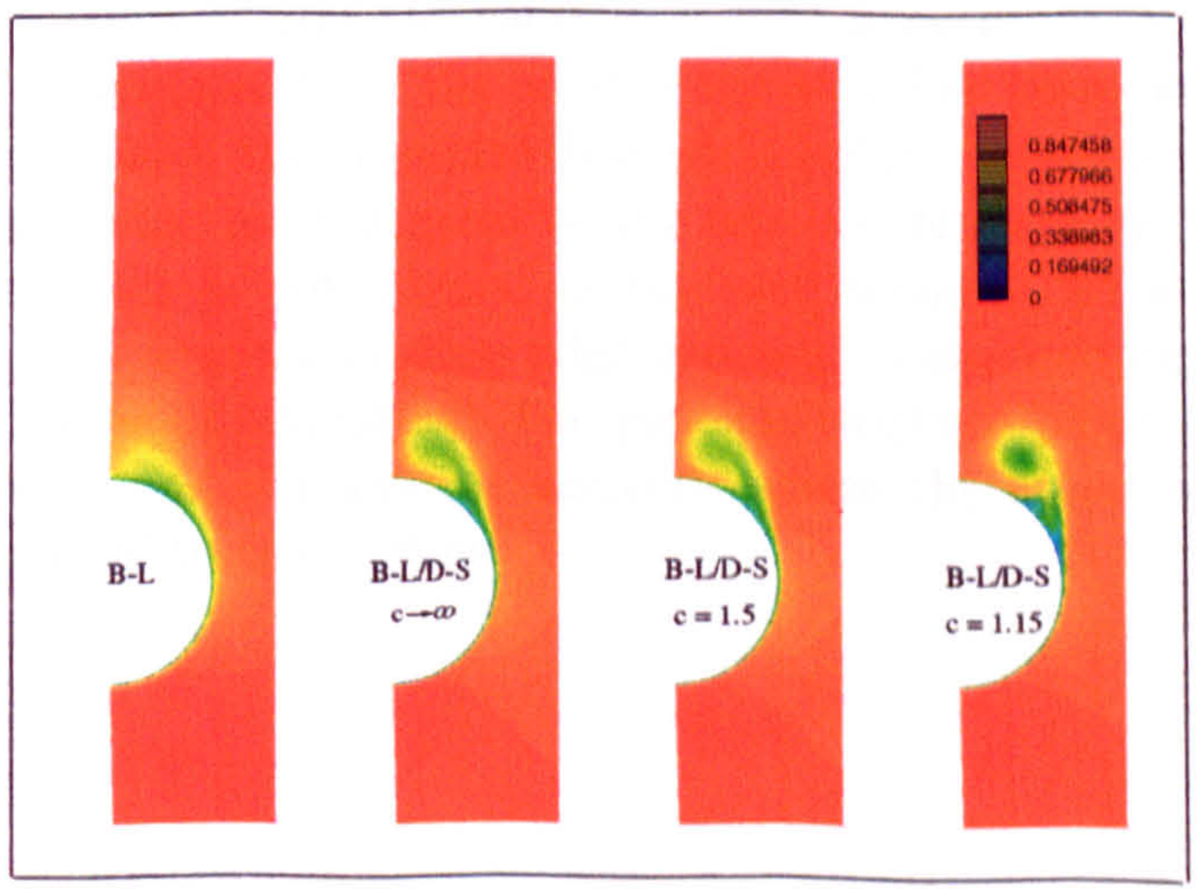

(c) Total Pressure Ratio $P_0/P_{0\infty}$

Figure 4.35: *Comparison of Results for Different Turbulence Models, B2 10°. x/D=9*

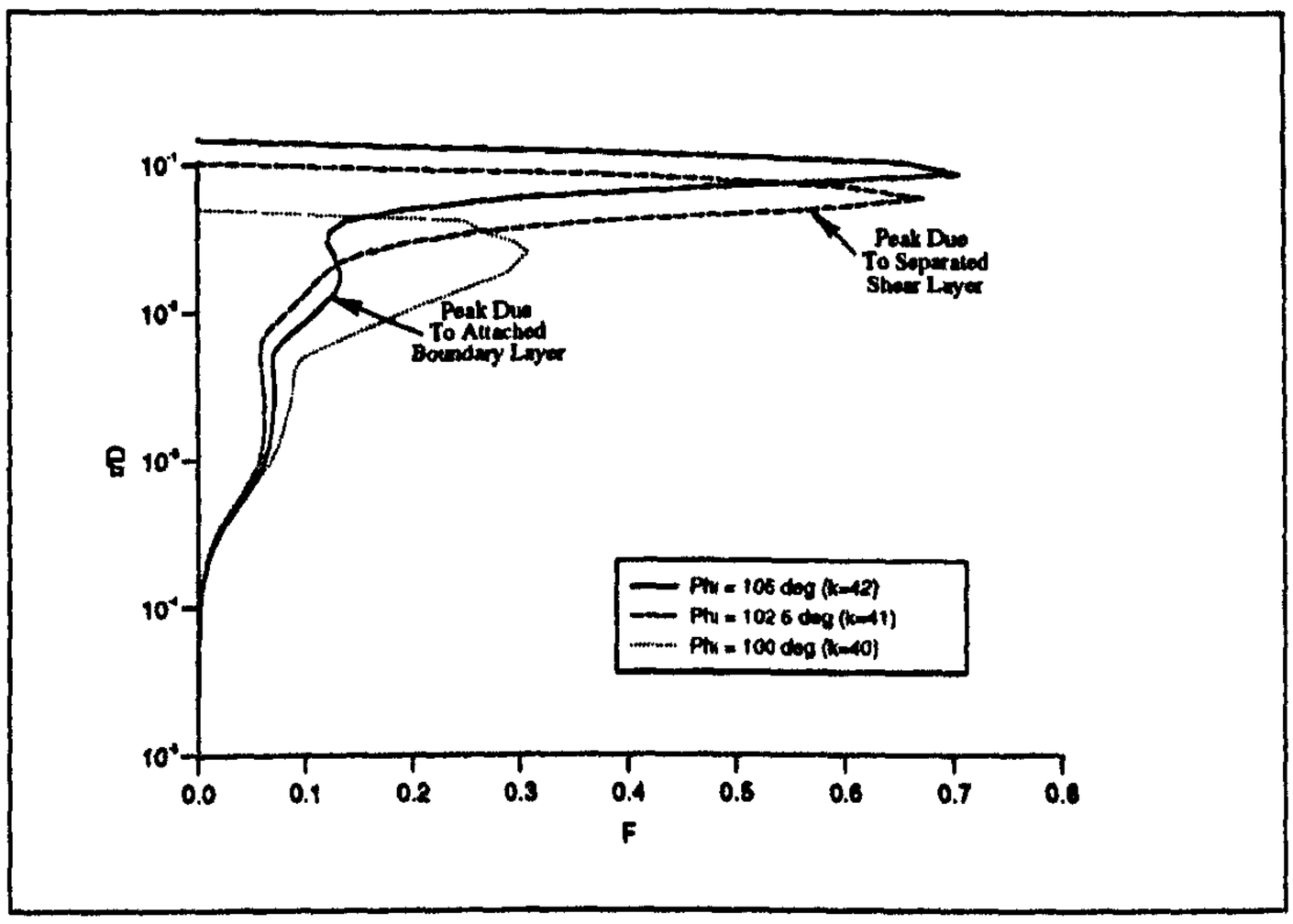

Figure 4.36: *Vorticity Moment Distributions at Three Circumferential Stations, x/D=6*

Further examination of the crossflow plots of turbulent viscosity ratio shown in Figure 4.35 a) demonstrates that the Degani-Schiff result with $C = 1.5$ and that with no cut-off at all are practically equivalent. In addition the crossflow plot of the turbulent viscosity ratio for the standard Baldwin-Lomax model clearly demonstrates its inadequacy to predict large separated turbulent flow fields. Figure 4.37 compares the radial vorticity moment distributions, on the windward symmetry plane, obtained using the standard Baldwin-Lomax approach and with the Degani-Schiff modification with $C = 1.15$. With the standard formulation, the Baldwin-Lomax model will choose the largest value of the F-function, $F_{y_{max2}}$ which is seen to occur due to the vorticity generation by the strong-curved bow shock wave out in the inviscid farstream. This will result in a vastly overpredicted turbulent length scale and the large region of extremely high turbulent viscosity which extends out to the bow-shock. The Degani-Schiff modification, however, acts to choose the first peak (chosen after the value of F falls back to 90 % of that peak value) $F_{y_{max1}}$ associated with the edge of the attached boundary layer.

The problem with the standard Baldwin-Lomax turbulence model thus outlined is suggested to be general to any flow where a strong curved shock wave exhists which is not normal to the wall surface. This includes supersonic sharp or blunted leading edge geometry flows and any supersonic flows about bodies of revolution. The problem may not be an issue for turbulent computations of transonic aerofoils where the upper surface shock sits almost normal to the surface.

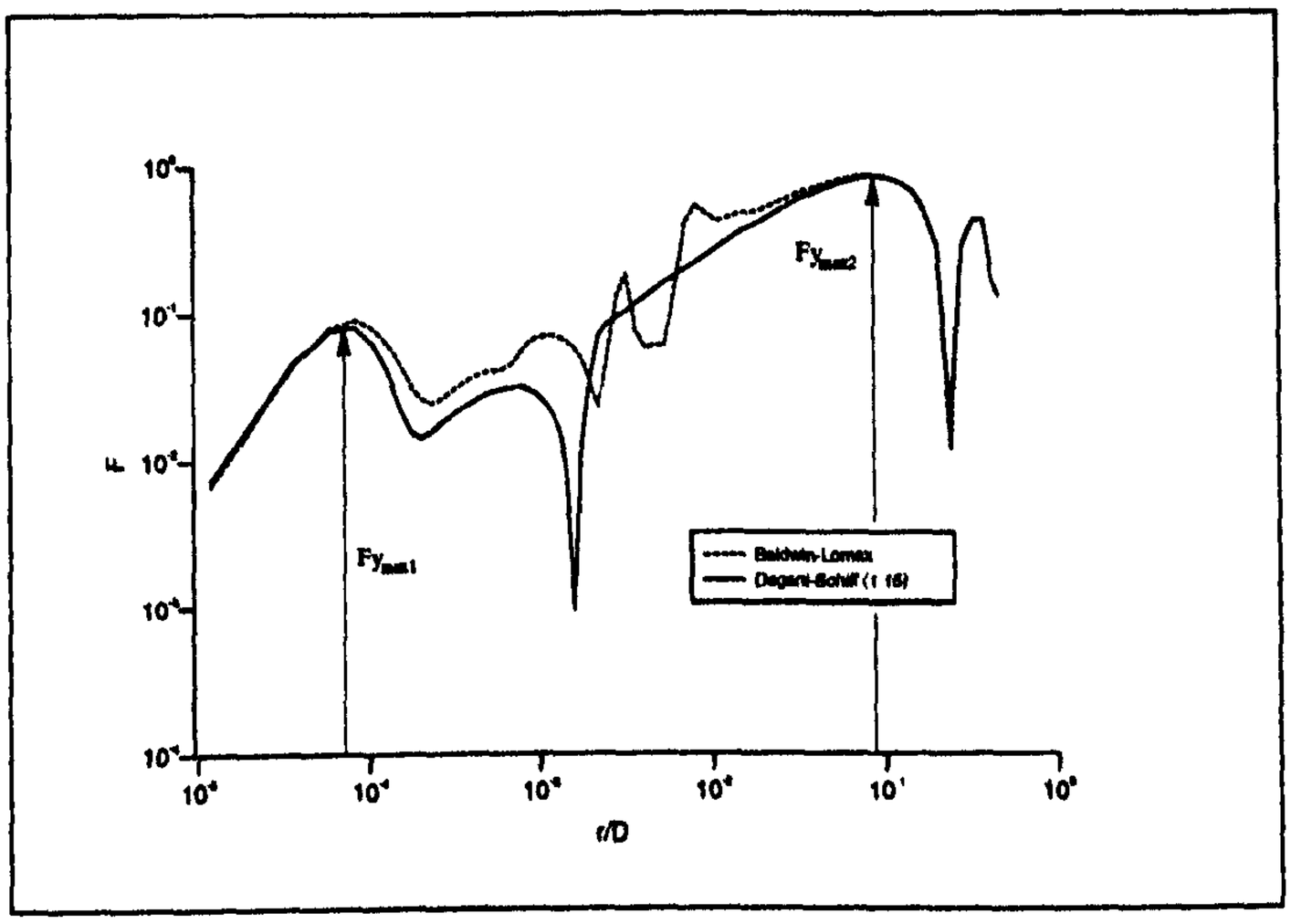

Figure 4.37: *Windward Symmetry Plane Vorticity Moment Distribution at Station I=1*

The comparison of the PNS surface pressure solutions for cut-off factors of 1.5 and 1.15, and the dramatic improvement when compared with experiment, is presented in Figure 4.38. Further reductions of the cut-off factor progressively made the solution too "laminar" in appearance, with primary separation occurring too early and at much higher values of C_p. The optimal value for the Degani-Schiff cut-off factor for this case is therefore 1.15.

CRANS3D was then employed using the intermediate grid ($60 \times 85 \times 73$) in order to see if the implementation of the cut-off factor of 1.15 could improve the NS result on a coarser grid. Figure 4.39 presents the cross-flow total pressure comparisons at the three measurement stations. The experimental contours are compared with the corresponding NS solutions employing the original value of the cut-off factor (1.5) and the figure of 1.15 suggested from the PNS study. The improvement can clearly be seen. The vortex structure appears to agree much better with experiment using the reduced cut-off factor, and is almost equivalent to the solution obtained on the finest grid. The only discernible difference between the experimental contours and the NS solution with modified Degani-Schiff appears to be that the suction in the core of the primary and secondary vortices, and the pressure within the feeding sheet is not as high as seen in experiment. A difference of about $\Delta P_0/P_{0\infty} \approx 0.05$ or an error of 12 % is observed in the primary vortex core. This compares with an experimental accuracy quoted at between 5 - 10 % in the vortex cores.

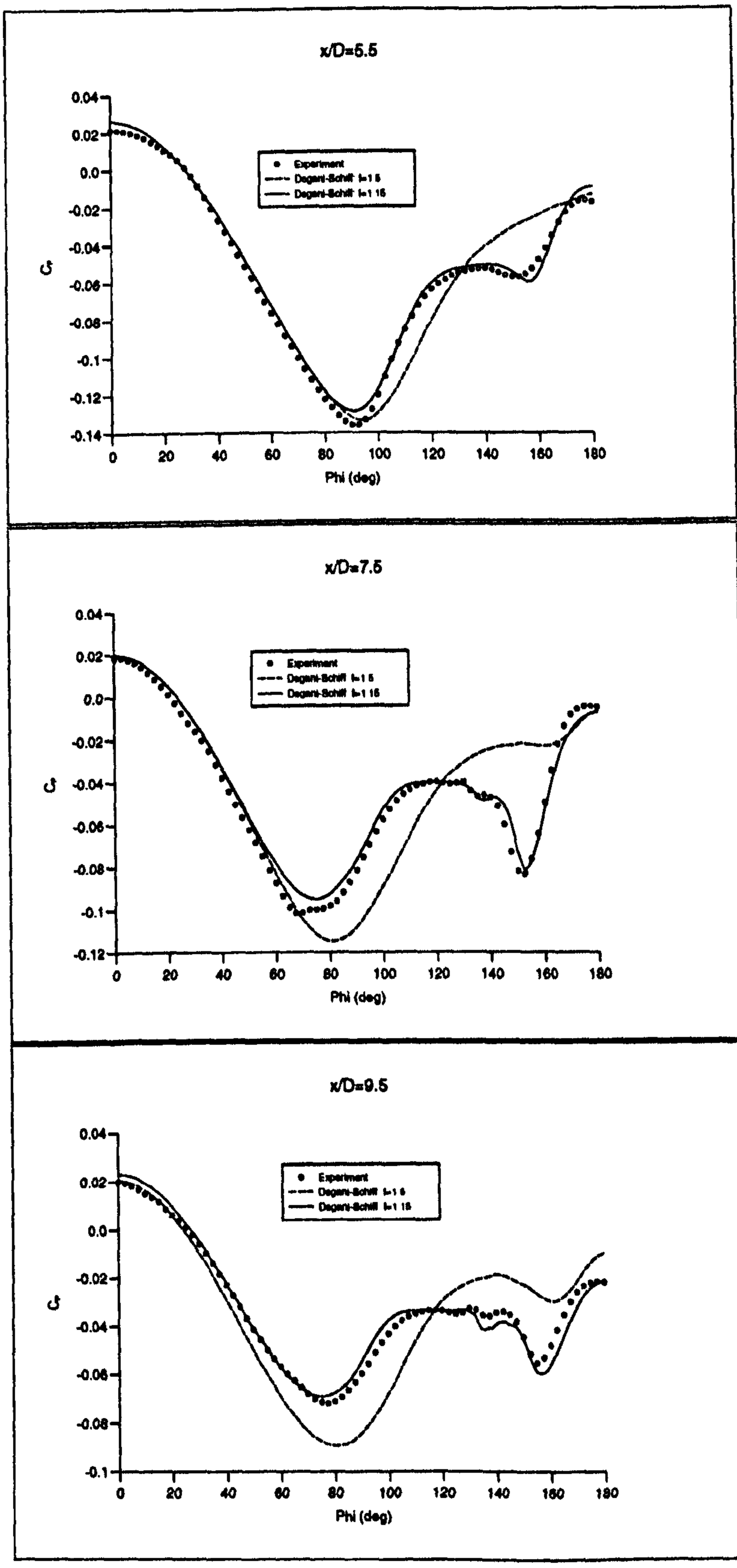

Figure 4.38: *Effect of Modified Degani-Schiff Parameter: Circumferential* C_P

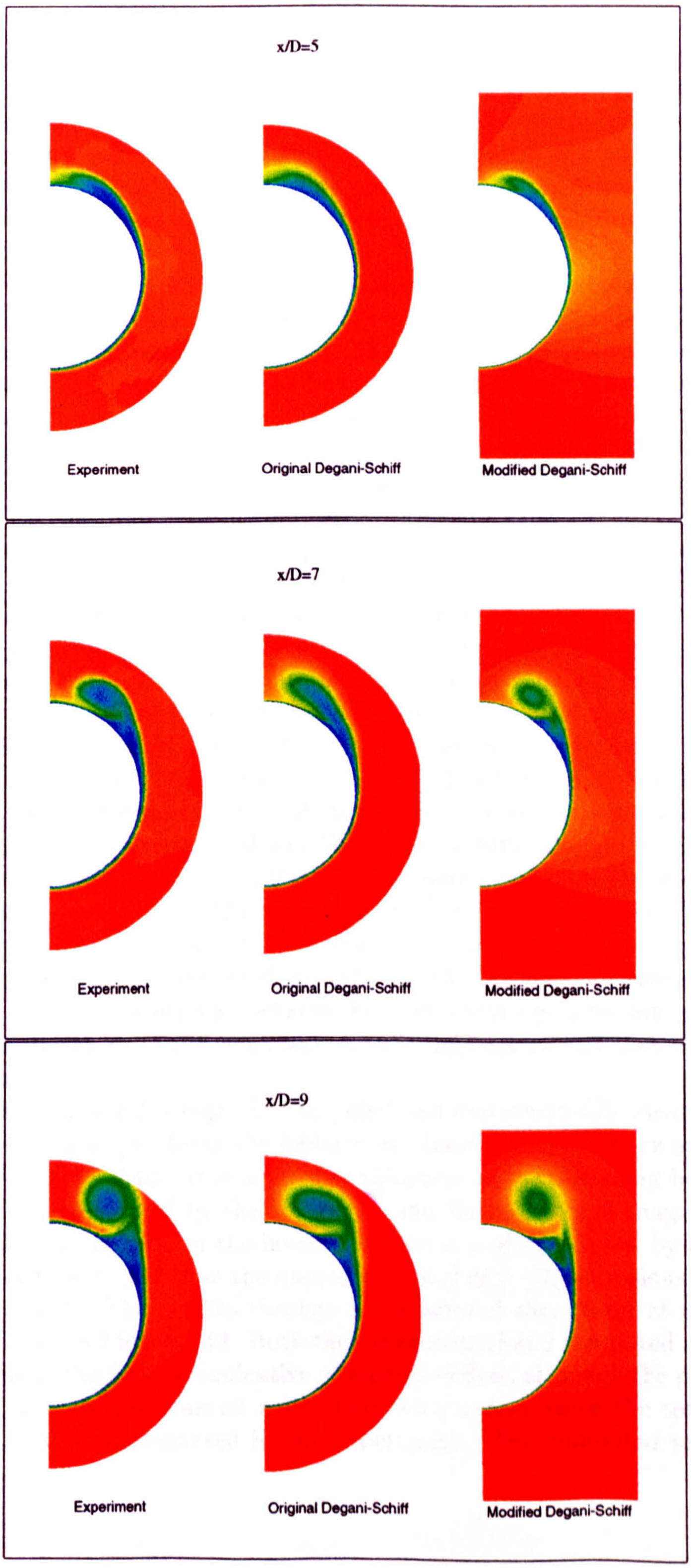

Figure 4.39: *Effect of Modified Degani-Schiff Parameter: Crossflow Total Pressure Ratio*

Figures 4.41 - 4.44 present the comparisons of the experimentally measured Mach number and total pressure ratio profiles within the leeside boundary layer and separated shear layer, and those predicted by CRANS3D using the modified Degani-Schiff turbulence model of the grid (60 × 85 × 73). Measurements were made at stations $x/D = 5, 7$ and 9 for $\phi = 90^o, 120^o, 135^o, 152.5^o$ and 180^o. The pressure probe traverses corresponding to these ϕ angles are represented on the leeward quadrant shown in Figure 4.40.

At station $x/D = 9$ the Mach number profiles are presented in Figures 4.41 - 4.42. For the boundary layer at $\phi = 90^o$ the correspondence between the experimental measurements and the NS solution is almost exact, with a maximum difference within the boundary layer of only $\Delta M \approx 0.1$. Further leeward, at $\phi = 120^o$, the S-shaped profile is correctly resolved, but the magnitude of the first Mach number peak is predicted about double that seen in the experiment, and appears to occur slightly higher above the surface than the experimental peak. The extent of the viscous region is also exaggerated by about 30%. At $\phi = 135^o$ the experimental profile exhibits a distinct double concavity between $r/D = 0.52 - 0.75$, corresponding to the secondary and primary vortices. The NS solution captures the concavity due to the effect of the primary vortex but fails to resolve the secondary concavity. The magnitude of the predicted Mach number in the viscous region differs from the corresponding experimental measurements by a maximum of $\Delta M \approx 0.2$ which is well over the experimental accuracy quoted at $\Delta M \pm 0.02$. The prediction at $\phi = 152.5^o$, which corresponds to a cut through the leeward portion of the primary vortex, appears to be much better. Both the experimental and NS profiles exhibit a large concavity between $r/D = 0.54$ and about 0.9 which corresponding to the outer region of the primary vortex. The Mach number minima obtained by the NS solver occurs at $r/D \approx 0.69$ which is equivalent to the measured position, but the magnitude is overpredicted by $\Delta M \approx 0.1$. At primary reattachment at $\phi = 180^o$ the agreement between the two curves is good although the predicted thickness of the boundary layer is only about half that measured experimentally.

The comparison between the computed and experimentally measured total pressure ratio profiles in the leeward quadrant at $x/D = 9$ are presented in Figures 4.43 - 4.44. At $\phi = 90^o$ the thickness of the oncoming boundary layer is underpredicted by the NS solver, and the subsequent magnitude of the total pressure ratio in the inviscid stream is underpredicted by as much as 10%. This is higher than the quoted accuracy of $2-3\%$ in regions of moderate gradients. The profiles through the separated shear layer at $\phi = 120^o$ are presented in Figure 4.43. Both the experimental and computed distributions include the S-shape indicative of separated flow, although the predicted S-profile is more pronounced and occurs with almost twice the total pressure ratio as that measured in the experiment. The computed separated

shear layer is also thicker than the corresponding measured shear layer, by an amount $\Delta r/D \approx 0.06$. Further leeward, at $\phi = 135^o$, the concavity attributed to the suction caused by the primary and secondary vortices, is not captured correctly by the NS solver. The magnitude within the region of this suction is overpredicted by as much as 250%. It is suggested that, while the experimental curve exhibits evidence of the effects of both primary and secondary vortices, the computed curve has captured only the suction from the primary vortex. In addition, the extent of the viscous region is considerably overpredicted by the NS solver, when compared with the measured profile. As with the Mach number distribution, the comparison for total pressure ratio is better at $\phi = 152.5^o$ than at the previous circumferential station. The predicted profile shape matches that measured in the experiment, although the primary suction, which is maximum in both cases at $r/D \approx 0.7$, is underpredicted by a maximum of about 200%. At primary reattachment at $\phi = 180^o$, the thickness of the boundary layer and the associated rise in pressure is not correctly resolved by CRANS3D which underpredicts the total pressure ratio by about 10% in the inviscid region.

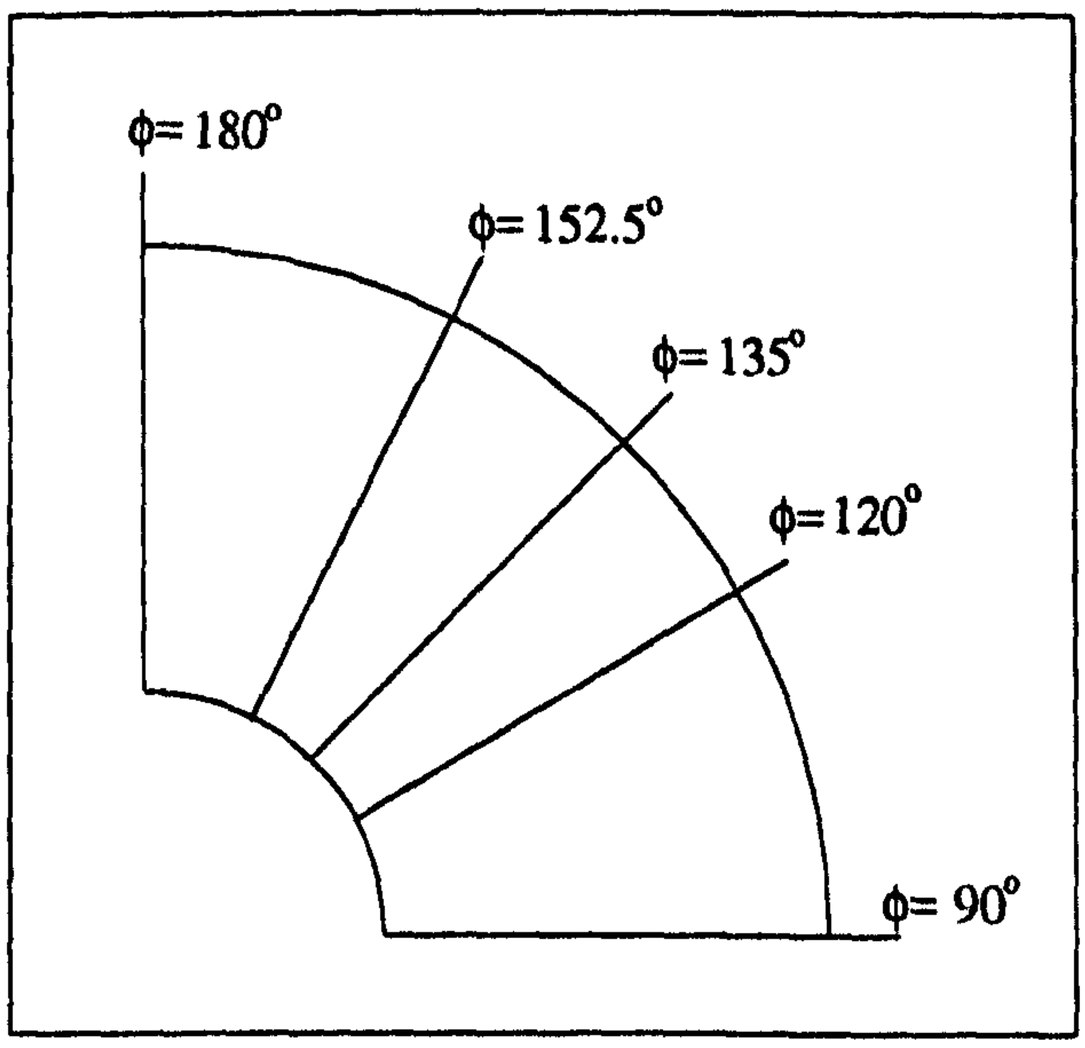

Figure 4.40: *Representation of the Measurement Traverses through the Leeward Quadrant*

When the flowfield for this case was examined in more detail, an anomalous windward feature appeared in the flowfield underneath the body. The available experimental data is unable to verify whether this is a physical feature, but results from other test cases will validate its existence. Section 4.4 will present the interpretation of this flow feature, explaining both its nature and its origin.

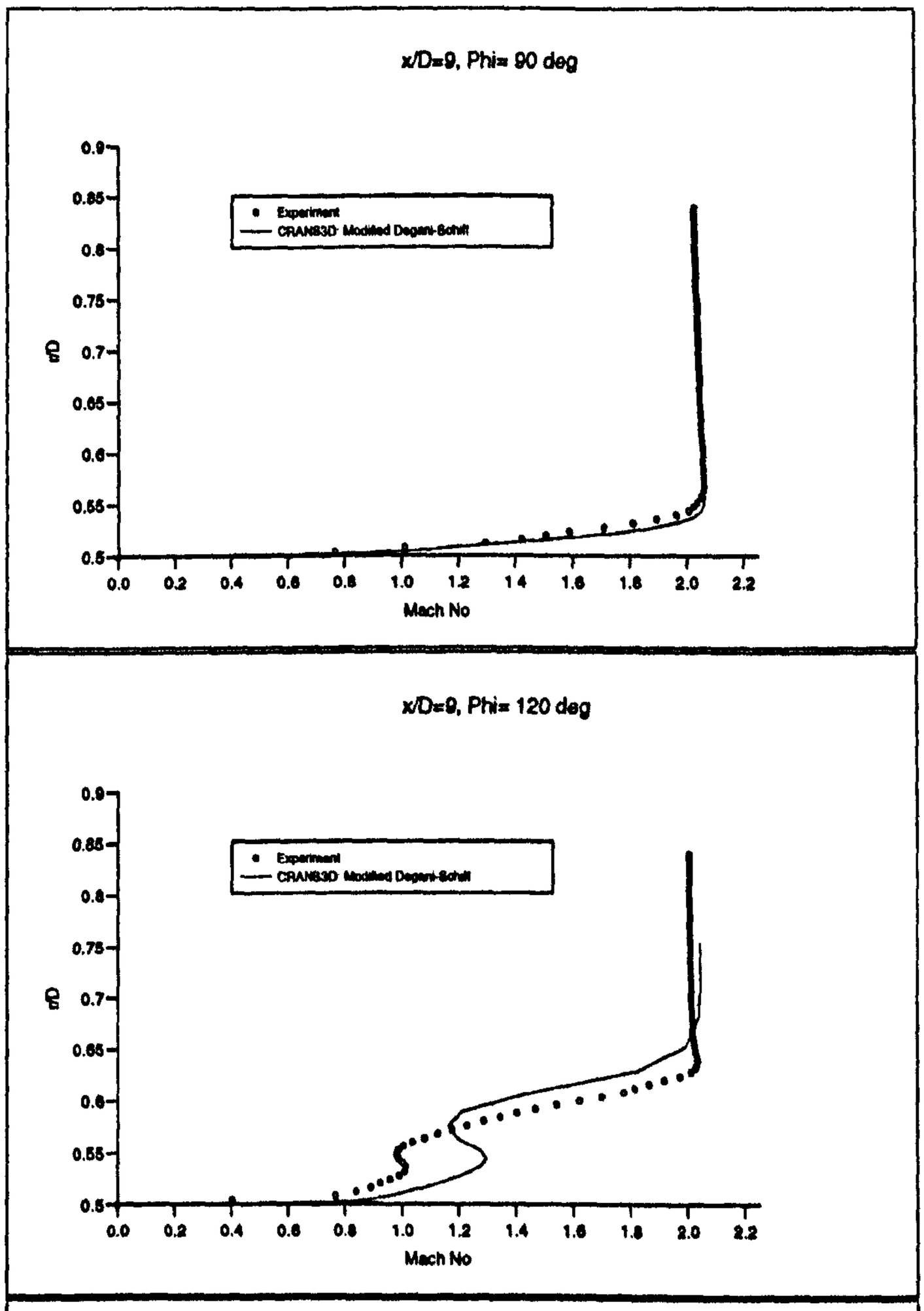

Figure 4.41: *Mach Number Profile: x/D=9*

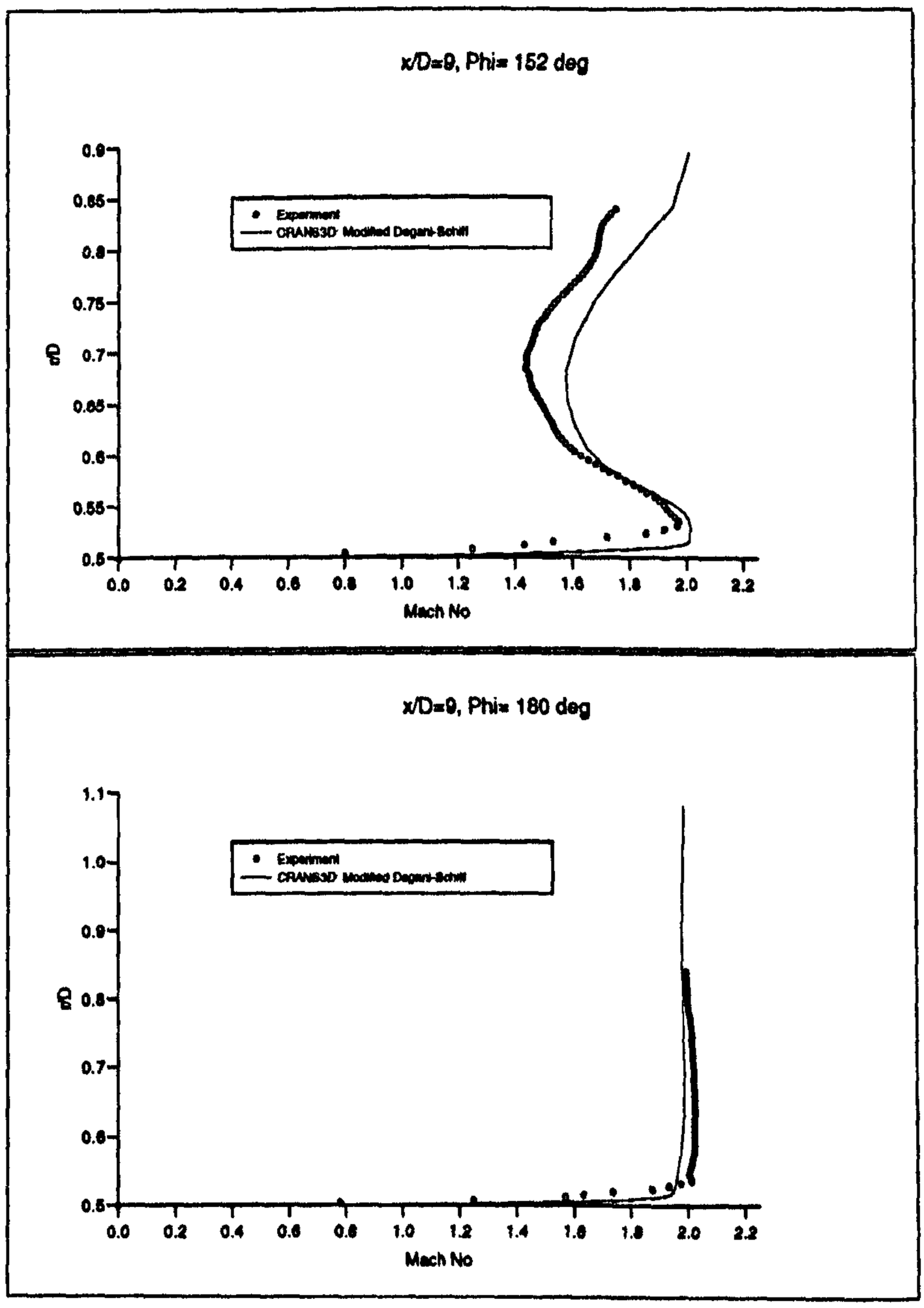

Figure 4.42: *Mach Number Profile: x/D=9, Continued*

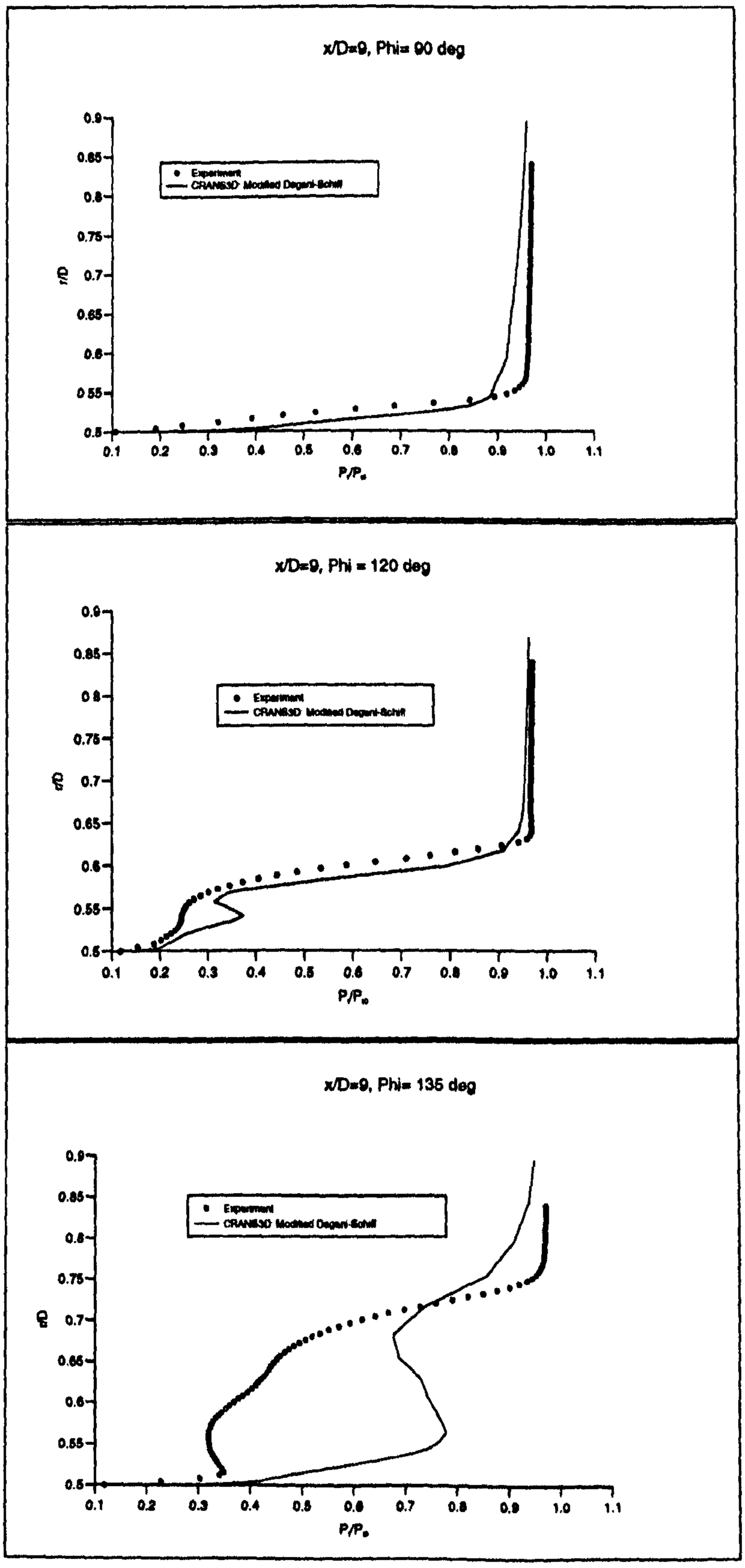

Figure 4.43: *Total Pressure Ratio Profile: x/D=9*

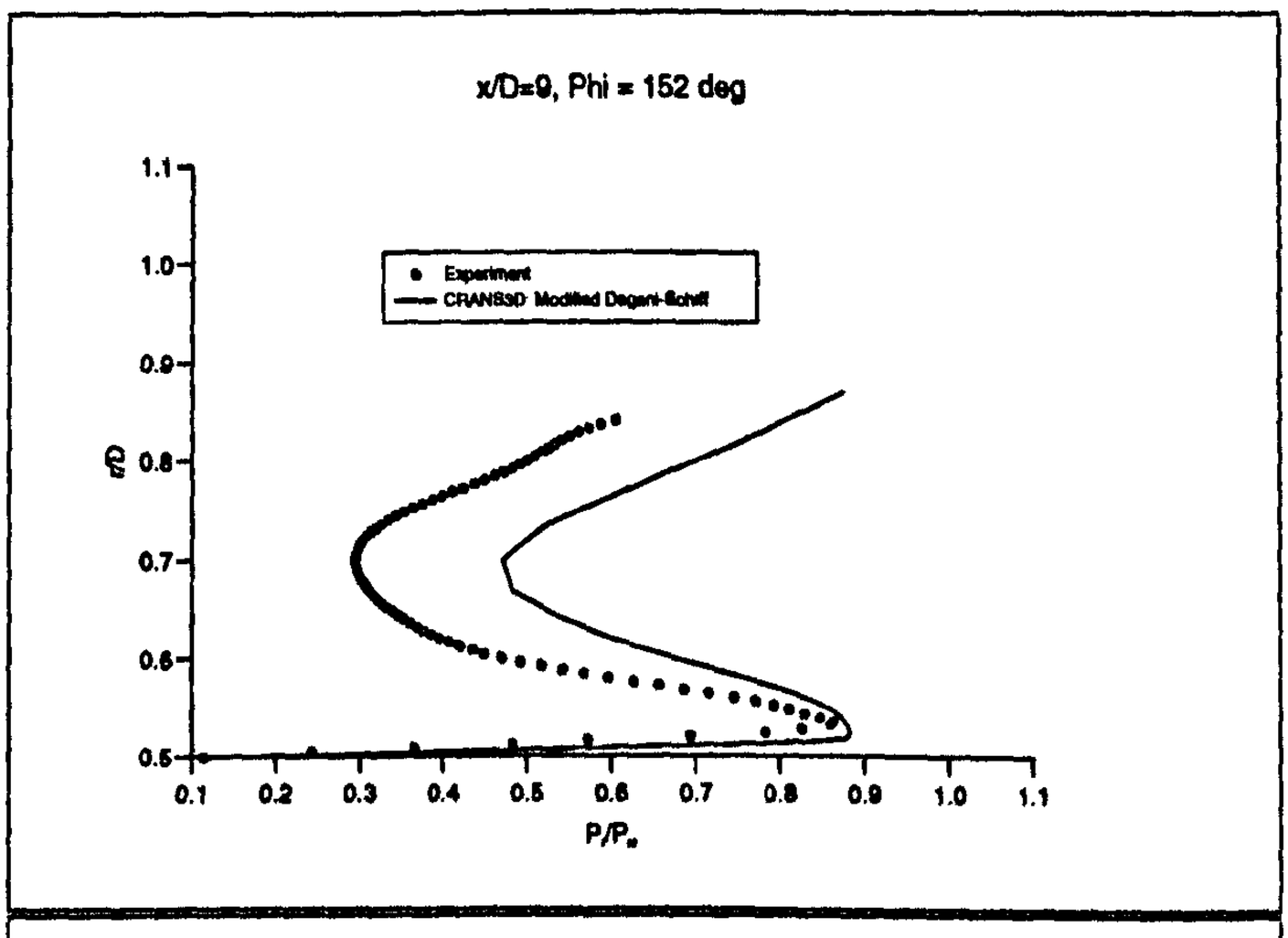

Figure 4.44: *Total Pressure Ratio Profile: x/D=9, Continued*

4.3.2 The RAE Forebody: Cases 5-8

The experimental studies which form test cases 5-8 are those performed at the Royal Aerospace Establishment, at Bedford, U.K., now the Defence Evaluation and Research Agency, by Ward et al [78] [23] [79]. The body investigated consisted of a 3 calibre ogive nose attached to a 10 calibre cylindrical section, and was tested in the 8ft × 8ft wind tunnel ($M_\infty = 0.7$ - 1.8) and the 3ft × 4ft High Speed Supersonic Tunnel ($M_\infty = 2.5$ - 4.5). The experiments were performed with a transition strip of carborundum grit of height 0.508mm at $x/D \approx 0.3$ in order to trip fully turbulent boundary layers further downstream. The experimental accuracy is quoted as follows:

Table 4.2: Experimental Accuracy

Property	Accuracy
C_p	± 0.003
$P_p/P_{p\infty}$	± 0.0025
M_∞	± 0.01
α	± 0.05°

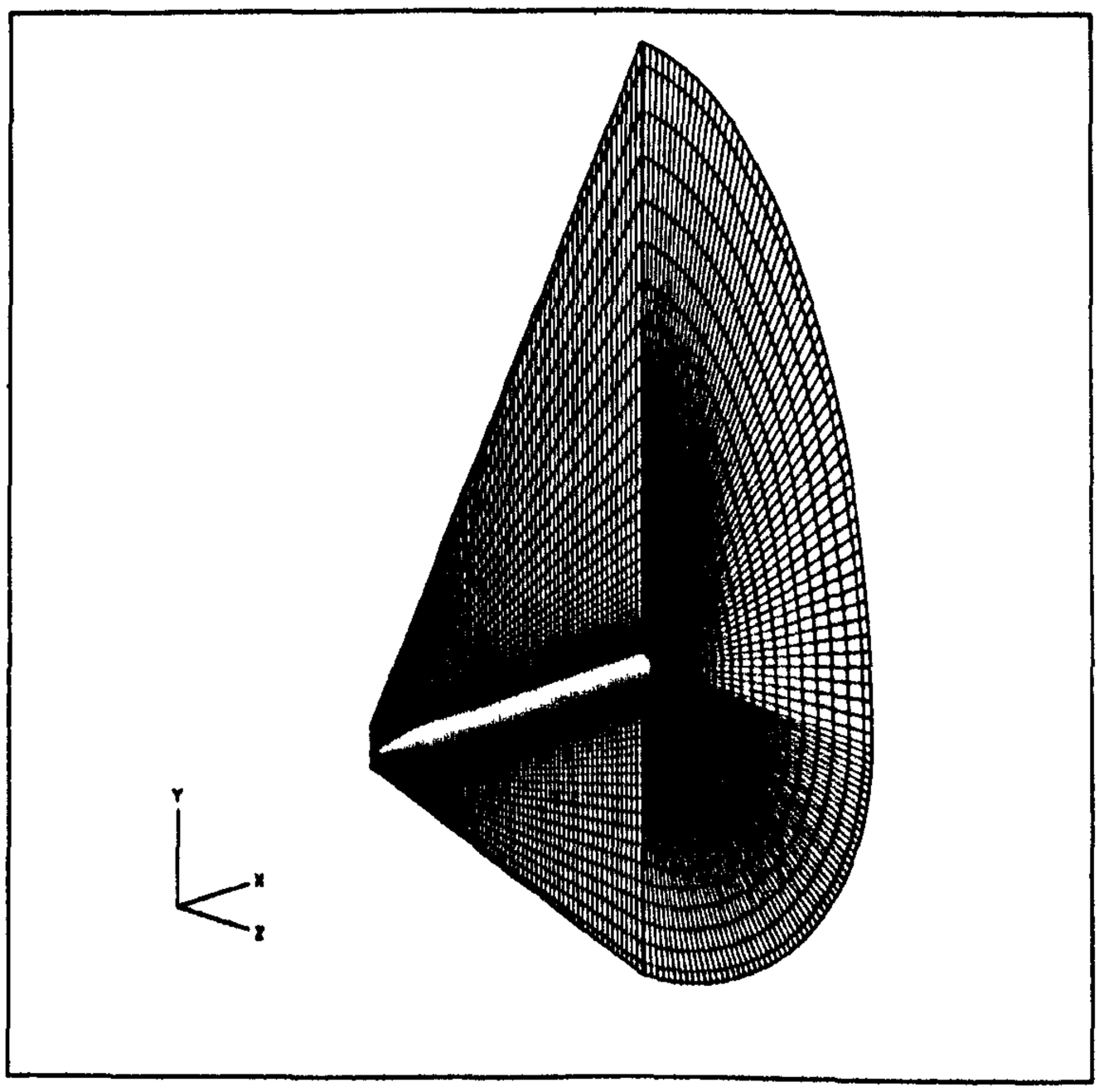

Figure 4.45: *B1A Supersonic NS Grid for Case 7 (89 × 89 × 119)*

The test cases were computed using both CRANS3D and PNS solver employed on the previous four cases, using various grids each with the first cell from the body surface with a radial size of $0.5 \times 10^{-5} D$ and the clustering performed using a *tanh* function. Figure 4.45 presents the finest grid used for the supersonic test case 7, while Figure 4.46 presents the finest transonic grid used in the study of test case 8.

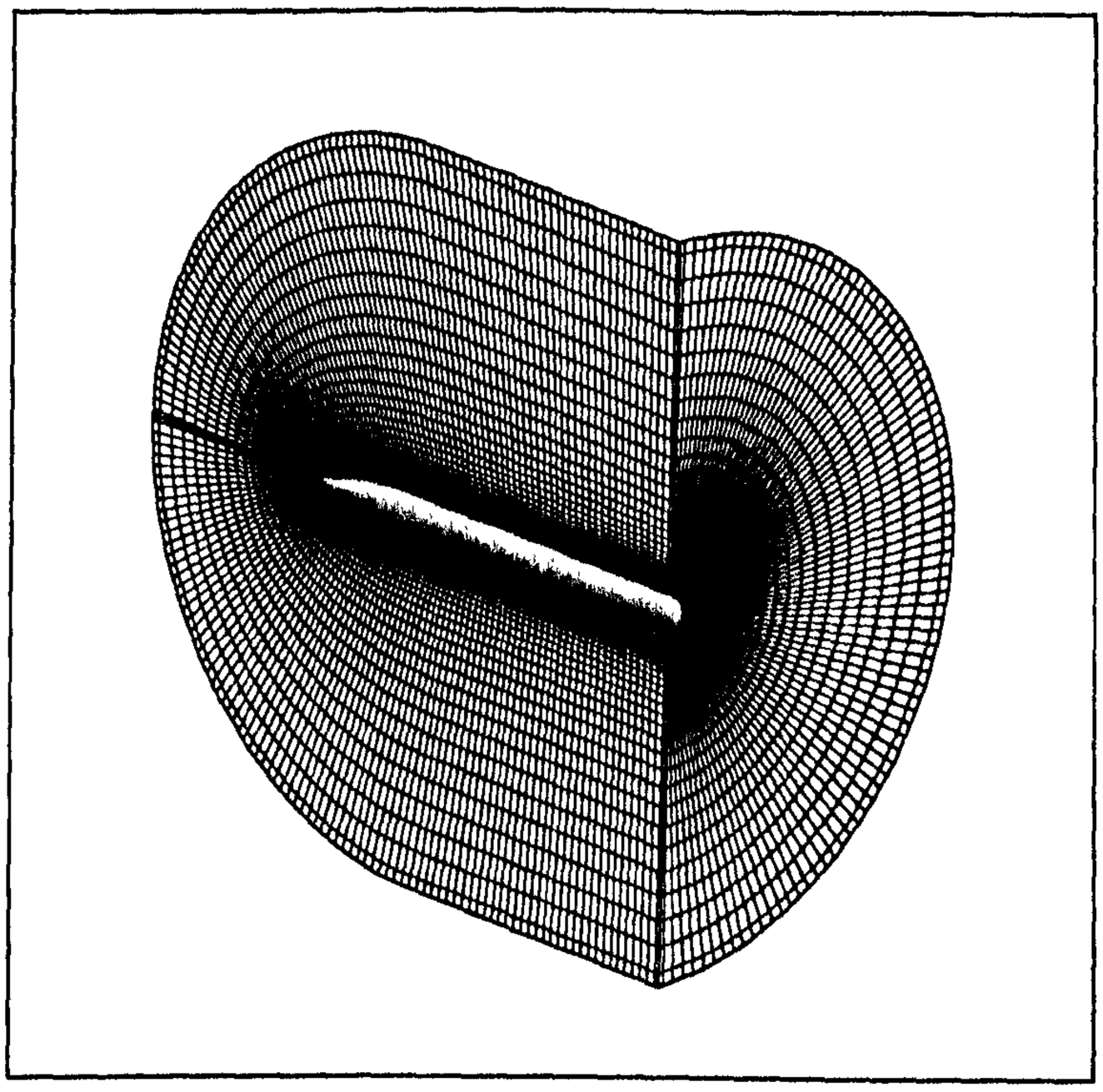

Figure 4.46: *B1A Transonic NS Grid for Case 8 (89 × 89 × 89)*

Case 5: B1A Body, Mach 2.5, 14° Angle of Attack

The test case was studied using 3 grids, the finest of which was (89 × 89 × 119). Figure 4.47 shows the results of the grid convergence study. A study of the effect of the cut-off factor was performed on this finest grid and it was found that, in terms of the surface pressure distribution along the whole body, and the resolution of the vortex structures at the three axial stations, a cut-off factor of 1.15 was found to be the optimal value. Figure 4.48 presents the comparison between the solution on the finest grid using both the standard, and modified Degani-Schiff formulation and clearly demonstrates the improvement made by reducing the cut-off factor to 1.15.

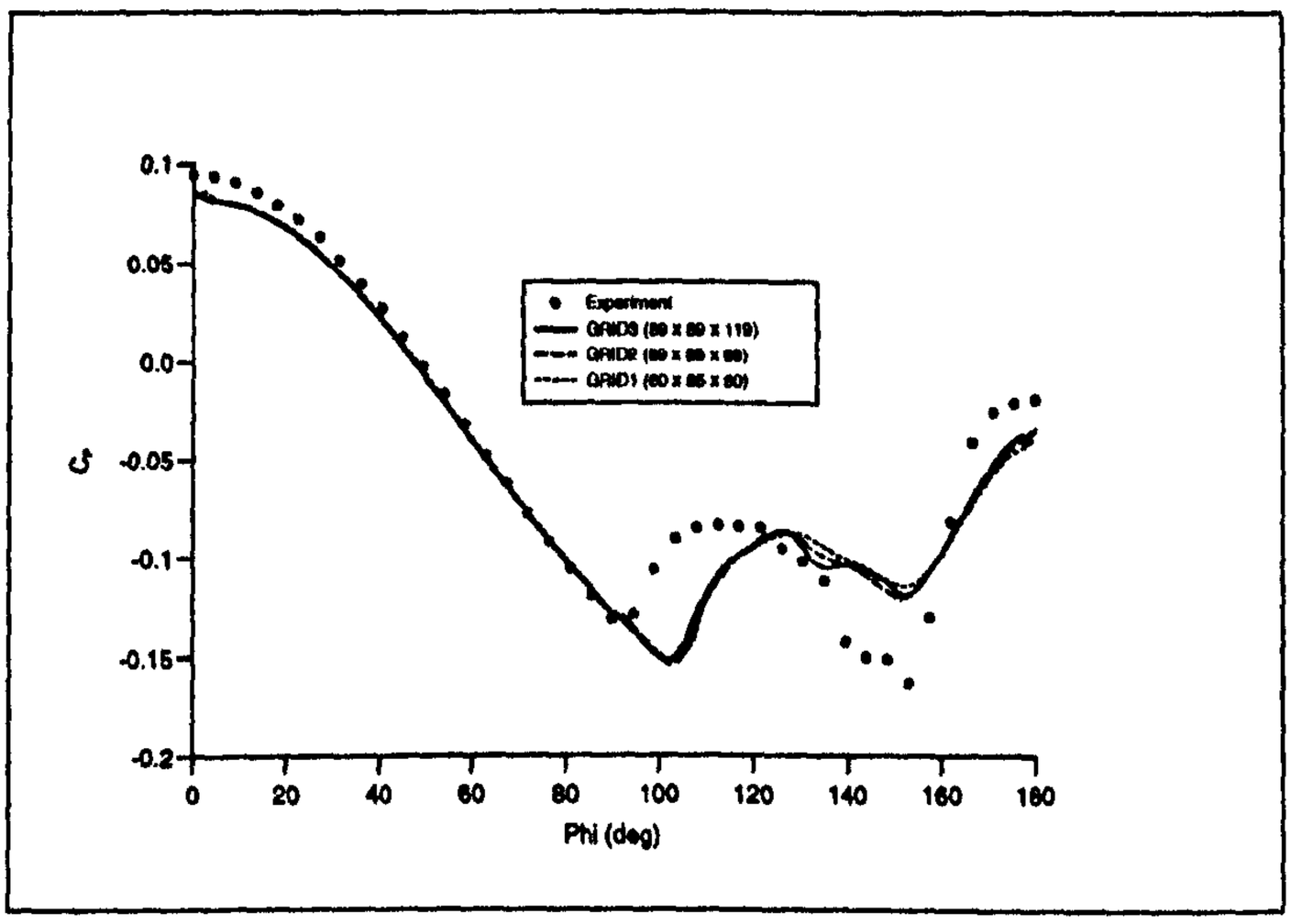

Figure 4.47: *Grid Convergence, Surface C_P at x/D=5, B1A, M_∞=2.5 14°*

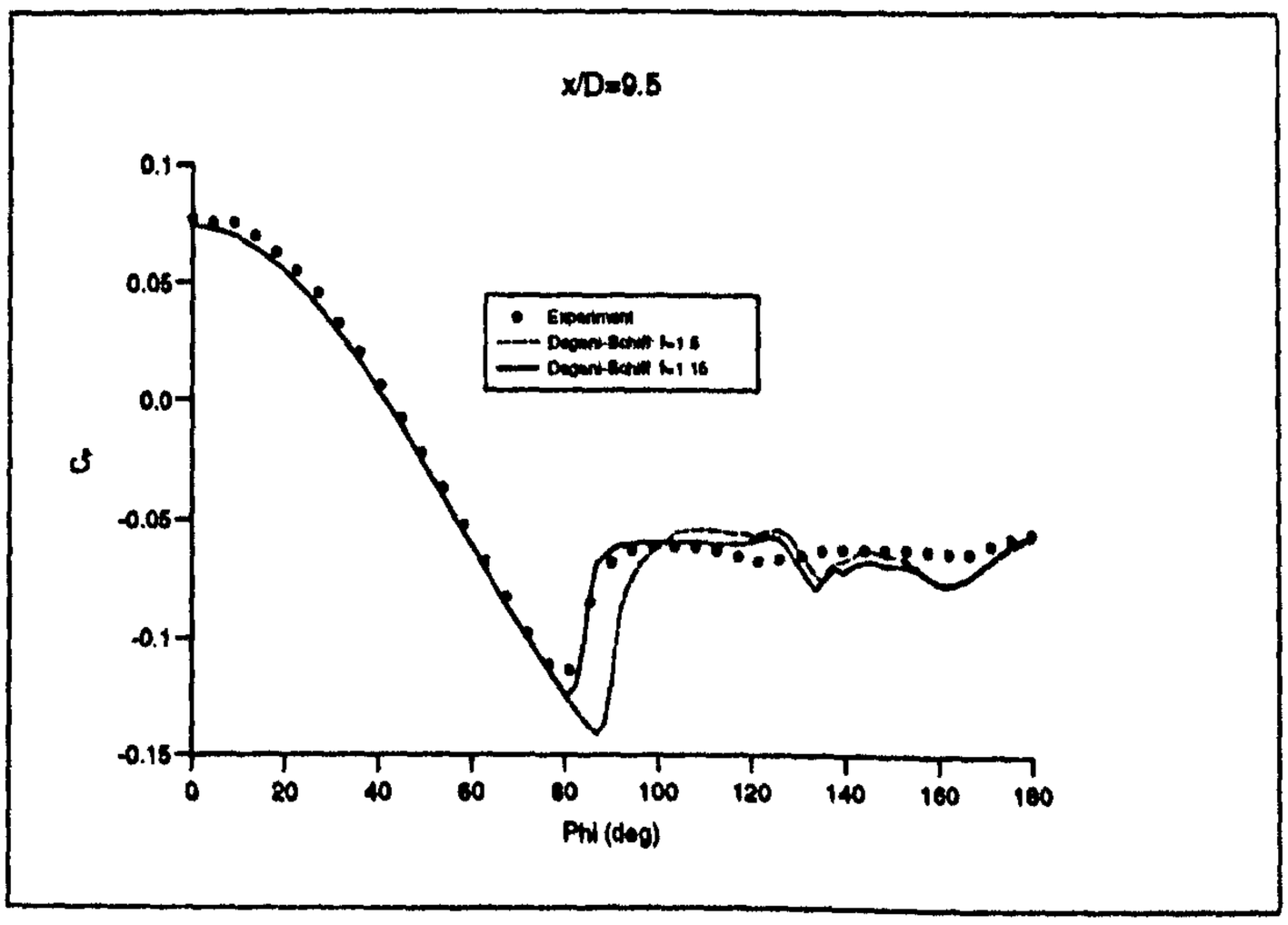

Figure 4.48: *Effect of Degani-Schiff Parameter, Surface C_P at x/D=9, B1A, M_∞=2.5 14°*

Figures 4.50 and 4.49 present the comparison of experimental with both laminar and turbulent CRANS3D circumferential surface pressure distributions. The flow is clearly turbulent, as the laminar result separates too early and does not exhibit the sharp pressure jump associated with the development of a crossflow shock between $80 - 90°$. The turbulent results using the modified cut-off factor consistently predicted the crossflow shock around $5 - 10°$ further leeward than experimental data would suggest. The main difference between the experimental and the computed surface pressures occurs in the leeward regions, in particular in the resolution of the vortex suctions. For instance, at $x/D = 7.5$ the vortex suction is overpredicted by as much as $\Delta C_p \approx 0.03$. This compares with an accuracy in C_p measurement quoted at ± 0.003.

The method outlined in Section 4.2 was used to investigate this difference between computation and experiment in the leeward regions. The NS solution was used to calculate the distribution, over the body, of displacement thickness and the local streamwise pressure gradient in the same manner as with cases 2 and 4. Figures 4.51 and 4.52 present examples of the circumferential distributions of displacement thickness and the local streamwise pressure gradient respectively.

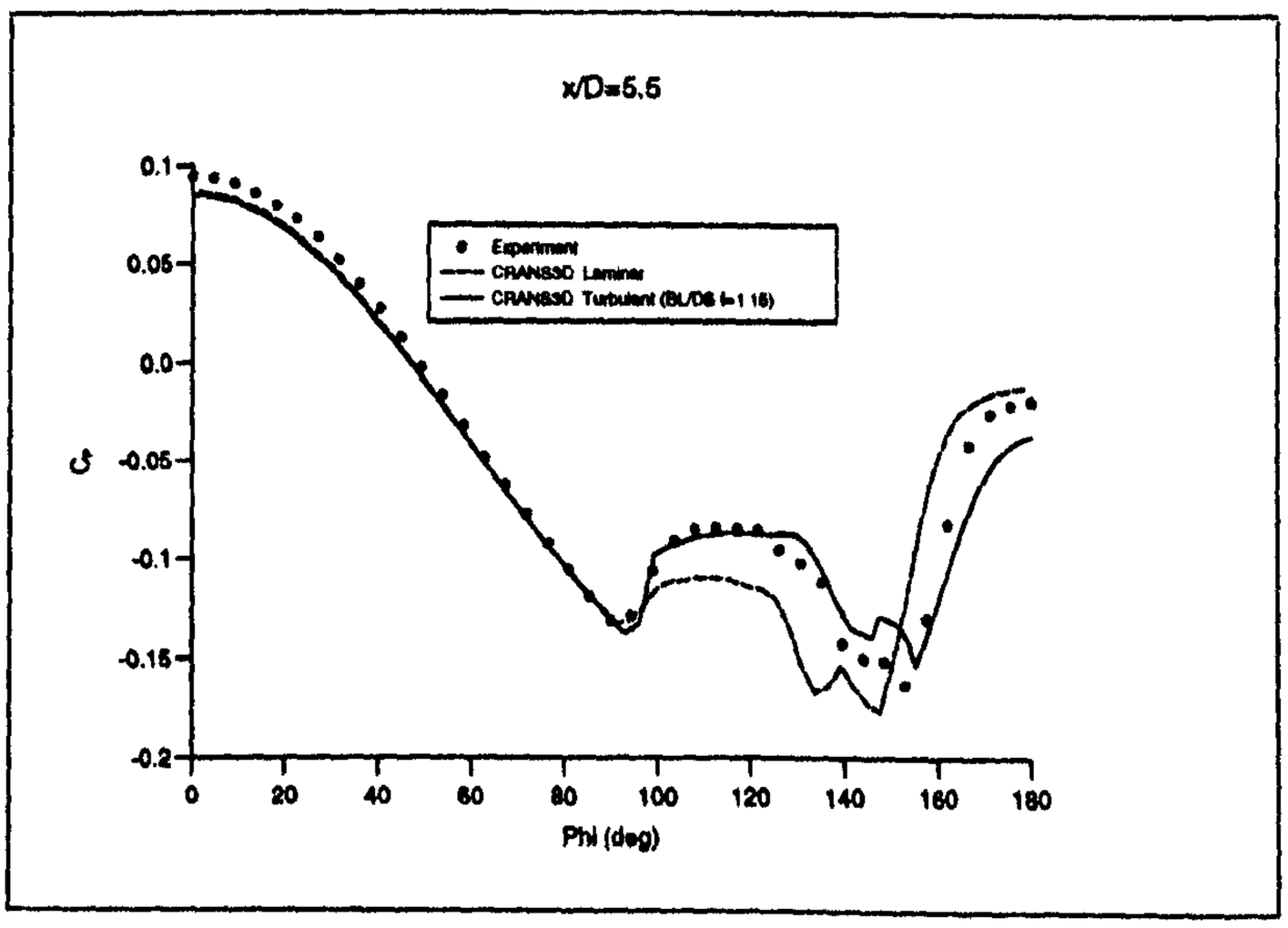

Figure 4.49: *Circumferential Surface Pressure Distribution, B1A, M_∞=2.5,* $14°$

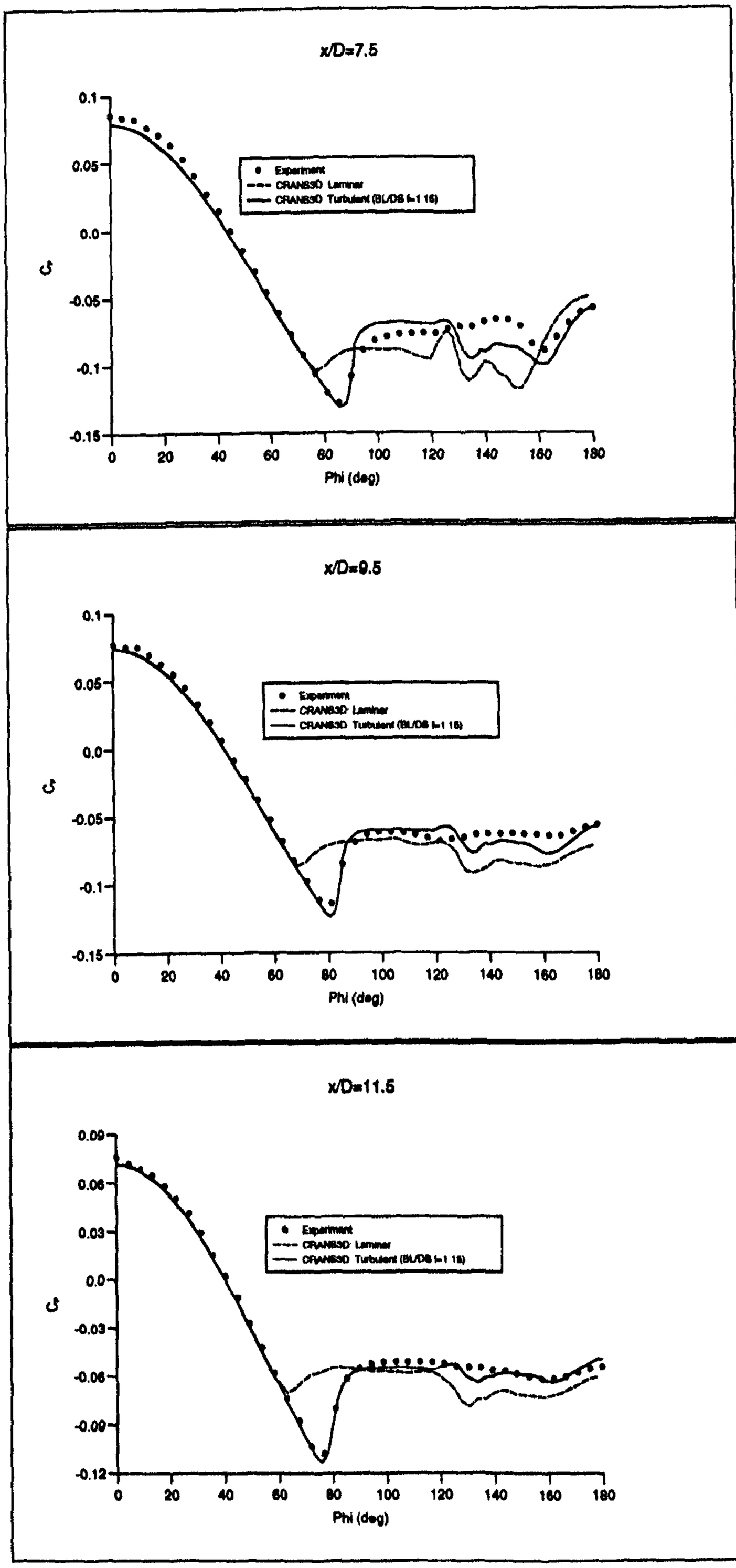

Figure 4.50: *Circumferential Surface Pressure Distribution, B1A, M_∞=2.5, 14°, continued*

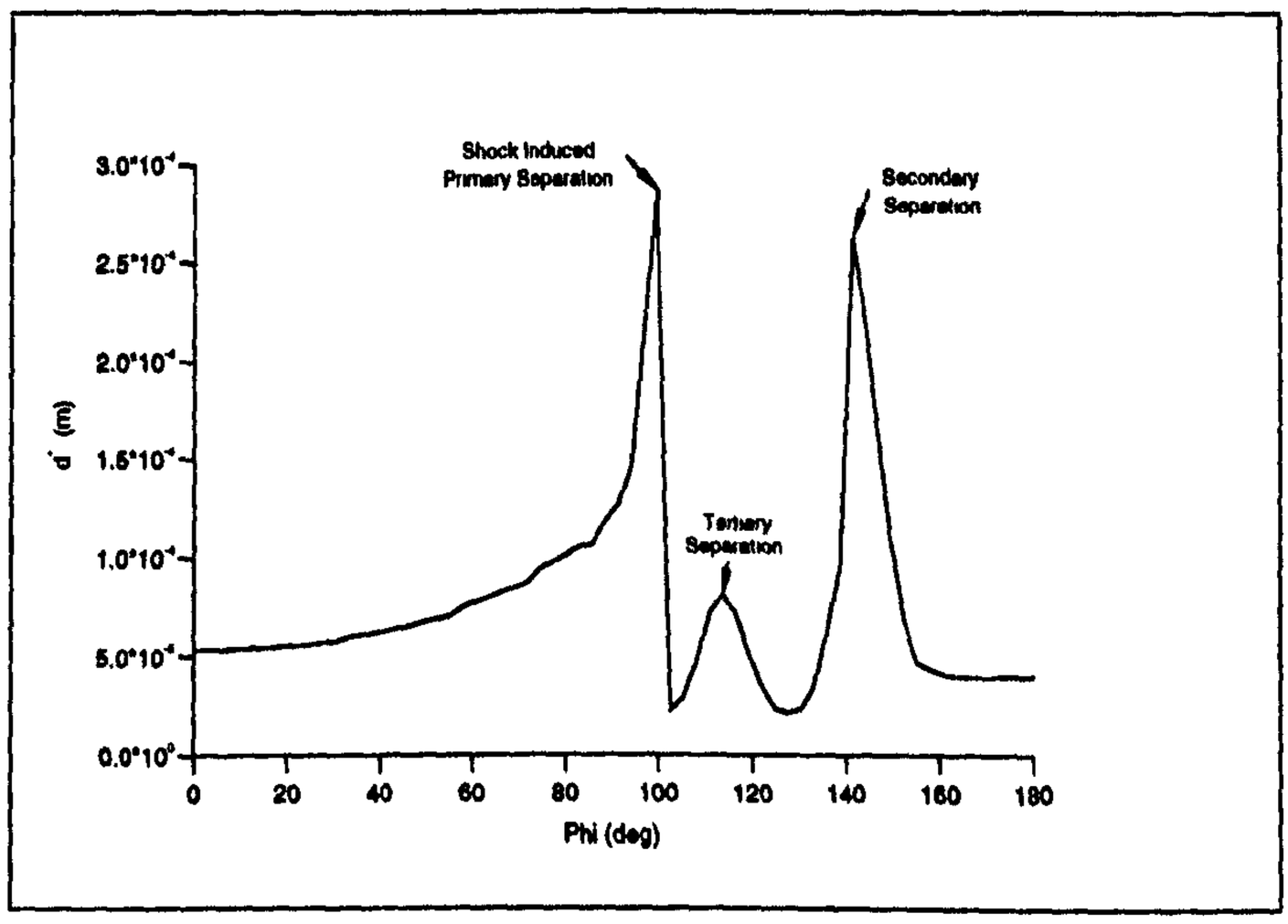

Figure 4.51: *Displacement Thickness: B1A, M_∞=2.5, 14°*

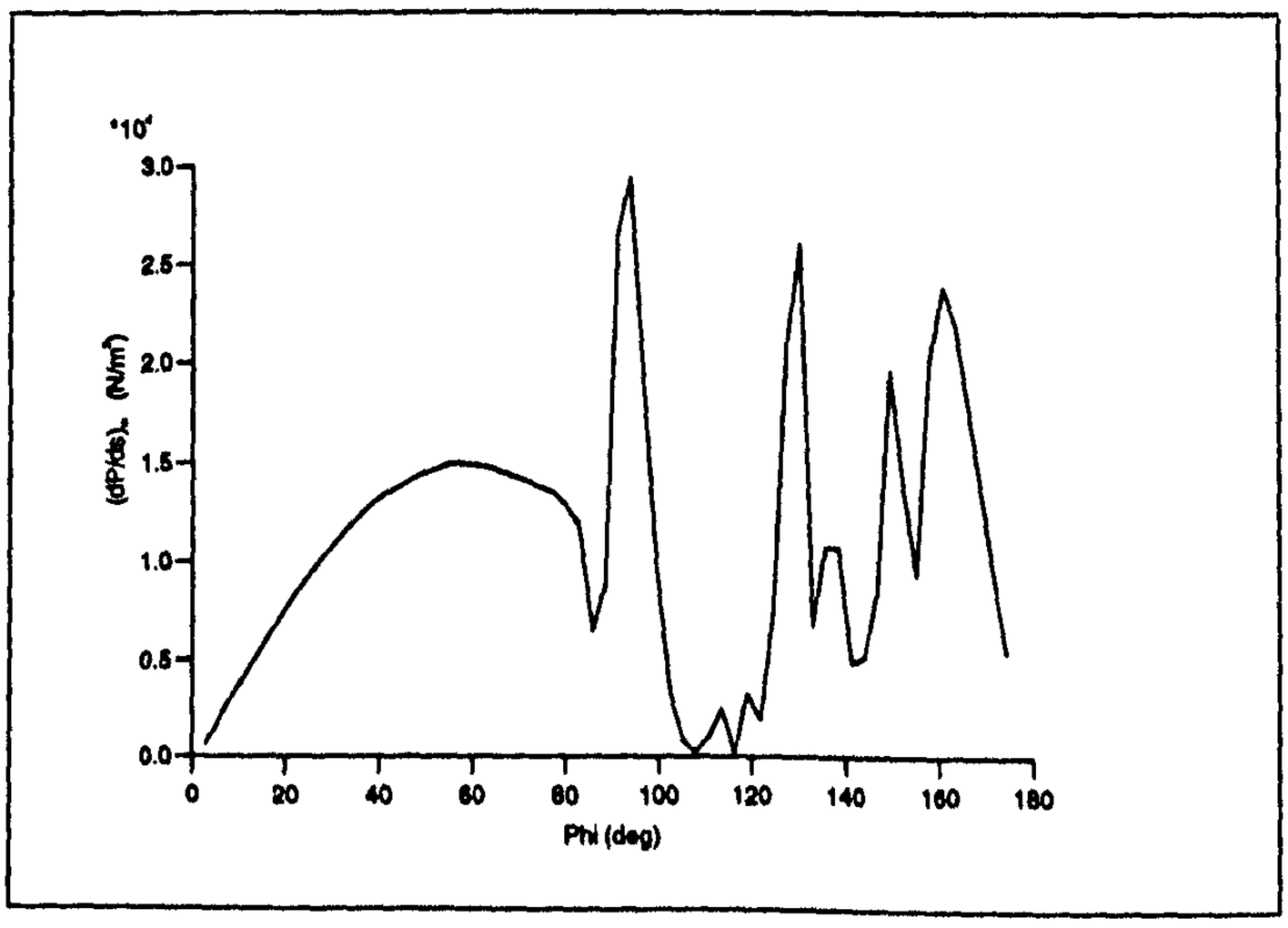

Figure 4.52: *Pressure Gradient: B1A, M_∞=2.5, 14°*

Figure 4.53 presents the resulting comparison between the computed surface pressure distributions and the experimental measurements with the estimated error bars. It can be seen that the computed curves lie generally within the bounds of the estimated experimental accuracy. In the regions where the computed curves depart from experiment, the corresponding error bars, which in some places are significantly greater than the quoted ± 0.003, are large enough that the computation is still within the error bounds. More confidence can therefore be placed in the numerical prediction.

Figure 4.54 presents the crossflow pitot pressure contours at stations $x/D = 5.5$ and 11.5, and compares experiment with the turbulent computations employing the original Degani-Schiff formulation, and that using a different cut-off factor. At station $x/D = 5.5$, the modified Degani-Schiff turbulence model clearly predicts the crossflow shock and both primary and secondary vortex structures better than the original formulation. At $x/D = 11.5$, the modified Degani-Schiff solution predicts a weaker crossflow shock slightly more windward than that appearing in the standard Degani-Schiff solution. The crossflow shock, however, although its effect is present in the corresponding surface pressure distribution, is not clearly evident in the experimental crossflow measurements.

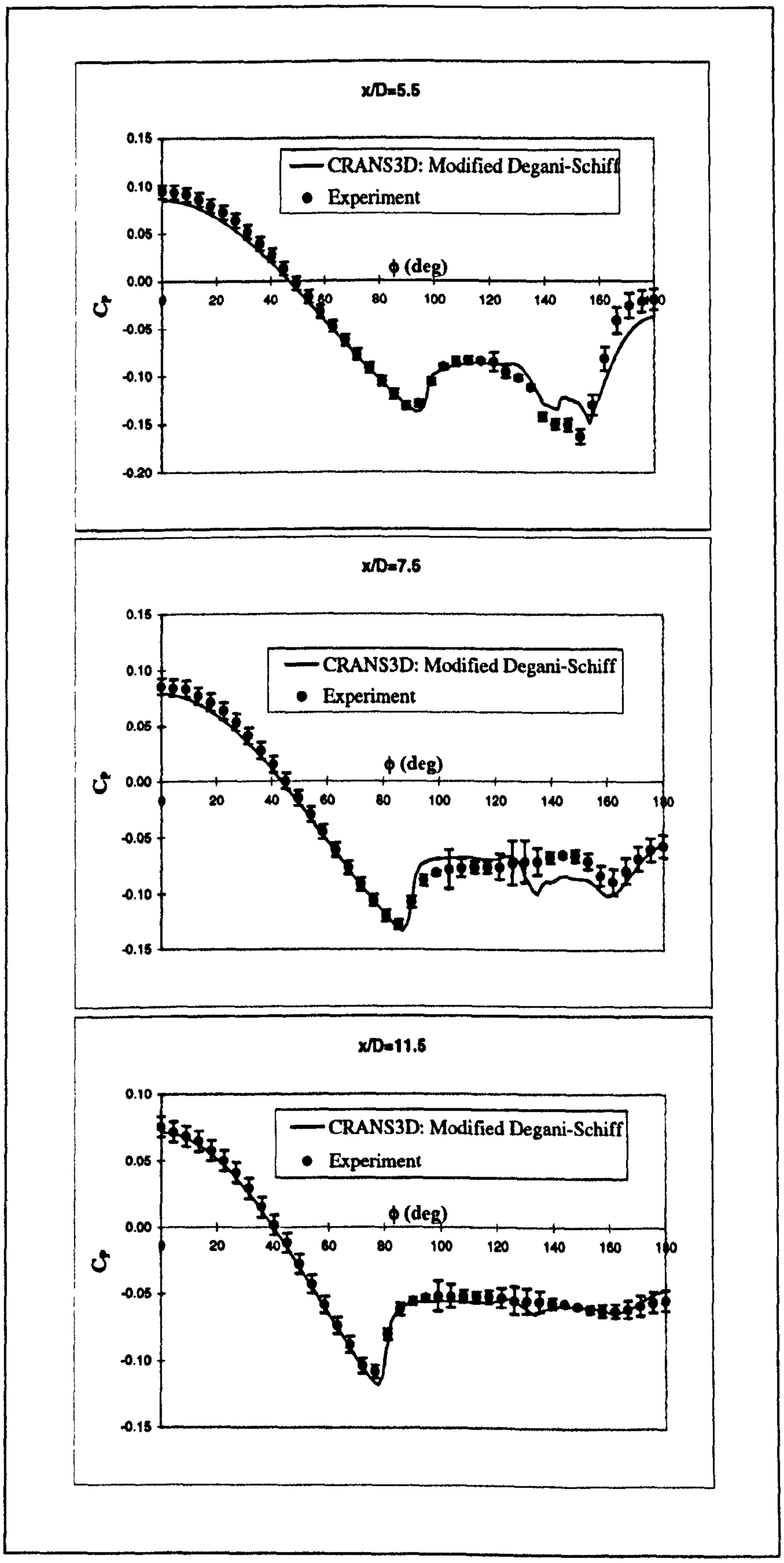

Figure 4.53: *Circumferential Surface Pressure, Experimental Error: B1A,* M_∞*=2.5,* 14°

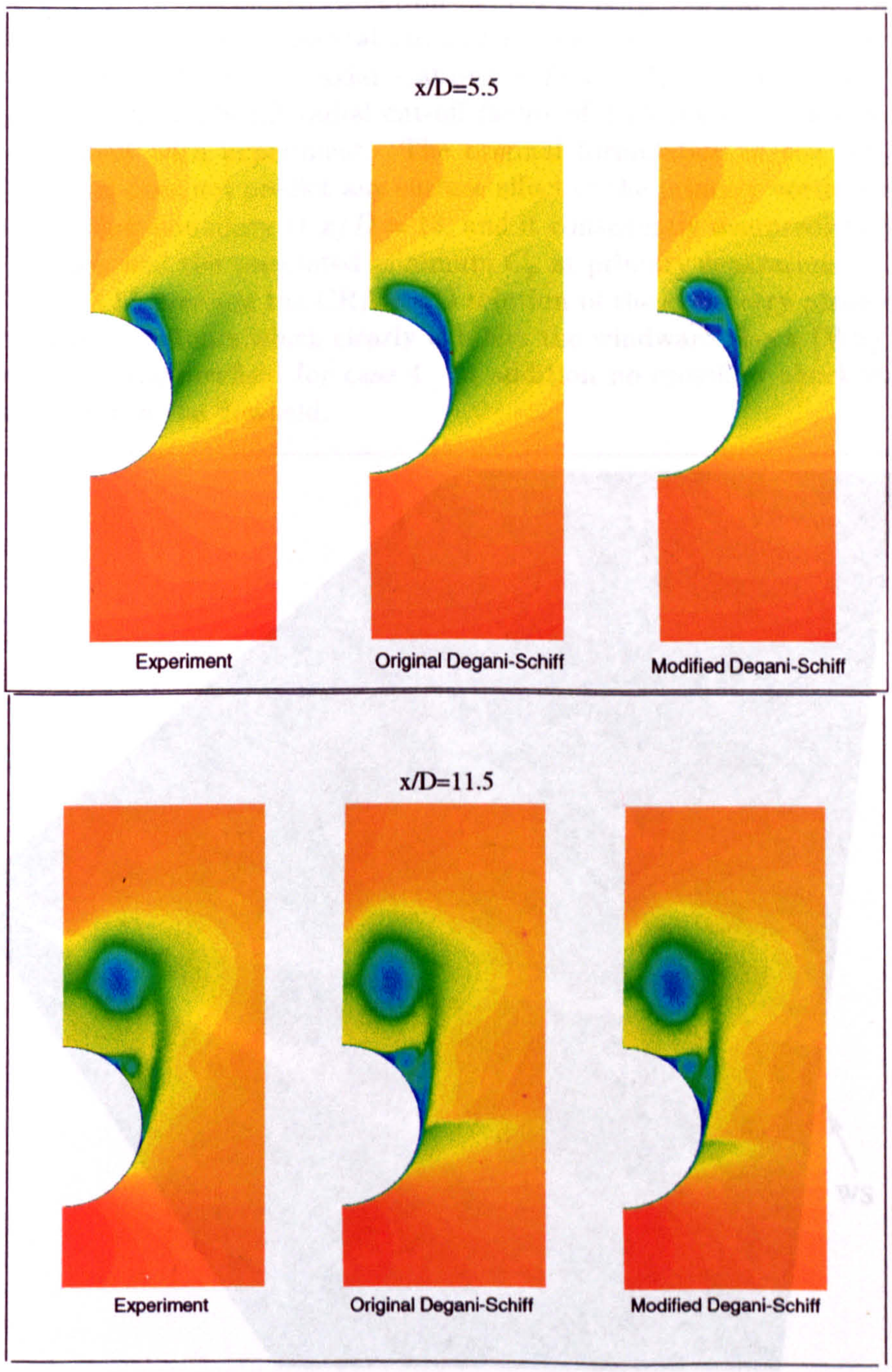

Figure 4.54: *Crossflow Pitot Pressure Contours: B1A, M_∞=2.5,* 14°

Case 6: B1A Body, Mach 2.5, 8^o angle of attack

Case 6 was computed using CRANS3D and the PNS solver on a grid (89 $\times$ 89 $\times$ 119) for Degani-Schiff cut-off factors of both 1.5 and 1.15. Figure 4.56 compares the experimental circumferential surface pressure with the computed distributions at axial stations x/D = 5.5, 8.5 and 11.5. The result for a Degani-Schiff radial cut-off factor of 1.15 is clearly superior in its agreement with experiment. The original formulation of the Degani-Schiff model does not predict any surface effect of the primary vortices even by the outflow boundary at $x/D = 13$, and it consistently overpredicts both the position and the associated minimum C_p at primary separation.

Figure 4.55 presents the CRANS3D solution of the symmetry plane density gradient contours which clearly exhibits the windward shock (WS) feature seen in the flowfield for case 4. In addition no crossflow shock-waves were evident in the flowfield.

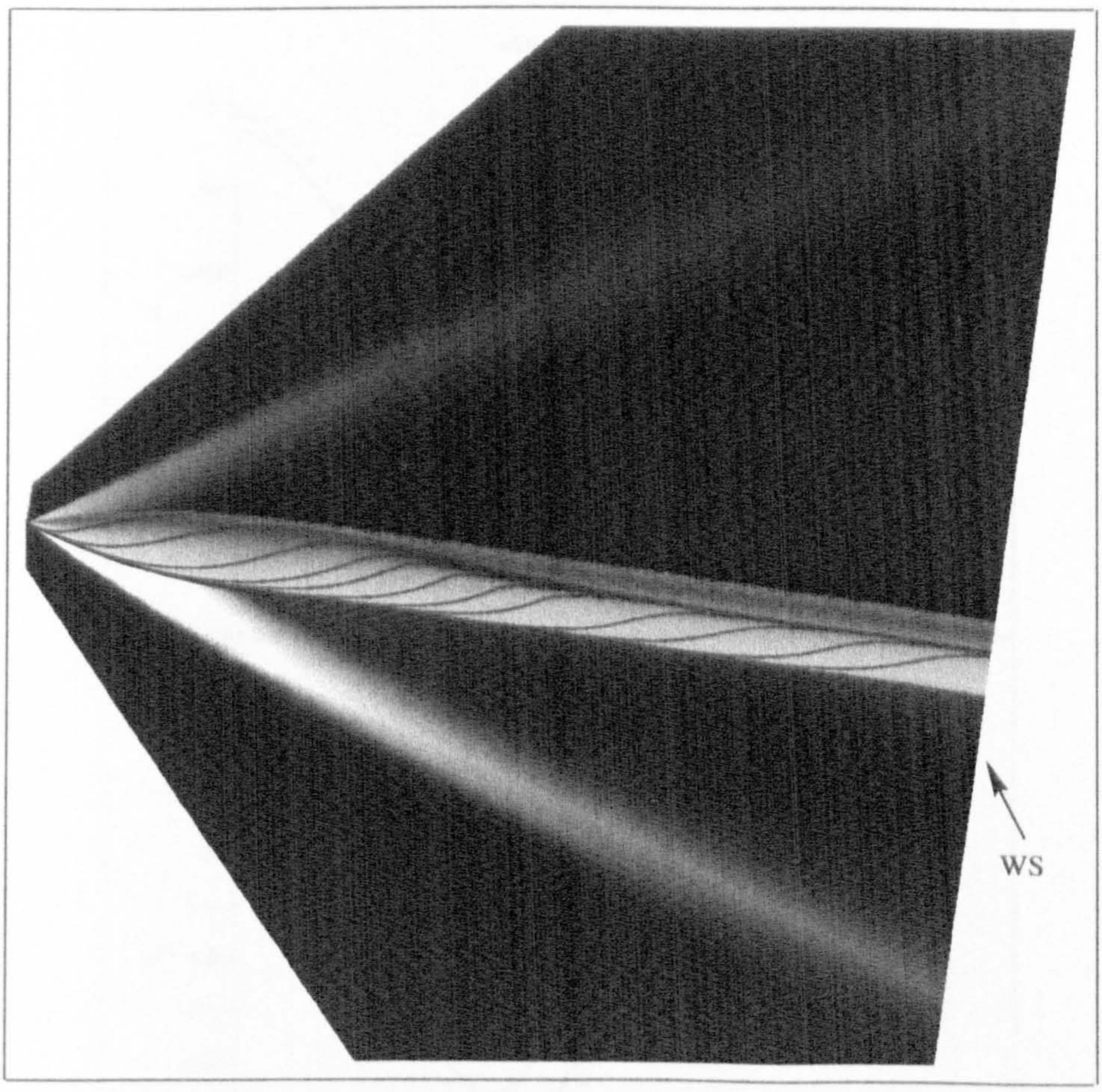

Figure 4.55: *Symmetry Plane Density Gradient and Skin Friction Lines: B1A, M_∞=2.5, 8^o*

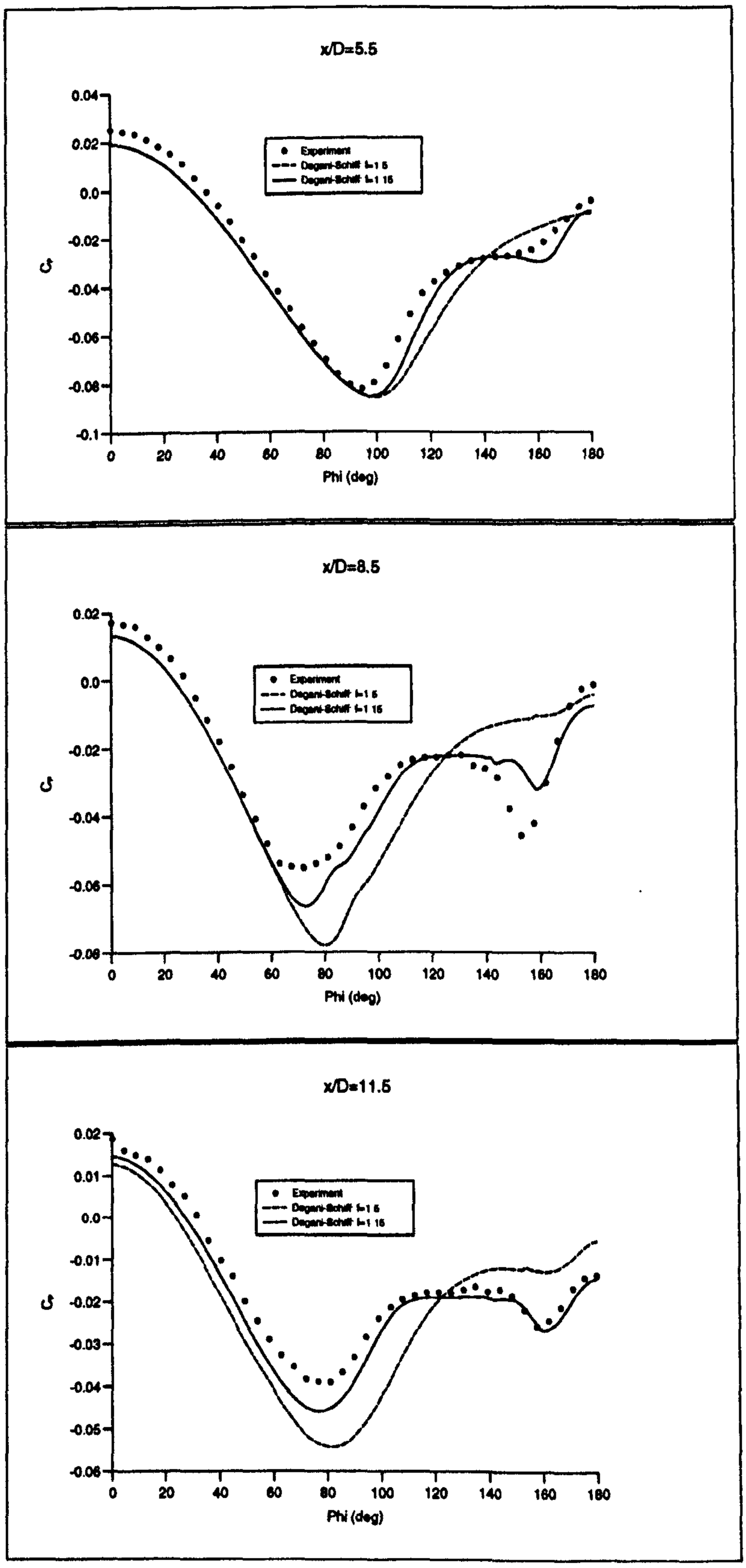

Figure 4.56: *Circumferential Surface Pressure Distribution, B1A, M_∞=2.5, 8°*

Case 7: B1A Body, Mach 1.8, 14° Angle of Attack

For the study of this case three grids were employed: (60 × 85 × 60),(89 × 89 × 89) and the finest being (89 × 89 × 119). The solutions on the two finest grids were practically equivalent using both NS and PNS solvers. Figure 4.57 shows the comparison of the experimental surface pressure measurements and the NS and PNS solutions at a number of values of the Degani-Schiff cut-off parameter. The NS solver is seen to consistently yield a better prediction, for a given value of the cut-off parameter, than that generated by the PNS solver. This is consistent with the findings from case 4. It can be seen for this case that a cut-off factor of 1.15, although producing a great improvement on the original value of 1.5, is not the optimal value which was found to be around 1.1 for the NS solver and about 1.05 of the PNS solver (though convergence is not certain for this result).

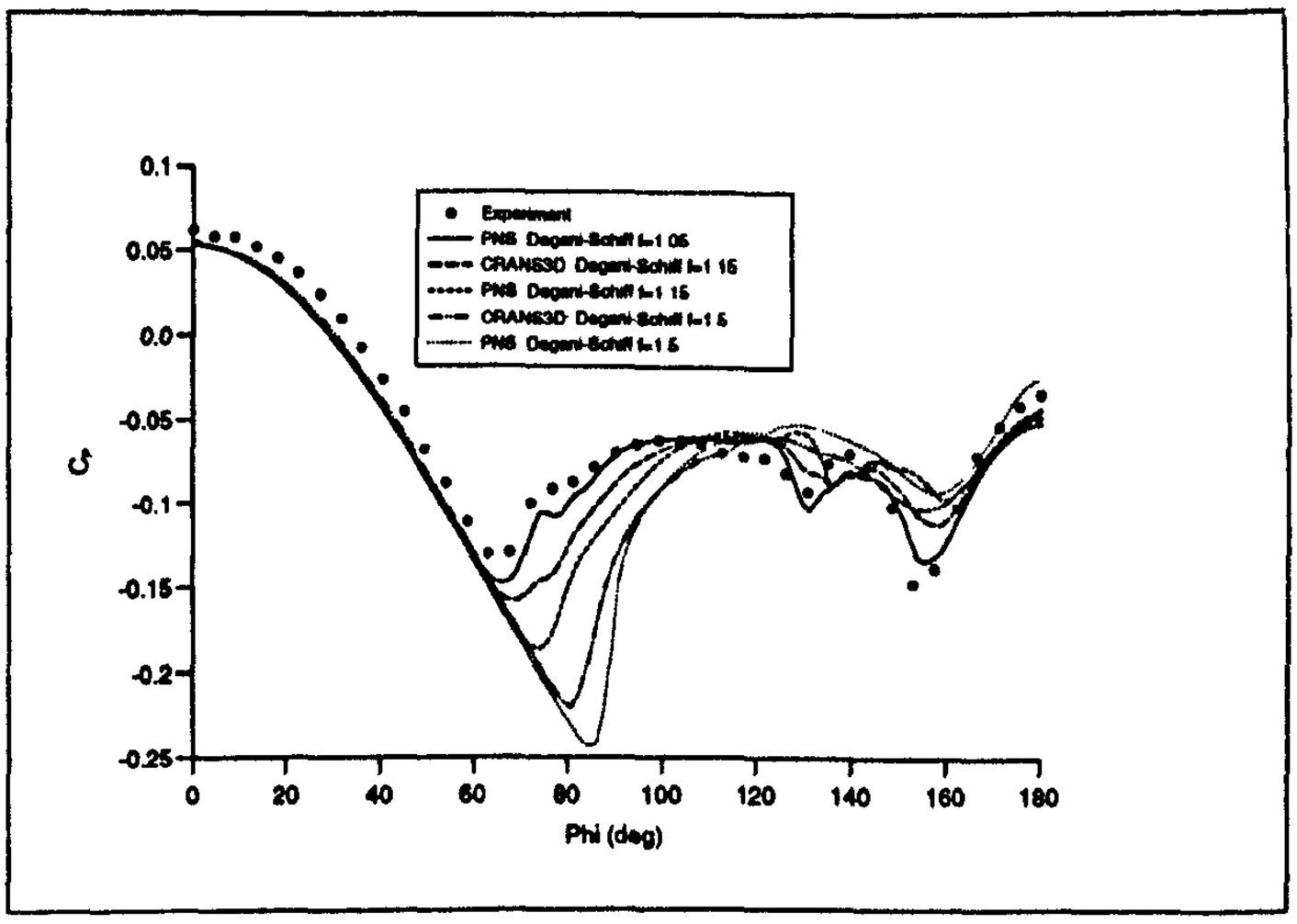

Figure 4.57: *Effect of Degani-Schiff Parameter, Surface C_P at x/D=7, B1A, M_∞=1.8,* 14°

Figures 4.58 and 4.59 compare the NS laminar and turbulent (cut-off factor=1.15) solutions for the circumferential surface pressure with the experimental measurements. Much better agreement is observed between experiment and the turbulent solution than between experiment and the laminar result. The laminar solution consistently underpredicts both the position and the magnitude of minimum C_p at primary separation which leads to poor predictions of the leeside pressure distributions. At station $x/D = 5.5$ the turbulent solution correctly captures the crossflow shock, but this is resolved by about 3° too leeward and with slightly too much strength. At $x/D = 7.5$ the crossflow shock is much weaker and has moved windward to around 70°. The NS solution successfully captures the crossflow shock, but the differ-

ence between experiment and computation is as much as $\Delta C_p = 0.05$ in its proximity, and the vortex suction is underpredicted by almost as much. At $x/D = 8.5$, the effect of a windward shock (WS), which appears in both the Schlieren picture taken during the experimental study (Figure 4.60) and the corresponding computed symmetry plane density gradient contours (Figure 4.61), is seen as a small inflexion in the surface pressure curves. The computed windward shock, however, appears about 15° more leeward than that measured in experiment, although they are both of similar strength. By the axial station $x/D = 9.5$ the windward shock has disappeared from the experimental and computed pressure distributions. At this station there is seen to be a large difference ($\Delta C_p \approx 0.03$) between the experimentally measured C_p and the value predicted by the NS solution which amounts to ten times the figure quoted as the experimental error in C_p measurement.

This extreme difference between experiment and computation is suggested to be associated with the incorrect resolution of the windward shock which is seen to pass under the body and stream off into the freestream. At station $x/D = 9.5$ the computed windward shock had only just moved off the underside of the body and its proximity will still affect the surface pressure, whereas the experimental windward shock is seen far from the surface such that it will not affect the surface pressure. The computational inability to predict the windward surface pressure distribution correctly leads to the disagreement between experiment and computation in the leeward regions.

At $x/D = 11.5$ the windward pressure distribution is within the experimental error of about $\Delta C_p \approx 0.01$ in the windward region predicted in the error analysis of case 5. The leeward pressures, however, are still overpredicted by as much as $\Delta C_p \approx 0.03$. If the experimental errors in the measurement of the leeward surface pressures for this case are similar to those estimated for the Mach 2.5 flow of case 5, then the error is expected to be of the order $\Delta C_p \approx 0.02 - 0.04$.

Figure 4.62 presents the three dimensional "carpet" plot of surface pressure predicted in the CRANS3D solution and clearly shows how the crossflow shock passes onto the windward side of the body, losing strength until it is no longer evident further downstream. Section 4.4 analyses the windward shock phenomena in the light of the study of all nine forebody test cases, and explains its origin. Interestingly, the laminar solution was seen to exhibit a windward shock, but this occurred almost at the outflow plane much further downstream than that resolved in the turbulent solution.

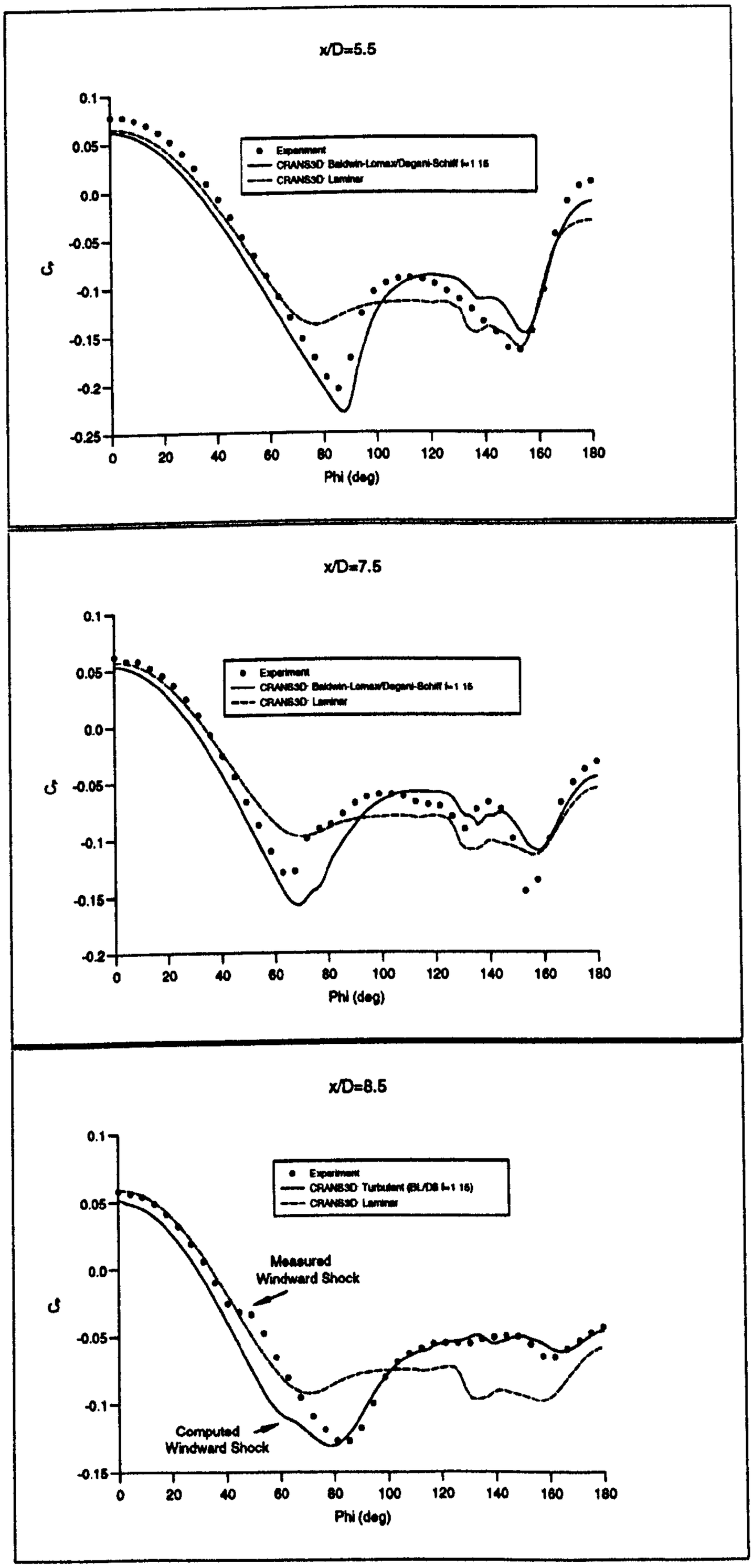

Figure 4.58: *Circumferential Surface Pressure Distribution, B1A, M_∞=1.8, 14°*

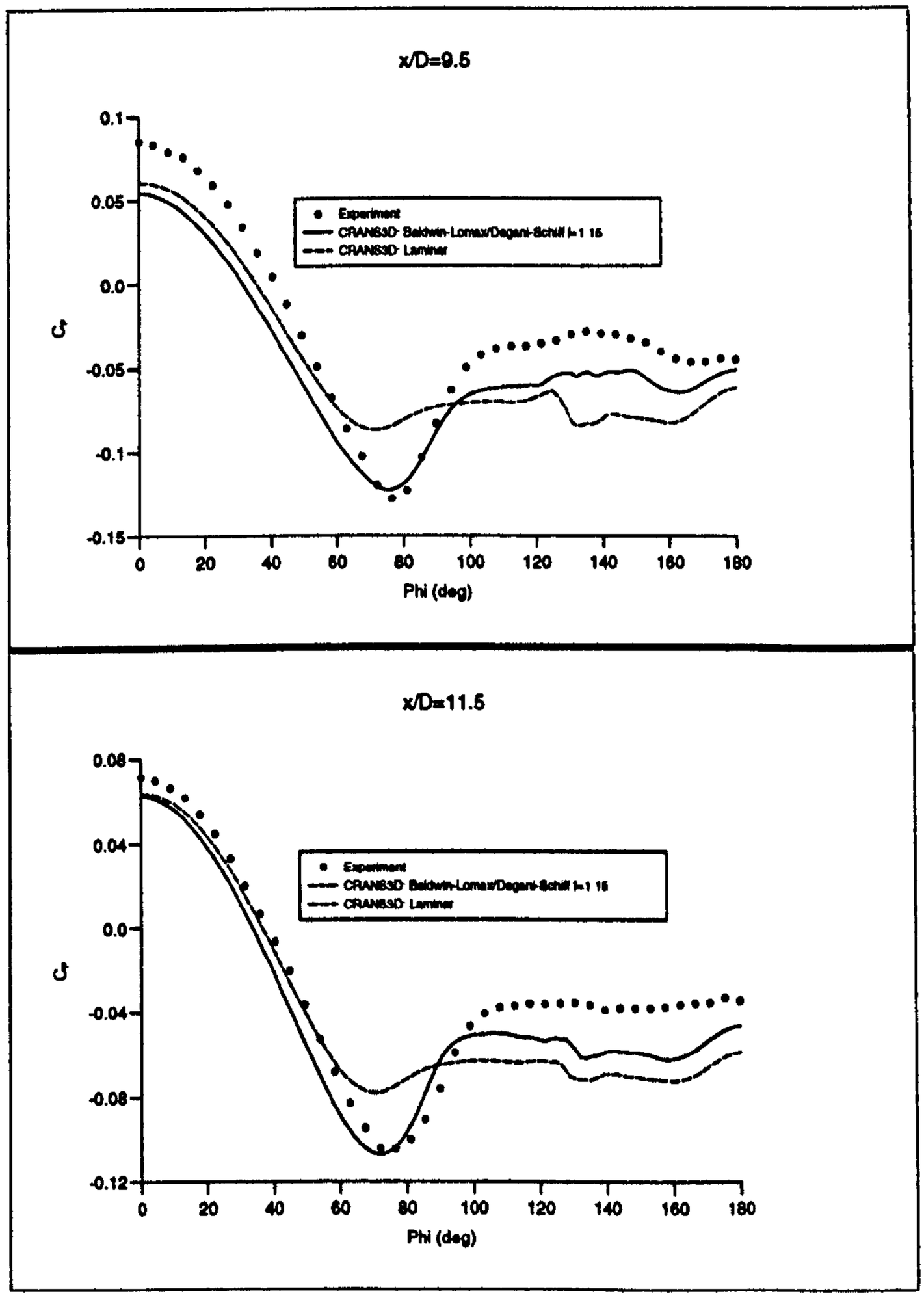

Figure 4.59: *Circumferential Surface Pressure Distribution, B1A, M_∞=1.8, 14°, continued*

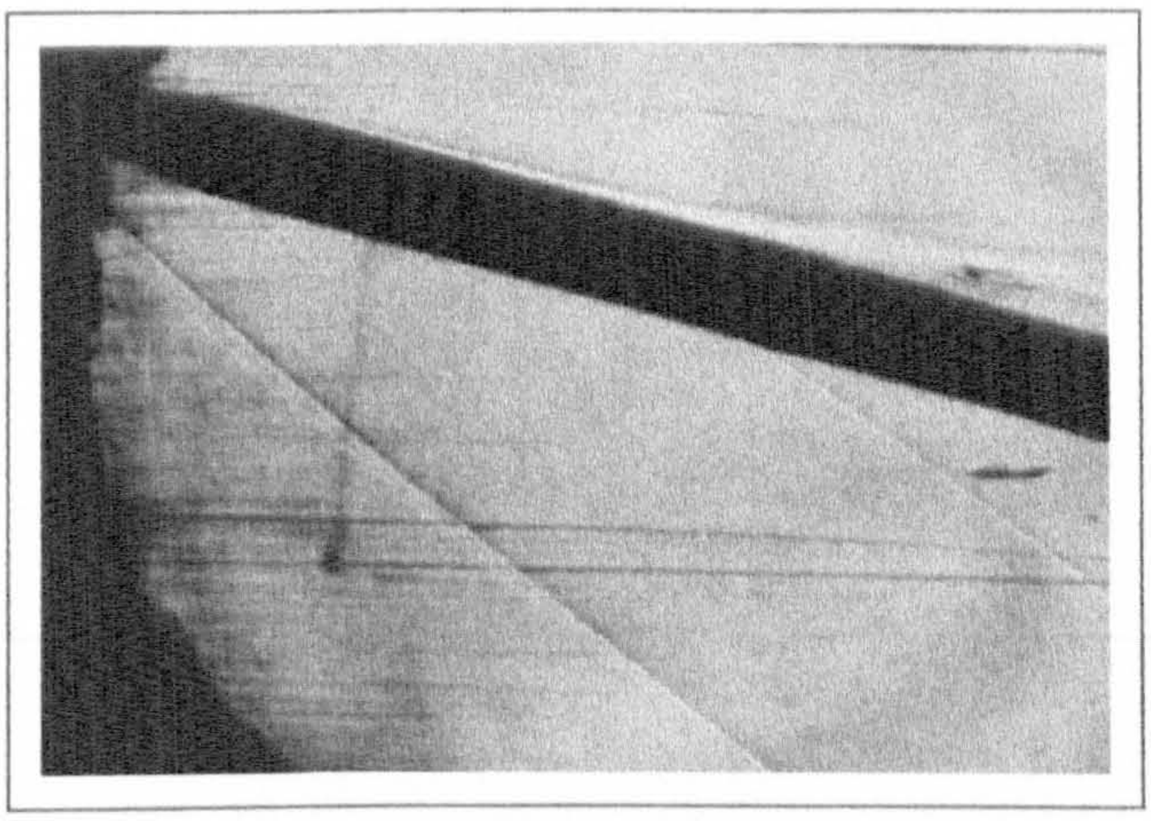

Figure 4.60: *Schlieren Photograph: B1A, M_∞=1.8,* 14°

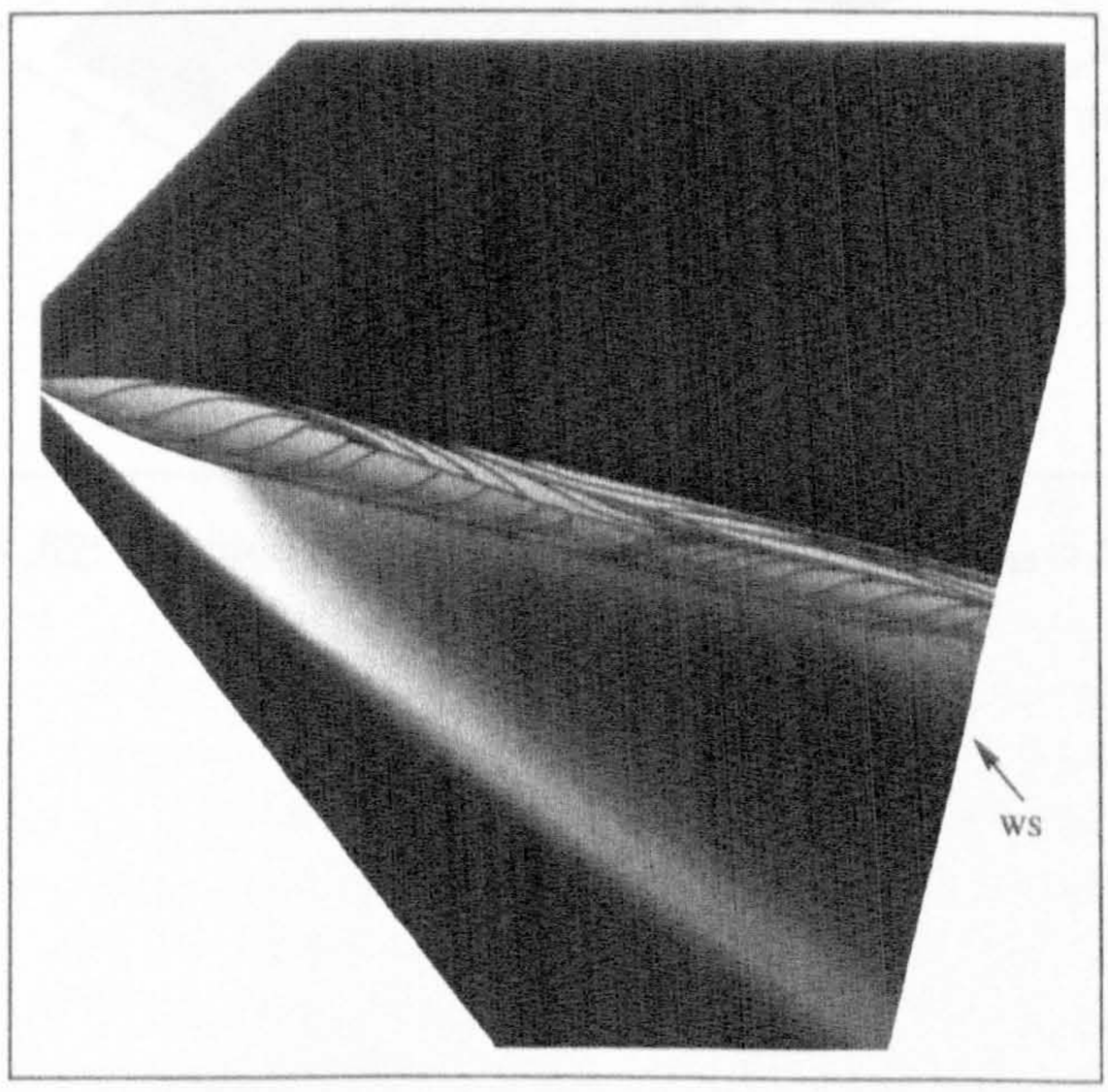

Figure 4.61: *Symmetry Plane Density Gradient: B1A, M_∞=1.8,* 14°

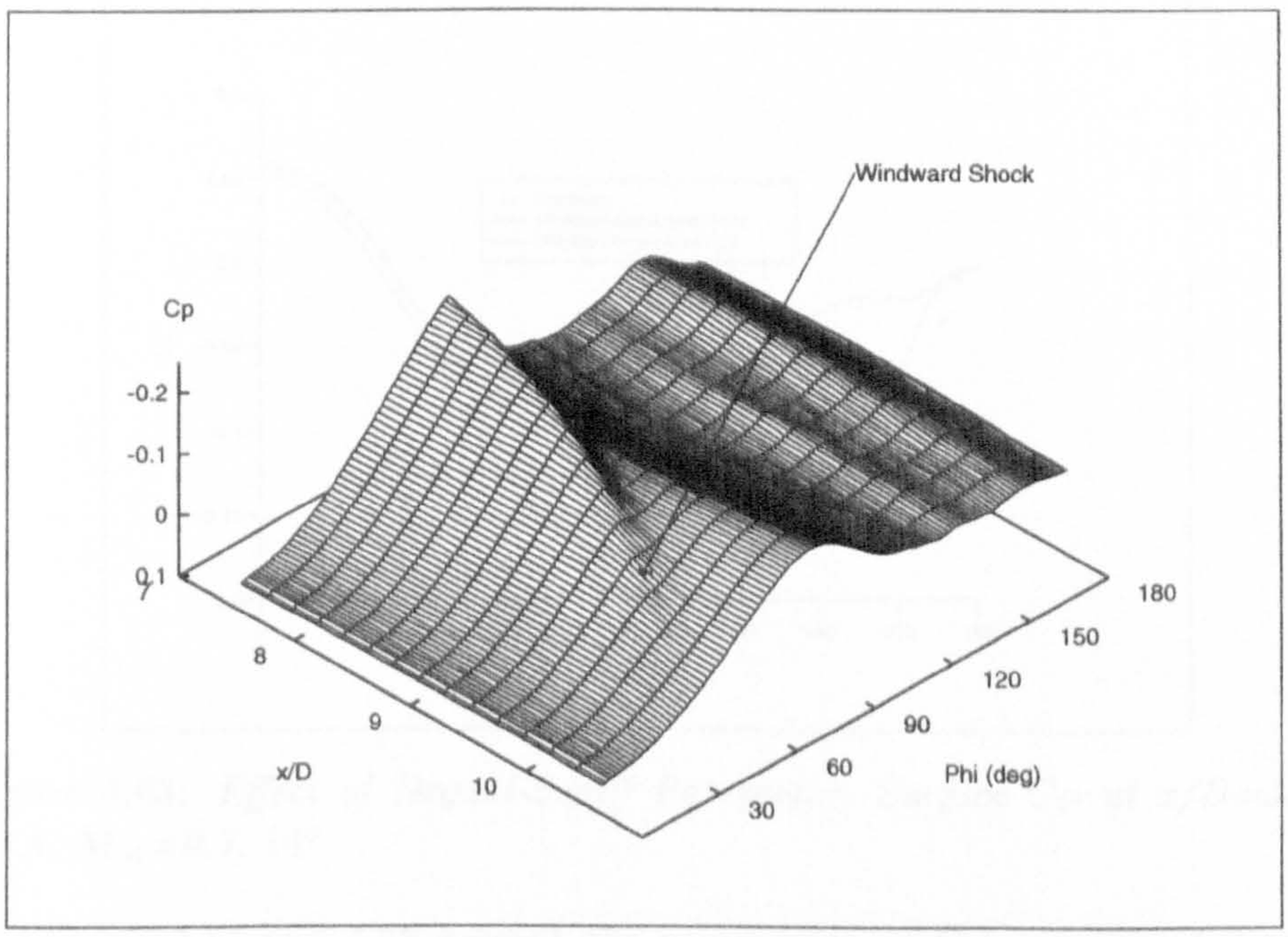

Figure 4.62: *Surface Pressure Carpet Plot: B1A, M_∞=1.8, 14°*

Case 8: Transonic Flow Past an Ogive-Cylinder Body

Since the PNS equations can solve for only steady supersonic flows, only the CRANS3D code was used in the analysis of this transonic test case. The inflow plane, outflow plane and farstream boundary conditions were implemented by evaluating the local sound speed for each boundary cell and solving the appropriate Riemann boundary problem - subsonic or supersonic inflow or outflow. The turbulent NS solutions were obtained on grids ($60 \times 85 \times 60$), ($89 \times 89 \times 89$) and ($89 \times 89 \times 119$) for the Degani-Schiff cut-off factor set at 1.5 and 1.15 and Figures 4.63 illustrates the improvement achieved by the lower value.

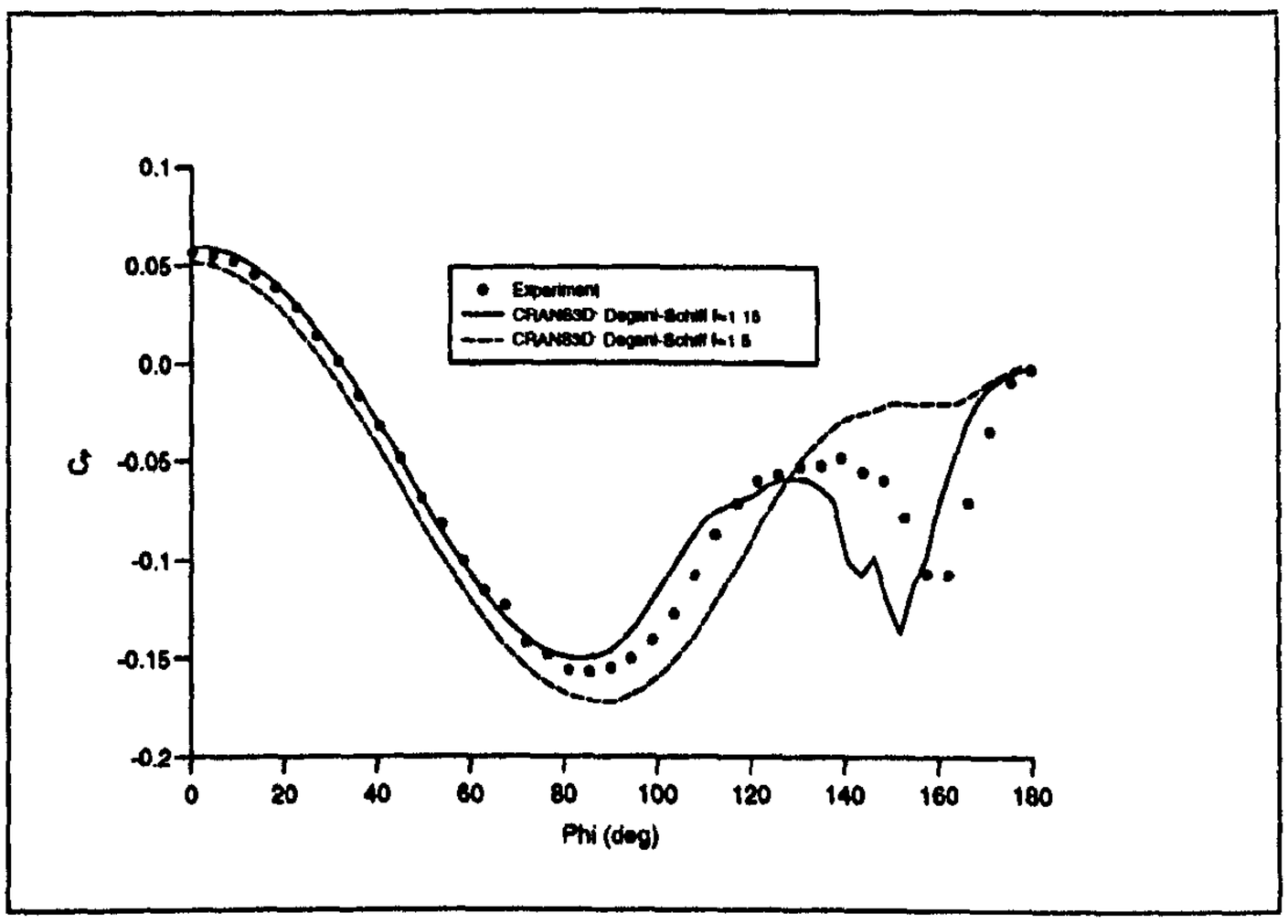

Figure 4.63: *Effect of Degani-Schiff Parameter, Surface C_P at x/D=5.5, B1A, M_∞=0.7,* 14°

Figures 4.64 and 4.65 present the comparison of the experimental and computed laminar and turbulent circumferential surface pressure at stations $x/D = 3.5, 5.5, 7.5, 9.5$ and 11.5. Better agreement is achieved by the turbulent computation which more correctly predicts the primary separation and separated leeside pressures. The turbulent solution follows the experimental surface pressure in the windward region very accurately at all five stations, but underpredicts the minimum C_p at primary separation which is computed $5-10\%$ too windward at the rearward three stations. At station $x/D = 5.5$ and 7.5 the magnitude of the vortex suction is accurately predicted, but the position at which it acts occurs almost 20° earlier than seen experimentally. This may be associated with the difference in the position of separation.

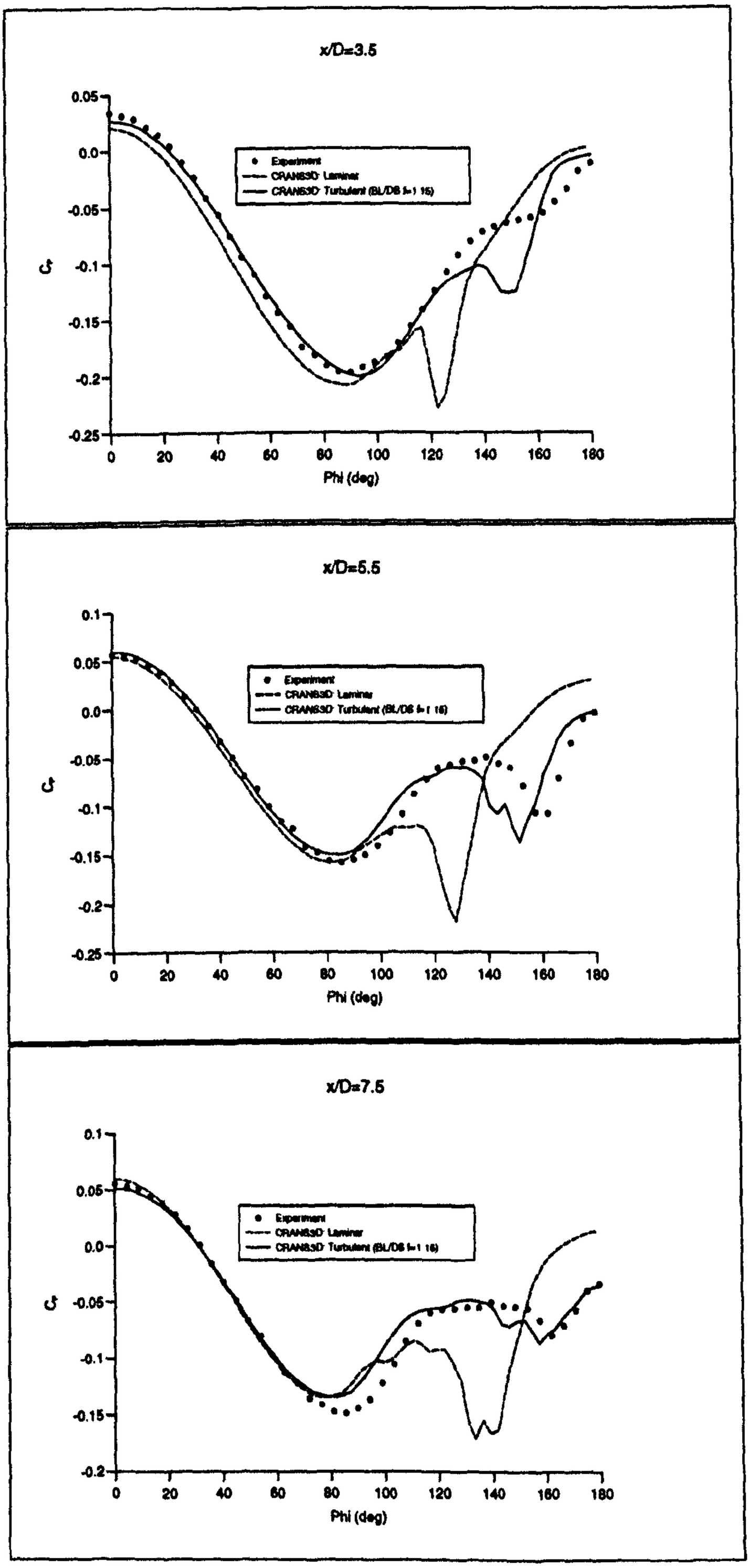

Figure 4.64: *Circumferential Surface Pressure Distribution, B1A, M_∞=0.7, 14°*

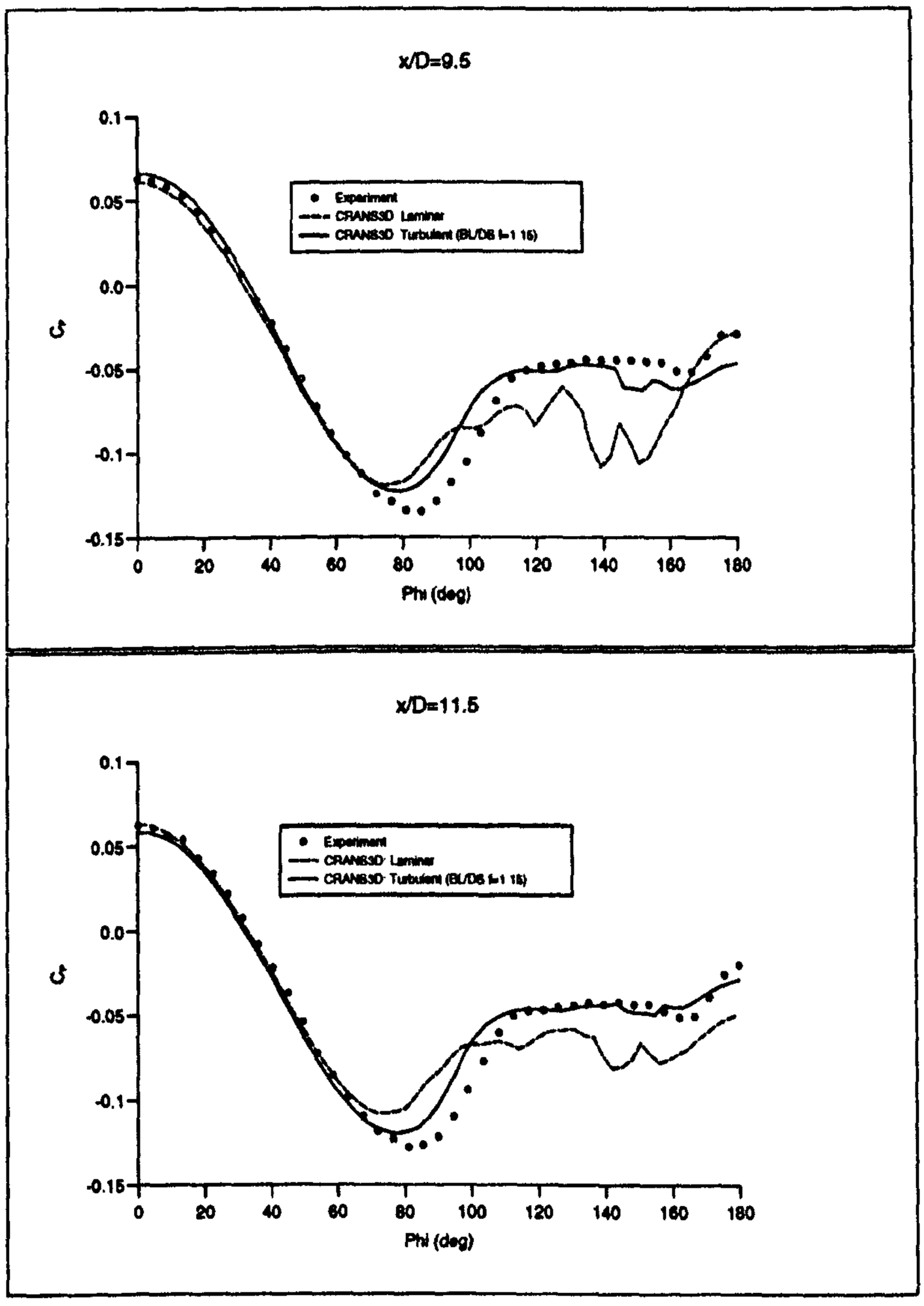

Figure 4.65: *Circumferential Surface Pressure Distribution, B1A, M_∞=0.7, 14°, continued*

Figure 4.66 compares the experimentally measured crossflow pitot pressure ratio with the corresponding results from laminar and turbulent computation. The turbulent solution employing the modified Degani-Schiff cut-off parameter is clearly superior to the laminar solution at both measurement stations. The computed turbulent vortex at $x/D = 8.5$, however occurs noticeably closer to the leeward symmetry plane than seen in experiment. The pressure in the vortex cores are underpredicted in the turbulent solution by about $\Delta P_p/P_{p\infty} \approx 0.003$ which compares with the quoted experimental accuracy of $\Delta P_p/P_{p\infty} \approx 0.0025$.

The results show that the CRANS3D solver can predict the transonic

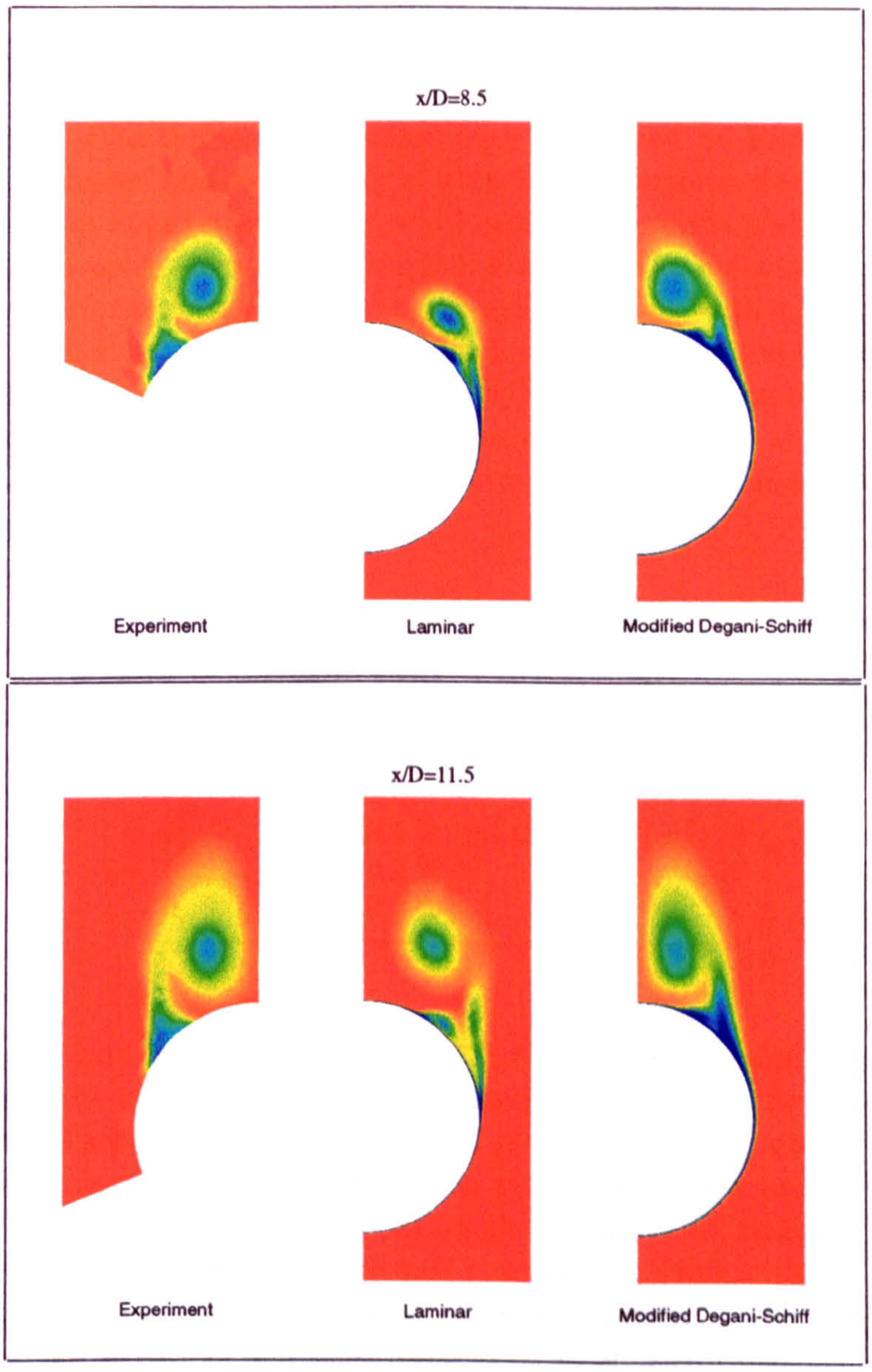

Figure 4.66: *Effect of Modified Degani-Schiff Parameter: Crossflow Pitot Pressure Ratio*

flow past a slender ogive-cylinder and that the reduced value of 1.15 for the Degani-Schiff cut-off factor, which was found to consistently give improved predictions for supersonic cases, performs equally well for transonic freestream cases.

4.3.3 The DLR Experimental Study of the Windward Shock Phenomenon

A number of wind tunnel experiments were performed by Esch [19] on various ogive-cylinder bodies at angle of attack in supersonic flows in order to investigate the appearance of the windward shock-waves which have been seen in the investigations of test cases 4, 6 and 7. The most comprehensive study was performed on a tangent-ogive-cylinder body with a fineness ratio of 3.5 at Mach numbers of 1.5 and 1.4, both of which exhibited the windward shocks streaming off under the body in the Schlieren photographs taken during the tests. The effect of this shock was clearly resolved as the inflexion in the measured windward surface pressure distributions. Esch quoted the experimental accuracy as follows:

Table 4.3: Experimental Accuracy

Property	Accuracy
C_p	$\pm$ 0.01
P_p	$\pm$ 0.1 % ($\pm 1.0 \times 10^5 N/m^2$)
M_∞	$\pm$ 0.5 %
α	$\pm$ 0.2 %

It was decided to compute the Mach 1.4 test case in order to gain more insight into the windward shock phenomena. For the study of this body only the PNS solver was used since, for a given size of computer memory, it can more efficiently obtain a solution on much finer grids, and has already been found to yield good results although not quite as accurate as those generated from CRANS3D. Figure 4.67 presents the ($150 \times 153 \times 153$) grid used in the computation. The radial cell size adjacent to the body surface was set as $0.5 \times 10^{-5} D$ and the radial clustering performed using a *tanh* function. The solution was resolved to 5 orders of convergence.

Case 9: DLR 3.5 Calibre Ogive, Mach 1.4, 16° Angle of Attack

Figure 4.68 presents the circumferential surface pressure distribution at $x/D = 7$ and compares the turbulent PNS solution with the experimental measurements. Although the numerical solution clearly resolved a windward shock, it was consistently predicted too late on the windward side resulting in a poor leeside pressure comparison. Figure 4.69 shows the experimental schlieren photograph together with the surface oil flow visualization which clearly highlights the primary separation line and the discontinuity in surface oil flow lines associated with the flow deflection through the windward

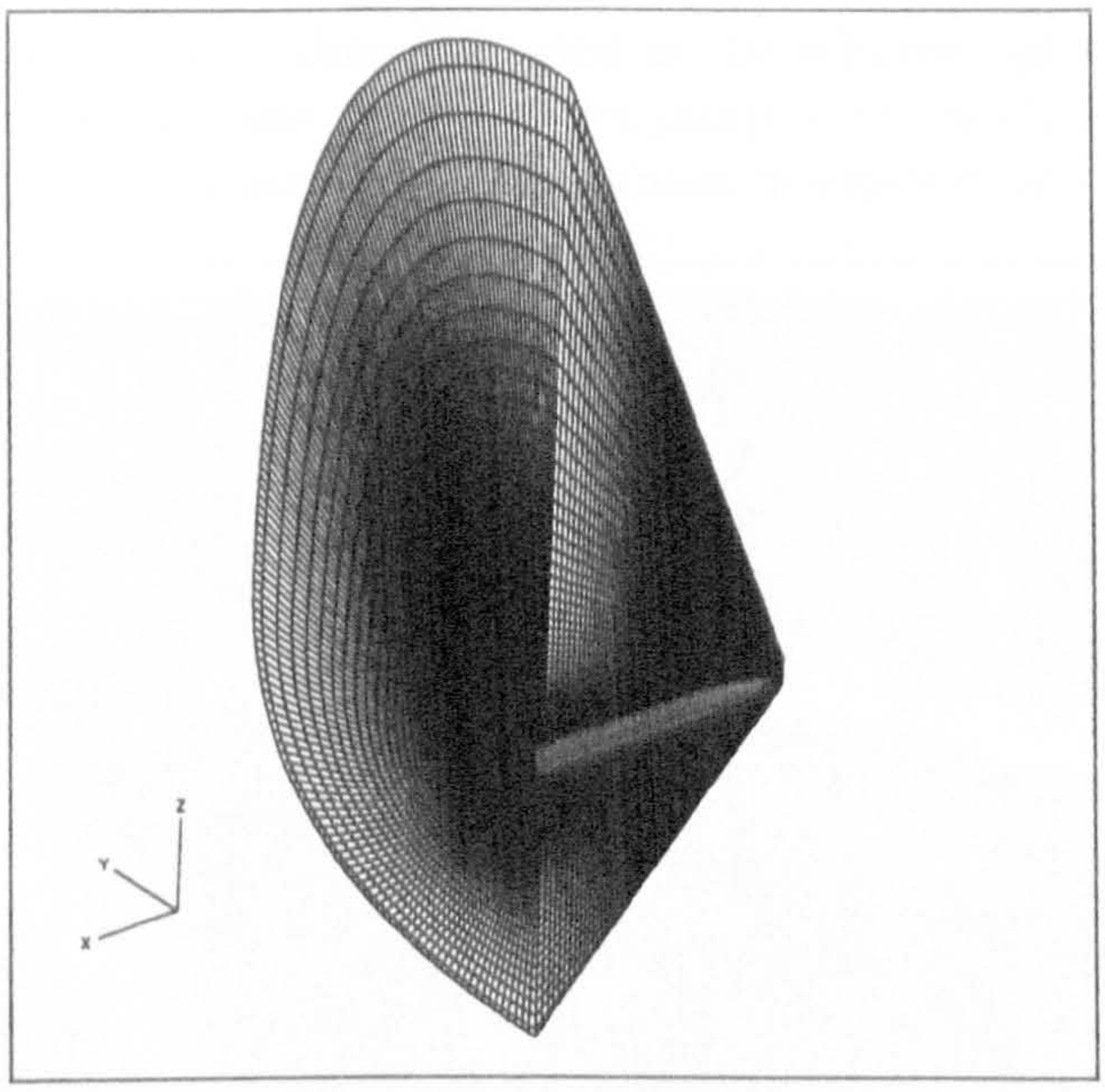

Figure 4.67: *DLR Body, Computational PNS Grid for Case 9 (150 × 153 × 153)*

shock.

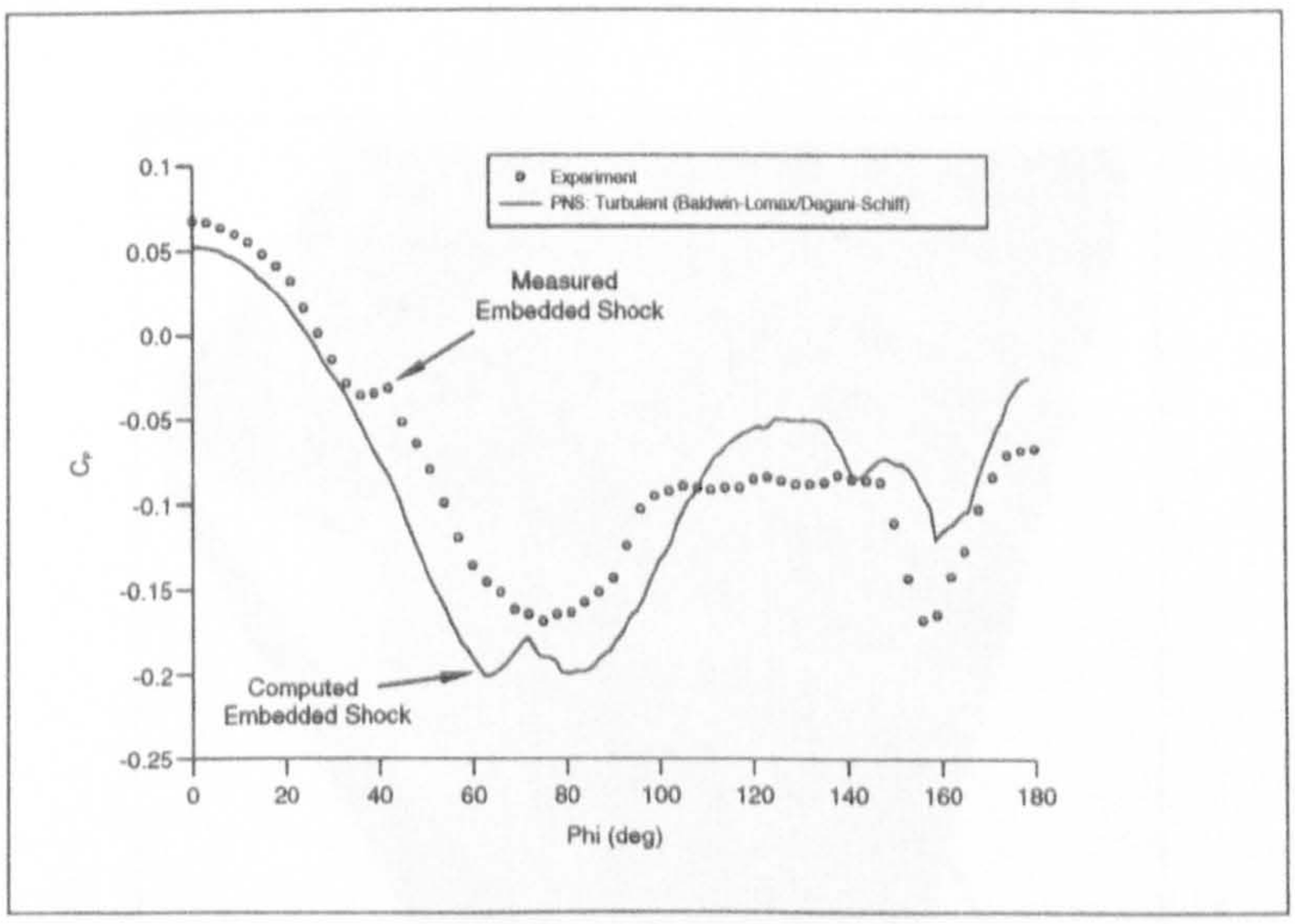

Figure 4.68: *Appearance of Windward Shock, Surface C_P at x/D=7, DLR Body, M_∞=1.4,* 16^o

Figure 4.70 presents the surface skin friction lines and the symmetry plane density gradient contours computed by the PNS solver. The windward shock (WS) can be discerned, although it is seen to leave the underside of the

body further downstream than that seen in the schlieren photograph. The turbulent computation also captured the jump in the surface skin friction lines in about the same position as those seen in experiment.

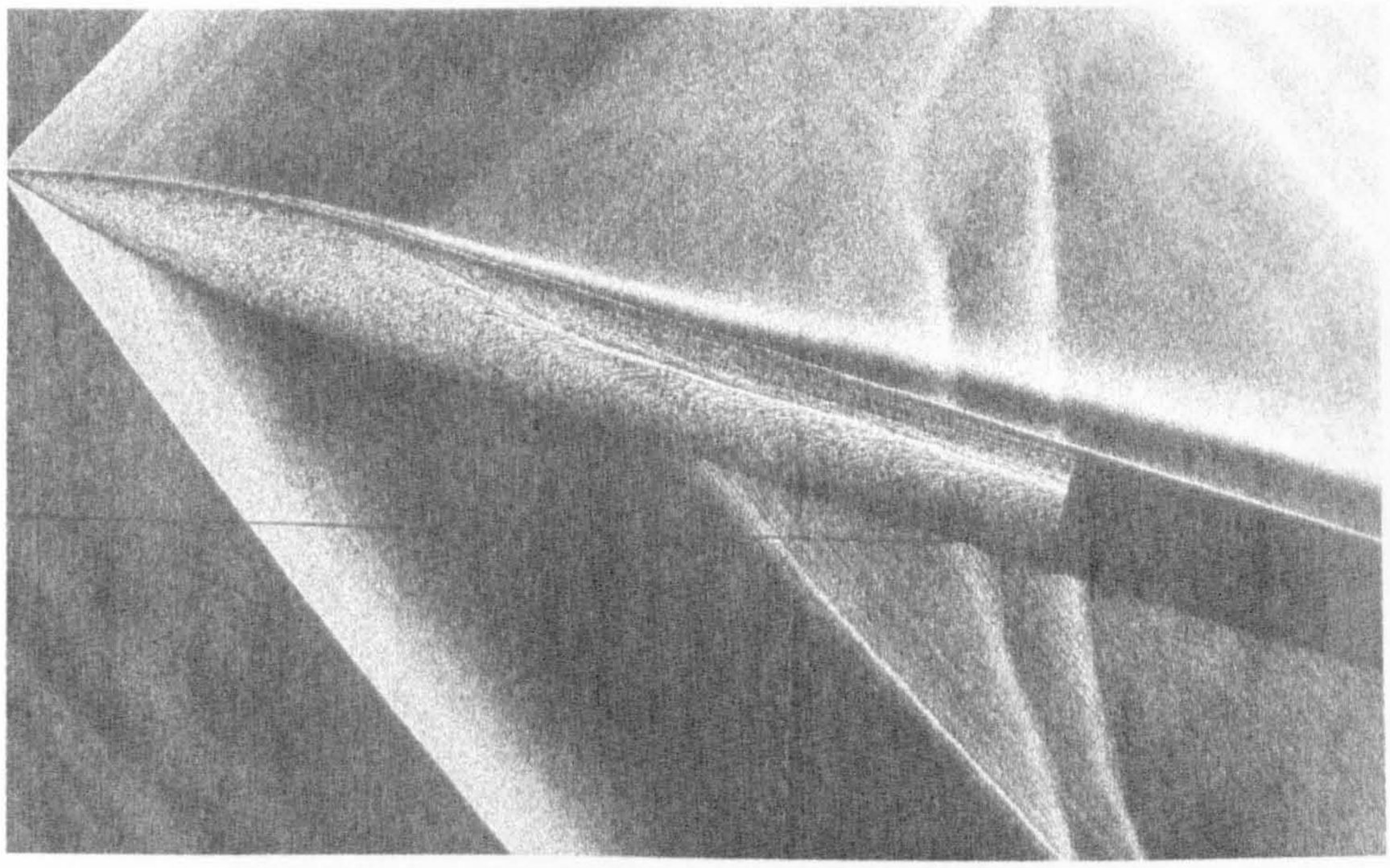

Figure 4.69: *Schlieren Photograph: DLR Body, M_∞=1.4,* 16^o

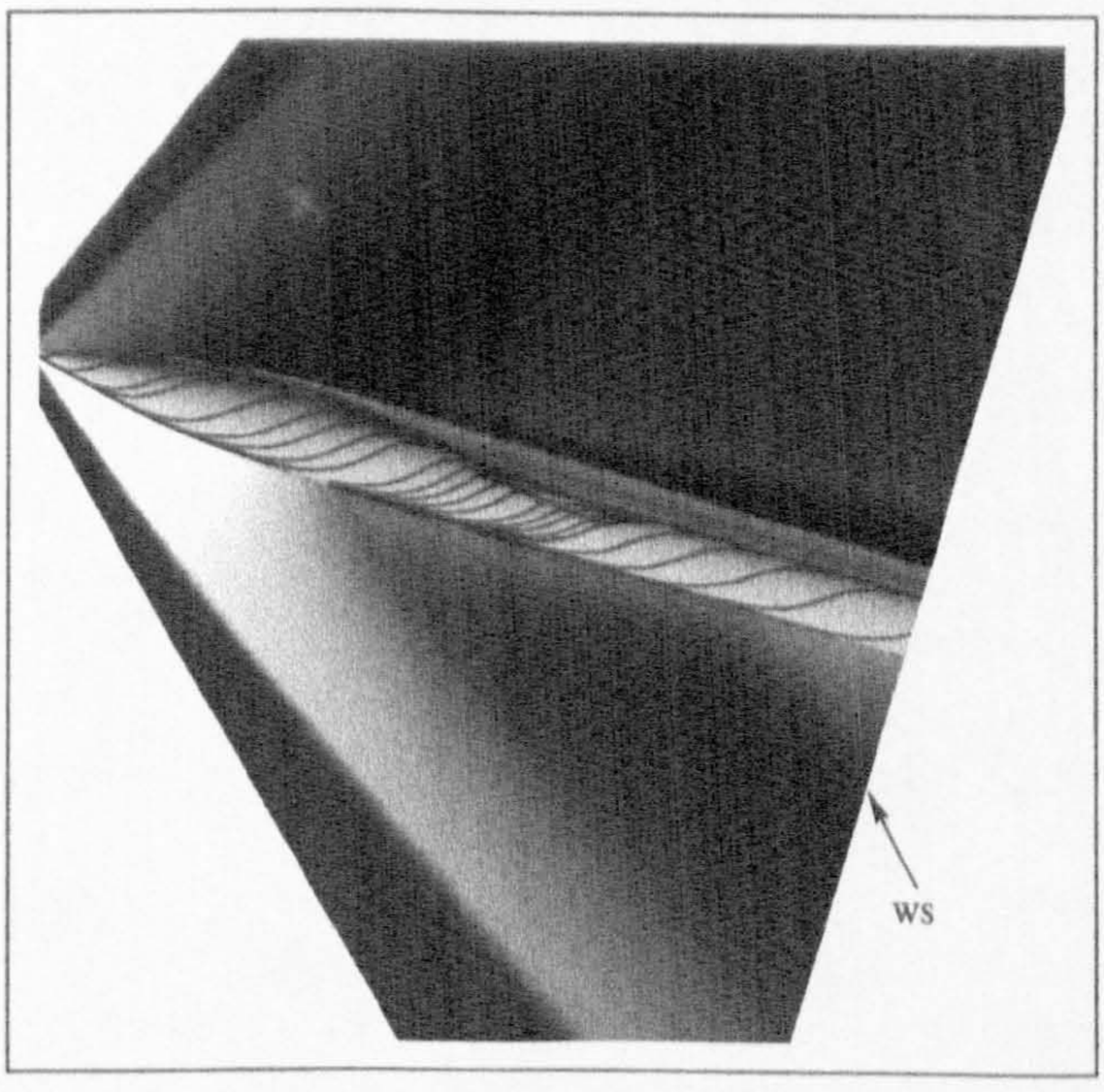

Figure 4.70: *Symmetry Plane Density Gradient: DLR Body, M_∞=1.4,* 16^o

4.4 Slender Forebodies and the Vortex Shock: An Aerodynamic Interpretation

The computational studies of the nine test cases, covering the Mach number and angle of attack ranges $0.7 \leq M_\infty \leq 2.5$ and $0^o \leq \alpha \leq 16^o$ respectively, proved to agree with experimental evidence well enough to enable the results to be used in the interpretation of the flow physics of inclined ogive-cylinders at these conditions. In particular, the windward shock feature observed in experiment under certain conditions can be analysed with the aim of describing its aerodynamic nature and its origin.

The most complete study of the phenomena was by Esch [19] at DLR, Cologne. Surface pressure distribution measurements were made together with schlieren and oil flow visualization in order to find an explanation for the formation of these shocks. Esch summarized that the shock exists when the crossflow Mach number is high enough for a crossflow shock to form in front of the wedge-like crossflow separation, and that under certain conditions the shock will detach from the primary separation line and move towards the windward side of the body. Figure 4.71 shows the effect of crossflow Mach number on the primary separation line and the near-surface flow.

Esch showed that as the freestream crossflow Mach number ($M_\infty sin\theta$) increased above about 0.31, a shock trace will appear in the oil flow as a discontinuity in the slope of the skin friction lines. This shock becomes strong enough that, by a freestream crossflow Mach number of 0.44, it will force the primary separation to follow it further windward. At even higher freestream crossflow Mach numbers at around 0.6, the embedded primary separation shock remains fixed to the separation line and is not seen to pass onto the windward side of the body. The fact that the numerical studies identified the windward shock in the flow fields of case 4, 6, 7 and 9 would seem to dispel the suspicion that it may be due to some imperfection on the body surface.

Considering case 4, it was shown that the numerical solution agreed very closely with experiment and the computed surface pressure at the three measurement stations lay consistently within the bounds of the estimated experimental error. The numerical results showed that at no point in the flow did the crossflow reach supersonic, and therefore no embedded crossflow shockwave developed. This agreed with experiment, where no evidence of any strong crossflow shock was apparent in either the surface data, or the three crossflow plane measurements. The numerical solution did, however, resolve a windward shock which is clearly visible in the numerical symmetry plane density gradient plot presented in Figure 4.72 together with the an interpretation of the flow features. Figure 4.73 presents the crossflow structure at different axial stations down the body together with an inter-

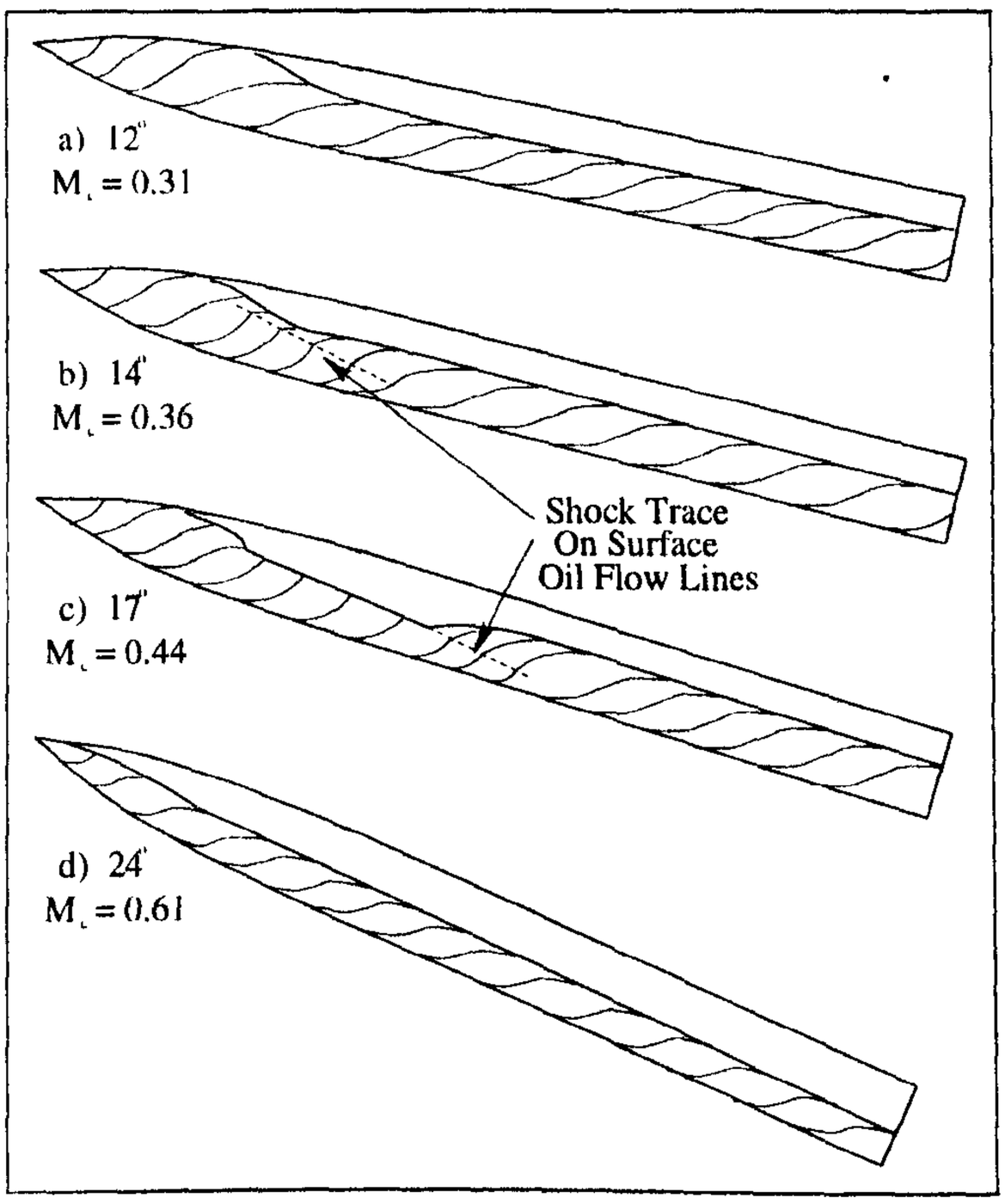

Figure 4.71: *Effect of Crossflow Mach Number on Primary Separation and Surface Skin Friction Lines [19]*

pretation of the flow. The development of a windward shock can clearly be discerned, and this windward feature is seen to originate around the primary vortices after their rapid growth as the flow expands past the ogive nose. This weak feature then streams off downstream in the same manner, and with the same slope as the bow shock wave, eventually passing under the body to appear in the symmetry plane as a windward shock trace. This evidence suggests that the windward shock forms because of the deflection of the supersonic stream caused by the virtual double-cone like modification of the leeside body shape by the primary vortices. The windward shock can therefore be renamed the *"vortex shock"*.

A similar situation was found with case 6, where the vortex shock appeared in the flowfield in the absence of any crossflow shock wave. It therefore seems that the windward appearance of the vortex shock is independent of the development of an embedded crossflow shock. Cases 4 and 6 correspond with the surface skin friction pattern of Figure 4.71 a).

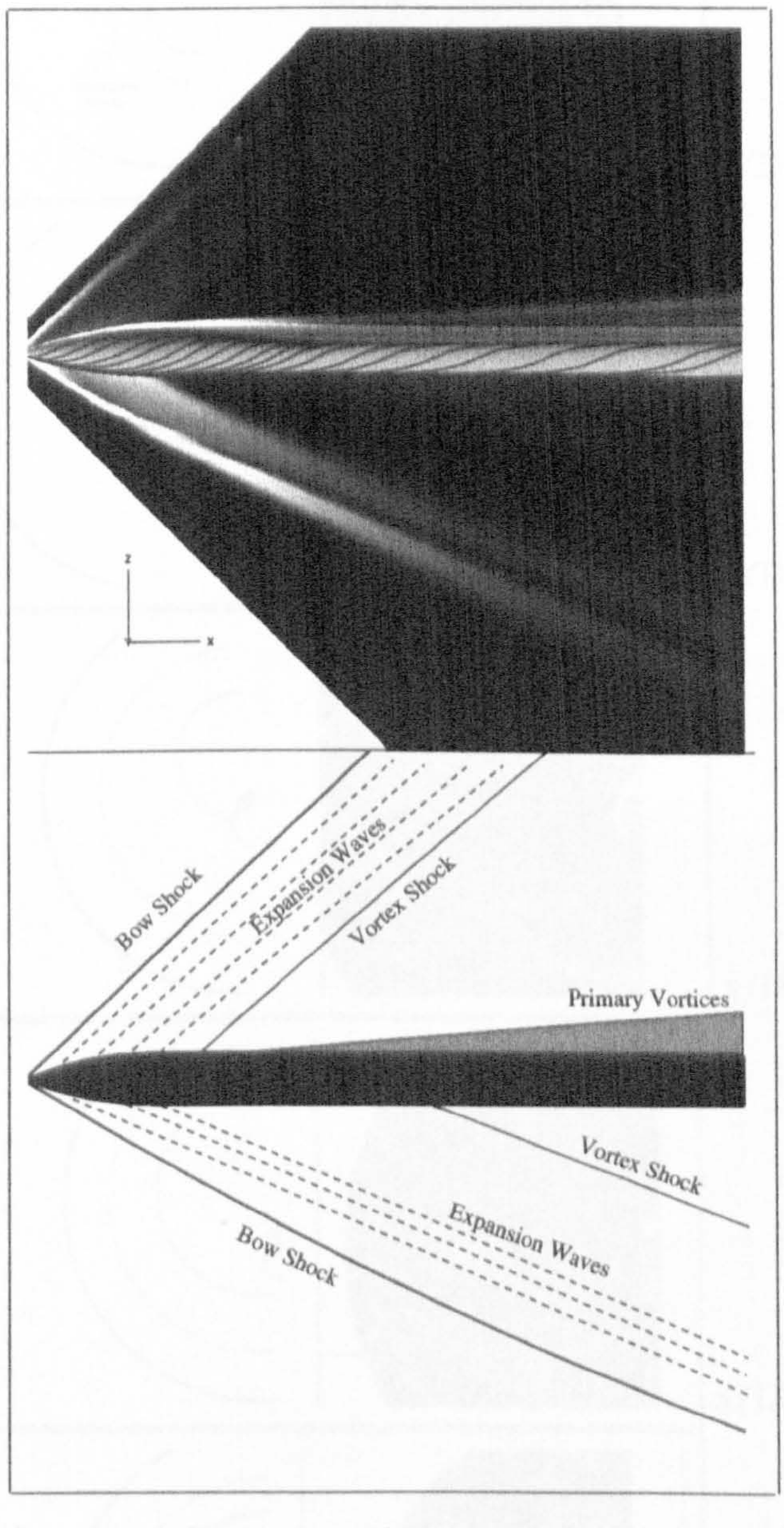

Figure 4.72: *Computed Symmetry Plane Density Gradient and Interpretation: B2,* 10^{o} *angle of attack*

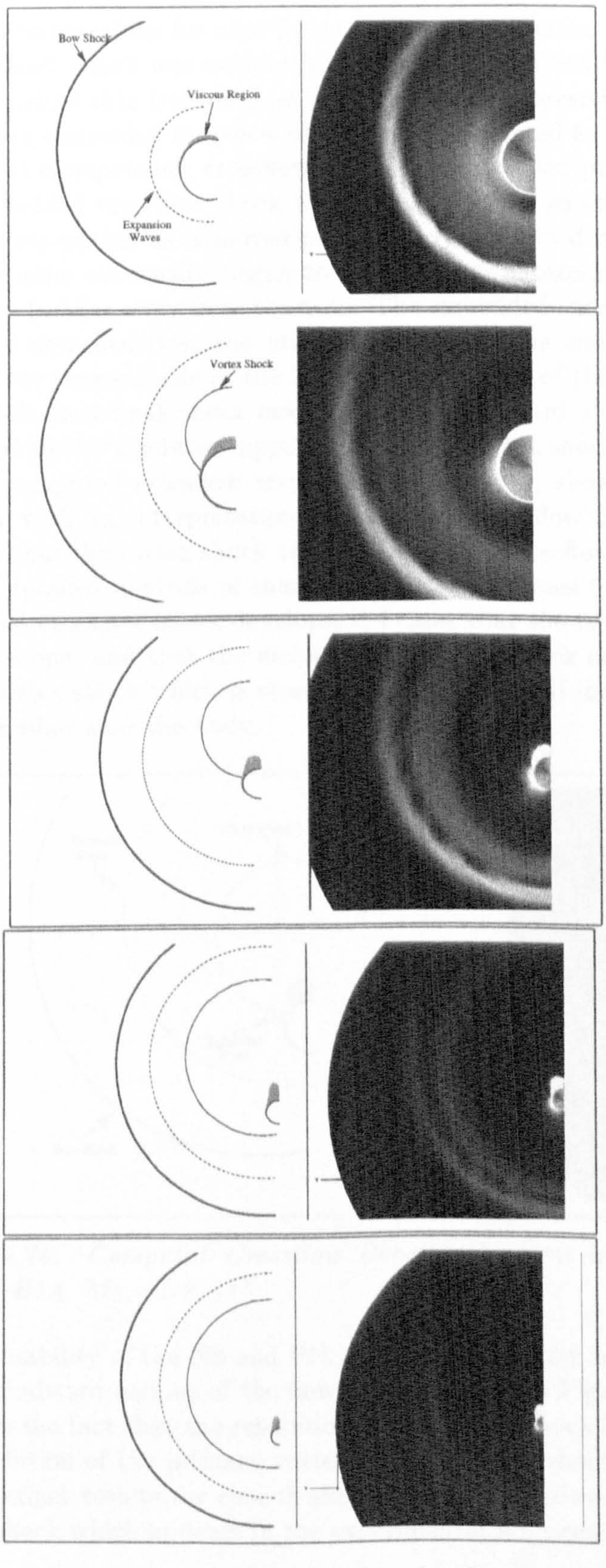

Figure 4.73: *Computed Crossflow Density Gradient and Interpretation*

The computations for case 7 also revealed the presence of the windward vortex shock which was evident in the experimental Schlieren photograph. The computed skin friction lines and the flowfield showed the development of a strong embedded crossflow shock which originated as a result of the development of supersonic crossflow as the flow expanded past the ogive nose. The embedded crossflow shock was seen to become so strong that it fixed primary separation as it moved progressively windward until the crossflow Mach number eventually began to reduce to its subsonic "2D cylindrical" condition further away from the nose. The embedded shock therefore weakened and detached from the primary separation line which moved rapidly back to the leeward side of the body. Continuation of the embedded crossflow shock, as a weak shock moving further windward along the body, can be traced to the windward appearance of the vortex shock.

The computed crossflow structure at $x/D = 5$, shown in Figure 4.74 together with an interpretation of the illustrated flow features, seems to indicate that the vortex shock and the embedded crossflow shock are linked. In fact, detailed analysis of this case and that of cases 5 and 9, where the embedded crossflow shock develops, indicates that the two features are one and the same, and that the embedded crossflow shock is actually the foot of the vortex shock which is strengthened by the local increase in crossflow Mach number near the body.

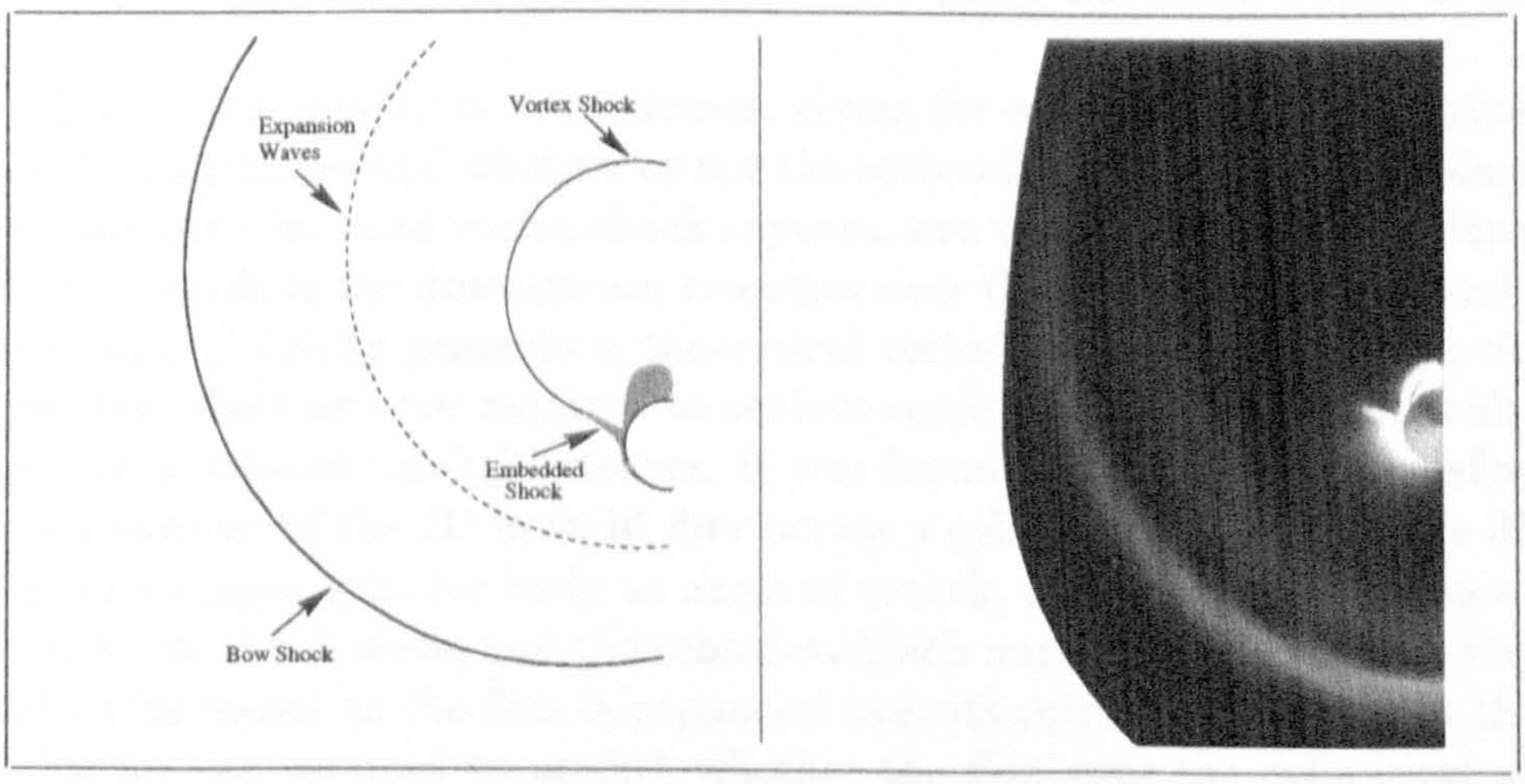

Figure 4.74: *Computed Crossflow Density Gradient and Interpretation: x/D=5, B1A, M_∞=1.8, 14°*

The inability of the NS and PNS solvers to correctly resolve the position of the windward regions of the flow, demonstrated in Figures 4.58 and 4.68, is due to the fact that the resolution of the vortex shock is very sensitive to the resolution of the primary vortex and its feeding sheet.

Numerical results for case 9 also resolve the windward presence of the vortex shock which appears in the experimental schlieren photographs. The

computed skin friction lines were in good agreement with experiments, and together with the flowfield solution, clearly showed the development of a weak crossflow shock emanating from the body surface close to but, significantly, prior to primary separation. This embedded shock was seen to develop as the crossflow reached supersonic condition soon after passing beyond the ogive-nose, and moved further windward as the crossflow Mach number in the critical region increased. After about 1 calibre beyond the station at which the shock first formed, the crossflow Mach number began to reduce, the shock became weaker until it practically disappeared when the crossflow became subsonic and stabilized to the equivalent "2D-cylindrical" condition far away from the nose. By this stage the embedded shock had passed a considerable distance onto the windward side of the body and again showed itself to be linked to the windward appearance of the vortex shock. This is further evidence that the embedded crossflow shock is part of the overall structure of the vortex shock. The foot of the vortex shock is strengthened by the increased crossflow Mach number close to the nose until it appears as the embedded crossflow shock as the crossflow becomes supersonic. The surface skin-friction lines for case 9 would appear to correspond with those of Figure 4.71 b), while the pattern predicted at the increased Mach number of case 7 appears close to that shown in Figure 4.71 c). The skin friction pattern of Figure 4.71 d) corresponds with that seen in case 5 where the embedded crossflow shock persists along the entire length of the body.

Table 4.4 summarizes the testcases, giving for each case the global crossflow Mach number and whether or not the embedded crossflow shock is seen, whether the windward vortex shock appears, and whether the computational solution predicts the downstream crossflow over the cylinder to be subsonic. Appendix C briefly presents a theoretical technique used to calculate the crossflow Mach number required to achieve sonic condition on a 2D circular body in a subsonic inviscid stream. It was found that the critical crossflow Mach number of the 2D inviscid flow across a cylinder is 0.418. For the 3D case of an ogive-cylinder body at angle of attack, the crossflow is processed by the bow shock wave, and the crossflow Mach number over the ogive nose will be increased as the flow is expanded over its surface. Nevertheless this technique can be used to predict whether the flow over the cylindrical afterbody, far away from the nose, is likely to exhibit an embedded crossflow shock. The critical freestream crossflow Mach number in this case is likely to be slightly larger than the 2D value of 0.418 due to the effect of both the nose expansion and the bow shock, and is suggested to be around 0.44.

Referring to table 4.4, the only case where locally supersonic crossflow is seen along the whole length of the cylinder is case 5 with a freestream crossflow Mach number of 0.605. Case 7, which exhibits a crossflow shock over a substantial portion of the cylinder body, has subsonic crossflow only over the rearward portions of the cylinder. The global crossflow Mach num-

Table 4.4: Testcase Summary

Case	M_∞	α (deg)	$M_\infty sin\alpha$	Crossflow Shock Appears	Windward Shock Appears	Local Subsonic Crossflow
1	2.0	0	0	-	-	-
2	2.0	10	0.347	×	? [2]	√
3	2.0	0	0	-	-	-
4	2.0	10	0.347	×	√	√
5	2.5	14	0.605	√	×	×
6	2.5	8	0.348	×	√	√
7	1.8	14	0.435	√	√	√
8	0.7	14	0.169	-	-	-
9	1.4	16	0.386	√	√	√

ber for case 7 is given as 0.435 and is likely to be very close to the figure required for critical flow to exist along the entire body length.

The effect of any supersonic patch over the body surface, which will be terminated by the embedded crossflow shock - the strengthened foot of the vortex shock, will be to prevent any disturbances on the leeward side, close to the body, from passing windward. It is suggested that the windward appearance of the vortex shock only occurs when the crossflow over a considerable length of the cylindrical afterbody is subsonic such that it can convect "upstream" into the windward flowfield. Table 4.4 demonstrates that for each case where the vortex shock appears on the windward side there is a substantial rearward portion of the cylinder afterbody with purely subsonic crossflow.

To summarize, the evidence from the study of the nine ogive-cylinder test cases suggests that the windward shock forms becuase of the deflection of the supersonic stream caused by the virtual double-cone like modification of the leeside body shape by the primary vortex system. The windward shock can therefore be named the *"vortex shock"*. In addition it would seem that the embedded shock, which appears in the crossflow, is the manifestation of the vortex shock which is strengthened in regions of supersonic crossflow. Figure 4.75 illustrates the flow topology when the crossflow over the rearward portion of the cylinder body is subsonic. Figure 4.76 presents the flow

[2]Body not long enough for windward appearance of vortex shock, but with a lengthened body, its windward appearance is expected.

features typically encountered when the crossflow over the whole body is transonic or supersonic. In this case the vortex shock never passes windward, and in cases of supersonic crossflow Mach number, a leeside shock forms over the primary vortices. The leeside shock, seen in the experimental studies of Ward et al [78] [23] [79] and computed by Hsieh et al [24] , occurs because the crossflow must turn parallel to the leeward symmetry plane.

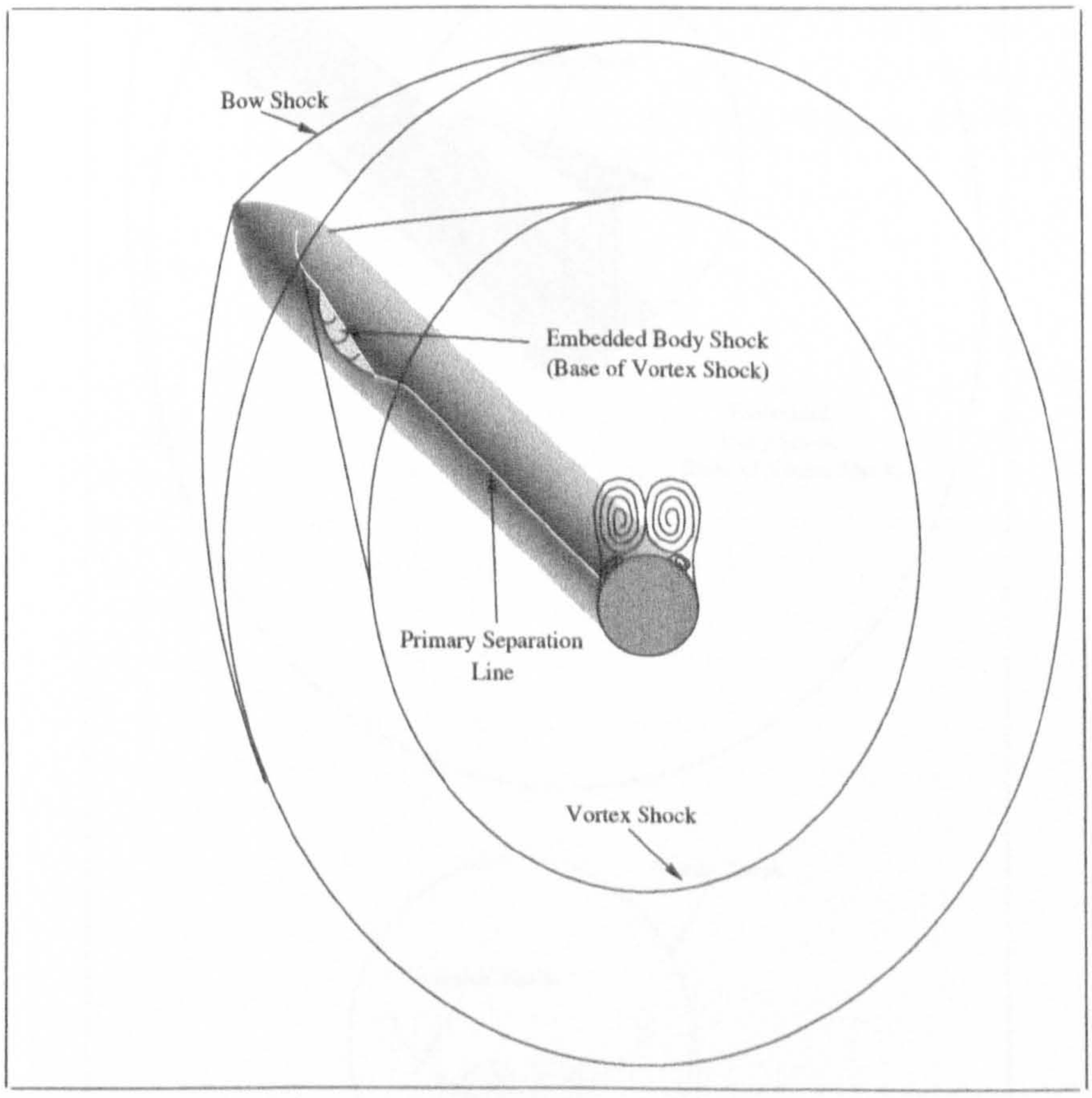

Figure 4.75: *Flow Topology for Subsonic Crossflow Over Rear of Cylinder Afterbody,* $M_\infty sin\alpha < 0.44$

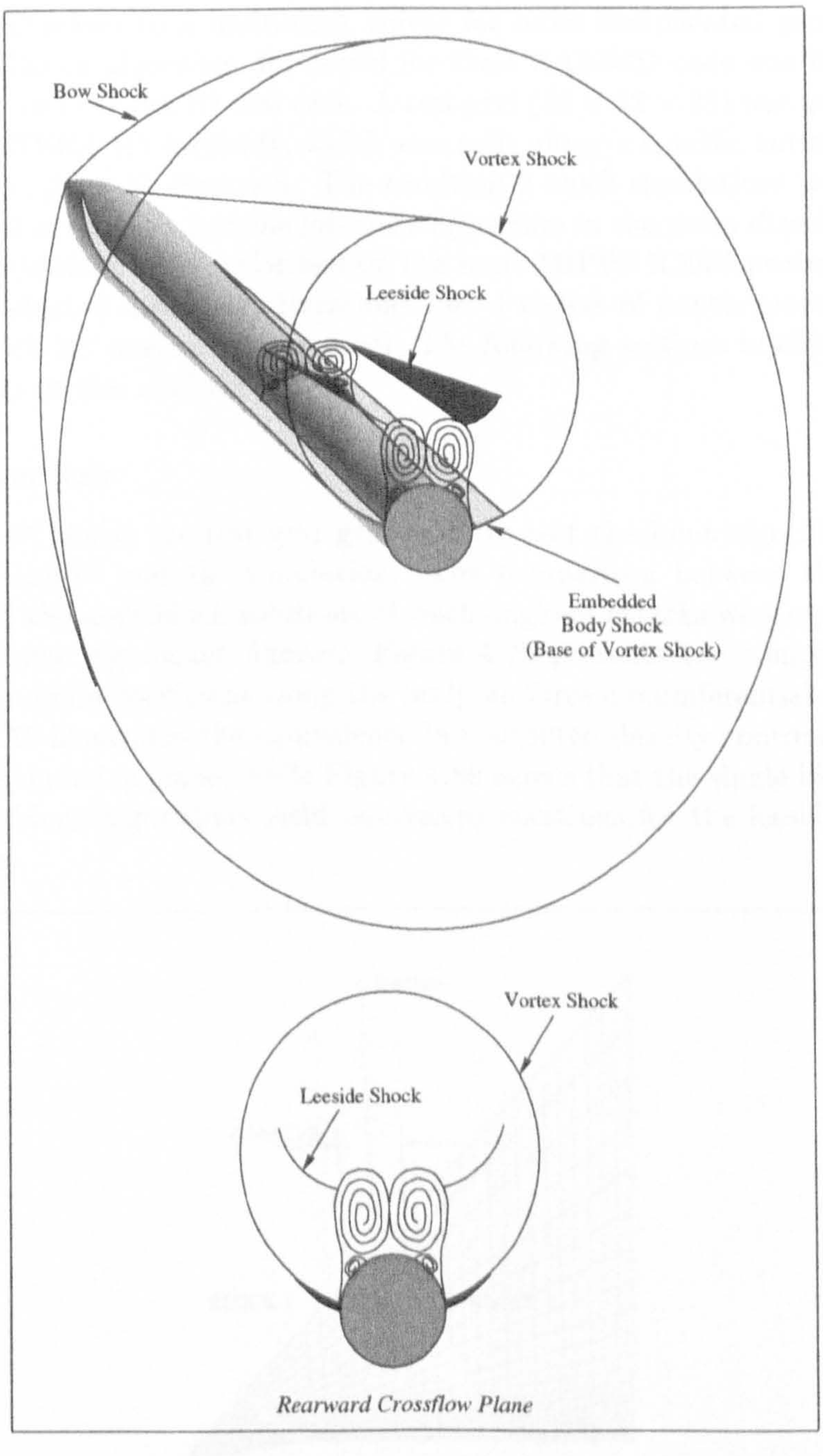

Figure 4.76: *Flow Structure Encountered with Transonic/Supersonic Crossflow Over Whole Body Length,* $M_\infty sin\alpha > 0.44$

4.5 Multiblock Validation: B1 and B2 Revisited

This section presents numerical tests associated with the extension of the CRANS3D solver to a multiblock solver for more complicated geometries. The multiblock algorithm developed for the CRANS3D code was first validated on the ONERA B1 test case. A test grid ($33 \times 33 \times 33$) was generated for the ONERA B1 forebody, which was split along a specific surface in either the I-, J- or K- direction. The resulting 2 block simulations were then performed in order to test the interface algorithm in the given direction. All the computations were performed on the same MIPPS R5000 processor and were terminated after 6000 iterations (ie: 4 orders of convergence for the single block 10^o angle of attack case). The following sections briefly present the results of this analysis.

I-Cut Analysis

Figure 4.77 shows the test grid generated to test the I-cut algorithm used for both the 0^o and 10^o simulation. The comparison between the single block and the multiblock solutions at both angle of attacks were equivalent, down to nine significant figures. Figure 4.78 presents the comparison of surface pressure coefficient along the body at three circumferential stations. Figure 4.79 illustrates the equivalence in computed density contours on the leeward symmetry plane, while Figure 4.80 shows that the single block, and the multiblock algorithms yield equivalent solutions for the leeside vortex structure.

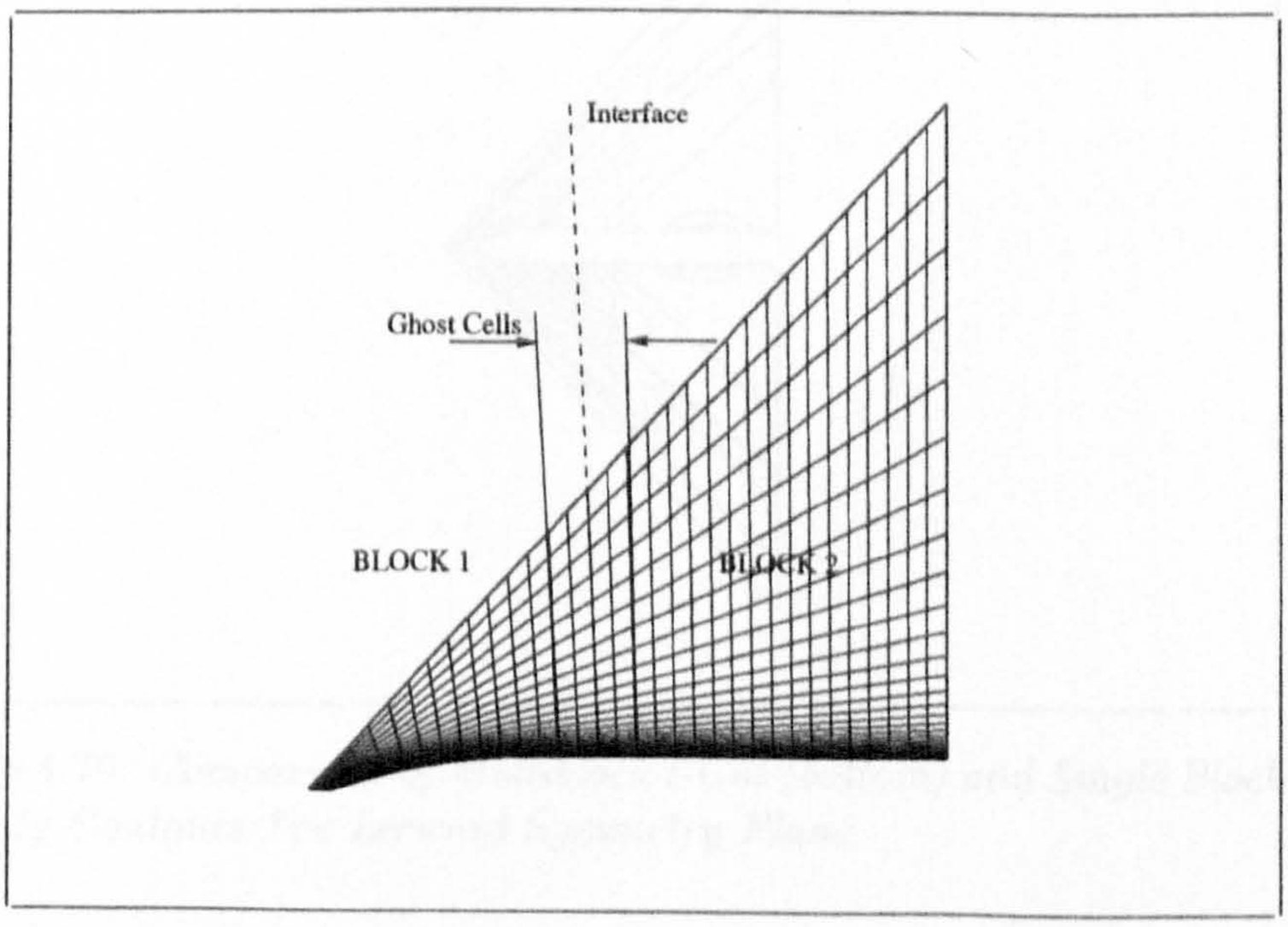

Figure 4.77: *Multiblock I-Cut test grid for Garteur B1 ($33 \times 33 \times 33$)*

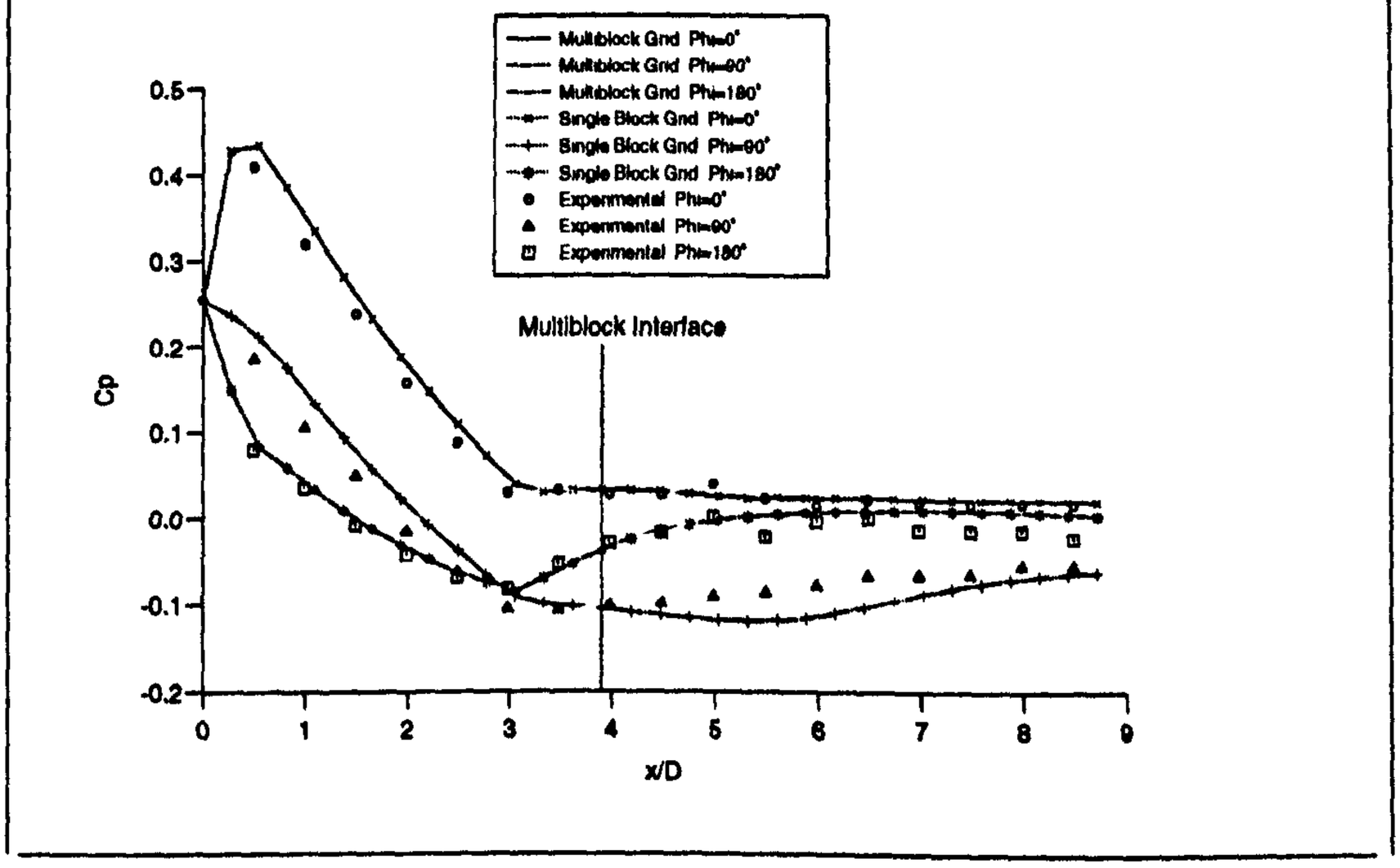

Figure 4.78: *Comparison of Axial Surface Pressure Coefficient*

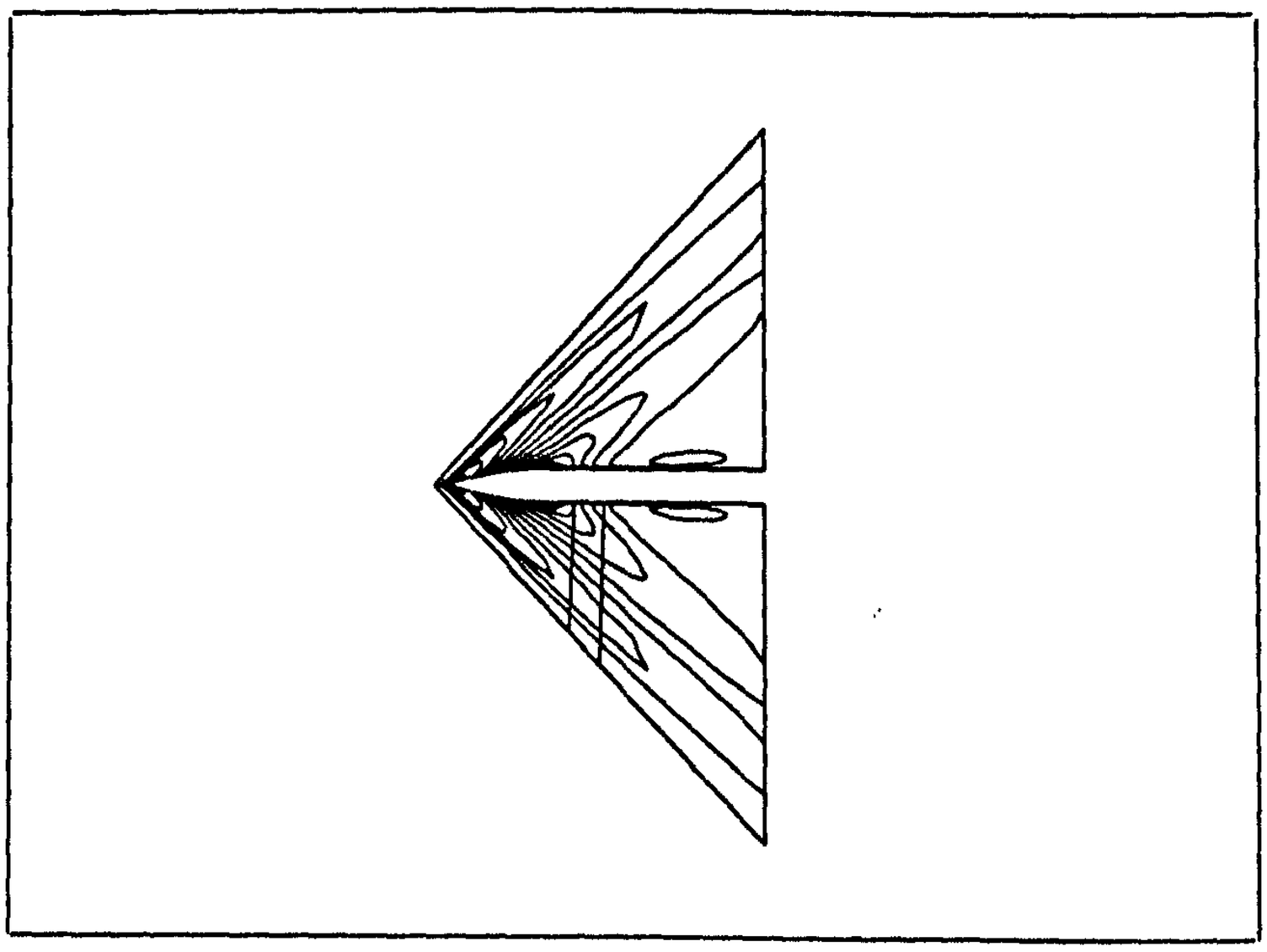

Figure 4.79: *Comparison of Multiblock I-Cut (bottom) and Single Block (top) Density Contours For Leeward Symmetry Plane*

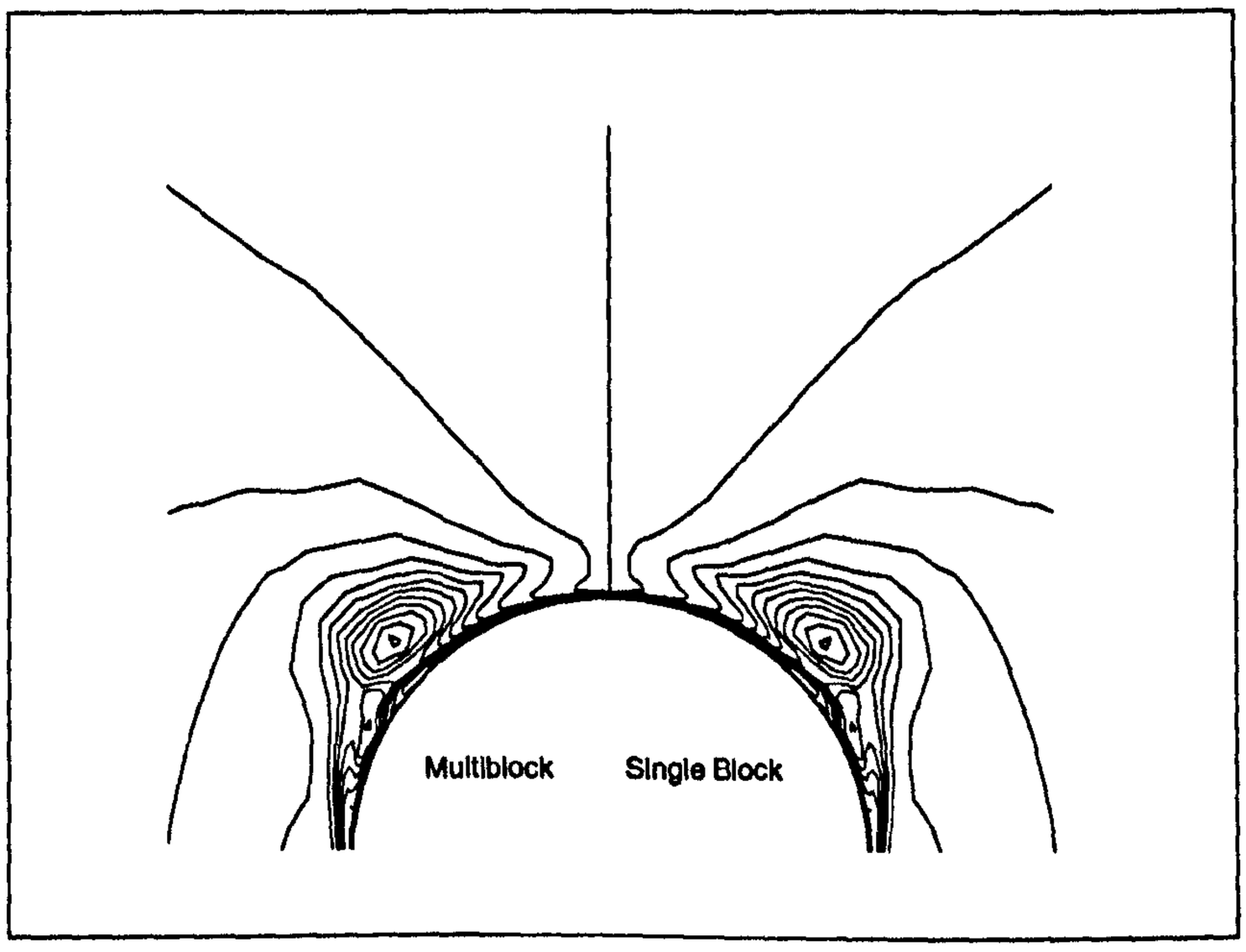

Figure 4.80: *Comparison of Crossflow Density Contour Resolution for Multiblock and Single Block Computations at Plane x/D=8*

J-Cut Analysis

The test grid for the J-cut analysis is shown in Figure 4.81, where the interface was set along a J-surface close to the body surface where flow variable gradients are highest. The J-cut algorithm was only tested on the 10° case with the more challenging flow physics. The simulation also proved to be equivalent to the corresponding single block case as shown in Figures 4.82 and 4.83. In addition, the same case was run with the Baldwin-Lomax/Degani-Schiff turbulence model implemented. The results for both single and multi-block solvers were, again, equivalent.

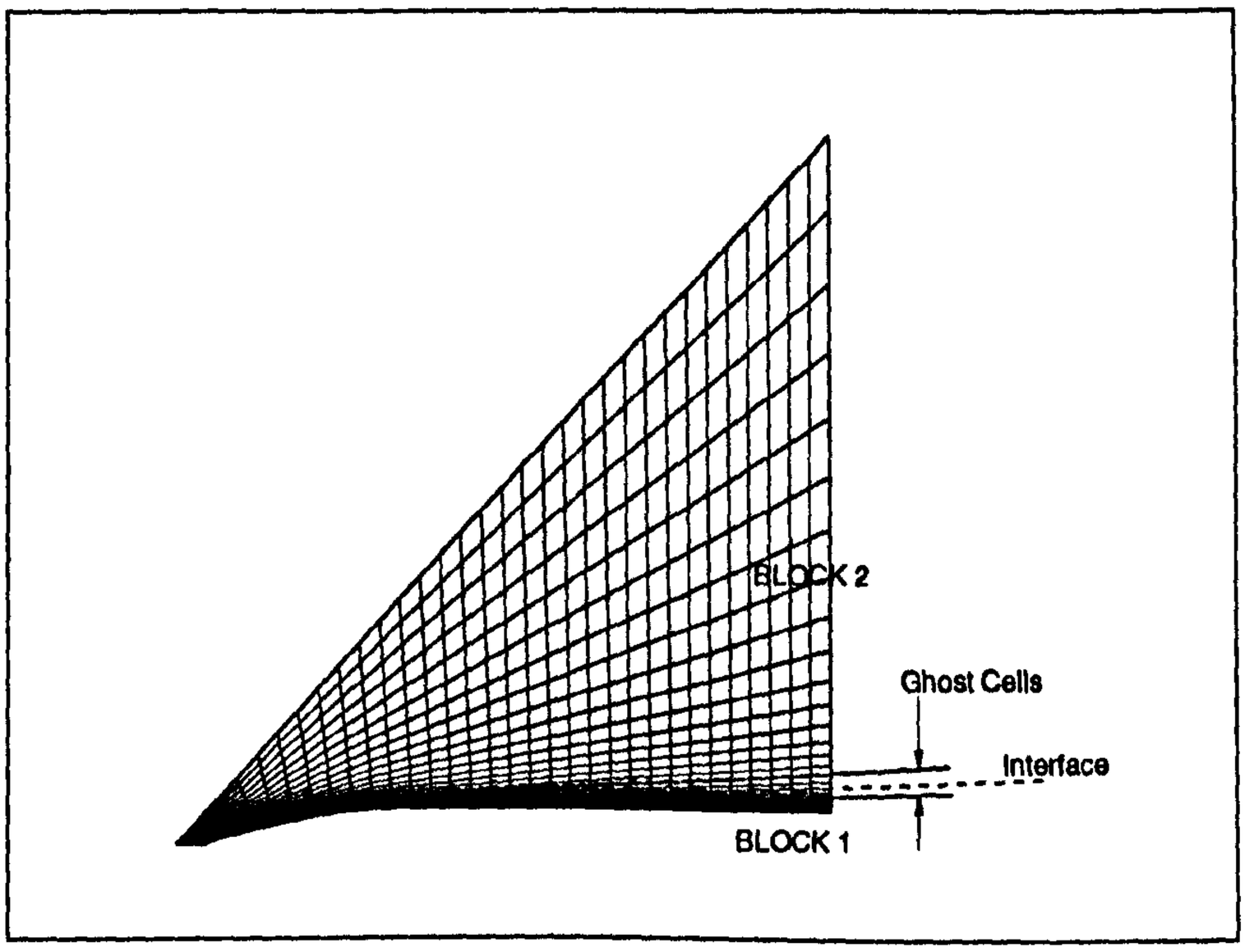

Figure 4.81: *Multiblock J-Cut test grid for Garteur B1 (33 × 33 × 33)*

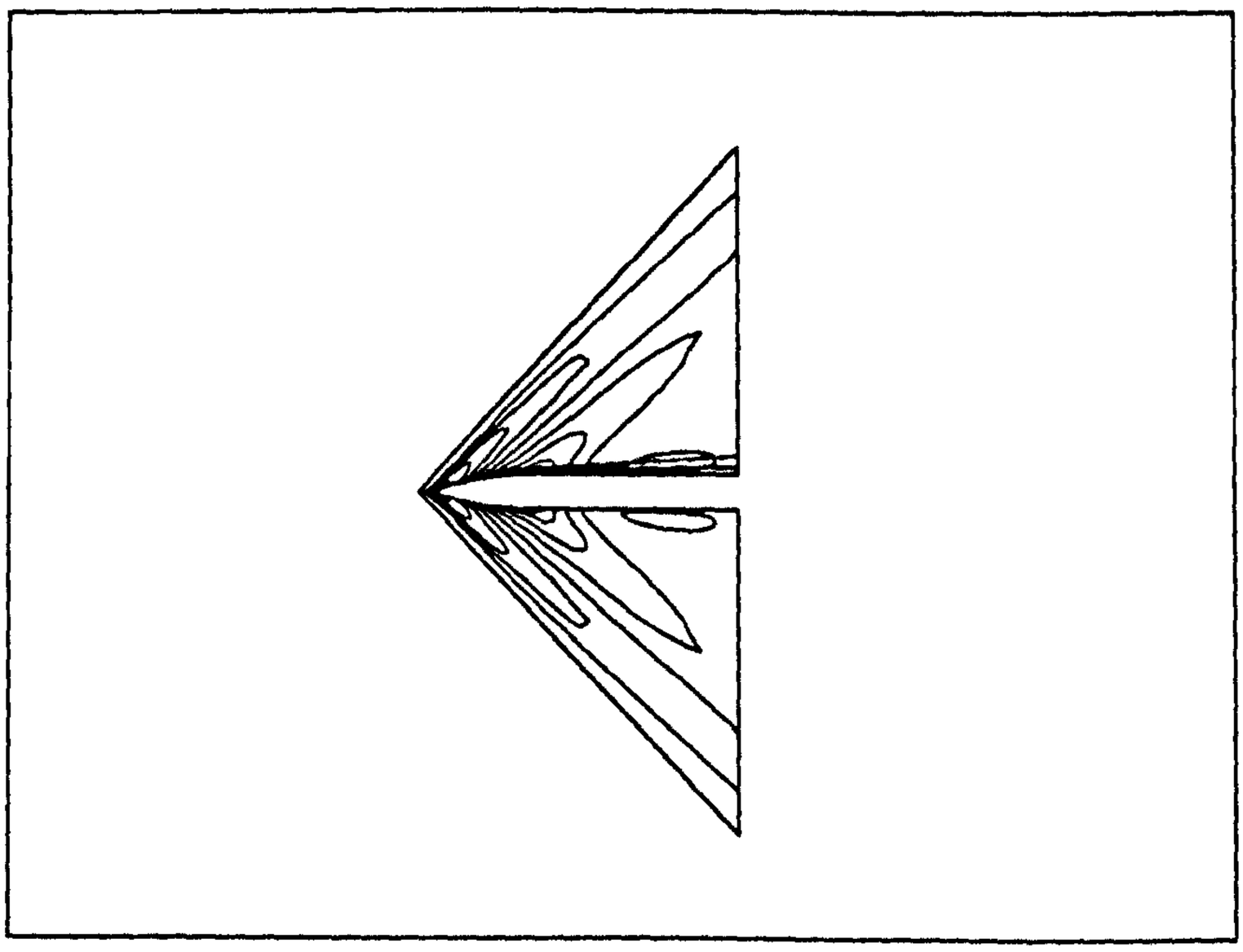

Figure 4.82: *Comparison of Multiblock J-Cut (top) and Single Block (bottom) Density Contours For Leeward Symmetry Plane*

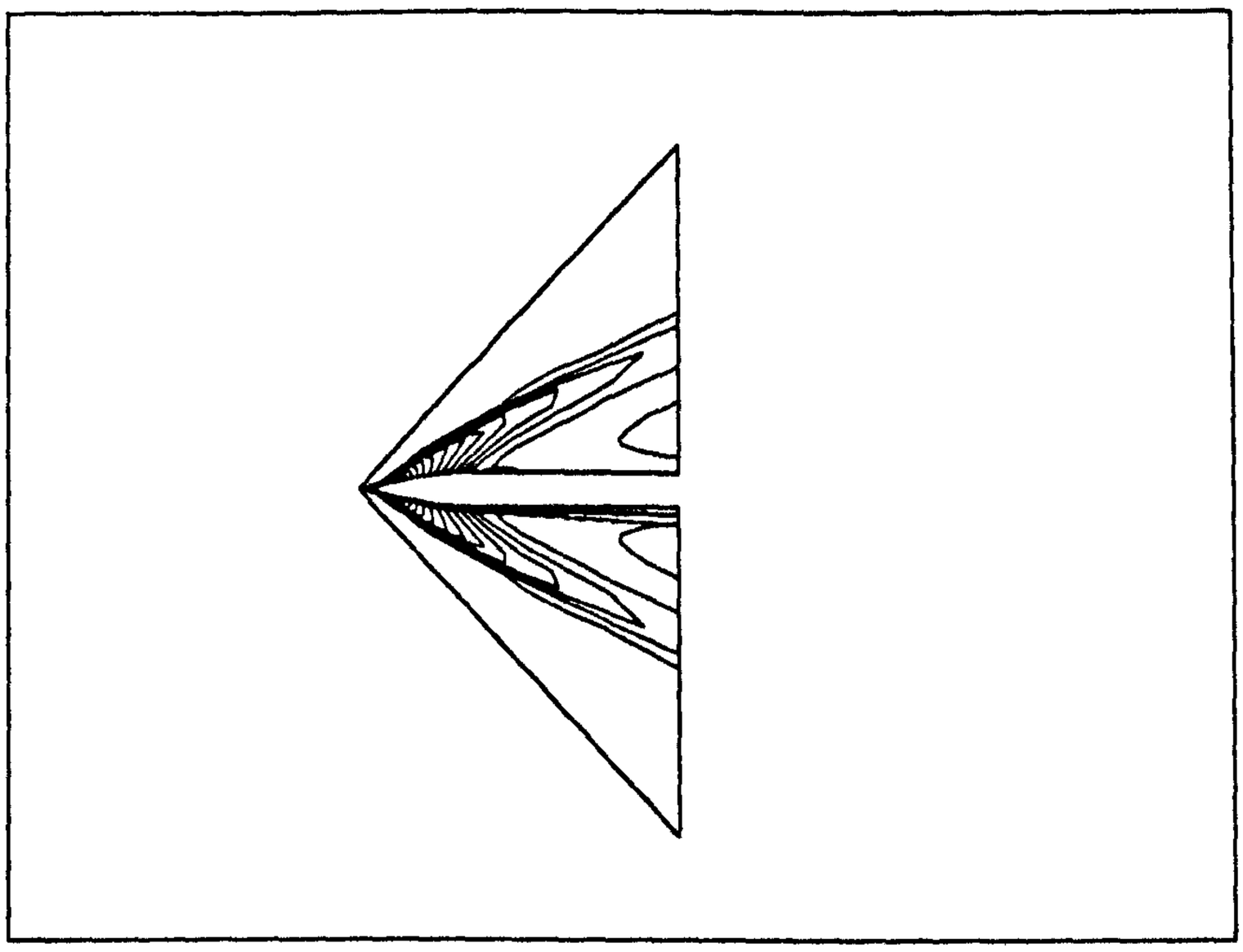

Figure 4.83: *Comparison of Multiblock J-Cut (bottom) and Single Block (top) Density Contours For Windward Symmetry Plane*

K-Cut Analysis

The grids for the K-cut test are shown in Figure 4.84. The test was again run only for the 10° case but with the interface set along a K-surface intersecting the vortex in order to provide a more challenging environment for the interface algorithm.

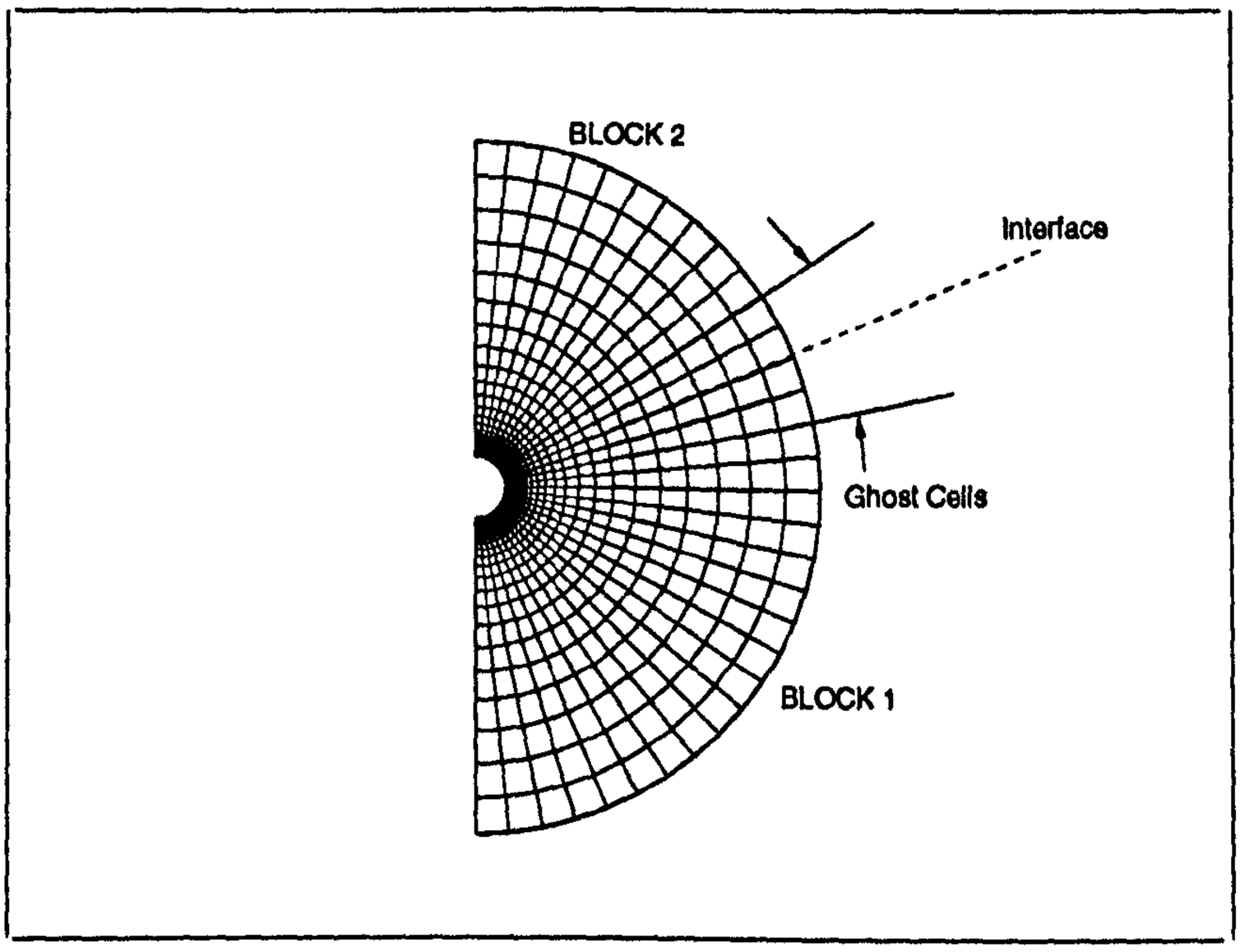

Figure 4.84: *Multiblock K-Cut test grid for Garteur B1 (33 × 33 × 33)*

The comparison between the K-cut multiblock solution and its single block counterpart are presented in Figures 4.85 to 4.88. The results show that the multiblock routine with the K-cut is equivalent to the single block case.

In conclusion, it has been demonstrated that for the case of the two block slender body test case, all three interface algorithms perform satisfactorily. The integration routine across each interface has been shown to yield the exact same solution, down to nine significant figures, as the corresponding single block routine, with the same processor and the same number of iterations at the same value of the CFL number. These numerical tests, therefore, validate the extension of CRANS3D to a multiblock solver.

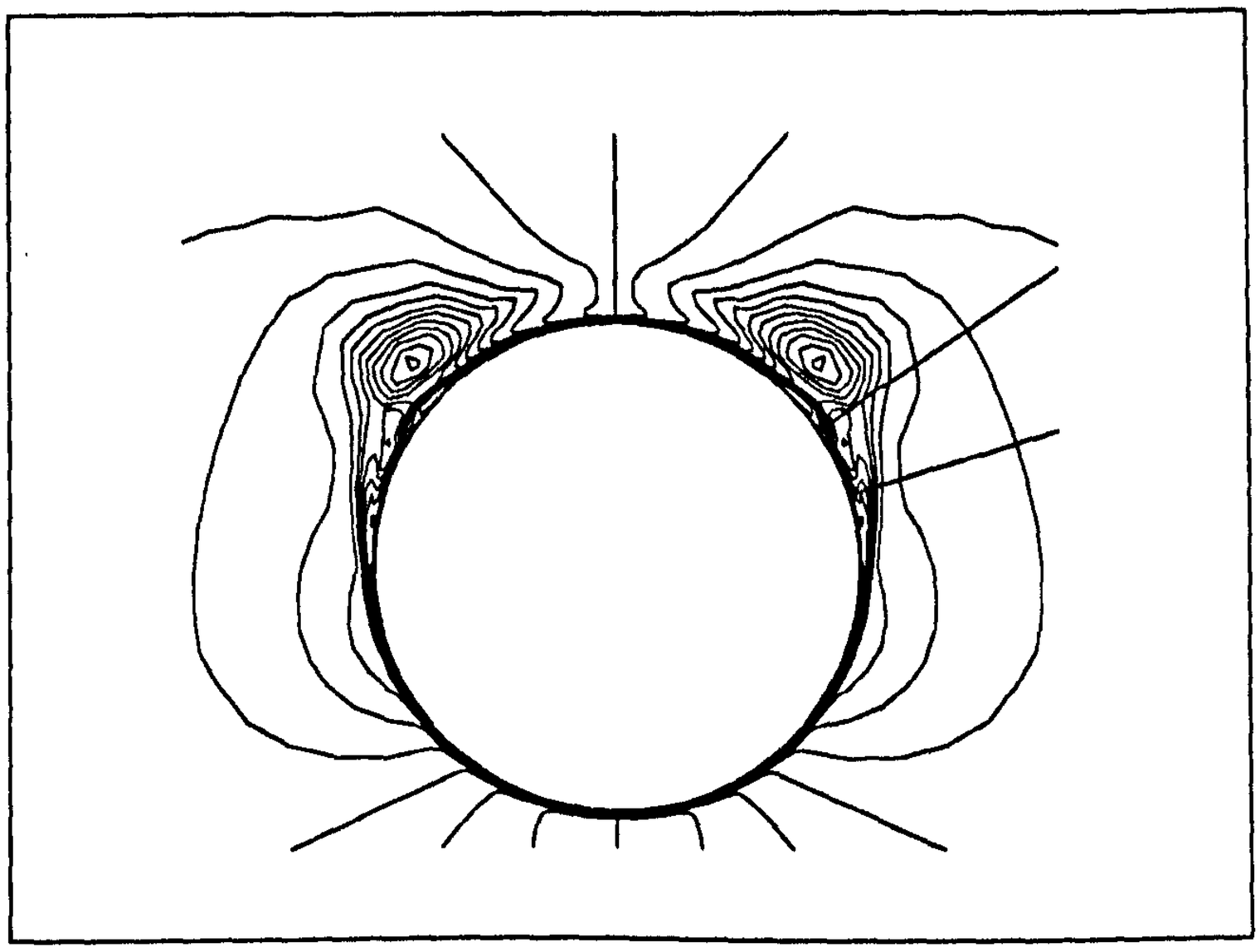

Figure 4.85: *Comparison of Vortex Density Contour Resolution for K-Cut Multiblock and Single Block Computations at Plane x/D=8*

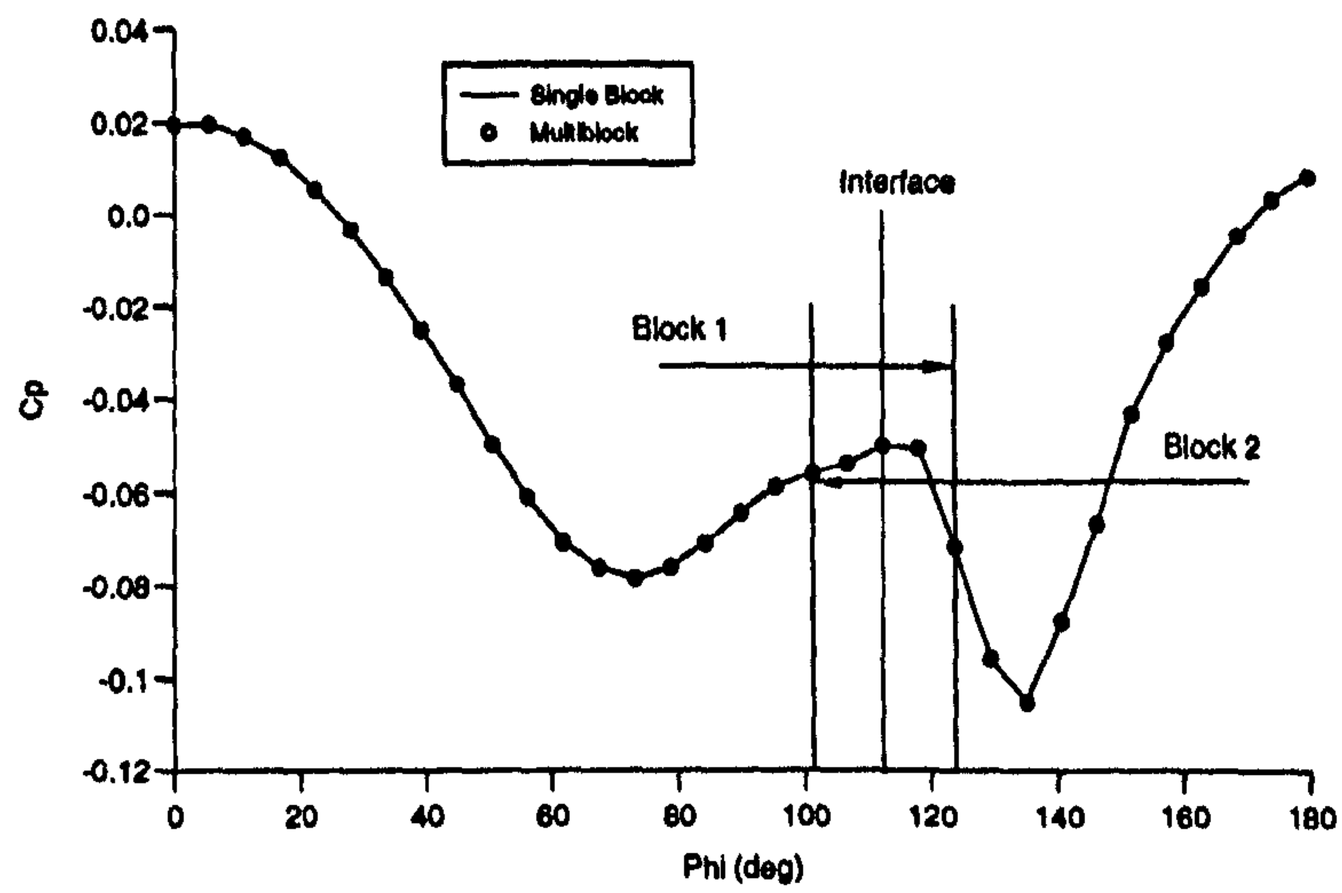

Figure 4.86: *Comparison of Circumferential Surface Pressure Coefficient, x/D=8*

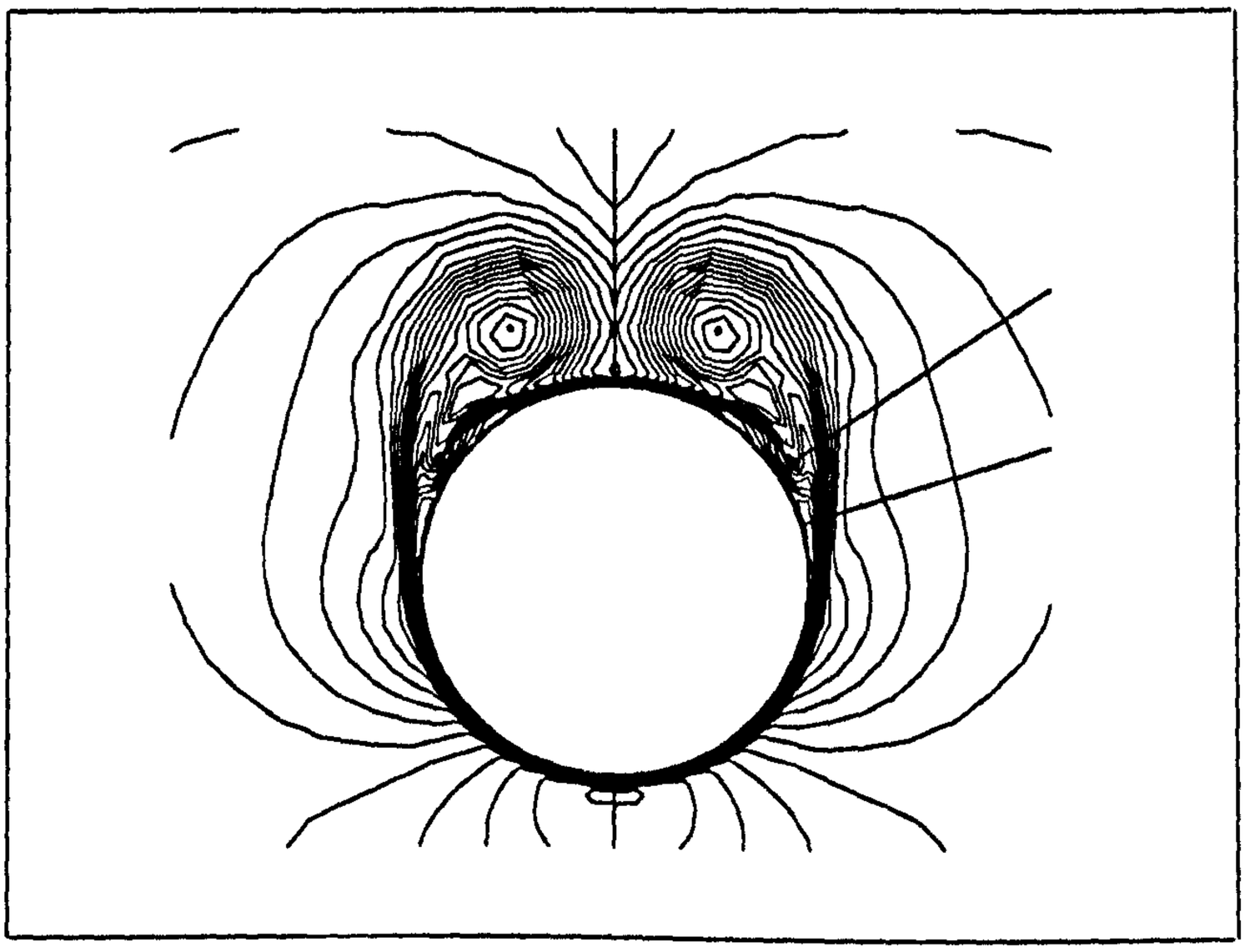

Figure 4.87: *Comparison of Turbulent Solutions for Vortex Resolution for K-Cut Multiblock and Single Block Computations at Plane x/D=9*

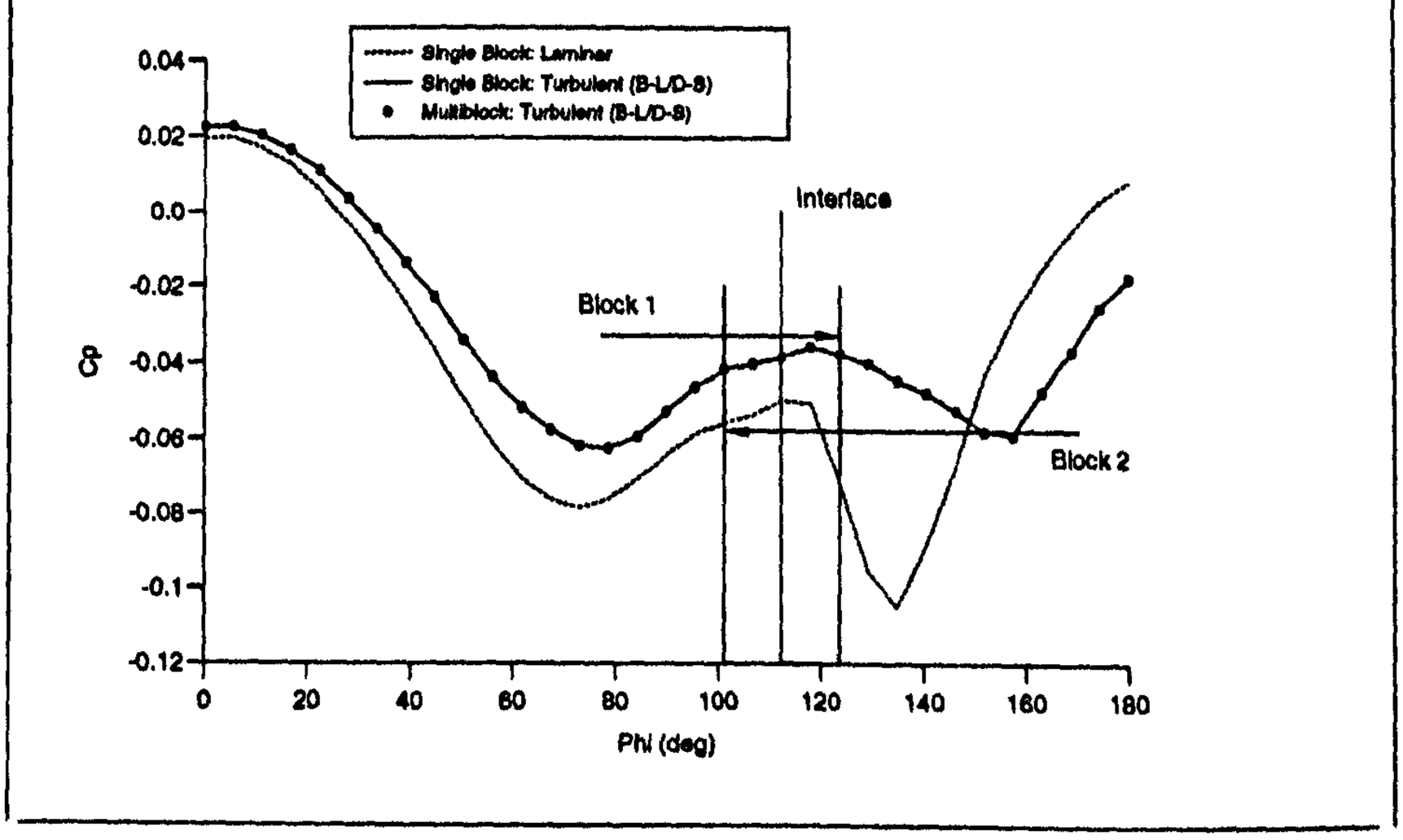

Figure 4.88: *Comparison of Circumferential Surface Pressure Coefficient, x/D=9*

Chapter 5

Euler Solutions and 'Phantom Vorticity' on Non-Uniform Grids

The phenomena of "phantom vorticity" in Euler solutions is introduced and linked to the stretching of the computational mesh. A new formulation of the higher order MUSCL scheme which accounts for grid non-uniformity is derived and applied to the alleviation of the phantom vorticity.

Several investigators have found that if the Euler equations are solved to predict the supersonic flow around smooth slender bodies at moderate to large angle of attack, anomalous leeside vortices can develop in the solution [34] [9]. In addition, the development of a "numerical" boundary layer has been observed, which grows at the body surface, even with the application of a slip boundary condition at the wall.

The inviscid character of the Euler equations, means that they cannot account for viscous vorticity generation. Numerical solution of the Euler equations can, however, involve mechanisms for the generation of vorticity "by mistake". In inviscid flow, curved shock-waves introduce circulation, entropy layers and vorticity into the solution. Marconi [34] demonstrated that for a conical-Euler solution on a slender cone at angle of attack in a supersonic stream, a crossflow shock will cause separation of the flow from the cone surface and a spiral vortex near the leeward symmetry plane. In addition, since numerical solutions are obtained from approximate, or discretised, forms of the governing equations, Euler solutions may include vorticity generation by the effect of truncation error. Once a vortex is formed, the Euler equations allow for its convection downstream but cannot simulate its

diffusion due to physical viscosity. All computational schemes, however, are dissipative and even without the addition of artificial viscosity, will diffuse and destroy vorticity. Numerical dissipation will diminish the concentration and strength of vortices, but not in a manner representative of a viscous flowfield.

Turkel [75] undertook a comprehensive investigation of the effect of grid stretching on the accuracy of modern schemes for compressible fluid flows. Turkel showed that many of the popular central and upwind methods reduce to first order spatial accuracy in regions where the grid is highly non-uniform. Various algebraic and exponential functions were investigated for the grid stretching. It was found that algebraic stretching was sufficiently smooth to allow second order techniques to maintain their formal accuracy. Exponential stretching functions, however, proved to deteriorate the spatial accuracy to first order unless special weighted formulas are used. In addition it was demonstrated that second order accuracy can be maintained with these schemes only if the mesh accurately reflects the properties of the solution.

Chinilov [13] investigated the phenomenon of the non-physical, numerical boundary layer which he found to develop near the body surface when a supersonic inviscid stream flows past a blunt body. A 2D, steady supersonic flow past a circular cylinder was investigated using several mesh resolutions by use of a first order finite volume numerical Godunov scheme. Chinilov, however, does not seem to have employed any appreciable grid stretching, and found that he could reduce the "phantom viscosity" by either refining the grid or employing second order spatial discretisation.

A number of investigators have developed techniques to account for grid stretching. Battina [6] developed improved algorithms for the spatial and temporal discretisation in his unstructured Euler solver for the investigation of the unsteady aerodynamics of a 2D pitching aerofoil. In particular he developed a simple interpolation of the primitive variables which he employed in the standard MUSCL scheme in order to treat highly skewed tetrahedral cells. This weighted interpolation of the primitive variables was based on the distance between the centroid and the midpoint of the appropriate edge. Battina [7] further developed this technique for 3-D flows, this time with a different MUSCL type scheme. Liou and Hau [31] developed a high resolution scheme for their time accurate, 3D, structured finite volume solver, based on Roe's upwind technique for flux difference splitting. Nonuniformity of cell sizes was accounted for by deriving a number of factors based on the sizes of each cell in the stencil.

The errors associated with "phantom vorticity" in Euler solutions on highly stretched grids, if large enough, may affect the viscous solutions, which employ very fine, highly stretched grids in the near wall region. It was therefore decided to investigate the affect of "phantom vorticity" on the solution of the Mach 2, 10° angle of attack flow over the ONERA B1 body

(Forebody Testcase 2).

5.1 The Numerical Investigation

The CRANS3D solver was employed in Euler mode to obtain solutions on five grids. The first "*Euler*" mesh was of size (60 × 54 × 45) and employed near wall cells of $0.00185D$ radial thickness and a *tanh* radial stretching function. The next four "*NS*" grids all used near wall cells of $2 \times 10^{-4}D$ radial thickness and again employed a *tanh* radial stretching function. The cells were spaced uniformly in the circumferential direction.

First of all, the solver was employed on all five grids using the standard MUSCL formulation with the κ factor set for third order spatial accuracy. It was found that for the first two grids the solution converged well down to five orders, whereas those on the finest three grids stalled at around 2-2.5 orders of convergence. The CFL number, set to 0.3, was successively reduced down to 0.05 in an attempt to converge the solutions further, but was found to have little affect. Analysis of the stalled solution, by checking after every 1000 iteration increment, revealed that the flow structure did not exhibit any appreciable change. Figure 5.1 presents the five solutions for the circumferential surface pressure at $x/D = 7$. It would be expected that as the grid is further refined, the solution would converge to the same circumferential distribution, but what is, in fact, observed is that the solution progressively deviates from the expected inviscid solution (Curve for Grid 1) and develops pronounced suction peaks due to the resolution of the phantom vortices on the leeside of the body.

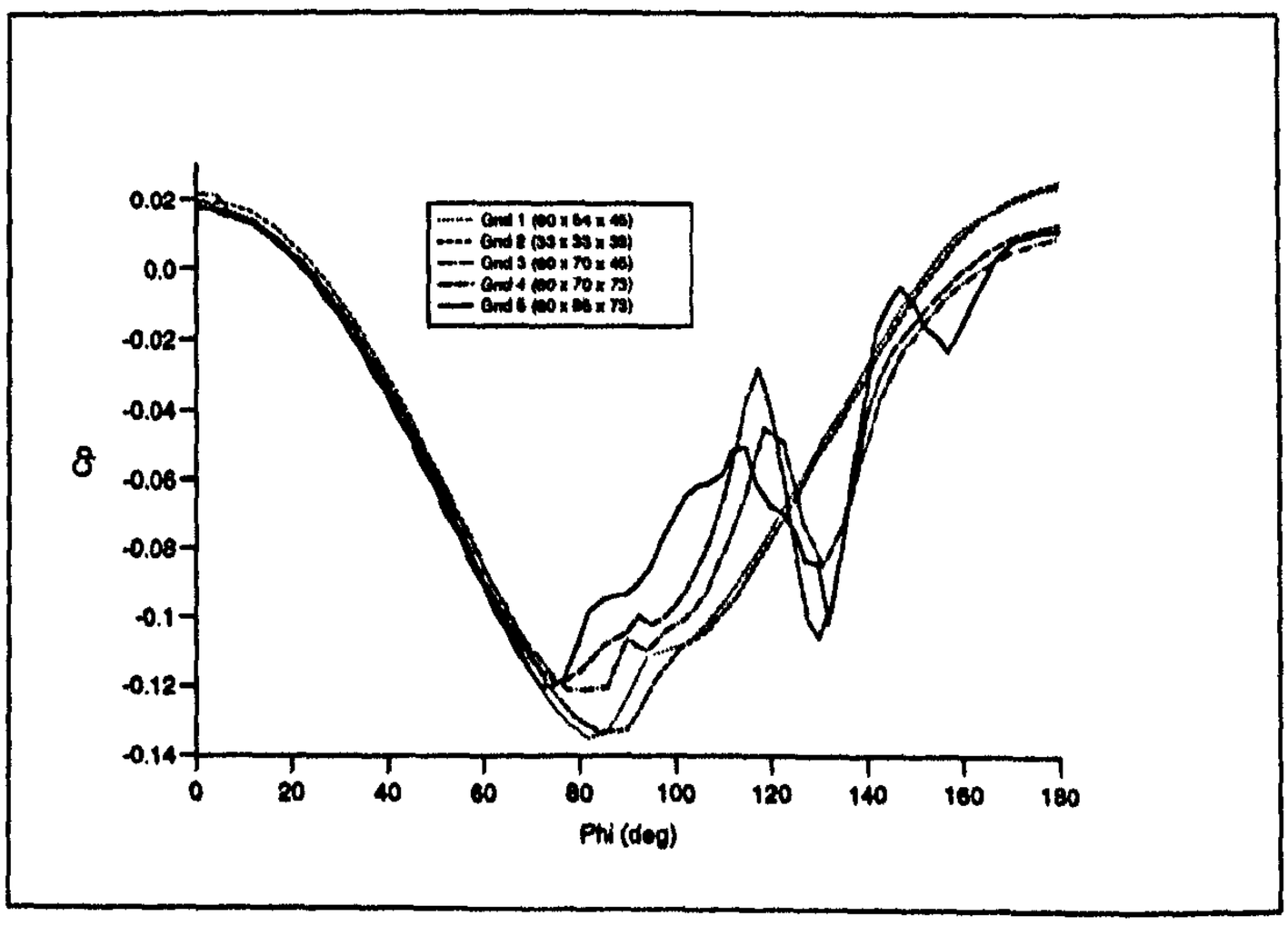

Figure 5.1: *Grid Convergence for Euler Solution, 3rd Order MUSCL*

Figure 5.2 presents the computational grid and density contours at $x/D = 8$ obtained by the fully converged Euler solution on grid 1. This solution appeared to yield the correct flow structure expected of an Euler solution, without any flow separation or leeward vortices. Close inspection of the crossflow velocity vectors, however, did show the presence of a slight velocity profile close to the leeward body surface.

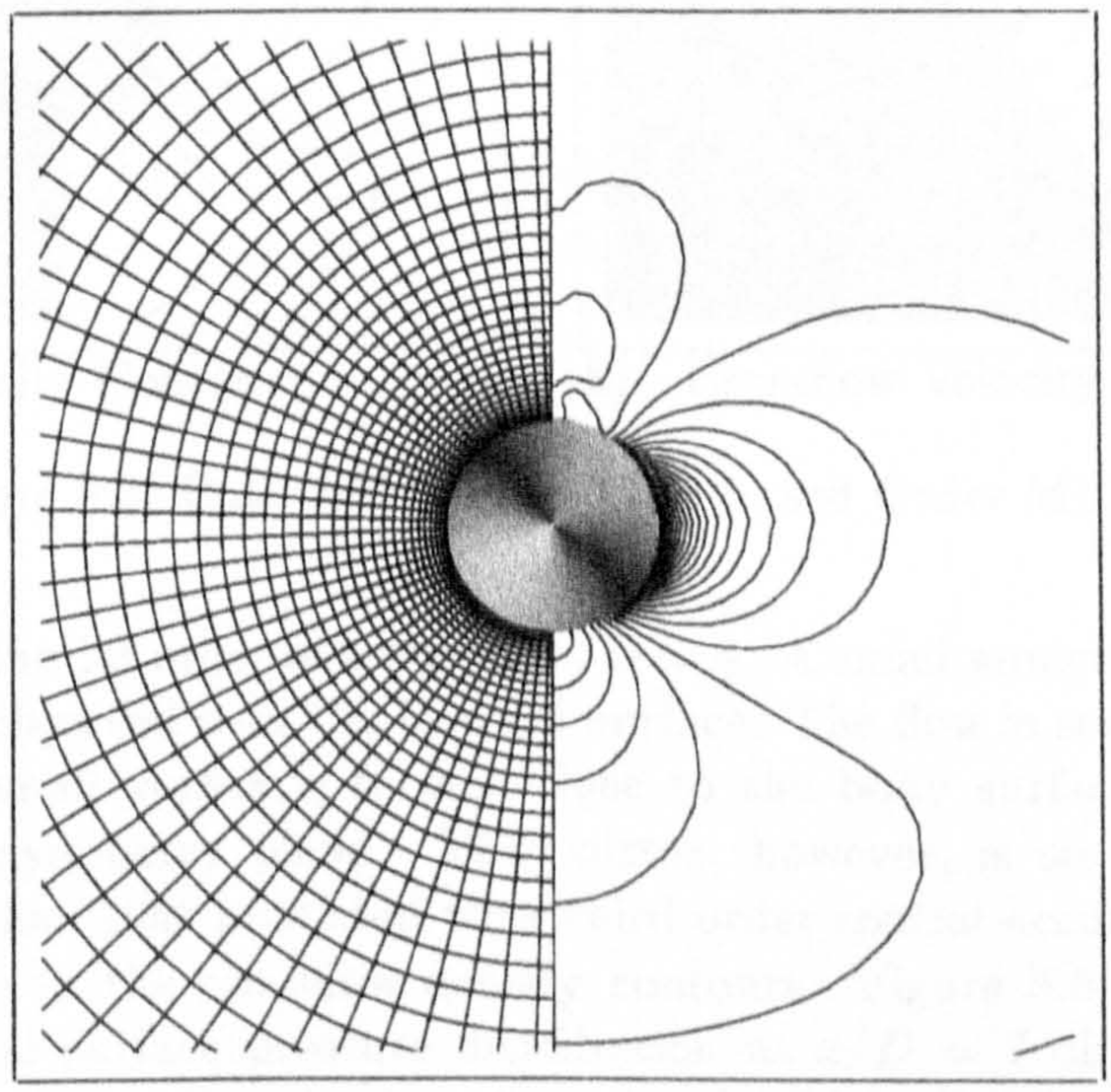

Figure 5.2: *Density Contours at x/D=8, 3rd Order MUSCL Euler Solution on Grid 1*

The corresponding crossflow solution on the finest NS grid ($60 \times 85 \times 73$) at the same axial station is presented in Figure 5.3.

The plot of leeward crossflow vectors clearly shows a well developed numerical boundary layer, which separates off the leeside of the body to form a well developed primary, secondary and tertiary vortex system similar to that expected of a viscous solution rather than an Euler solution. Since the origin of the vorticity is non-physical, the resulting vortex pattern does not agree with either experiment, or with the laminar NS solution for the same grid. The primary vortex is resolved too strongly, and no tertiary vortex was resolved in either experiment or the viscous solution. Solutions were also obtained using a different formulation for the Euler wall slip boundary condition, and using the Roe Approximate Riemann solver instead of the Osher solver. Neither changes had any appreciable affect on the solution.

The next step in the investigation was to look at the effect of spatial accuracy. By altering the κ factor in the MUSCL scheme one can obtain solutions of second order spatial accuracy, and by switching off the MUSCL scheme altogether one gets a solution of first order spatial accuracy. Figure

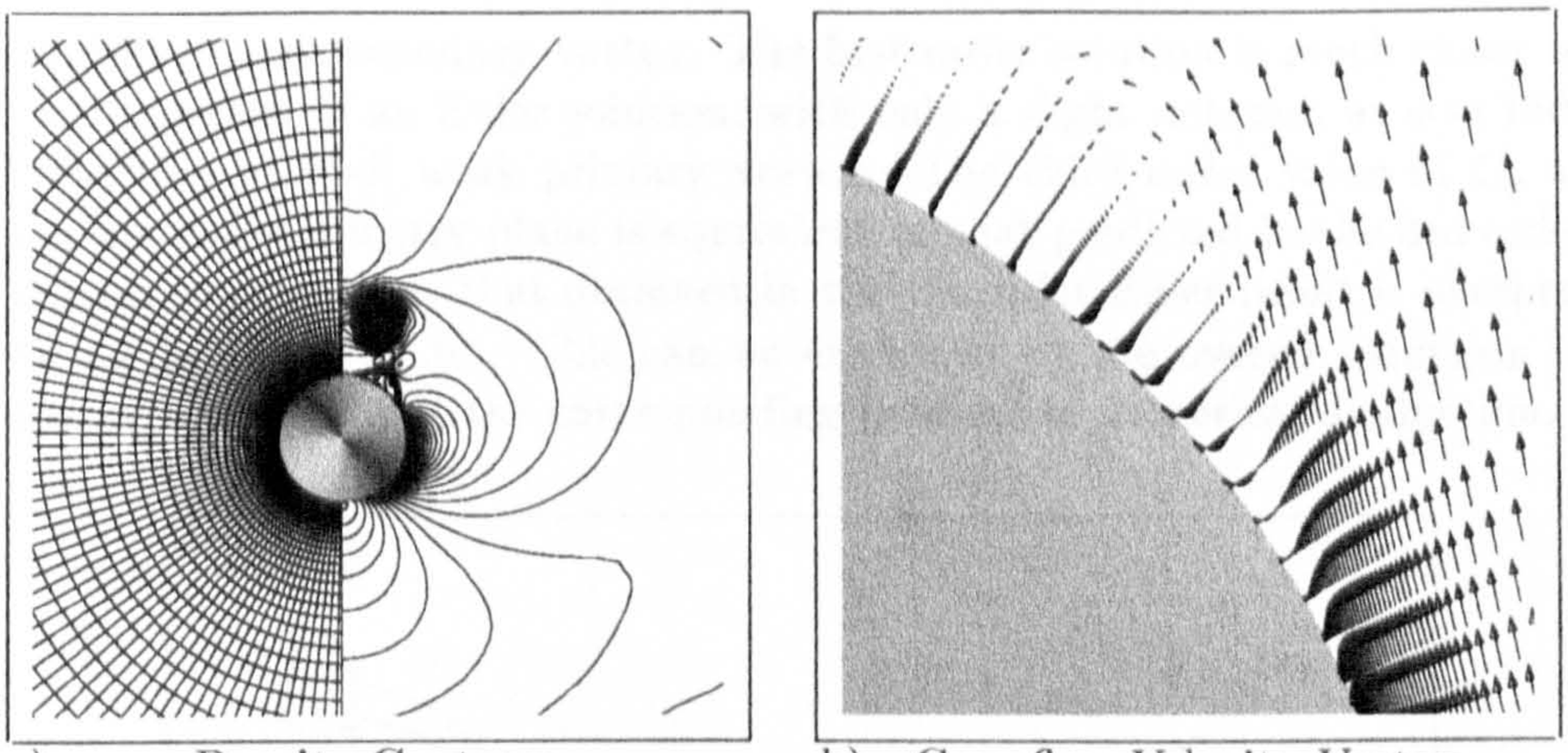

a) Density Contours b) Crossflow Velocity Vectors

Figure 5.3: Euler Solution on Grid 5, 3rd Order MUSCL

5.4 presents the 1st order solution at $x/D = 8$. A small numerical boundary layer is still observed over the leeward surface. The flow is seen to separate and a very small vortex is formed close to the body surface adjacent to the leeward symmetry plane. This vortex, however, is so much smaller and weaker than that predicted with third order spatial accuracy that it is hardly visible in the crossflow density contours. Figure 5.5 compares the circumferential surface pressure distribution at $x/D = 7$ obtained for 1st order spatial accuracy, and using the 3rd order MUSCL scheme.

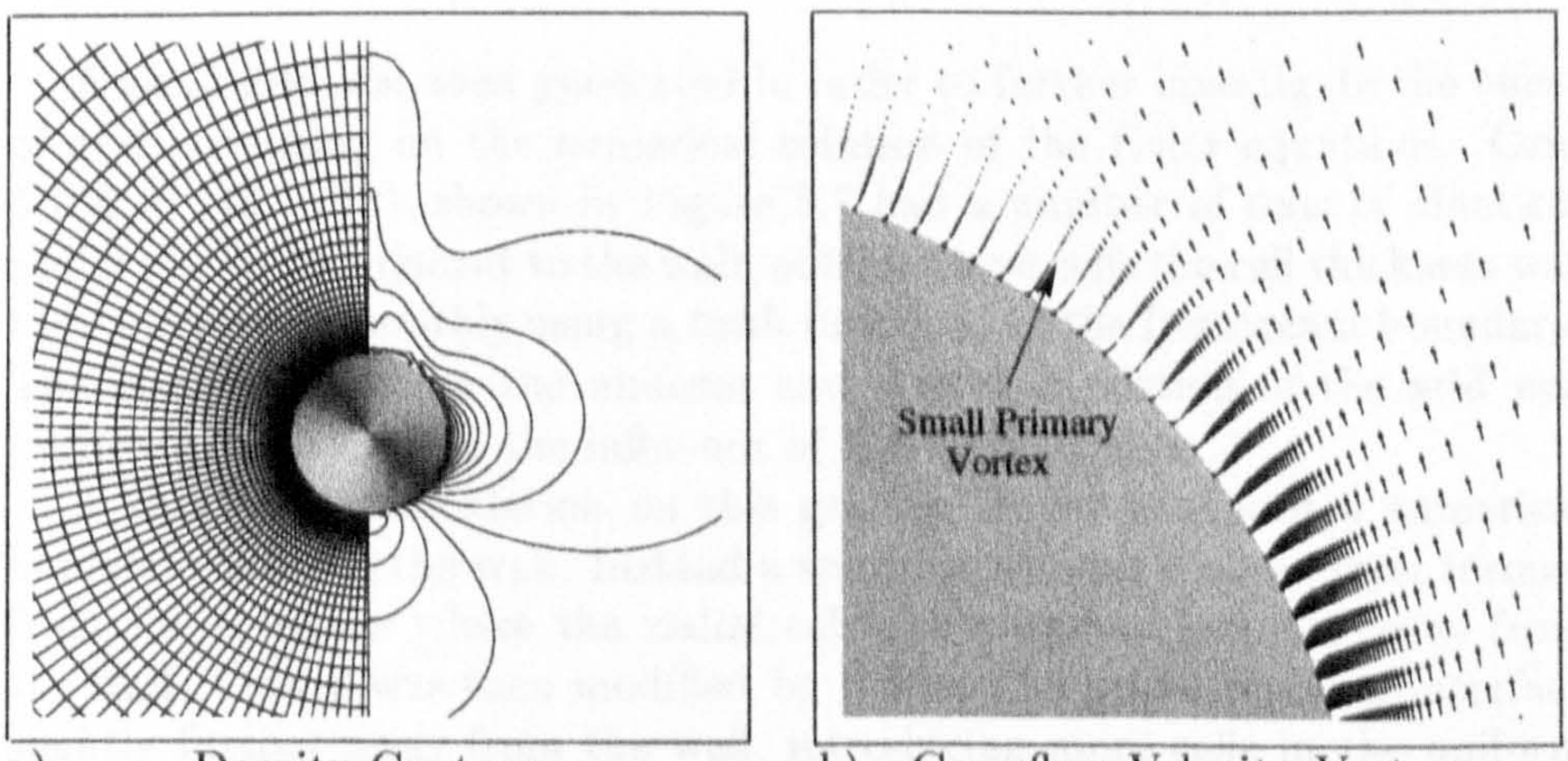

a) Density Contours b) Crossflow Velocity Vectors

Figure 5.4: B1, First Order Euler Solution on Grid 5

The first order solution and that predicted using the 3rd Order MUSCL scheme are seen to be dramatically different. The higher order result predicts separation at around $\phi \approx 100^o$ and two suction peaks associated with

a primary and secondary vortex. The first order solution is much closer to that expected of an Euler solution, with only a slight inflexion at $\phi \approx 150°$ indicating a small weak primary vortex. The third order value of C_p at the leeward symmetry plane is equivalent to that predicted in the 3rd order viscous solution, but that obtained in the 1st order Euler result is overpredicted by $\Delta C_p \approx 0.01$. This can be explained by the overall reduction in spatial accuracy, and the corresponding increase in numerical dissipation.

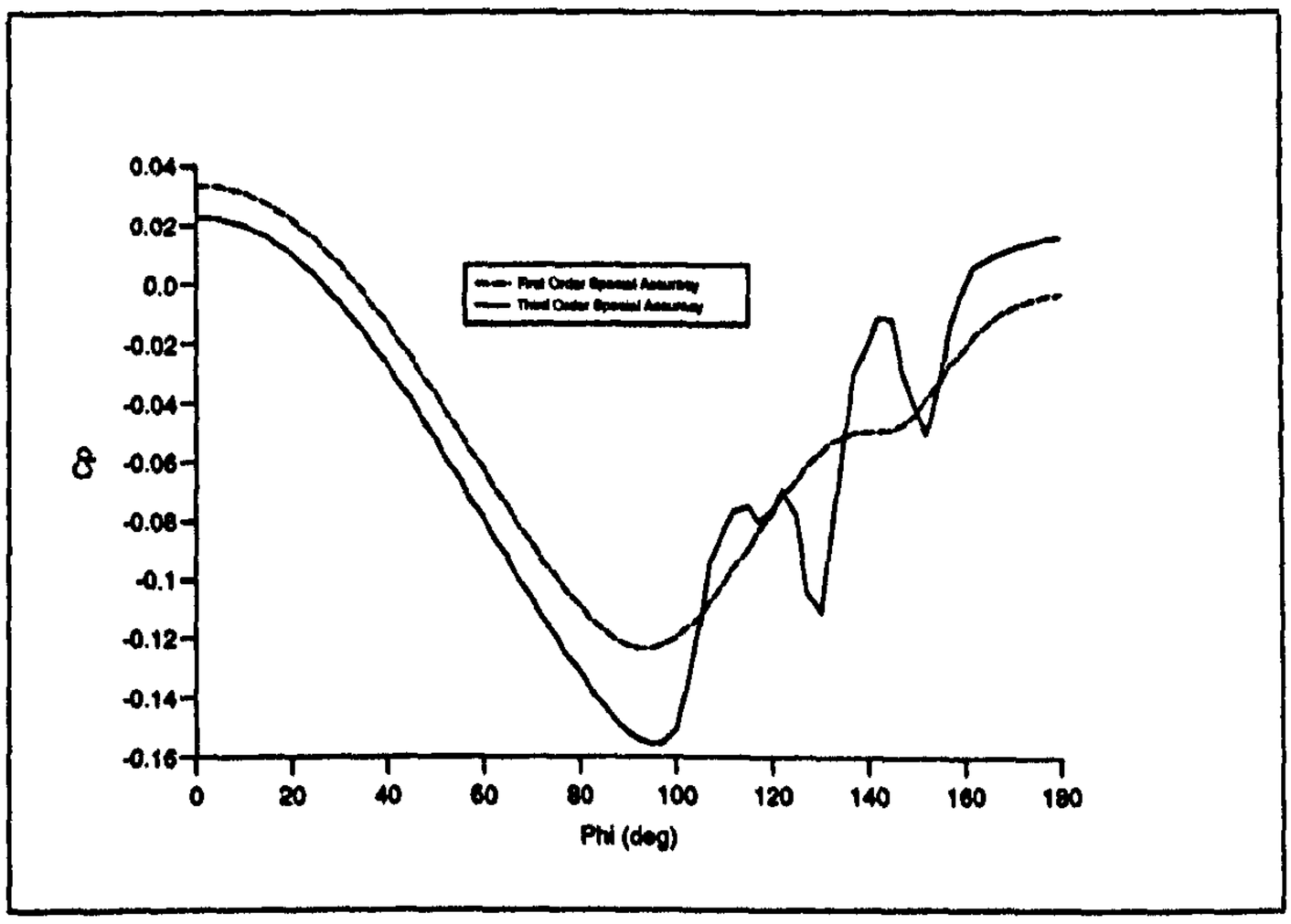

Figure 5.5: *Euler Solution on Grid 5, 1st Order vs. 3rd Order MUSCL*

A sixth grid was then generated in order to further investigate the effect of grid stretching on the numerical solution of the Euler equations. Grid 6 ($60 \times 140 \times 73$), shown in Figure 5.7 had a number of cells of identical radial thickness adjacent to the wall; outside these cells the cell thickness was then increased smoothly,using a *tanh* function, to the freestream boundary. The interface between the uniform and stretched portion of the grid was positioned well beyond the influence of the body surface.

A third order calculation on this grid no longer produced a numerical boundary layer at the wall. Instead a spurious numerical shear layer formed from the interface where the radial cell size began to increase away from the wall. Grid 6 was then modified by pulling the grid stretching interface slightly further away from the wall, introducing more cells in the uniform regions such that the uniform cell size of grid 6 was maintained. It was found that the numerical shear layer moved with the stretching interface. In effect, the numerical boundary layer was moved away from the wall and followed the position of the discontinuity in the gradient of cell size.It was noted that the solution could only be converged down to 2.5 orders before it stalled. The solution remained the same after iterating a further 3000 time

steps with a CFL number reduced from 0.3 to 0.1.

It was postulated that the numerical boundary layer and the resultant phantom vorticity is due to excessive numerical dissipation associated with the localized loss of spatial accuracy when using the standard high resolution MUSCL scheme in regions where the grid is highly stretched. In order to test this hypothesis, it was decided to derive a modified MUSCL scheme to account for grid stretching. Section 5.1.1 presents the derivation of a high resolution MUSCL scheme which uses a weighted formulation of each cell size in the stencil.

5.1.1 A New Formulation of the MUSCL Scheme for Non-Uniform Grids

The original formulation of the MUSCL scheme was derived from the piecewise quadratic distribution for the variable U in a cell i given by equation (5.1).

$$U = U_i + (x - x_i)\left.\frac{\partial U}{\partial x}\right|_i + \frac{3\kappa}{2}\left[(x - x_i)^2 - \frac{\Delta x^2}{12}\right]\left.\frac{\partial^2 U}{\partial x^2}\right|_i \tag{5.1}$$

where U_i is the average value defined by:

$$U_i = \frac{1}{\Delta x}\int_{i-\frac{1}{2}}^{i+\frac{1}{2}} U(x)dx$$

The above expression assumes that each cell is the same size, that is - there is no grid stretching. Figure 5.6 shows a 1D computational stencil about cell i for a stretched grid, where the length of cell i is denoted by s_i.

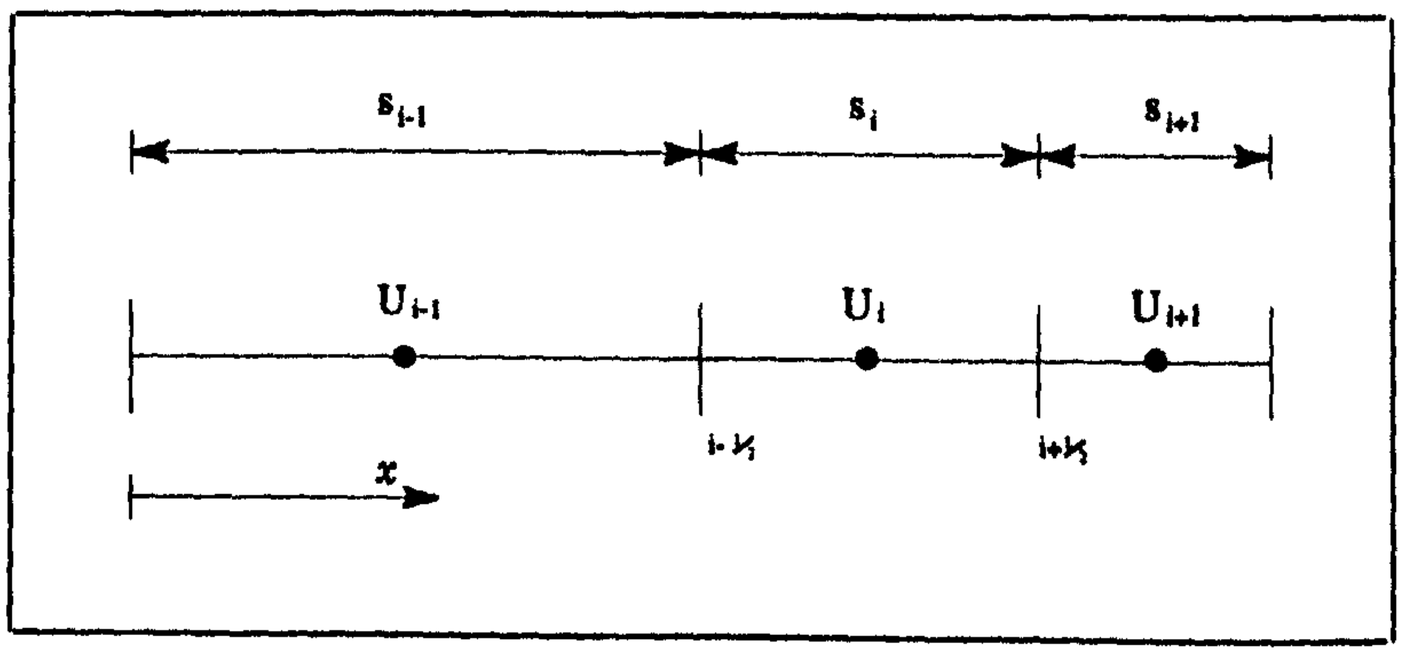

Figure 5.6: *Finite Volume Representation of Stretched Grid About Cell i*

Taking the function $f(x)$ to be a quadratic function of U of the form $dU = Adx^2 + Bdx$ gives the following relation:

$$U - U_i = A\,(x - x_i)^2 + B\,(x - x_i) \tag{5.2}$$

To evaluate the required derivatives of U with respect to x:

$$\frac{\partial U}{\partial x} = 2Adx + B$$
$$\frac{\partial^2 U}{\partial x^2} = 2A$$

Expressions for the factors A and B can be obtained by applying equation (5.2) about point i:

$$\begin{aligned} U_{i+1} - U_i &= A\,(x_{i+1} - x_i)^2 + B\,(x_{i+1} - x_i) \\ U_{i-1} - U_i &= A\,(x_{i-1} - x_i)^2 + B\,(x_{i-1} - x_i) \end{aligned} \tag{5.3}$$

yielding the following result:

$$A = \frac{1}{x_{i+1} - x_{i-1}} \left(\left(\frac{U_{i+1} - U_i}{x_{i+1} - x_i} \right) - \left(\frac{U_{i-1} - U_i}{x_{i-1} - x_i} \right) \right)$$

and:

$$B = \frac{1}{x_{i+1} - x_{i-1}} \left(\left(\frac{x_i - x_{i-1}}{x_{i+1} - x_i} \right) (U_{i+1} - U_i) + \left(\frac{x_{i+1} - x_i}{x_i - x_{i-1}} \right) (U_i - U_{i-1}) \right)$$

The required derivatives at i (where $x - x_i = 0$) are then given by:

$$\left.\frac{\partial U}{\partial x}\right|_i = B \qquad\qquad \left.\frac{\partial^2 U}{\partial x^2}\right|_i = 2A$$

For a stretched grid the Δx term in equation (5.1) becomes the size of cell i - s_i. The cell sizes can then be given by

$$\begin{aligned} s_{i-1} &= x_{i-\frac{1}{2}} - x_{i-\frac{3}{2}} = 2\left(x_{i-\frac{1}{2}} - x_{i-1}\right) \\ s_i &= x_{i+\frac{1}{2}} - x_{i-\frac{1}{2}} = 2\left(x_i - x_{i-\frac{1}{2}}\right) \\ s_{i+1} &= x_{i+\frac{3}{2}} - x_{i+\frac{1}{2}} = 2\left(x_{i+1} - x_{i+\frac{1}{2}}\right) \end{aligned}$$

Setting:

$$\tilde{\Delta}^+ = \frac{2s_i(U_{i+1} - U_i)}{(s_{i+1} + s_i)}$$

$$\tilde{\Delta}^- = \frac{2s_i(U_i - U_{i-1})}{(s_i + s_{i-1})} \tag{5.4}$$

Equations (5.4) can then be substituted into equation (5.1). For the evaluation of the variables at the interfaces of cell i, the value of x is set as $x = x_i \pm s_i/2$. For the left hand side of interface $i + 1/2$, this results in the following relation.

$$U^L_{i+\frac{1}{2}} = U_i + \frac{1}{\left(\frac{s_i+s_{i-1}}{s_i}\right) + \left(\frac{s_i+s_{i+1}}{s_i}\right)} \left(\left(\left(\frac{s_i + s_{i-1}}{2s_i}\right) + \kappa\right)\tilde{\Delta}^+ + \left(\left(\frac{s_i + s_{i+1}}{2s_i}\right) - \kappa\right)\tilde{\Delta}^-\right) \tag{5.5}$$

A corresponding expression can be derived for the values of the right hand side of interface $i + 1/2$ (ie: by a similar treatment for cell $i + 1$):

$$U^R_{i+\frac{1}{2}} = U_{i+1} - \frac{1}{\left(\frac{s_{i+1}+s_i}{s_{i+1}}\right) + \left(\frac{s_{i+1}+s_{i+2}}{s_{i+1}}\right)} \left(\left(\left(\frac{s_{i+1} + s_i}{2s_{i+1}}\right) - \kappa\right)\tilde{\tilde{\Delta}}^+ + \left(\left(\frac{s_{i+1} + s_{i+2}}{2s_{i+1}}\right) + \kappa\right)\tilde{\tilde{\Delta}}^-\right) \tag{5.6}$$

Where:

$$\tilde{\tilde{\Delta}}^+ = \frac{2s_{i+1}(U_{i+2}-U_{i+1})}{(s_{i+2}+s_{i+1})}$$

$$\tilde{\tilde{\Delta}}^- = \frac{2s_{i+1}(U_{i+1}-U_i)}{(s_{i+1}+s_i)} \tag{5.7}$$

Equation (5.5) and (5.6), represent the modified MUSCL scheme for non-uniform grids, based on a quadratic distribution of U across the cell.

The modified MUSCL scheme was employed on grid 6. Figure 5.8 presents the $x/D = 8$ crossflow solution and clearly demonstrates the dramatic improvement the modified MUSCL scheme produced. The numerical shear layer and the associated vortices, which appeared as intermediate solutions, were convected out of the solution as it converged down to five orders. The final solution was comparable, even better, than the standard 3rd order MUSCL solution on the Euler grid (grid 1) despite the large cell stretching.

A further calculation was performed, employing the modified MUSCL scheme on grid 5. This time the numerical boundary layer and resultant phantom vortices appeared only as an intermediate solution, and disappeared as the solution converged down to five orders.

A further test was carried out using grid 5 to obtain a laminar solution with the modified MUSCL scheme. The result showed that the solution was equivalent to that presented for that grid in the study of forebody testcase 2, indicating that the "phantom viscosity" is less of a problem for NS solutions.

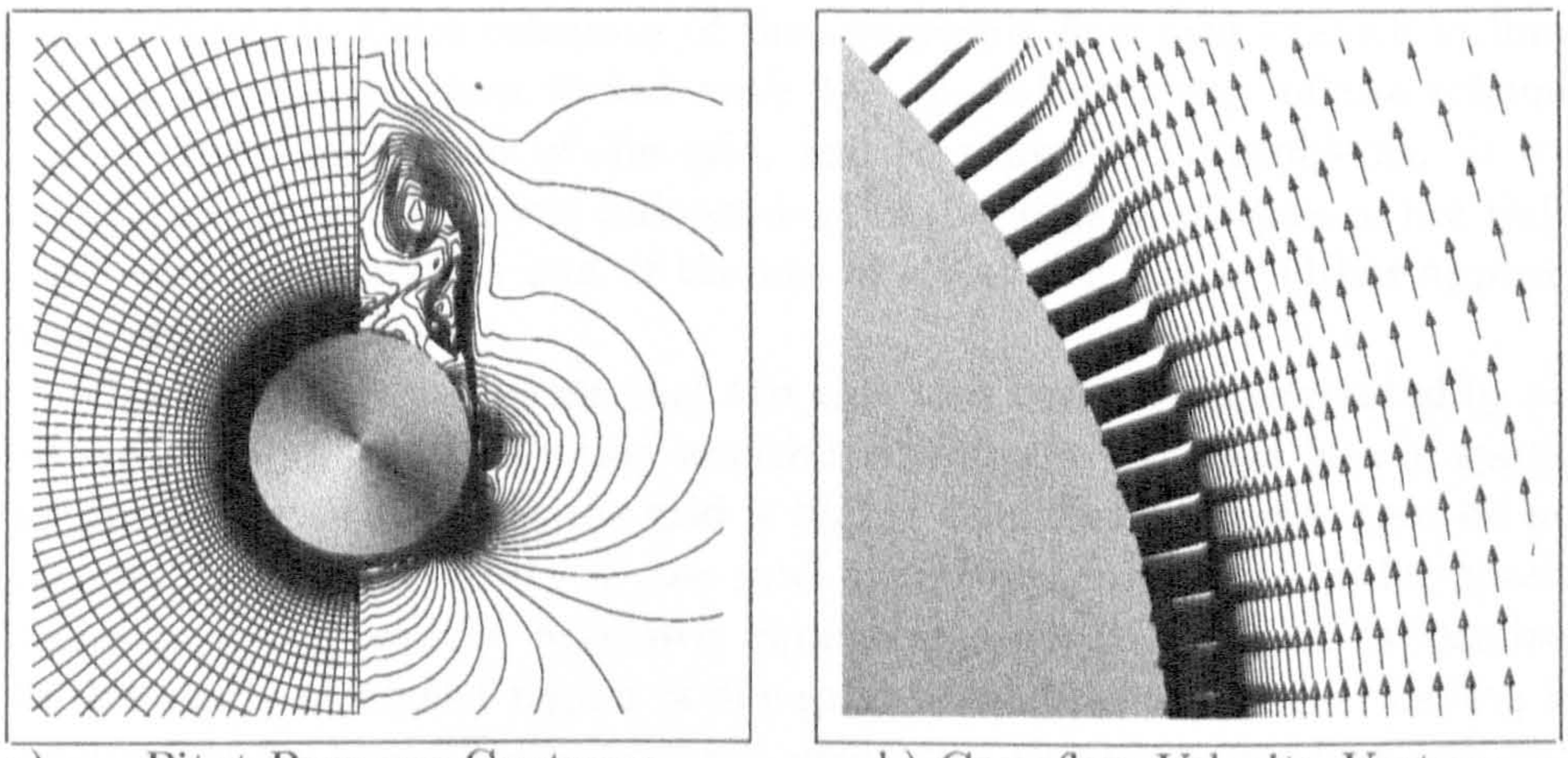

a) Pitot Pressure Contours b) Crossflow Velocity Vectors

Figure 5.7: *Euler Solution on Grid 6, x/D=8, 3rd Order Original MUSCL Scheme*

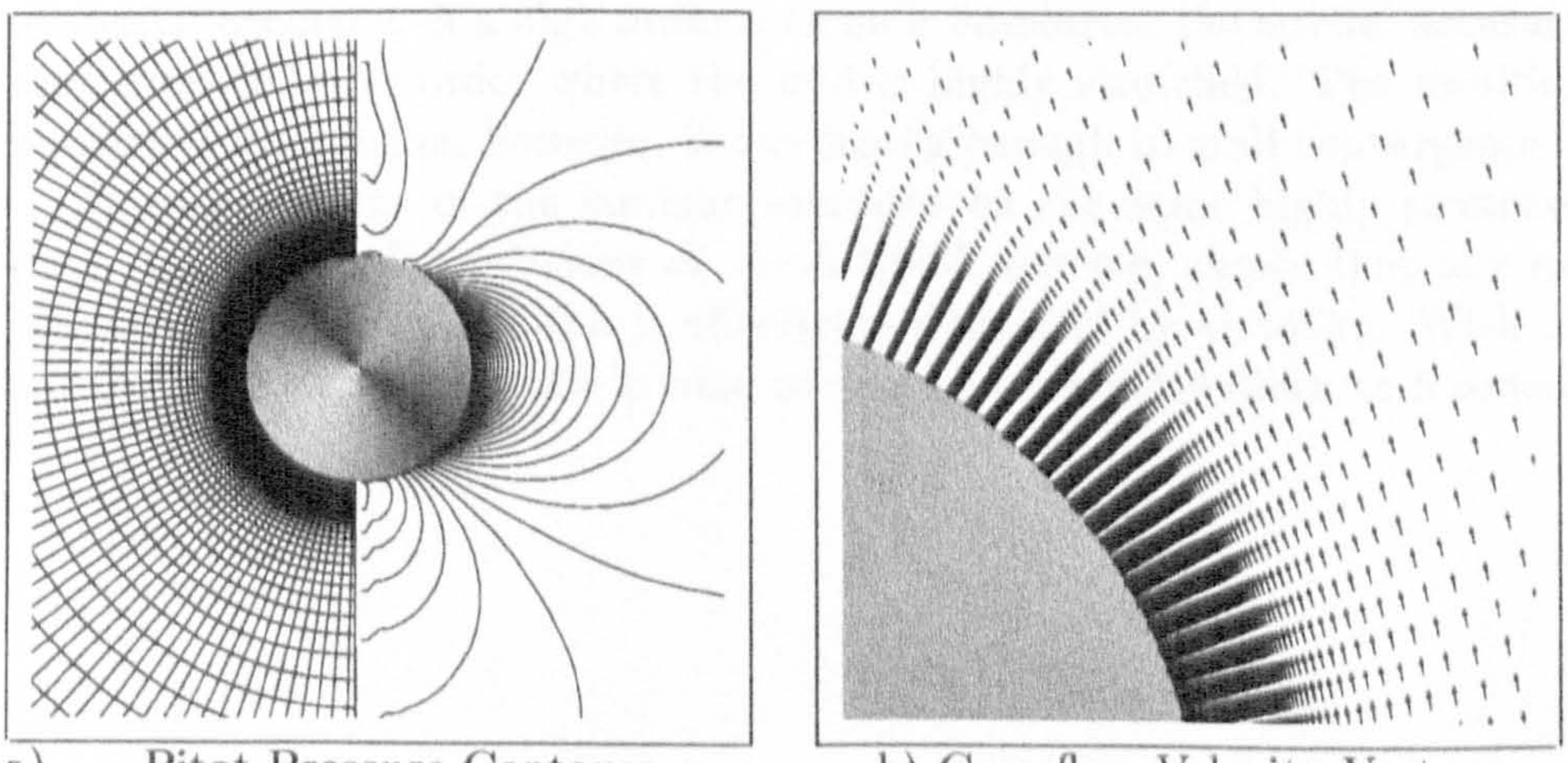

a) Pitot Pressure Contours b) Crossflow Velocity Vectors

Figure 5.8: *Euler Solution on Grid 6, x/D=8, 3rd Order Modified MUSCL Scheme*

5.2 Phantom Vorticity: An Interpretation

The phenomenon of the numerical boundary/shear layer and resultant phantom vorticity in Euler solutions of the supersonic flow past smooth inclined slender bodies has been linked with the spatial accuracy of the scheme, highly stretched regions of the grid, and to convergence problems. It was found that the problem was independent of the implementation of the Euler slip boundary condition and of the use of either the Roe or Osher approximate Riemann Solver.

This information suggests that the phantom vorticity is generated by the excessive numerical dissipation associated with the localized loss of spatial accuracy in regions where the grid is highly stretched. Schemes that do not account for nonuniformity of the grid cannot maintain high order spatial accuracy and introduce excessive numerical dissipation which is localized to the highly stretched region of the grid. The Euler equations, having no mechanism for the diffusion, cannot delocalize these errors which can only convect through the flowfield in the streamwise direction. Since the source of the numerical dissipation - highly stretched grids with an inconsistent numerical scheme - remains as the flow develops, more and more numerical dissipation is generated and eventually the solution cannot converge any further.

Application of a scheme which accounts for grid nonuniformity will maintain higher order spatial accuracy in highly nonuniform areas of the mesh. The fact that numerical vorticity does occur but dies away as the solution is converged beyond three orders indicates that there is still a localized loss of spatial accuracy. If a high order scheme is employed, the spatial accuracy may drop to lower order where the grid is highly stretched. The resulting numerical dissipation, however, is not strong enough to stall convergence.

The equivalence of the laminar solutions on the same highly stretched mesh using both formulations of the MUSCL scheme, shows that any excessive numerical dissipation is effectively dispersed by viscosity. With no localized errors, the solution is able to converge correctly down to 5 orders.

Chapter 6

Delta Wings At High Speed

The supersonic flow past sharp leading edge delta wings is investigated. In particular the NASA 75° Delta Wing test cases, which correspond closely to the geometry of the wings on the B1AW20A3 configuration, are computed.

6.1 The Supersonic Flow About Delta Wings

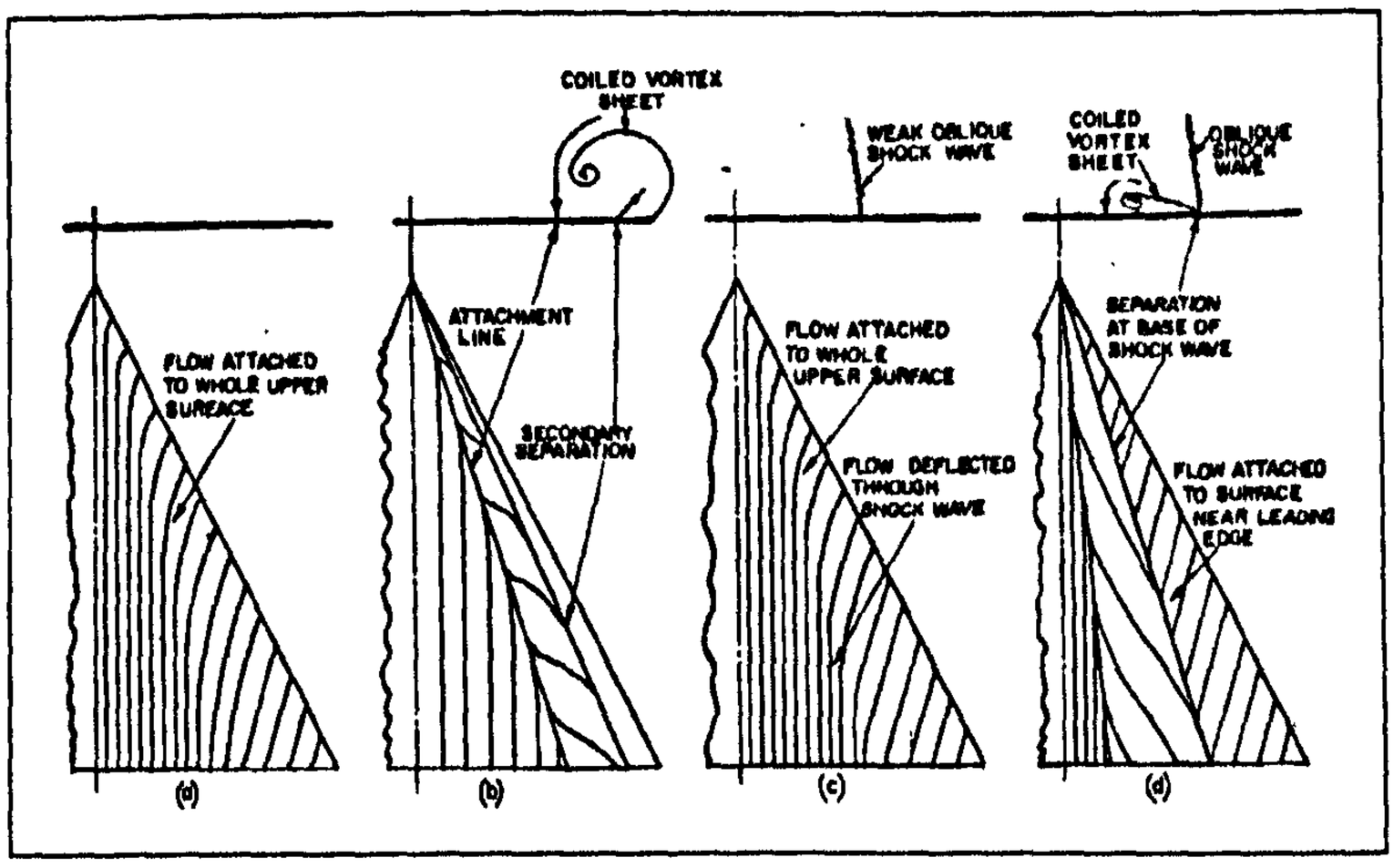

Figure 6.1: *Separation Mechanisms Identified by Stanbrook and Squire [70].*

Stanbrook and Squire [70] performed an analysis of experimental data existing in the early 1960's on the structure of the flow around the leading edges of swept wings. It was shown that, as the Mach number increased at a given angle of attack, the leeside flow changed from a separated to an attached flow while the Mach number normal to the leading edge, M_N, was subsonic. This transition between separated and attached flows is associated

with the occurrence of a supersonic expansion around the leading edge, and the Mach number at which it was found to occur increased with angle of attack.

Four distinct types of leeside flow were identified, as shown in Figure 6.1. At low Mach numbers and almost zero angle of attack the flow is attached and exhibits no crossflow shock as shown for case a). For higher angles of attack the flow separates from the leading edge and the resulting separated shear layer rolls up to form a strong primary vortex. The primary vortex induces a spanwise outflow beneath it which can then separate to form a smaller secondary vortex. This structure, case b), is known as the classical vortex structure and is illustrated in Figure 6.2.

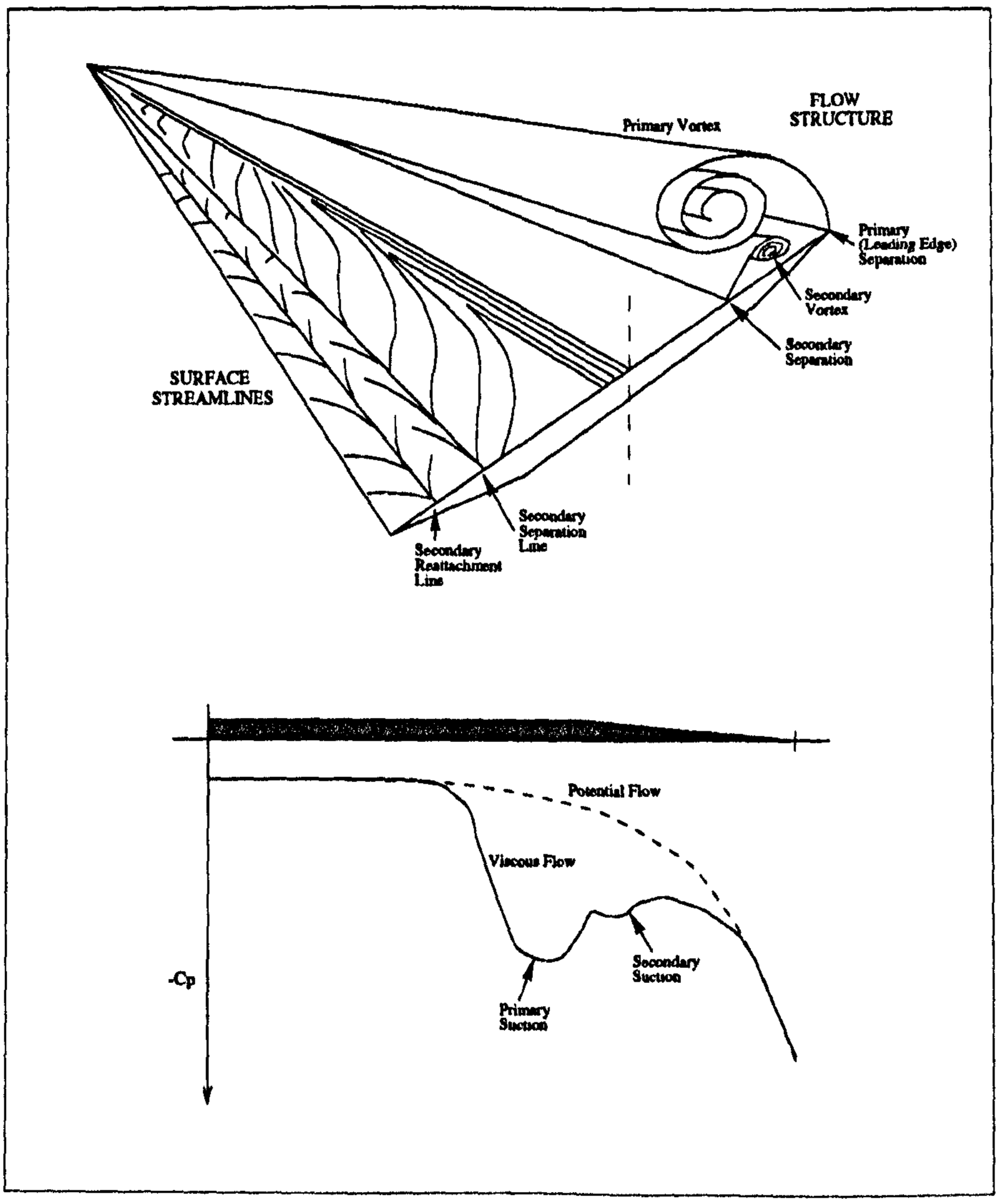

Figure 6.2: *Classical Swept Leading Edge Separation Flow Structure and Surface Pressure Distribution.*

At lower angles of attack there exists a regime where the separated shear layer reattaches to the surface, forming a long bubble similar to that formed in two dimensional flow. For higher Mach numbers, when the leading edge becomes supersonic, the leeside flow in the vicinity of the leading edge remains attached due to the swept supersonic expansion around the leading edge. An oblique crossflow shock will occur from the surface, originating close to the wing apex. If this shock is weak, then there will only be a thickening of the boundary layer around the shock foot and the flow will remain attached as in case c). If the shock is strong enough, however, it will induce boundary layer separation and the resulting free shear layer will either roll up to form a vortex or reattach to the surface forming a bubble, depending on the flow angle of attack. This case is illustrated in Figure 6.1, case d).

Stanbrook and Squire correlated data for sharp, swept leading edge separation on a graph of the angle of attack normal to the leading edge, α_N, against the corresponding normal Mach number M_N. This graph is reproduced in Figure 6.3 and shows the boundaries within which the transition from separated to attached leeside flow was found to occur. This boundary has since become known as the Stanbrook-Squire separation boundary.

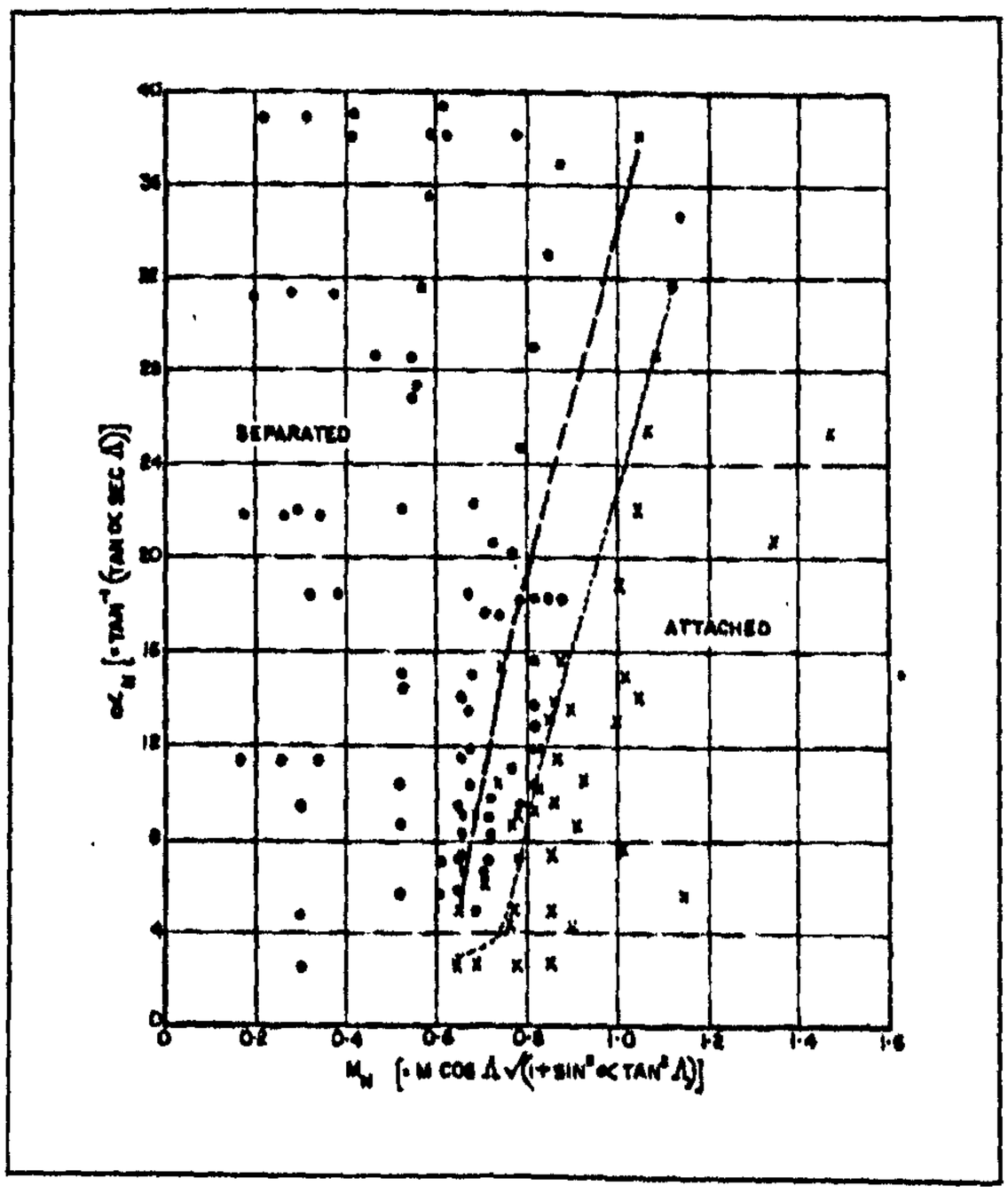

Figure 6.3: *The Variation with angle of attack of Mach Number for Flow Attachment on Swept Sharp Leading Edge Wings. [70].*

An extensive experimental program was performed at NASA Langley by

Miller and Wood [38], studying the leeside flow structures about sharp leading edge delta wings at supersonic speeds. The spanwise surface pressure coefficient was measured at the rear of the model, and the flow structure was visualised by means of vapour screen, oil flow and surface tuft techniques. Four geometries with sweepback angles Λ of 75°, 67.5°, 60° and 52.5° were tested at Mach numbers between 1.5 and 2.8. The four sweepback angle geometries enabled the experimental results to straddle the Stanbrook-Squire separation boundary, and so provide more insight into the mechanisms of the leading edge separation or expansion.

The experimental data enabled Miller and Wood to classify the flow structures into seven distinct regimes, based on the flow mechanisms observed on the leeward side. This classification was later modified by McMillin et-al [36] who performed a comprehensive CFD analysis of all of Miller and Woods experimental cases. These classifications are presented in Figure 6.4 a), which shows the vapour screen photographs of the rearward leeside flow structures. The $\alpha_N - M_N$ graph, marking the regions within which the seven identified regimes occur is presented in Figure 6.4 b). The case of a leeside flow with no leading edge separation and no crossflow shock or resultant separation (ie: subsonic leading edge), was found to occur only at low Mach numbers and extremely low angle of attacks ($\alpha < 1°$). The classical vortex structure as shown in Figure 6.2, with primary and secondary features, occurred above about 5° angle of attack for low subsonic Mach numbers. For smaller angle of attack only a leading edge bubble was evident. For Higher Mach numbers and large angle of attacks above 10°, and for both subsonic and supersonic leading edges, the classical vortex can exhibit a strong crossflow shock embedded on the top of the vortex. This shockwave has not been found to affect the wing surface, but will certainly have an effect on the vortices from a missile forebody in the case when the wing is attached to a body.

A similar situation can occur with a separation bubble where, for higher Mach numbers, embedded crossflow shocks can develop above the bubble. For these cases, Miller and Wood were able to identify effects in both the surface oil flow pattern and surface pressure distribution due to the appearance of the shock. The shock wave was distinguished in the oil flow pattern by an accumulation line within the separated region and in the surface pressure by a large jump in the distribution.

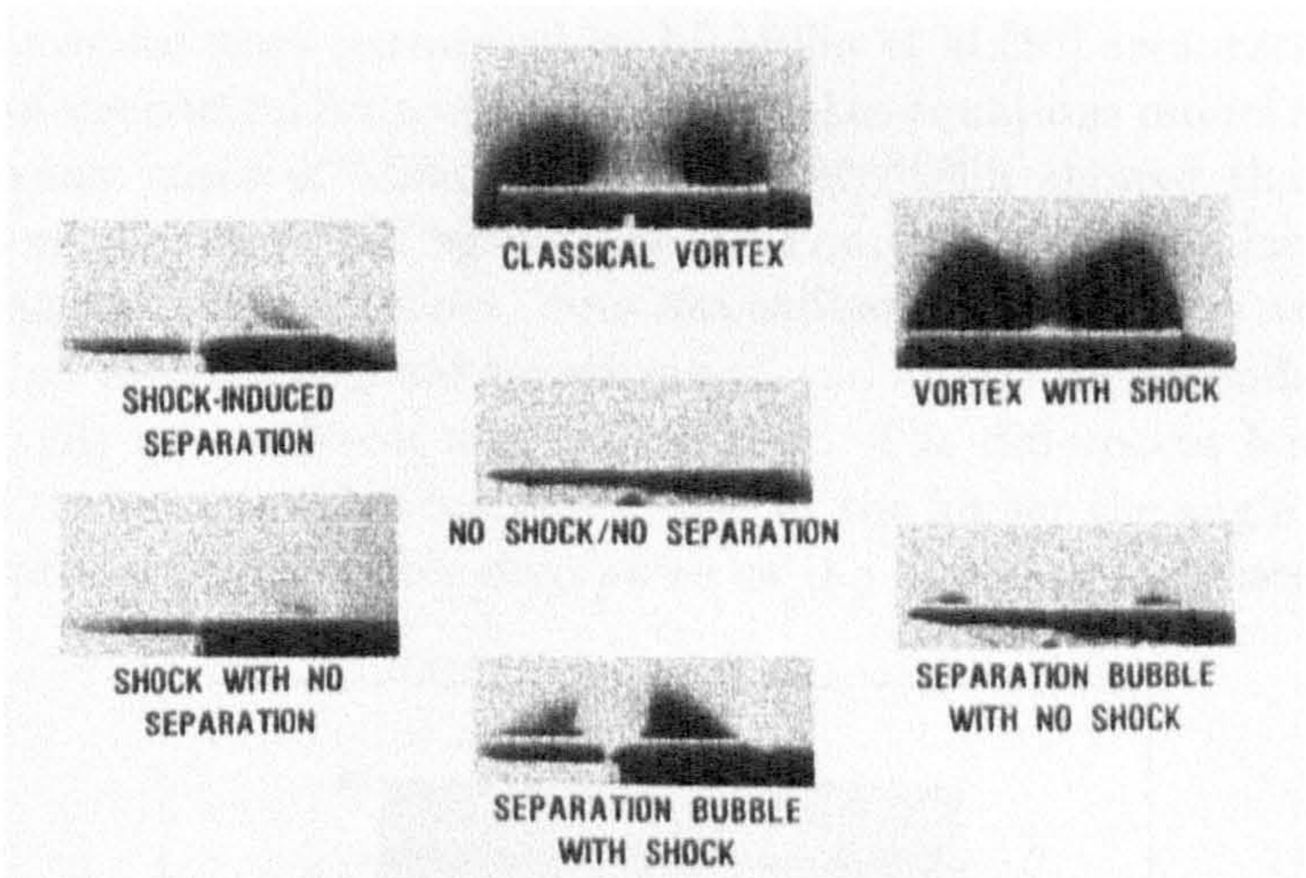

a) Vapour Screen Flow Visualisation

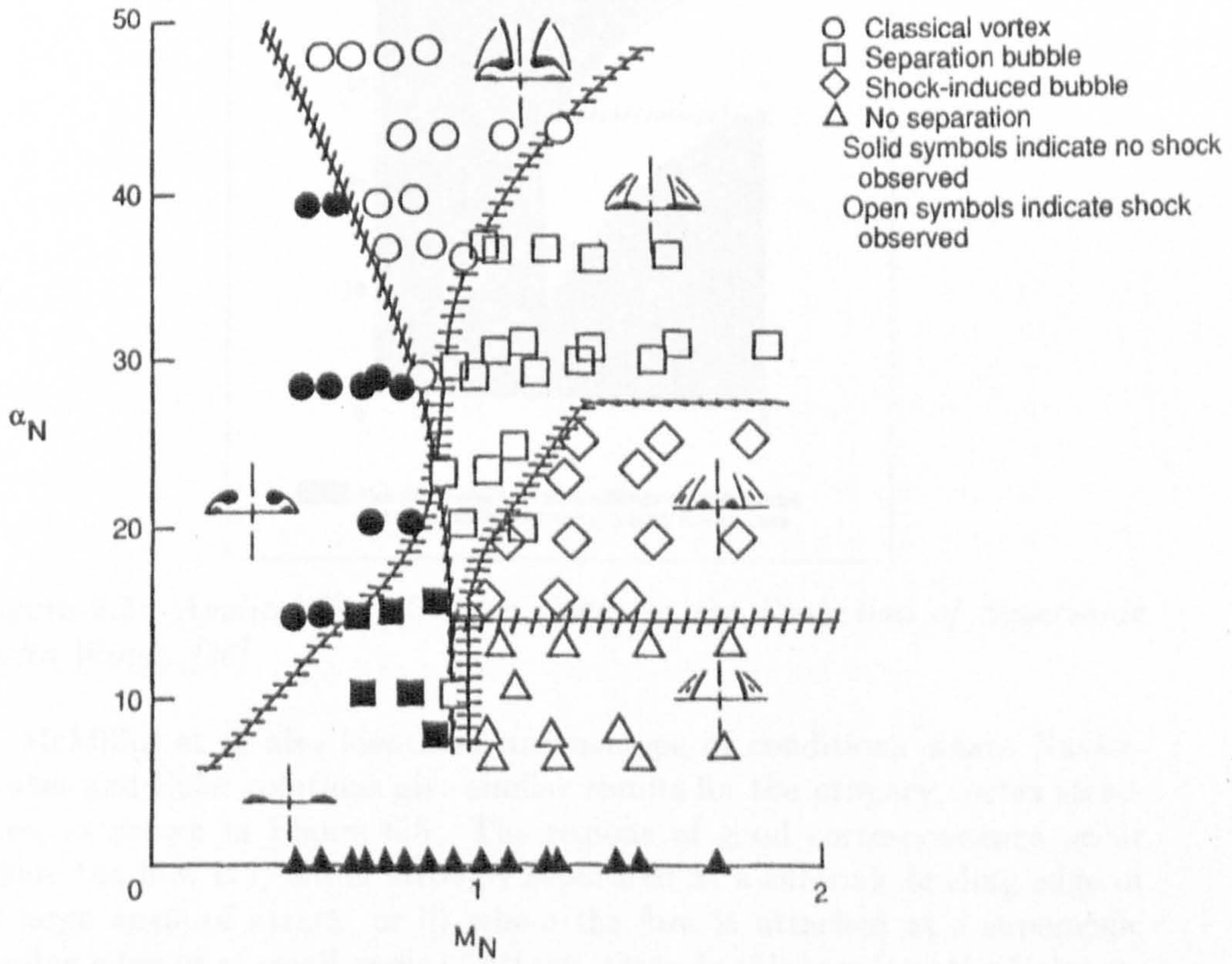

b) $\alpha_N - M_N$ Plot

Figure 6.4: *Classification of Leeside Flow on Swept Sharp Leading Edge Delta Wings. [38] [36]*

The numerical work performed by McMillin et al [36] demonstrated that solutions of the conical form of the Navier-Stokes equations model accurately the supersonic cases of Miller and Wood. McMillin showed that because of the nature of sharp leading edge separation, the boundary layer model, whether laminar and turbulent, does not influence the primary vortex flow field solution over the angle of attack range, and affects the secondary vortex flow field only at the lower angle of attacks. The differences between the Euler and the viscous solutions diminished at the higher the angle of attack, since the primary vortex flow dominates as the crossflow increases.

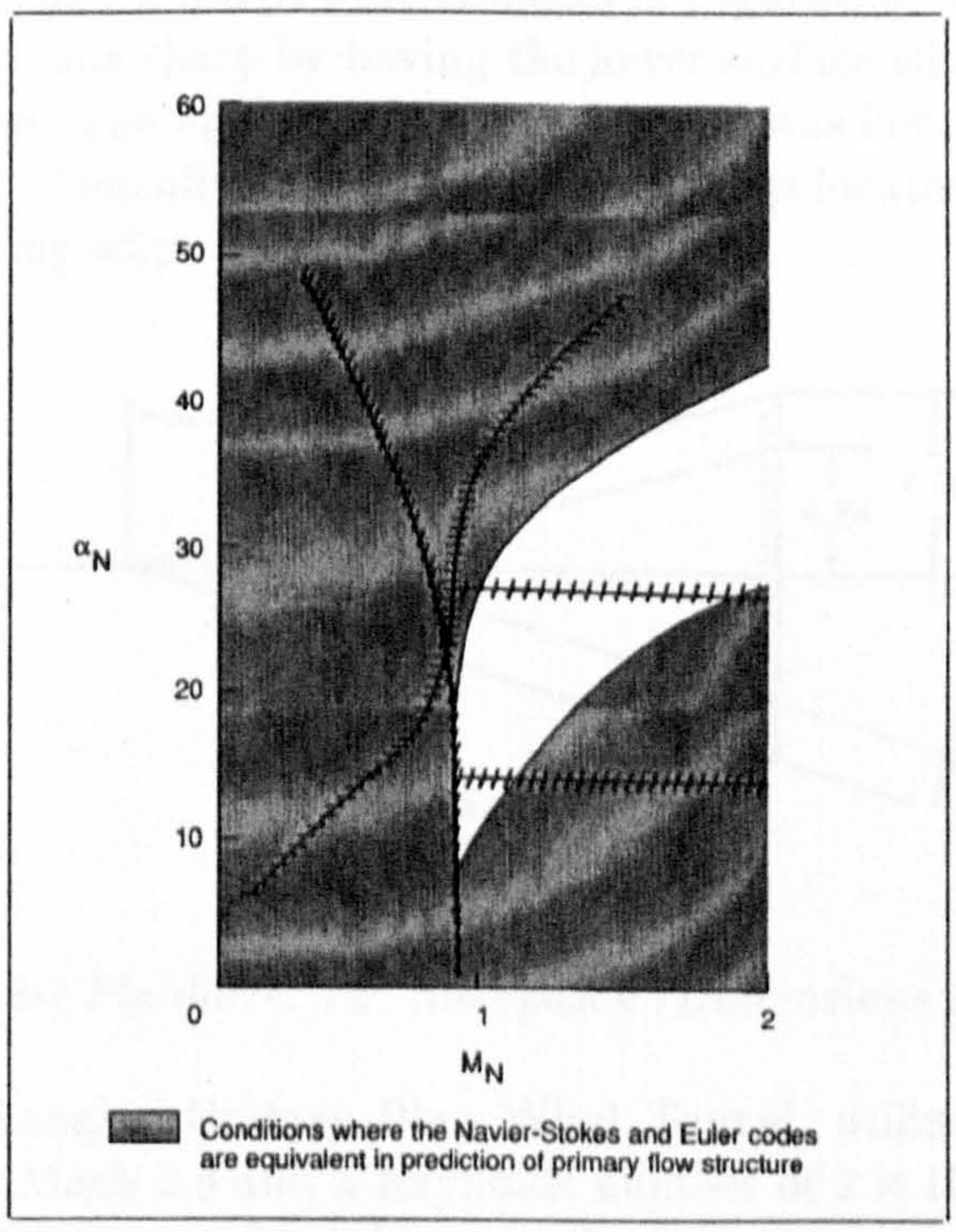

Figure 6.5: *Applicability of Euler Codes to the Prediction of Supersonic Delta Wings. [36]*

McMillin et al also identified an envelope of conditions where Navier-Stokes and Euler solutions give similar results for the primary vortex structure, as shown in Figure 6.5. The regions of good correspondence occur where the flow is i) either strongly separated at a subsonic leading edge or at large angle of attack, or ii) where the flow is attached at a supersonic leading edge or at small angle of attack. Outside this envelope the Euler solutions were incapable of correctly resolving the primary flow features or the shock induced separations, and there were marked differences in the laminar and turbulent viscous solutions.

6.2 Wing Alone: The NASA 75° Swept Delta Wing

The CRANS3D solver was employed to compute the Miller and Wood, 75° Sweepback, Mach 2.8, experimental test case for angle of attacks of 8° and 16°. This provides a fundamental study of the physics of a wing alone geometry similar to, and under similar flow conditions as the B1AW20A3 geometry fin to be studied in the next chapter.

6.2.1 The Experimental Test Case

The planform of the 75° swept wing is shown in Figure 6.6. The leading edge of the wing was made sharp by having the lower surface with a 10° angle to the upper surface. The upper surface was flat and was instrumented with a spanwise row of 19 equally spaced pressure tappings located 1 inch forward of the wing trailing edge.

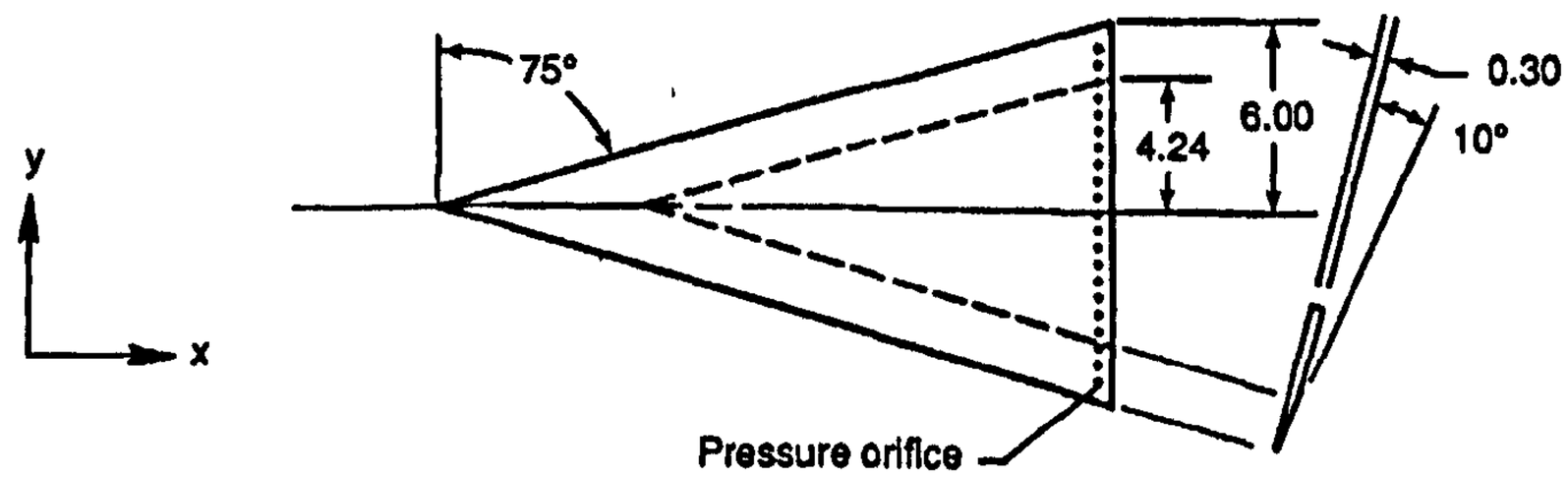

Figure 6.6: *Model Planform, 75° Sweepback (Dimensions in Inches) [38].*

The NASA Langley Unitary Plan Wind Tunnel, utilized in the study, was operated at Mach 2.8 and a Reynolds number of 2×10^6 per foot. The operating total pressure and total temperature was measured at 1875 lb/ft^2 and 125°F respectively. Turbulent conditions were tripped using a strip of No. 60 carborundum grit 0.2 inches behind the leading edge.

The vapour screen technique was employed to visualize the compressible and vortical flow features. This technique is described in more detail in Chapter 7. Figure 6.7 presents the set-up in the working section. For the 8° and 16° test cases investigated, the geometric measurements are given in Figure 6.7. From this figure it is important to note that the view through the flowfield presented by the vapour screen is not strictly the crossflow since the light sheet is not normal to the wing surface and is also viewed from an oblique angle. The result is that vortex features will be "flattened" slightly and appear more elongated.

α (deg)	e (deg)	b (in)	a (in)	$c(\alpha)$ (in)
8	14.27	8.55	32.78	27.25
16	14.27	8.55	32.78	28.50

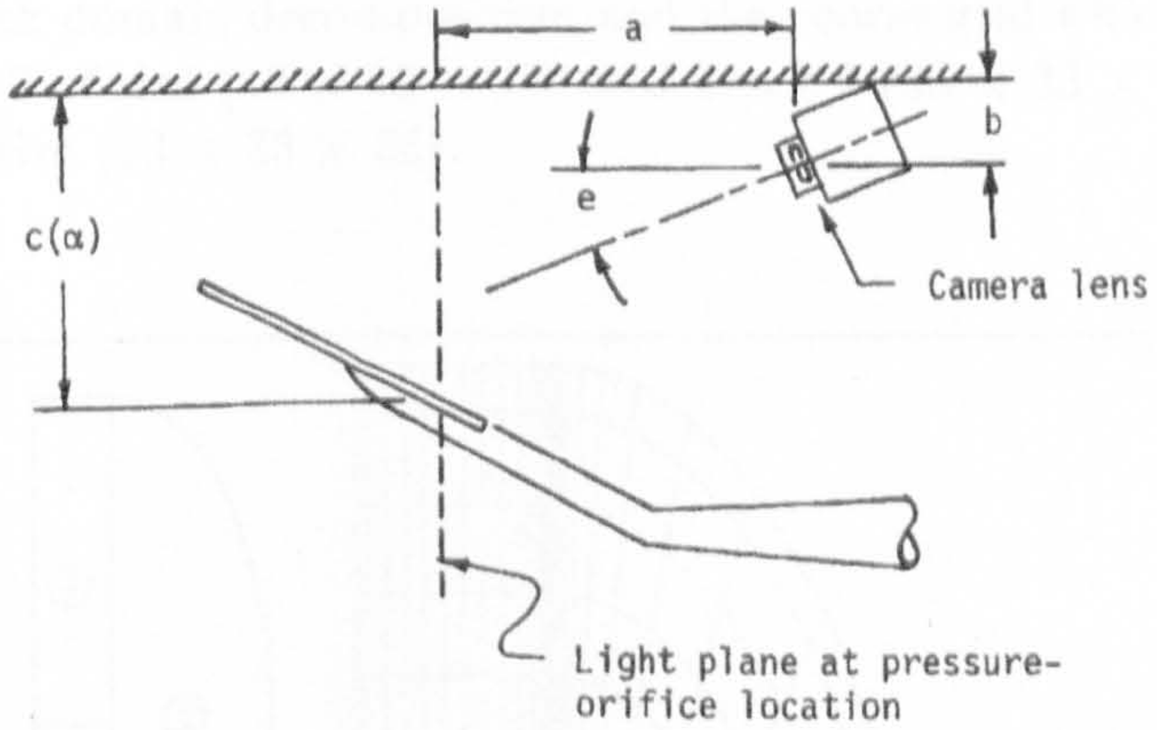

Figure 6.7: *Vapour Screen Photographic Apparatus [38].*

6.2.2 The Computational Model

Various grids were used for each angle of attack case. Initially a single block grid ($90 \times 86 \times 94$) was generated, where the mesh in the K-direction was wrapped around the sharp wing. Figure 6.8 shows the grid used for the 16^o angle of attack case together with the grid in the close vicinity of the wing tip.

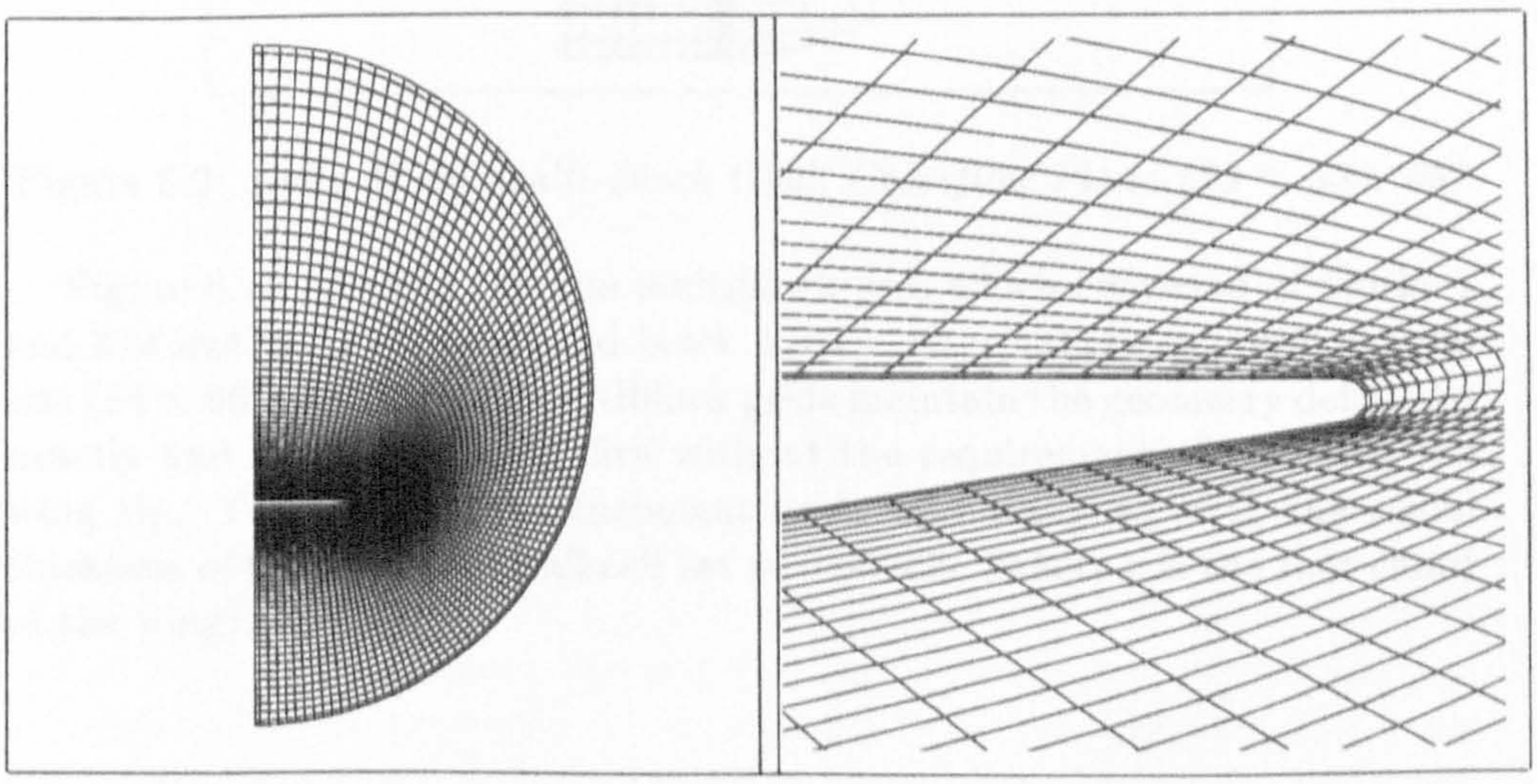

Figure 6.8: *Delta Wing Single Block Grid, Crossflow Plane ($90 \times 86 \times 94$)*

Clearly the quality of the grid in the wing tip region is poor, even with the rounding of the tip as illustrated. Considerable time was spent trying to improve the grid quality in this region, but without seriously compromising the geometry definition, the radial J-lines could not be made normal to the wall. It was therefore decided to decompose the domain into three blocks. Figure 6.9 presents the multiblock grid in the crossflow plane and shows the three block domain decomposition and the coarse grid which comprised blocks 1 and 3 of size $(33 \times 33 \times 17)$ and block 2 $(33 \times 33 \times 32)$ giving a grid of total size $(33 \times 33 \times 66)$.

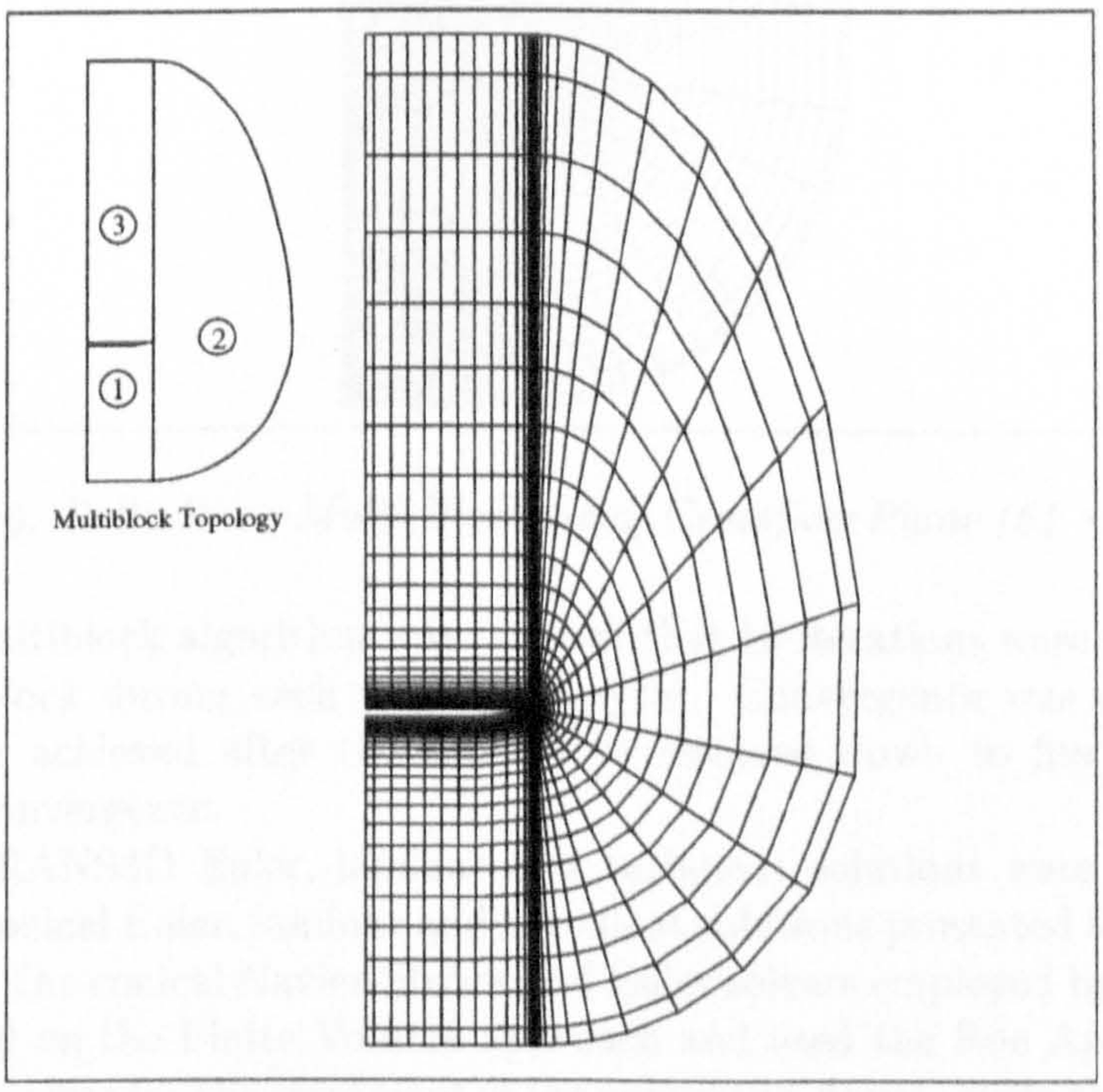

Figure 6.9: *Delta Wing Multi-Block Grid, Crossflow Plane (33 × 33× 66)*

Figure 6.10 presents the fine multiblock grid which consisted of blocks 1 and 3 of size $(64 \times 86 \times 48)$ and block 2 $(64 \times 86 \times 52)$ giving a grid of total size $(64 \times 86 \times 148)$. Both multiblock grids maintain the geometry definition exactly and allow wall normality without the requirement of rounding the wing tip. The laminar and turbulent grids were designed with the radial thickness of the first near wall cell set to $0.00003c$ (where c is the root chord of the wing).

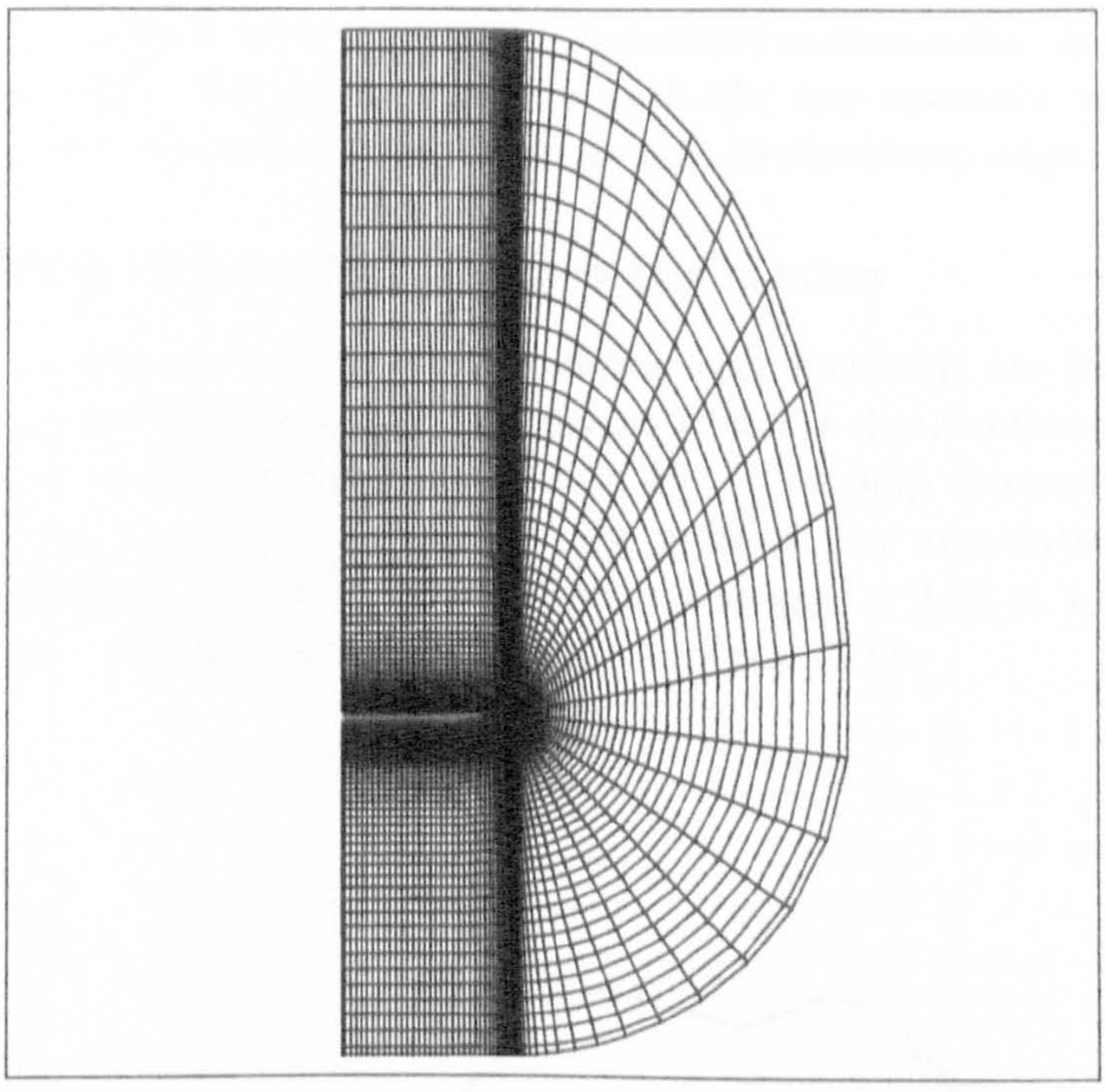

Figure 6.10: *Delta Wing Multi-Block Grid, Crossflow Plane (64 × 86× 148)*

The multiblock algorithm was set such that 10 iterations were performed on each block during each multiblock cycle. Convergence was deemed to have been achieved after the solution is resolved down to five orders of residual convergence.

The CRANS3D Euler, laminar and turbulent solutions were compared with the conical Euler, laminar and turbulent solutions presented by McMillin et al [36]. The conical Navier-Stokes and Euler solvers employed by McMillin were based on the Finite Volume approach and used the Roe Approximate Riemman solver for the treatment of the convective fluxes, while the diffusive fluxes were centrally differenced. Third order spatial accuracy was achieved by interpolation of the primitive variables. Turbulence was modelled by the Baldwin-Lomax turbulence model with the Degani-Schiff modification for crossflow separation capturing.

Both CRANS3D and McMillin's Euler solver enforce the Kutta condition for inviscid flow at the sharp edge, by the manner in which the boundary conditions are implemented. The grids employed in the NASA study consisted of 75 radial and 151 circumferential (75 × 151) points for the viscous calculations and (128 × 128) points for the inviscid calculations. For the laminar computations the near wall cell was set with a radial thickness of $0.00005c$ while for turbulent flow this size was set as $0.00003c$. These single block grids were wrapped around the sharp edge geometry in an O-grid topology, which required the sharp edge to be rounded with a radius of

0.00002c and elliptic grid smoothing to achieve a reasonable mesh around the leading edge. The grids, however, still did not maintain wall normal radial lines or a smooth cell distribution around the sharp edge.

6.2.3 Wing Alone: Results and Discussion

Figure 6.11 confirms that supersonic delta wing flowfields are indeed near-conical in nature by presenting the surface pressure distributions at several axial stations along the wing inclined at 16°. The only discernible change along the wing is that the location of the pressure rise associated with secondary separation, which is seen to begin at $y/y_{LE} \approx 0.86$ at $x/y_{LE} = 12$, moves further inboard, to $y/y_{LE} \approx 0.83$ at $x/y_{LE} = 22$.

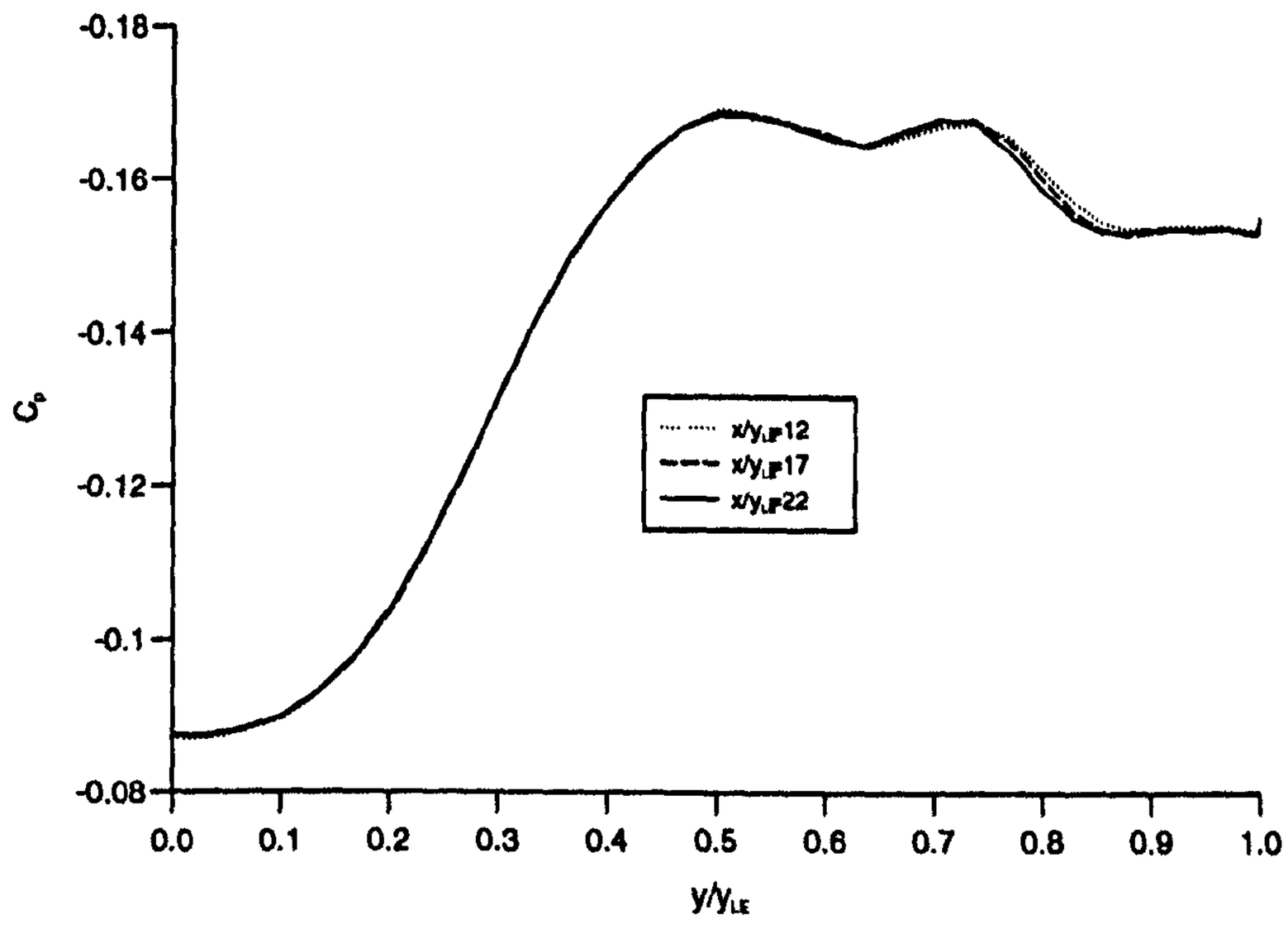

Figure 6.11: *Demonstration of Conical Flow Past Supersonic Delta Wings, 16° angle of attack*

Mach 2.8, 8° Angle of Attack

The effect of grid topology is outlined in Figure 6.12 which compares laminar crossflow solutions obtained on the single block grid and the 3 block grid. Both solutions appear to predict the primary vortex and its structure very well when comparing with the vapour screen photograph. Comparison with the NASA conical solution, however, shows that the total pressure outside

the primary vortex is resolved too low in the single block solutions, appearing as the large pink region in Figure 6.12c). The weak primary crossflow shock which is resolved above the primary vortex in both solutions appears much stronger in the single block case.

The secondary vortex is clearly resolved in the multiblock solution at the correct spanwise location and with a size and structure which matches that observed experimentally. The single block solution, however, captures a much smaller secondary vortex which appears too close to the leading edge.

Since both grids have similar cell resolution in the crossflow plane, one would expect the solutions, converged down to the same value of residual, to be practically the same. The results, however, demonstrate a clear topology dependence between the single and multiblock grids. Similar evidence was found by comparison of the single and multiblock solutions for the 16° angle of attack case, while the single block Euler computations consistently failed with over-expansion around the leading edge resulting in negative pressures and densities. Apart from the fact that it is impossible to maintain the definition of the sharp leading edge with a single block grid, it can be concluded that the highly skewed cells, which cannot be avoided in this region, introduce localized errors which adversely affect the accurate resolution of primary separation and its associated expansion. In addition, the inability of a single block grid to maintain wall normal radial grid lines, especially close to the leading edge, may account for the poor prediction of secondary separation and resulting secondary vortex. The rest of this chapter will, therefore, focus on the comparison and interpretation of the multiblock 3D solutions with experiment and the conical results of McMillin *et al.*

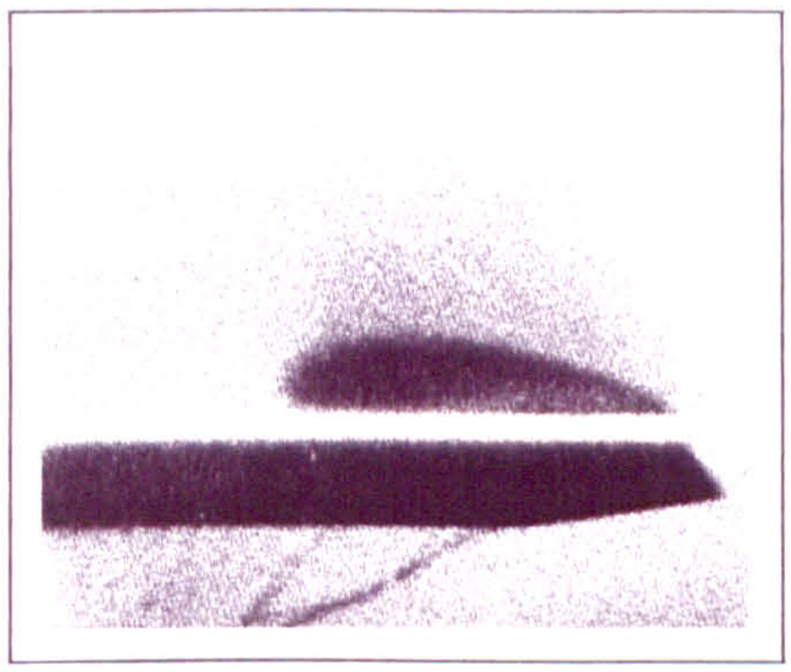

(a) *Delta Wing: Vapour Screen, M=2.8, 8° angle of attack [38].*

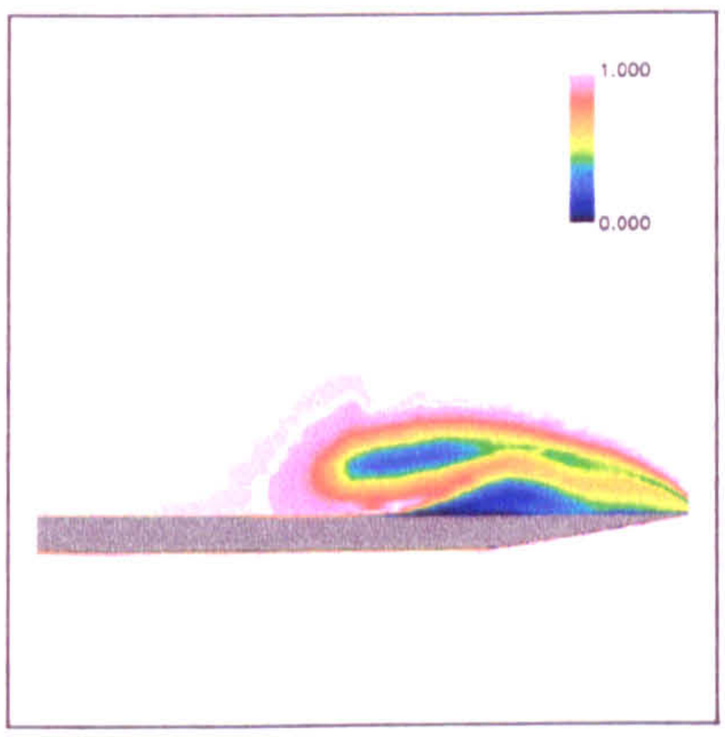

(b) Laminar, Multiblock Grid

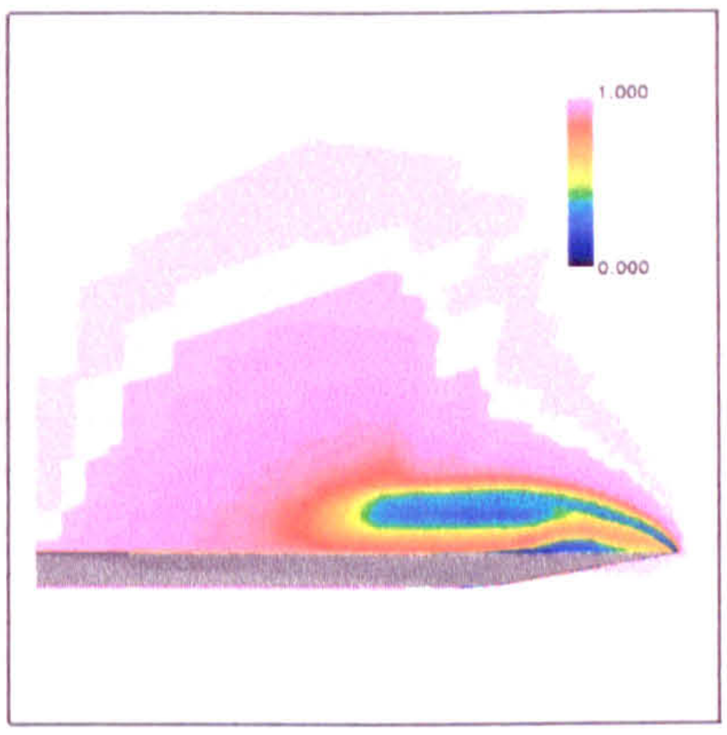

(c) Laminar, Single Block Grid

$P_0/P_{0\infty}$ Contours

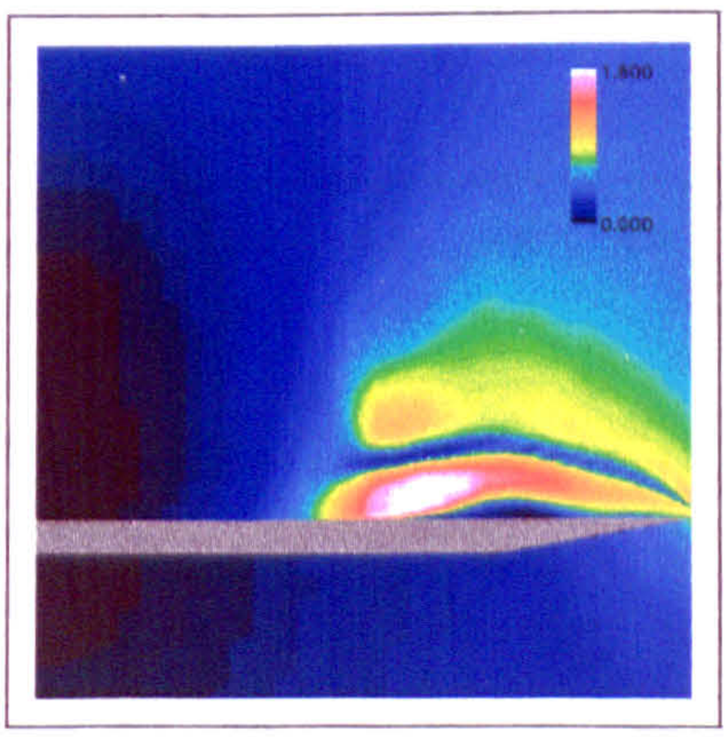

(d) Laminar, Multiblock Grid

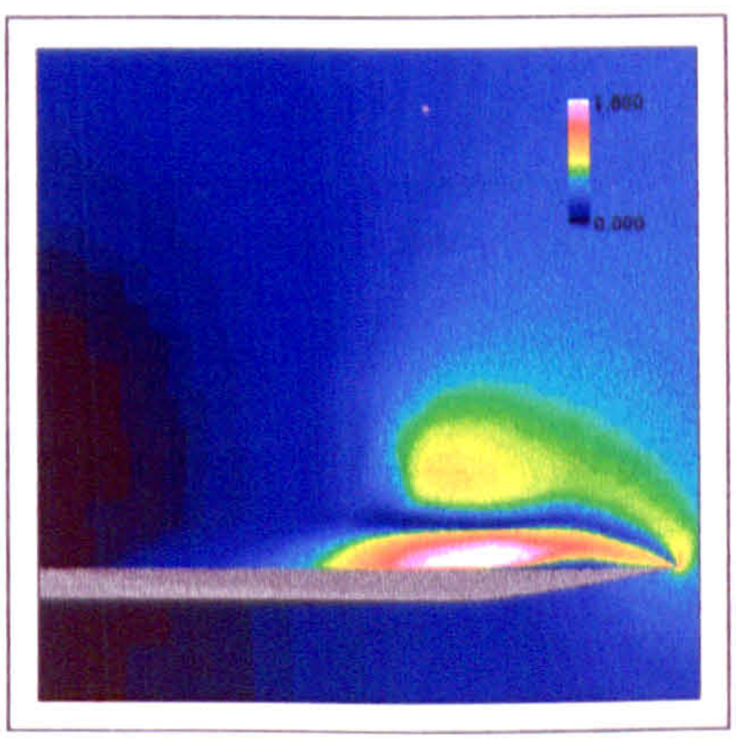

(e) Laminar, Single Block Grid

M_c Contours

Figure 6.12: *Comparison of Grid Topologies,* $\alpha = 8^o$

The spanwise surface pressure pressure distribution is presented in Figure 6.13 which compares the experimental measurements with the laminar, turbulent and inviscid CRANS3D solutions. The computed curves are almost identical with the conical results presented by McMillin. The laminar and turbulent solutions are equivalent from the centreline until primary reattachment at a spanwise position around $y/y_{LE} \approx 0.5$. The difference between the two solutions at y/y_{LE} from $0.55 - 0.85$ are due to the differences in the prescription of the boundary layer and the resulting secondary separation and vortex. After secondary reattachment the solutions are, again, equivalent.

The Euler solution fails to correctly resolve the position of primary reattachment and overpredicts the level of primary vortex suction. In addition the Euler solution indicates a slight over-expansion at the leading edge which is consistent with the inviscid nature of the Euler equations.

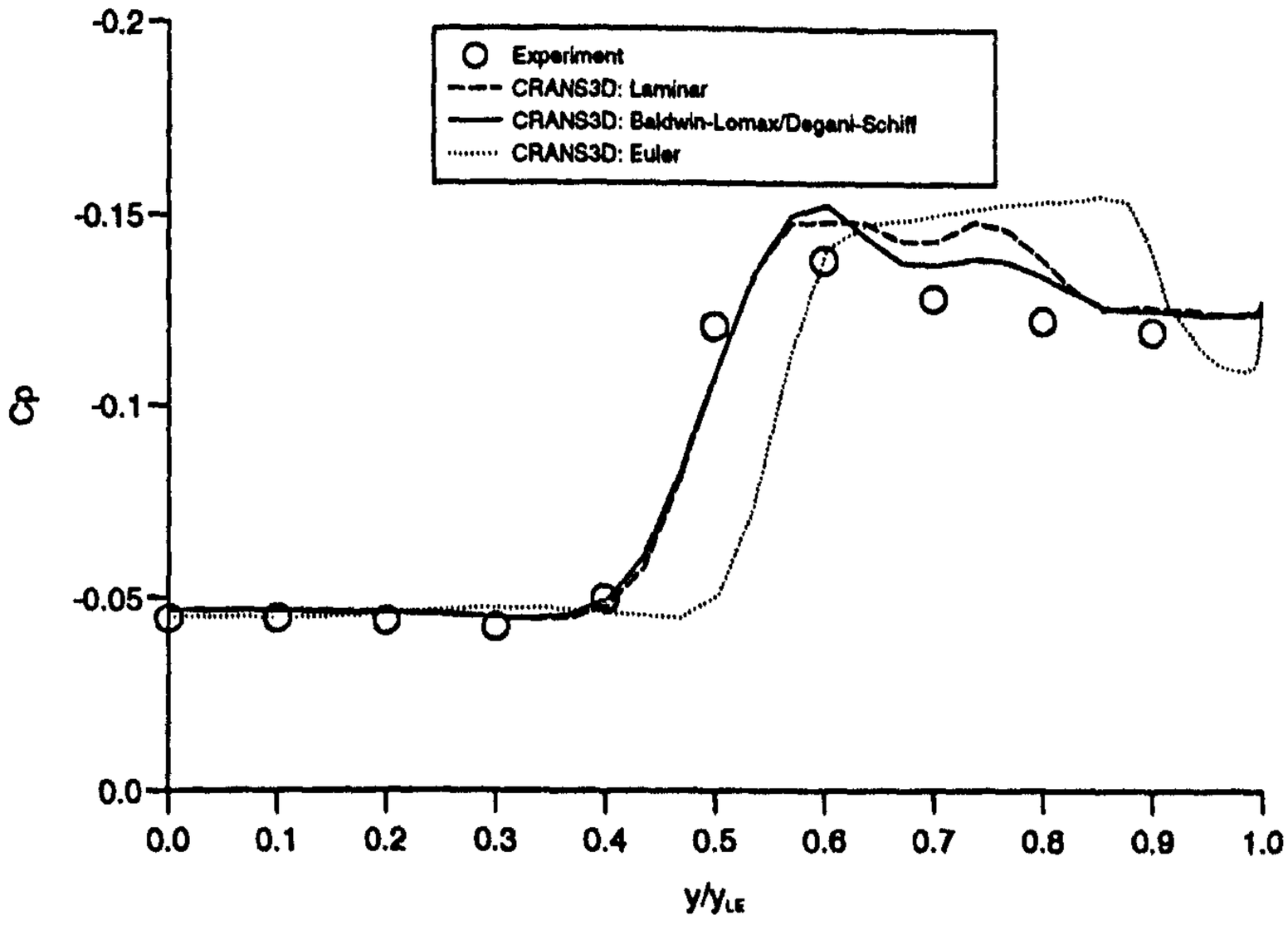

Figure 6.13: *Delta Wing: C_p Distribution Comparison, M=2.8, 8° angle of attack.*

Figures 6.14 - 6.16 present the CRANS3D solutions which are contrasted with the experimental vapour screen picture and the conical solutions of McMillin *et al.* The comparison of the viscous crossflow plots of total pressure ratio is given in Figure 6.14, while the corresponding inviscid solutions are compared in Figure 6.15.

Figure 6.14 reveals that a good comparison exists between the 3D-NS and conical NS solutions. The laminar and turbulent primary vortex structures resolved by both solvers appear to be very similar. This similarity demonstrates that the wall boundary layer model (laminar or turbulent) does not significantly influence the primary vortex flowfield. The primary crossflow shock appears sufficiently weak that it is only just evident in the total pressure ratio data.

The difference between laminar and turbulent results appears in the prediction of the secondary features. The boundary layer model affects the extent of secondary separation beneath the primary vortex. The turbulent secondary vortex appears slightly larger and stronger than its laminar counterpart. Closer inspection of the laminar solutions reveal the existence of a double-secondary vortex system. The extra secondary vortex, which appears beneath the primary feeding sheet close to the sharp leading edge, is much more pronounced in the conical solution but a very small feature does appear in the 3D result as well. This complex secondary flow pattern is not seen with the turbulent boundary layers since the turbulent flow beneath the primary vortex is more resistant to separation. Another difference between the laminar and turbulent solutions appears with the prediction of the reattached boundary layer after primary crossflow reattachment. The turbulent boundary layer predicted by both the 3D and conical codes appears to become much thicker than that seen in the corresponding laminar solutions. This will be important if one is interested in accurately predicting skin friction and heat transfer rates. Unfortunately the experimental vapour screen results do not indicate whether the boundary layer is laminar or turbulent in this region, although the operating Reynolds number of 2 million/ft would suggest a turbulent case.

Figure 6.15 presents the Euler solutions of the crossflow total pressure ratio. The 3D and conical inviscid solutions appear very similar with each other, but markedly different to the viscous solutions. The primary vortices appear as long thin features close to the upper surface, much different to the "droplet" shaped vortices evident in experiment and predicted by the viscous calculations. While the sharp leading edge provides the mechanism for primary flow separation, the absence of boundary layers results in the absence of any secondary vortical flow.

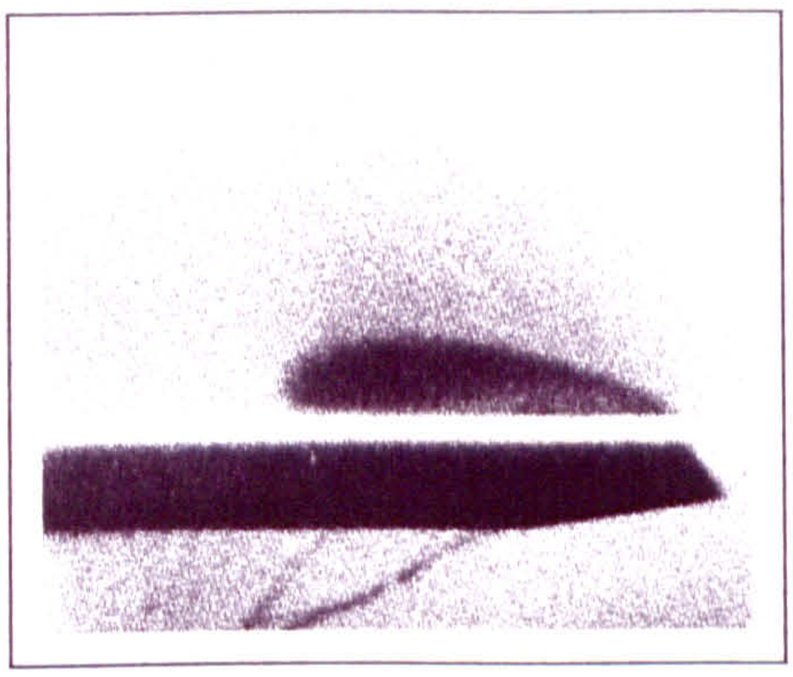

(a) *Delta Wing: Vapour Screen, M=2.8, 8° angle of attack [38].*

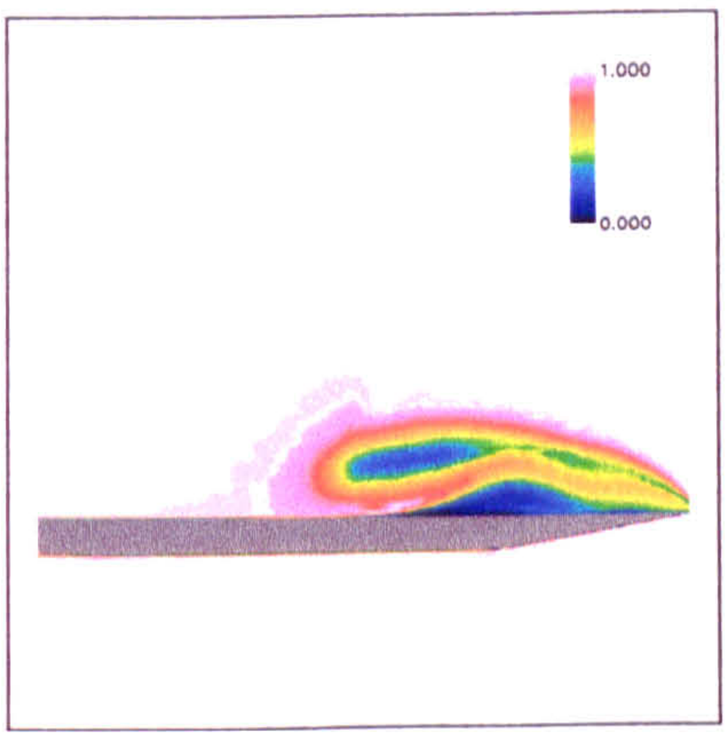

(b) Laminar, 3D-NS

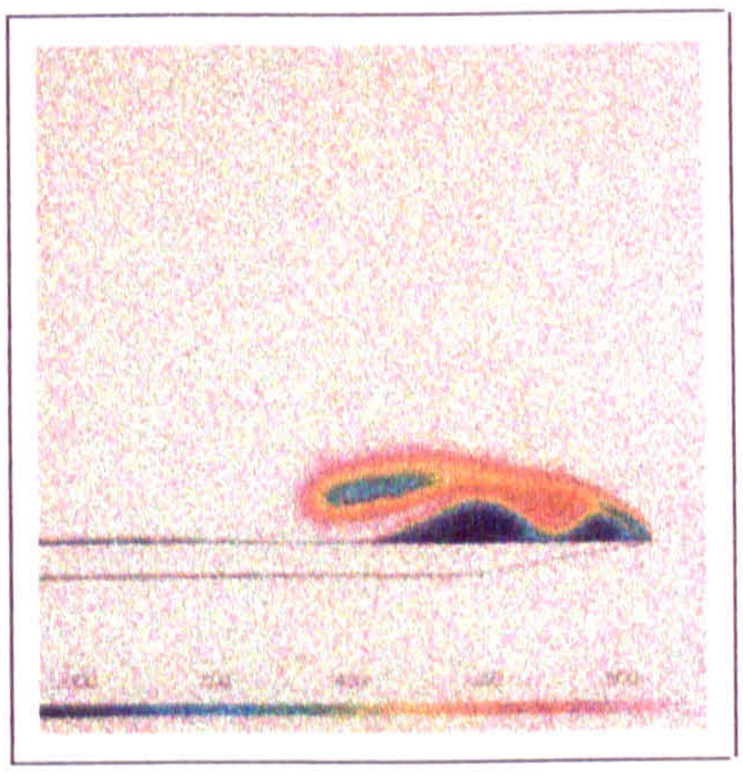

(c) Laminar, Conical NS

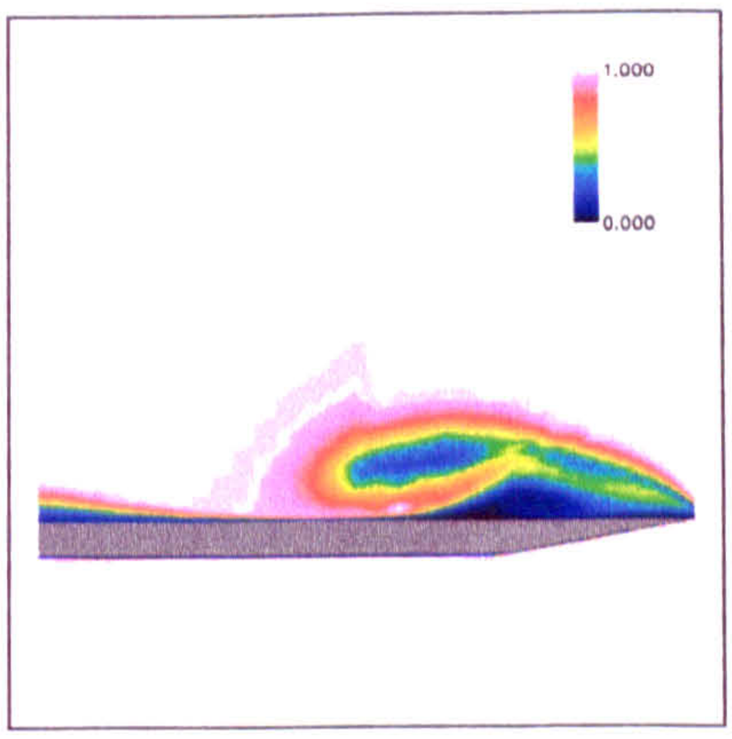

(d) Turbulent, 3D-NS

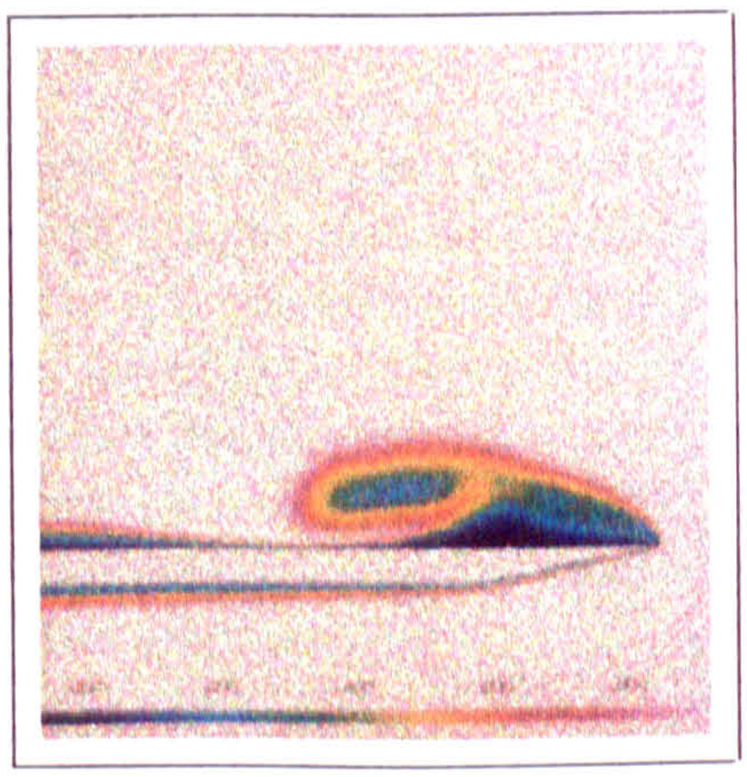

(e) Turbulent, Conical NS

Figure 6.14: *$P_0/P_{0\infty}$ Contours, $\alpha = 8^o$, 3D vs Conical NS*

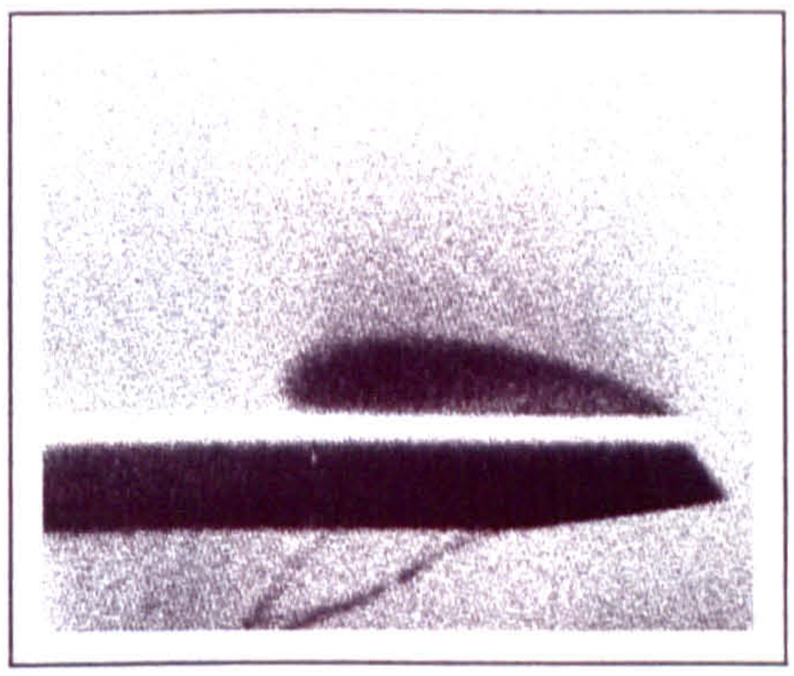

(a) *Delta Wing: Vapour Screen, M=2.8, 8° angle of attack [38].*

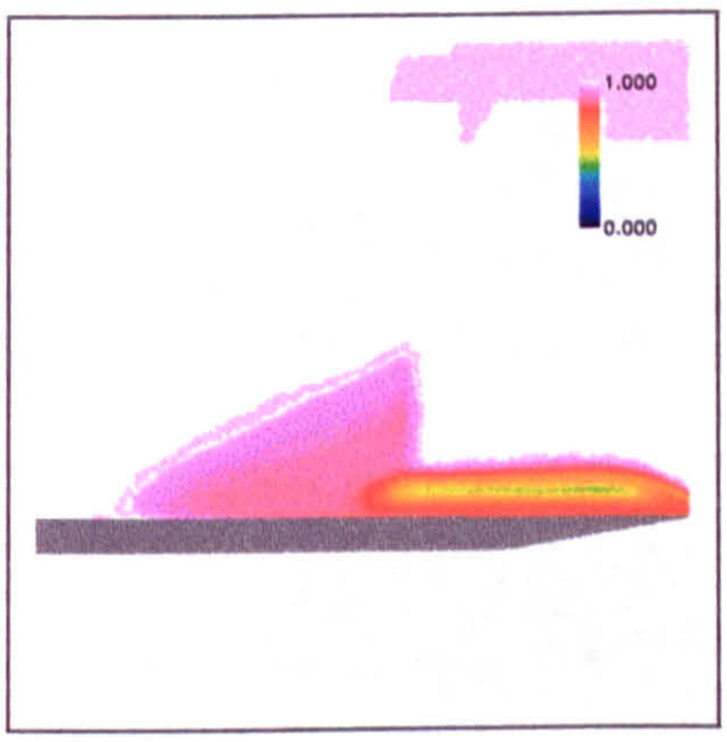

(b) 3D Euler

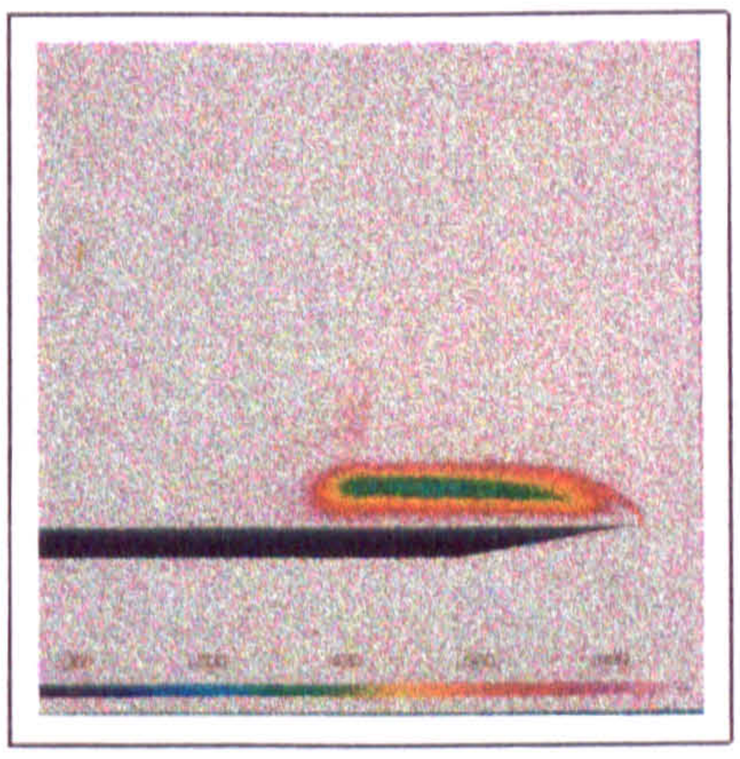

(c) Conical Euler

Figure 6.15: $P_0/P_{0\infty}$ *Contours,* $\alpha = 8°$*, 3D vs Conical Euler*

The comparison of the crossflow Mach number contour plots is presented in Figure 6.16. The correspondence between the viscous 3D and conical solutions is seen to be very good, the differences in colour levels most likely attributable to the different plotting software employed rather than differences in solutions. Both laminar and turbulent resolved primary crossflow shocks are seen to be equivalent. The inviscid solutions, however, are clearly different from the viscous solutions, with a larger and stronger primary crossflow shock and no evidence of any secondary vortical features.

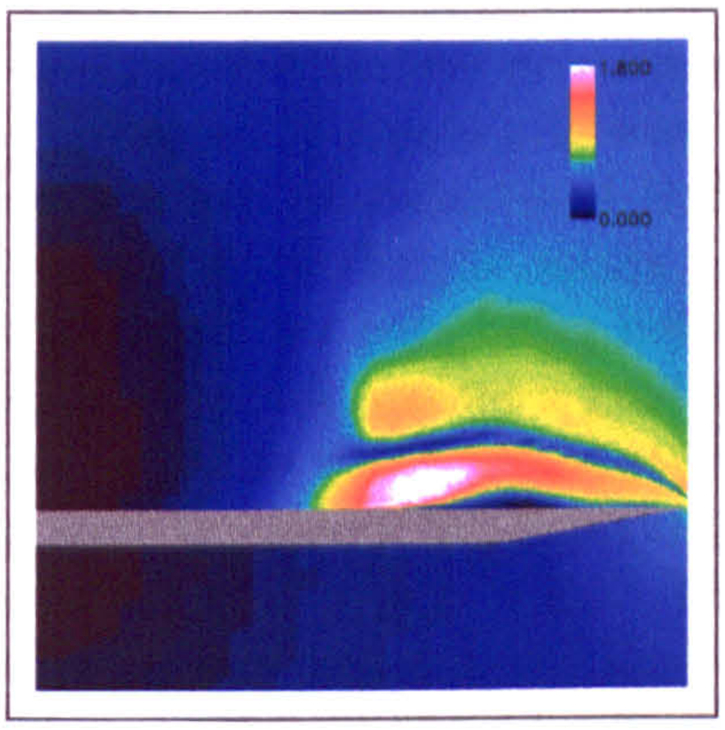

(a) Laminar, 3D-NS

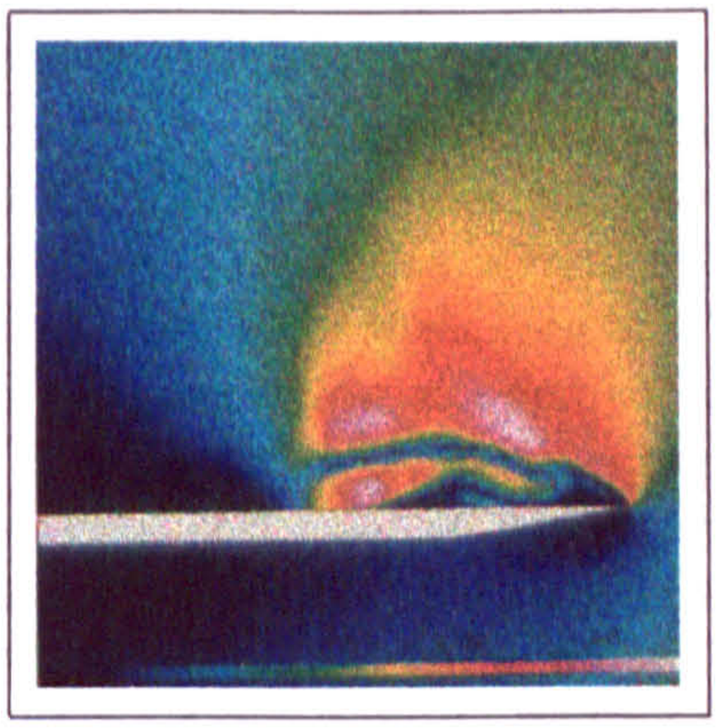

(b) Laminar, Conical NS

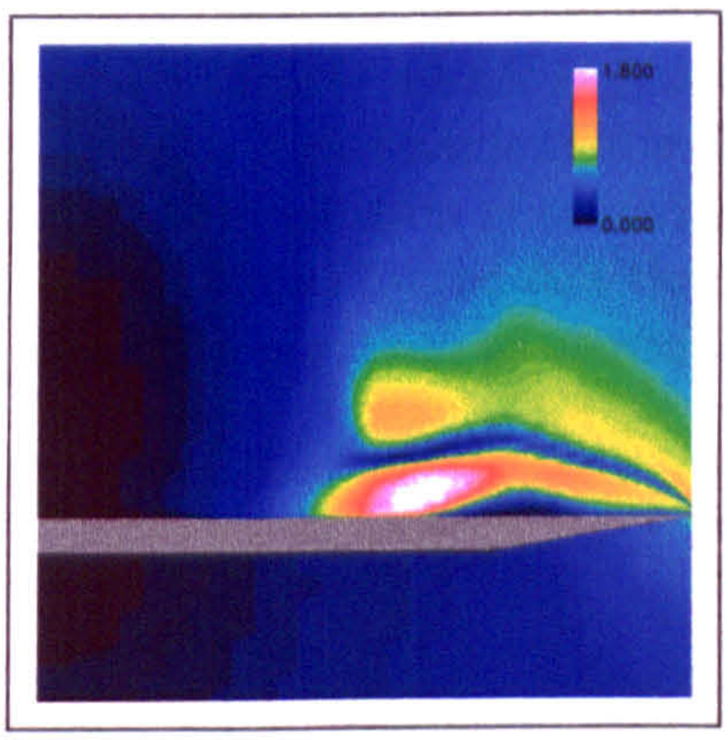

(c) Turbulent, 3D-NS

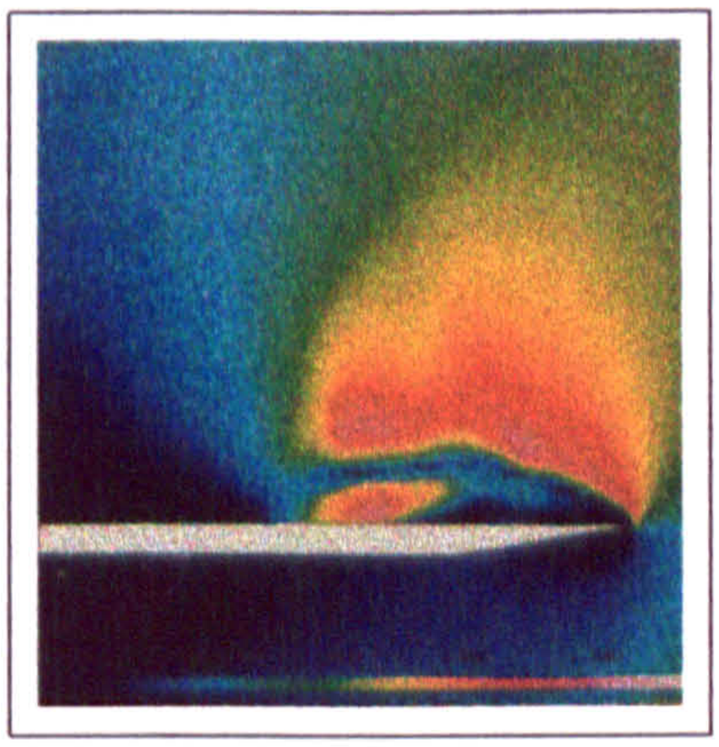

(d) Turbulent, Conical NS

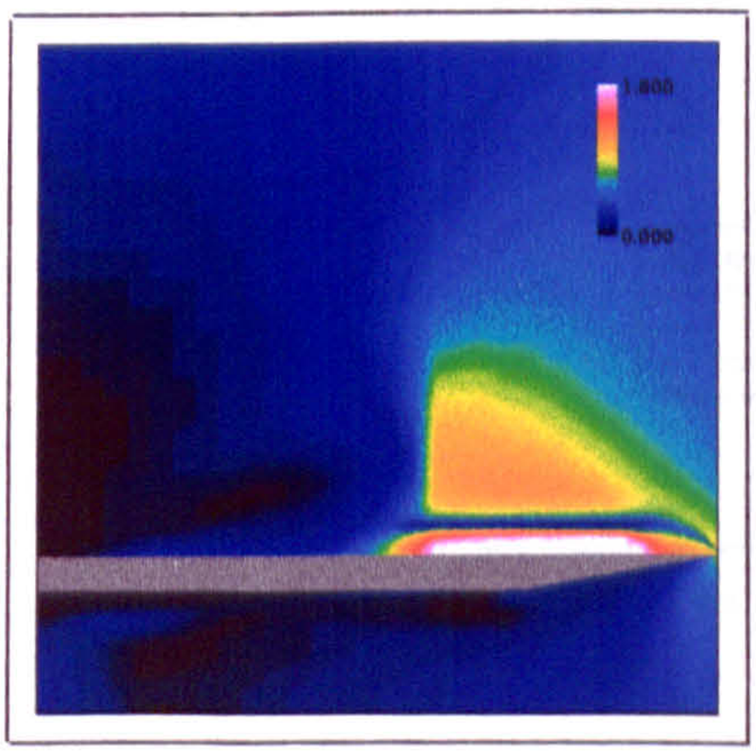

(e) 3D-Euler

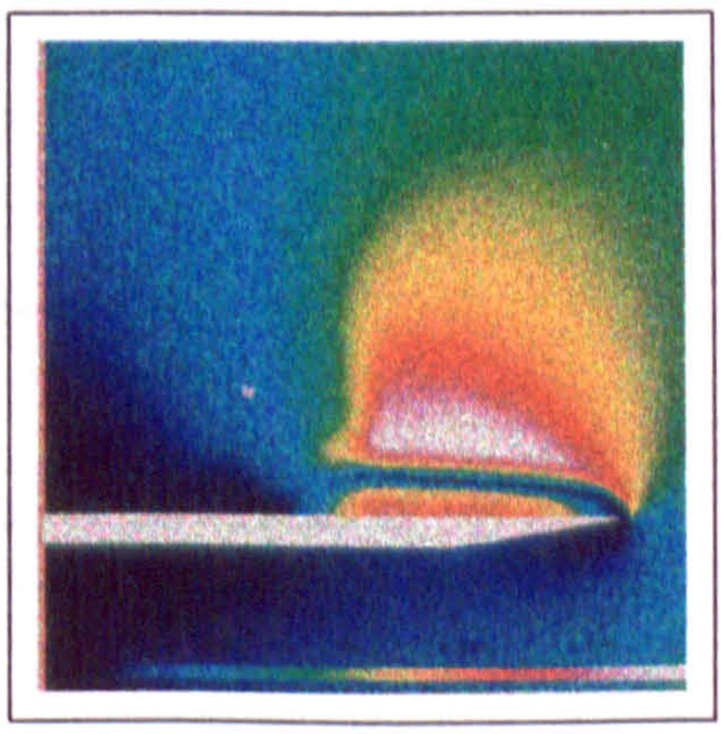

(f) Conical Euler

Figure 6.16: *M_C Contours, $\alpha = 8^o$, 3D vs Conical*

Mach 2.8, 16° Angle of Attack

The spanwise surface pressure distribution for the 16° angle of attack case is presented in Figure 6.17 which compares experimental measurement with the laminar, turbulent and inviscid CRANS3D calculations. For this case primary reattachment occurs along the centreline of the delta wing. The primary vortex core being much further above the surface than seen at 8° angle of attack, causes a gradual increase in surface suction as opposed to the rapid rise which occurs at 8° inclination. The predicted primary suction is seen to exceed the experimental measurements just prior to secondary separation at $y/y_{LE} \approx 0.5$. This may be indicative of the late prediction of secondary separation. Beyond secondary separation, all three numerical predictions begin to differ. The best prediction, when compared with the measurements, is the turbulent solution where the overshoot of suction quickly drops back close to the measured level. The laminar solution overpredicts the secondary suction over the whole extent of the secondary region, only reducing to match experiment after secondary reattachment.

For this higher angle of attack case, although an Euler prediction gives the worst overprediction of secondary suction, the Euler solution is surprisingly good, not least by the fact that it does actually resolve a secondary (shock induced) separation, as shown in Figures 6.20 e) and f).

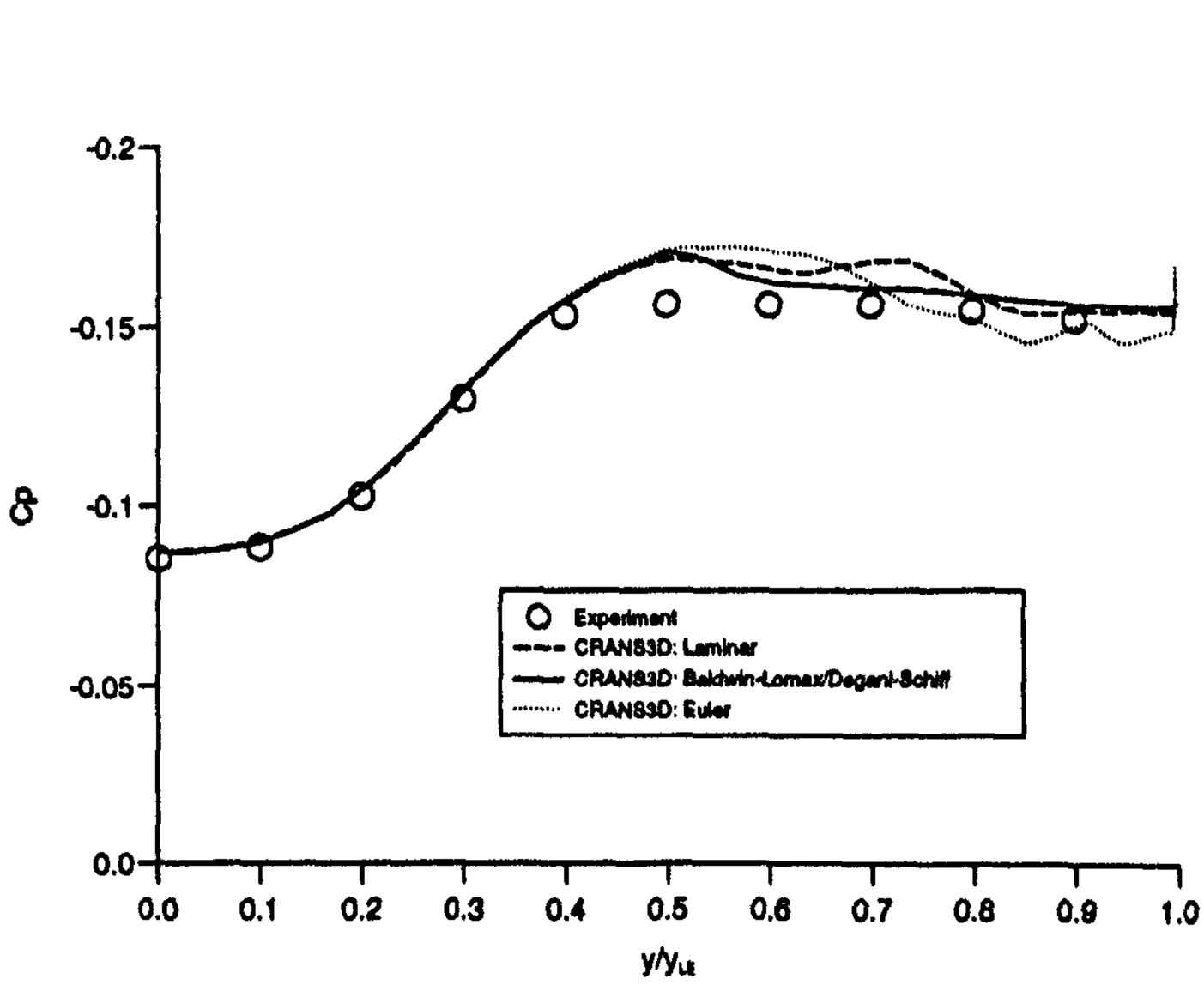

Figure 6.17: *Delta Wing: C_p Distribution Comparison, M=2.8,* 16° *angle of attack.*

The crossflow contours of total pressure ratio for the 16° angle of attack viscous calculations are compared in Figure 6.18. Both the conical and 3D solutions predicted the large "droplet" shaped primary vortex and the large secondary separated region underneath, which are evident in the vapour screen photograph. In addition, the viscous solutions correctly resolved the strong primary crossflow shock sitting above the primary vortex, turning the flow back towards the freestream direction.

The boundary layer model was, again, found only to affect the extent of secondary separation. The laminar solution resolved a double secondary system with a large secondary vortex formed beneath the primary feature, and an extra, very small secondary vortex formed after the reattachment of the first, located beneath the primary feeding sheet. The turbulent secondary separated region, although approximately the same size as the laminar region, results in a slightly stronger vortex with a higher core suction. In addition, no extra secondary vortex was resolved in the turbulent solution, and this agreed with experiment where no double secondary vortex system was evident in either vapour screen or oil flow visualisation.

Figure 6.19 presents the 3D Euler solution and the conical result of McMillin *et al*. Both solutions agree very well in the resolution of the primary vortex and the primary crossflow shock, but a significant difference is observed in the flow structure beneath the primary vortex. The 3D Euler solution, surprisingly, captures a small secondary vortex, much smaller than seen in experiment or in the viscous solutions. Closer examination of the 3D inviscid solution revealed that a weak secondary shock was resolved above the secondary vortex. Although no wall boundary layer existed in the Euler solutions, the development of a crossflow shock induced secondary separation can explain the formation of the secondary vortex. As the inviscid solution developed, a curved secondary shock was resolved, which imparted a rotation into the flow beneath the primary vortex, eventually causing secondary separation and a secondary vortex in the steady converged solution. The conical calculation failed to capture any secondary shock induced separation, perhaps because the secondary crossflow shock was never curved enough for any vorticity to be generated in the crossflow. Another source of vorticity generation in the Euler solution, as described in Chapter 5, is that of "phantom vorticity" due to strong cell stretching. The grids employed by McMillin *et al* for the conical investigations were much finer in the near wall region, with much less cell stretching.

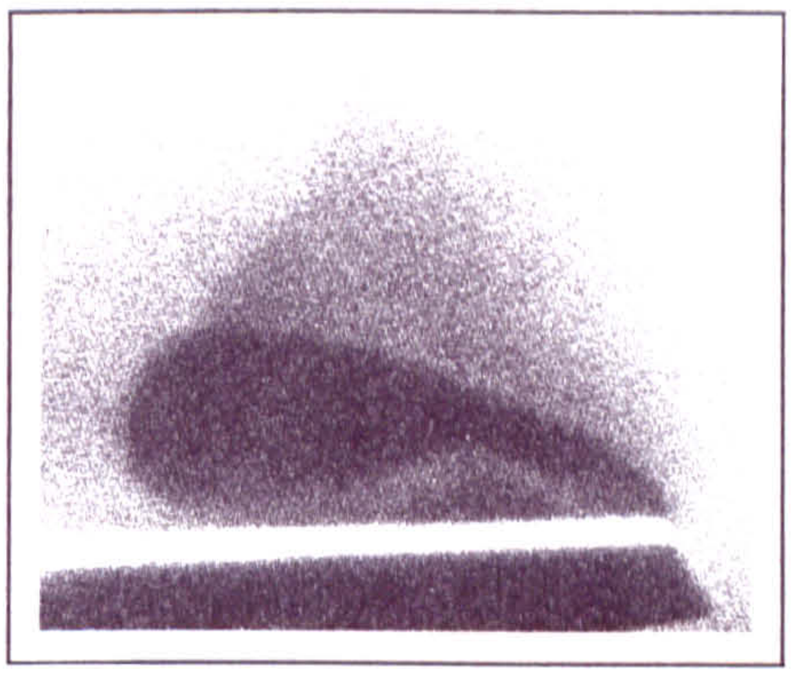

(a) *Delta Wing: Vapour Screen, M=2.8, 16° angle of attack [38].*

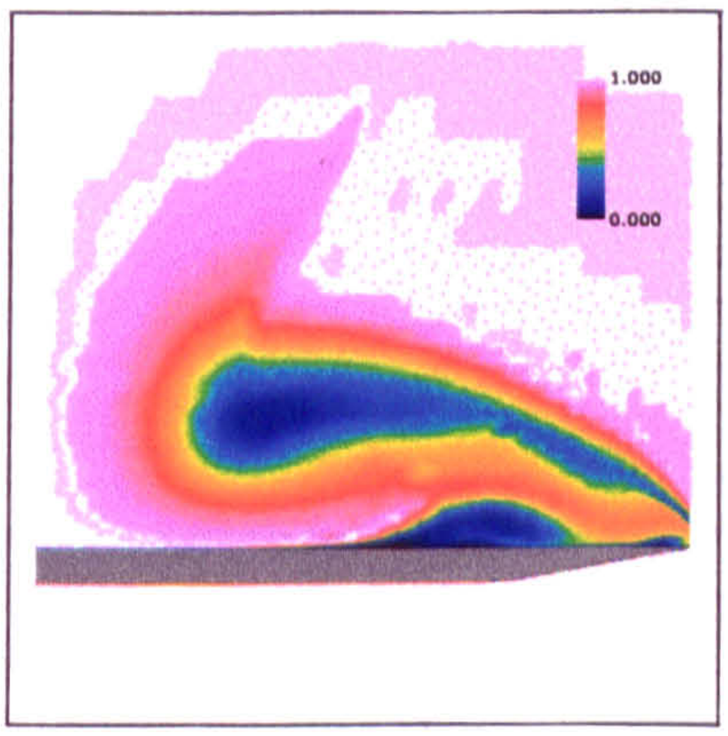

(b) Laminar, 3D-NS

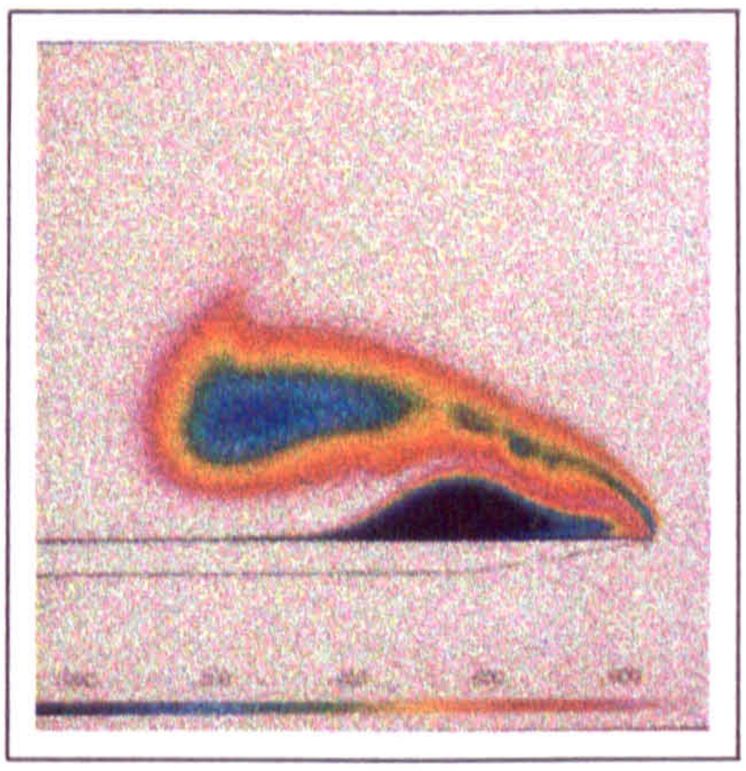

(c) Laminar, Conical NS

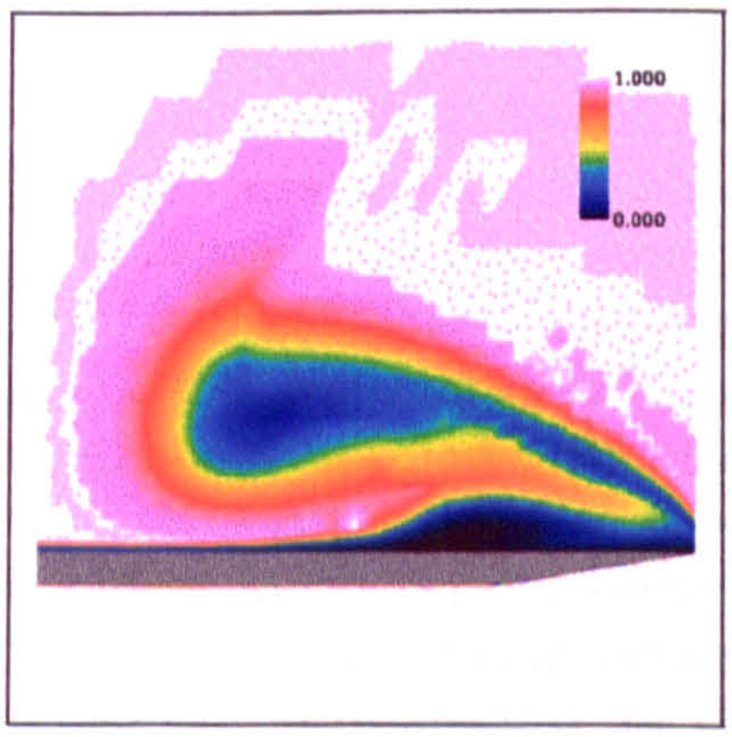

(d) Turbulent, 3D-NS

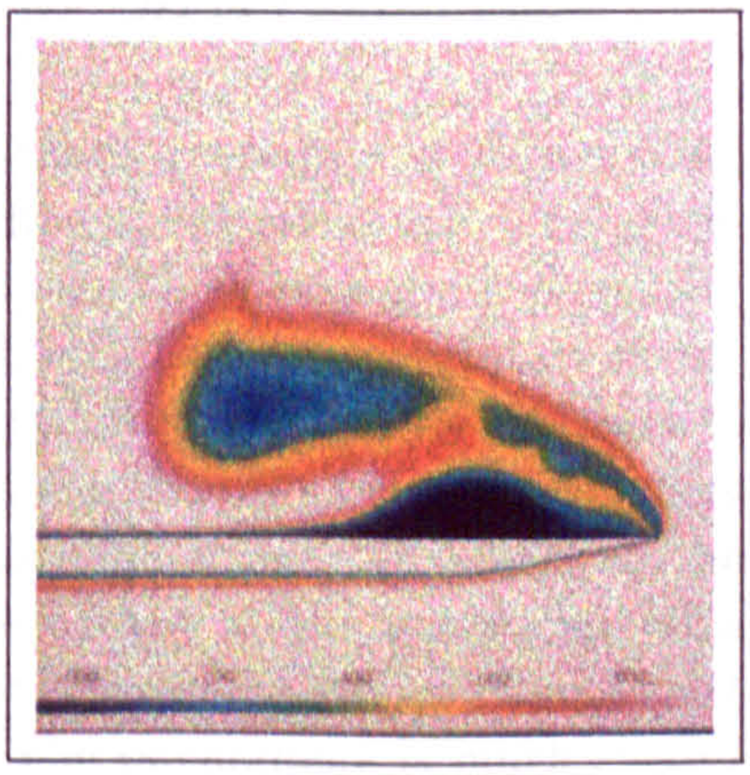

(e) Turbulent, Conical NS

Figure 6.18: *$P_0/P_{0\infty}$ Contours, $\alpha = 16°$, 3D vs Conical NS*

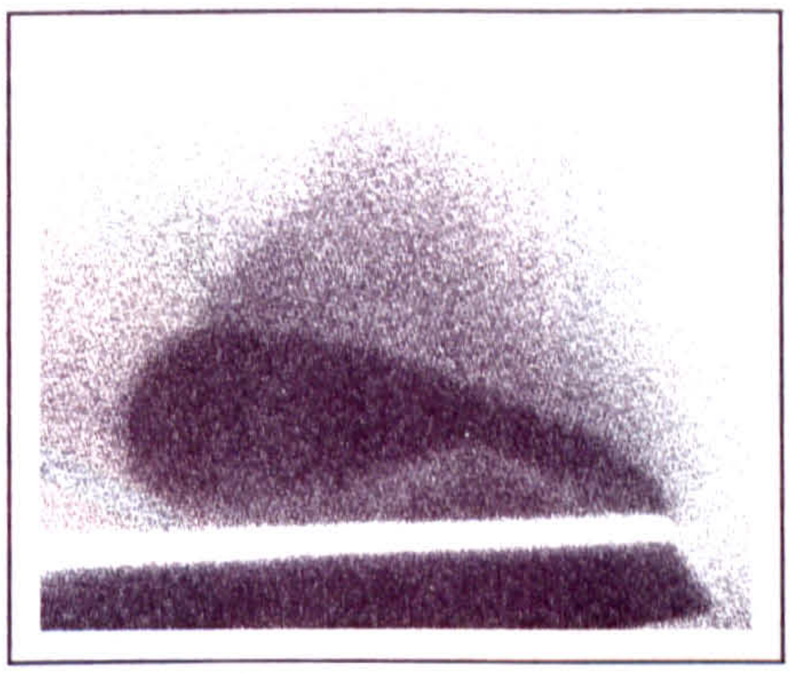

(a) *Delta Wing: Vapour Screen, M=2.8, 16° angle of attack [38].*

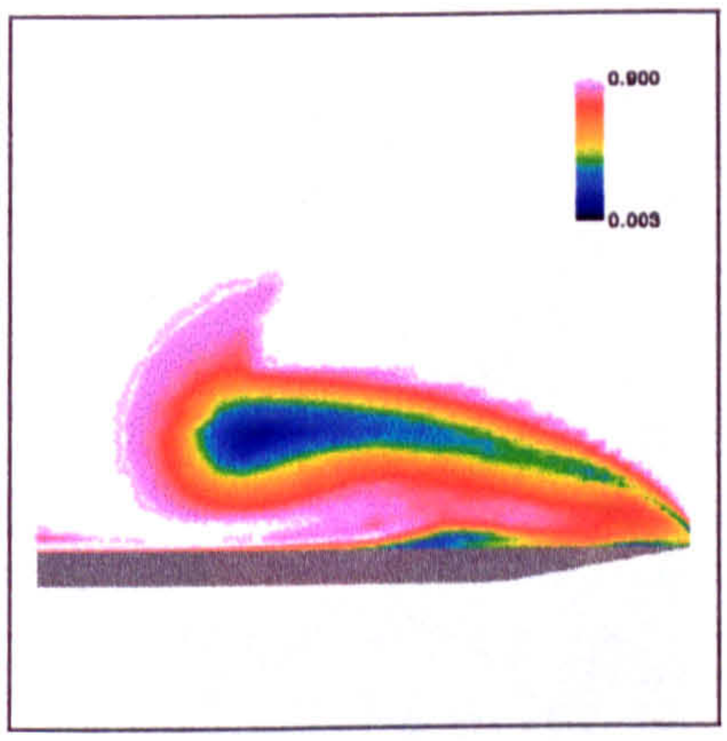

(b) 3D Euler

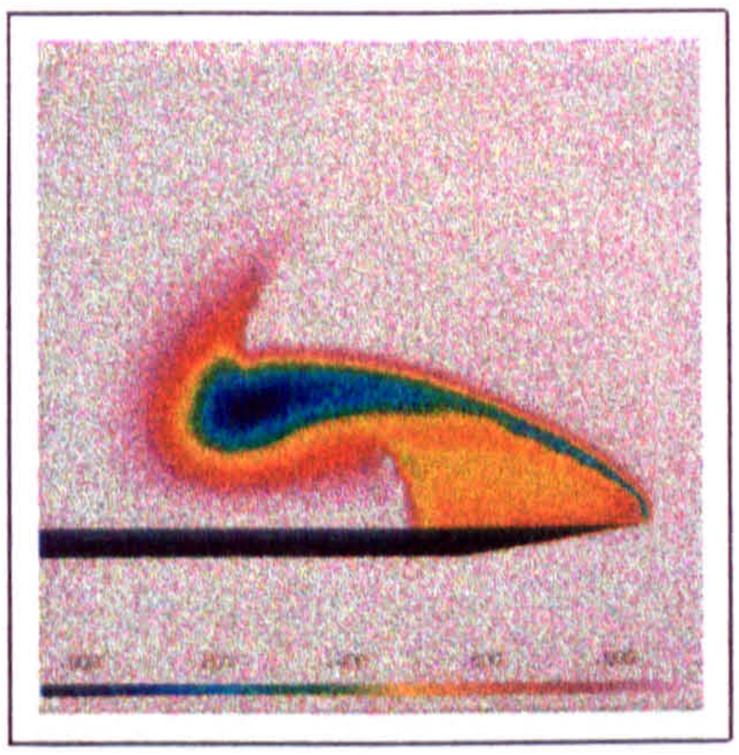

(c) Conical Euler

Figure 6.19: *$P_0/P_{0\infty}$ Contours, $\alpha = 16^o$, 3D vs Conical Euler*

The plots of crossflow Mach number contours, presented in Figure 6.20, provide the best means to visualize the crossflow shock structure. The agreement between the 3D and conical solution is seen to be very good, especially with the resolution of the primary flowfield with the strong primary crossflow shock. Not evident in the vapour screen photographs is the existence of a secondary crossflow shock sandwiched between the primary and secondary vortices, which is resolved in all the viscous simulations. In addition, the crossflow Mach number contours provide evidence of the generation of a crossflow shock forming between the primary vortex and its counterpart across the longitudinal plane of symmetry. The phenomena is much clearer in McMillin's solutions at $\alpha = 20^o$, and was reported by Szodruch [72].

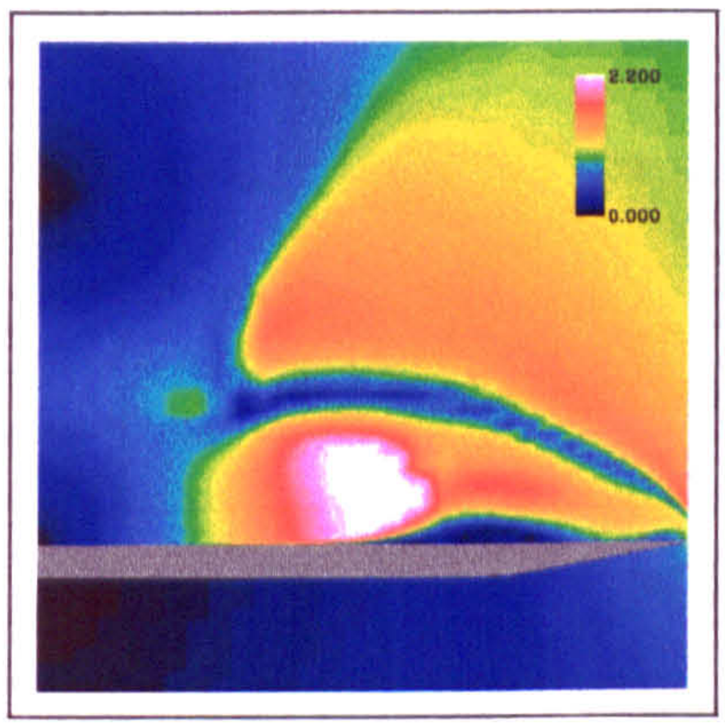

(a) Laminar, 3D-NS

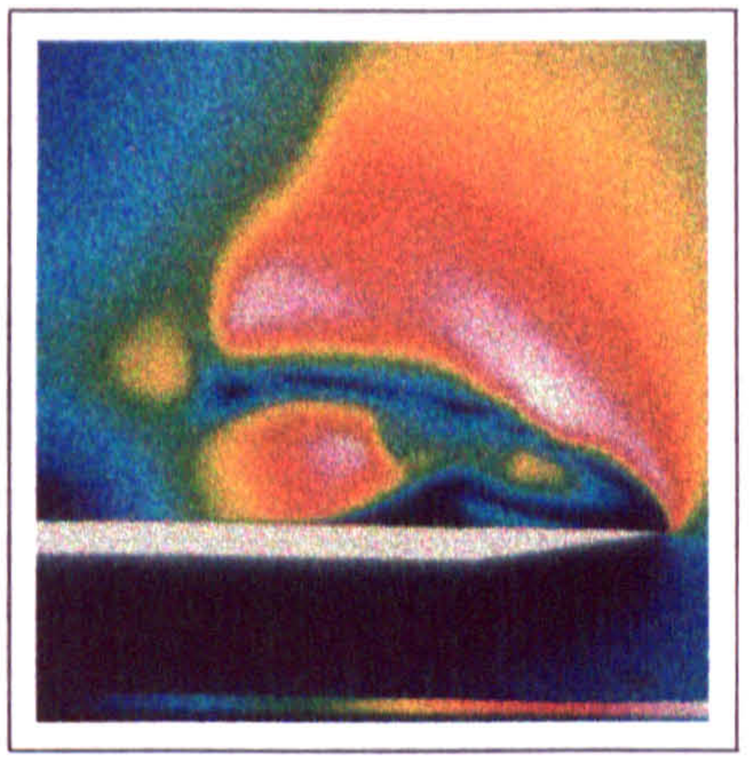

(b) Laminar, Conical NS

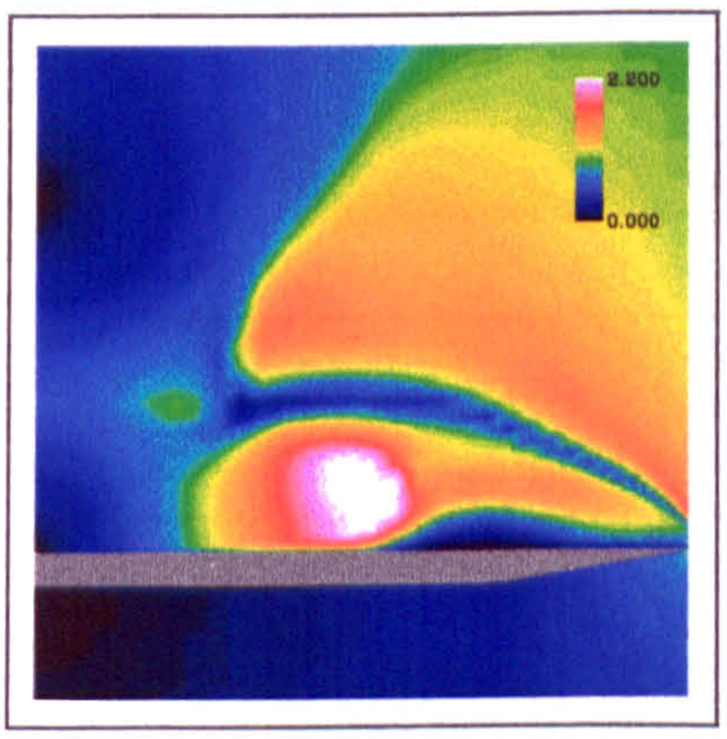

(c) Turbulent, 3D-NS

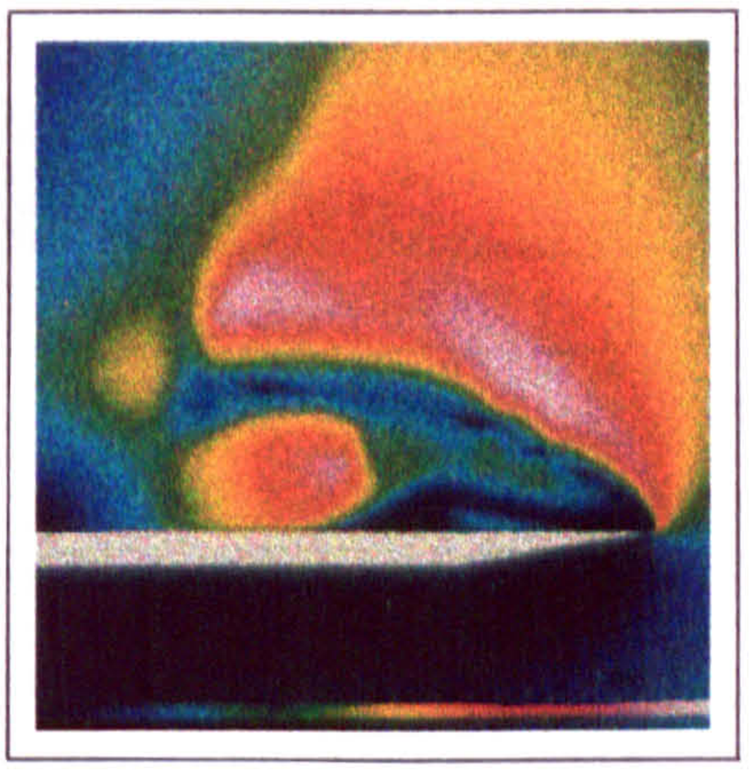

(d) Turbulent, Conical NS

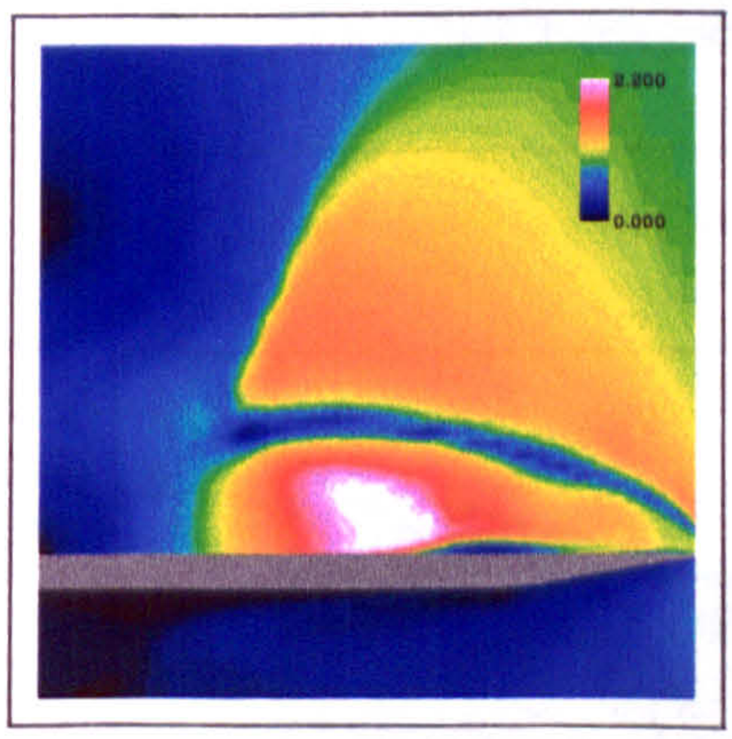

(e) 3D-Euler

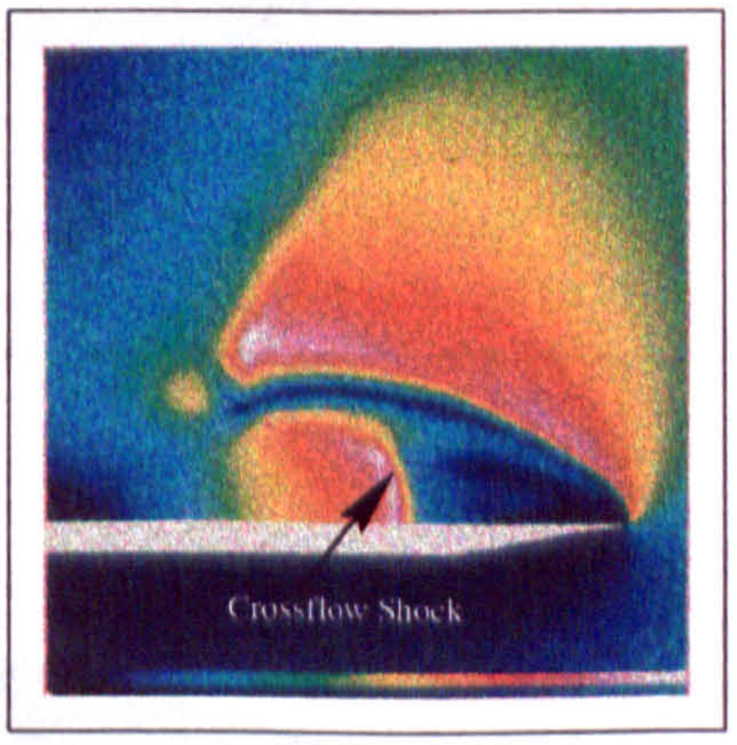

(f) Conical Euler

Figure 6.20: *M_C Contours, $\alpha = 16°$, 3D vs Conical*

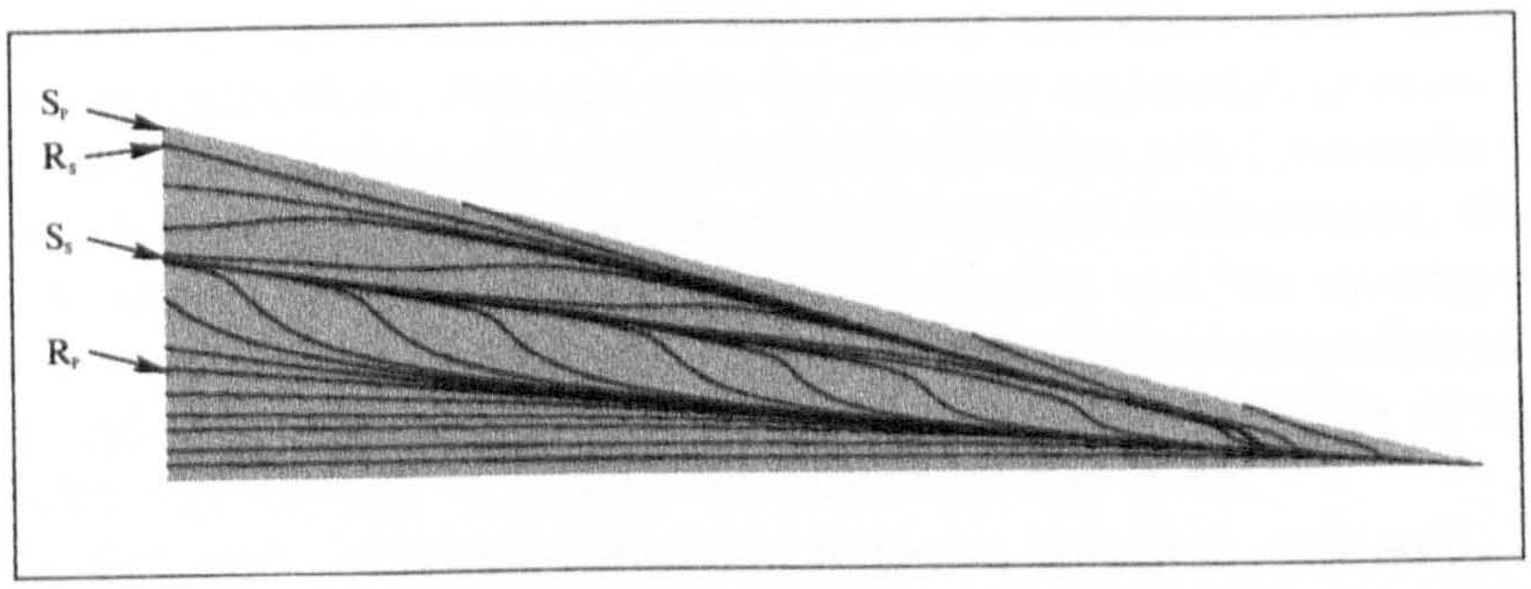

(a) Turbulent NS, $\alpha = 8^o$

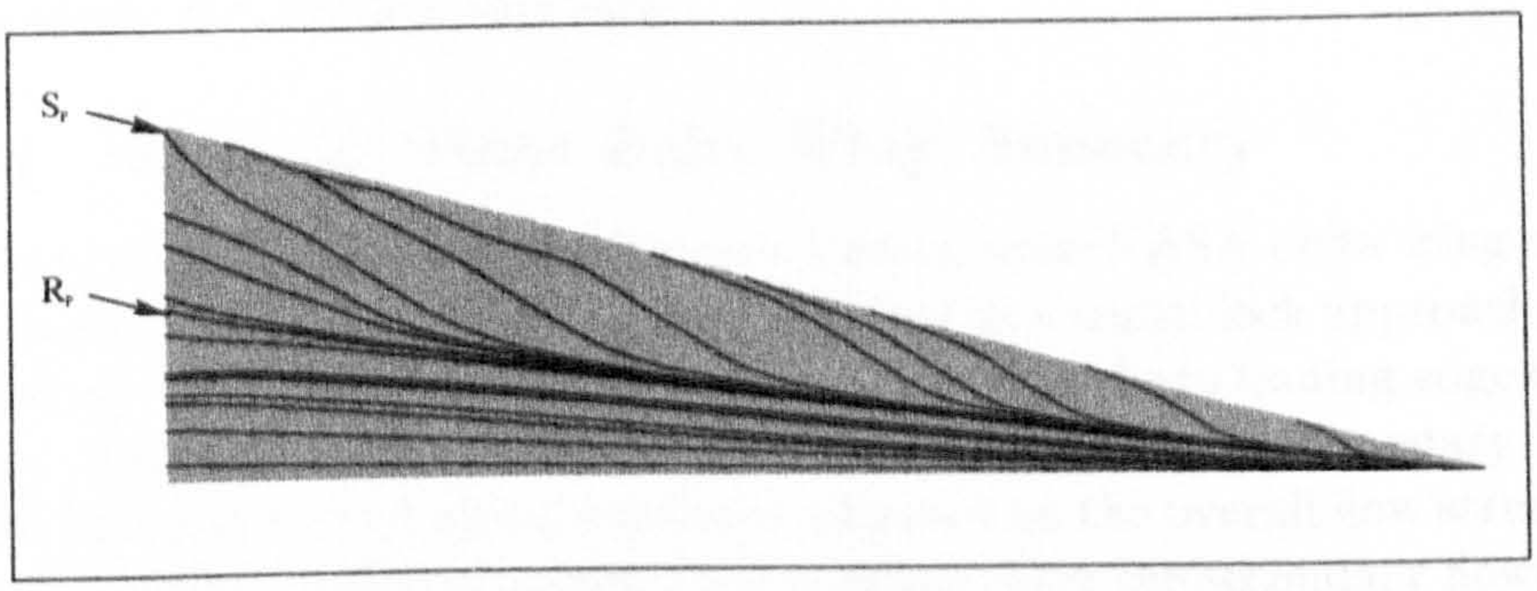

(b) Euler, $\alpha = 8^o$

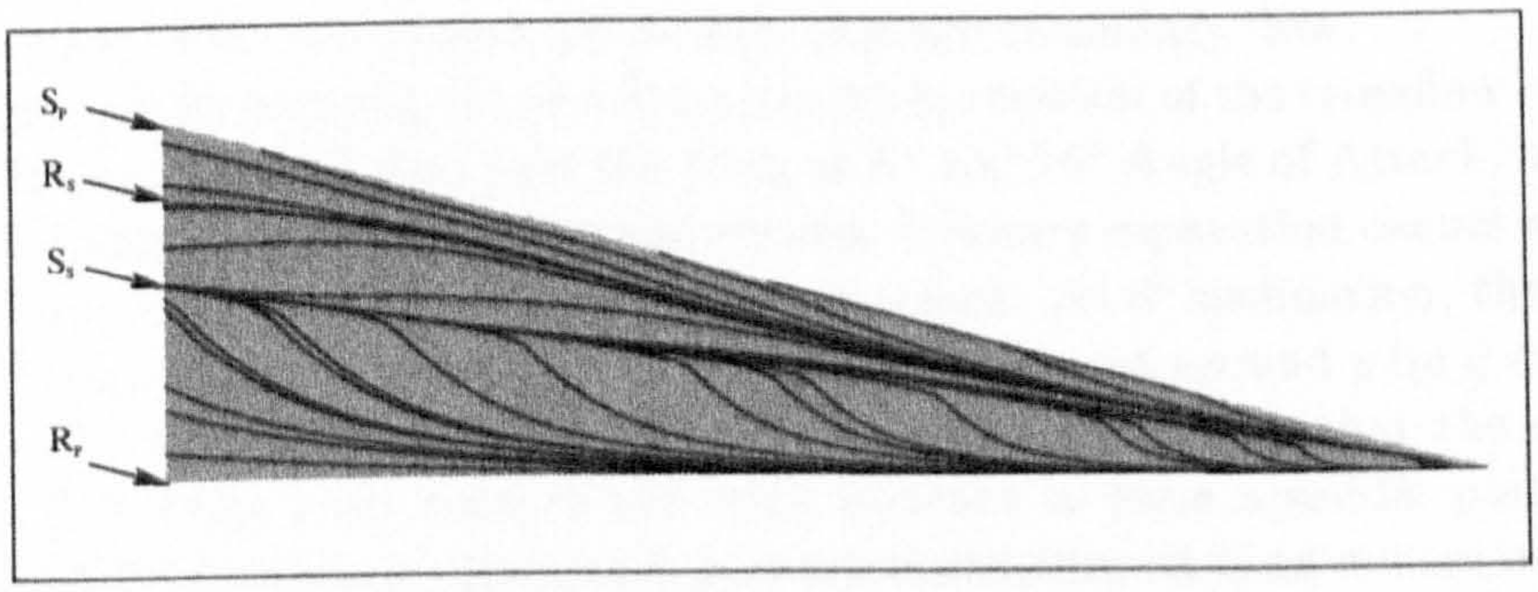

(c) Turbulent NS, $\alpha = 16^o$

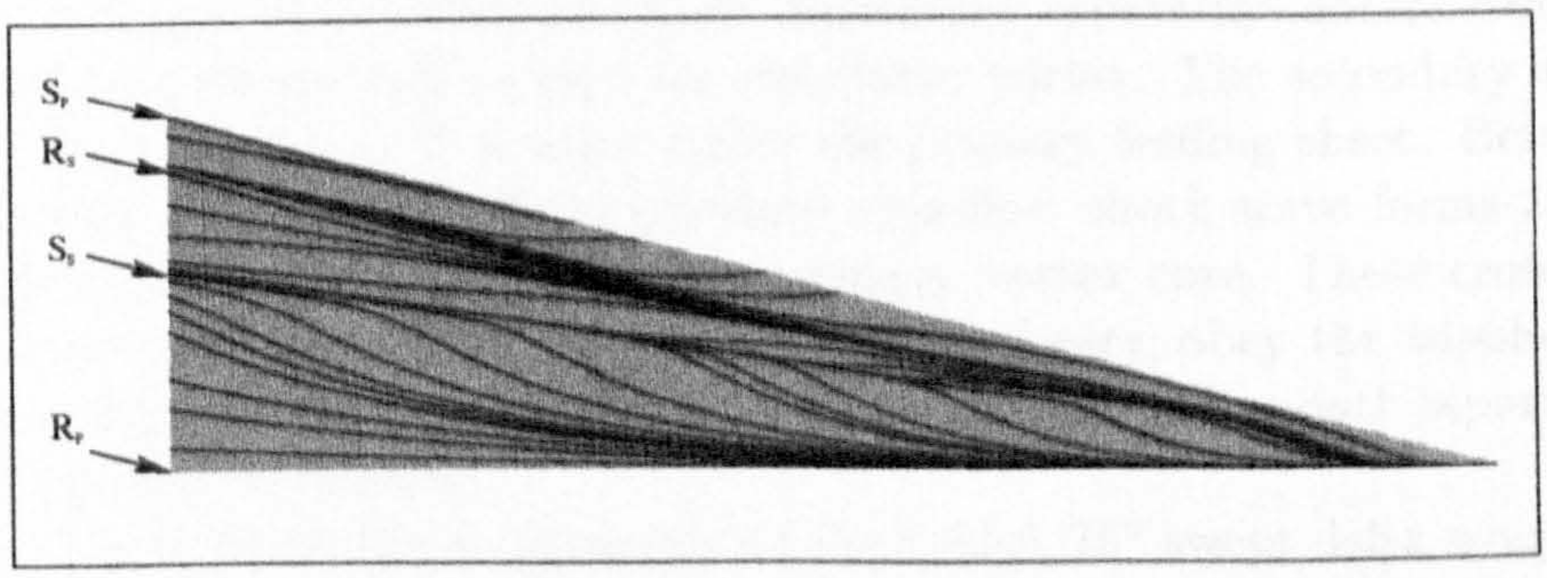

(d) Euler, $\alpha = 16^o$

Figure 6.21: *Surface Streamline Comparisons, Turbulent NS vs Euler*

The surface streamlines for the 3D turbulent and Euler solutions are examined in Figure 6.21. For each case the primary separation (S_P) occurred along the sharp leading edge. Primary reattachment (R_P), secondary separation (S_S) and secondary reattachment (R_S) lines are indicated. For the lower 8° angle of attack, the turbulent NS solution and the corresponding inviscid result are clearly different. The turbulent surface streamline pattern agrees well with the particle trace study presented by McMillin et al, but the Euler solution fails to predict the secondary flow field.

The 16° angle of attack solutions, however, compare very well. Both turbulent and inviscid calculations capture secondary separation and reattachment lines which appear almost equivalent and agree with the particle trace study of McMillin very well.

6.2.4 NASA 75° Swept Delta Wing: Summary

The investigation of the two 75° swept leading edge NASA delta wing cases has shown that the CRANS3D solver, employing a multiblock approach, can accurately calculate the steady supersonic flow past sharp leading edge delta wings. Consistent with the findings of McMillin *et al.*, the boundary layer model (laminar or turbulent) has little influence on the overall flow structure except at higher angles of attack when it affects only the secondary flowfield. In addition it has been shown that the solution of the Euler equations for these sharp leading edge geometries can predict the primary vortex structure reasonably well, but cannot accurately capture secondary flow.

Figure 6.22 presents the aerodynamic interpretation of the crossflow structure of the Mach 8.2 flow past the wing at 8° and 16° Angle of Attack, based on the experimental and numerical results. Primary separation occurs along the sharp leading edge for both angles of attack. At 8° inclination, the primary separated flow reattaches on the wing surface at around $y/y_{LE} \approx 0.4$, while at 16° angle of attack the primary vortex is so large that the separated flow from both sides of the wing interact to form a saddle point on the leeward symmetry plane and primary reattachment then occurs on the surface on that plane. Both flow fields exhibit a primary crossflow shock which sits above the primary vortex, with the higher inclination producing a stronger, more extensive shock. Secondary separation occurs beneath the primary vortex and induces an associated vortex. The secondary separated flow reattaches at a point under the primary feeding sheet. Between 8° and 16° angle of attack a secondary crossflow shock wave forms above the secondary vortex and below the primary vortex core. These crossflow structures, when analysed using critical point theory, obey the topological relationship of Shen et al [62] given by equation (4.2) for smooth separation off cylindrical forebodies.

The close similarity in geometry of the NASA 75° swept delta wing and the RAE W20 wing incorporated into the missile configuration investigated

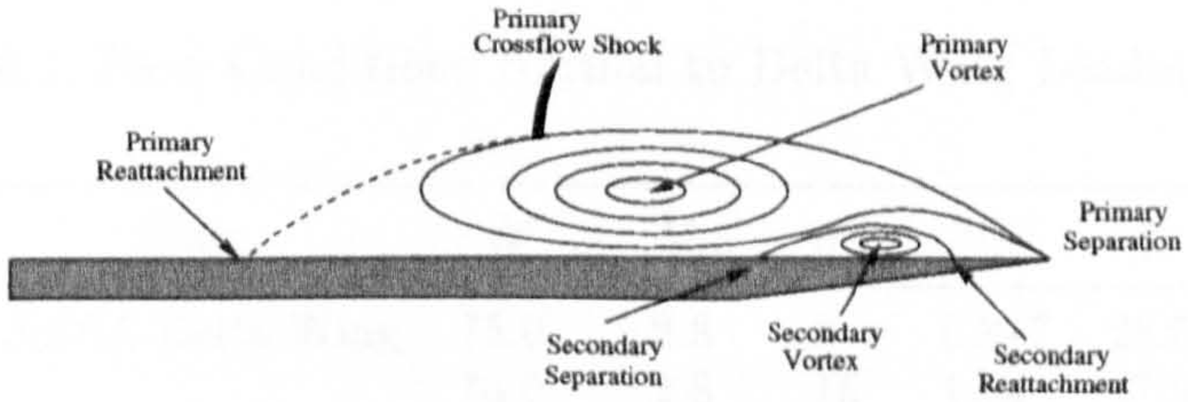

a) Crossflow Structure, $\alpha = 8^{o}$

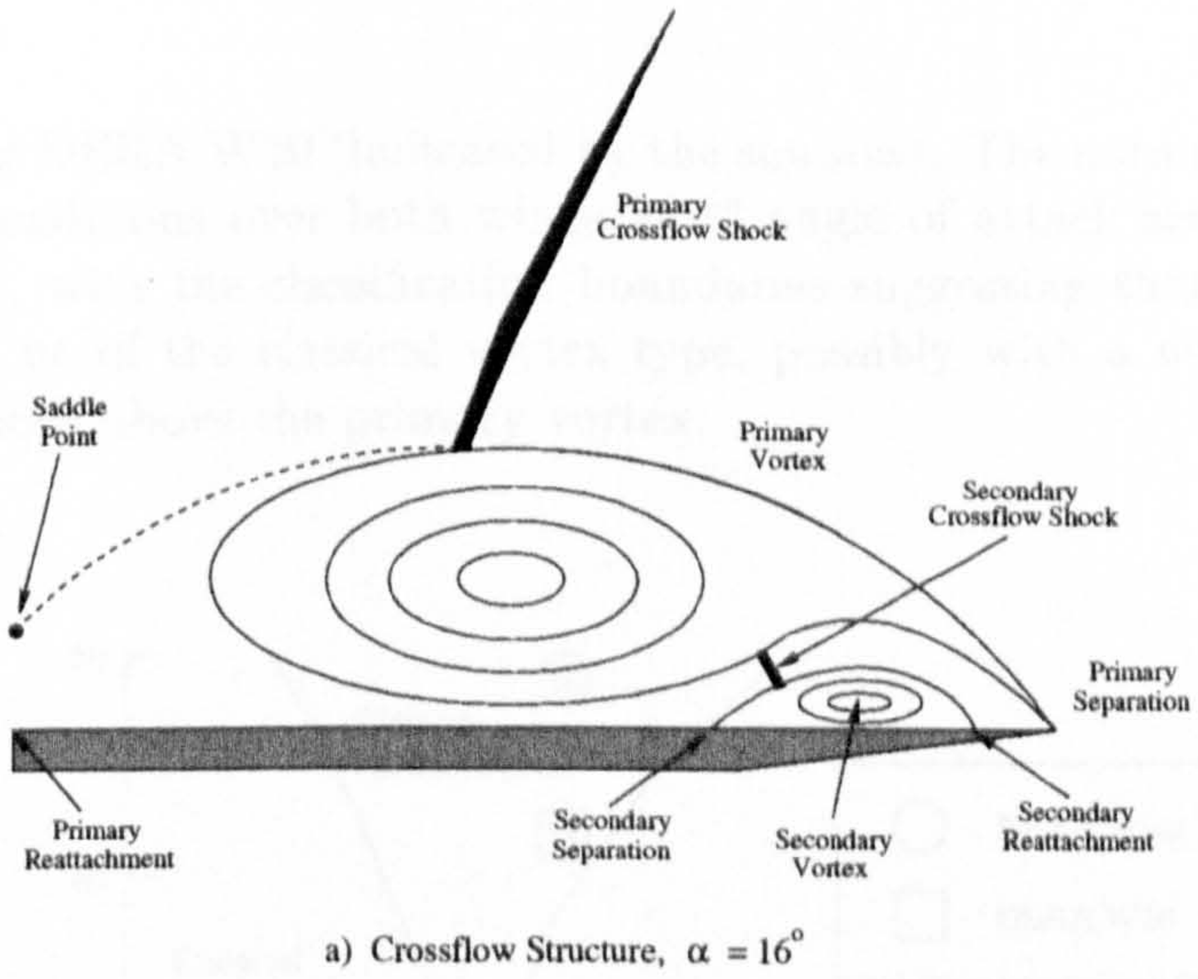

a) Crossflow Structure, $\alpha = 16^{o}$

Figure 6.22: *NASA* 75^{o} *Swept Delta Wing: Flow Structures at* 8^{o} *and* 16^{o} *Angle of Attack*

in Chapter 7, and the similar test flow conditions suggests that the flow over the leeside of both geometries, at a given angle of attack, will be very similar. To assess whether the Mach 2.5 flow over the RAE W20 wing at 8^{o} and 14^{o} angle of attack are likely to be similar to those observed on the NASA delta wing at 8^{o} and 16^{o}, the $\alpha_N - M_N$ classification of McMillin et al (Figure 6.4) can be employed. Table 6.1 presents the required flow conditions normal to the leading edge, given by:

$$M_N = M_\infty cos\Lambda \left(1 + sin^2\alpha\ tan^2\Lambda\right)^{\frac{1}{2}}$$

$$\alpha_N = tan^{-1}\left(tan\alpha / cos\Lambda\right)$$

where Λ is the leading edge sweep back angle and α is the angle of attack. Figure 6.23 reproduces the $\alpha_N - M_N$ graph showing the NASA delta wing conditions (indicated by the circles with the angle of attack given inside) and

Table 6.1: Flow Conditions Normal to Delta Wing Leading Edge

Case	Λ^o	M_∞	α^o	M_N	α_N^o
NASA Delta Wing	75.0	2.8	8	0.817	28.5
	75.0	2.8	16	1.04	47.9
RAE W20	71.565	2.5	8	0.857	24
	71.565	2.5	14	0.977	38.3

those for the DERA W20 (indicated by the squares). The normal to leading edge flow conditions over both wings at 8° angle of attack are seen to be very similar, with the classification boundaries suggesting that the leeside flow should be of the classical vortex type, possibly with a weak primary crossflow shock above the primary vortex.

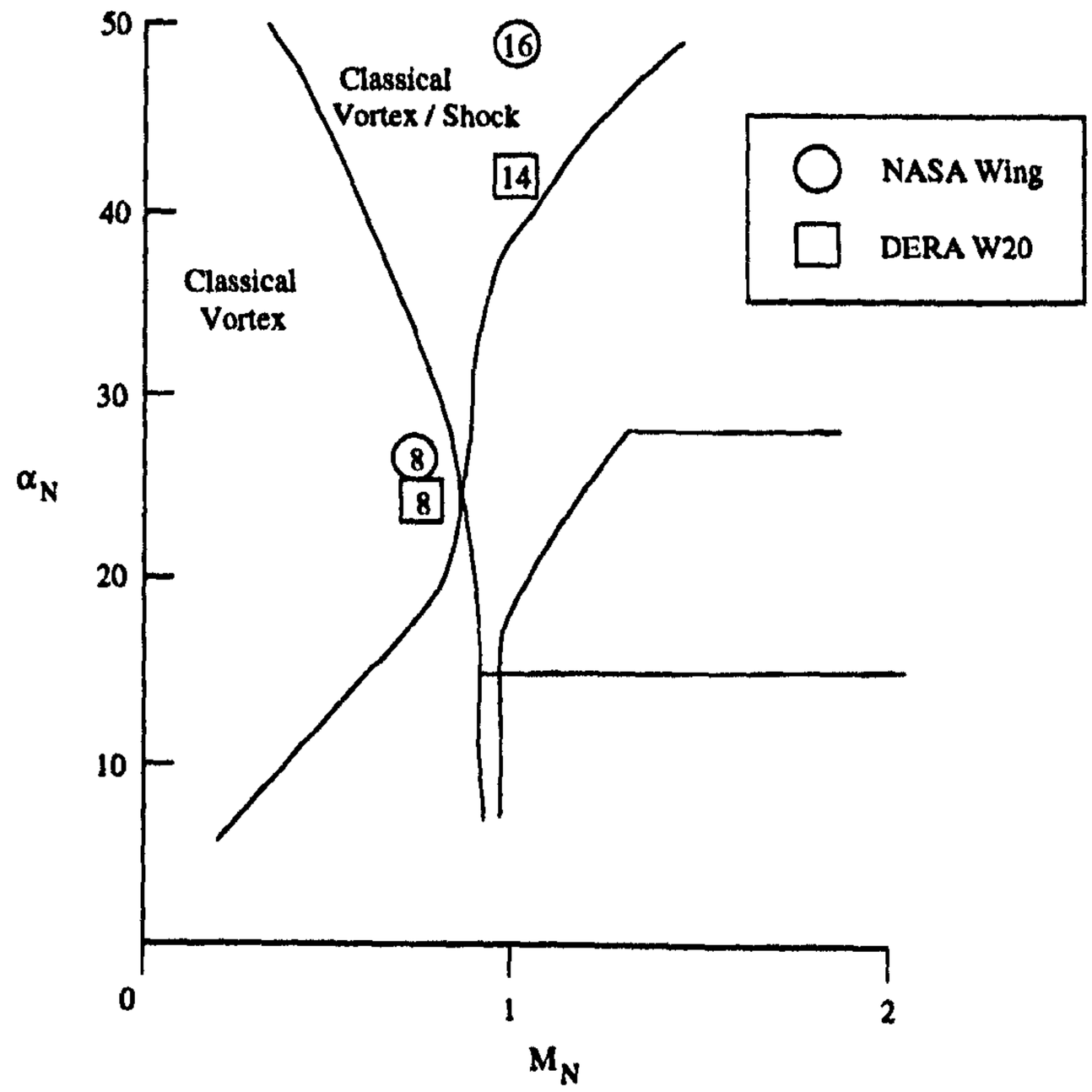

Figure 6.23: *Classification of Leeside Flow for the NASA and RAE W20 Delta Wing Cases*

For the higher angle of attack cases the Mach number normal to the leading edge appears to be similar, but the corresponding angle of attack

for the NASA case is almost 20% higher than that for the DERA case. The flow classification for both geometries, at their respective higher angle of attack conditions, appears to be the same - a classical vortex pattern on the leeside surface with a strong crossflow shock. The $\alpha_N - M_N$ plot, therefore, suggests that the 8° angle of attack crossflow structure for both wing cases will, indeed, be the same and that the crossflow structure for the NASA delta wing at 16°, Mach 2.8 will be the same as that encountered by the DERA W20 wing at 14°, Mach 2.5.

Chapter 7

Full Configuration: The Body/Wing

The aerodynamics of the B1AW20A3 cruciform wing missile configuration is studied. Both the experimental study and the corresponding numerical investigation is presented together with an interpretation of the shock-wave/shear-layer/vortex interactions occurring due to the interference of the body and wing flowfields.

The previous chapters have investigated the complicated vortical flows around the simple geometries of the isolated components of conventional cruciform wing missile configurations. When these isolated components are brought together to form the full configuration, there is mutual interference between the body and the wing flowfields, making the flow even more complex for the complete system. The body vortices will induce an additional crossflow component on lifting surfaces and so influence the flowfield on the wing which, in turn, affects the body vortices. The following section reviews some of the work performed to date, on the study of the flows about conventional cruciform wing missiles.

7.1 Vortical Body/Wing Flowfields: A Review

A number of publications exist concerning the vortical aerodynamics of cruciform wing missile configurations. Allen and Dillenius [2] used vapour screen flow visualisation in the analysis of the supersonic flow, and in particular the longitudinal vortex development, past a cruciform wing-body-tail missile. The results were compared with the predictions of the longitudinal vortex trajectories provided by linear theory. Figure 7.1 presents the results of the vapour screen study of the longitudinal vortex development for 11.4° angle of attack and 0° roll and demonstrates that the technique is a powerful method for the visualisation of the large scale shock wave/vortical structures

in complicated crossflows.

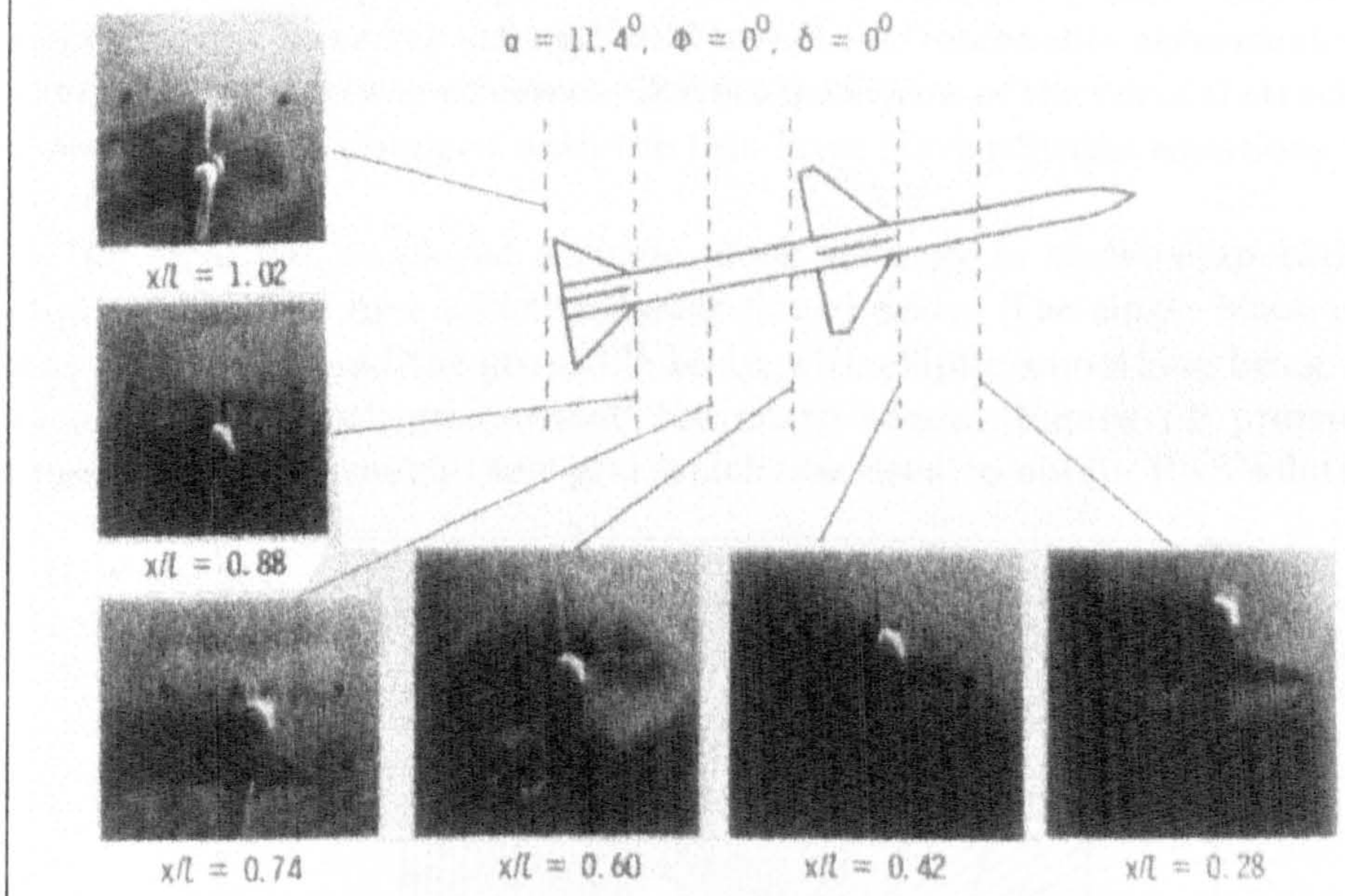

Figure 7.1: *Vapour Screen Study of Longitudinal Vortex Development, M_∞=1.3. [2]*

Various body-wing configurations have been computed using space marching Euler solvers, and have been presented in the review of Wardlaw et al [82]. Reasonable agreement has been obtained between calculation and experiment for many different missile configurations, and the method can give accurate predictions of the force and moment characteristics at low angles of attack ($< 5^o$) but provides poor results where viscous effects become large at moderate to high angle of attack.

Lijewski [30] presented a multiblock numerical study of the mutual interference between cruciform finned missiles in a variety of closely spaced positions. In particular, the grid generation aspects and the multiblock topology issues were addressed. Lijewski employed the EAGLE grid generation package, the forerunner to the EAGLEView software used in the present study, to develop blocking schemes for single missiles and the 2-3 missile combinations investigated.

In their review of the "aeromechanical design of modern missiles", Hennig and Lacau [22] presented a series of numerical investigations of the aerodynamics of the ASTER surface to air missile. Various solvers were employed including a single-block space marching Euler code, a coupled Euler/Boundary layer solver and a multiblock thin-layer Navier-Stokes code. It

was found during the inviscid computational study that the sharp wing tips enabled the Euler solver to successfully predict primary separation on the wings and fins and, although the vortices were captured unphysically and so resolved with incorrect strength and structure, reasonable agreement with experimental data was achieved. Correct resolution of the vortical structure, however, was not obtained until the thin layer Navier-Stokes equations were solved.

Rai et al [56] employed a single block strategy in their computational study of the flow over a cone-cylinder finned body. The single block mesh was wrapped around the projectile body, with elliptic smoothing being used to obtain a smooth grid around the sharp edges. Figure 7.2 presents a crossflow plane through their grid which was used to obtain PNS solutions.

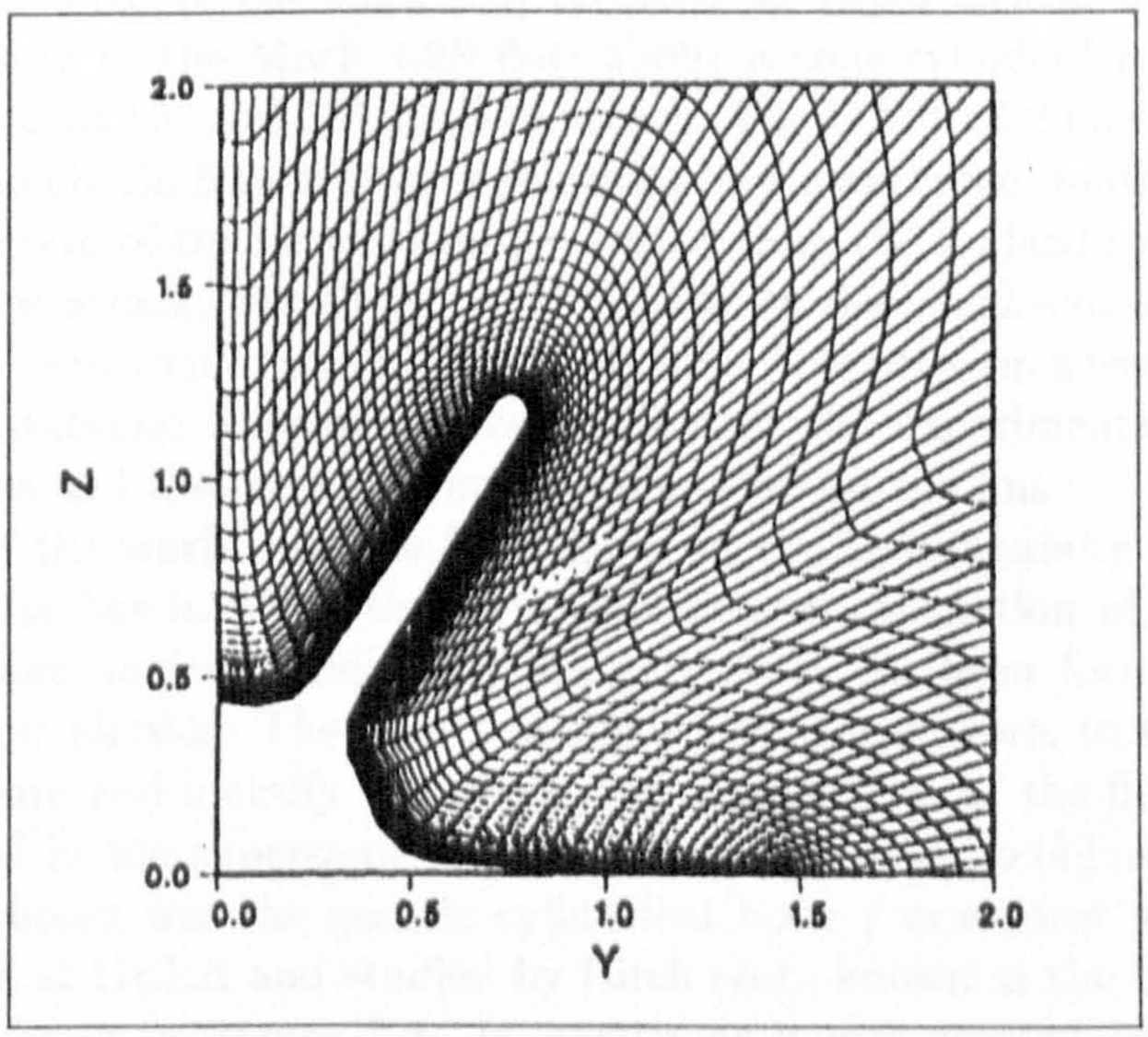

Figure 7.2: *Single Block Mesh Around a Finned Body [56]*

Birch [9] at DERA, Bedford in the UK. has, over a number of years, been involved in collaborations with industry and a number of Universities in the development of multiblock PNS technologies for missile configurations. It has been demonstrated that PNS solvers can successfully calculate the supersonic vortical flows about winged-bodies including the complex shock-vortex and shock-shock interactions that occur in the vicinity of wings and fins. For the validation of computational solvers Ward, Birch and Hodges [78] [23] [79] performed a number of experiments on body/wing configurations, measuring surface pressure distributions on the body and wings and the total pressure ratio in a crossflow plane in the wake of cruciform wing arrangements. The results from these studies revealed a complex flow structure involving shock-shock, shock-vortex and shock-boundary layer interactions, forebody,

afterbody and leading and trailing edge vortices together with a plethora of smaller vortical structures.

Priolo and Wardlaw [51] employed the multiblock method in their aerodynamic study of a body-canard-tail arrangement at Mach 2.5 and 20° angle of attack. The time-marching Navier-Stokes solutions successfully captured both the body vortices and the leading edge vortices over the canard and tail surfaces. At such high angles of attack, the PNS assumption becomes less valid since streamwise separation becomes more probable, and the longitudinal Mach number (which must be supersonic) is reduced with increasing angle of attack. Such restrictions do not apply to time marching solvers.

Bertin has recently published a number of papers on a series of investigations of the flowfield about missile configurations employing rectangular wings. The most recent work [50] involved an experimental and computational study of the Mach 4.28 flow about a cone-cylinder/cruciform fin configuration at 10° and 20° angle of attack. The GASPv3.2 flow solver was employed to obtain Navier-Stokes solutions on a structured multiblock grid. The interaction of the shockwaves generated from the fin leading edges, for zero angle of attack, was shown to be similar to the shock-shock iterations which have been seen to occur in the supersonic flow between a wedge-corner. The computational solutions agreed well with the experimental schlieren photographs and the measured surface pressures on the fins.

Much of the work that has been done on the aerodynamics of winged-body missiles has involved the measurement and calculation of forces and moments, and surface conditions, but very little has been focused on the complex flow physics. The object of this study, is therefore, to classify the flow structure and identify the origin and mechanisms of the flow features encountered in the supersonic flow about a body/wing configuration. The geometry chosen was the generic cylindrical body / cruciform wing design constructed at DERA and studied by Birch *etal.*, known as the B1AW20A3 geometry shown in Figure 7.3. In particular it was decided to study the flow at the two basic roll orientations for which measurements had already be taken: 0° (a + configuration with the wings in and at right angles to the crossflow) and 45° (an × configuration).

Access to the NASA Langley Unitary Plan Wind Tunnel enabled a series of experimental flow visualisation studies to be performed in conjunction with a comprehensive study of two angle of attack cases using the multiblock CRANS3D Navier-Stokes solver. The following sections describe the experiments and computations performed together with the results and an aerodynamic interpretation of the complex flow structures observed.

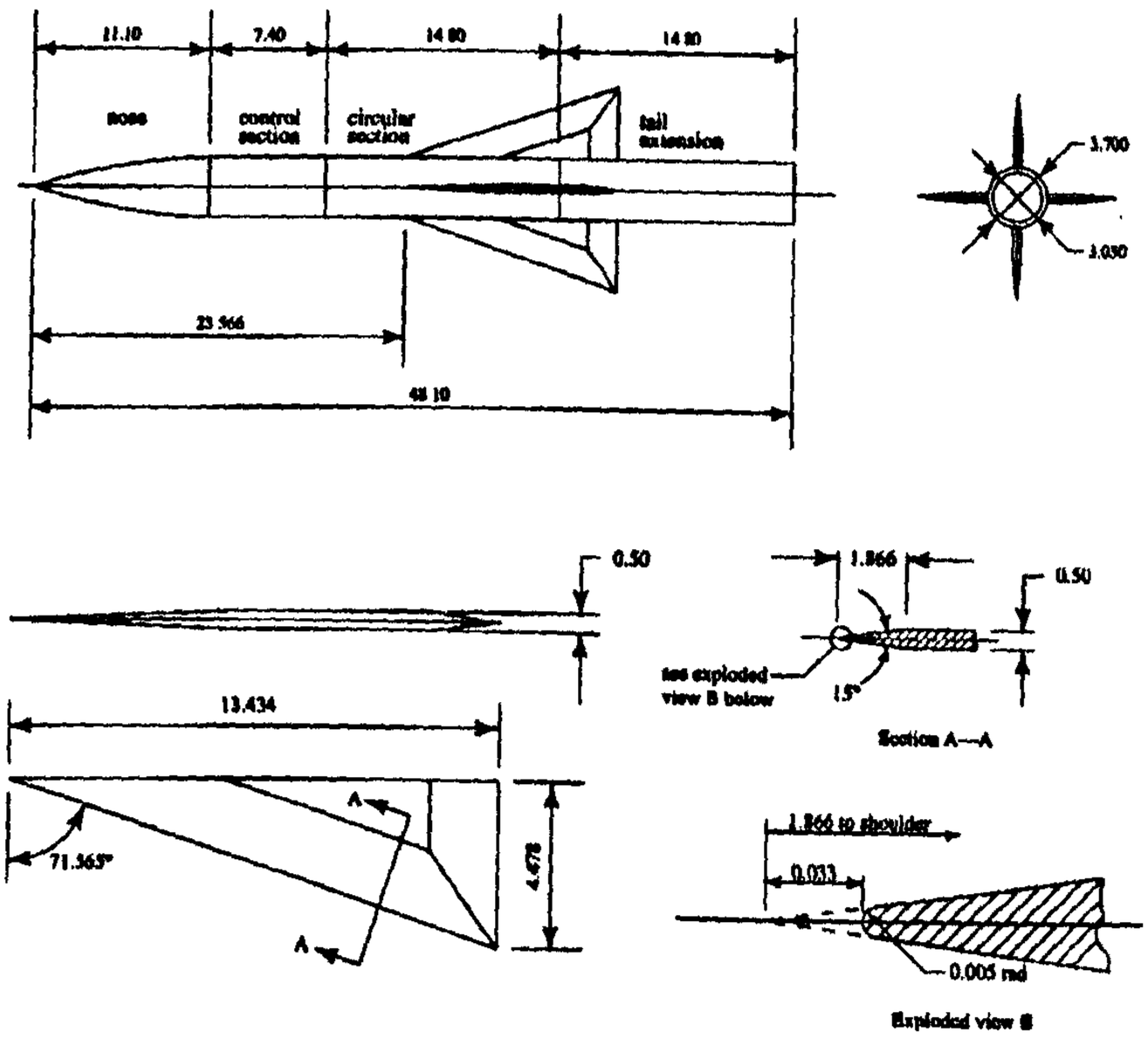

Figure 7.3: *The B1AW20A3 Generic Missile Configuration (Dimension in Inches)*

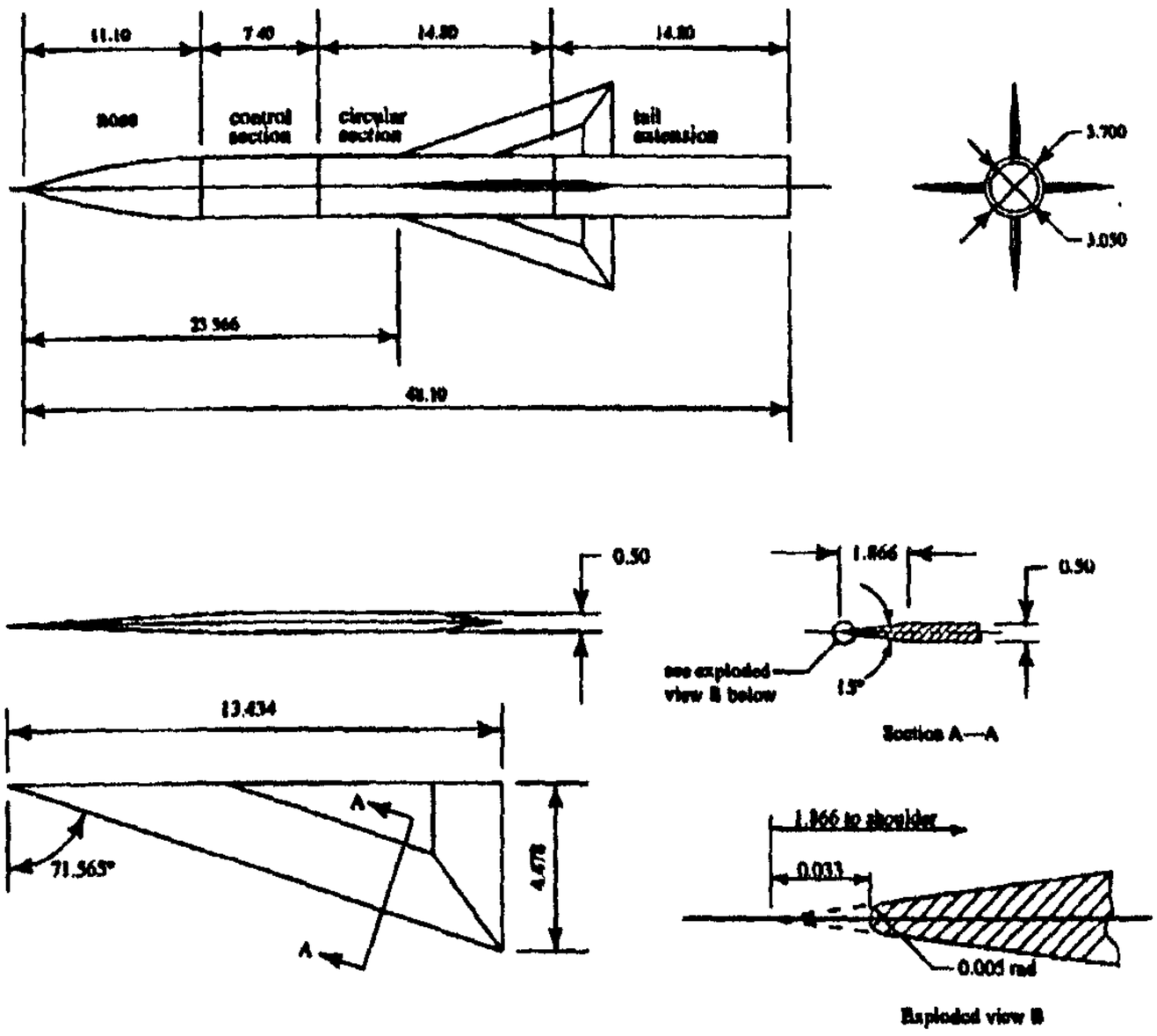

Figure 7.3: *The B1AW20A3 Generic Missile Configuration (Dimension in Inches)*

7.2 The Experimental Study

7.2.1 The Langley Unitary Plan Wind Tunnel

The experimental flow visualisation studies were performed on the B1AW20A3 model in the Unitary Plan Wind Tunnel (UPWT) at the NASA Langley Research Center, Hampton, Virginia, USA. The facility is a continuous, variable pressure, supersonic windtunnel, feeding two test section of 4 × 4 ft cross section, and was the same tunnel used for the NASA delta wing experiments presented in the previous chapter. A sliding block nozzle ahead of the test section allows continuous variation of Mach number during the test. The higher Mach number test section was employed, allowing Mach numbers between 2.36 and 4.63. The tunnel dew point was monitored and maintained at levels to minimize condensation. Table 7.1 presents the average freestream conditions measured during the experiments. Conditions were chosen to match the experiments previously performed on the model at DERA, Bedford.

Table 7.1: B1AW20A3 Experiments: Freestream Flow Conditions

M_∞	Re_∞ (per ft)	P_0 (lb/ft^2)	P_0 (^oF)
2.50	4.0	3928	138

7.2.2 The B1AW20A3 Model And Instrumentation

Figure 7.4 shows the experimental model mounted within the test section ready for force and moment measurements. The model comprised several sections that were combined together before the test. A separate section was manufactured to adapt the model to the tunnels force/moment balance which was attached to the cylindrical sting as shown in Figure 7.5. The roll coupling allowed the model to be rolled to 45° during tunnel operation. Force and moment measurements were obtained with the Langley UT-65B 6-component electrical strain gauge balance which is described in more detail by Wilcox [84].

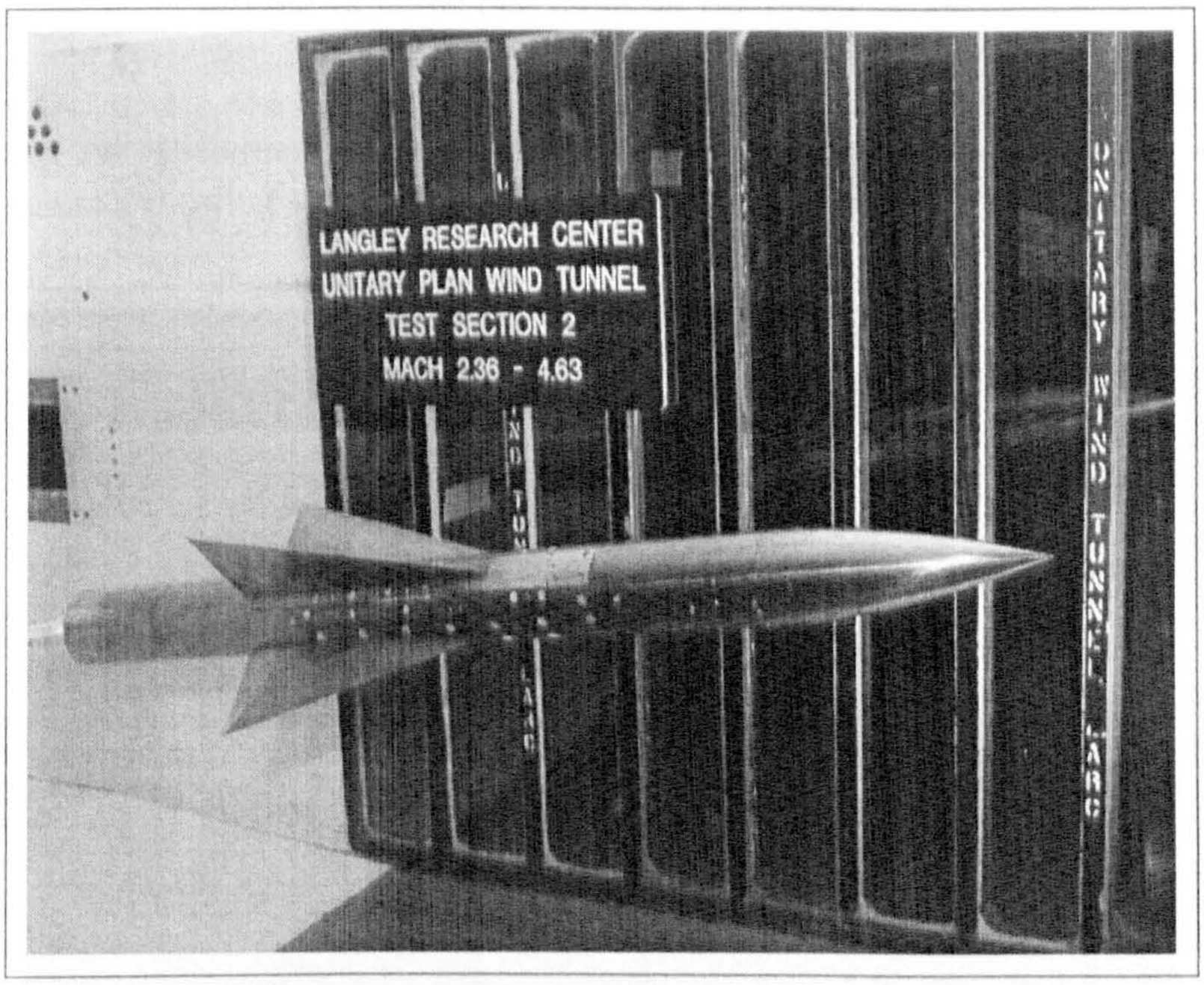

Figure 7.4: *The B1AW20A3 Model Mounted in the Unitary Wind Tunnel Test Section*

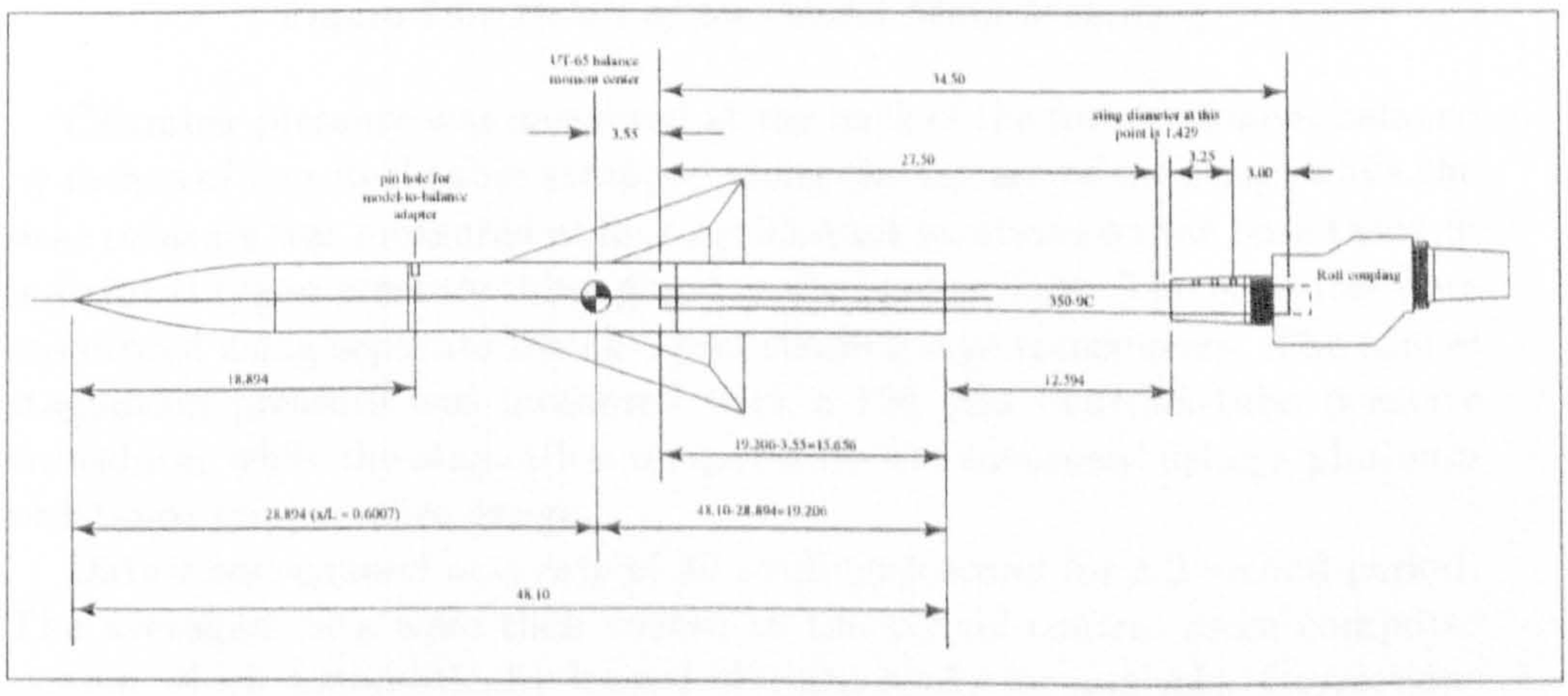

Figure 7.5: *Tunnel Installation (Dimension in Inches) [84]*

Temperature sensitivity was monitored using three platinum resistance thermometers located in three positions on the balance. Force and moment data was corrected for base effects by measurement of the pressures on the base and within the chamber between the sting and the model base/shroud. Figure 7.6 reproduces the photograph taken of the sting-base-chamber arrangement showing the base and chamber pressure tubes.

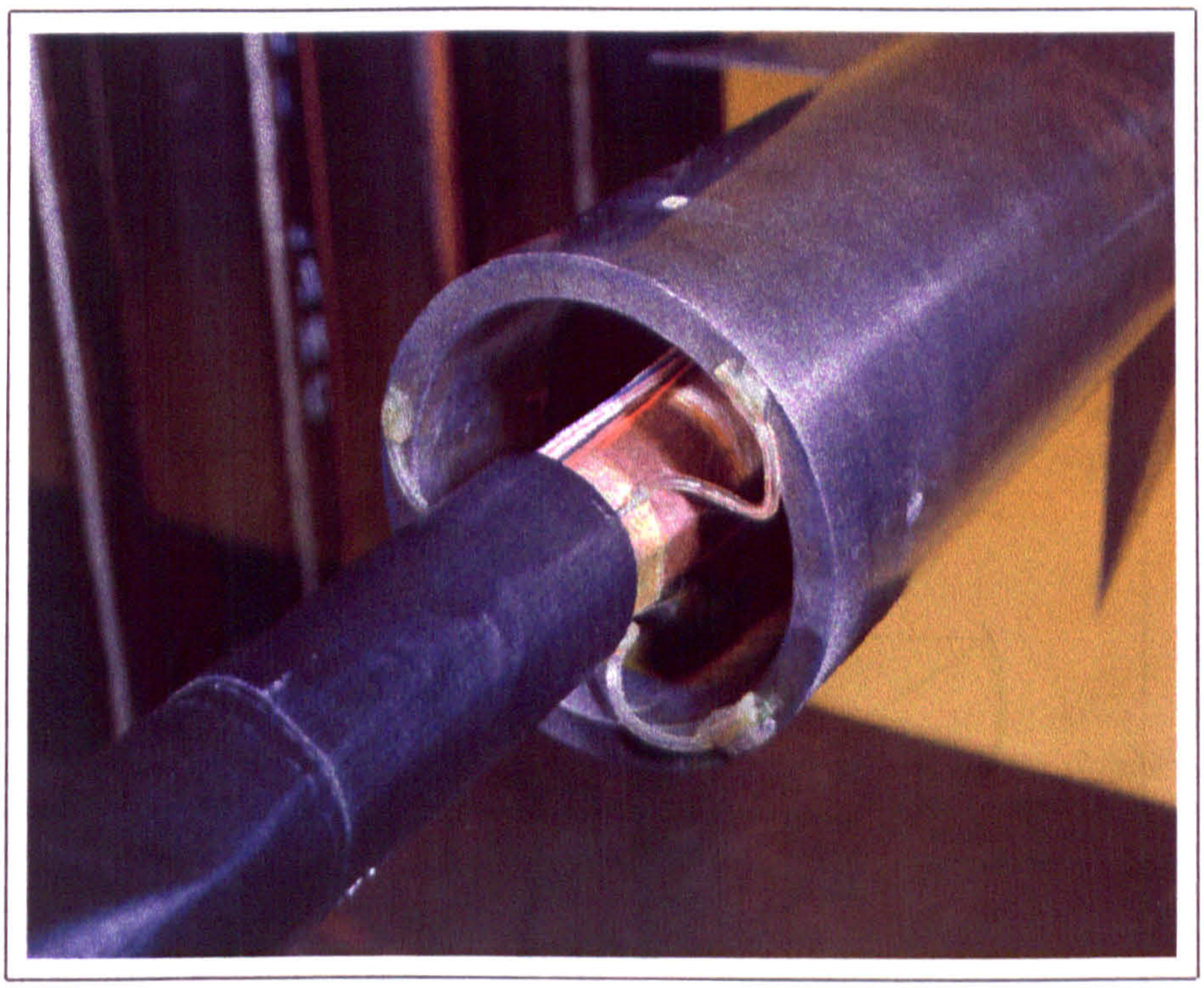

Figure 7.6: *Detail of the Model Sting Mounting*

Chamber pressure was measured at the back of the force/moment balance by means of two steel tubes strapped along the surface of the sting, while the base pressure was measured at four equidistant locations on the base through individual tygon pressure tubes glued to the base surface. The pressures were monitored using separate Druck 5 psia strain gauge transducers. The tunnel stagnation pressure was measured with a 150 psia bourdon-tube pressure transducer while the stagnation temperature was measured using a platinum resistance temperature gauge.

Data were scanned at a rate of 30 readings/second for a 2 second period. The averaged data were then routed to the tunnel control room computer system which automatically logged all data ready for analysis. Corrections to the data were then made for effects of flow angularity and model deflection, details of which are presented by Wilcox [84].

7.2.3 Flow Visualisation Techniques

Schlieren Photography

A schematic of the Unitary Plan Wind Tunnel schlieren system is presented in Figure 7.7. The light source was provided by a continuous running Xenon vapour arc lamp. An optical beam splitter was employed to provide a schlieren image for the photographic Hasselblad camera (70mm ASA 400 black and white film) and for a video camera for viewing in the control room. The schlieren system knife-edge was oriented approximately parallel to the freestream flow direction, thus highlighting the density gradients normal to the freestream. Increasing density gradients normal to the freestream therefore appeared white in the photographs (the vertical black lines which appear in the schlieren photographs being the test section support arms).

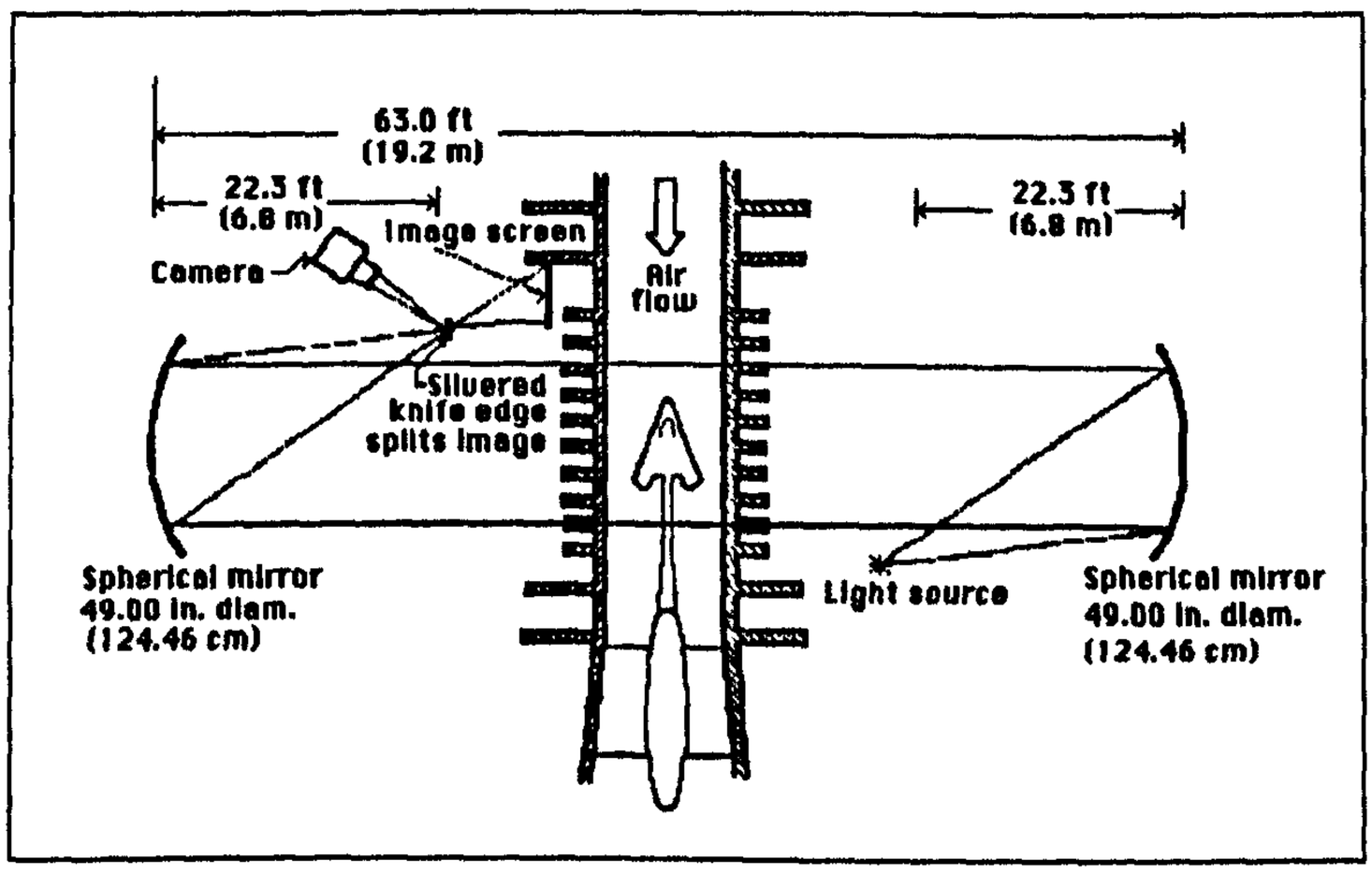

Figure 7.7: *Schematic of the UPWT schlieren System [42]*

Vapour Screen Visualisation

The vapour screen technique has been successfully used for flow visualization of vortices and shock structures in high speed flow [43] [1] [38]. For this technique the whole wind tunnel is seeded with an aerosol, usually water vapour for high speed flows but smoke can be used at low speeds. Water vapour is introduced into the air stream just ahead of the supersonic nozzle. As the moist air expands through the nozzle it cools and the water vapour condenses to form a uniform fog throughout the test section. A cross-section of the test section is illuminated by a thin light sheet, as depicted in Figure 7.8. Any disturbances in the flow field will cause variations in the density of the water vapour which will show up in the illuminated sheet as variations in the intensity of the scattered light.

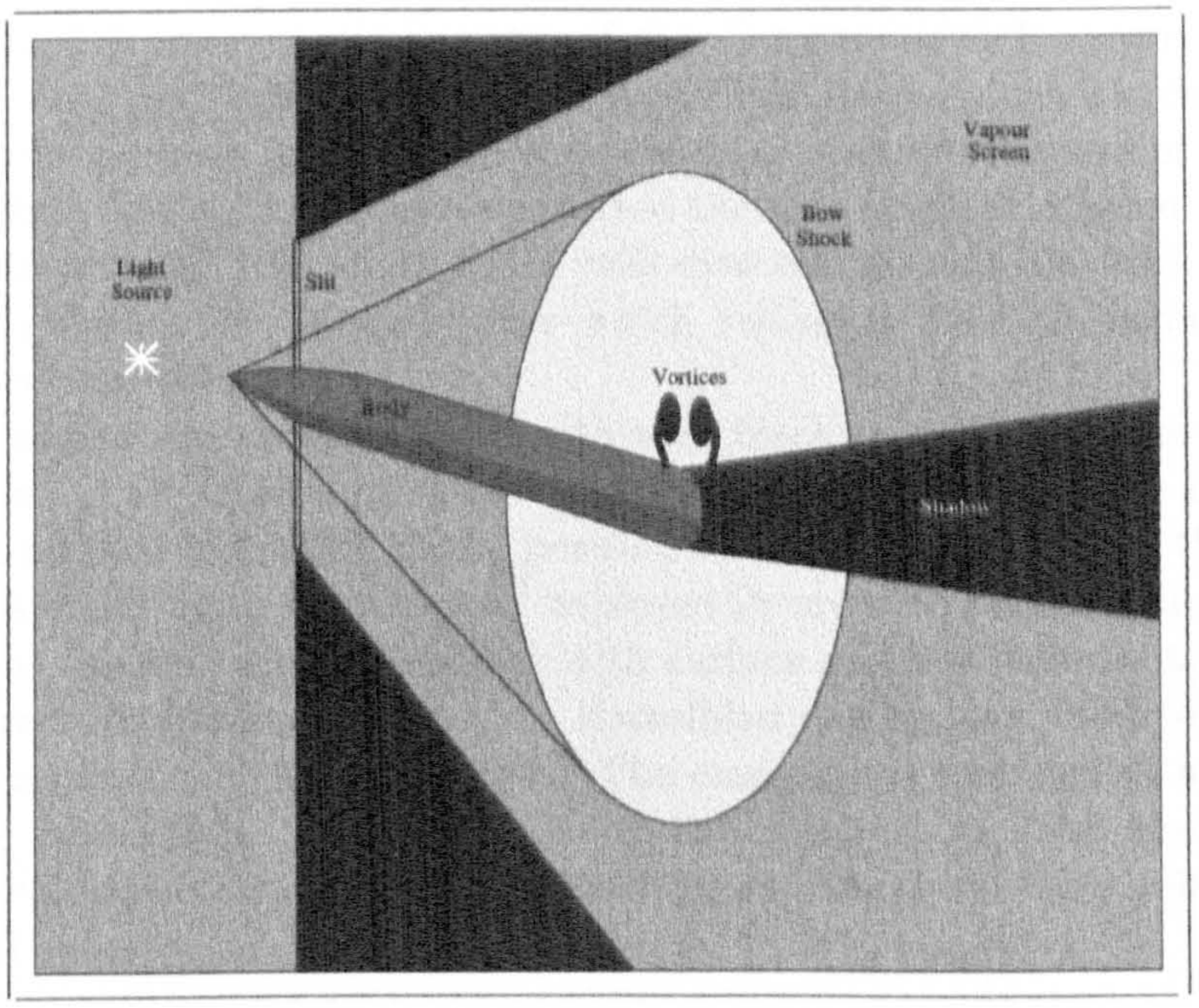

Figure 7.8: *The Vapour Screen Flow Visualization Technique*

Vortices intersecting the light sheet appear as dark spots in the flow field. It is suggested [43] that the centripetal acceleration due to spinning action in the vortices pulls the water droplets away from the core region resulting in reduced light scattering. Shock waves appear as light curves in the flow field due to the increased density behind the shock and thus increased light scattering.

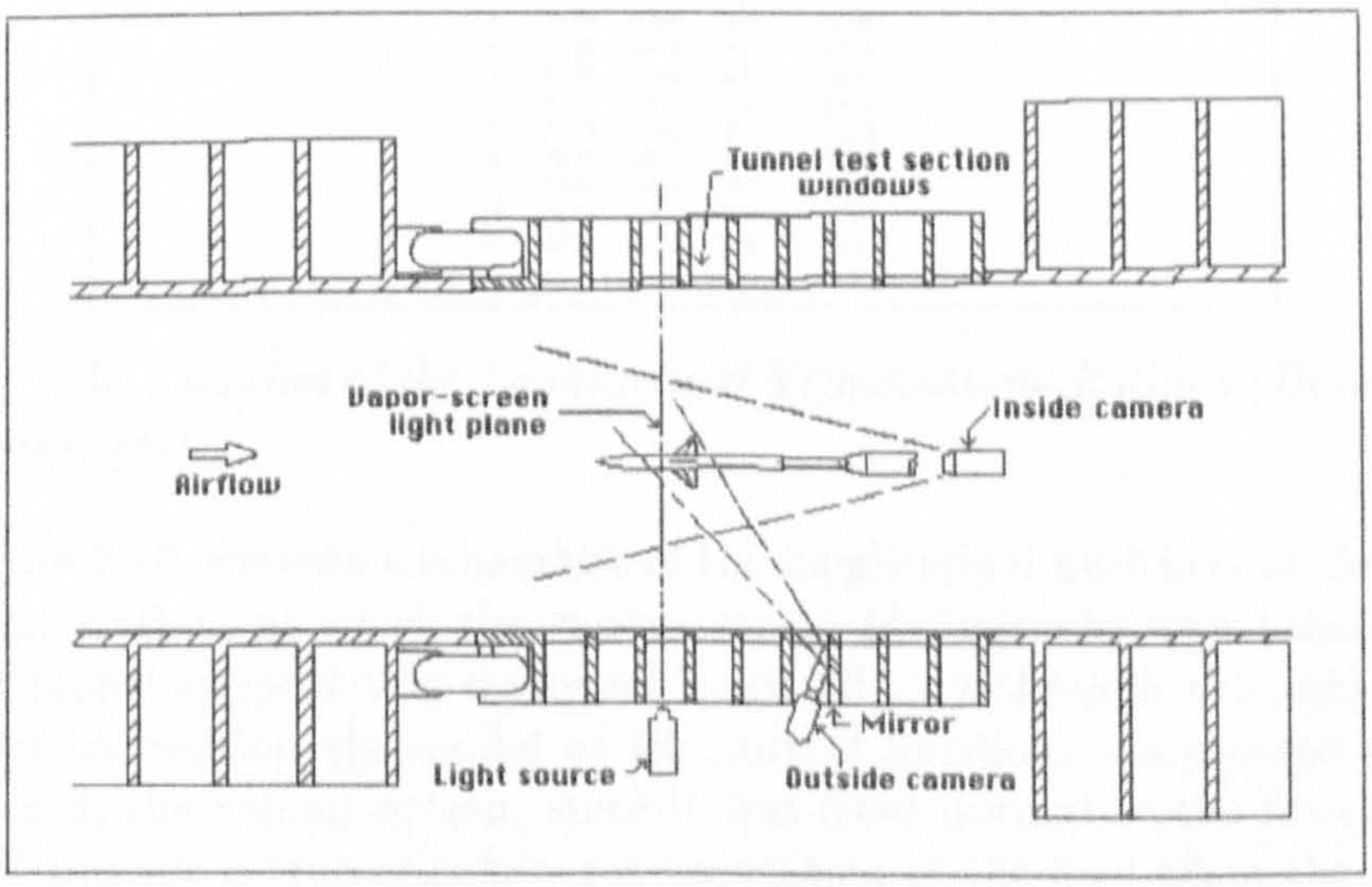

Figure 7.9: *Schematic of the UPWT Vapour Screen Setup [42]*

Figure 7.9 presents a schematic of the Langley UPWT vapour screen system. An Argon laser was employed as the light source which was delivered to an optics package attached to the test section window by means of a fibre-optic cable. The optics package converted the thin cylindrical beam of laser light into a broad thin sheet which was directed through the test section in an approximately vertical plane which remained fixed throughout the vapour screen tests.

The model was spray painted with mat black paint in order to reduce reflections of the laser light sheet. White dots were painted on the body to provide a visual indication of the position of the model relative to the light sheet. A small video camera was employed in order to position the model such that the light sheet coincided with surface markers in order to locate the correct longitudinal station. A Hasselblad camera was used to obtain photographic vapour screen images. The camera was installed in a cooled housing mounted in the tunnel approximately 12 inches from the tunnel ceiling just downstream of the test section and remained fixed relative to the light sheet.

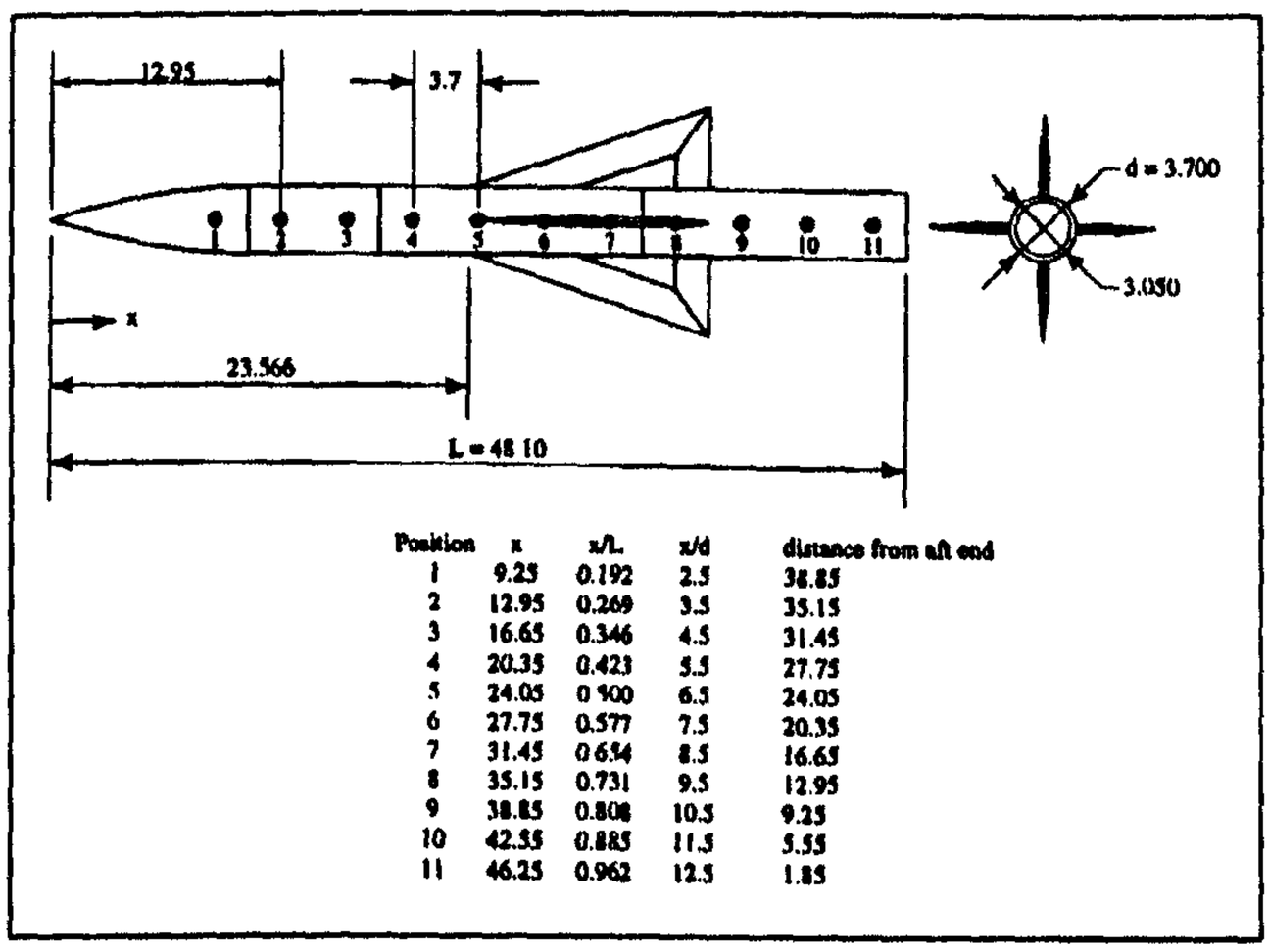

Position	x	x/L	x/d	distance from aft end
1	9.25	0.192	2.5	38.85
2	12.95	0.269	3.5	35.15
3	16.65	0.346	4.5	31.45
4	20.35	0.423	5.5	27.75
5	24.05	0.500	6.5	24.05
6	27.75	0.577	7.5	20.35
7	31.45	0.654	8.5	16.65
8	35.15	0.731	9.5	12.95
9	38.85	0.808	10.5	9.25
10	42.55	0.885	11.5	5.55
11	46.25	0.962	12.5	1.85

Figure 7.10: *Location of the Longitudinal Visualisation Stations (Dimension in Inches) [84]*

Figure 7.10 presents a schematic of the longitudinal positions of the visualisation stations at which the vapour screen photographs were taken. The tunnel model support was traversed longitudinally through the light sheet in order to position the model at the correct location. As pointed out in Chapter 6, the vapour screen, since it was fixed normal to the freestream, did not provide a true crossflow representation of the flow when the model was pitched. The photographic camera was also positioned obliquely to the light sheet. The vapour screen flow visualisation study is, therefore, a

qualitative study employed only to visualise the flow structure and not to spatially locate individual features by measurement.

Oil Flow Visualisation

Ultra-Violet oil flow visualisation was also performed in order to obtain more insight into flow separation and surface effects due to shock waves and vortices. The results of this study are omitted due to problems with the photographic output.

7.2.4 Experimental Procedure

Force and Moment Measurement

The longitudinal aerodynamic coefficients (C_L, C_D, C_M, C_N and C_A) were measured in order to analyse the longitudinal characteristics of the configuration and as a means to check repeatability to determine if the day to day fluctuation in data was significant compared to short term variations.

Data was obtained first at 0^o angle of attack, α, and then the model was pitched down to $\alpha = -4^o$ where data was taken. The model was then pitched from -4^o up to 18^o angle of attack, taking data at 2^o intervals in a pitch/pause manner in order to allow time for the model to stop any pitch induced vibration. The angle of attack was then reduced back down to -4^o, taking data at 2^o intervals in a similar fashion. The longitudinal characteristics were measured for the three configurations: the body alone, the body/wing at zero roll and the body/wing at 45^o roll.

Schlieren Study

Schlieren photographs were taken during the force/moment measurement runs for $0^o, 4^o, 8^o$ and 14^o at each of the three configurations.

Vapour Screen Study

Vapour screen photographs were taken at each of the longitudinal visualisation stations at angles of attack of $4^o, 8^o$ and 14^o for the three configurations. The same pitch/pause technique was employed as used in the force/moment runs.

Flow Condition Investigation

The boundary layer flow condition was investigated by performing force/moment measurement and vapour screen visualisation runs for the body alone with grade 45 sand grit glued in a narrow strip around the nose approximately 3 inches from the nose apex.

7.3 The Numerical Study

A computational study was performed in conjunction with the experimental program in order to investigate the supersonic flow structure around cruciform wing missile configurations in more detail, and assess the capability of CFD to accurately predict such flows. The CRANS3D multiblock solver was employed to compute the Mach 2.5 flow over the B1AW20A3 configuration at 8° and 14° angle of attack and for roll angles of 0° and 45°.

7.3.1 Block Topology and Grid Generation

It was decided to use a similar grid topology as was employed by Lijewski [30] and later by Pluntze et al [50]. The EAGLEView grid generation package was employed to develop a series of multiblock grids. Two grids designed for Euler computations were developed, one for 0° roll and another for 45° roll. Two more grids were developed for laminar computations for the two roll cases and a further two grids generated for turbulent computation.

The block topologies employed in the study are illustrated in Figures 7.11 and 7.12. The topology of the grid in the crossflow plane is shown in Figure 7.11. The symmetric nature of the geometry/flow means that, as with the forebody investigations, only half of the flowfield needs to be computed, with symmetric boundary conditions applied to the appropriate symmetry planes. The crossflow is then split radially, out from the sharp wing tips, and circumferentially from the wing leading edge and from the ridge in the wing cross-section. The crossflow is therefore decomposed into six blocks for the + configuration and nine blocks for the × configuration.

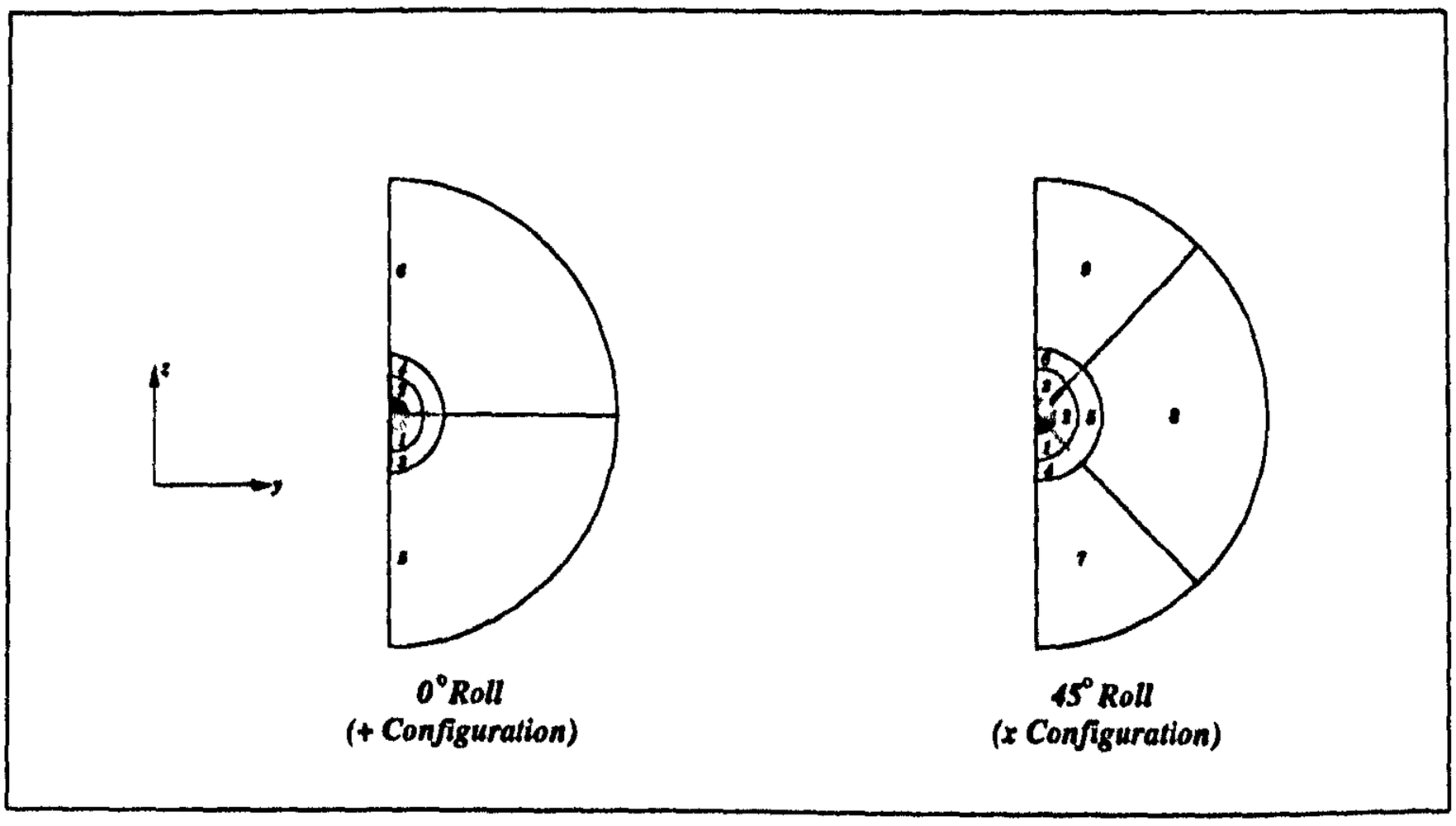

Figure 7.11: *Block Topology, Forward View*

Figure 7.12 presents the block topology in the xz-plane for the + configu-

ration case and highlights the longitudinal decomposition which is common to both roll configurations. The result is a grid with 22 blocks for the zero roll case and 33 blocks for the 45° roll configuration.

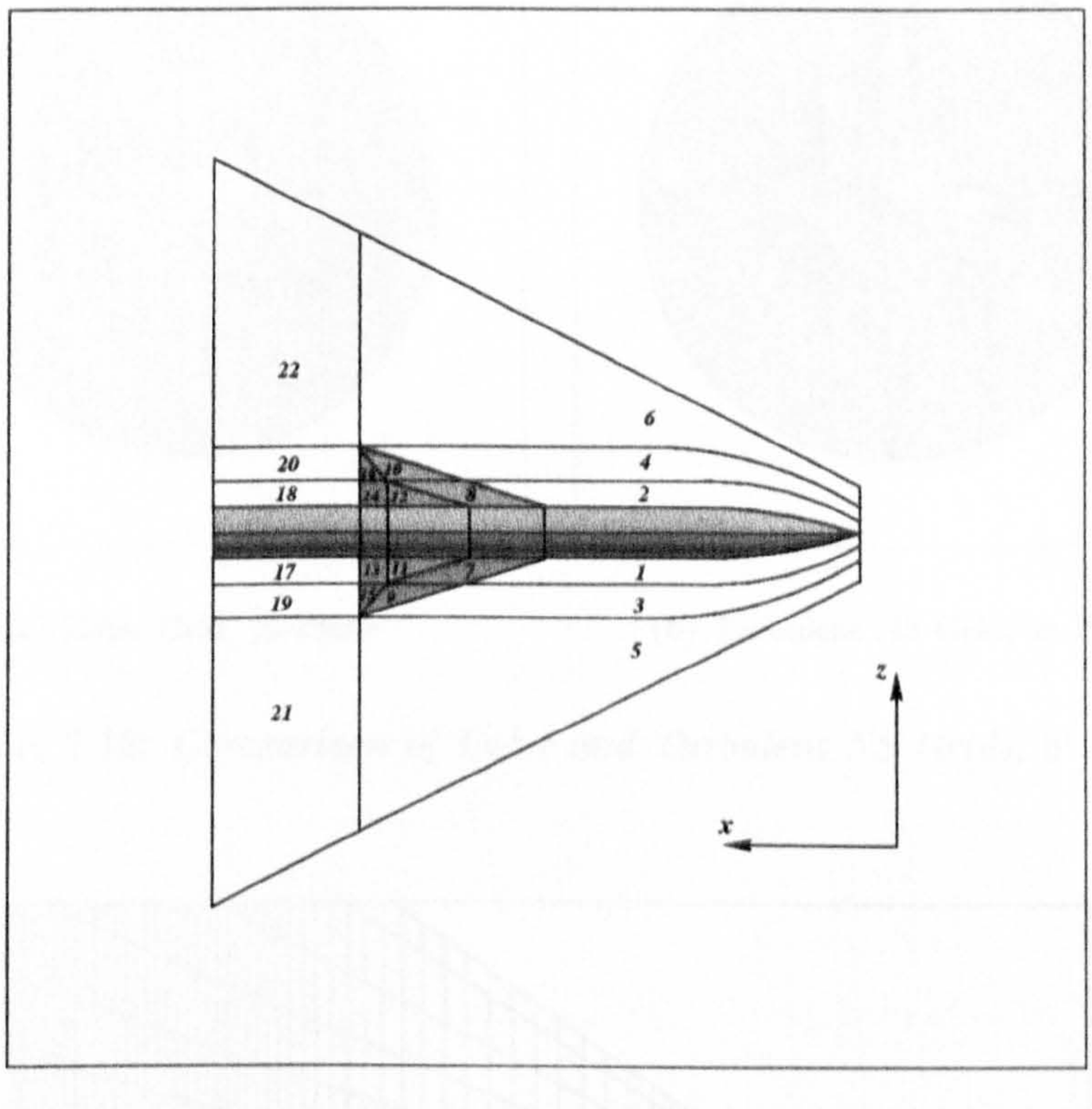

Figure 7.12: *Block Topology, 0° Roll Case, xz-Plane*

Figure 7.13 compares the Euler and turbulent grids, plotting the crossflow plane grids of the inner blocks around the wings. The viscous and inviscid grids differ only in the number of cells and the clustering employed in the radial J-direction and the circumferential K-direction. All of the grids have the equivalent number of cells and the same clustering in the I-direction. The wall normal thickness of the first cell adjacent to a solid boundary (ie: the body and wing surfaces) was set as $6 \times 10^{-3}D$ for the Euler grids and $8 \times 10^{-6}D$ and $5 \times 10^{-6}D$ for the laminar and turbulent grids respectively. A further 30 points were introduced to the radial index for the viscous grid, and maintaining the radial size of the cell JN with a *tanh* clustering function ensured that a much finer grid resolution was achieved at the body surface. A similar approach was used for the K-index where a further 30 points were introduced.

Figure 7.13 presents the turbulent NS grid for the zero roll case, in the xz-plane (ie: the leeward and windward symmetry planes). The total size of the grids, combining all of the blocks together, was 579,000 cells for the Euler grids and 1,254,000 cells for the viscous grids.

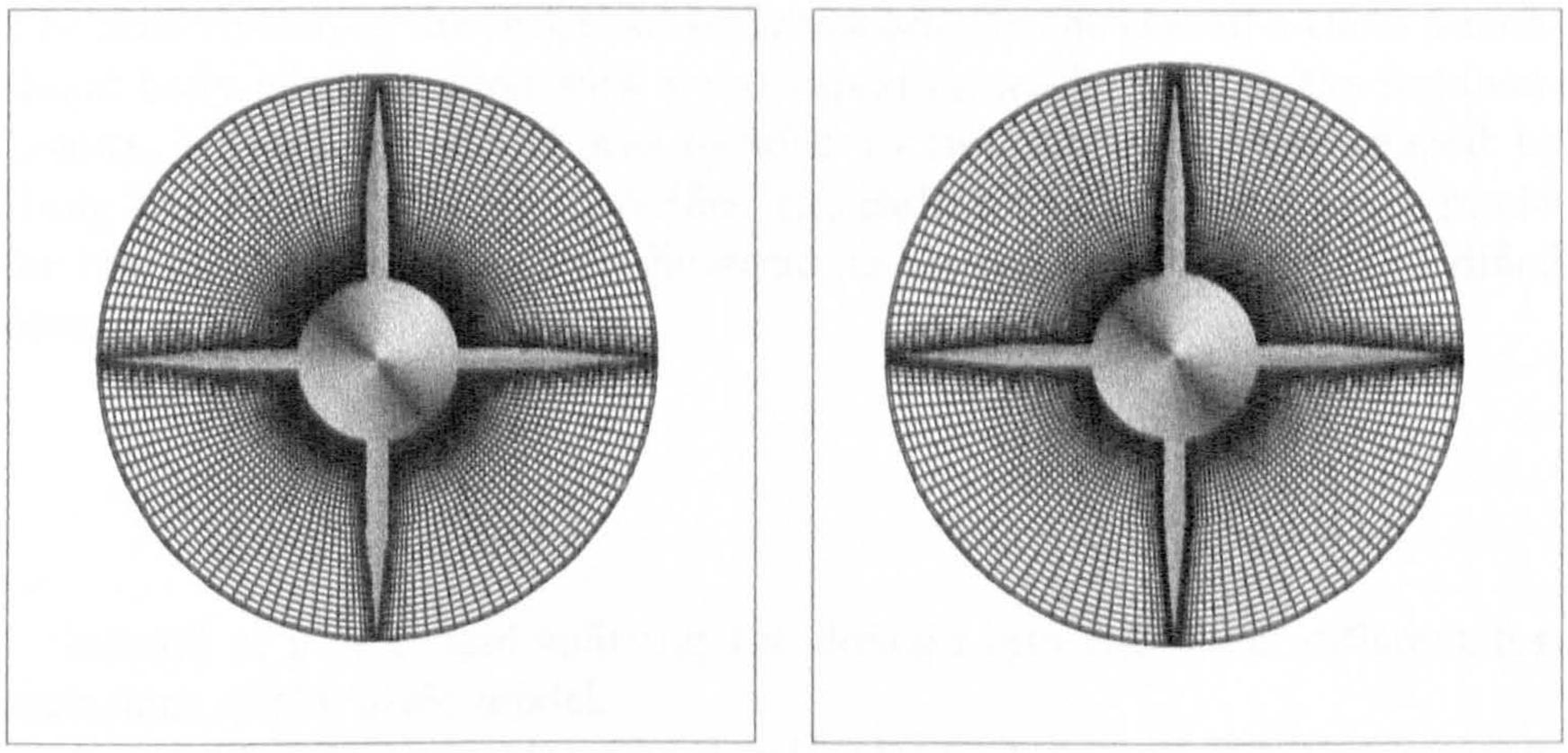

(a) Euler Grid, yz-Plane

(b) Turbulent NS Grid, yz-Plane

Figure 7.13: *Comparison of Euler and Turbulent NS Grids,* 0^o *Roll*

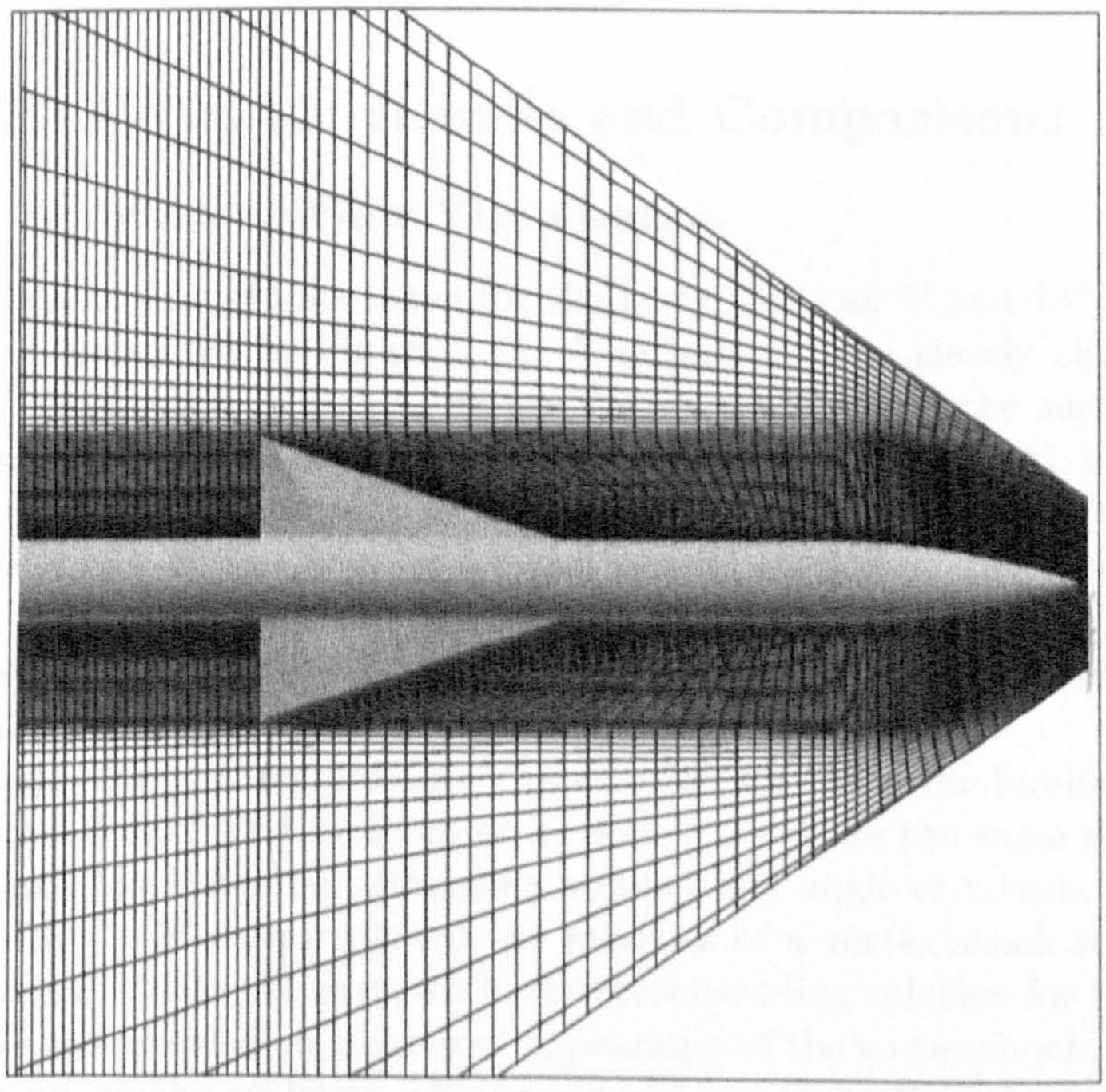

Figure 7.14: *Turbulent NS Grid,* 0^o *Roll, xz-Plane*

7.3.2 Turbulence Modelling Issues

The prescription of the turbulent eddy viscosity in the case of a three dimensional body-wing junction with a zero-equation model such as the Baldwin-Lomax, is complicated. It was decided to test the method developed by Hung and Buning [25] who modified the Baldwin-Lomax turbulence model for the application of a three-dimensional corner flow, using the modified distance:

$$\eta = \frac{2yz}{y + z + (y^2 + z^2)^{\frac{1}{2}}}$$

instead of y or z, and splitting the domain into regions of different formulations of the basic model.

A simplification was also tested, whereby turbulence modelling was employed only to capture the correct forebody and afterbody boundary layer profiles and corresponding smooth surface separations. The assumption in this case is that, since the delta wing studies of Chapter 6 showed that turbulent boundary layers have only a minor affect on the secondary flowfield, little difference will be perceived in the body/wing flow structure with and without turbulence modelling on the wings.

7.4 B1AW20A3: Results and Comparisons

7.4.1 Body Alone Flow Visualisation

The schlieren photographs taken for the body alone at 8° and 14° angle of attack are presented in Figure 7.15. The photographs clearly show both the bow shock wave and the primary vortex core leaving the surface and streaming off above the body. Additional features are also evident, including a wave appearing on the top of the body emanating from the position of the intersection of the first (nose) and second section of the model, two features corresponding to the intersection of the second and third sections and another wave further downstream emanating from the intersection of the third section and the base section.

The body alone cases presented here correspond with the forebody test-cases 5 and 6 described in Chapter 4, that is, they are the same geometry at the same Mach number, Reynolds number and angle of attack. The NS solution for the 8° case indicated the presence of a vortex shock streaming under the body near the base, while the corresponding solution for 14° angle of attack case revealed no windward appearance of the vortex shock. Further examination of the schlieren photographs shows that the wave emanating from the rearward intersection appears, at $\alpha = 8°$, much more pronounced than the others and much stronger than the corresponding feature seen at

$\alpha = 14^o$ where it is hardly evident. The feature also manifests itself very clearly above the body at 8^o angle of attack, while at 14^o it is not visible at all.

It is possible that the under-surface detachment of the vortex shock is coincident with the intersection of the two rearward model components. This is speculation, however, and further evidence must be provided to prove or disprove the theory.

Figures 7.16 and 7.17 present the results of the body alone vapour screen study of the longitudinal development of the leeside body vortices. The 8^o angle of attack results are reproduced in Figure 7.16 which shows, at $x/D = 5.5$, the light ring around the body which is the bow shock wave. The body and its black shadow can clearly be seen as can the developing primary vortex structure. The vapour screen photographic technique is not sensitive enough to capture the small secondary features. The CFD study of forebody testcase 6 showed that there was no formation of any crossflow primary separation shock for the 8^o angle of attack case and this result agrees with Figure 7.16 where no such feature is evident. In addition, no vortex shock is evident which would be seen circling round the primary vortex structure as demonstrated in Figure 4.74. This is not surprising since the vapour screen technique only captures the strong bow shock wave very faintly.

Figure 7.17 presents the results of the vapour screen study of the body alone at 14^o angle of attack. At $x/D = 5.5$ the primary vortices are seen to be well developed and a crossflow separation shock is evident. Further downstream the primary vortices are seen to have moved further leeward away from the body and the crossflow shock can still be discerned curving out a considerable distance into the freestream in a manner similar to that shown in Figure 4.74. The primary vortex development shown in Figure 7.17 can be compared with its computational equivalent, Figure 4.54. The qualitative agreement between computation and experimental vapour screen is seen to be very good.

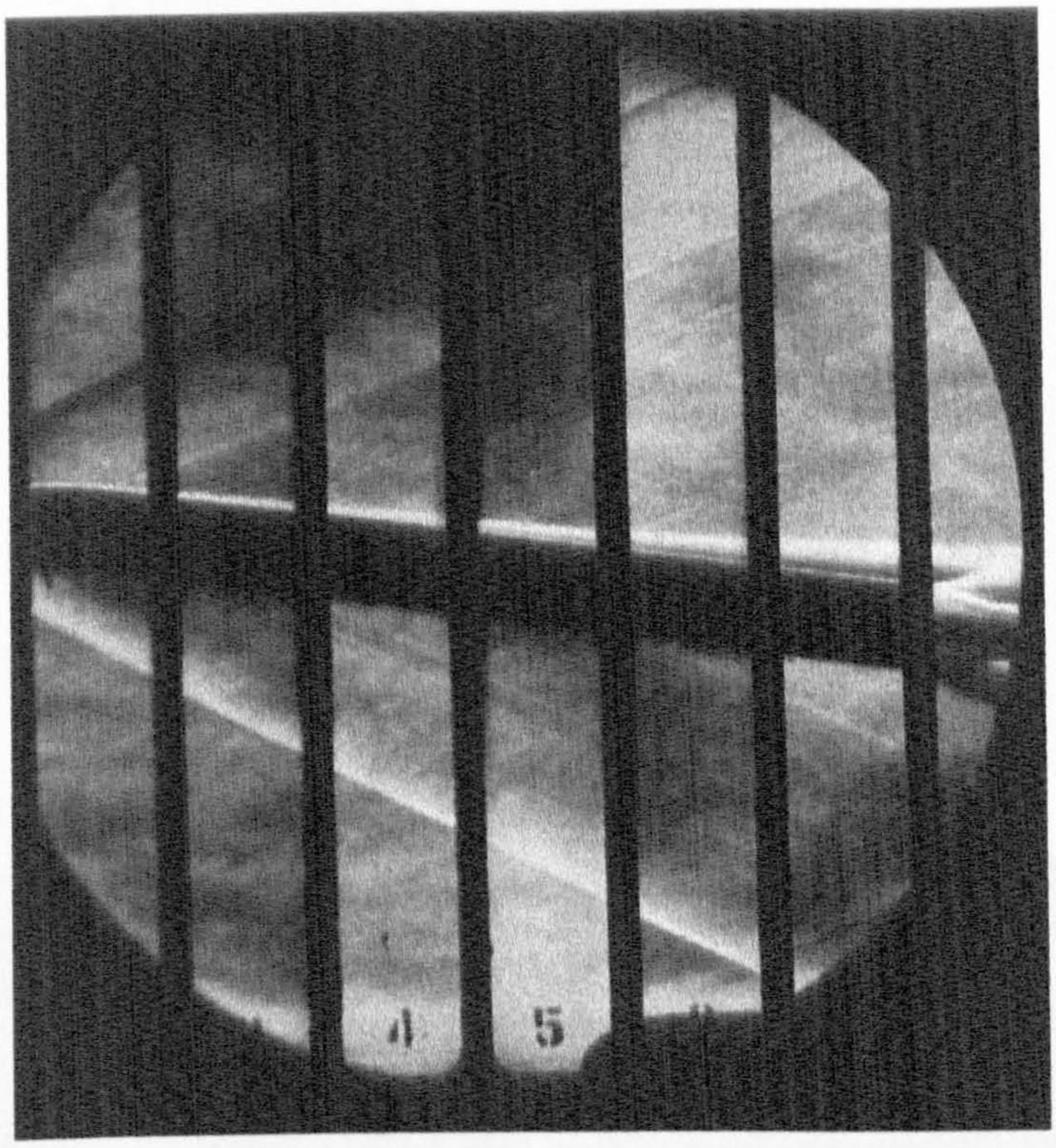

(a) 8° Incidence

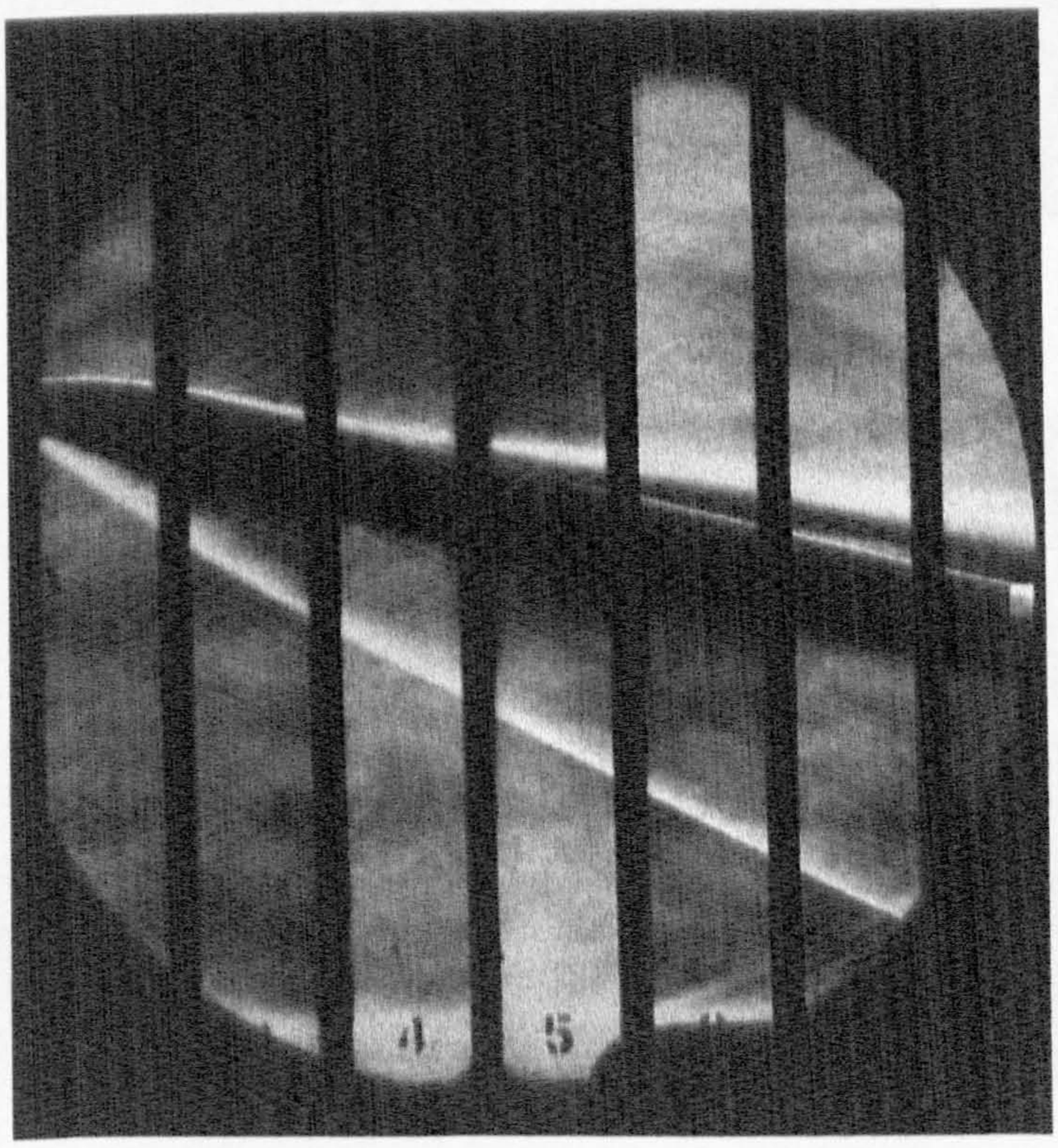

(b) 14° Incidence

Figure 7.15: *Body Alone: schlieren Photographs,* 8° *and* 14° *Incidence*

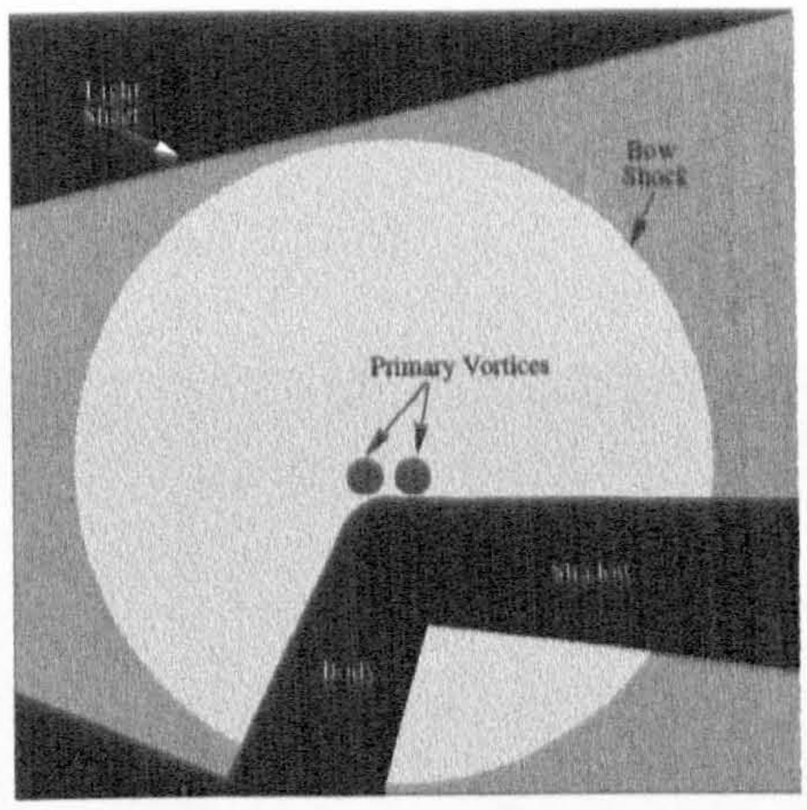

(a) General Interpretation

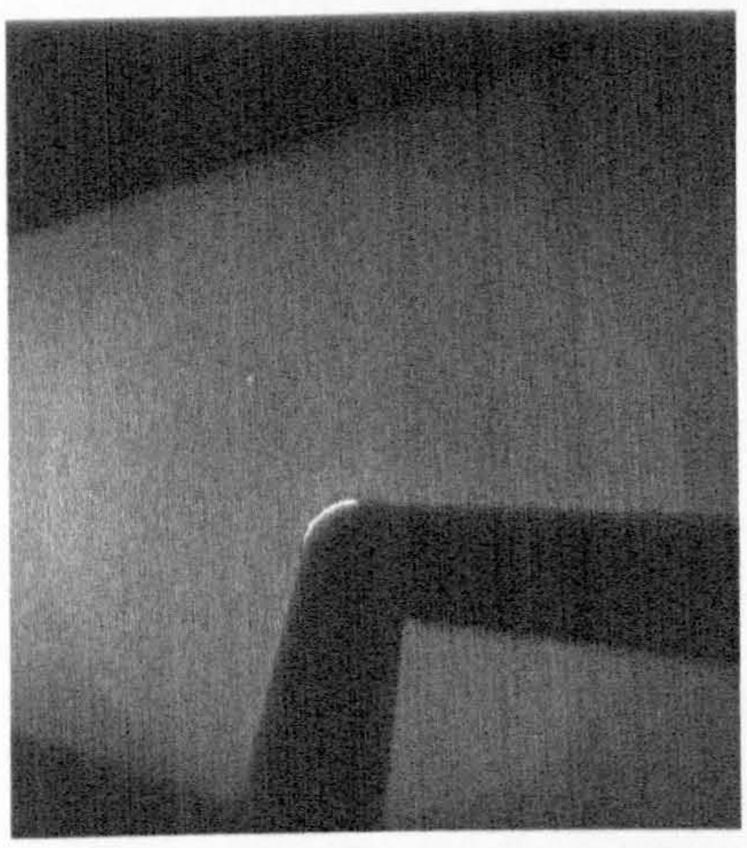

(b) $x/D = 5.5$

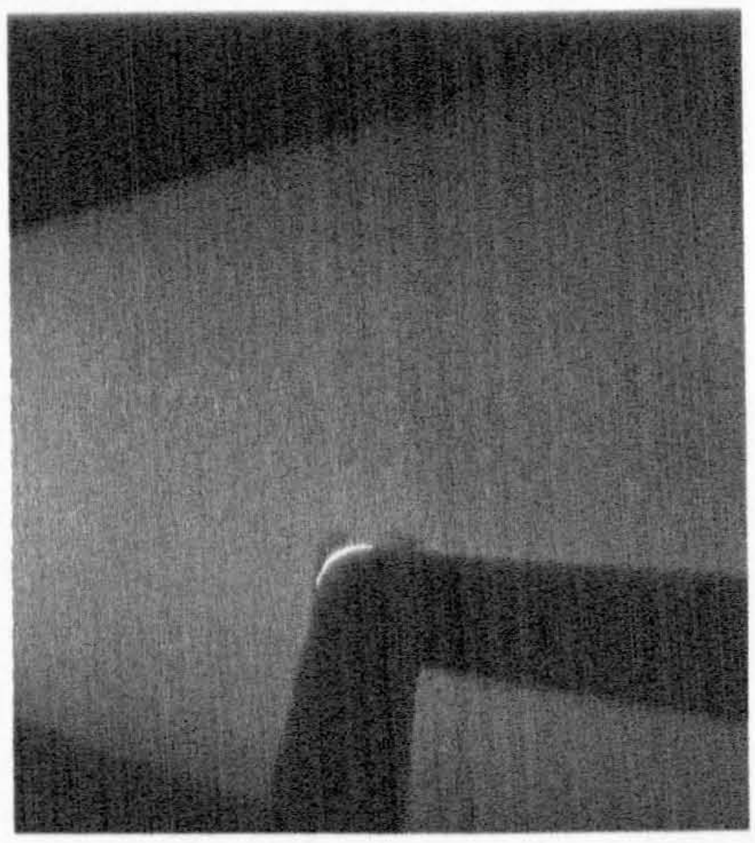

(c) $x/D = 7.5$

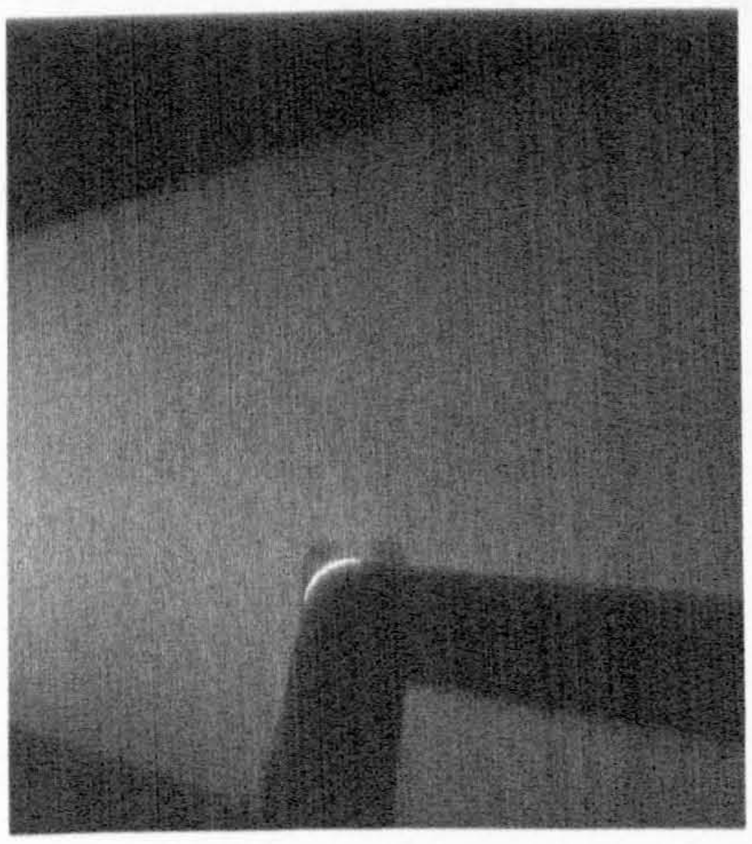

(d) $x/D = 9.5$

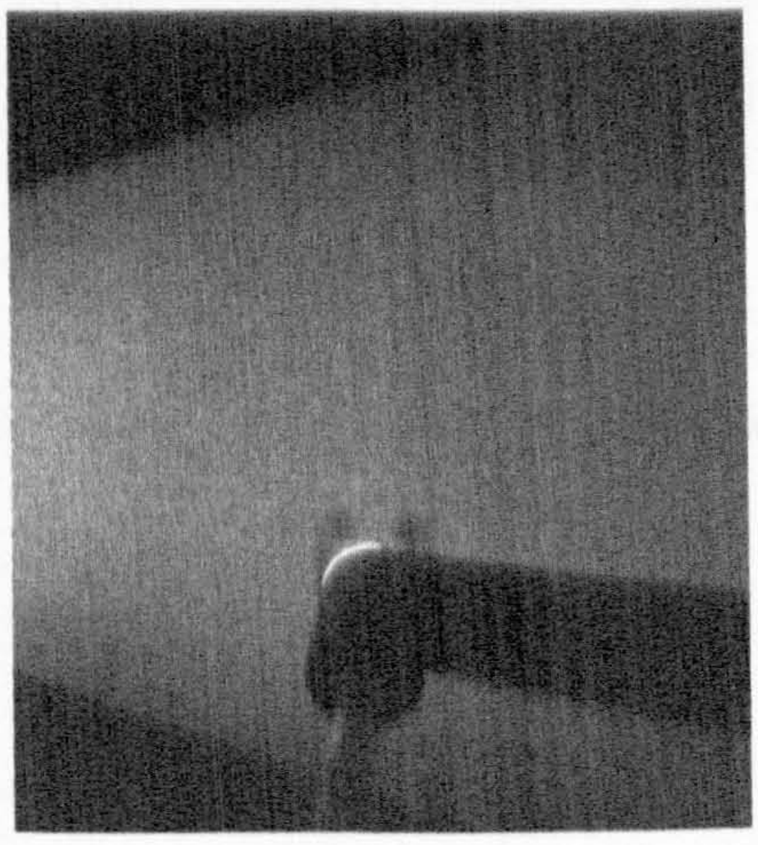

(e) $x/D = 11.5$

Figure 7.16: *Body Alone: Vapour Screen Photographs, 8° Incidence*

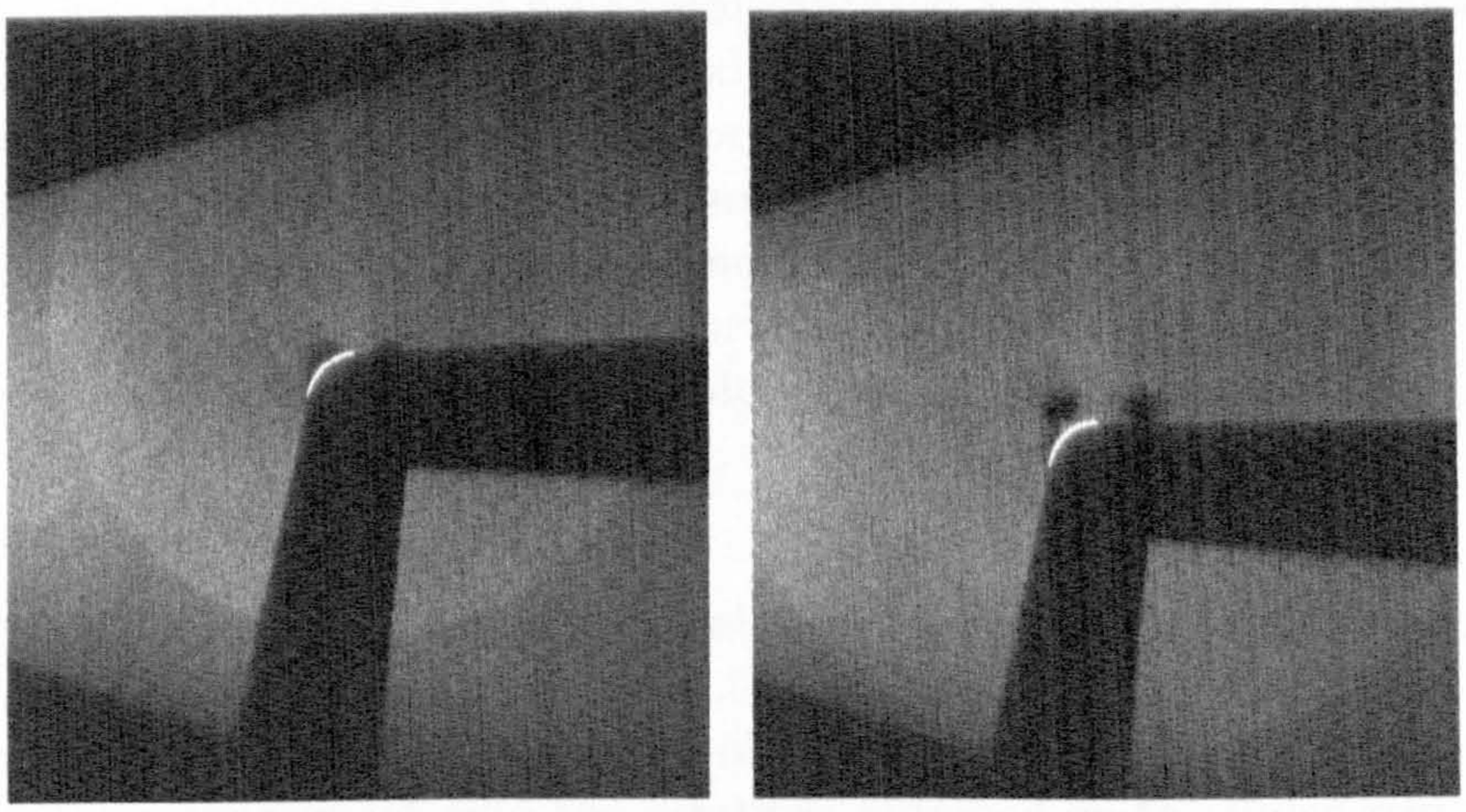

(a) $x/D = 5.5$

(b) $x/D = 7.5$

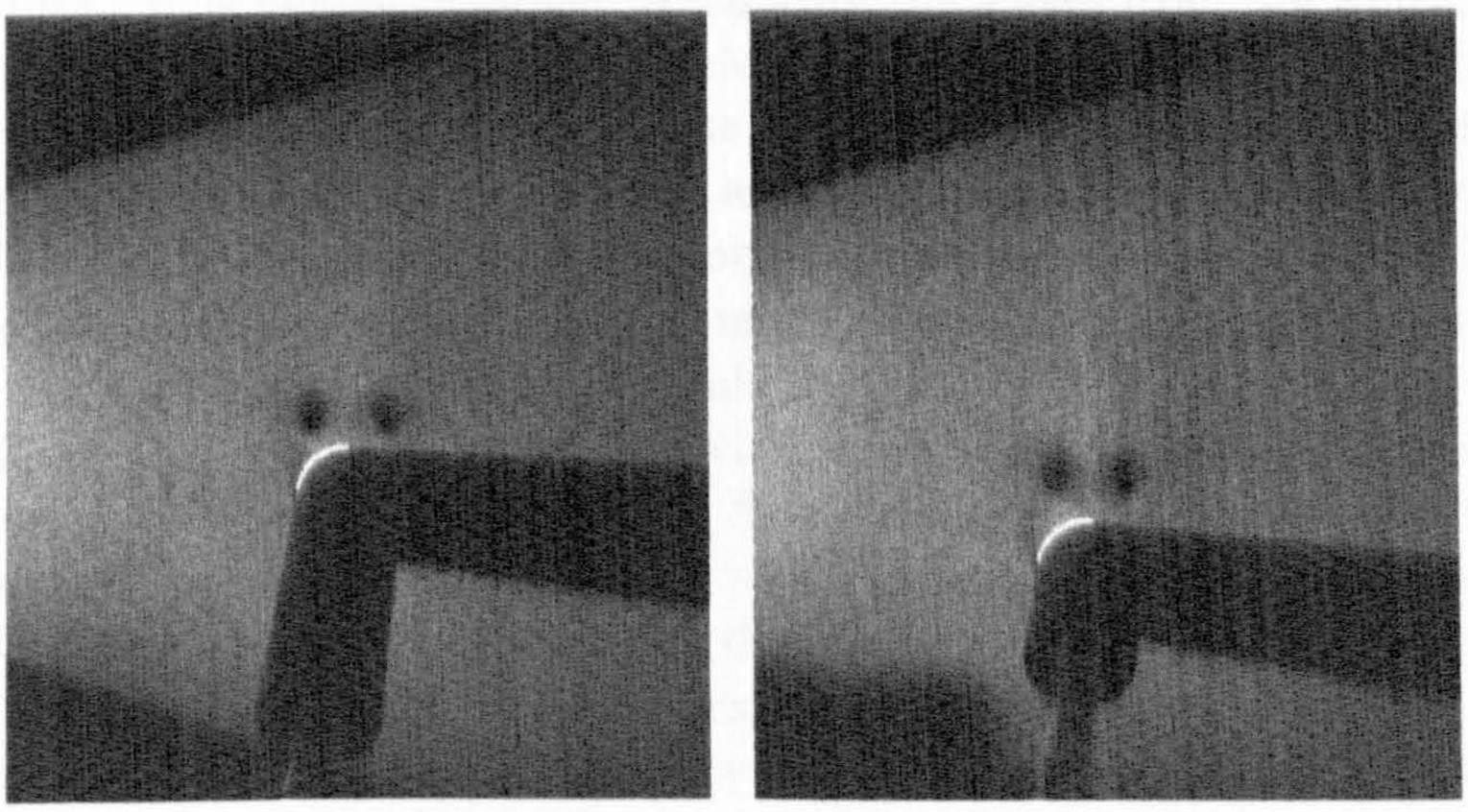

(c) $x/D = 9.5$

(d) $x/D = 11.5$

Figure 7.17: *Body Alone: Vapour Screen Photographs,* 14^o *Incidence*

7.4.2 B1AW20A3 Zero Roll Investigation

In conjunction with the experimental program, several computations were performed for the 8^o and 14^o angle of attack cases. The Euler grid was used to obtain both an inviscid solution and a laminar NS solution. The NS grids were employed to generate both laminar and turbulent solutions. Although the laminar solutions on the Euler grid captured 3-4 points in the boundary layer they did, however, generate good solutions compared with experiment and correctly resolved the appearance of all the large crossflow structures. The investigation of the turbulence modelling issues showed that there were no appreciable differences between modelling turbulence on the body and over the wings, and just modelling turbulence on the body alone. The only difference was a slightly larger wake downstream of the vertical wings.

8^o Angle of Attack

Figure 7.18 compares the experimental measurements of total pressure ratio [9], at a crossflow plane $x/D = 11.5$ in the wake of the cruciform wing structure, with the numerical results obtained from CRANS3D. Figure 7.18 a) compares experiment with the solutions obtained on the Euler grid. The Euler solution appears to predict the flowfield surprisingly well, capturing the leading edge vortex from the horizontal wing and the overall inviscid flow structure . It is unable, however, to capture the wakes from the wings, any smooth separation and resulting vortices or the double trailing edge vortex system. The laminar solution on the Euler grid, however, resolved all of the large flow structures observed in experiment including the body vortex and the swept-wing shock induced vortex (described in section 7.4.4). The latter feature, however, is observed much closer to the windward vertical wing than experimental evidence would suggest.

Figure 7.18 b) presents the fine viscous computational results in comparison with experiment. What is at first striking is the similarity between the laminar and turbulent solutions, which in fact appear to be equivalent. Both solutions correctly capture the double vortex system emanating from the horizontal wing, the body vortex and the swept-wing shock induced vortex, together with the inviscid flow structure. The difference in the two solutions lies in the slightly different strengths of the vortices and a slightly more extensive wake from the vertical wings. Although both solutions captured the body vortex, it appears much smaller than the feature measured in experiment. The experimentally measured double vortex system appears as two separate and distinct vortices, with the inner (leading edge) vortex having a crossflow shock feature sat above it. The computationally resolved feature, however, although it does predict two vortices, has them merged closer together such that they are almost indistinguishable from each other. The strength (core suction) of the two NS resolved vortices is less than

measurement would suggest, although the turbulent solution does predict a weak crossflow shock above the leading edge vortex. The double vortex system is described in section 7.4.4.

Figure 7.19 presents the experimental schlieren photographs and the corresponding plot of computed symmetry plane density contours together with body skin friction lines. The schlieren photograph, being a view through the whole 3D flowfield, appears somewhat messy downstream of the wings. The computed skin friction pattern under the horizontal wing clearly shows the separation line due to the effect of the windward leading edge shock generated by that wing. The skin friction lines also indicate the shock induced upwash behind the horizontal wing trailing edge and the development of a primary separation line over the rearward portion of the afterbody. The horizontal wing leading and trailing edge shocks are clearly visible in the schlieren photograph, streaming off behind the wings. The computational solution also captures the effect of these shock waves on the leeward and windward symmetry planes downstream of the wings, where they interact with the low density wake from the vertical wings.

Figure 7.20 plots the density contours looking downstream in the xz-plane, with the skin friction lines calculated on the leeside of the wings. The bow shock wave and those generated by the horizontal wings are clearly visible as are the wakes from the wings and the affect of the vortex system. The skin friction pattern highlights the primary reattachment as well as the secondary separation and reattachment lines, and appears similar to that calculated for the 8^o angle of attack NASA case. This is to be expected since both cases were shown to be occupy similar positions on an $\alpha_N - M_N$ plot, both being subsonic leading edge cases.

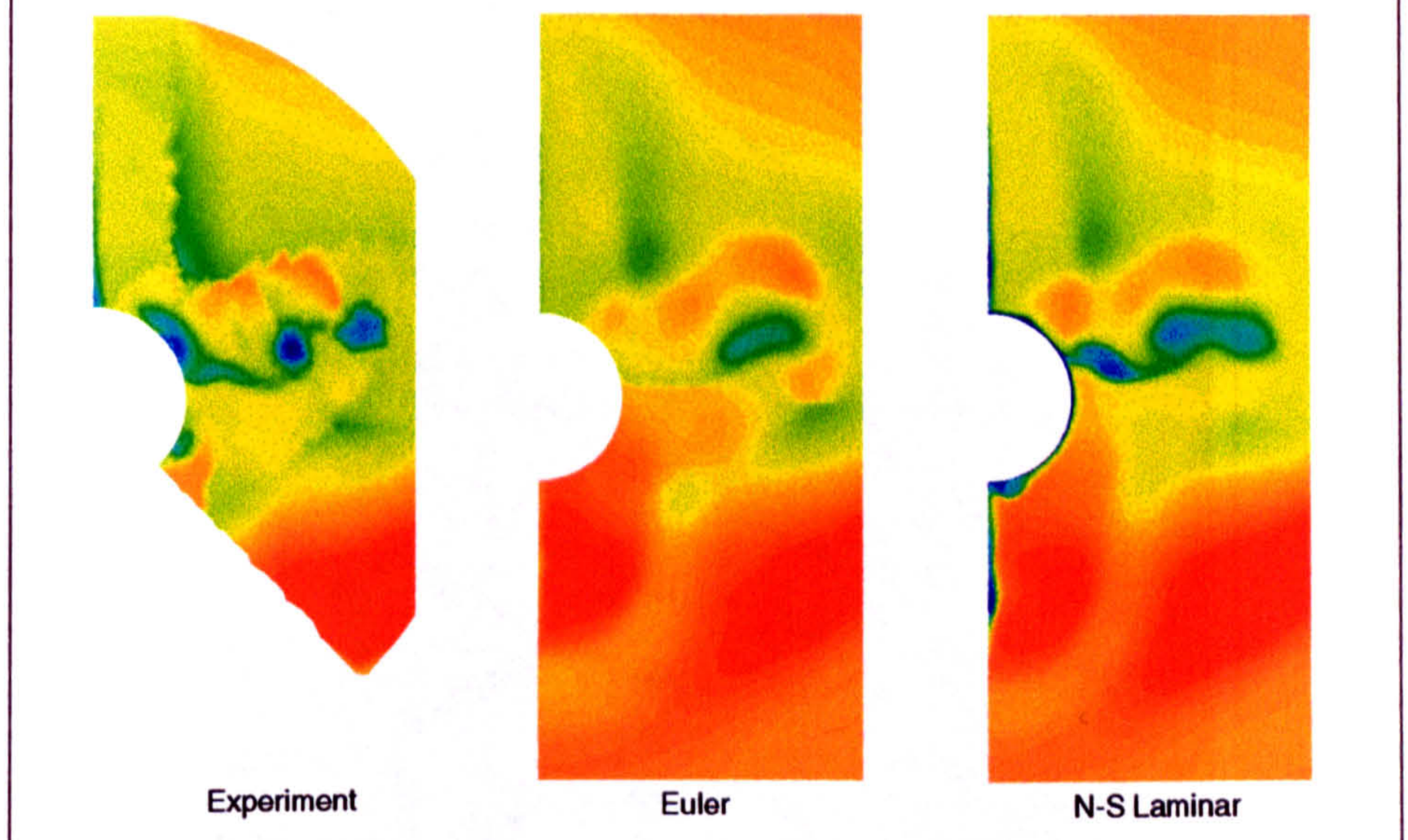

(a) Euler Grid Solutions

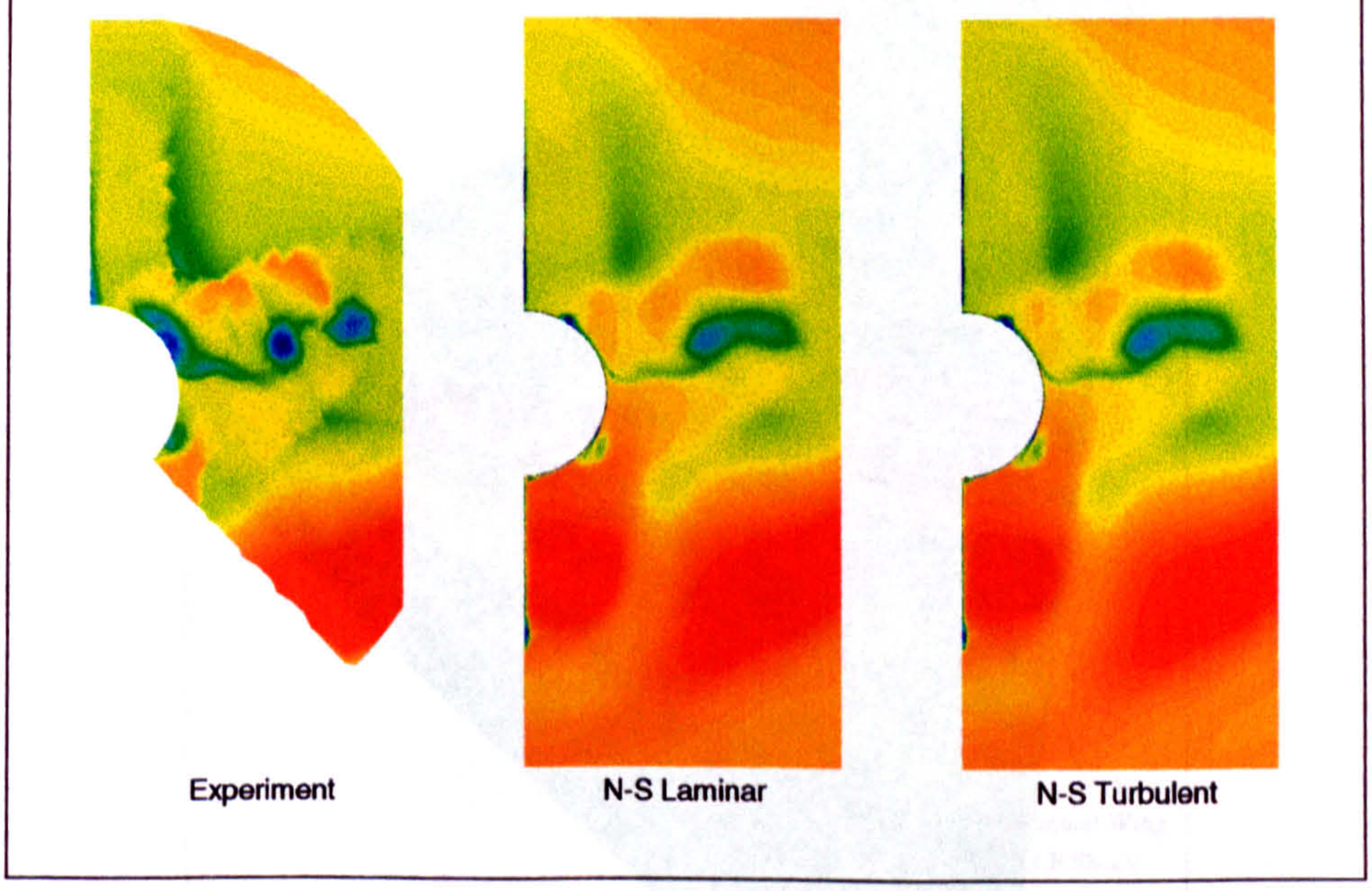

(b) NS Grid Solutions

Figure 7.18: *Total Pressure Ratio Contours Comparison, 0° Roll, x/D=11.5, 8° Incidence*

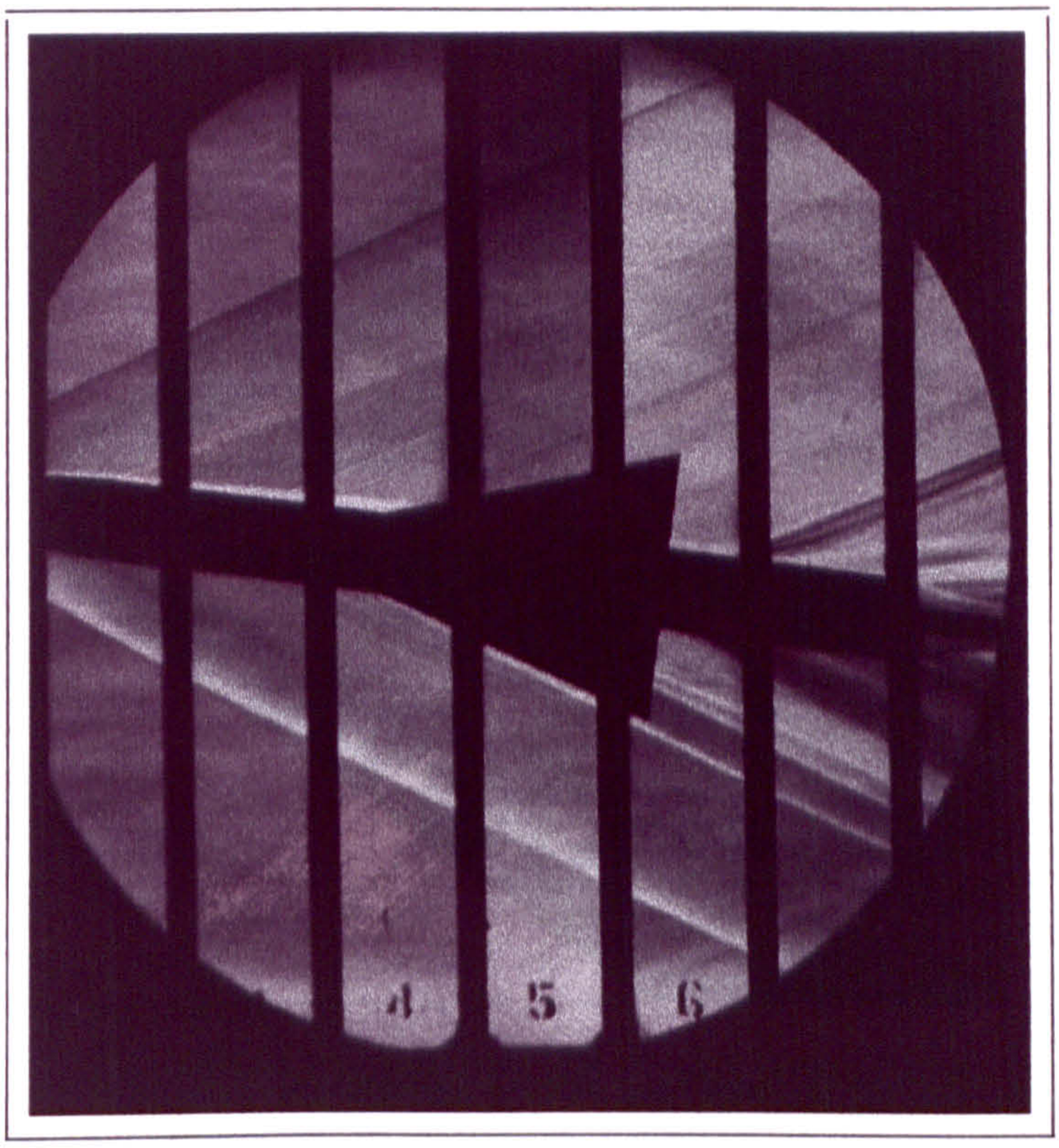

(a) Experimental schlieren

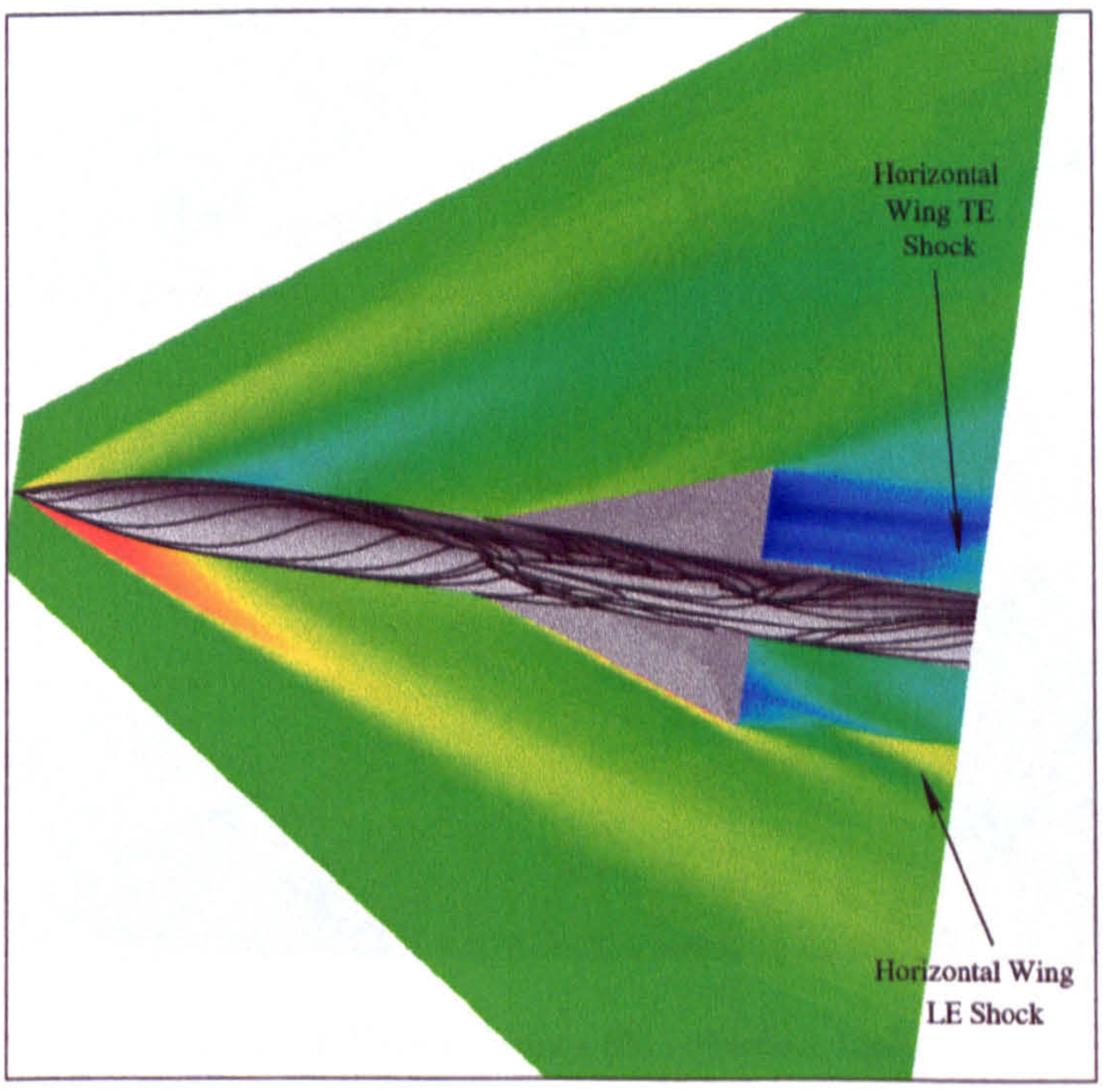

(b) Symmetry Plane (xz-Plane) Density Contours

Figure 7.19: *Computation vs Experimental schlieren,* 0° *Roll,* 8° *Incidence*

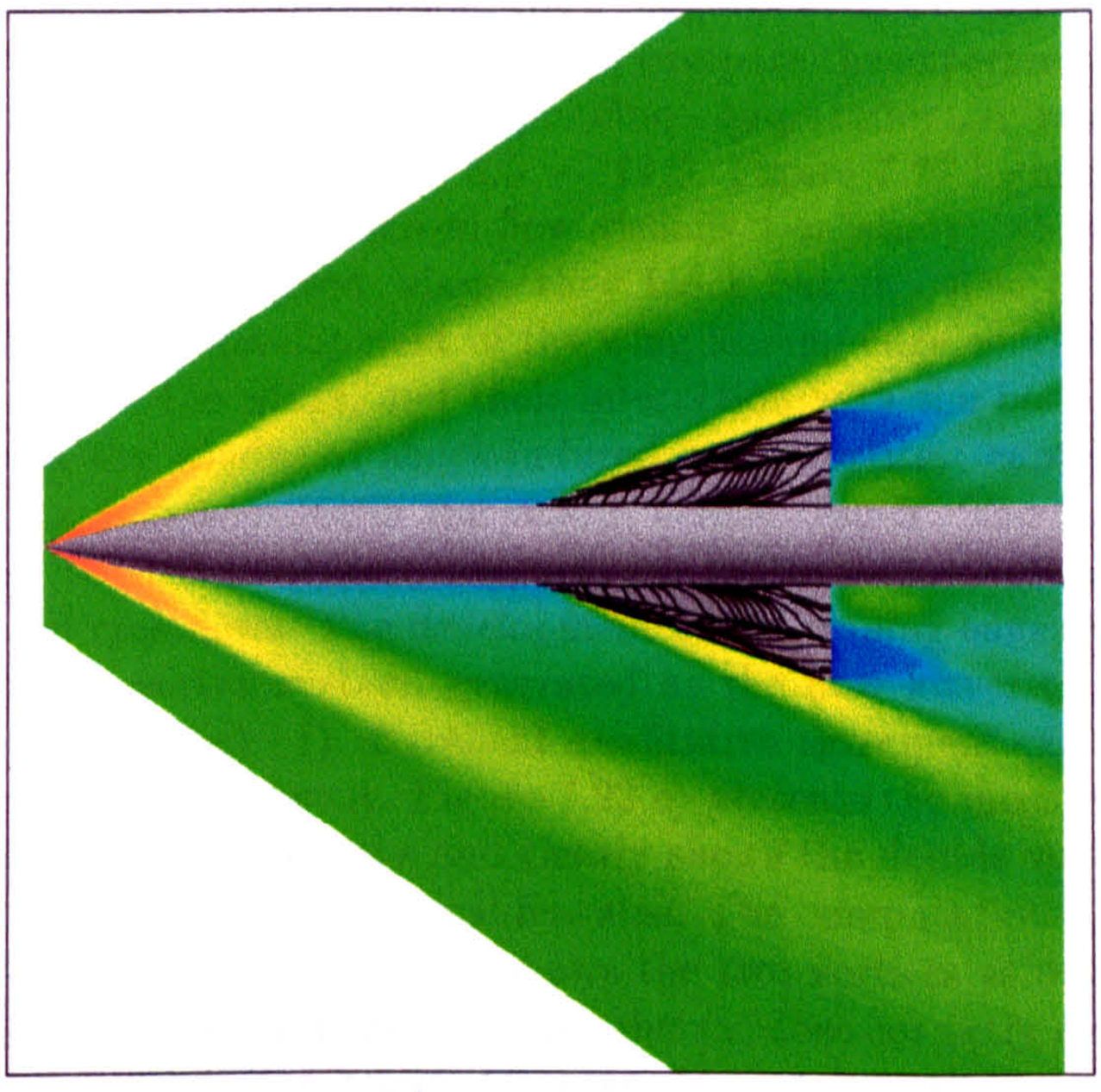

(a) Density Contours (xz-Plane)

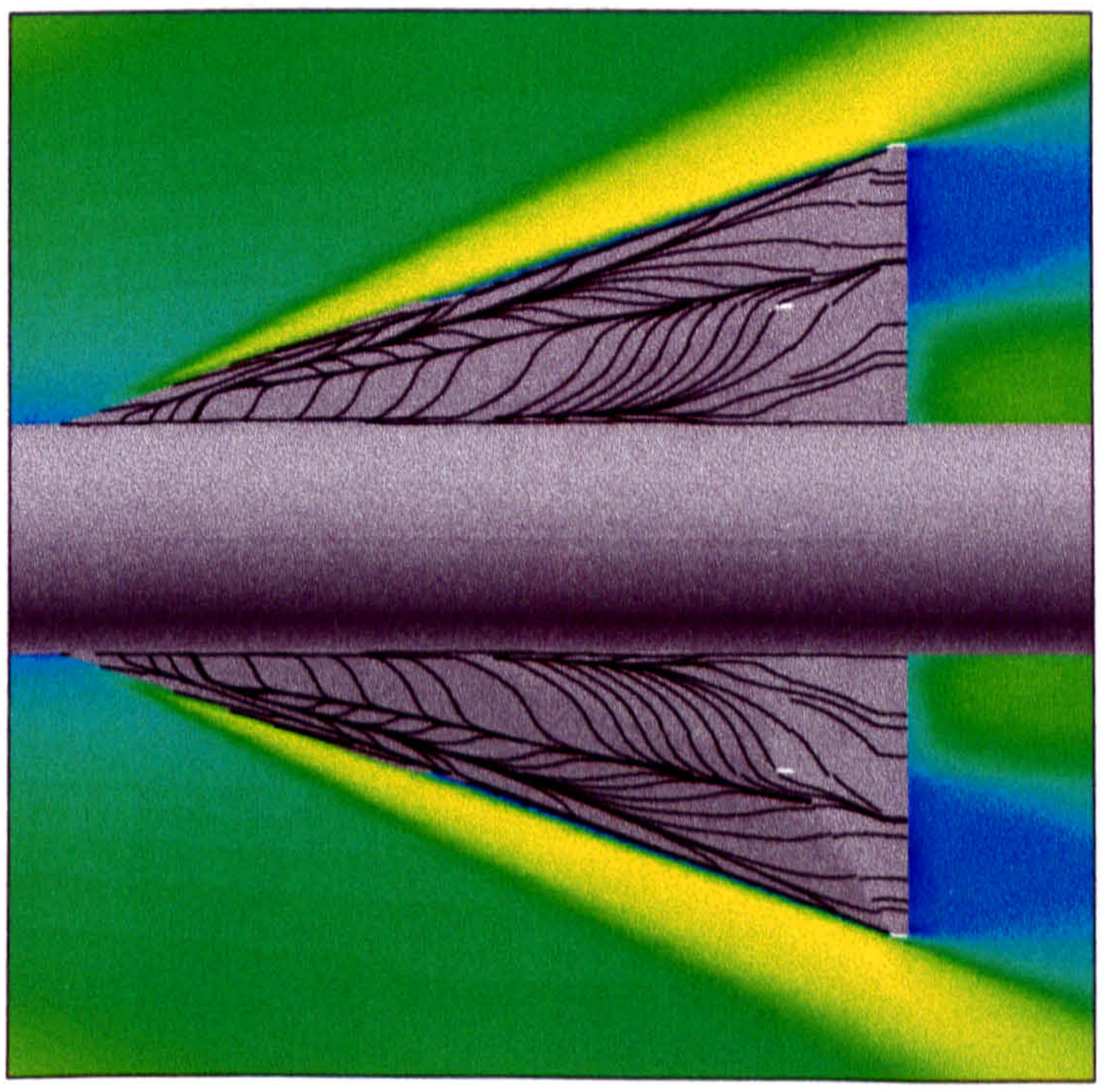

(b) Wing Upper Surface Skin Friction Lines

Figure 7.20: *Computational Solution (xz-Plane), 0° Roll, 8° Incidence*

The longitudinal development of the 8° angle of attack crossflow structure is analysed in Figures 7.21 and 7.22 which compare the experimental vapour screen photographs with the corresponding computationally resolved density contours at stations, $x/D = 6.5 - 11.5$. Figure 7.21 highlights one of the problems of the vapour screen flow visualisation study: where the light sheet intersects the inclined wings, they block out the view of the windward flowfield. The development of the wing leading edge shocks under the windward side of the wings, and their interaction with the body boundary layer to form the windward shock-induced body vortices, captured in the computations, is not visible in the vapour screen results. The leeside body vortices and the wing vortices, however, are visible and compare well with the computed crossflows. The development of the trailing edge shock waves and the double vortex system, generated as the flow leaves the wings, is seen in Figures 7.22 c) - f). Excellent qualitative agreement exists between computation and experiment. Figure 7.22 e) presents the most rearward of the vapour screen photographs and clearly shows the double vortex system as two linked, but separate vortical features. The computational equivalent shown in Figure 7.22 f), however, shows the two vortices as one extended feature. The numerical turbulent result, shown, does correctly capture capture the two vortices as separate features, but resolves their cores slightly too close together with the inner vortex with less strength than experimentally measured. This flowfield, together with those of the other cases will be described in more detail in section 7.4.4.

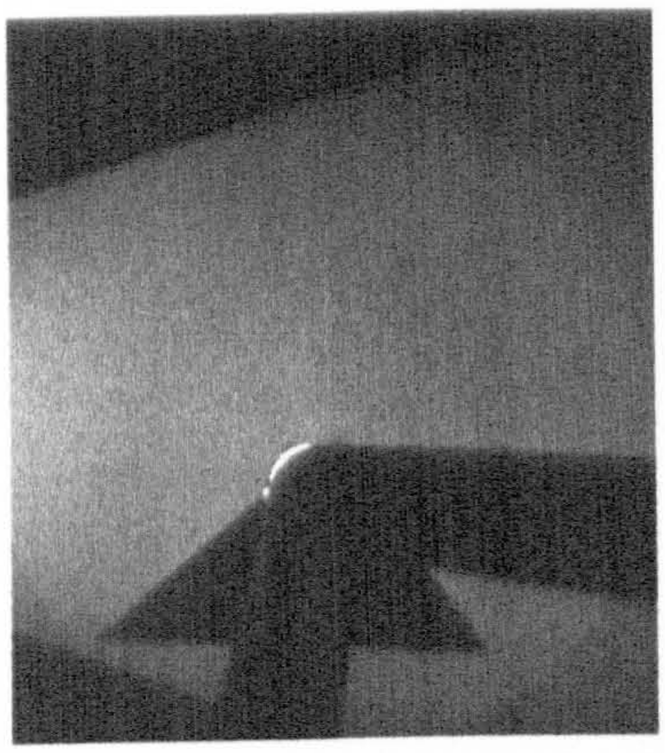

(a) Experiment, $x/D = 6.5$

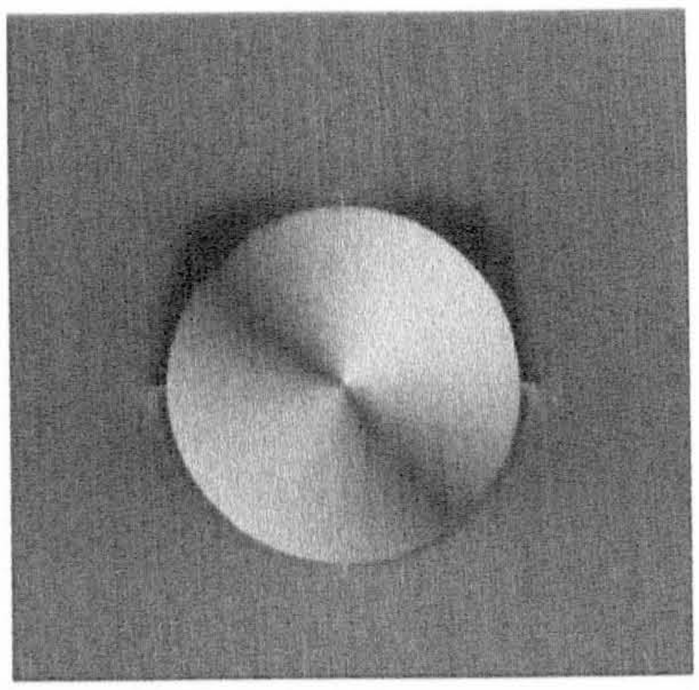

(b) Computation, $x/D = 6.5$

(c) Experiment, $x/D = 7.5$

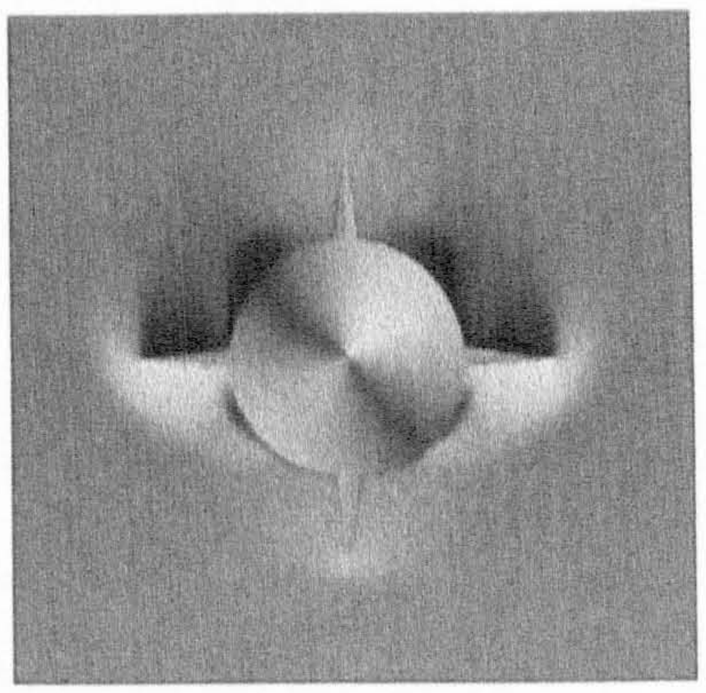

(d) Computation, $x/D = 7.5$

(e) Experiment, $x/D = 8.5$

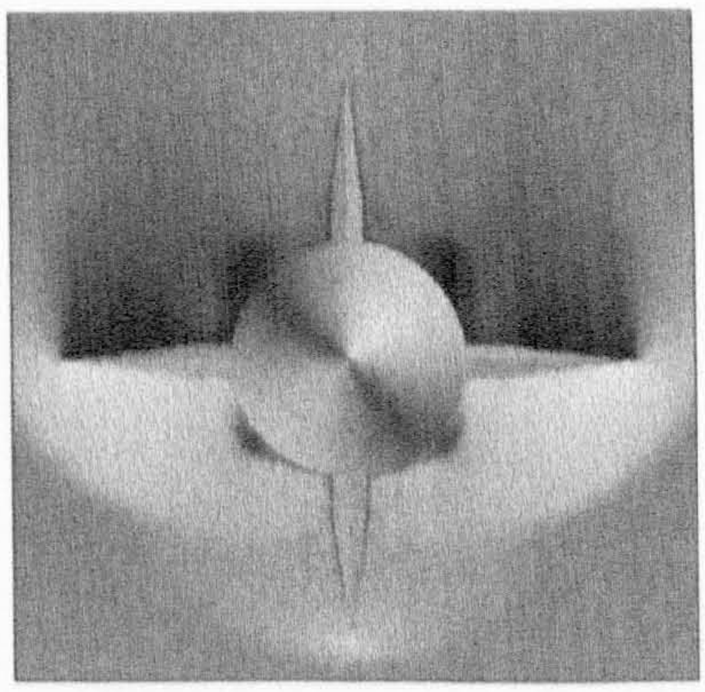

(f) Computation, $x/D = 8.5$

Figure 7.21: *Comparison of Computational and Experimental Vapour Screen Visualisation, Zero Roll, 8° Incidence*

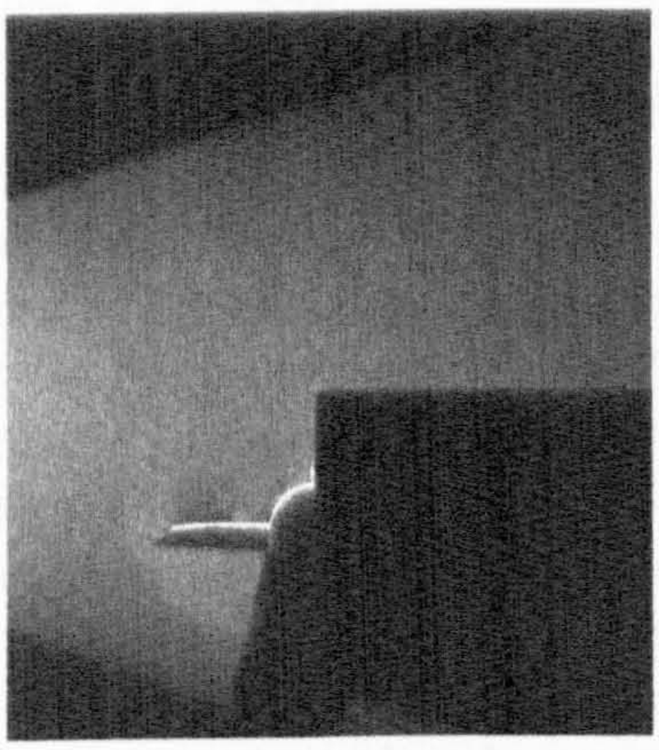

(a) Experiment, $x/D = 9.5$

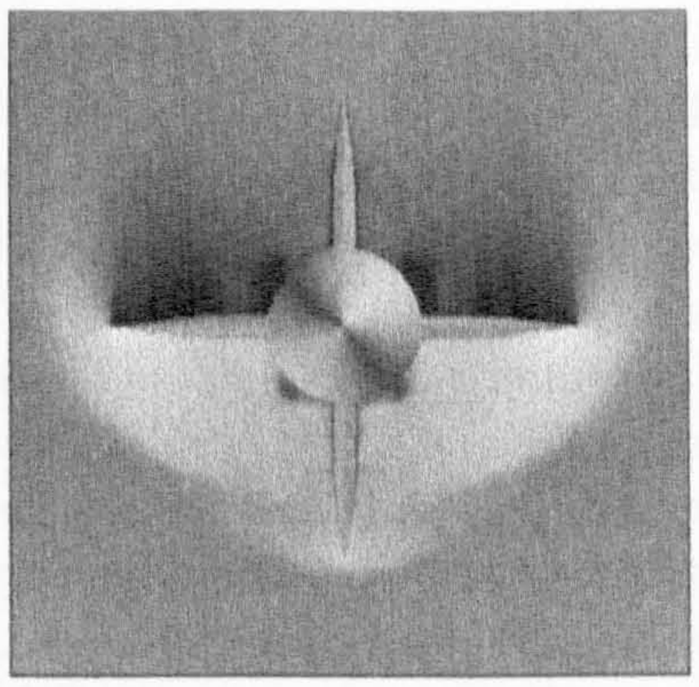

(b) Computation, $x/D = 9.5$

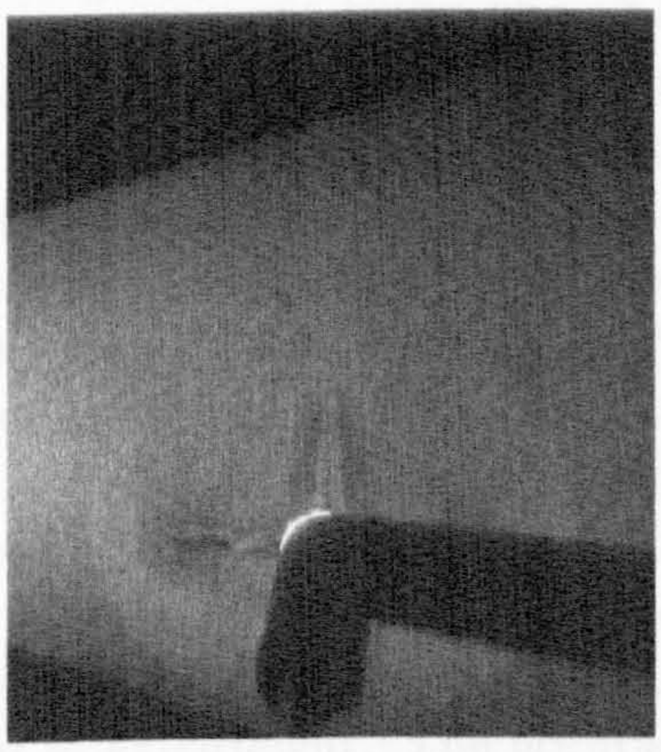

(c) Experiment, $x/D = 10.5$

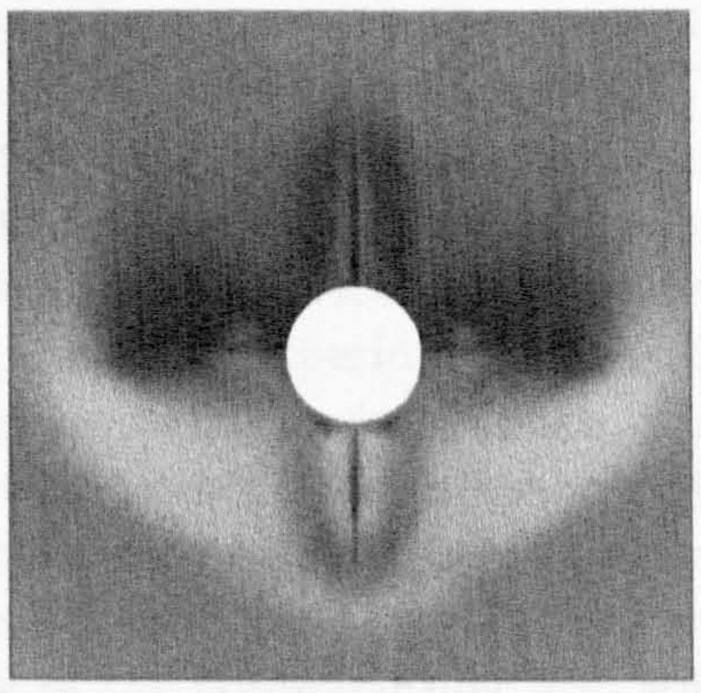

(d) Computation, $x/D = 10.5$

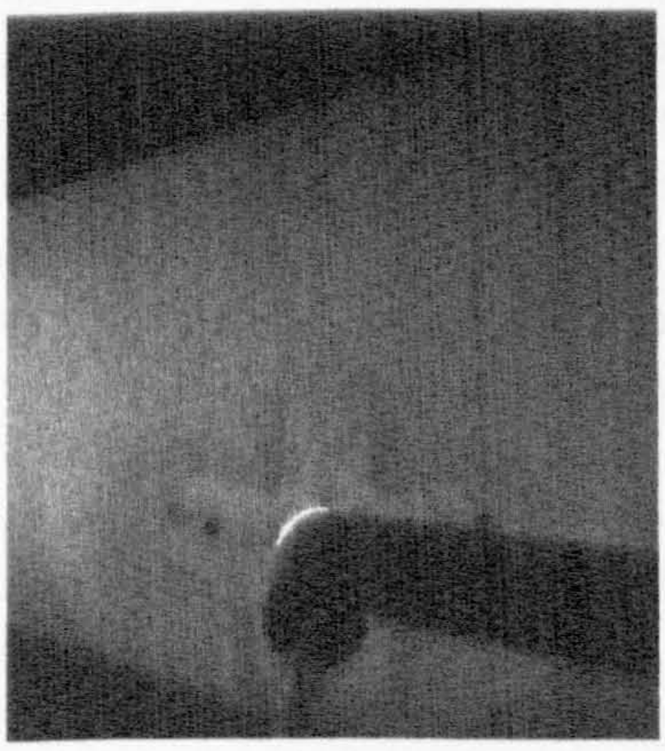

(e) Experiment, $x/D = 11.5$

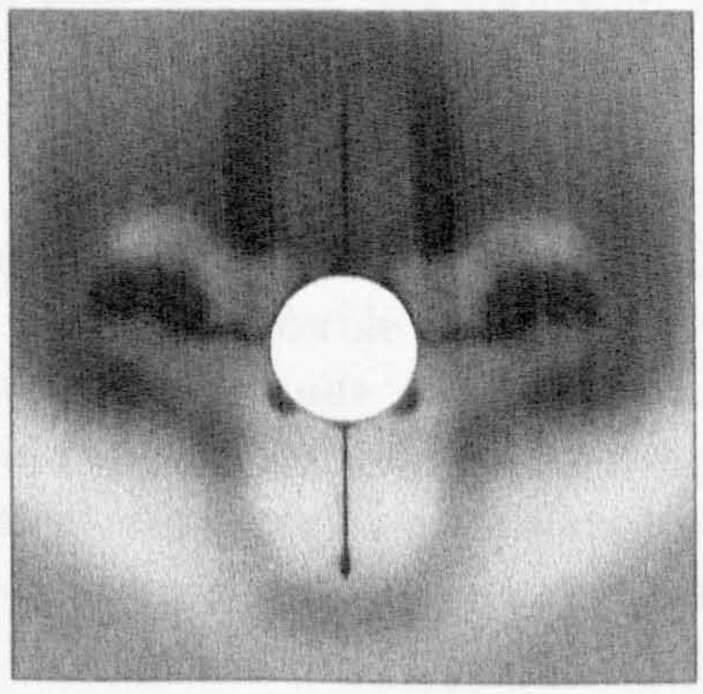

(f) Computation, $x/D = 11.5$

Figure 7.22: *Comparison of Computational and Experimental Vapour Screen Visualisation, Zero Roll, 8° Incidence (continued)*

14° Angle of Attack

The structure of the flow past the body/wing in the + configuration was found to be much the same for both 8° and 14° angle of attack. Differences exist not in the type of flow features present, but in their size, strength, and location. Figure 7.23 presents the comparisons between the experimentally measured crossflow plane ($x/D = 11.5$) total pressure ratio and the corresponding computational solutions. The Euler grid solutions (laminar and inviscid) are plotted with experiment in Figure 7.23 a). The agreement between the inviscid Euler solution and experiment is remarkable, with the correct prediction of a twin vortex system generated by the horizontal wing trailing edge, together with the accurate resolution of the inviscid flow structure. The Euler calculation, however, failed to capture any of the other viscous flow structures such as the wing wakes or the leeside or windward body vortices. The laminar solution on the Euler grid for total pressure ratio at $x/D = 11.5$, appears to be almost equivalent with experiment. The twin vortex system is resolved in the correct location with the same structure as that measured experimentally, but at slightly lower strength. The core suctions are computed marginally lower than experimental measurement, but the solution captures the horizontal wing wake structure remarkably well. The leeside body vortex is predicted and appears almost equivalent in shape, strength and location, to that measured experimentally, as does the secondary feature it induces on the leeward vertical wing surface. The windward body vortex, generated by the interaction of the strong horizontal wing leading edge shock wave and the body boundary layer, is resolved with the correct shape and strength but appears about 5° further windward than that observed in experiment. The accuracy of the laminar-Euler grid solution is misleading since the boundary layers are captured with between 3-4 points - clearly insufficient to correctly resolve the smooth surface separations or shock-boundary layer interactions correctly.

Figure 7.23 b) presents the comparisons between experimental pressure measurement at $x/D = 11.5$, and the NS grid solutions which resolve boundary layers with between 15-25 points depending on their state (laminar or turbulent) and their location in the flowfield. The turbulent solution is clearly the better, having resolved a stronger horizontal wing leading edge vortex, and stronger shock structures above the double vortices which more closely resemble experiment. Both solutions include the wing wakes, the windward and leeward body vortices and the vortex induced by the primary leeward body vortex on the top vertical wing surface. Comparison with experiment, however, shows that both laminar and turbulent NS resolved primary leeward body vortices are smaller, weaker and more elongated than those measured in experiment. The windward body vortex, though resolved in approximately the correct circumferential position, is captured as a much weaker feature. In general, the fine NS solutions successfully predict all

flow features observed experimentally, demonstrating excellent qualitative agreement.

The schlieren photograph for the 0° roll, 14° angle of attack case is reproduced in Figure 7.24 together with the turbulent NS computed symmetry plane density contours and skin friction lines on the body. The computed body skin friction pattern clearly highlight primary separation over the forebody and afterbody. The shock induced separation line under the horizontal wing is apparent as is the strong shock induced upwash just downstream of its trailing edge. The pattern is very similar to that shown for the 8° angle of attack as is the flowfield solution on the symmetry plane. The horizontal wing leading edge shock wave can be seen streaming away under the afterbody, together with its interaction with the wake from the lower vertical wing. The horizontal trailing edge shock wave appears, streaming away above the afterbody. The experimental schlieren photograph illustrates both of these phenomena. The experimental photograph appears to show the trailing edge feature emanating directly from the trailing edge of the horizontal wing. The computational plot, however, only shows its affect on the symmetry plane, and so appears much further downstream where it detaches from the afterbody surface.

The density contours in the xz-plane are plotted in Figure 7.25 together with the computed skin friction lines on the leeside of the horizontal wings. The bow shock wave and the xz-plane trace of the windward leading edge shock are clearly evident. The wakes from the horizontal wings appear as the low density (blue) flow behind the wings together with the effect of the trailing edge double vortex system which appears as the darker blue region. The skin friction pattern shows that the flow, which separates at the sharp leading edge of the wing, reattaches close to the wing root. Secondary separation occurs at almost mid chord while secondary reattachment occurs almost at the leading edge. The flow pattern is very similar to that observed for the 75° swept NASA delta wing at 16° angle of attack investigated in Chapter 6. The leading edge is just subsonic, with the Mach number normal to the leading edge calculated at $M_N \approx 0.977$ while that for the NASA case was marginally supersonic with $M_N \approx 1.04$.

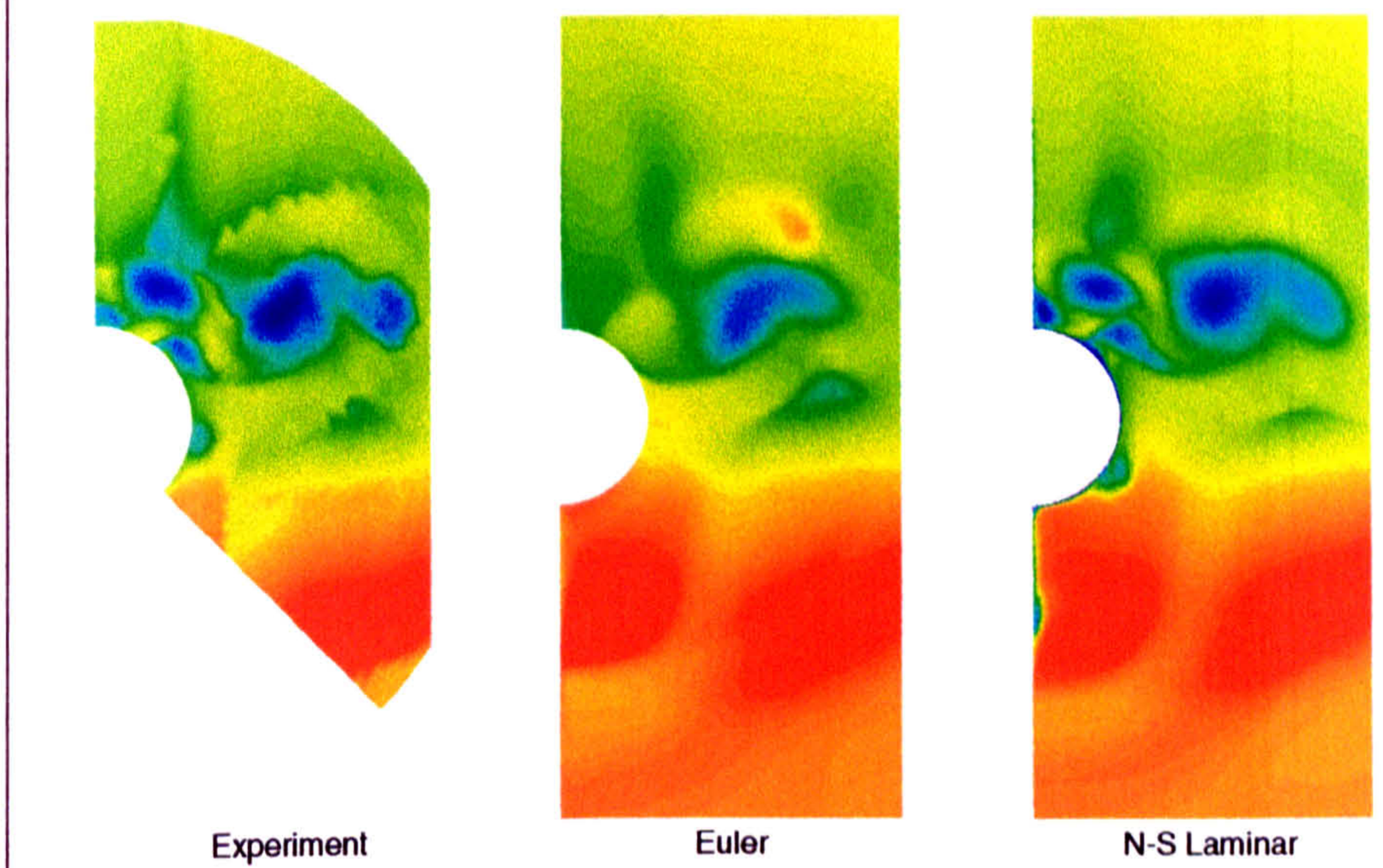

(a) Euler Grid Solutions

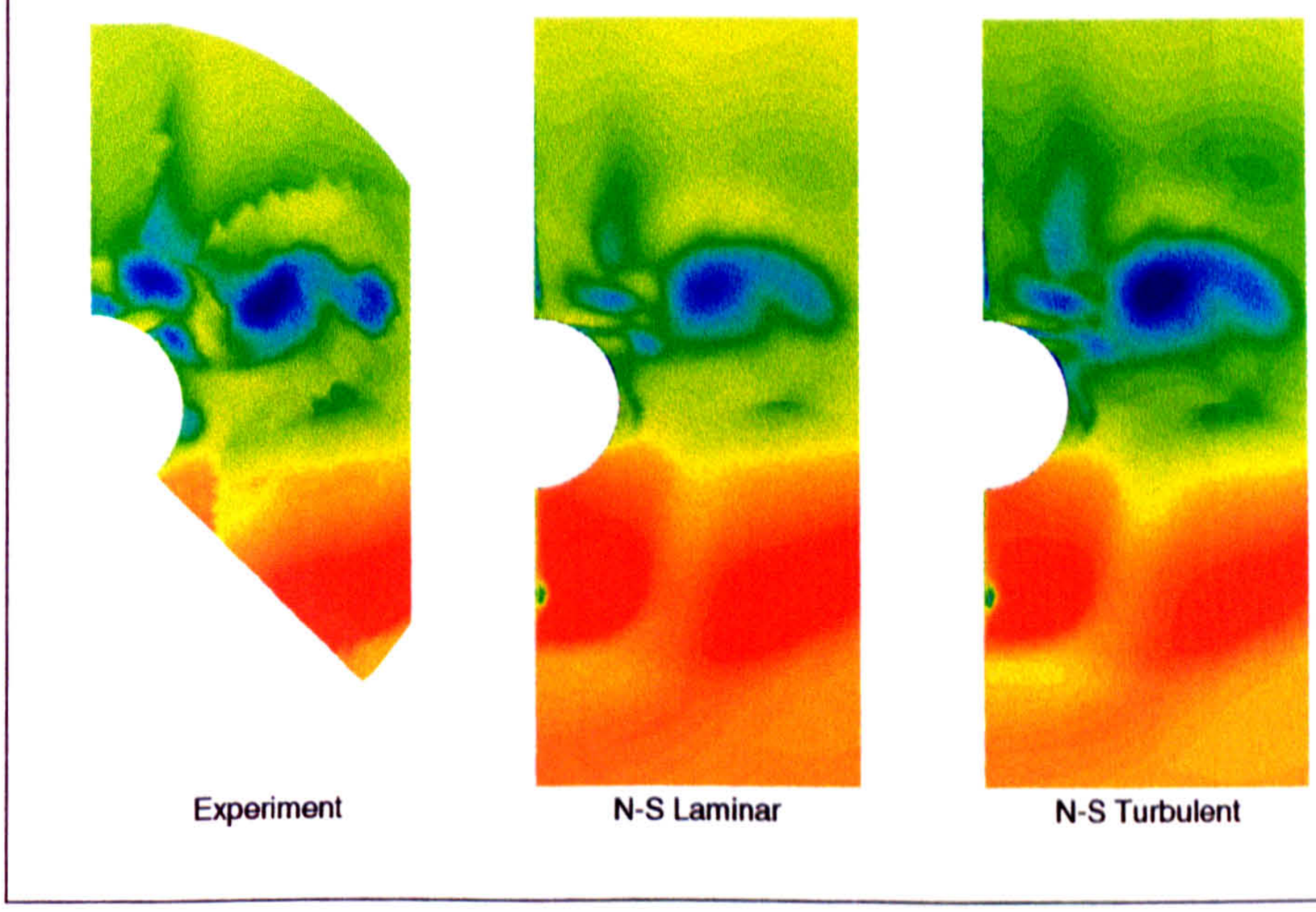

(b) NS Grid Solutions

Figure 7.23: *Total Pressure Contours Comparison,* 0^o *Roll,* x/D*=11.5,* 14^o *Incidence*

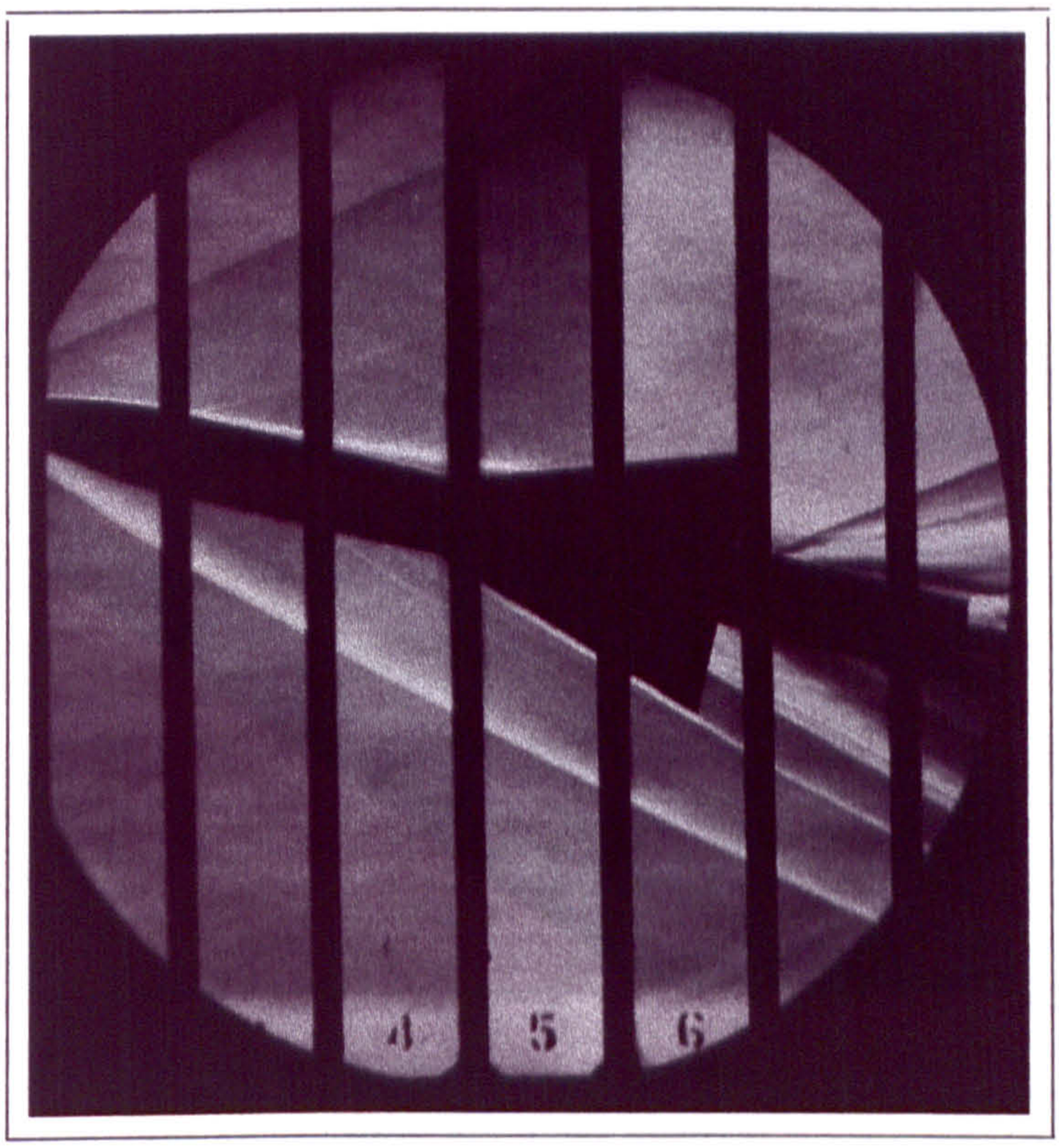

(a) Experimental schlieren

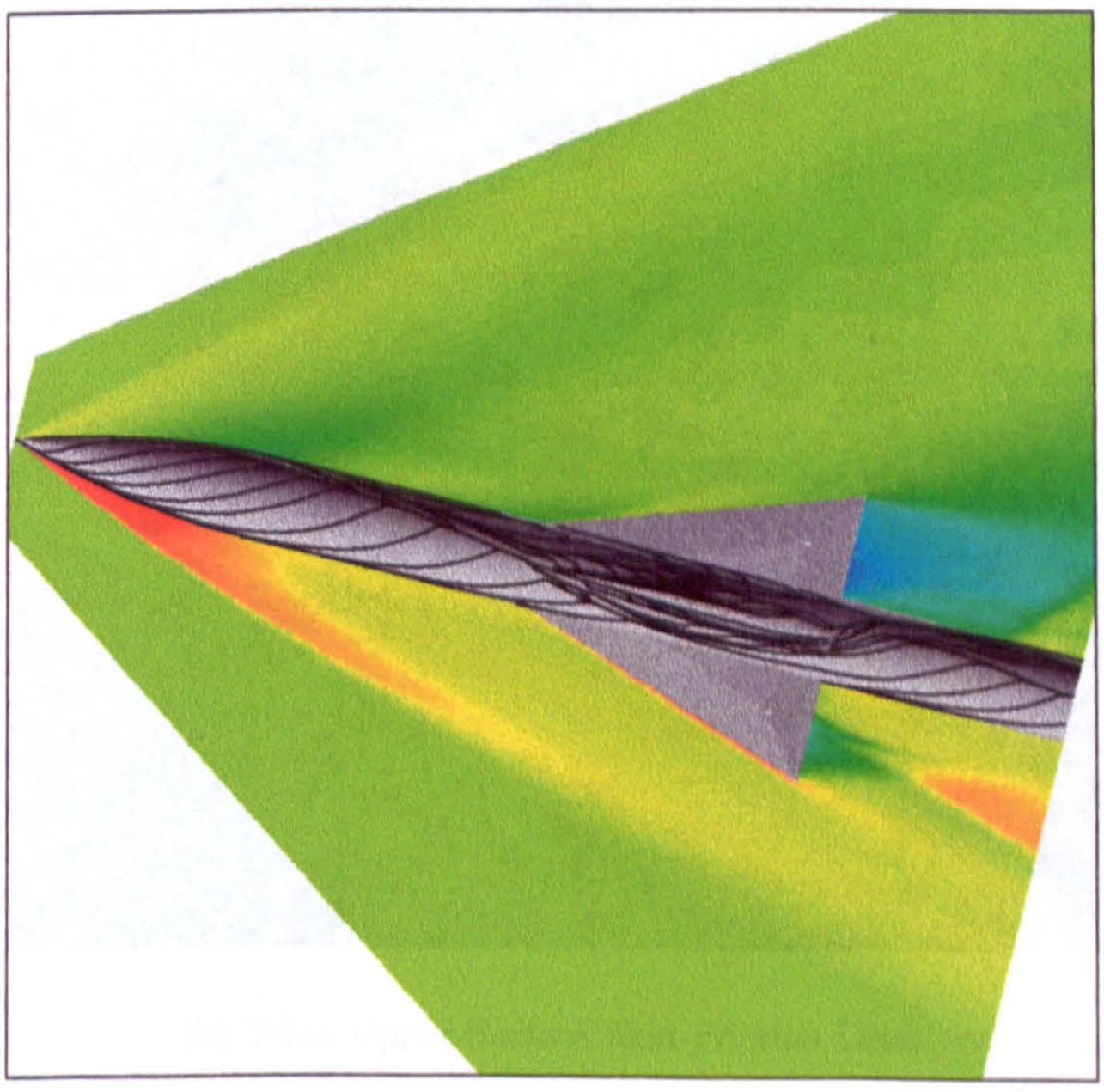

(b) Symmetry Plane (xz-Plane) Density Contours

Figure 7.24: *Computation vs Experimental schlieren*, 0° *Roll*, 14° *Incidence*

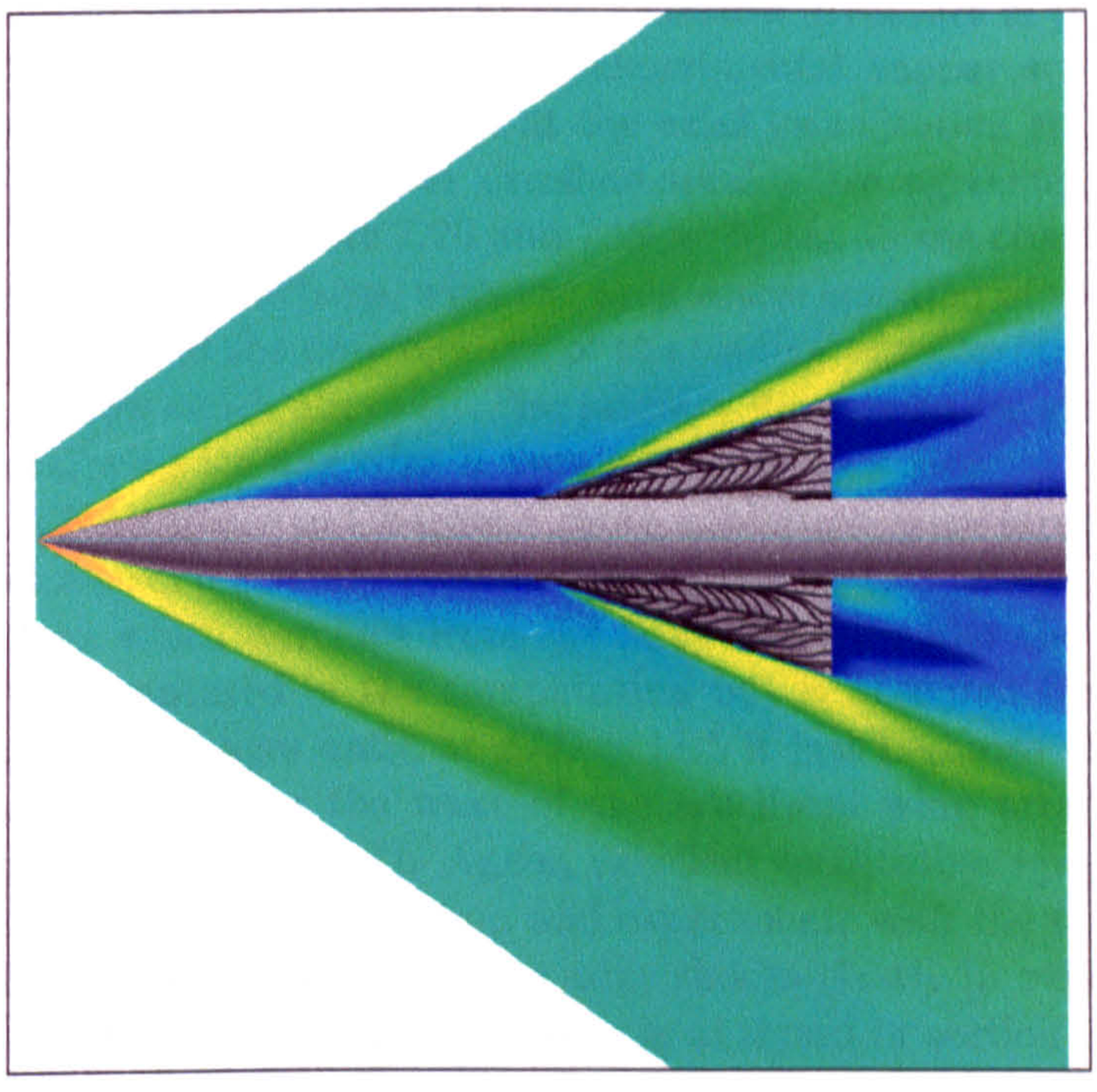

(a) Density Contours (xz-Plane)

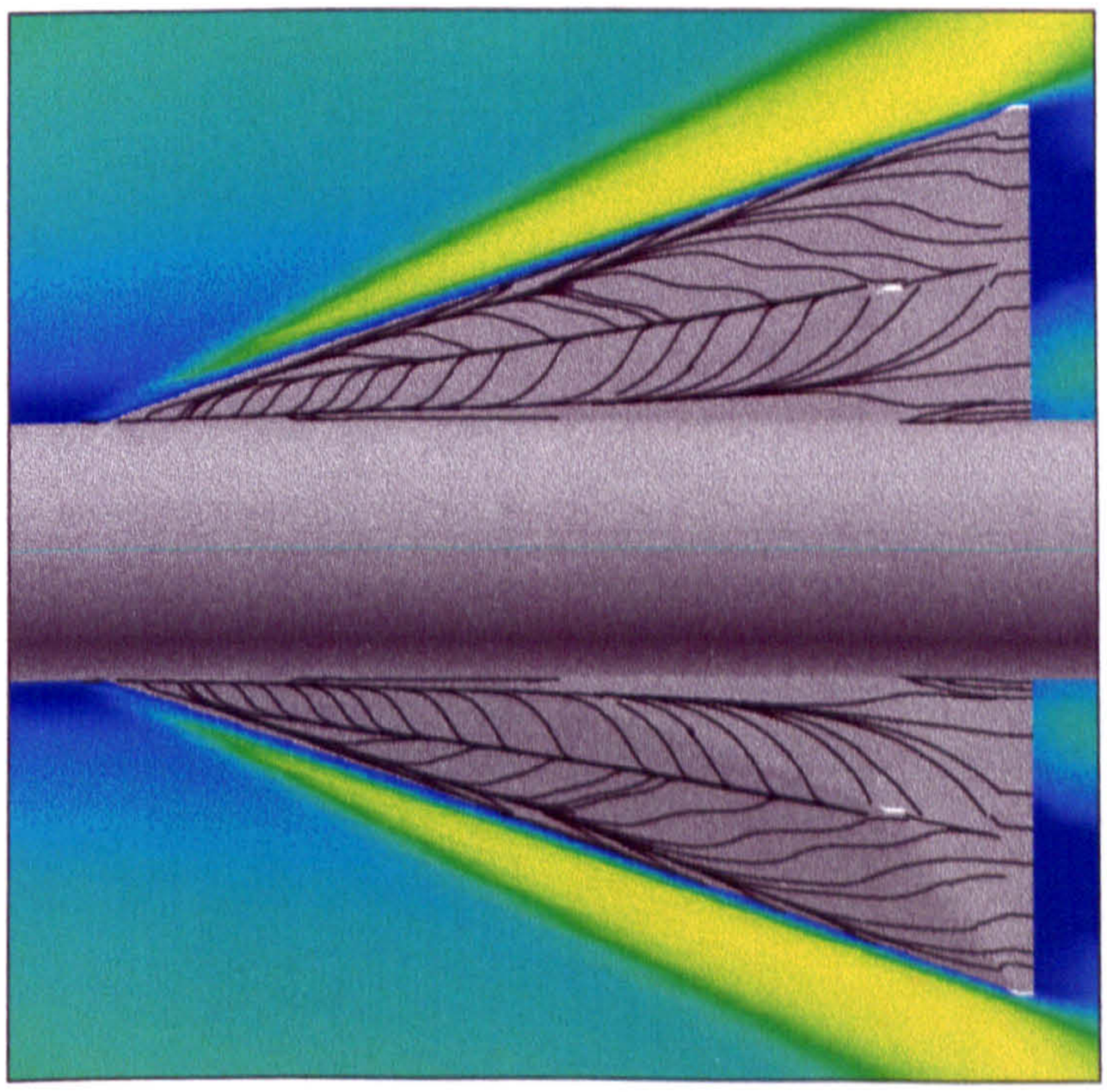

(b) Wing Upper Surface Skin Friction Lines

Figure 7.25: *Computational Solution (xz-Plane),* 0° *Roll,* 14° *Incidence*

The longitudinal development of the crossflow structure is presented in Figures 7.26 and 7.27, comparing the experimental vapour screen results and the computed density contours at the axial visualisation stations. The computed flowfield demonstrates excellent qualitative agreement with the vapour screen images. Figure 7.26 and 7.27 a)-b) shows the crossflow development over the wing surfaces, with the progressive isolation of the forebody primary vortices and the development of the leading edge vortex and strong primary crossflow shock above it. The primary flow structure generated by the horizontal wing leading edge is very similar to that seen for the 16^o angle of attack NASA case in Chapter 6, both exhibiting large strong primary vortices and a strong primary crossflow shock sitting just above. The shock induced vortex which develops from the body surface under the horizontal wing is clearly captured in the computation but is obscured from view in the vapour screen images until, at $x/D = 11.5$ it just becomes visible. The crossflow development in the wake of the cruciform wing arrangement is presented in Figures 7.27 c)-f). Again, excellent qualitative agreement was demonstrated between computation and experiment, with the trailing edge double vortex system and the trailing edge shocks clearly in evidence. The longitudinal development of the crossflow is analysed in section 7.4.4.

(a) Experiment, $x/D = 6.5$

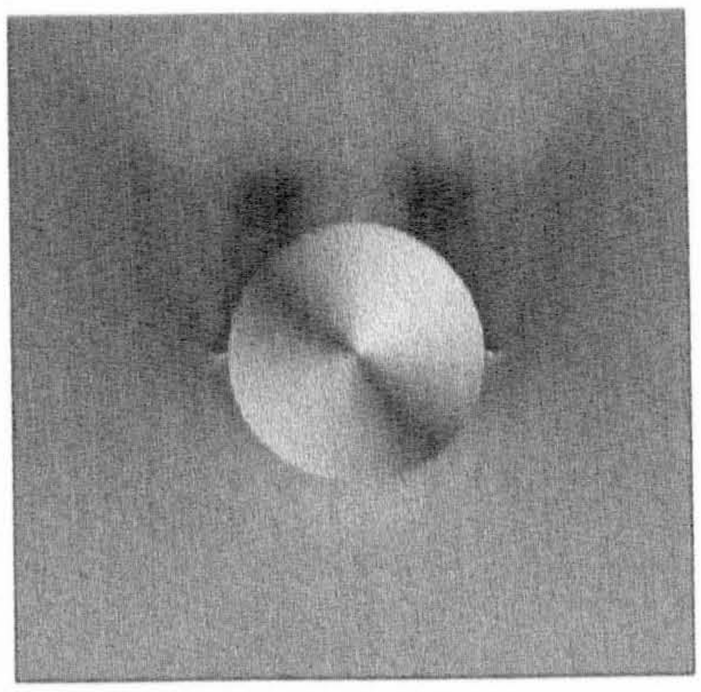

(b) Computation, $x/D = 6.5$

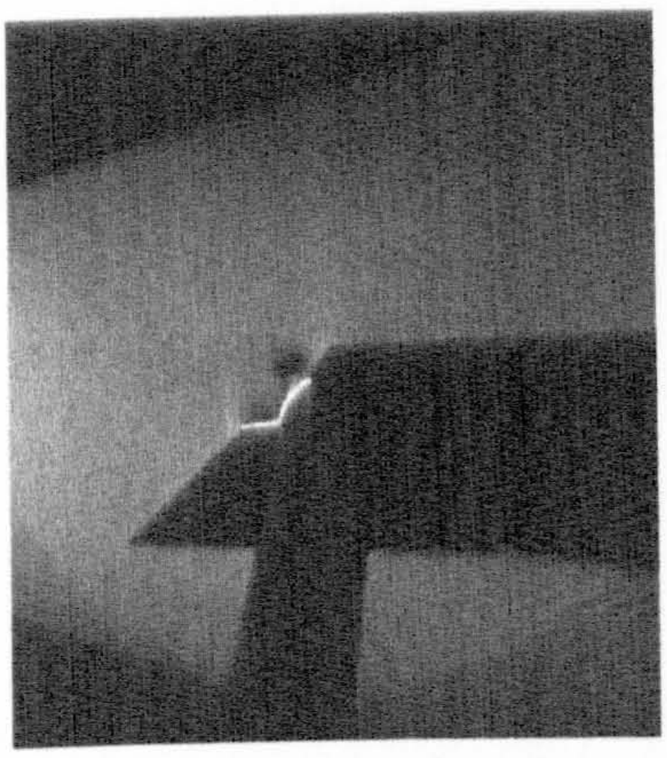

(c) Experiment, $x/D = 7.5$

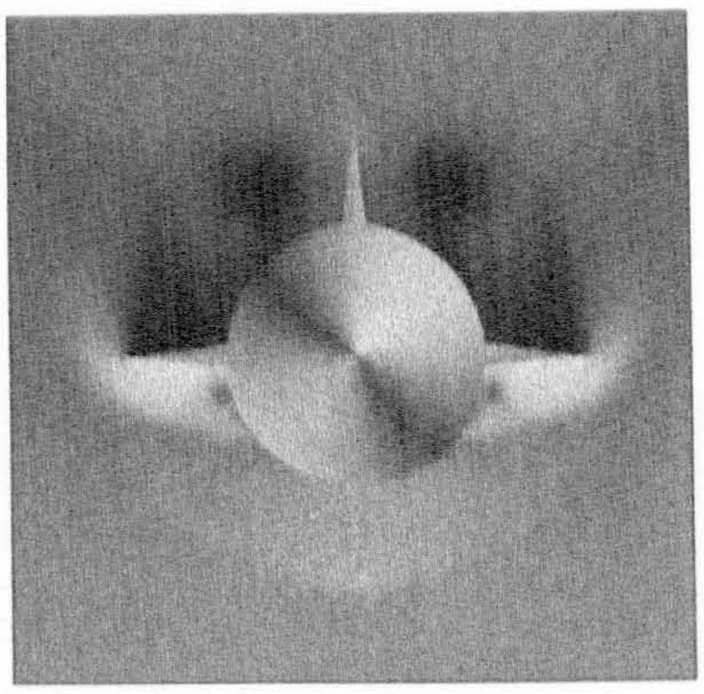

(d) Computation, $x/D = 7.5$

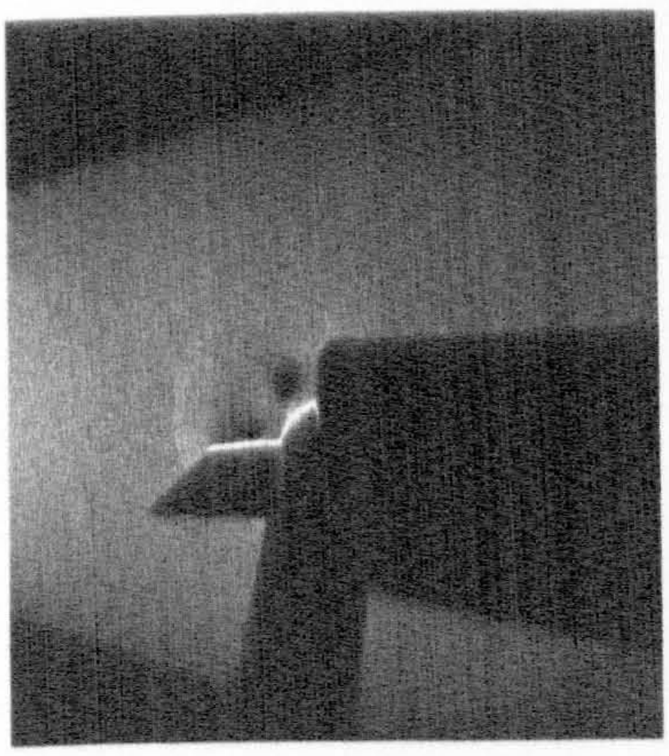

(e) Experiment, $x/D = 8.5$

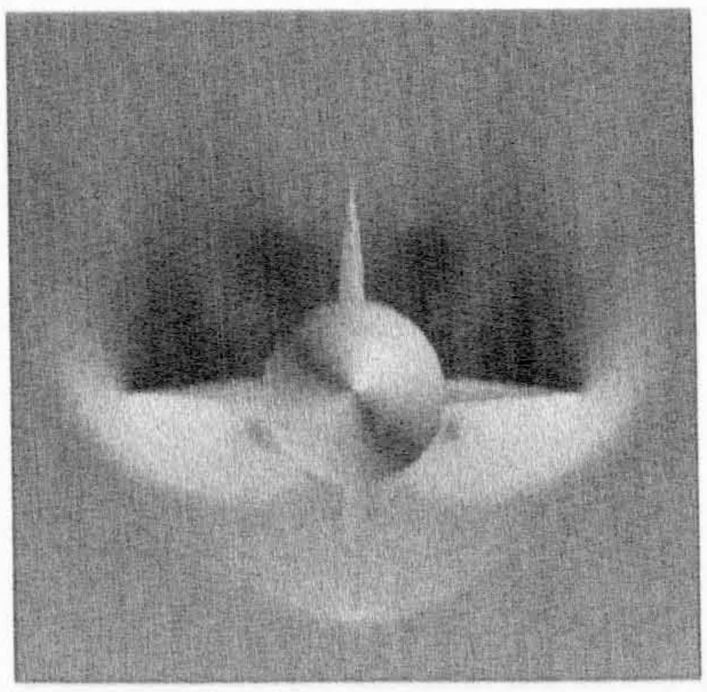

(f) Computation, $x/D = 8.5$

Figure 7.26: *Comparison of Computational and Experimental Vapour Screen Visualisation, Zero Roll,* 14° *Incidence*

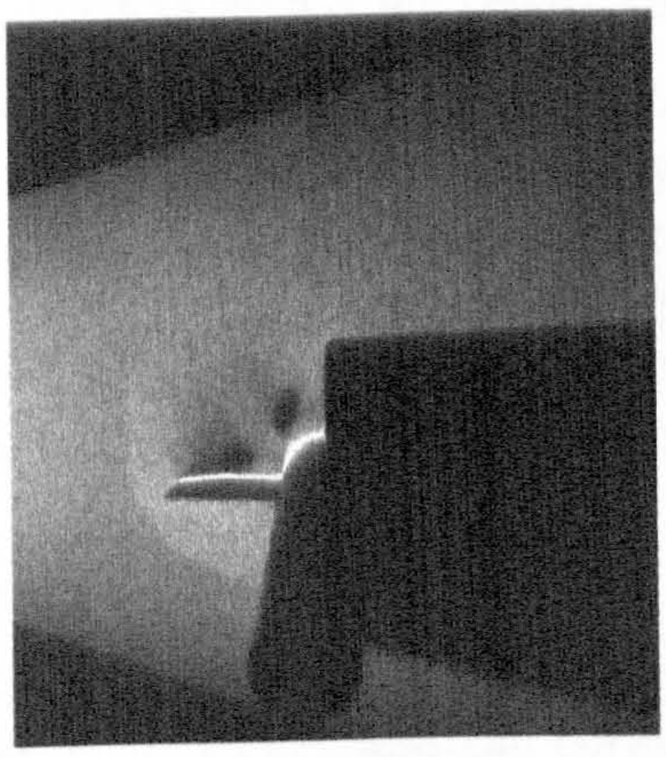

(a) Experiment, $x/D = 9.5$

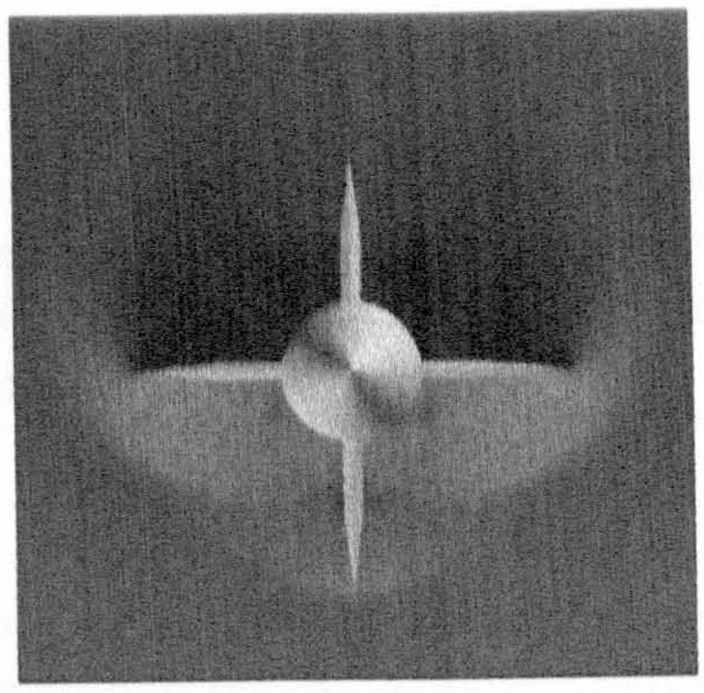

(b) Computation, $x/D = 9.5$

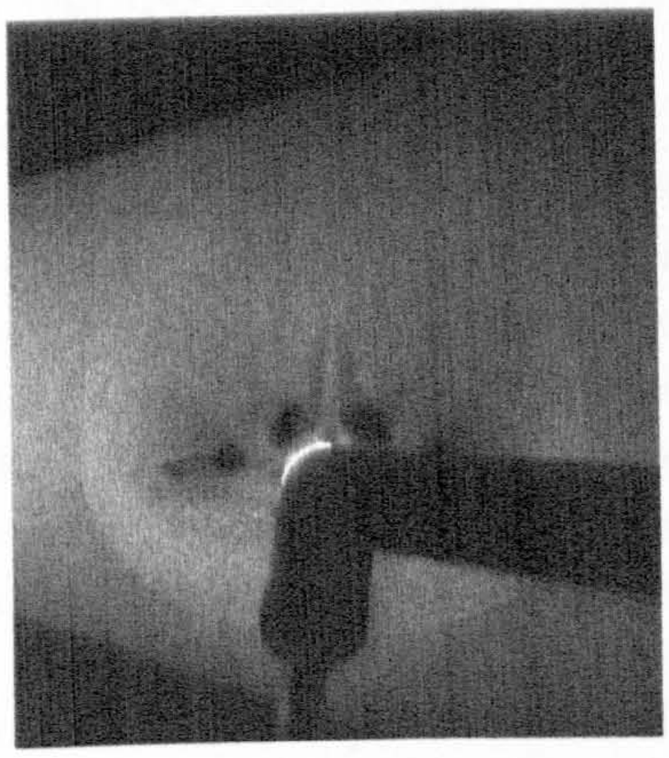

(c) Experiment, $x/D = 10.5$

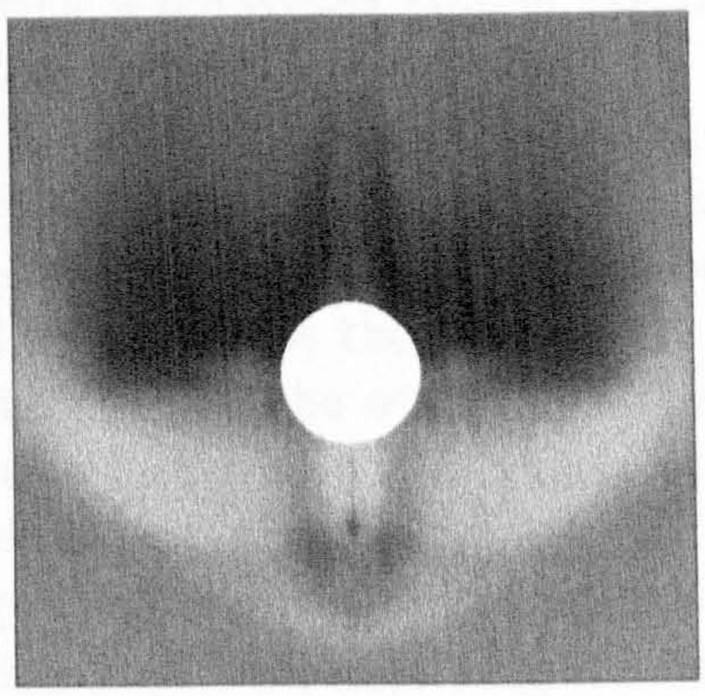

(d) Computation, $x/D = 10.5$

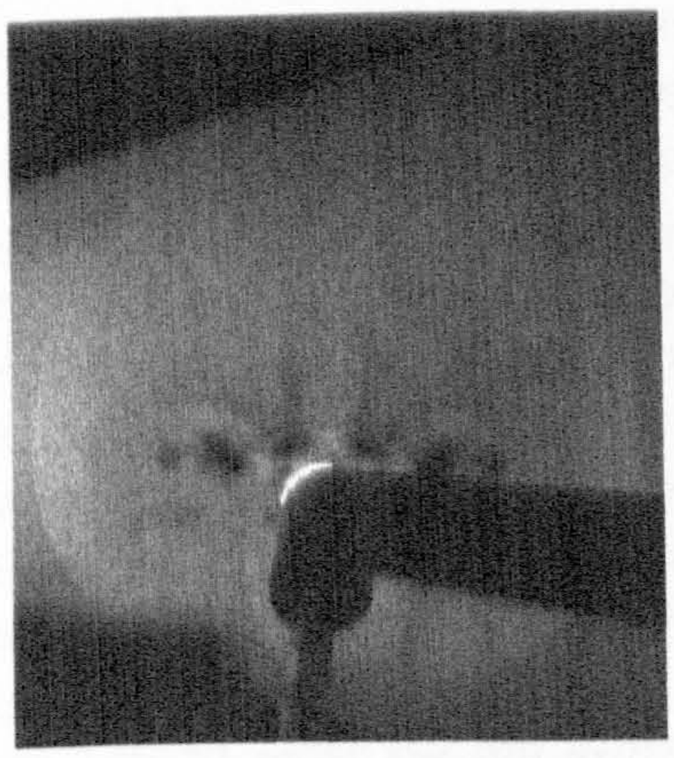

(e) Experiment, $x/D = 11.5$

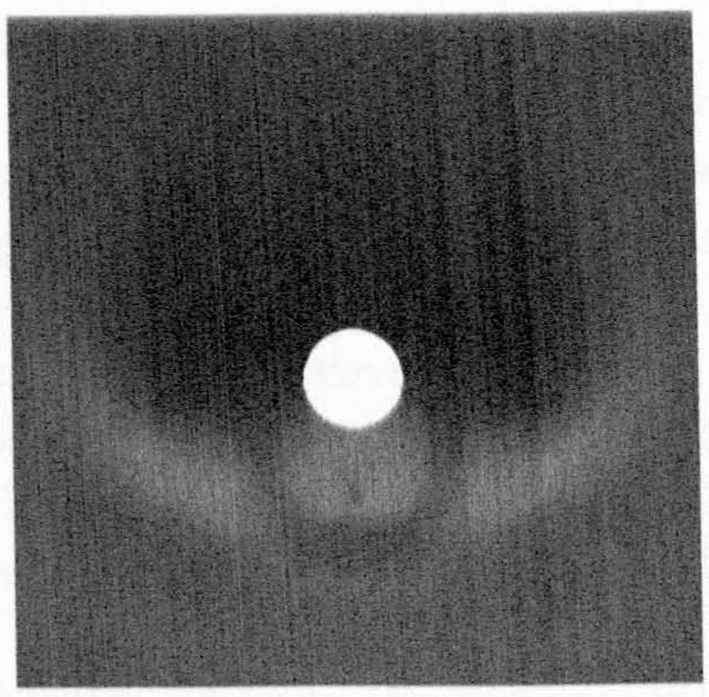

(f) Computation, $x/D = 11.5$

Figure 7.27: *Comparison of Computational and Experimental Vapour Screen Visualisation, Zero Roll,* 14^o *Incidence (continued)*

7.4.3 B1AW20A3 45° Roll Investigation

The numerical investigation methodology employed for the study of the 0° roll cases was also used for the study of the body/wing at 45° roll. Inviscid and laminar calculations were performed on the Euler grid while finer laminar and turbulent calculations were performed on their respective grids. On the basis of the findings in the 0° roll investigation, turbulence modelling was invoked only on the forebody and afterbody.

8° Angle of Attack

The comparison between the experimentally measured total pressure ratio [9] at $x/D = 11.5$, and the corresponding computational predictions, is presented in Figure 7.28. The experimental resolution of the upper wing wake-vortex system is difficult to interpret but appears to show two small vortical features, one acting from the wing tip and another one induced further inboard. Similarly the lower wing wake-vortex system can be interpreted as having two vortices acting together.

Measurement of a pressure field in the wake of a body involves the use of intrusive pitot tubes which will perturb the flowfield especially in supersonic flow when a tube acts as a blunt body and a bow shock will form before it. The pitot tubes are of finite size and measure not the pressure at a point in the flow, but the average pressure acting over the width of the orifice. It is, therefore, impossible to capture sharp features such as shock waves and thin wakes with any degree of precision.

The inviscid and laminar, Euler grid, solutions are presented in Figure 7.28 a) beside the experimentally measured contours. Again, the Euler prediction compares surprisingly well with experiment, resolving the sharp leading edge separation from both upper and lower wings and the resulting vortices together with the multiple shock interaction occurring between the wings. Only one vortex is generated off each wing, however, and the calculation did not predict the development of any body vortices seen in the viscous results and in experiment. The laminar, Euler grid, result better captured the shape and strength of the wing vortices. The upper wing outboard vortex agreed well with experiment, while the solution included a very small thin vortex embedded within the wake further inboard in the position indicated in experiment. This vortex, however, was much smaller and weaker than that indicated by experimental measurement. In addition the laminar result included the shock induced vortical features seen beneath the lower wing and above the upper wing, and the body vortex in between the wings.

Figure 7.28 b) plots the NS grid solutions beside the experimental measurements. The laminar result resolves a slightly smaller outboard vortex formed off the upper wing, while the second vortex is almost non-existent.

Both laminar results predict the double vortex system formed by the trailing edge of the lower wing. The turbulent solution appears similar to the laminar except that the effect of the second, inboard, vortex from the upper wing is more extensive. Examination of the computed velocity vectors reveals that the thicker boundary layer on the body leads to a more pronounced inboard vortical structure in better agreement with experiment. The turbulent calculation reveals a weaker body vortex in between the two wings, appearing 5° more leeward than the laminar counterpart. This is in better agreement with its experimentally resolved position. In general, the three viscous results are in excellent qualitative agreement with experiment, the turbulent case being slightly superior.

The schlieren photograph for the × configuration at 8° angle of attack is reproduced together with the computed symmetry plane density contours in Figure 7.29. The schlieren photograph, being a view through the whole 3D flowfield, appears somewhat messy downstream of the wings where leading edge and trailing edge shock waves from both upper and lower wings stream off and interact. The turbulent NS calculation resolved the effect of the strong lower wing leading edge shock and the upper wing leading and trailing edge shock waves.

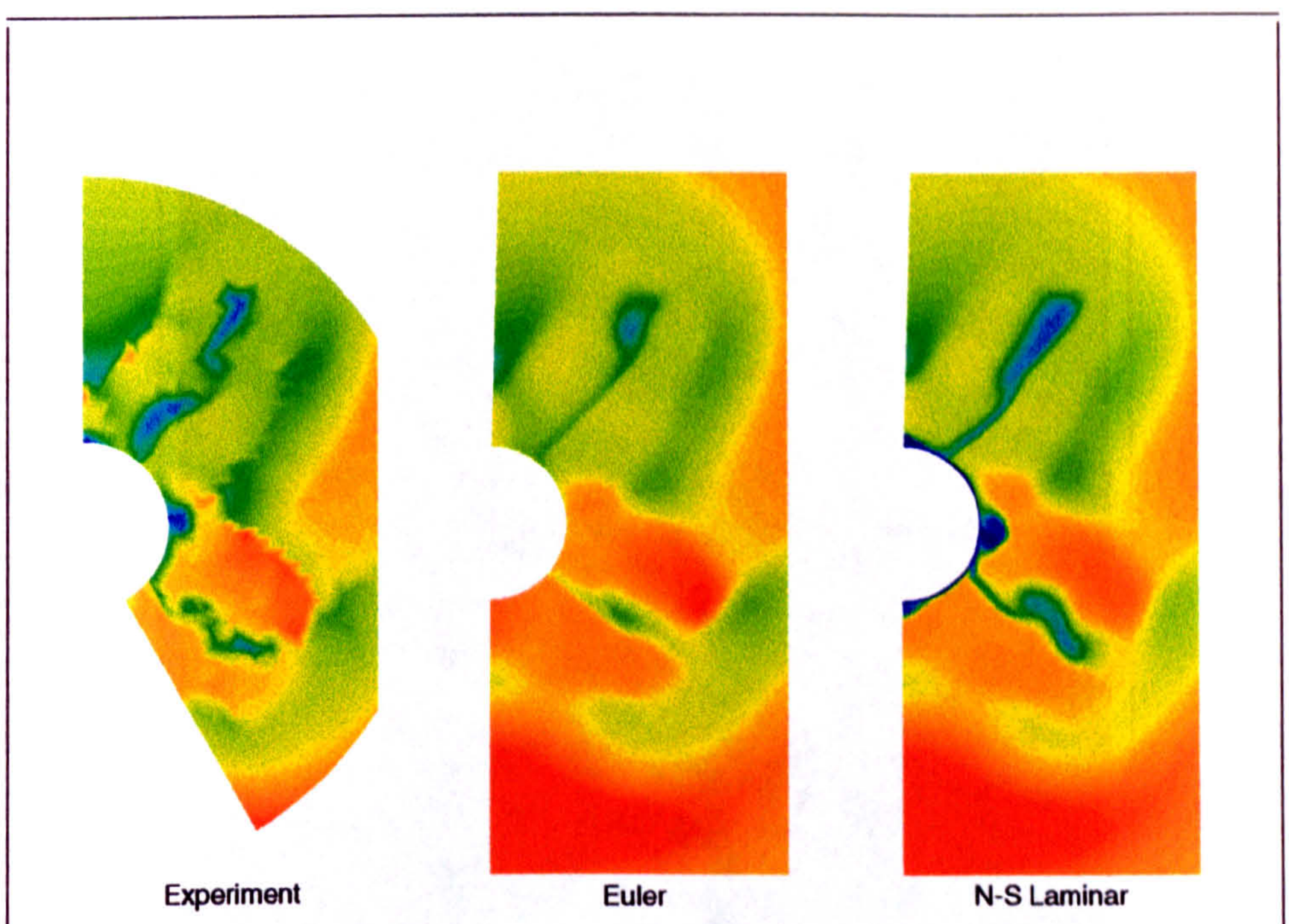

(a) Euler Grid Solutions

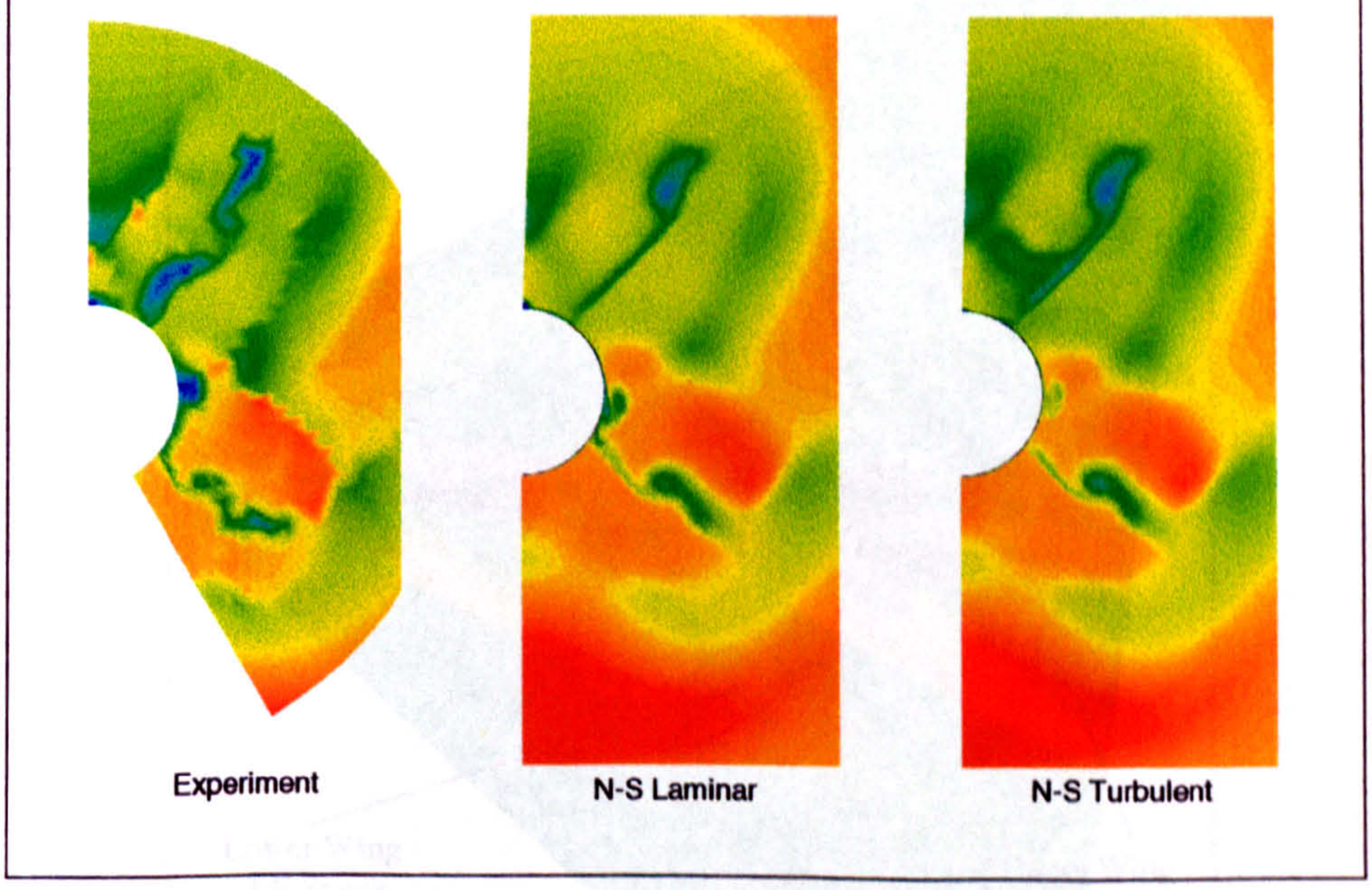

(b) NS Grid Solutions

Figure 7.28: *Total Pressure Contours Comparison,* 45° *Roll, x/D=11.5,* 8° *Incidence*

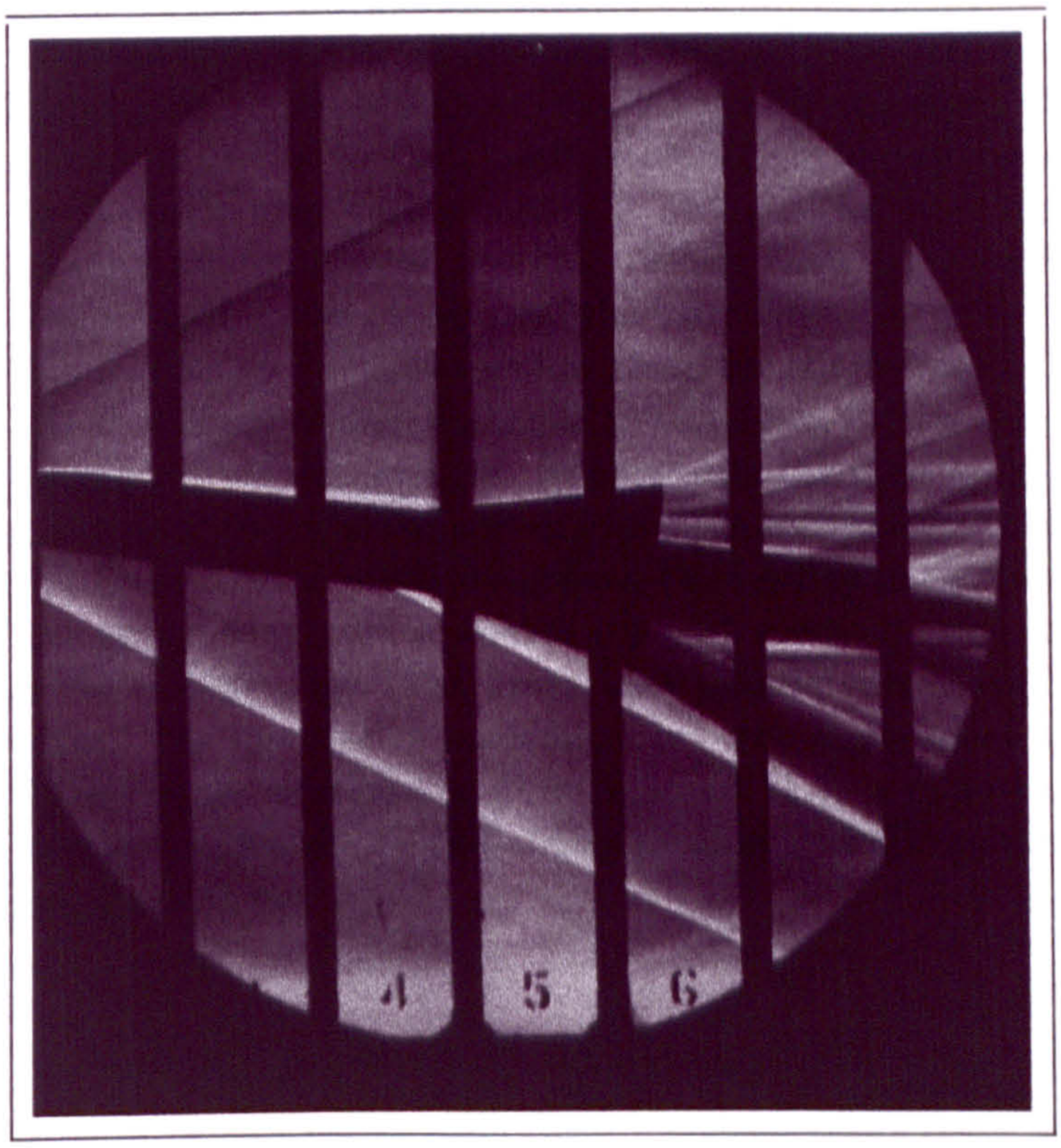

(a) Experimental schlieren

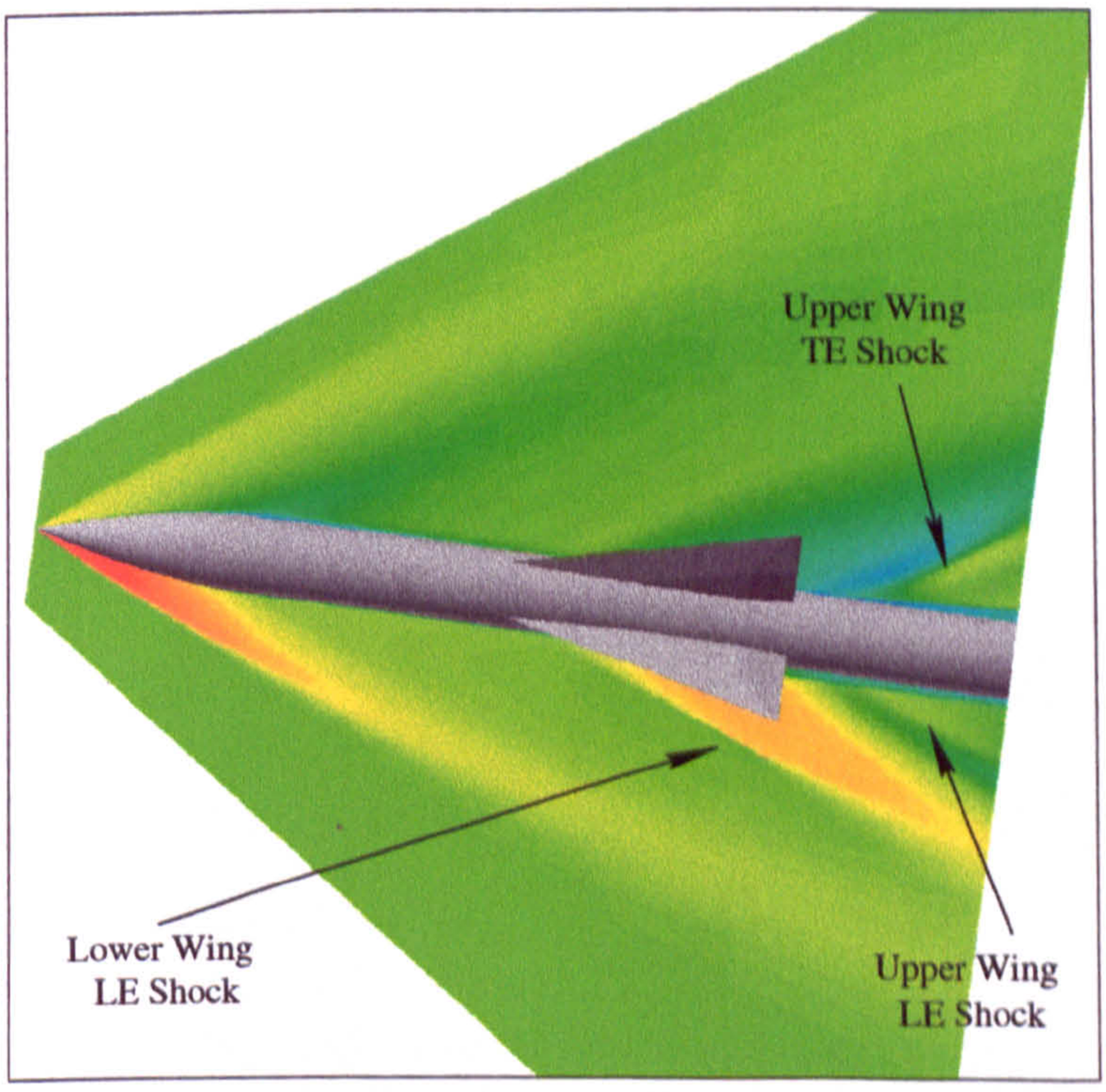

(b) Symmetry Plane (xz-Plane) Density Contours

Figure 7.29: *Computation vs Experimental schlieren*, 45° *Roll*, 8° *Incidence*

Figures 7.30 and 7.31 present the longitudinal development of the crossflow structure and compare the experimental vapour screen images with the computed density contours. It is clear that, for the 45° roll cases, the vapour screen technique is useless in the crossflow planes cutting across the wings because the shadows they cast completely obscure the view of the flowfield. The computational results, however, clearly show the development of the various shock and vortex structures which are described in section 7.4.4. The vapour screen images of the crossflow structure in the wake of the wings (Figures 7.31 c) and e)) clearly highlight the complex interactions between shock waves and the viscous features. In particular the experimental images reveal that the upper wing wake-vortex system is composed of two vortices - a strong outboard vortex originating from the leading edge vortex on the leeside of the upper wing, and a weaker inboard vortex formed as the flow passes over the trailing edge. The lower wing double vortex system is also clearly evident. The qualitative agreement between experiment and calculation at the presented stations, $x/D = 10.5$ and 11.5, is remarkably good, providing further confidence in the ability of modern CFD to resolve such complex compressible flows.

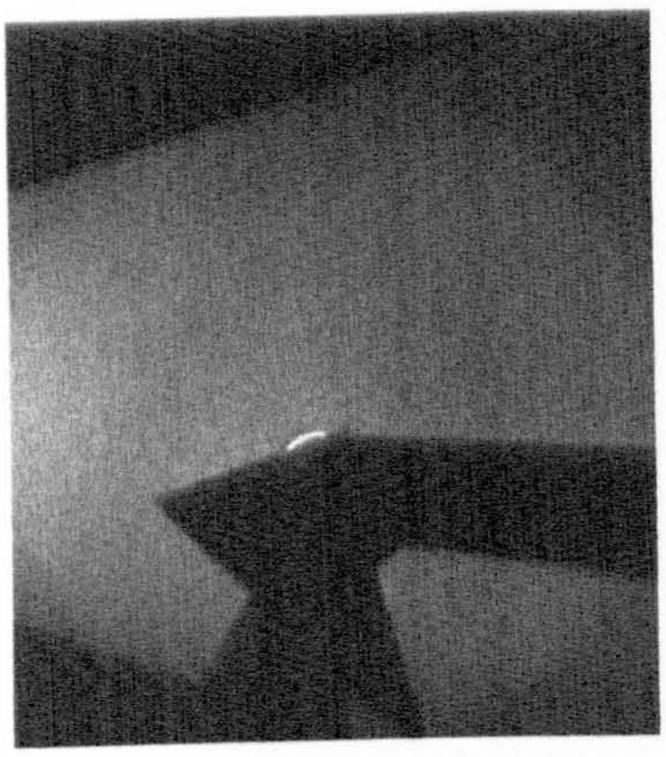

(a) Experiment, $x/D = 6.5$

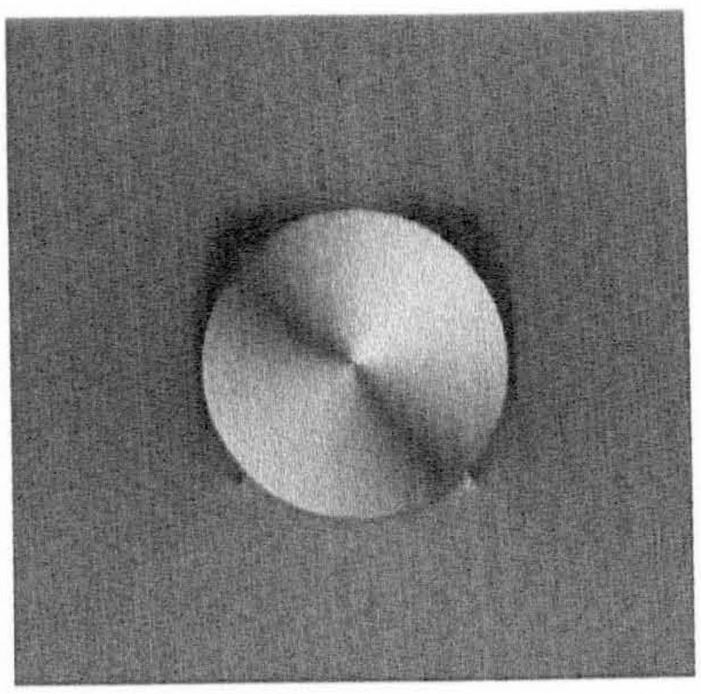

(b) Computation, $x/D = 6.5$

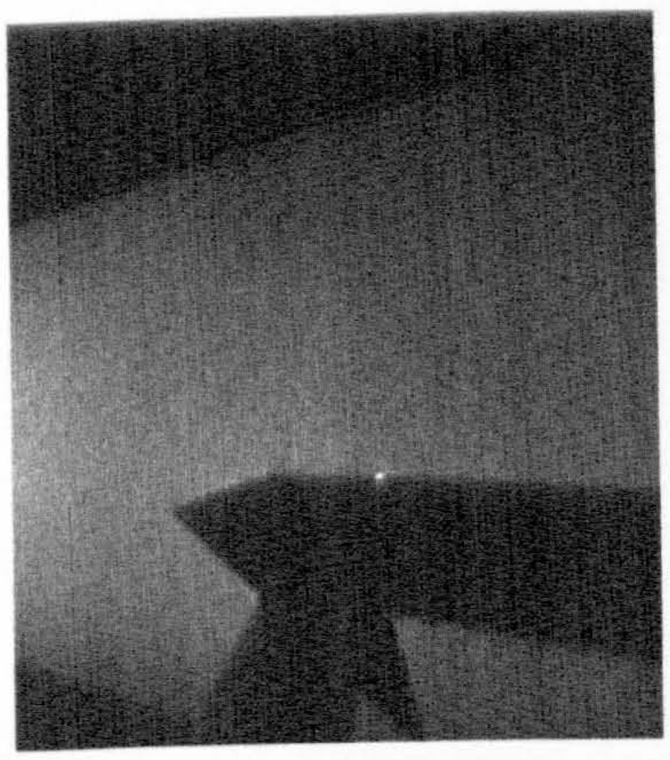

(c) Experiment, $x/D = 7.5$

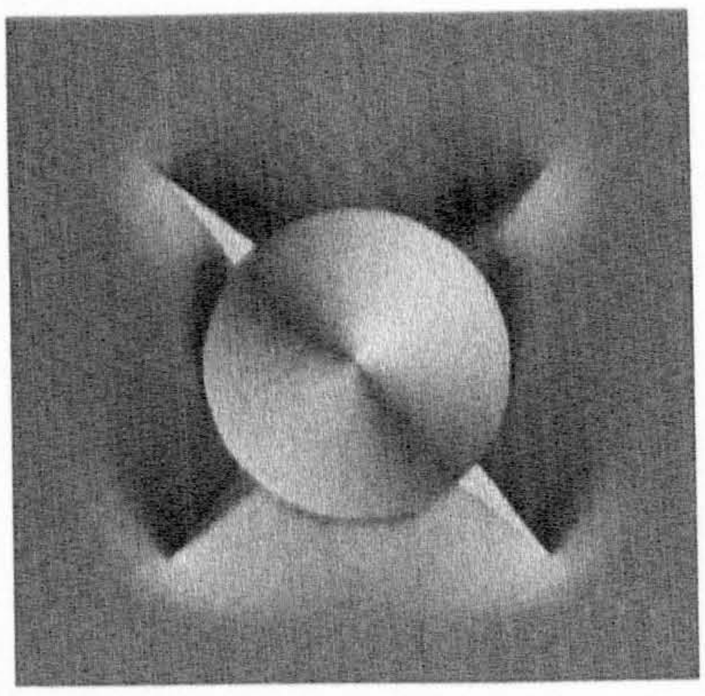

(d) Computation, $x/D = 7.5$

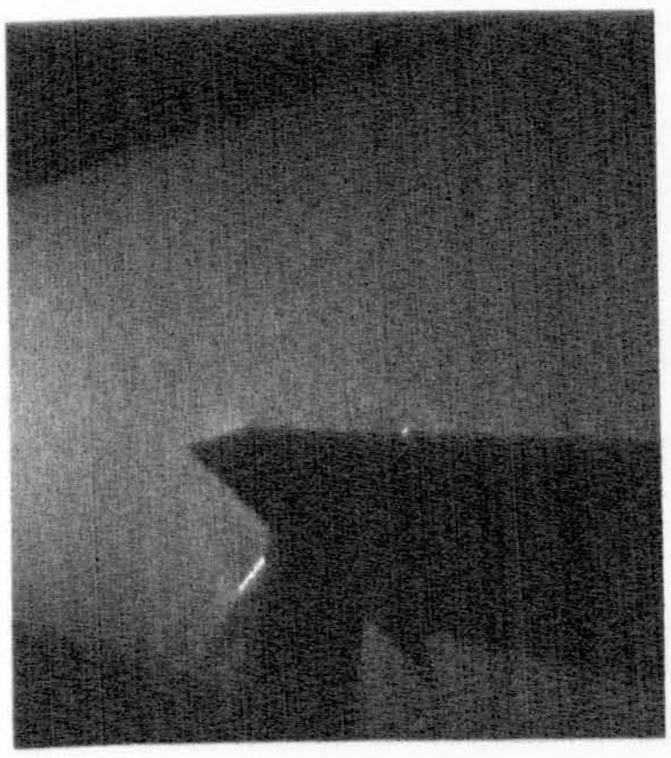

(e) Experiment, $x/D = 8.5$

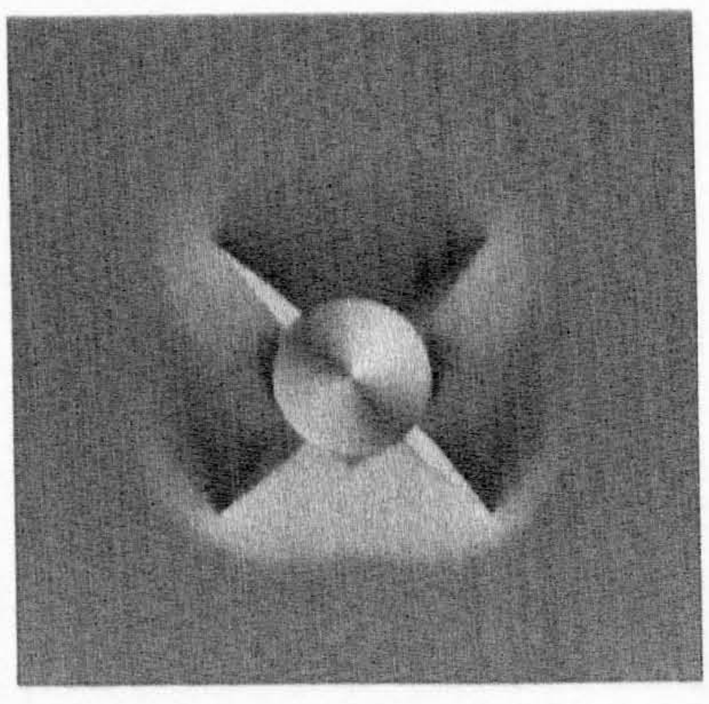

(f) Computation, $x/D = 8.5$

Figure 7.30: *Comparison of Computational and Experimental Vapour Screen Visualisation,* 45^o *Roll,* 8^o *Incidence*

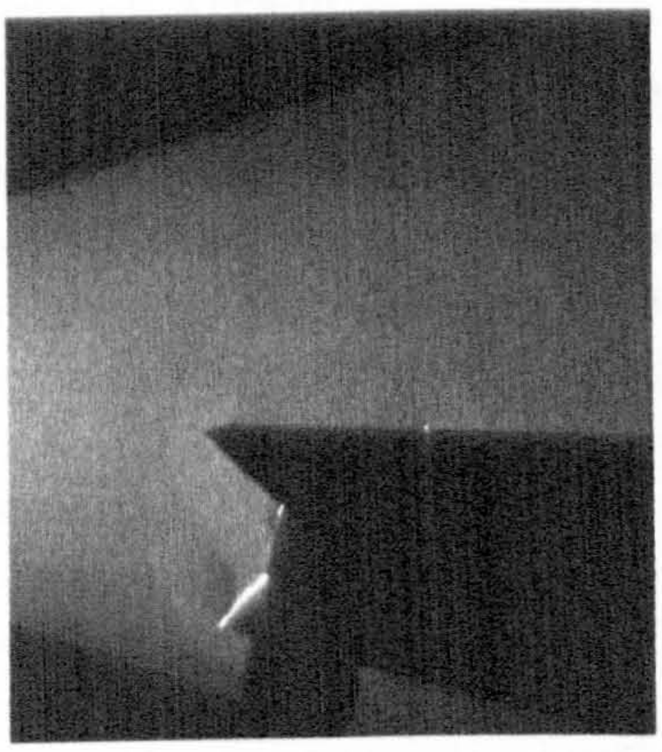

(a) Experiment, $x/D = 9.5$

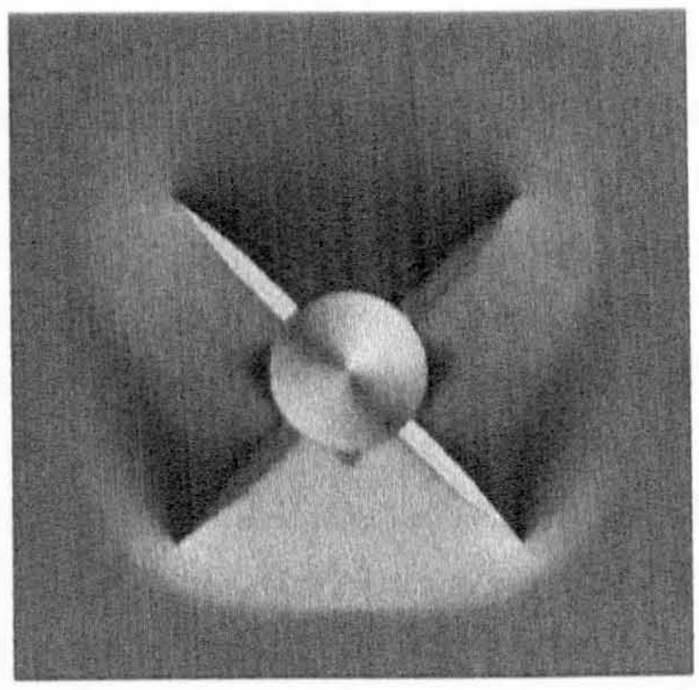

(b) Computation, $x/D = 9.5$

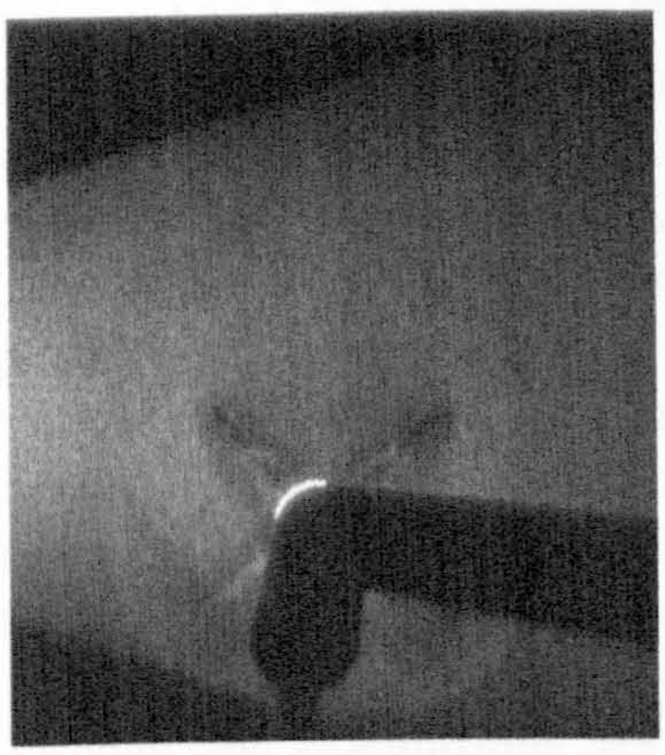

(c) Experiment, $x/D = 10.5$

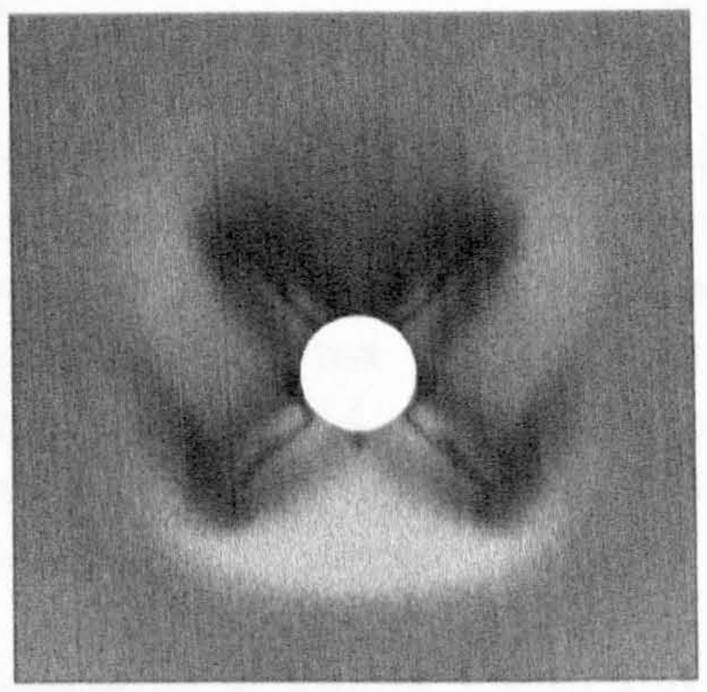

(d) Computation, $x/D = 10.5$

(e) Experiment, $x/D = 11.5$

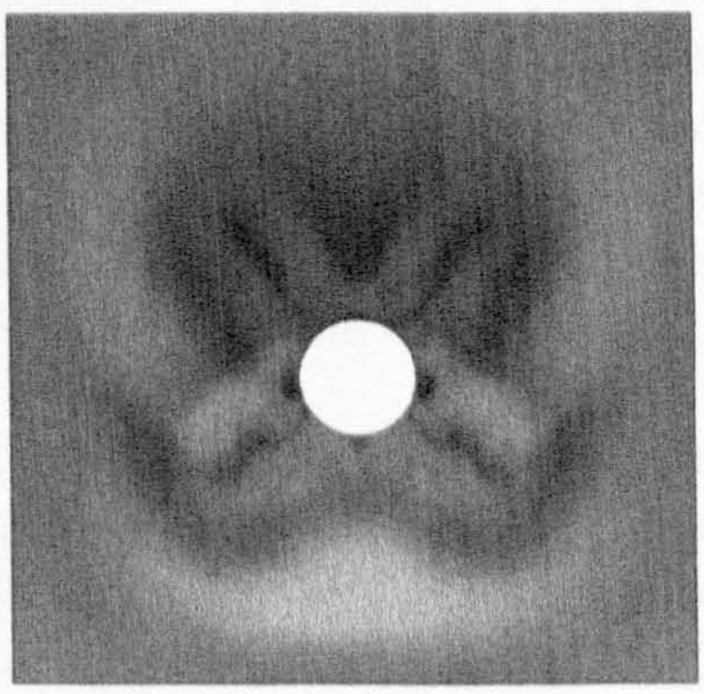

(f) Computation, $x/D = 11.5$

Figure 7.31: *Comparison of Computational and Experimental Vapour Screen Visualisation,* 45^o *Roll,* 8^o *Incidence (continued)*

14° Angle of Attack

The structure of the flow past the body/wing at 45° roll was found to be very similar for both 8° and 14° angle of attack. Figure 7.32 compares the experimental total pressure measurements at $x/D = 11.5$ with the corresponding numerical predictions. The experimental total pressure contours again revealed the existence of a large vortical feature generated by the upper wing leading edge, and a much weaker double vortex system formed by the lower wing.

The computational solutions calculated on the Euler grid are plotted with the experimental contours in Figure 7.32a). The inviscid solution provides a good prediction of inviscid and wing primary viscous flow structure, resolving the large leading edge vortex from the upper wing and a single vortex generated by the lower wing. In addition, the inviscid calculation correctly predicts the strong multiple shock interaction which occurs above the lower wing vortices, but fails to predict the existence of any body vortices. The laminar, Euler grid, solution captured a much stronger and extensive upper wing vortex which agrees better with experiment. No second vortex feature is resolved, however, suggesting that, as angle of attack is increased the weak inboard vortex observed for 8° angle of attack, either bursts and disappears or merges with the larger outboard vortex. The lower wing wake reveals a double vortex structure with a strong inboard vortex and an induced outboard feature. In addition, the laminar, Euler grid, calculation correctly predicts the appearance of a shock induced vortex beneath the lower wing and a strong body vortex, matched in experiment, located between the two wings.

The viscous grid calculations are presented in Figure 7.32b) and demonstrate good qualitative agreement with experiment. Both viscous results resemble the laminar, Euler grid, solution except that the upper wing leading edge vortex is slightly weaker, and an extra small vortex is captured at the leeside of the upper body/wing junction. This feature originates from the secondary leeside forebody vortex. The fine NS solutions better resolve the size, strength and location of the body vortex formed in between the wings. The turbulent result appears equivalent to the laminar except that it agrees with experiment in the prediction of a slightly larger, stronger upper wing vortex. Both viscous grid solutions include the double vortex system generated by the lower wing.

The schlieren photograph for the × configuration at 14° angle of attack is reproduced together with the computed symmetry plane density contours in Figure 7.33. The observed flow structure appears very similar to that for 8° angle of attack. The symmetry plane affect of the strong lower wing leading edge shock and the upper wing leading and trailing edge shock waves are, again, evident in the computed plot.

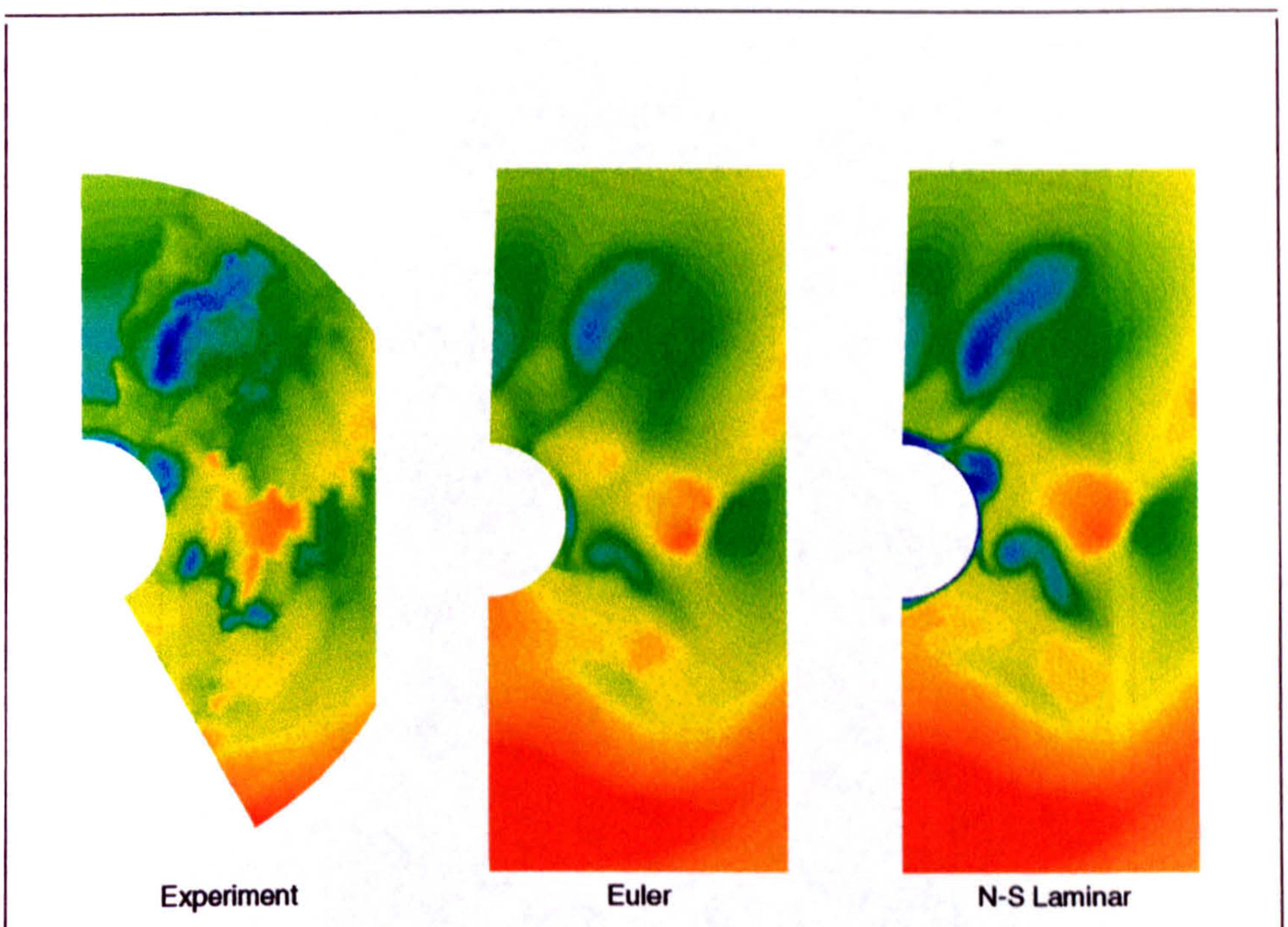

(a) Euler Grid Solutions

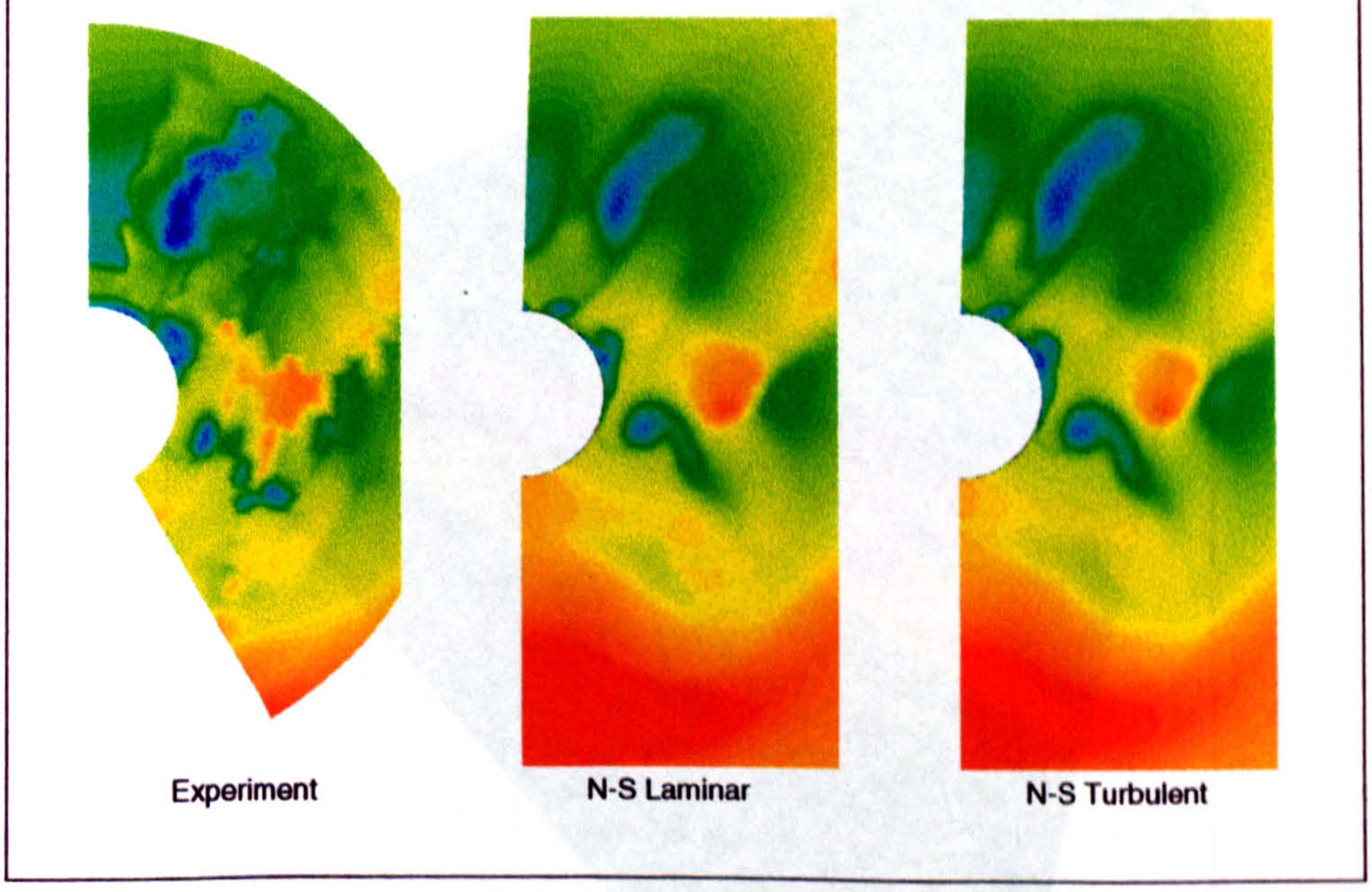

(b) Fine NS Grid Solutions

Figure 7.32: *Total Pressure Contours Comparison,* 45° *Roll, x/D=11.5,* 14° *Incidence*

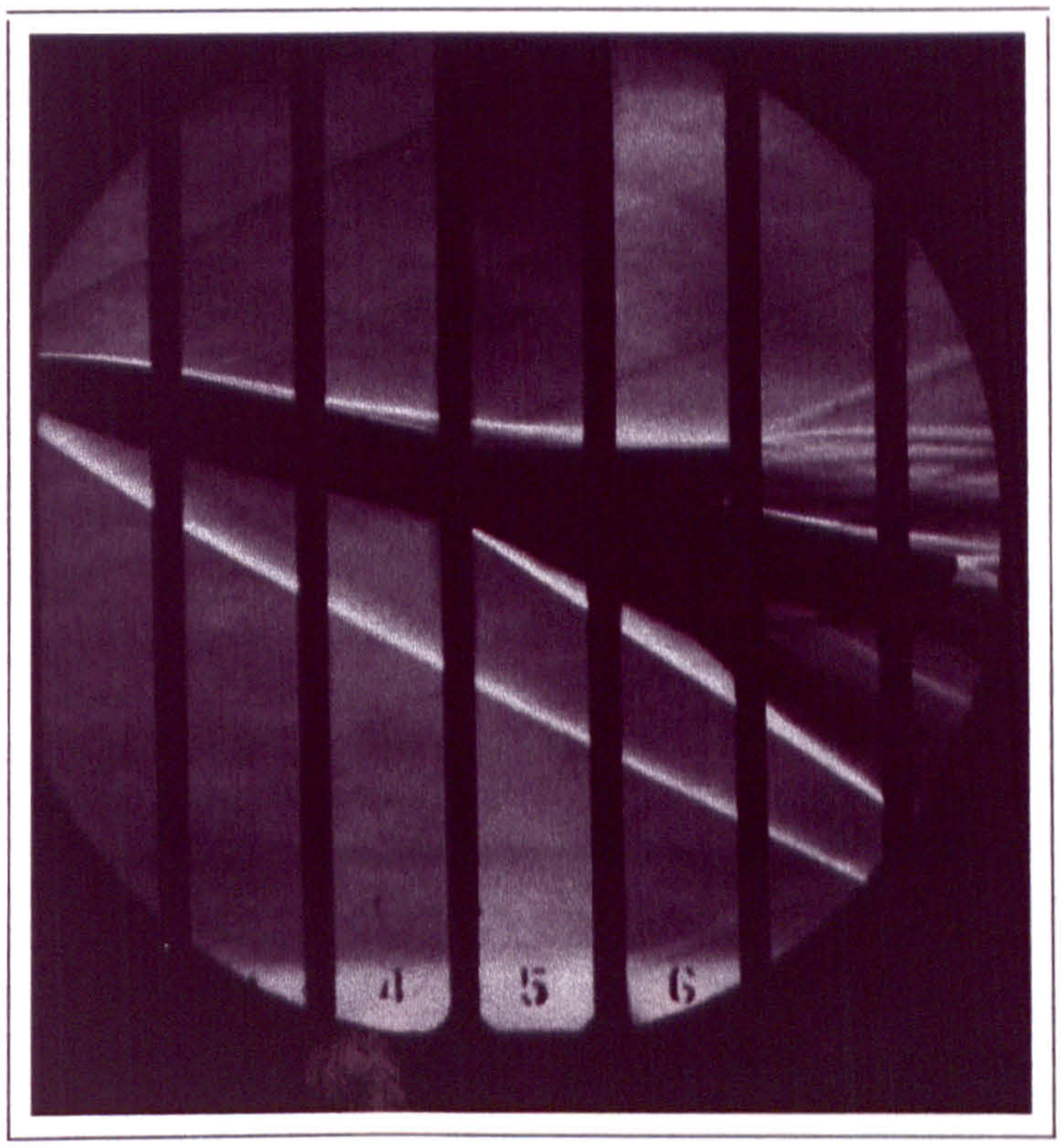

(a) Experimental schlieren

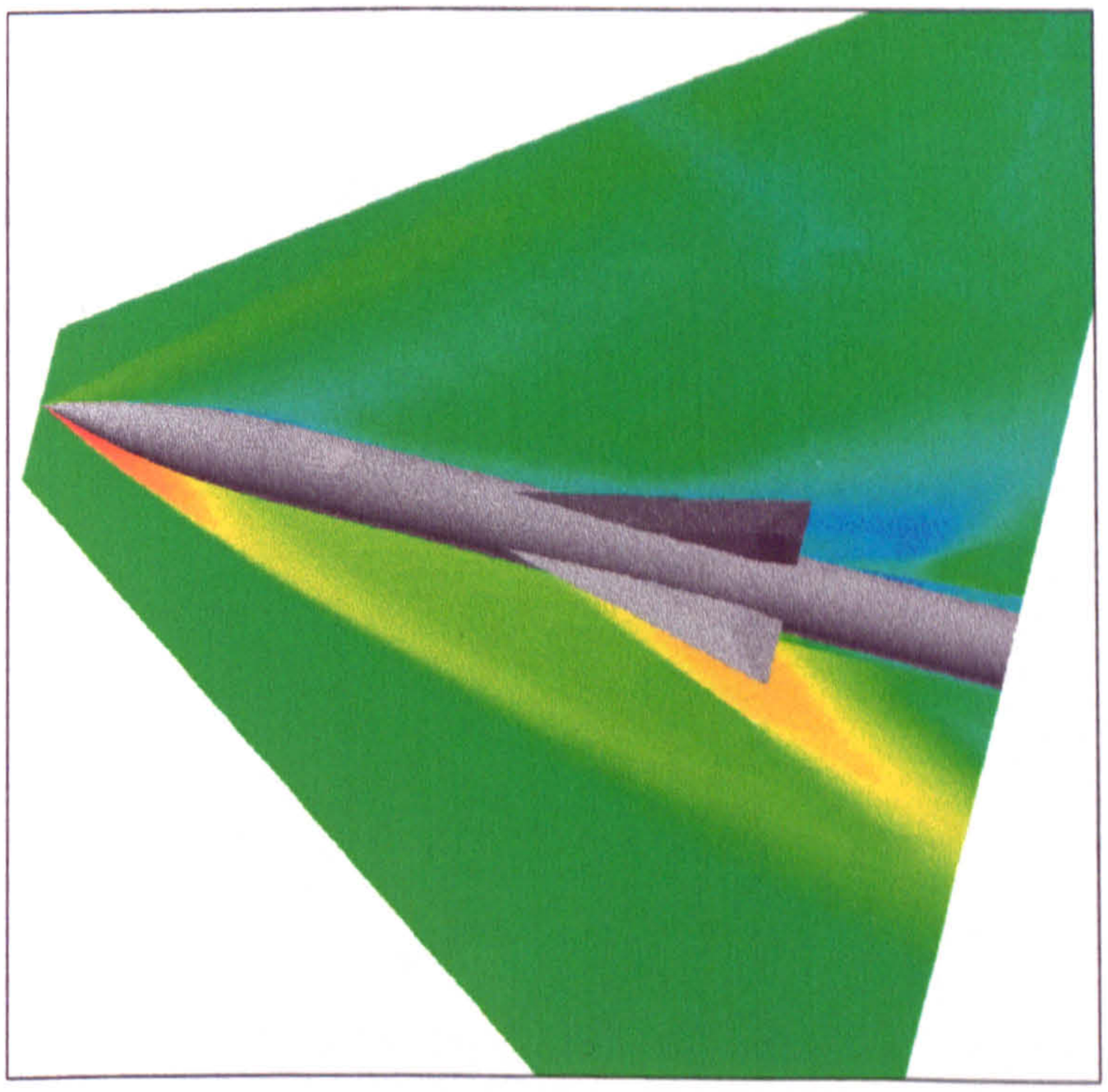

(b) Symmetry Plane (xz-Plane) Density Gradient

Figure 7.33: *Computation vs Experimental schlieren*, 45° *Roll*, 14° *Incidence*

The longitudinal development of the crossflow structure at the higher 14° angle of attack is illustrated in Figures 7.34 and 7.35 which reproduce the experimental vapour screen images and the corresponding computational density contours at the six x/D stations of interest. Although the flowfield is obscured by the shadows from the wings in the first four vapour screen images, the computational results are in excellent qualitative agreement with experiment. The turbulent computational solution, shown, clearly highlights the development of the various shock wave and vortical structures which develop over the wings. These will be described in section 7.4.4. The vapour screen images of the crossflow structure in the wake of the wings clearly distinguish the shock wave and vortical flow structures. The upper wing vortical structure can clearly be seen to be composed of the single large vortex indicated in experimental pressure measurements. The lower wing vortical structure, however, indicates the existence of a strong inboard vortex and a much weaker outboard vortex which was also resolved in the experimental pressure measurements. The computational resolution of the flow in the wake of the wings, again, appears to agree very well with the experimental vapour screen images.

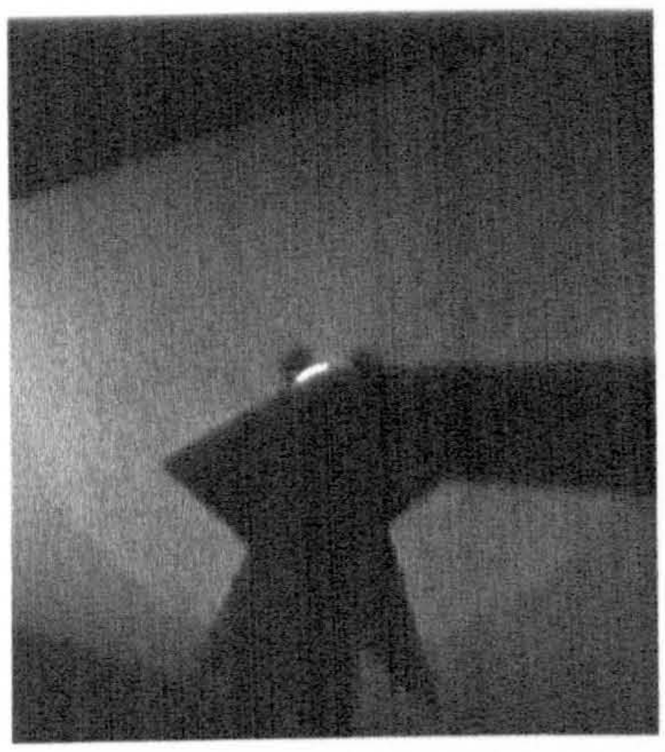

(a) Experiment, $x/D = 6.5$

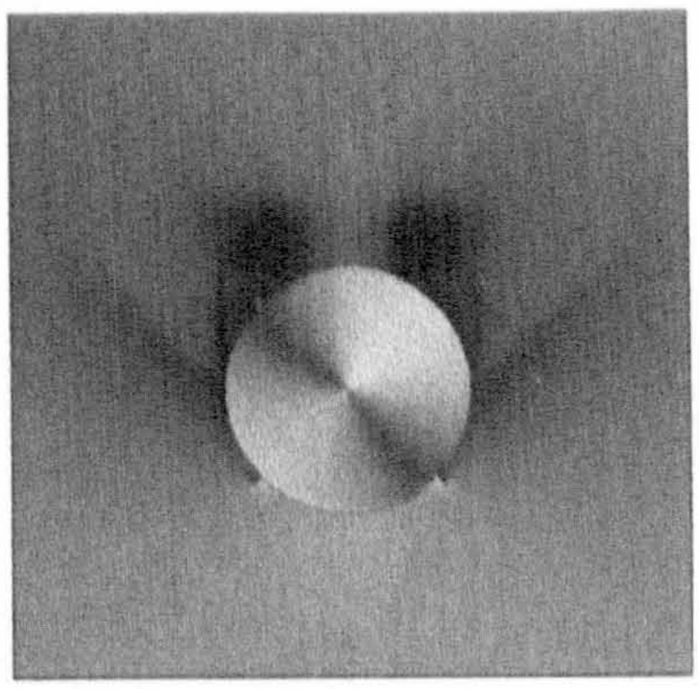

(b) Computation, $x/D = 6.5$

(c) Experiment, $x/D = 7.5$

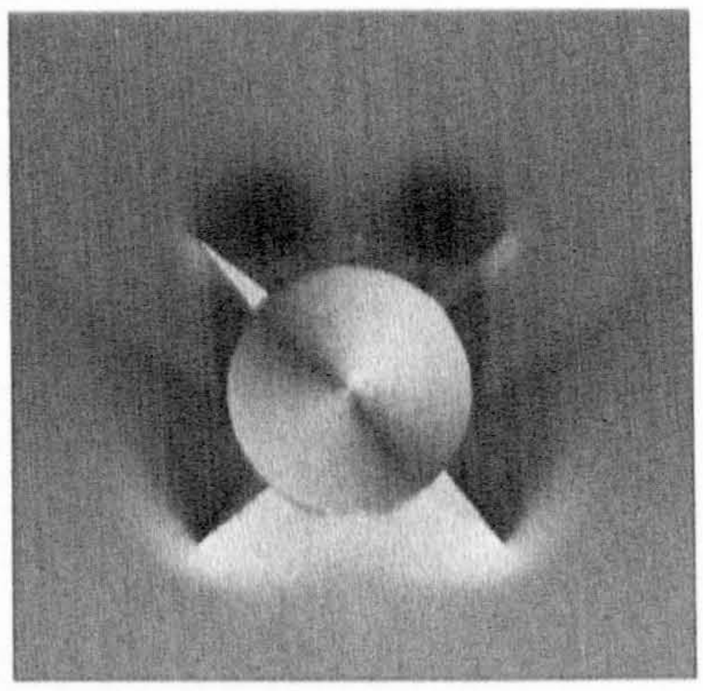

(d) Computation, $x/D = 7.5$

(e) Experiment, $x/D = 8.5$

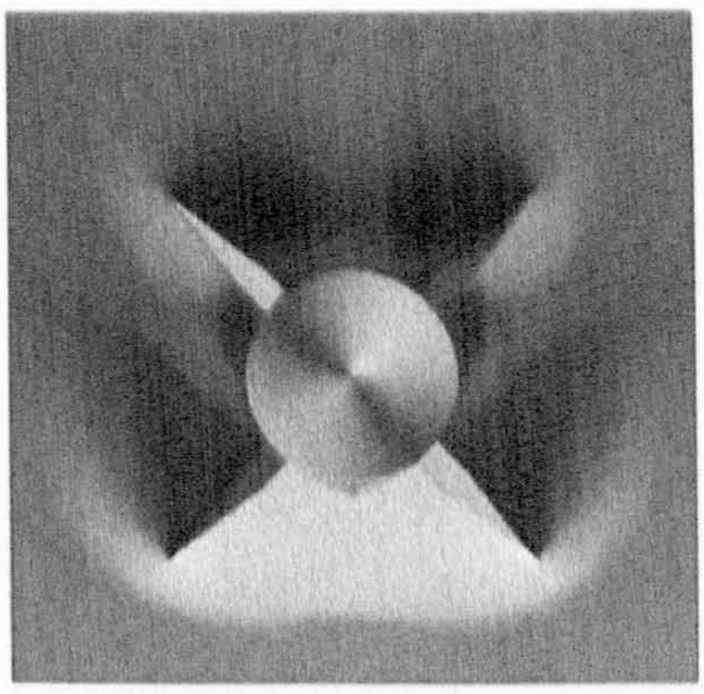

(f) Computation, $x/D = 8.5$

Figure 7.34: *Comparison of Computational and Experimental Vapour Screen Visualisation,* 45° *Roll,* 14° *Incidence*

(a) Experiment, $x/D = 9.5$

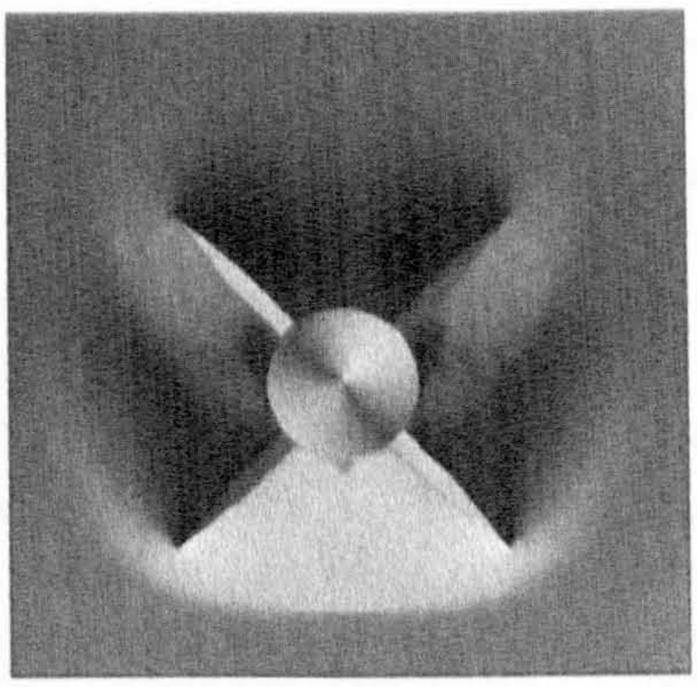

(b) Computation, $x/D = 9.5$

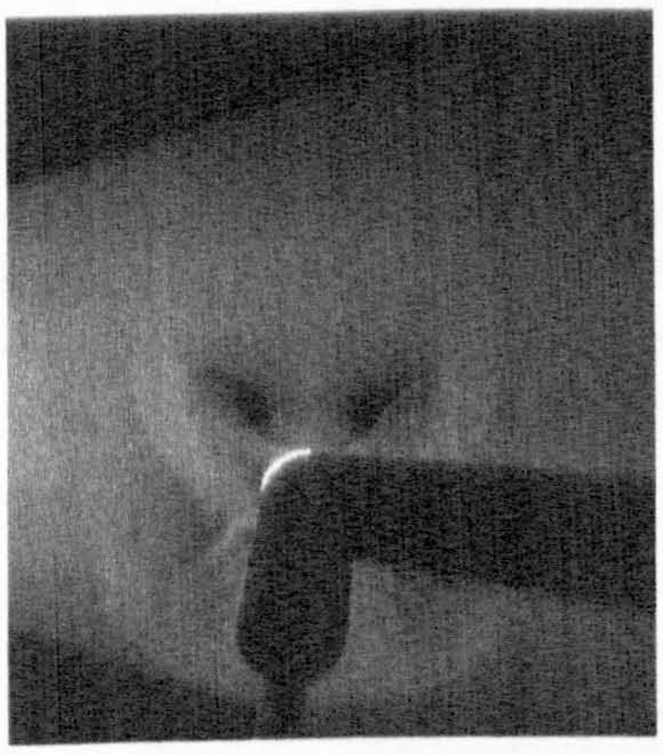

(c) Experiment, $x/D = 10.5$

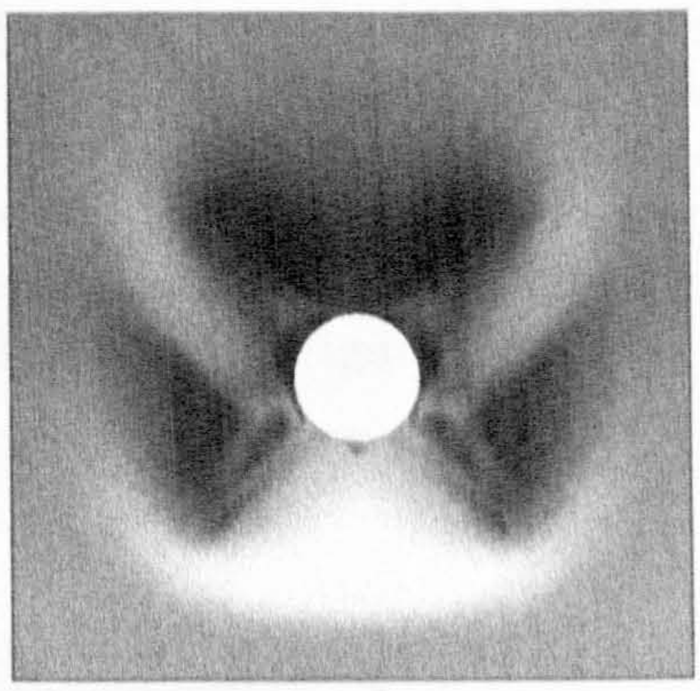

(d) Computation, $x/D = 10.5$

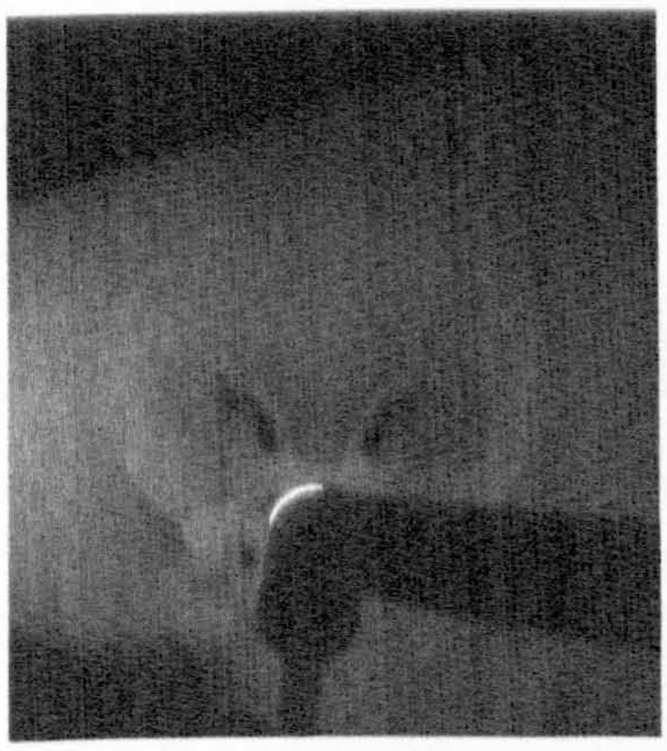

(e) Experiment, $x/D = 11.5$

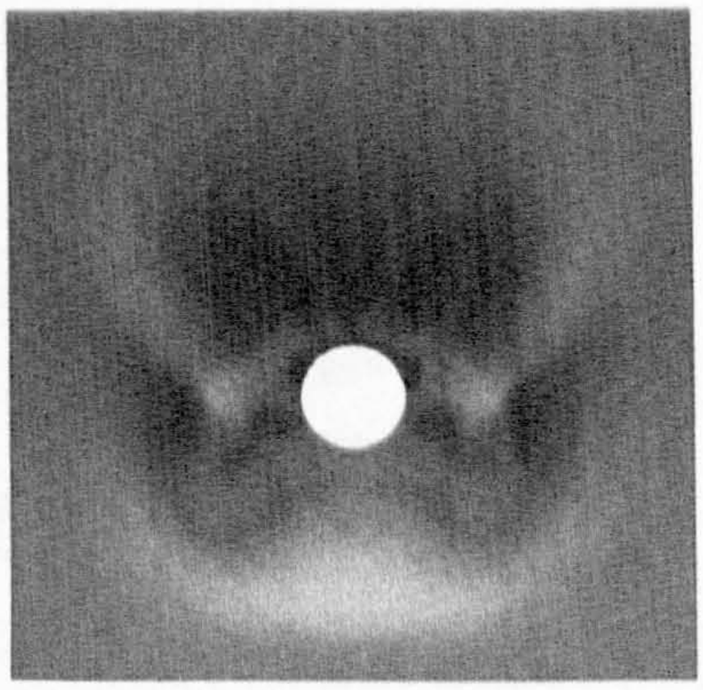

(f) Computation, $x/D = 11.5$

Figure 7.35: *Comparison of Computational and Experimental Vapour Screen Visualisation,* 45° *Roll,* 14° *Incidence (continued)*

7.4.4 B1AW20A3: Aerodynamic Interpretation

The longitudinal development of the crossflow past the inclined B1AW20A3 has been illustrated in sections 7.4.2. and 7.4.3. This section goes on to describe where and how the individual shock wave and vortex features originate.

The supersonic flow over a cruciform, sharp leading edge, swept wing /cylindrical body geometry, historically employed in missile design, begins with the separated vortical flow on the forebody. This portion of the flow is well known and has been described in Chapter 4. The supersonic flow over the cylindrical forebody is independent of the wing geometry or of roll angle, so the flow structure as the supersonic stream encounters the wings at zero roll will be the same as that encountered by the wings at 45° roll for a given incidence.

The vortical flow over the leeside of a sharp swept leading edge delta wing is also well known. The wing geometry incorporated into the B1AW20A3 design, however, differs from the delta wing investigated in Chapter 6, in that the leeside surfaces will not be flat. The study of the NASA delta wing did not involve the trailing edge flow structure, which is important to the understanding of the flow structure in the wake of the cruciform wing arrangement. Consider the inviscid supersonic flow past the 2D wing section employed in the B1AW20A3 design illustrated in Figure 7.36.

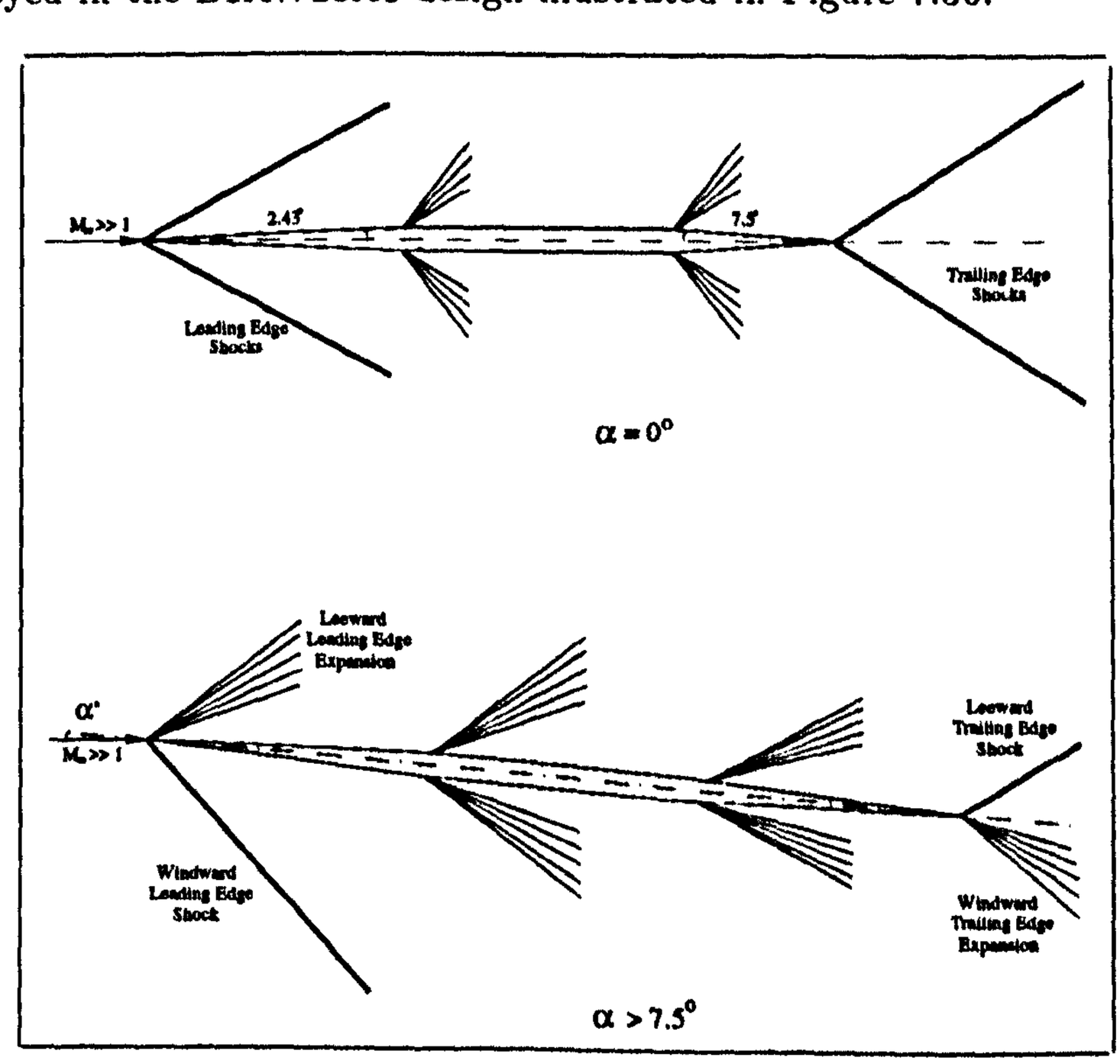

Figure 7.36: *Supersonic Flow Over the RAE W20 Wing Section*

For zero angle of attack, such as the flow past the vertical wings in the + configuration, the leading and trailing edges will create shock waves which will stream off on either side of the wing as shown. If the angle of attack is increased to above 2.43° but below 7.5°, a leading edge shock will exist only in the windward flowfield, the leading edge generating an expansion on the leeward side. The trailing edge will continue to generate two shock waves until above 7.5° angle of attack when the windward trailing edge shock disappears and an expansion fan is generated.

The interaction of the supersonic flowfield around the wing and that around the body leads to the interaction of shocks waves and surface boundary layers, and the interaction of shocks with shocks. When a shock wave impinges on a surface with a viscous layer, the two features will interact. The large pressure rise across the shock wave acts as a severe adverse pressure gradient which is imposed on the boundary layer. If the shock is strong enough it will cause boundary layer separation. Since the near wall portions of the boundary layer will be at subsonic speeds, the high pressure behind the shock feeds upstream forcing boundary layer separation to occur ahead of the impingement of the incident shock. This will, in turn, generate a separation shock wave which will interact with the incident shock. The reattachment of the boundary layer will generate a compression fan which may form a further shock wave which may also interfere with the induced separation shock. If the interaction is purely two-dimensional (ie: no transverse flow), as shown in Figure 7.37, the separated flow will form a separation bubble, whereas a three-dimensional separation will induce a vortex.

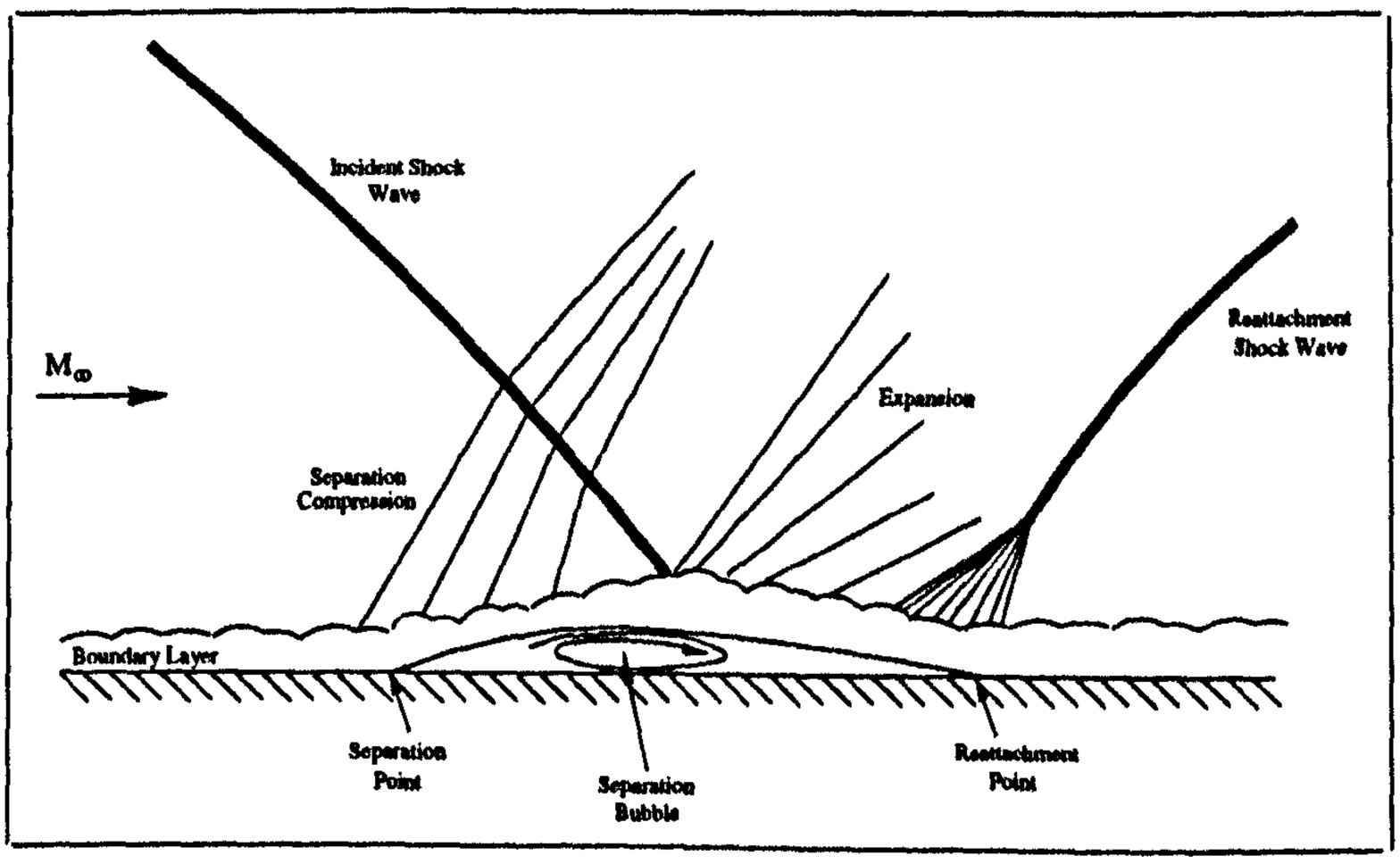

Figure 7.37: *Schematic of a 2D Shock Wave/Boundary Layer Interaction*

The three-dimensional swept shock wave/boundary layer interaction is

extremely significant in missile aerodynamics and has recieved much academic attention in recent decades. The interaction of the flow under a wing connected to a cylindrical body can at first be studied by neglecting body curvature, leading to the simplified model of a flat plate with a sharp fin attached at right angles. A review of this class of flow together with other three-dimensional interactions was written by Peake and Tobak [47] and by Settles and Dolling [64]. The accepted flowfield model can be adapted to describe how the wing leading edge shock interacts with the boundary layer on the side of a cylindrical body.

Figure 7.38 presents the computationally resolved (density contours) shock-boundary layer interaction occurring under the horizontal wing of the + configuration at 14° angle of attack and a schematic interpretation of the resulting flowfield based on the numerical and experimental results. The shock wave generated from the sharp leading edge of the wing acts as the incident shock wave on the cylindrical body creating an even larger adverse pressure gradient resulting in boundary layer separation. Close to the wing leading edge the separated layer will reattach on the wing surface as illustrated. As the wing shock wave moves downstream it simultaneously moves away from the wing such that its interaction with the body boundary layer will progressively more windward, bringing the associated separation point and separated vortical structure with it. Eventually the reattachment point will move off the wing onto the body. As the shock travels further downstream it will become weaker and eventually detach from the separation point on the body. This movement of the separation point traces a separation line on the body surface, as was seen in Figures 7.19 and 7.24. The interaction will be different for different configurations of wing-body junction and will be sensitive to both crossflow Mach number and Reynolds number. In addition to the primary shock induced vortex, secondary features may develop under the primary vortex and on the wing surface where the primary feature may induce secondary separation.

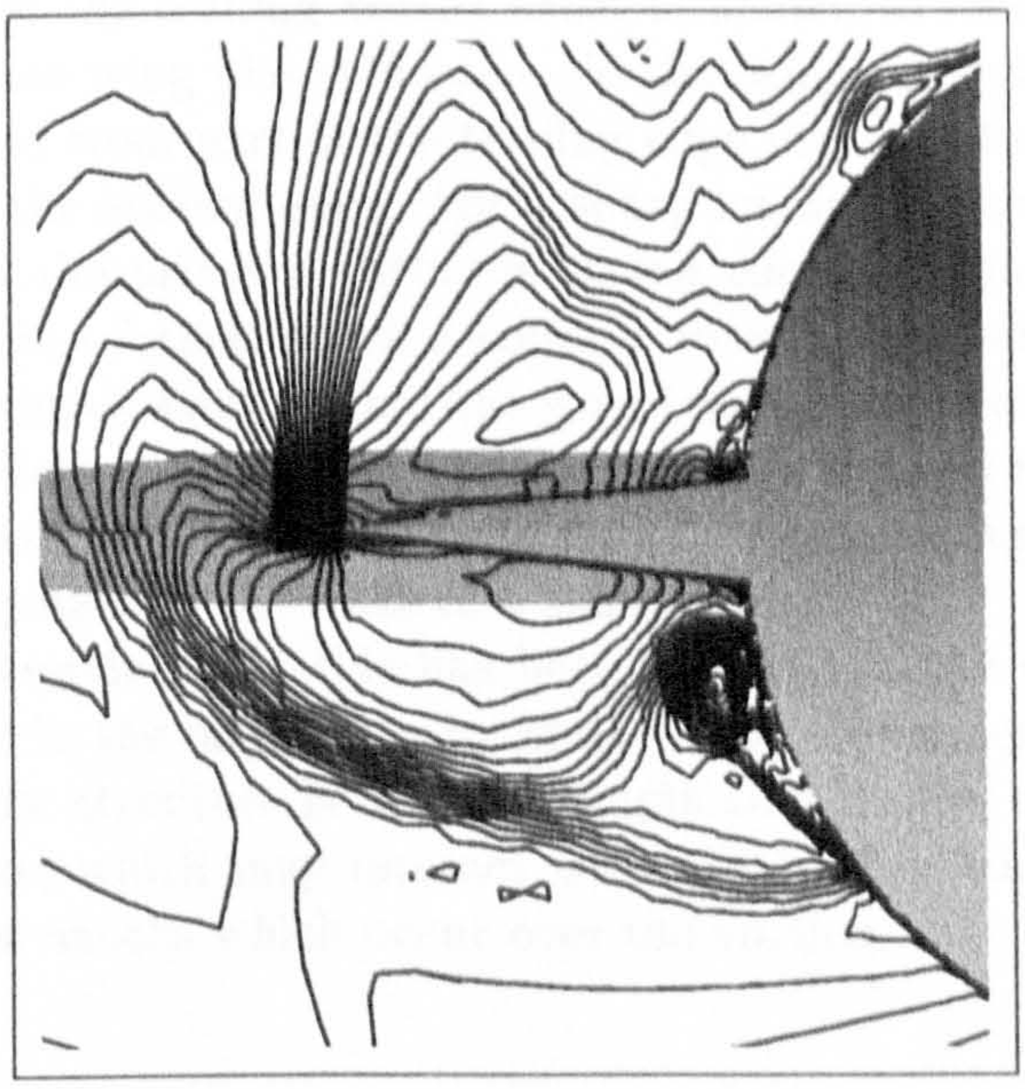

(a) Computation: Density Contours, $\alpha = 14^o$, Zero Roll, $x/D = 7.5$

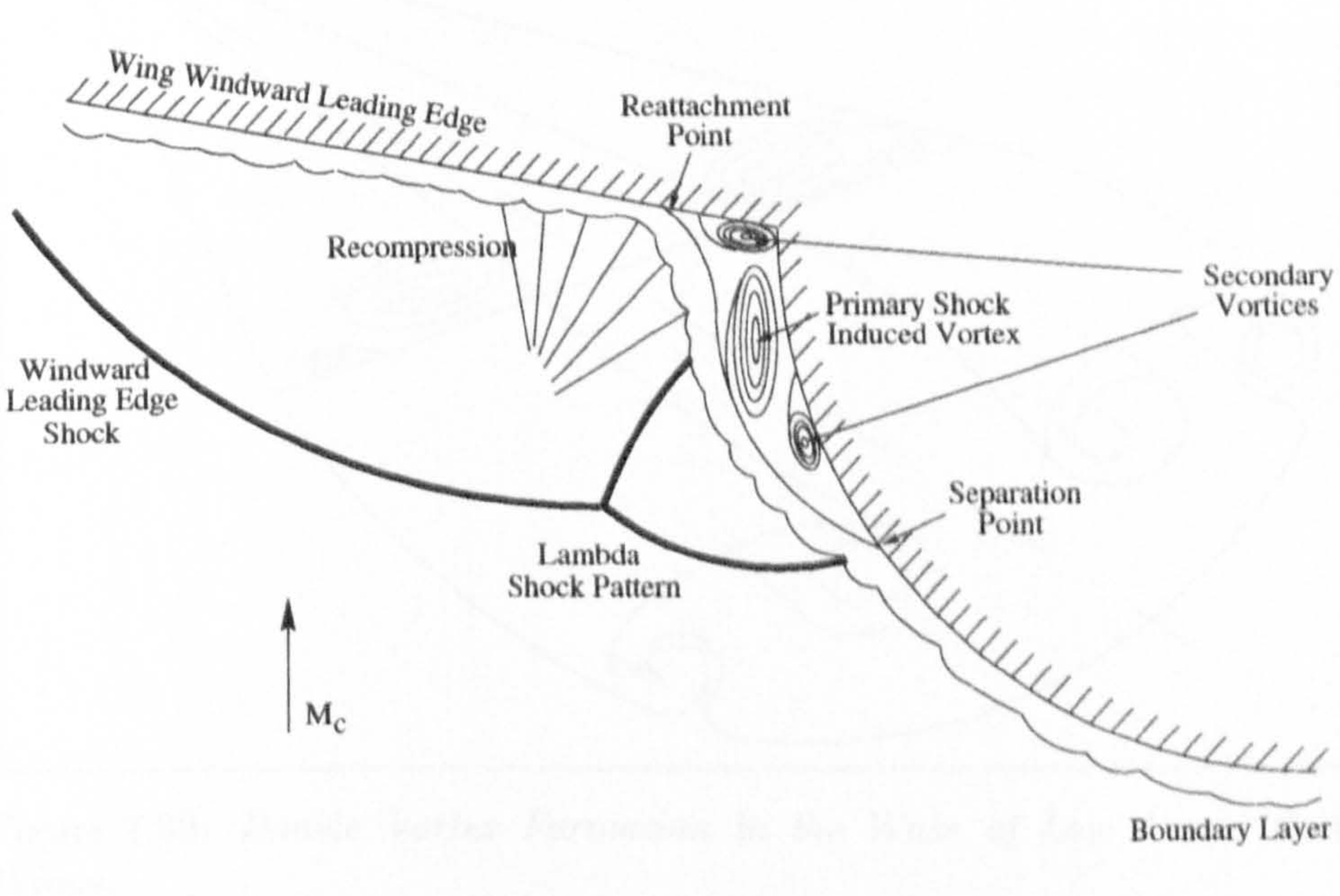

(b) Schematic Interpretation

Figure 7.38: *Sharp Wing-Cylindrical Body Shock-Boundary Layer Interaction*

The roll-up of the trailing vortex sheet is known to be sensitive to the aspect ratio of the wing [69]. On some slender wings of small aspect ratio, the vorticity shed from part of the trailing edge may be of opposite sign to that shed from the leading edge. For a sharp leading edge delta wing, this can occur when the primary vortex is strong enough to induce secondary separation and the formation of a counter rotating secondary vortex. In these cases the vortex sheet behind the wing trailing edge produces two pairs of rolled up vortices as shown in Figure 7.39. Even without the formation of secondary vortices, the bound vorticity may be strong enough to generate a double vortex system in the wake of a slender wing.

For incompressible flows, this has been observed in the wake from Concorde wings and in the laboratory by Maltby [33]. For supersonic flows, the trailing edge flow structure is further complicated by the affect of trailing edge shock waves which may interact with the trailing edge vortex sheet, and by crossflow shocks which occur over the vortices.

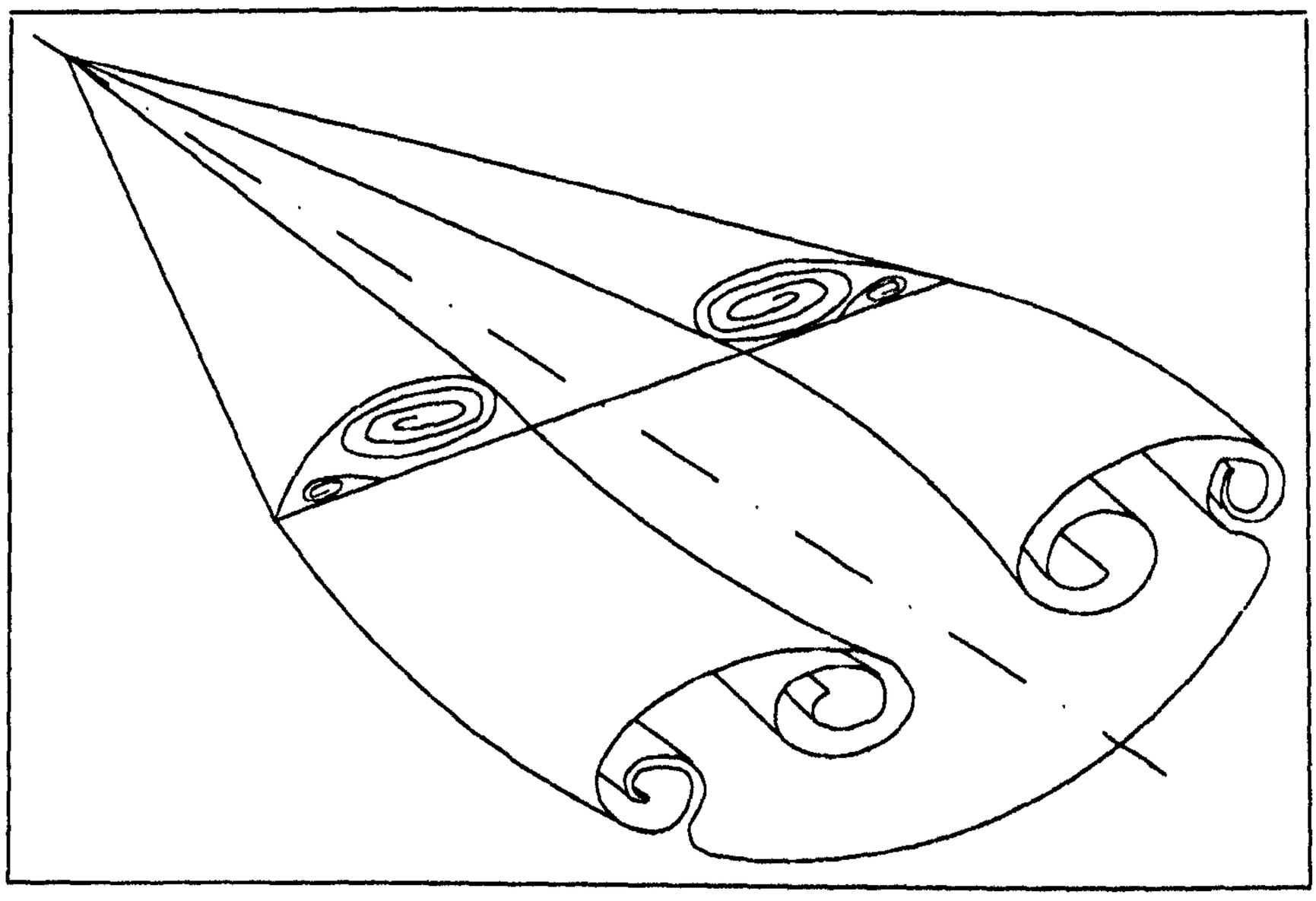

Figure 7.39: *Double Vortex Formation In the Wake of Low Aspect Ratio Wings.*

Further downstream, beyond the cruciform wing arrangement, the shocks generated by the wing leading edges, and those originating from the trailing edges may impinge and interfere with each other. Edney [17] made a seminal study of the interference patterns when two oblique shocks of different strength interact. The analysis of his experimental results and the corresponding heart (pressure-deflection) diagrams identified six different shock interference patterns. Although the hypersonic hemisphere and swept cylinder flows investigated by Edney differ somewhat from the supersonic flows encountered about the inclined body-wing, the shock interaction patterns observed appear similar in both cases, in particular the types I, II and VI of Edneys classification. It is, therefore, useful to review these three types of shock-shock interactions.

Consider the type I interaction shown in Figure 7.40 a) between two oblique shocks waves where shock 1 is the stronger. The impingement takes place at point P, and results in two transmitted shocks, PR and PS, and a slip line, or shear layer, either side of which the density, temperature, entropy and velocity magnitude, but not the pressure or flow direction, will be different. Downstream of the shock impingement the flow will remain supersonic.

If shock 1 becomes much stronger than shock 2, a type II interaction can occur as in Figure 7.40 b). Here the interaction of the two shocks forms a Mach surface, downstream of which the flow will be subsonic. Two transmitted shocks, PS and PQ, are produced together with two slip lines. Both types I and II shock interactions occur when the two impinging shocks are of opposite families, that is, they turn the flow in opposite directions. A Type VI interaction, as illustrated in Figure 7.40 c), occurs when two weak shocks of the same family intersect such that they coalesce to form a single shock wave outboard of the impingement. A slip line will originate from the impingement point together with an expansion fan.

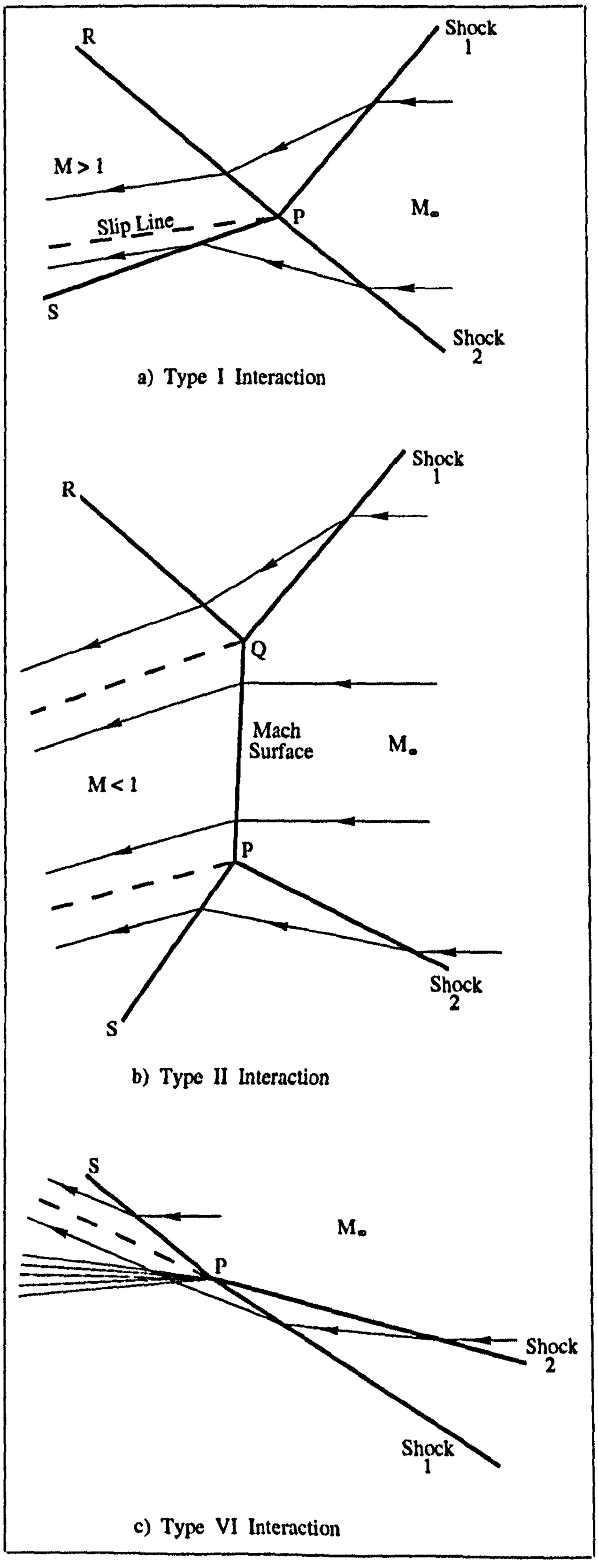

Figure 7.10: Shock Shock Interaction Classifications

The results from the experimental and computational investigation showed that the crossflow structures of a given roll angle (either 0° or 45°) appeared very similar at both 8° or 14° angle of attack. The following sections present an interpretation, for the two roll angles, of the shock-viscous interactions and vortical phenomena that occurred as the flow passed over the body-wing.

Crossflow Development: + Configuration

The longitudinal development of the complex vortical flow, as interpreted from the experimental and computational results, is presented in Figure 7.41 at three rearward longitudinal stations. As the flow passes over the wings the primary forebody vortices are isolated from their feeding sheets. The leading edge vortices develop over the horizontal wing while the associated leading edge shock induces separation and a vortex system to form under the wing. A weak shock wave is also observed under the lower vertical wing. Further downstream, at x/D=9.5, the leading edge shock wave from the horizontal wing and the weak shock generated from the lower vertical wing undergo a type VI shock-shock interaction. A separation bubble is also seen to form on the lower vertical wing, as the flow separates from the beveled edge and reattaches soon after. By the station x/D=11.5 the flow has passed over the wing trailing edges and the double vortex system from the horizontal wing is clearly evident. The primary forebody vortices and the windward shock induced vortices are still seen to be very strong, while the separation bubbles on either side of the lower vertical wing appear to come together in a double vortex system resembling the figure ∞. Trailing edge shock waves have formed above the double vortex system from the horizontal wing and from both upper and lower vertical wings. The lower vertical wing trailing edge shock impinges on the horizontal wing leading edge shock in a type I shock-shock interaction.

An attempt was made to apply the critical point analysis equation of Visbal [62], given by equation (4.2), to these crossflows. For the first two stations shown, the equation could be shown to hold if the small scale vortices (not shown) are neglected. Further downstream in the wake of the wings, the small scale features and the difficulty in locating saddle or half-saddle points, made the task impossible.

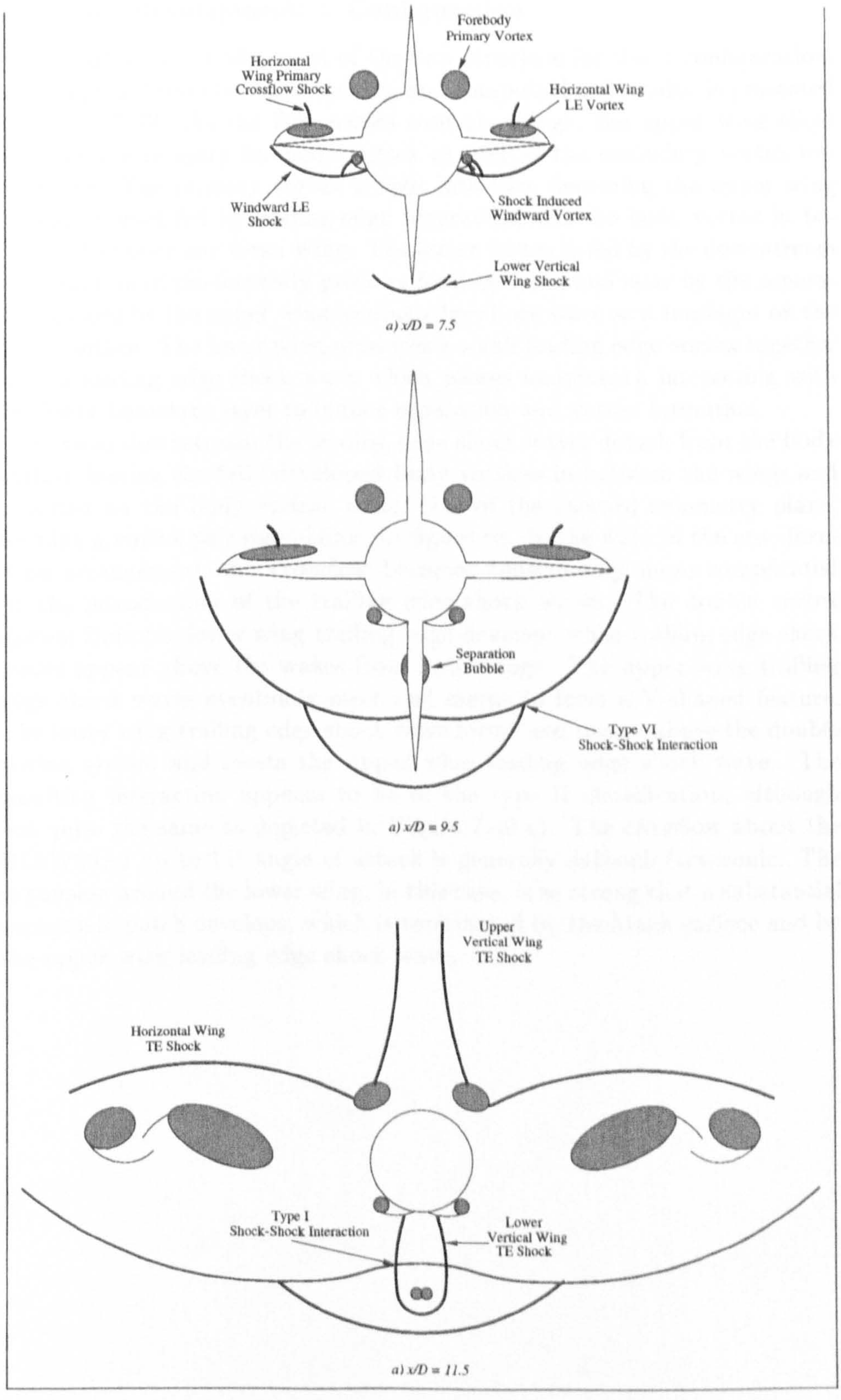

Figure 7.41: *Interpretation of Longitudinal Flow Structure: + Configuration*

Crossflow Development: × Configuration

The longitudinal development of the flow structure for the × configuration, as interpreted from the experimental and computational results, is presented in Figure 7.42. As the flow passes over the wings, the upper wing slices through the primary forebody vortex as well as the secondary vortex underneath. The primary vortex is split into two, becoming the upper wing primary vortex fed by leading edge separation, and the body vortex in between the upper and lower wing. The latter vortex is fed by the downstream continuation of the forebody primary feeding sheet, and later by the separation caused by the upper wing leading edge shock wave as it impinges on the body surface. The lower wing produces a small leading edge vortex together with a leading edge shock wave which passes underneath interacting with the body boundary layer to induce separation and vortex formation.

Further downstream the leading edge shock waves detach from the body surface leaving the fully developed body vortices in between the wings and a vortex on the body surface either side of the leeward symmetry plane, forming a vortex pair resembling the figure ∞. In the wake of the cruciform wing arrangement, the crossflow becomes considerably more complicated by the introduction of the trailing edge shock waves. The double vortex system from the lower wing trailing edge develops while trailing edge shock waves appear above the wakes from both wings. The upper wing trailing edge shock waves eventually meet and merge to form a V-shaped feature. The lower wing trailing edge shock wave forms and passes above the double vortex system and meets the upper wing leading edge shock wave. The resulting interaction appears to be of the type II classification, although not quite the same as depicted in Figure 7.40 c). The crossflow about the B1AW20A3 up to 14° angle of attack is generally subsonic/transonic. The expansion around the lower wing, in this case, is so strong that a substantial supersonic patch develops, which is terminated by the Mach surface and by the upper wing leading edge shock wave.

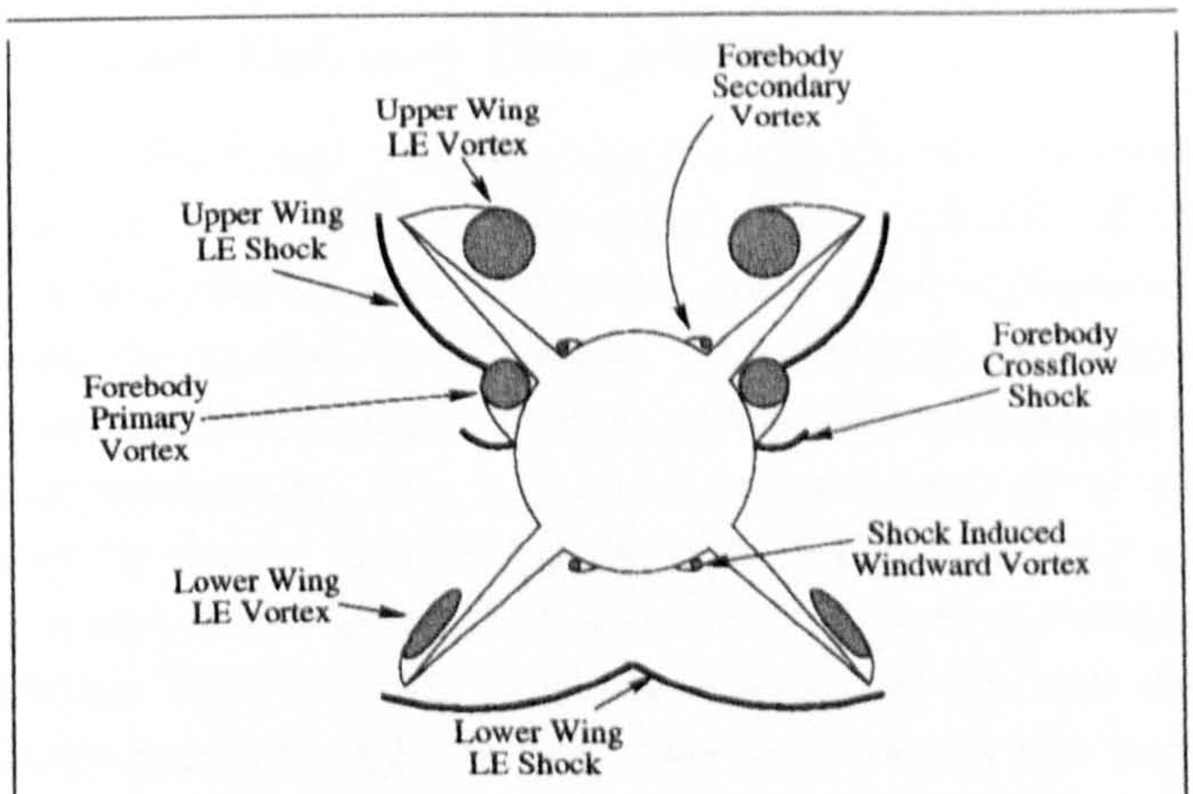

a) x/D = 7.5

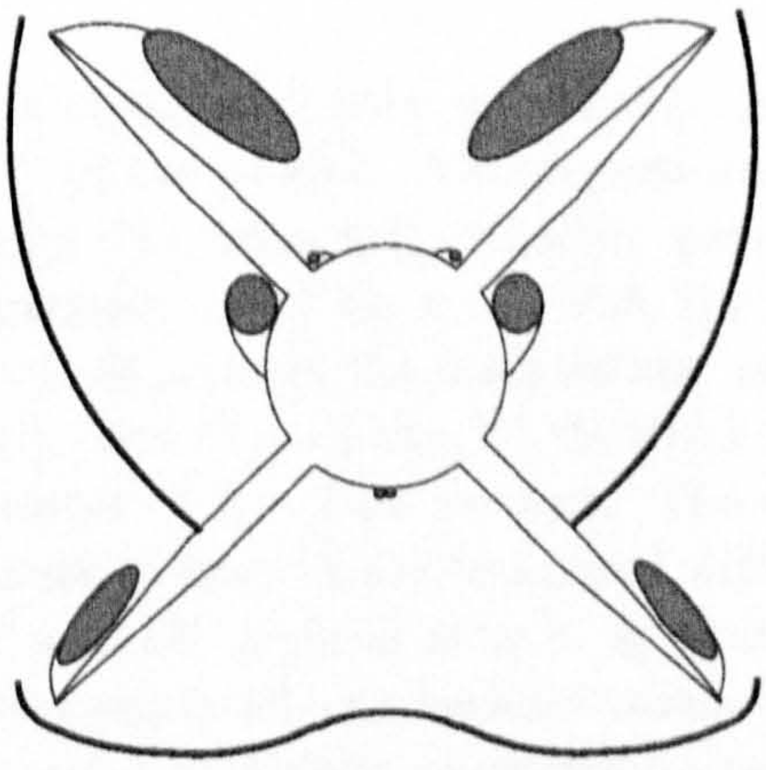

a) x/D = 9.5

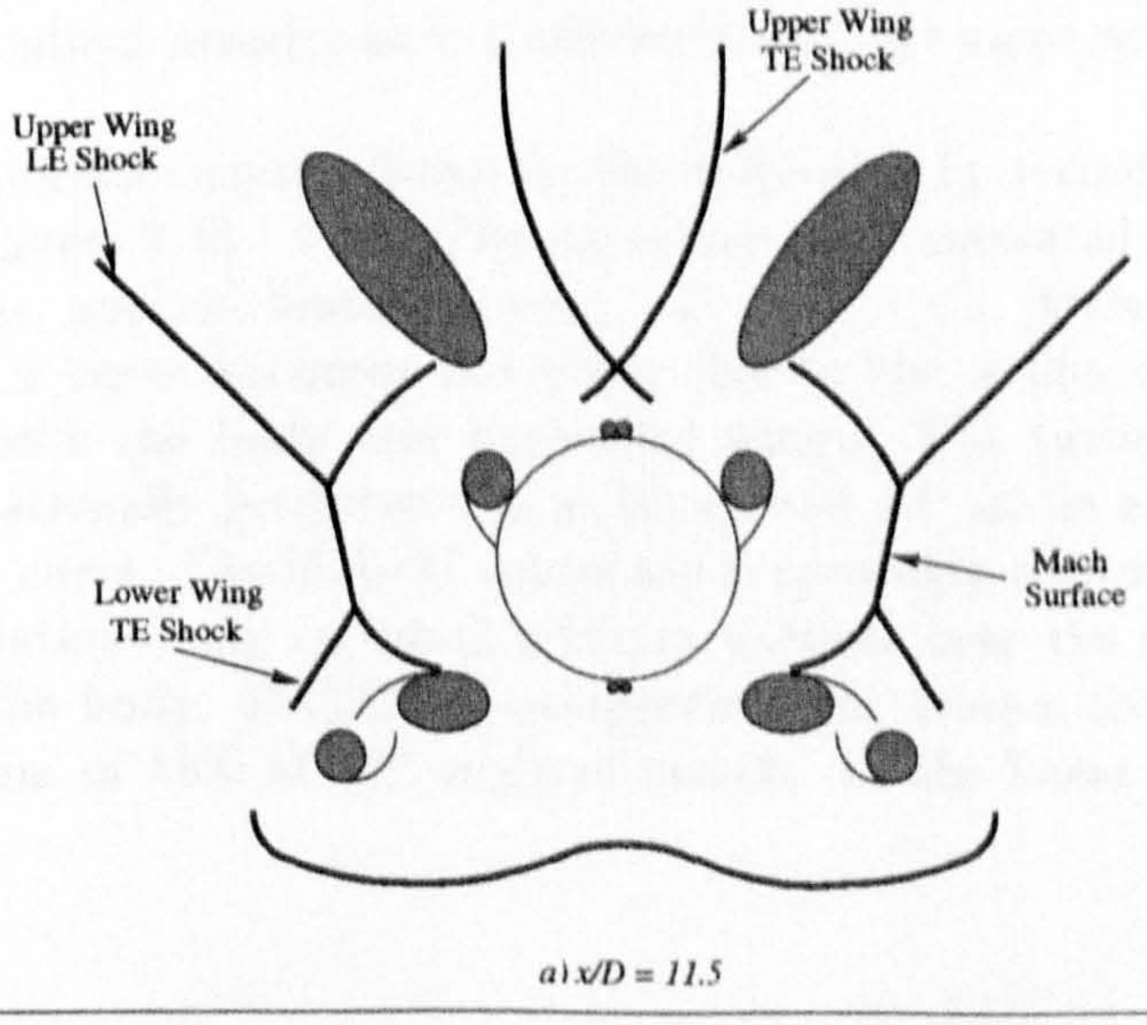

a) x/D = 11.5

Figure 7.42: *Interpretation of Longitudinal Flow Structure: × Configuration*

7.4.5 Force and Moment Prediction

The longitudinal force and moment measurements were repeated 14 times and demonstrated repeatability to within a few percent of the measured values. The experimental measurements were later compared with those calculated from the numerical solutions. The inviscid and viscous contributions to the forces and moments, obtained from the computational solutions, were calculated separately. The x, y and z components of the inviscid forces were calculated by simply evaluating the product of the computed wall pressure and the relevant component of the cell face area corresponding to the wall. The viscous force contribution was calculated by first evaluating the required velocity gradients which were used to work out the wall shear stress components τ_{xx}, τ_{xy} etc. The x, y and z components of the wall shear stress could then be evaluated. Given the viscous and inviscid forces acting in the x, y and z directions, it was then possible to work out the axial (x) and normal (z) force characteristics and the pitching moment about the centre of gravity.

The computational investigation took no account of the flow past and around the base section of the model. The experimental force data was, therefore, corrected using the base and chamber pressure measurements such that a direct comparison could be made with the computational predictions. Figures 7.43 - 7.46 present the longitudinal aerodynamic characteristics (C_L, C_D, C_M, C_N and C_A) of the B1AW20A3 at Mach 2.5 with a freestream Reynolds number of 4 million per foot. The experimental curves (between -4^o and 18^o angle of attack) are compared with the numerical predictions obtained for 8^o and 14^o angle of attack. In addition a further three zero incidence cases were calculated - an inviscid computation using the Euler grid and a laminar and a turbulent computation using their respective grids, providing extra drag and axial force data. Turbulent PNS predicted results at 8^o and 14^o angle of attack were obtained from Ludlow [32] who applied the multiblock version of the PNS solver on these cases. The DATCOM97 aerodynamic prediction program was also used to obtain predictions for the longitudinal aerodynamic coefficients over the same angle of attack range.

The longitudinal characteristics for the body-wing in + configuration are plotted in Figures 7.43 - 7.44. The experimentally measured normal force coefficient C_N, appears linear between $-4^o > \alpha > 4^o$. Above 4^o angle of attack the C_N curve becomes non-linear due to the action of the leeside vortices on both the body and horizontal wings. The turbulent NS and PNS computationally predicted C_N at 0^o, 8^o and 14^o all lie exactly on the experimental curve. The inviscid values are surprisingly accurate given that the Euler solutions only captured primary vortices over the wing surfaces and not on the body. DATCOM overpredicts the normal force coefficient by a maximum of 15% at 18^o angle of attack. In the linear region below

$\alpha = 5^o$, however, DATCOM compares much better, with a maximum error of about 8% at 5^o angle of attack.

The axial force coefficient C_A is not predicted very accurately by CFD. The inviscid predictions give values of only half those measured experimentally. This is not surprising since they will only account for the pressure contribution to the axial force. The viscous NS and PNS results, which should match experiment much more accurately, are better but underpredict experiment by a maximum of about 15%. The DATCOM result follows the experimental curve with an accuracy of about ±5%. The experimental variation in the 14 sets of C_A measurements was assessed by Wilcox [84] who observed a variation of about $\Delta C_A \approx \pm 0.006$ which approximates to about 2% of the measured values. The differences between the NS resolved axial force and the experimental measurements can therefore arise only as a result of either the numerical resolution of the viscous layers, or the experimental errors due to the axial force balance load limit which is close to the measured values and the treatment of the base and chamber contribution to the axial force. The pronounced rise in the experimental curve occurring around zero angle of attack is the result of flow separation on the leeside of the body and over the leading edges of the wings.

The pitching moment coefficient C_M taken about the centre of gravity position is predicted very well by the viscous computations. The numerical NS values for 8^o angle of attack are almost equivalent to the experimental result, but at $\alpha = 14^o$ the NS computations predict values about 3% too low. The inviscid result correctly predicts the pitching moment coefficient up to 8^o angle of attack but fails to correctly capture the non-linearity due to the affect of the leeside body vortices. The DATCOM prediction gives the correct trend, but consistently underpredicts the magnitude of C_M, the maximum error of about 60% occurring at about $\alpha = 12^o$.

The lift coefficient C_L, resolved from its axial and normal components, is predicted almost exactly by all three numerical methods - the turbulent NS and PNS and the Euler calculations. The DATCOM result matches experiment up to 2^o and then begins to overpredict C_L as angle of attack is increased. At $\alpha = 18^o$ the semi-empirical code overpredicts experiment by $\Delta C_L \approx 1.0$ which amounts to about 20% of the experimental value. The drag coefficient C_D , resolved from its axial and normal components, is also predicted very well by the two NS solvers, both of which give results equivalent to experiment. The inviscid solution, as expected, underpredicts the drag since it does not account for any viscous contribution. The Euler results, however, still correctly resolved the characteristic shape of the C_D vs α curve, as does the DATCOM result which provides the worst match with experiment. The DATCOM results match experiment up to about 4^o angle of attack above which it overpredicts the drag coefficient until, at $\alpha = 18^o$ the difference is $\Delta C_D \approx 0.5$ or about 25%.

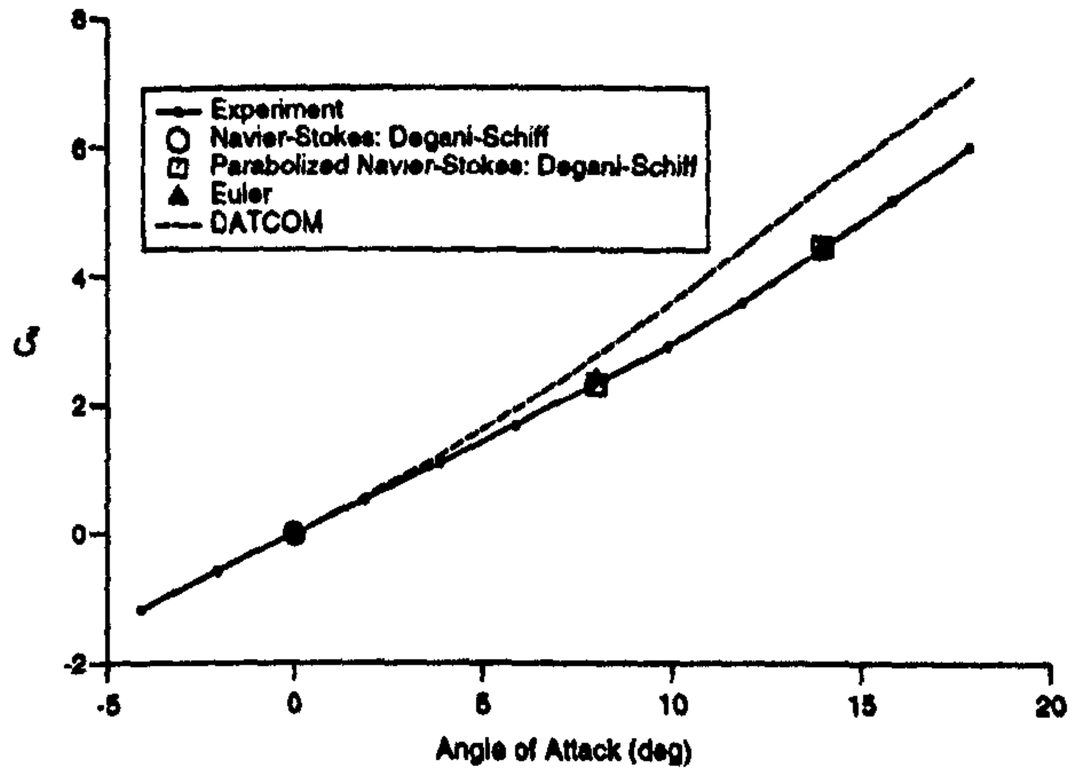

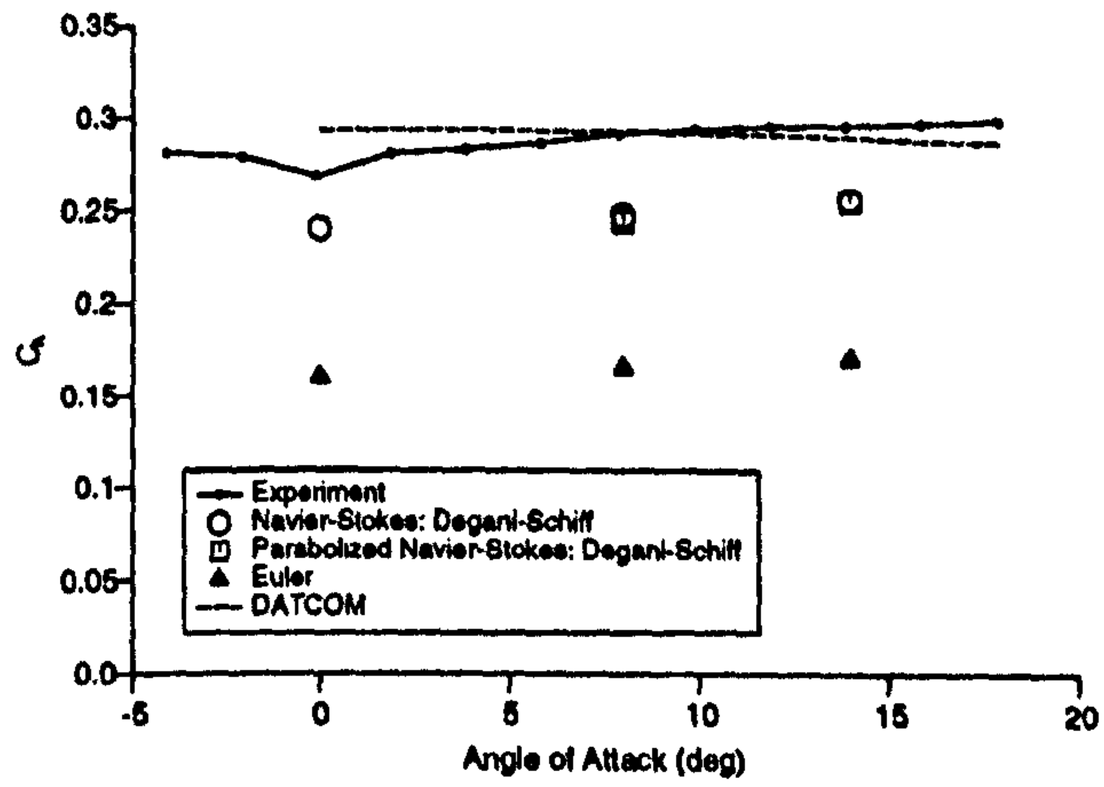

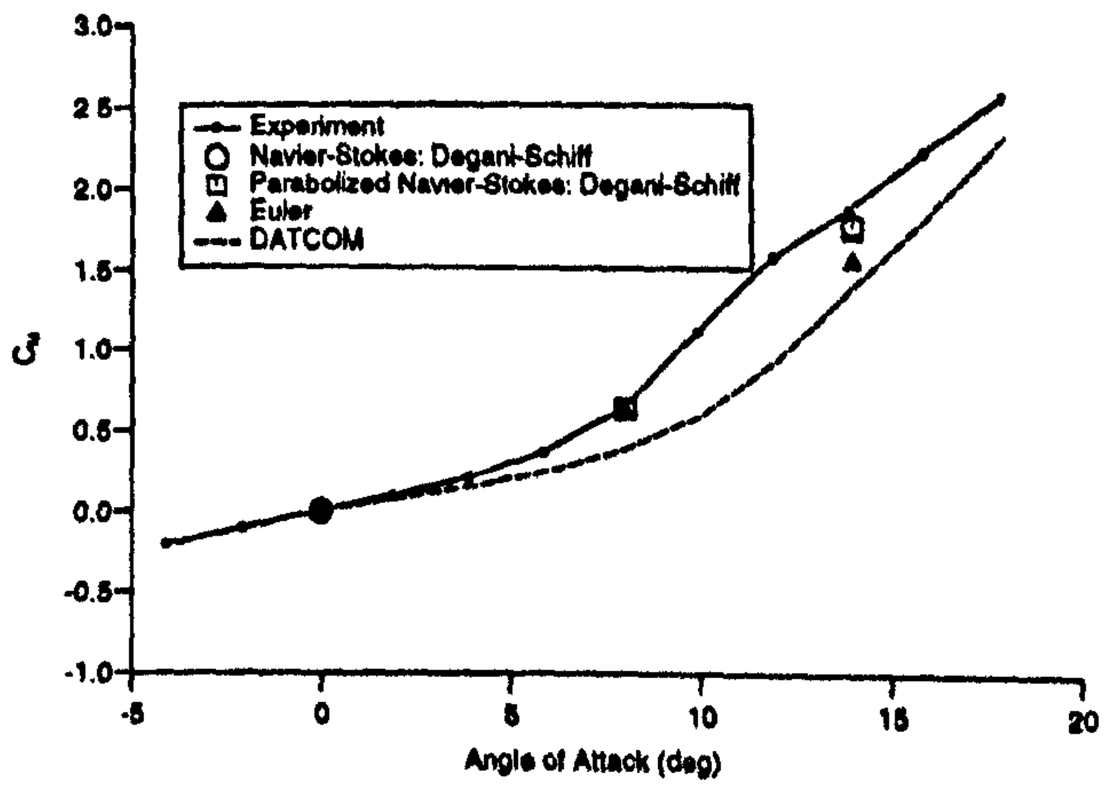

Figure 7.43: *Force Coefficients: Plus Configuration*

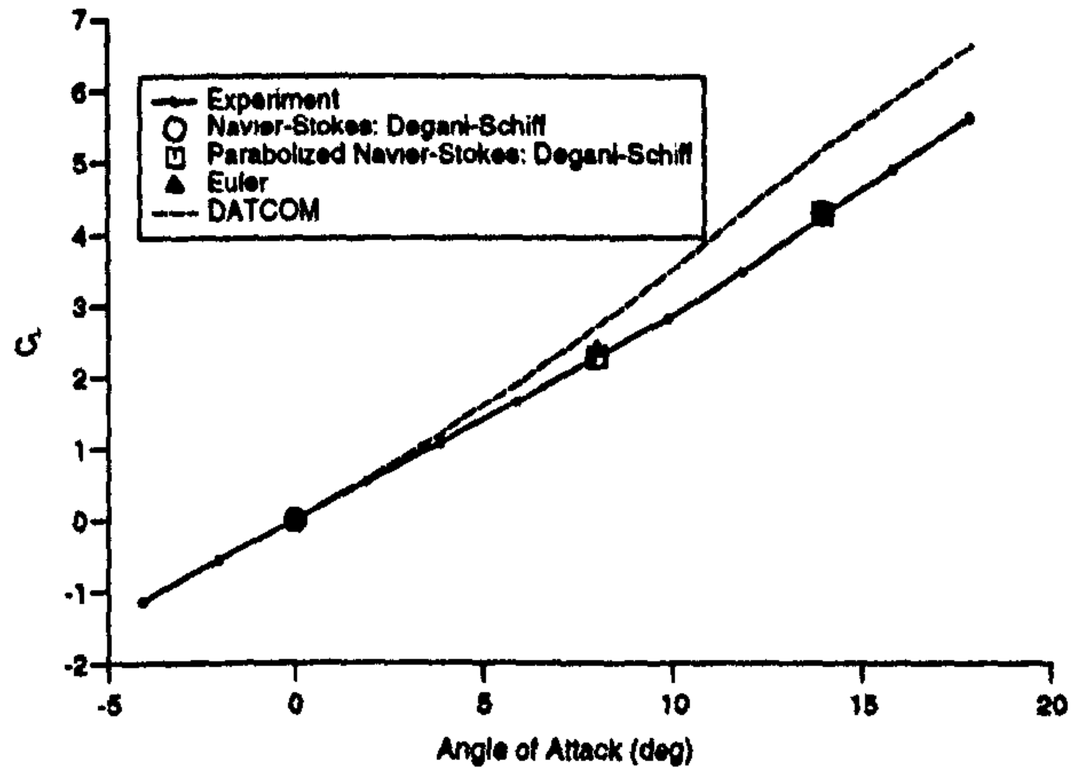

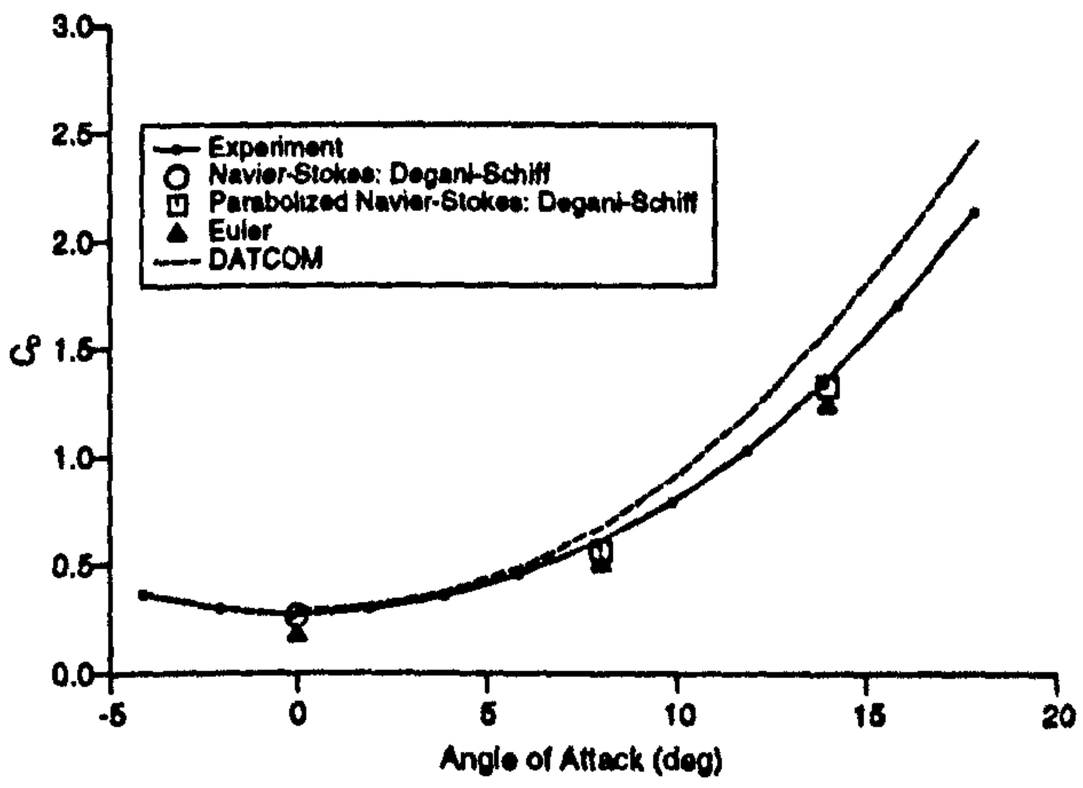

Figure 7.44: *Force Coefficients: Plus Configuration, continued*

The longitudinal characteristics for the body-wing in × configuration are plotted in Figures 7.45 - 7.46. The normal force coefficient is accurately calculated by both NS solvers, while the inviscid calculation which captures the primary vortices generated by the sharp leading edge separation, matches experiment to within 10%. The normal force coefficient for the + and × configuration at a given angle of attack is equivalent up to 10° angle of attack, above which the + configuration produces more normal force. At 18° angle of attack the difference in normal force coefficient is about 0.5.

The same trends appear in the prediction of axial force coefficient for the × configuration as were seen for the + configuration. The best prediction is provided by DATCOM which is within ±5% accuracy over the whole range of angle of attack. The turbulent NS and PNS predictions, which are both equivalent, underpredict the experimental measurements by as much

as 20%, while the inviscid calculation predicts only the pressure contribution. Comparison of the experimental curves for both roll configurations shows that, within the accuracy indicated by repeatability, they are almost equivalent over the α range. The experimental pitching moment coefficient demonstrates a dramatic change which occurs around $5-6^o$ angle of attack. This is due to both the increased effectiveness of the upper wing (which is somewhat shielded by the lower wing) and also to the emergence of strong leeside forebody vortices. The turbulent NS predictions at 8^o and 14^o angle of attack both compare well with experiment and appear to capture the rapid rise in pitching moment. The inviscid computation also captures the non-linearity since it successfully resolves the primary vortices generated by the sharp leading edges of both wings, but fails to predict the magnitude of the rise. At 14^o angle of attack the Euler result underpredicts the experimental measurement by as much as 20%. The DATCOM prediction appears very similar to the Euler result, both failing to resolve the extent of the viscous effects. Comparison of the experimental C_M measurements for the two roll angles shows that below 6^o angle of attack both results are equivalent. Above $\alpha = 6^o$, however, the $\times$ configuration begins to generate greater pitching moments until, at 18^o angle of attack the $\times$ configuration C_M is 40% greater than that generated by the corresponding + configuration.

The lift and drag coefficient characteristics are plotted in Figure 7.46. The lift coefficient appears to vary almost linearly with angle of attack up to 18^o. Both NS and PNS turbulent solutions compare almost equivalently with experiment at 8^o and 14^o angle of attack. The inviscid solutions compare almost as well, predicting C_L to within 3%. The DATCOM result overpredicts the effect of vortex suction above 2^o angle of attack with a lift coefficient at $\alpha = 18^o$ about 20% greater than experiment. Comparison between the + and $\times$ configuration lift curves shows that up to 10^o angle of attack the lift coefficients are equivalent, and beyond this the + configuration generates higher values of C_L. The drag coefficient for the $\times$ configuration is predicted very well by the two NS solvers, both of which give results equivalent to experiment at the two angles of attack investigated numerically. The inviscid solution, as expected, underpredicts the drag since it does not account for any viscous contribution, but still successfully resolves the characteristic shape of the C_D vs α curve. DATCOM is seen to perform well at very low incidences up to about 5^o, after which it begins to depart from the experimental curve. The DATCOM results overpredict the drag coefficient at high angles of attack, and at $\alpha = 18^o$ the difference is $\Delta C_D \approx 0.6$ above experiment, equating to an inaccuracy of about 10%. As with the lift curves, the drag coefficient at a given angle of attack is equivalent up to 10^o angle of attack, above which the + configuration generated a higher value of C_D.

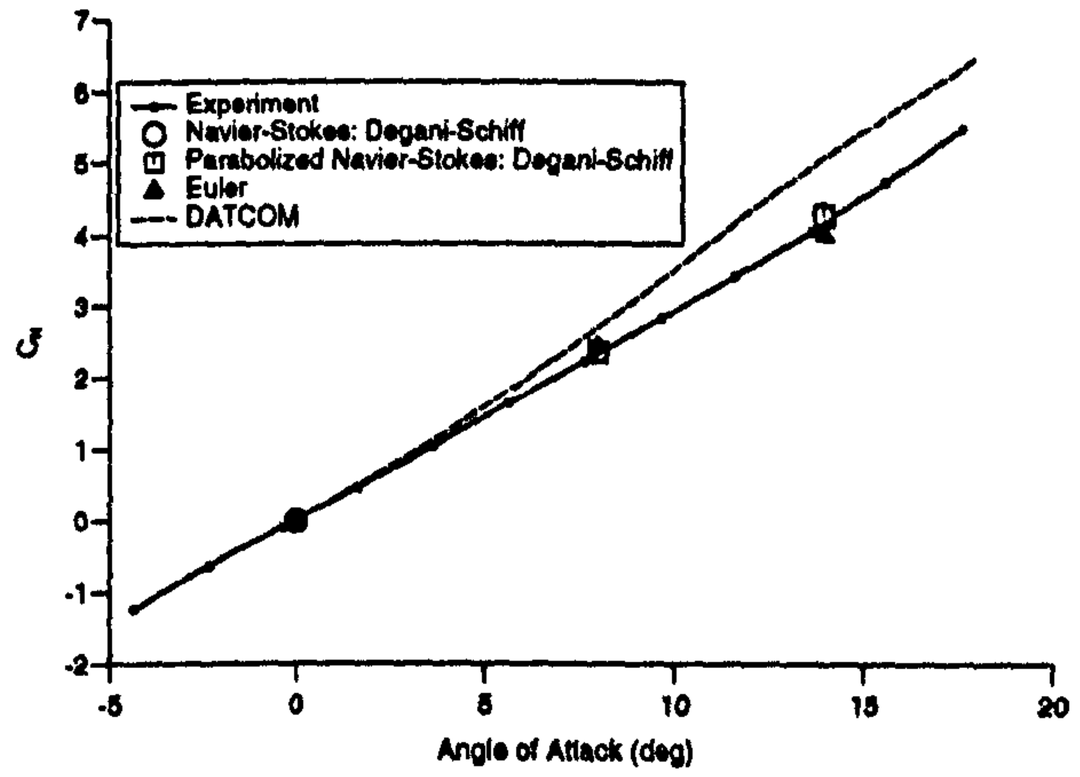

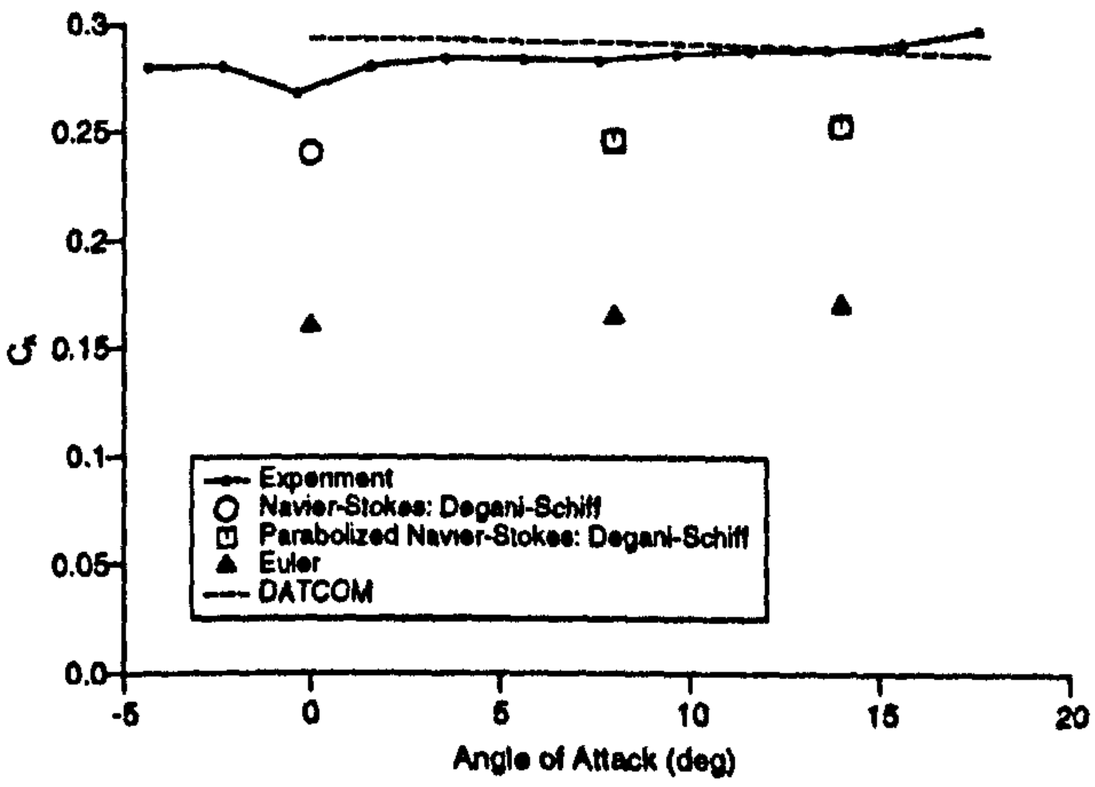

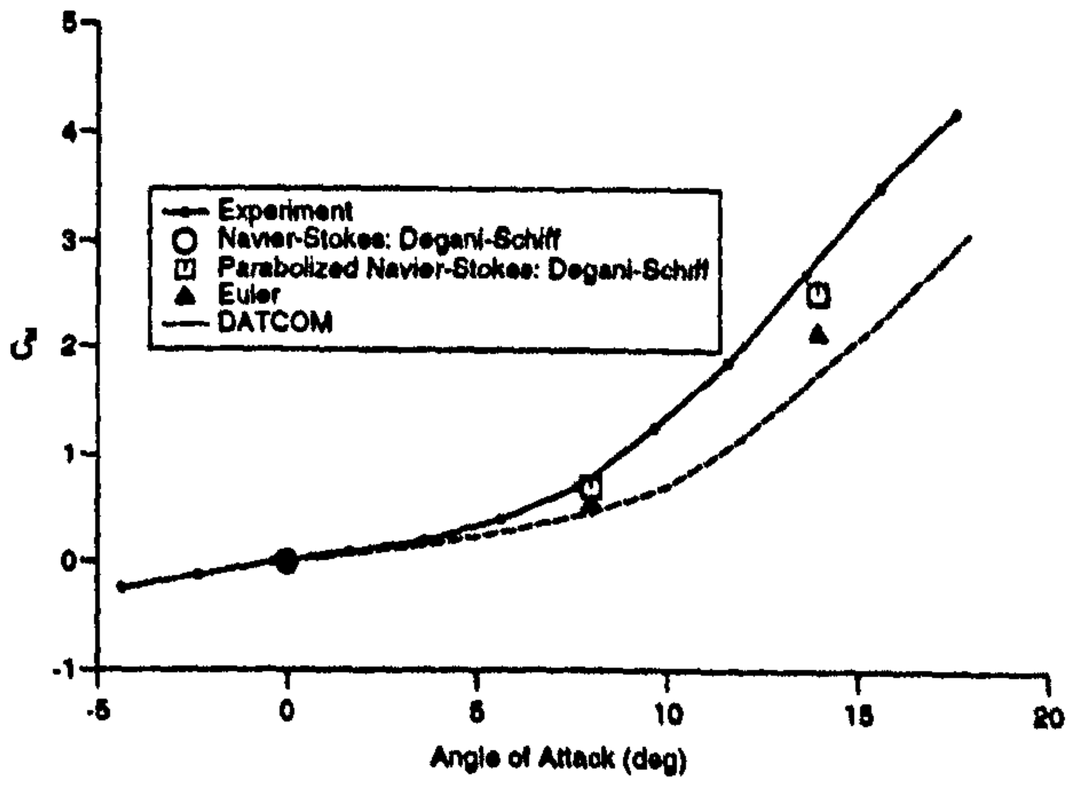

Figure 7.45: *Force Coefficients:* × *Configuration*

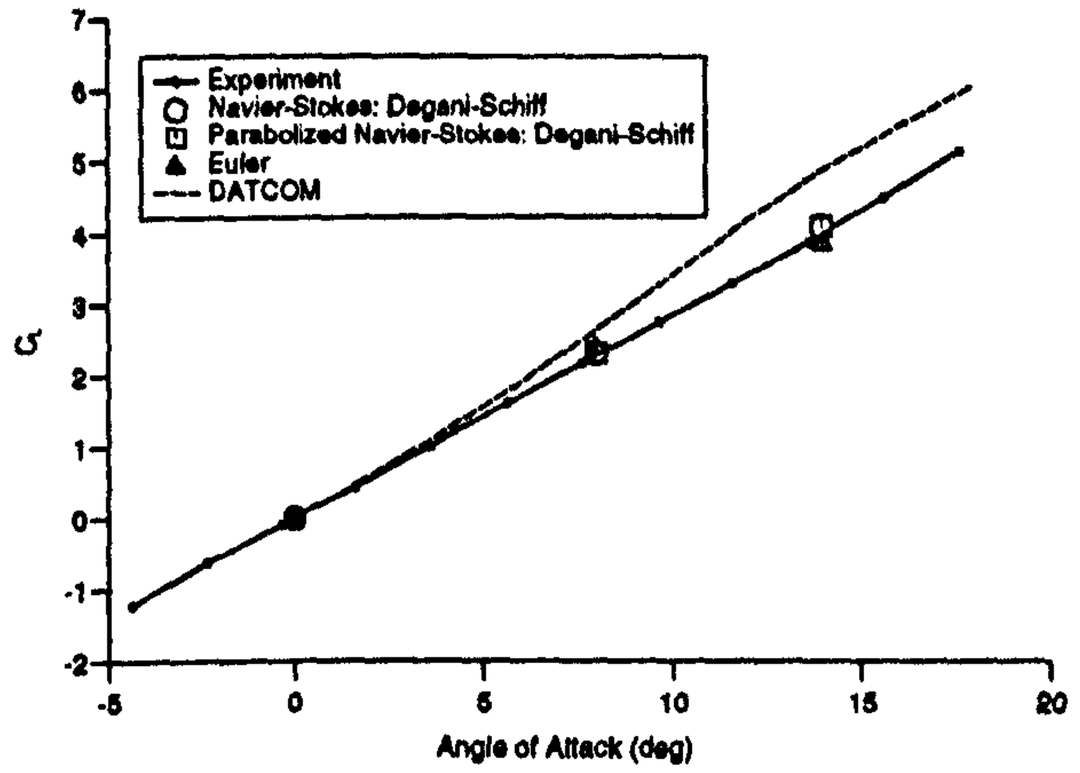

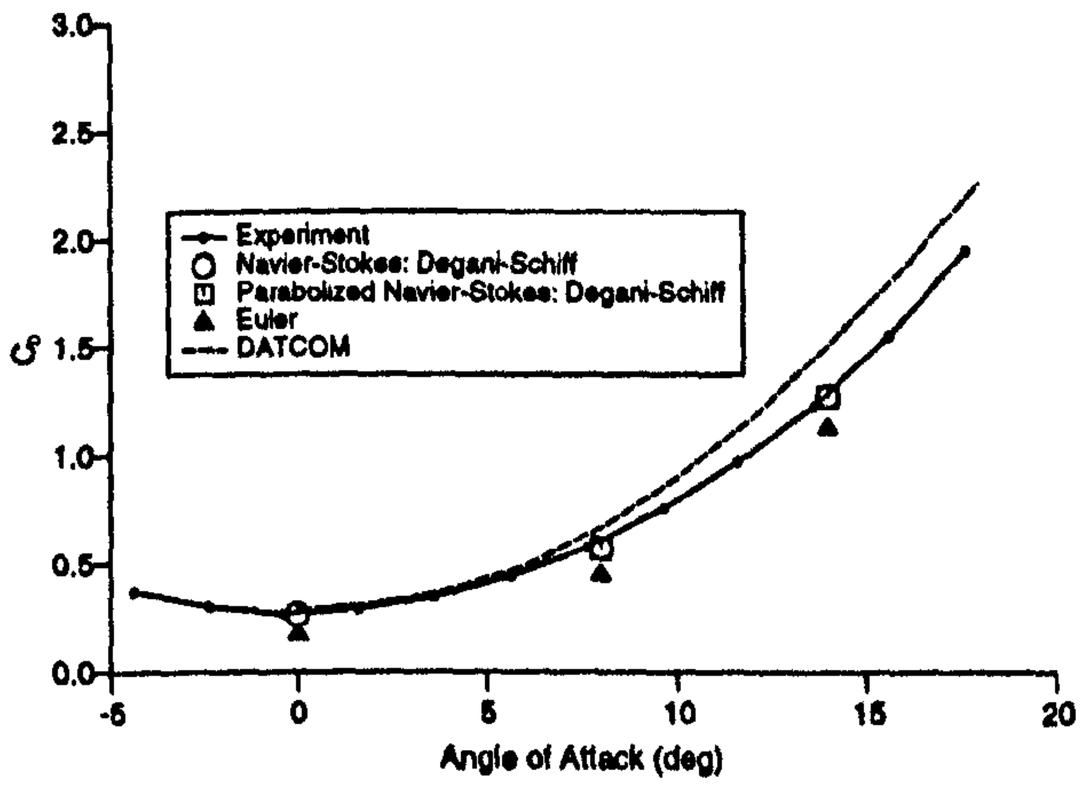

Figure 7.46: *Force Coefficients:* × *Configuration, continued*

The results of this study indicate that the NS and PNS solvers are highly capable of predicting the longitudinal force and moment characteristics of a missile configuration in supersonic flow. Apart from the axial force coefficient prediction, both NS and PNS results appeared consistently within 3% of the experimentally measured value. The discrepency with the axial force measurement can be attributed to the fact that the axial force balance load limit was close to the measured force. The inviscid normal force, lift and pitching moment predictions were almost as accurate as the NS results, below about 10° angle of attack, but failed to accurately predict the non-linear effects. The prediction of axial force and drag, however, cannot be obtained from Euler solvers. The DATCOM prediction code successfully achieved 10 – 15% accuracy below about 6° angle of attack, but conspicuously failed to predict the high angle of attack characteristics with the same accuracy.

At 18° angle of attack only the axial force coefficient was predicted within 20% of the experimentally measured value.

The normal force is a measure of the lateral acceleration of a missile, and it has been shown that the normal force characteristics are very similar in both + and × configuration up until 10° angle of attack, beyond which the + configuration generated marginally higher normal forces. For most modern air defense missiles, drag and axial force are of little importance. If range and cruising speed are important, however, then drag and axial force prediction will assume great importance. Comparison of the experimental results for the two roll configurations shows that axial forces are almost equivalent as are the drag coefficients below 10° angle of attack. Above this, however, the + configuration induces slightly more drag.

Accurate prediction of pitching moment is of considerable importance in determining the stability and controllability of a missile. For a missile to possess satisfactory longitudinal static stability characteristics, the slope of the C_M (about the centre of gravity) vs α curve must be negative over the operating α range. The B1AW20A3 geometry investigated is evidently statically unstable and becomes even more so beyond 10° angle of attack, and would therefore require the addition of a tail fin arrangement for it to become a useable design. Comparison of the C_{M_α} curves for the two roll configurations shows that above about 6° angle of attack the × configuration becomes dramatically more statically unstable.

7.4.6 Multiblock Efficiency Issues

The efficiency of the serial multiblock technique employed in the CRANS3D solver will be very much dependent on the time it takes to read in the grid and flow files each time the solver computes another block in the multiblock cycle, and then to pass the required information from the adjacent blocks. If the solver performs only one iteration in each block before moving to the next, much more time will be spent reading and writing data, per iteration, than if several iterations are performed before moving to the next block. Reading and writing data, especially formatted data, is extremely expensive in time. It was found that in a block (58 × 25 × 61) with three adjacent blocks, for each iteration, 80% of the CPU time was employed in reading and writing formatted data. If the data format was changed to "unformatted", this proportion was reduced to about 60%. In the case where only one iteration is performed in each block before moving to the next, that is, only one iteration per multiblock cycle, then only 20 – 40% of the computational time is spent actually solving the governing flow equations. This is evidently unacceptable. It was therefore decided to investigated the effect of increasing the number of iterations performed within a block during each multiblock cycle. This was done before any of the body-wing calculations were performed in order to ensure that the 36 cases required would be run

in the most efficient manner. Initially an Euler calculation was performed for zero angle of attack with only one iteration per multiblock cycle, such that the CPU time and the total number of iterations required to achieve 1st order residual convergence was recorded. The computation was repeated for 2, 5, 10, 15, 20, 30 and 50 iterations per multiblock cycle. The different solutions were compared with the single iteration/multiblock cycle case, and were found to be almost identical.

Figure 7.47 presents the plots of the affect of the number of iterations in each block in the multiblock cycle on the CPU time and overall number of iterations required to obtain a solution of one order of residual convergence, ie: $||R|| = 1 \times 10^{-1}$. If the number of iterations required to achieve first order convergence is plotted against the number of iterations in each multiblock cycle, there is an initial jump of about 50 iterations between 1 and 2 iterations per cycle. There appears to be only a modest affect on convergence of varying the number of iterations per multiblock cycles from 2 to 20. Having more than 20 iterations per cycle, however, seems to significantly increase the number of iterations required for convergence. This suggests that the more iterations that are performed without transferring information between blocks, impinges the flow of information throughout the flow field and increases the computational effort required to achieve convergence.

The plot of the CPU time required to achieve first order convergence against the number of iterations in each multiblock cycle, is more revealing. It is shown that increasing the number of iterations per cycle up to 20 dramatically reduces the required CPU time to achieve convergence. Further increases in the number of iterations per cycle, however, were found to cause a slight increase in the required CPU to convergence. The evidence from this plot would suggest that for the inviscid, 0^o body-wing case investigated, there is an optimum number of iterations per multiblock cycle of about 20. This study was repeated during the laminar investigation of the + configuration at 8^o angle of attack, using the NS laminar grid. It was found that the optimum number of iterations per multiblock cycle was around $15 - 20$. It was decided that for the rest of the 34 calculations the solver would be set to operate at this optimum value in order to achieve the best serial efficiency. Figure 7.48 presents a typical convergence history for one of the inclined body-wing calculations with 20 iterations per multiblock cycle.

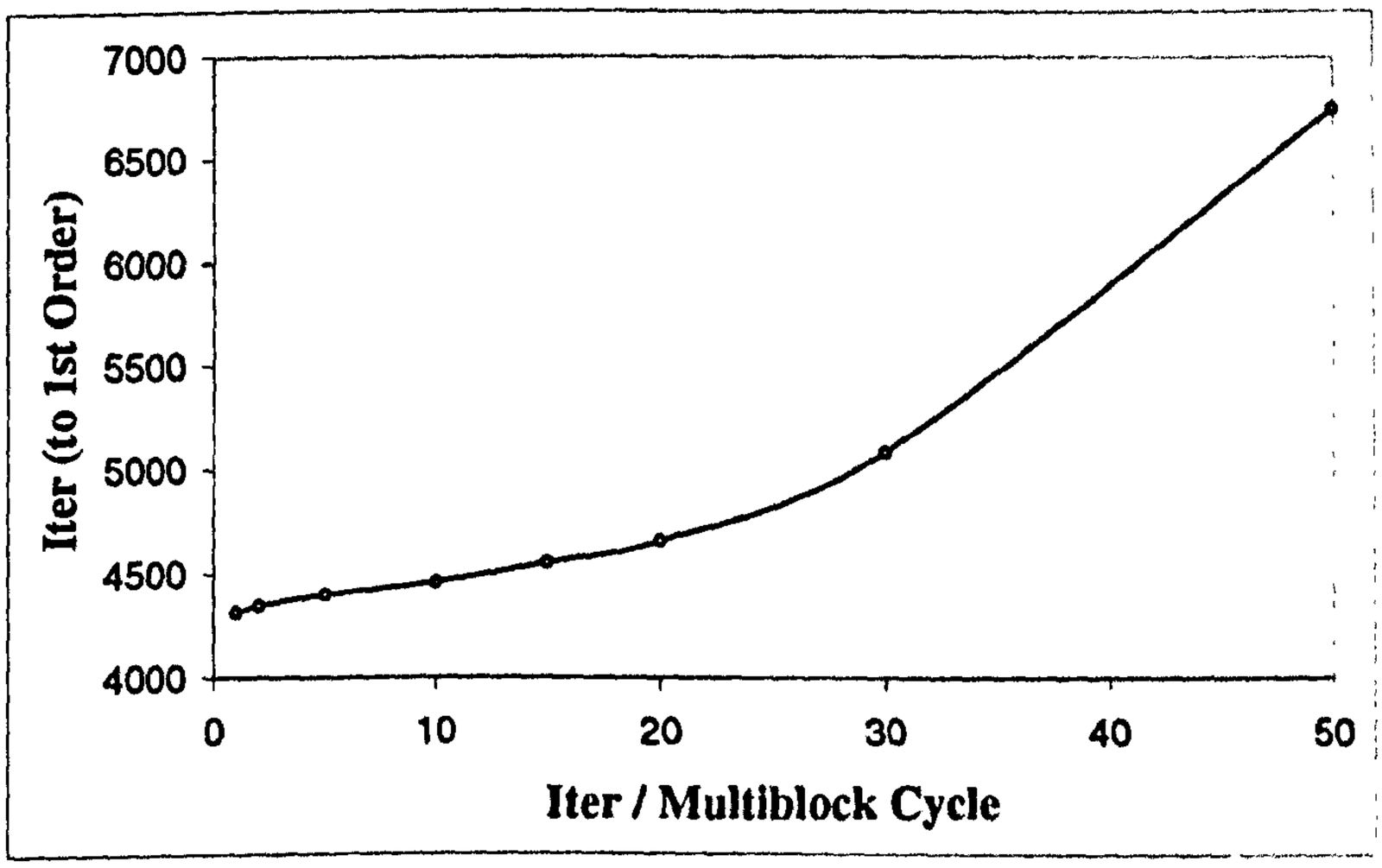

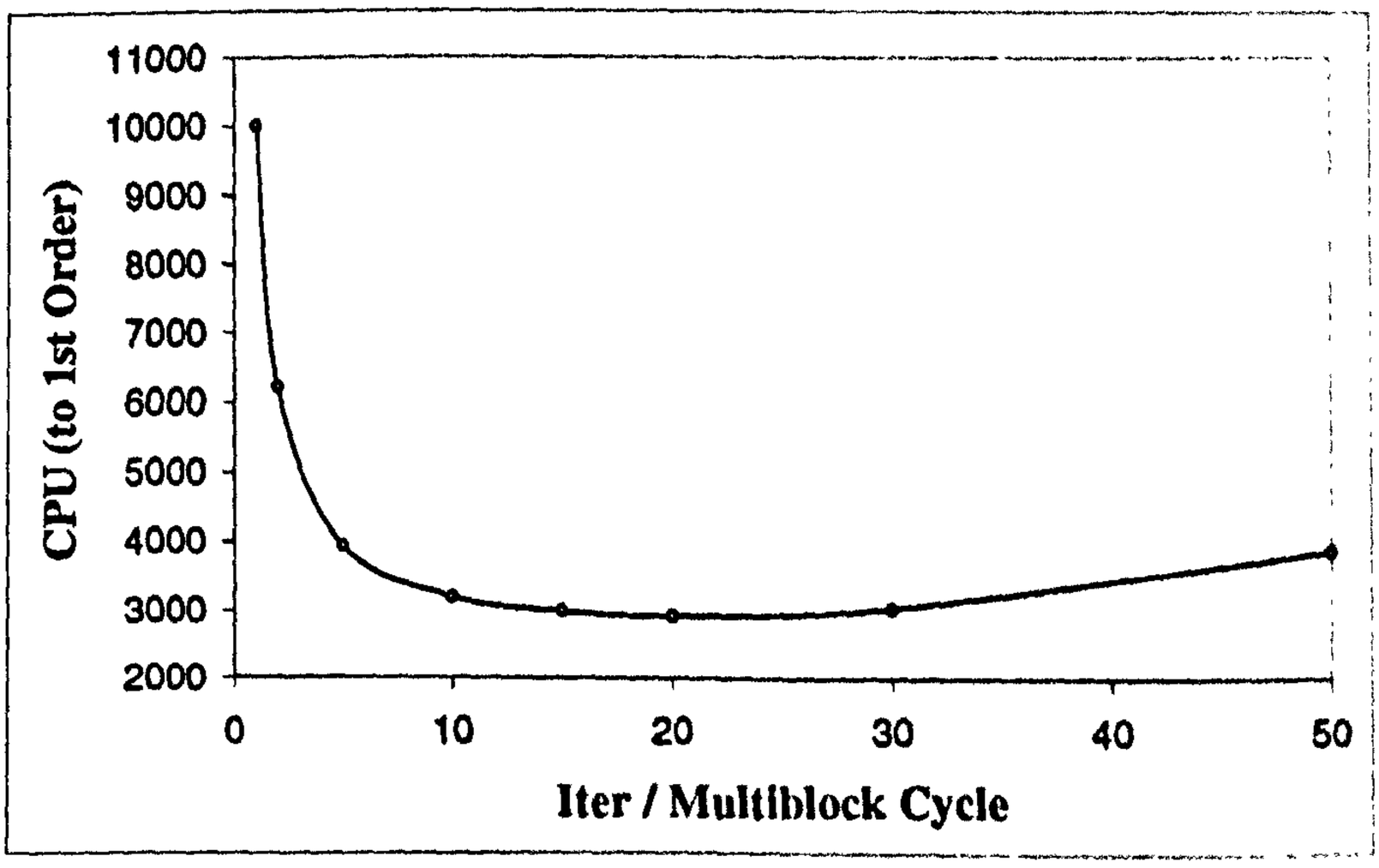

Figure 7.47: *Investigation of Serial Multiblock Efficiency*

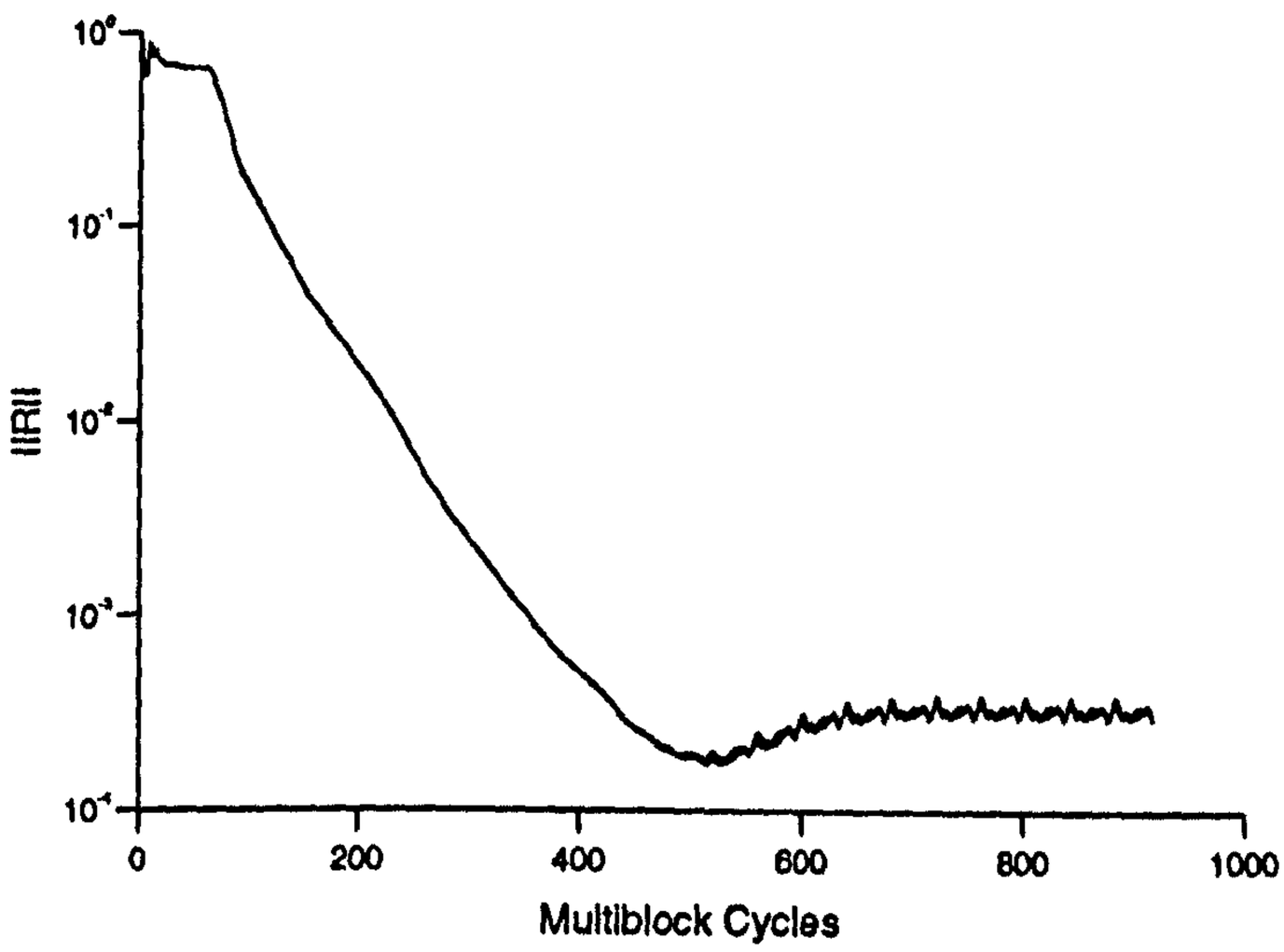

Figure 7.48: *B1AW20A3 Calculations: Typical Convergence History*

Chapter 8

General Discussion

This section presents a discussion on the applicability of the various prediction methods employed in the study, to the cost effective design of aerial weapons.

In Chapter 4 it was shown that for the computation of the vortical flows around inclined ogive-cylinder bodies, both the 3D-NS and PNS solvers employed were equally capable in the accurate prediction of those flows. This is true for both laminar and turbulent flows and for small to moderate angles of attack. The superior computational efficiency of the PNS approach, however, makes it more useful in the design environment than time marching. The same was found for the calculations performed for the B1AW20A3 body-wing where the PNS solver, using similar grids as those generated for the time marching solver, performed with equivalent accuracy but with far superior efficiency. The reduction in CPU time by using an explicit PNS solver over a 3D-NS solver has been found to be around 4 times [53]. Implementation of an implicit scheme together with multigrid convergence acceleration will further improve the efficiency.

A cost estimation exercise was performed in order to compare the cost effectiveness of the various methods for obtaining the longitudinal force and moment characteristics and a flowfield description for the B1AW20A3 at angles of attack from -4° to 18° at every 2° increment. Cost estimations were made for the experimental study and for the DATCOM analysis and CFD investigations using a turbulent 3D-NS solver, a turbulent PNS code and a 3D Euler solver. The experimental cost was estimated, including the cost of the model manufacture and of the experiments in the Langley tunnel. Costs for the DATCOM and CFD analyses assumed that the cost of man hours for set-up time was £20,000 per year and computer time on the Silicon Graphics Origin 200 used in the study, was charged at £0.5 per hour. This figure was evaluated assuming that one has to buy the Origin 200 machine which has an efficient lifetime of about 3 years and costs about £10,000. Overhead costs including software and other maintenance are taken at 10%

while electricity costs for its 805W requirement amounts to about 5.25p per hour. The resulting £0.5 per hour cost can be compared with the £100 per hour charged by the Cranfield University Computing Service for use on their CRAY II computer. The computer time assumes that all 12 angle of attack cases were calculated. Table 8.1 gives the results of the cost estimation, together with the accuracy associated with each method. The quoted accuracy is based on the accuracy, for moderate to high incidences, of the measurement instrumentation used in experiment and, for the computer prediction techniques, on the average accuracy (not including those for axial force) of the predictions to meet experimental force and moment measurements.

Table 8.1: Cost Analysis: B1AW20A3 Investigation

Solver	Set-up Time	Run Time	Cost (£)	Accuracy
Experiment	months	2 weeks	≈ 1,000,000	< 1%
Turbulent NS	5 weeks	1440 hrs.	2,600	< 3%
Turbulent Explicit PNS	5 weeks	280 hrs.	2,000	< 3%
Turbulent Implicit PNS [1]	5 weeks	60 hrs.	1,950	< 3%
3D Euler	4 weeks	580 hrs.	1,800	< 20%
DATCOM	0.5 day	1 sec.	30	10 – 60%

The table shows that, as far as the current programme is concerned, the implicit PNS solver is the most cost effective method for satisfactory engineering design. This analysis, however, is not realistic since experimental design programs would involve much more than measurements at just 12 angles of attack and 2 roll angles. A more realistic set of experiments would involve the aerodynamic measurements for 20 angles of attack, 15 roll angles, 10 fin deflections and 5 different Mach numbers. This amounts to 15,000 sets of data, or 15,000 CFD calculations. Having manufactured and installed the model in the tunnel, it would not require much extra cost, in either time or money, to obtain the extra experimental measurements for this more extensive study. The CFD investigation, however, if only performed on the one processor machine, would take much more time to predict the full 15,000 cases. If the 3D-NS solver were employed, it would take 1.8 million hours to complete, whereas the much more efficient implicit PNS would take 75,000 hours. The cost of the study would also dramatically increase. The cost in time is quite evidently unacceptable for the requirements of design. If the computing time were to be reduced by performing the computations in parallel, or by running several cases simultaneously the initial computing cost would increase. For instance, if 100 SGI Origin 200 processors were

[1] Calculation uses a much finer mesh than that for the other cases.

purchased for the study the cost would be around £1,000,000 and the reduction in the computing time would be 100 ×. The cost of a CFD study, however, would then be greater than the experimental costs. It seems clear that CFD is not in a position to be able to replace the wind tunnel for large scale tests covering the entire operating envelope of a given configuration. Its role in design is, therefore, limited to the investigation of configurations over a small range of conditions, and for analysis of the effect of small geometry changes in the optimisation of a design.

The analysis shows that although it provides the least accurate predictions of the longitudinal force and moment characteristics the DATCOM aeroprediction code is the most efficient method for the engineering analysis of conventional missile geometries. A whole series of aerodynamic data for various angles of attack, roll angles and wing and fin deflections can be obtained at nominal cost. Semi-empirical codes are, therefore, ideal for the conceptual design stage as long as the configurations are of the type for which large experimental databases are available. This is a severe limitation for their applicability since most modern missile designs, especially those designed for subsonic cruise to long range, now incorporate intakes, strakes and sharp corners for low radar observability. For such complex geometries with little experimental data, the only other alternative at the conceptual design stage is an efficient CFD method employed at a few operating conditions in the flight envelope of the configuration.

The 3D Navier-Stokes solver, being far too inefficient is evidently unsuitable for use in conceptual design where rapid synthesis is preferred over accuracy. Comparison of the other three structured CFD methods investigated shows that a similar physical prediction is obtained much more rapidly at only slightly higher cost by the implicit PNS solver. The only disadvantage with the use of this solver, as with all structured solvers, is that the grid generation is a tedious and time consuming process. In recent years special grid generation techniques have been developed for use with the PNS approach [67]. Since a PNS calculation in effect consists of a series of 2D crossflow computations, so the grid generation can be treated as the generation of a series of crossflow grids. This method of grid generation coupled with a fast PNS solver would be an extremely efficient numerical method for the engineering analysis of missile configurations in supersonic flows with no streamwise separation or large adverse pressure gradients.

The structured 3D Euler solver, although the grid generation time was less since there is no requirement for fine grid resolution near body surfaces, took much longer to obtain the 12 flow solutions. In addition, with an accuracy of $< 20\%$ and a cost only marginally less than that for the explicit and implicit PNS solvers, there appears to be no reason why a 3D structured Euler solver should be used in the design process at all, if the PNS approach is applicable. A 3D unstructured Euler solver might be more useful, but for

sharp nosed geometries in supersonic flows, the demonstrated efficiency of PNS solvers coupled with plane by plane structured grid generation might also render them unfeasible for cost effective missile design. Blunt nosed configurations can be treated by solving the 3D-NS equations in a time marching approach on a block around the blunt region, and using the rearward station as the starting solution for a PNS calculation of the supersonic flow in the downstream blocks away from the subsonic patch formed by the normal shock in front of the nose. If semi-empirical codes are employed in the conceptual design study, it would be sound practice to calculate a few cases using an NS or PNS solver in order to investigate the accuracy of the results obtained, especially at high angle of attack. This will, in addition provide detailed information on the vortical flow structure which will not be available from semi-empirical methods.

The missile conceptual design study should employ only semi-empirical methods, where applicable, and fast and efficient CFD solvers in order to gain more accurate data and insight into the flow structure at a few conditions in the flight envelope. In this manner the conceptual design allows for various aerodynamic configurations to be analysed in an iterative process until an optimum design is achieved. Experiments and large grid NS calculations which provide excellent accuracy but require a lot of time and therefore a large cost, should be left until the preliminary design stage. During preliminary design the optimum configuration can at first be calculated using NS or PNS solvers on fine grids at conditions where the conceptual design indicates a requirement for more data or information on the flow structure. With the addition of all other conceptually designed engineering systems, the configuration might require "fine tuning". This can be achieved using CFD before any wind tunnel models are built. In this manner the costly and lengthy, iterative experimental test-modify practices employed until recently are taken out of the design process such that, ideally, only one set of experiments will be required to obtain aerodynamic data over the entire operating range such that the flight dynamic characteristics of the configuration can be evaluated. In this manner, the introduction of efficient CFD methods into the early stages of design is expected to provide aerodynamic configurations which better meet design requirements quicker, and at much reduced costs.

To look in more detail at the typical workload involved in the process of a structured CFD analysis, both the time spent setting up, monitoring and post-processing the calculation and the corresponding CPU time was recorded for one of the body-wing explicit NS calculations. Figure 8.1 presents the pie charts for the workloads in terms of man-hours and CPU hours spent for each of the component tasks required for a flow solution.

The largest number of man-hours, almost 60% of the total, was spent generating the volume grids. Surface grid generation was found to be the

next largest contribution. In fact the total man hours spent generating the grid, including the geometry definition, amounted to 93% of the total man hours spent performing the CFD analysis. The cost analysis clearly showed that for complex multiblock geometries, the cost due to the total man-hours required to set-up the computation is by far the major contribution to the total cost of performing the CFD analysis. Any significant reductions in the amount of time an aerodynamicist is required to sit and generate the grid will considerably reduce the total cost. It is for this reason that much effort is currently being focused on efficient grid generation technologies for complex geometries, and why unstructured grids (which require much less user input) have proved to be so useful.

Figure 8.1 *b*) shows a typical pie chart of the CPU hours spent for each of the component tasks required for a structured flow solution. The flow solution is seen to take 99% of the total CPU hours spent performing the CFD analysis. This figure would be reduced somewhat if the implicit PNS solver was employed, but the CPU time spent solving the governing flow equations would still be, by far, the largest contribution to the total CPU time. Together with the man-hours required for the grid generation, the CPU time spent on solving the flow equations defines how many cases one can perform in a given amount of time, and therefore the usefulness of the method to the designer. Faster, more powerful computer processors and more efficient numerical algorithms are required to reduce the computational workload associated with the flow solution. In particular, parallel algorithms have proved to significantly reduce the flow solution times and are now popular in CFD and other numerical engineering fields.

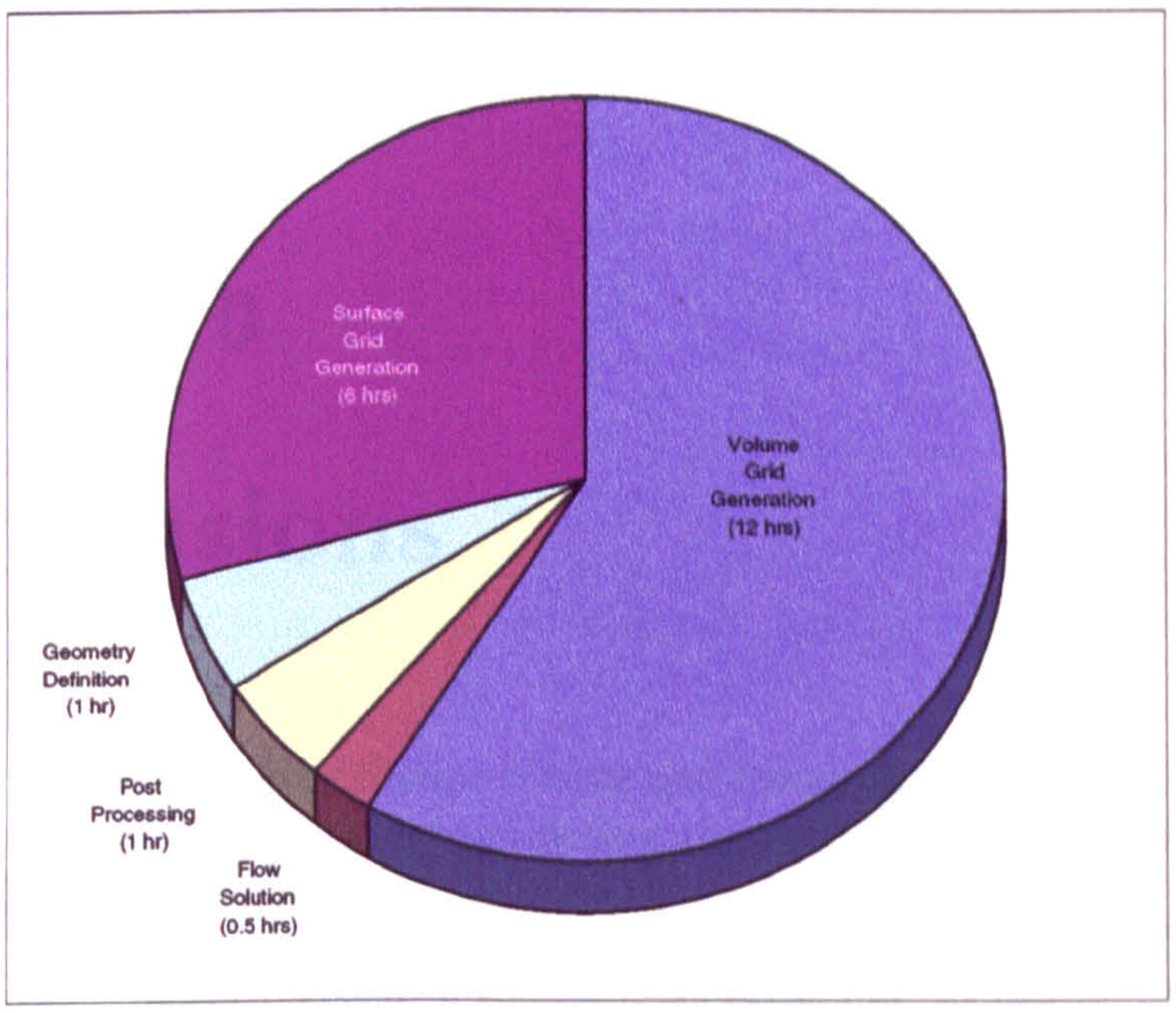

a) Man Hours

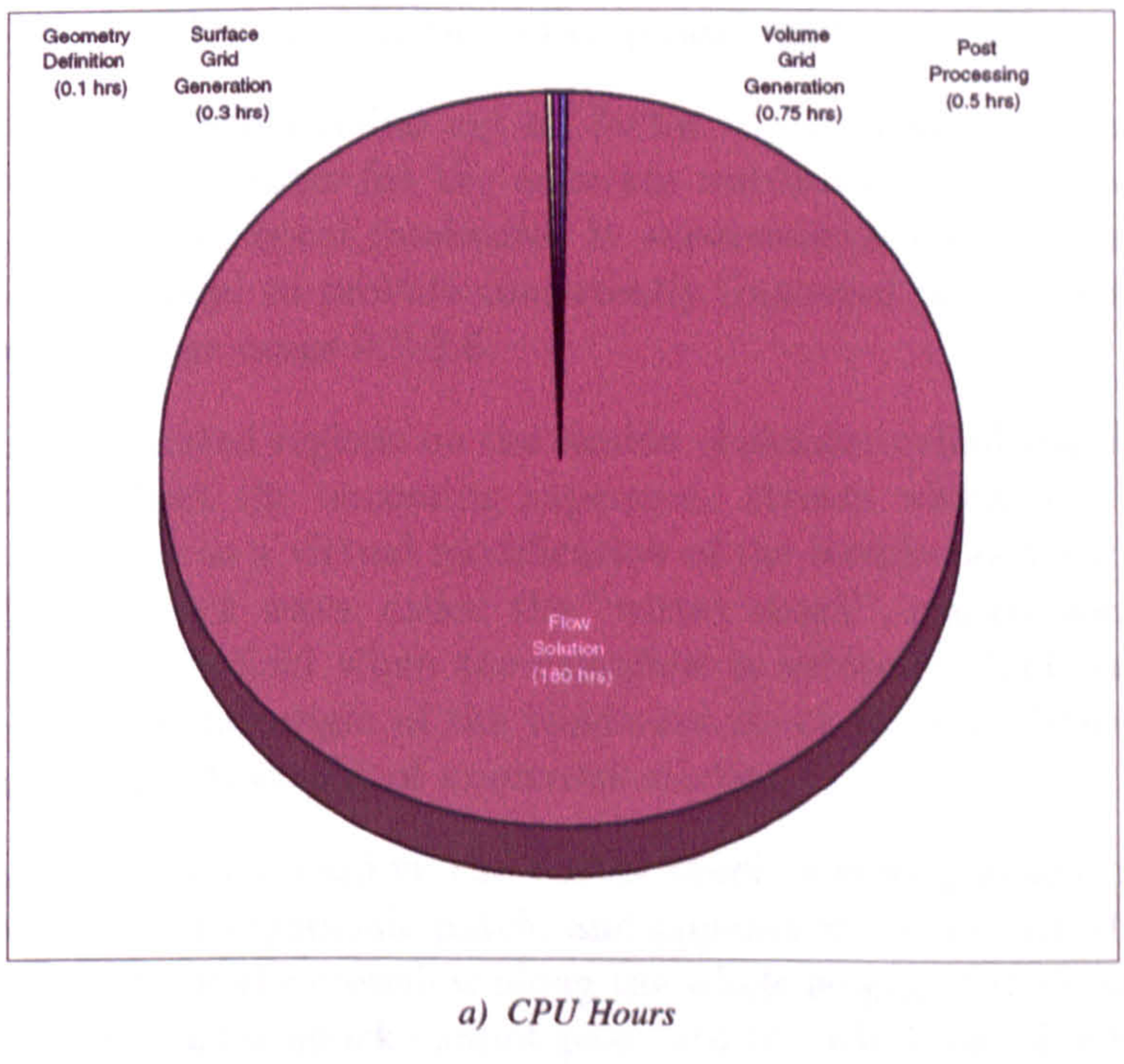

a) CPU Hours

Figure 8.1: *Typical Workload, Structured 3D-NS Body-Wing Calculation*

Chapter 9

Conclusions

- Both time marching Navier-Stokes and Parabolized Navier-Stokes solvers are capable of accurately predicting the vortical supersonic flow about inclined slender bodies.

- The maximum possible measurement error due to the finite size of a surface pressure tapping and the pressure gradient across it, can be estimated using Navier-Stokes solutions of the local boundary layer together with a combination of empirical relationships.

- The Degani-Schiff radial cut off factor of 1.5, quoted in many publications, is too large for the accurate resolution of the smooth separation off cylindrical forebodies in supersonic flows. A value of 1.15 has been found to provide consistently improved predictions over the Mach number range 0.7-2.5.

- Large separated regions on the leeside of slender cylindrical forebodies act to deflect the oncoming supersonic stream which sees the separated region as a virtual modification of the leeside body surface. The resulting shock wave, called the "vortex shock", can convect into the windward flowfield when the crossflow is subsonic. This reveals the mechanism and origin of the windward shock feature observed in the schlieren photographs of numerous studies.

- With transonic crossflow the vortex shock is strengthened by the appearance of a supersonic patch, and appears as an embedded crossflow shock wave. If the crossflow along the whole length of the body is transonic, the vortex shock cannot pass into the windward flowfield.

- The phenomenon of the numerical boundary layer/shear layer and resultant "phantom vortices" in Euler solutions of the supersonic flow past smooth inclined slender bodies has been linked to the spatial accuracy of the solution scheme. Excessive numerical dissipation caused

by the localized loss of spatial accuracy in regions where the grid is highly stretched can be alleviated by employing a high order MUSCL scheme which accounts for grid non-uniformity.

- The conical flow assumption for the supersonic flow past sharp inclined delta wings has been validated using the time marching solutions of the full Navier-Stokes equations of two NASA test cases.

- Euler solutions of supersonic flows past sharp corners can resolve the flow separation that occurs at that sharp edge. For sharp leading edge delta wings the resulting primary vortex structure can effectively be predicted, but the induced secondary flow due to the separation of the reattached boundary layer cannot be predicted.

- Vapour Screen flow visualisation is an effective technique for the qualitative analysis of compressible separated flow structures.

- The supersonic flow in the wake of the cruciform delta wing arrangement of the body-wing configuration involves the development of double vortex systems and complicated systems of leading and trailing edge shock waves. The double vortex systems observed are seen to be generated from the large leading edge vortices and secondary separation on the leeside of the low aspect ratio delta wings.

- CFD is an effective tool in the conceptual and preliminary design process for analysing the aerodynamics at a small number of conditions, and for design optimisation exercises, but cannot replace the wind tunnel when data over the entire flight envelope is required.

Bibliography

[1] Allen, H. J. and Perkins, E. W. A Study of the Effects of Viscosity on the Flow Over Slender Inclined Bodies of Revolution *NACA TR-1048*, 1951.

[2] Allen, T. M. and Dillenius, M. F. E. Vortex Development on Slender Missiles at Supersonic Speeds. *AIAA Paper 79-0360*, Jan 1979.

[3] Anderson, W. K., Thomas, J. L. and van Leer, B. A Comparison of Finite Volume Flux Vector Splittings for the Euler Equations *AIAA Journal*, 24(9):1453–1460, 1986.

[4] Baldwin B. S. and Lomax H. Thin Layer Approximation and Algebraic Turbulence Model for Separated Turbulent Flows *AIAA-78-257*, 1978.

[5] Test Case C5: Supersonic Vortex Flow Around A Missile Body A Selection of Experimental Test Cases for the Validation of CFD Codes *AGARD AR 303*, August 1994.

[6] Battina, John, T. Implicit Flux-Split Schemes For Unsteady Aerodynamic Analysis Involving Unstructured Dynamic Meshes *AIAA-90-0936-CP*, 1990.

[7] Battina, John, T. A Fast Implicit Upwind Solution Algorithm For Three-Dimensional Unstructured Dynamic Meshes *AIAA-92-0447*, 1992.

[8] Birch T. J., Qin N. and Jin X. Computation of Supersonic Viscous Flows Around a Slender Body at Incidence *AIAA-94-1938*, 1994.

[9] Birch, T. J. Unpublished TTCP Report 1998.

[10] Blake, W. B, Missile Datcom: User's Manual: FORTRAN 90 1997 em Air Force Research Lab Wright-Patterson AFB, OH USA, Feb 01, 1998

[11] Cebici T. and Smith A. M. O. Analysis of Turbulent Boundary Layers *Ser. in Appl. Math. and Mech.*, Vol. XV, Academic Press 1974.

[12] Navier-Stokes Calculations of the Flow about Slender Configurations. *GARTEUR AG-24 Report*, December 1995.

[13] Chinilov A. On Numerical Boundary Layers of Numerical Schemes Applied to the Euler Equations. *Proceedings of the Seventh International Symposium on Computational Fluid Dynamics*, Beijing, Sep. 15-19, 1997. pp 84-90.

[14] Degani D. and Schiff L. B. Computation of Turbulent Supersonic Flows Around Pointed Bodies Having Crossflow Separation. *J. Computational Phys.*, 66(3):173–196, 1986.

[15] Deniau H., Lafon A. and Moschetta J. M. Progress in the Development And Validation of Turbulence Models for the Computation of Supersonic Flows With Crossflow Separation. *AIAA-95-0090*, 1995.

[16] Dubuc, L., Richards, B. E. Mesh Sequencing and Multigrid Acceleration Techniques for Three-Dimensional Navier-Stokes Solver *Glasgow University Aerospace Engineering Report 9421.*

[17] Edney, Barry. Anomalous Heat Transfer And Pressure Distributions on Blunt Bodies At Hypersonic Speeds in the Presence of An Impinging Shock. *FFA Report-115*, February 1968.

[18] Esch H. Bodies. *AGARD Lecture Series-98.*, (Missile Aerodynamics), 1979.

[19] Esch H. Wind Tunnel Investigations of the Appearance of Shocks in the Windward Region of Bodies with Circular Cross Section at Angle of Attack. *AGARD AR-303, A Selection of Experimental Test Cases for the Validation* , 1994.

[20] Goldstein S. (Ed.) Modern Developments In Fluid Dynamics *Volumes 1 and 2, Oxford 1938*

[21] Hartwich, P. M., Hall, R. M. and Hemsch, M. J. Navier-Stokes Computations of Vortex Asymmetries Controlled By Small Surface Imperfections *AIAA-90-0385*, 1990.

[22] Hennig, P. and Lacau, P. G. Aeromechanical Design of Modern Missiles. *AGARD Report 804*, Special Course on Missile Aerodynamics, June 1994.

[23] Hodges, J., Ward, L. C. and Birch, T. J. Pressure Measurements on an Slender Bodies at Supersonic Speeds and Developments of Flow Separation Criteria for Euler Codes. *RAE TM Aero 2177*, 1990.

[24] Hsieh T., Wardlaw A. B. and Birch T. J. Vortical Flows About a Long Ogive Cylinder at M=3.5 and $\alpha = 18^{\circ}$ *AIAA-91-1808*, 1991.

[25] Hung, C. M. and Buning, P. G. Simulation of Blunt Fin Induced Shock-Wave and Turbulent Boundary Layer Interaction. *J. Fluid Mechanics*, Vol. 154, 1985, pp163-185.

[26] Jorgensen L. H. Prediction of Static Aerodynamic Characteristics for Space-Shuttle-Like and Other Bodies At Angles of Attack from 0° to 180° *NASA TN D-6996, 1973*

[27] Josyula, Eswar. Computations of Supersonic Vortical Flows Around Ogive Cylinders Using Central and Upwind Differences *Wright Laboratory Tech Report: WL-TR-96-3061*, March 1997.

[28] Lamont P. J., and Hunt B. L. Pressure and Force Distributions on a Sharp-Nosed Circular Cylinder at Large Angles of Inclination to a Uniform Supersonic Stream *Journal of Fluid Mech*, 76(3):519-559, 1976.

[29] van Leer, B. Upwind-difference Methods for Aerodynamic Problems Governed by the Euler Equations Lect. Applied Mathematics, 22:327-336, 1985.

[30] Lijewski, L. E. Transonic Solutions on Mutually Interfereing Finned Bodies. *AIAA Journal*,Vol. 28, No. 6, June 1990, pp928-988.

[31] Meng-Sing Liou and Andrew T. Hau A Time Accurate Finite Volume High Resolution Scheme for Three Dimensional Navier-Stokes Equations *AIAA-89-1994-CP*, 1989.

[32] Ludlow, D. K. Personal Communication

[33] Maltby, R. L. A Visualisation Technique for Flows Separating from Highly Swept Edges. *J. R.Aero.Soc.*, v18, 21. 1951.

[34] Marconi F. Conical, Separated Flows with Shock and Shed Vorticity. *AIAA Journal*,Vol. 25, No. 1, January 1987, pp173-175.

[35] Marshall M. R., and Deffenbaugh F. D. Separated Flow over a Body of Revolution *Journal of Aircraft*, 12(2):78-85, 1975.

[36] McMillin S. N., Thomas, J. L. and Murman E. M. Navier-Stokes and Euler Solutions for Lee-Side Flow Over Supersonic Delta Wings: A Correlation With Experiment. *NASA TP-3035*, December 1990.

[37] Mendenhall J. F., and Nielsen J. N. Effect of Symmetrical Vortex Shedding on the Longitudinal Aerodynamic Characterstics of Wing-Body-Tail Combinations *NASA CR-2473*, January 1976.

[38] Miller D. S., and Wood R. M. Lee-Side Flow Over Delta Wings at Supersonic Speeds *NASA TP-2430*, June 1985.

[39] Moore F. G. Engineering Codes For Aeroprediction: State of the Art and New Methods. *AGARD AR-804*, (Special Cource on Missile Aerodynamics), June 1994.

[40] Morrison, D. F., Sheppard, L. M. and Williams, M. J. Hole Size on Hemisphere Pressure Distributions. *Journal of the Royal Aeronautical Society* Vol. 21, pp 317 - 319, April 1967.

[41] Moschetta J. M., Lafon A. and Deniau H. Detailed Numerical Investigation of Supersonic Crossflow Separation *AIAA-94-2382*, 1994.

[42] NASA Langley Web Site http://www.nasa.gov

[43] Nelson, R. C. and Malcolm, G. N. Visualization of High Anlge-of-Attack Flow Phenomena. *Tactical Missile Aerodynamics*, AIAA Progress in Astronautics and Aeronautics Vol. 141.

[44] Osher, S., Chakravarthy S. R. Upwind Schemes and Boundary Conditions with Applications to Euler Equations in General Coordinates *J. Computational Phys.*, 50:447–481, 1983.

[45] Pagan D. and Moltan P. Basic Experiment on a Supersonic Vortex Flow Around A Missile Body *AIAA-91-0287*, 1991.

[46] Pagan D. Molton P. and Delery J. Basic Experiment on a Supersonic Vortex Flow Around a Missile Body *J. Spacecraft and Rockets*, 29(3) 1992.

[47] Peake, D.J. and Tobak, M. Three Dimensional Interaction And Vortical Flows With Emphasis on High Speeds. *NASA TM-81169*, March 1980.

[48] Peto, J. W., Pugh, P. G. and Ward, L. C. Experimental Verification of Predicted Static Hole Size Effects on A Model with Large Streamwise Pressure Gradients. *NPL Aero Report 1313* UK National Physical Laboratory, February 1970.

[49] Peto, J. W. and Pugh, P. G. The Effects of the Presence of Static Holes on the Measurement of Static Pressures on the Models at Supersonic Speeds. *NPL Aero Report 1292* UK National Physical Laboratory, March 1969.

[50] Pluntze, S. C., Zuber, M. E., Bertin J.J. and Erick Gilbert, R. Flowfield For Rectangular Fins of a Generic Missile Configuration. *AIAA Paper 99-0993*, Jan. 1999.

[51] Priolo, F. J. and Wardlaw, A. B. Vortical Flowfields for Missiles Computed Using GRIDGEN and GASP *AIAA Paper 92-4351*, August 1992.

[52] Qin, N. User Guide for the NS3D Code Dept. Aero. Eng. Glasgow University, 1991.

[53] Qin, N. Ludlow, D. K., Zhong, B., and Shaw, S. T. and Birch, T. J. Multigrid Accelleration of a Preconditioned GMRES Implicit PNS Solver *AIAA-99-0779*, Jan. 1999.

[54] Qin, N., Scriba, K. W. and Richards, B. E. Shock-Shock, Shock-Vortex Interaction and Aerodynamic Heating in Hypersonic Corner Flow. *The Aeronautical Journal*, Vol. 95, No.945, 1991.

[55] Qin, N., and Jayatunga, C. Algebraic Turbulence Modelling for Vortical Flows around Slender Bodies. *RTO AVT Symosium on "Missile Aerodynamics"*, Sorento, 11-14 May 1998.

[56] Rai, M. M., Chausee, D. S. and Rizk, Y. M. Calculations of Viscous Supersonic Flows over Finned Bodies. *AIAA Paper 83-1667*, July 1983.

[57] Rainbird, W. J. Errors in Measurement of Mean Static Pressure of a Moving Fluid due to Pressure Holes *DME/NAE Report 1967(3). Quarterly Bulletin of the Division of Mechanical Engineering and the National Aeronautical Establishment* pp 55-89, 1 July - 30 Sept. 1967.

[58] Rizzi, A., Eliasson, P., Lindblad, I., Hirsch, C., Lacor, C. and Haeuser, J. The Engineering of Multiblock/Multigrid Software for Naier-Stokes Flows on Structured Meshes *Computers and Fluids*, Volume 22, No 2/3, 1993.

[59] Roe, P. L. Approximate Riemann Solvers *J. Computational Phys.*, 43:357–372, 1981.

[60] Rom Josef. High Angle of Attack Aerodynamics: Subsonic, Transonic and Supersonic Flows *Springer-Verlag*, 1994.

[61] Shaw, S. and Qin, N. A Matrix-Free Preconditioned Krylov-Subspace Method for the PNS Equations *AIAA-98-0111*, Jan. 1998.

[62] Shen G. and Philpott D. The Application of Topology to the Interpretation of Crossflows and Some New Extensions *AIAA-89-0568*, 1989.

[63] Schlichting H. Boundary Layer Theory *First English Edition, Pergamon Press, 1955*

[64] Settles, G. S. and Dolling, D. S. Swept Shock-Wave/Boundary-Layer Interactions. *Tactical Missile Aerodynamics: General Topics*, Chapter 12, AIAA Progress in Astronautics and Aeronautics, Volume 141, 1991.

[65] Shang J. S. and Hankey W. L. Jr. Numerical Solution for Supersonic Turbulent Flow Over A Compression Ramp *AIAA Journal*, 13(10):1368-1374, 1975.

[66] Siclari M. J., Marconi F. Computation of Navier-Stokes Solutions Exhibiting Asymmetric Vortices *AIAA Journal*, 29(1), Jan. 1991.

[67] Sowa, J. GEMINI - General Missile Navier-Stokes Integrator *Proceedings of the International Congress on the Aeronautical Sciences*, 1992 pp483-492.

[68] Spekreijse, S. P. Multigrid Solution of the Steady Euler Equations *CWI Tract 46*, Centre for Mathematics and Computer Science, Amsterdam.

[69] Spreiter, J. R. and Sacks, A. H. The Rolling-up of the Trailing Edge Vortex Sheet and its Effect on Downwash Behind Wings. *J. Aero.Sc.*, v18, 21. 1951.

[70] Stanbrook, A. and Squire, L. C. Possible Types of Flow At Swept Leading Edges. *Aeronautical Quarterly*, Vol. XV, Pt. 1, pp 72-82, Feb 1964.

[71] Sturek W.B., Birch T., Lauzon M., Housh C., Mantor J., Josyula E. and Soni B. The Application of CFD to the Prediction of Missile Body Vortices. *AIAA Paper 97-0637*, 1997.

[72] Szodruch, Joachim Leeside Flow for Slender Delta Wings of Finite Thickness. *NASA TM-75753*, 1980.

[73] Thompson, J. F. and Weatherill, N. P. Aspects of Numerical Grid Generation: Current Science and Art *AIAA-CP-93-3539*, 11th AIAA Applied Aerodynamics Conference, Monterey, Aug. 1993.

[74] Thornburg, Hugh J. and Soni, Bharat K. A Structured Grid Based Solution-Adaptive Technique for Complex Separated Flows *12th AIAA Computational Fluid Dynamics Conference*, San Diego 1995.

[75] Turkel, E. Accuracy of Schemes with Nonuniform Meshes For Compressible Fluid Flows. *Applied Numerical Mathematics 2*, North-Holland Publishing (1996) pp529-550

[76] Vigneron, Y. C., Rakich, J. V. and Tannehill, J. C. Calculation of Supersoinc Viscous Flows around a Delta Wings with Sharp Subsonic Leading Edges *AIAA-78-1137*, July 1978.

[77] Visbal M. R. and Gornier R. E. Crossflow Topology of Vortical Flows *AIAA Journal*, 32(5):1085-1087, 1994.

[78] Ward, L. C. Pressure Measurements on an Axisymmetric Body at Mach Numbers from 2.5 to 4.5 *RAE TM Aero 2174*, 1990.

[79] Ward, L. C. and Birch, T. J. An Investigation of Reynolds Number Effects On a Tangent-Ogive Cylinder Body. *DRA TM Aero/Prop 4*, May 1992.

[80] Wardlaw A. B. High Angle of Attack Missile Aerodynamics. *AGARD Lecture Series-98.*, (Missile Aerodynamics), 1979.

[81] Wardlaw A. B., and Morrison A. M. Induced Side Forces on Bodies of Revolution at High Angle of Attack *NSWC TR 75-176, 1975*

[82] Wardlaw A. B., Baltakis, F. P., Priolo, F. J. and Solomon, J. M. Space Marching Euler Solvers. *Tactical Missile Aerodynamics: Prediction Methodology*, Chapter 9, AIAA Progress in Astronautics and Aeronautics, Volume 142, 1991.

[83] Weatherill, N. P. Numerical Grid Generation *Von Karman Institute for Fluid Dynamics Lecture Series*, June 11th-15th 1990.

[84] Wilcox, Floyd. Unitary Plan Wind Tunnel Test 1709 Experiment Notebook, December 1998.

Appendix A

A Brief History of Aerial Weapons

The aerial weapon, is one of mans oldest inventions, conceivably even predating the discovery of fire. Modern ICBM's (Intercontinental Ballistic Missiles) have ranges of over 7000 miles, are capable of speeds of some 15,000 mph and have come a long way from Palaeolithic man hurling rocks in ancient prehistory. The principles of motion, however, as well as the basic human urges that brought about their use, are very much the same.

The first spears were developed by smoothing and sharpening wooden shafts, but together with rocks and other hand held weapons, they were adequate only at close range and were of little use in bringing down agile and fast moving prey. The bow and arrow appeared some 4000 years ago and revolutionised both hunting and warfare, playing a pivotal roll in over a thousand years of British military history. Early forms of artillery were the catapult and the trebuchet which hurled large stones against enemy defenses.

All of these early aerial weapons were projectiles aimed directly and relied on momentum to pierce or demolish the target. With the discovery of gun powder the first experiments were performed on firing projectiles through tubes. The earliest "gun" used in the West was the *pot-de-fer*, first employed in the 14th century, it fired a bolt or heavy arrow and was similar to much earlier Chinese weapons. The cannons which were developed throughout the following three decades certainly changed the way land and naval warfare was conducted, but they still relied on the momentum of the projectile, and were still highly inaccurate. It was the cannon ball, however, and the development of artillery, that prompted the birth of ballistics as a scientific field. Perhaps the most monumental contribution to the understanding of both ballistics and indeed the much more contemporary fields of rocketry and aerodynamics, was Isaac Newton's laws of motion.

The advent of gun powder also brought about the invention of the shell,

the first of which were simple hollow metal balls filled with explosive and detonated by a fuse. The advantages of the exploding shell over simple cannon balls were twofold; its effect does not depend on its weight or the speed at which it leaves the barrel, and it can destroy multiple targets over a wide area.

The first accounts of rockets date back to the use, by the Greeks in the defense of Constantinople in the 7th Century, of "flaming arrows" - arrows propelled by rockets tied to their shafts. The Chinese are known to have employed bamboo tubes filled with explosive powder during the 10th Century, pioneering the field of solid propellant technology. The use of gunpowder and its application to rocket propulsion was the subject of many investigators including the German Albertus Magnus and the Englishman Roger Bacon in the 13th Century, and Leonardo de Vinci who sketched designs in the 15th Century. Less than a hundred years later, Conrad Haas first discussed the concept of multiple stage rockets and developed swept back fins attached to the forebody of his designs to improve stability and accuracy of his rockets.

The British Army, having been subjected to Indian rocket fire during the Siege of Seringapatam in 1799, commissioned Colonel William Congrieve to develop a rocket system for use by the Royal Artillery. Congrieve came up with the design of a rocket on the end of a long shaft which acted to stabilize the rocket in flight over a 1km range. This type of stabilization is still employed today on display rockets. In his studies Congrieve reported that the thrust of the rocket is exerted without a recoil on the point from which it is launched. The Royal Navy, therefore, adopted his designs and during the Napoleonic Campaign Admiral Gambier's Fleet bombarded Copenhagen with 25,000-45,000 ship launched rockets during a three day siege in 1807. Congrieve Rockets, however, had a bad reputation. Not only did the long sticks make them cumbersome, the rockets proved unreliable and erratic to the extent that they often turned back on the firer.

Further developments were made by William Hale in the early 1800's who invented the technique of spin stabilization. Spin stabilization was already widely used in artillery, where the gun barrel was "rifled", thus spinning the projectile and improving its accuracy. Hale spun his rockets by placing gas vents at the base of his designs, each arranged to cause a tangential efflux and thus impart a rotary motion. Hale rockets were successfully tested during the British campaigns in Abyssinia and in the Crimea.

Rockets were extensively used by both sides in the American Civil War. Accounts exist that the Confederate Army attempted to fire a Ballistic missile at Washington DC from their capital in Richmond, Virginia. Confederate President Jefferson Davis was supposed to have been present at the launch of the 12 foot high, solid fueled rocket, and watched as it was ignited and accelerated up into the air and out of site. No mention was made as to where the rocket impacted.

During the 1890's, the Swedish engineer Wilhelm Unge made pioneering developments in solid propellant technology. He employed stabilizers to increase storage life and plasticizers to make the powders safer to handle. His propellants were the first to be designed for controlled burn rates which enabled rockets to be delivered at much greater accuracy. This innovation together with that of spin stabilization meant that by the turn of the century, rockets could be delivered with the same accuracy as artillery shells.

The British Royal Flying Corps and the French Air Force developed experimental rockets during World War One, launched from the outboard struts of their bi-plane wings, to destroy observation balloons, they met only limited success. The First World War and the threat posed by German Zeppelins, however, brought about the first truly guided aerial weapon. The Flying Target, developed by a British Professor, A. M. Lowe, was essentially a monoplane flying bomb, powered by a propeller and guided by radio from the ground. The weapon, though successfully tested, was never employed in anger.

The principal drawback of rocket propulsion during this time was that of the propellant. Solid propellants were limited in the amount of power they could provide. During the early postwar years, two men began work on the concept of liquid fueled rockets. In Germany, Herman Oberth published work on high altitude liquid fueled rockets, as did Robert Goddard in America. By 1935, Goddards' rockets were achieving altitudes of 75,000 feet, having accelerated to over 700 mph.

Following on Oberth's work, a small group of German scientists continued to develop liquid propellant technology, one of whom was Werner Von Braun, a young scientist from the Berlin Institute of Technology. After graduating, the German Army offered to fund Von Braun's work on liquid rocket motors, and in November 1932 he founded Germany's ballistic missile program at Peenemunde on the Baltic coast of Germany. With increased funding and more scientists, a series of rockets were launched culminating in the successful launch of the A-4 on October 3rd 1942. The rocket accelerated to a Mach number of 4.7, and an altitude of 275,000 feet and became the first man-made object to breach the Earth's atmosphere.

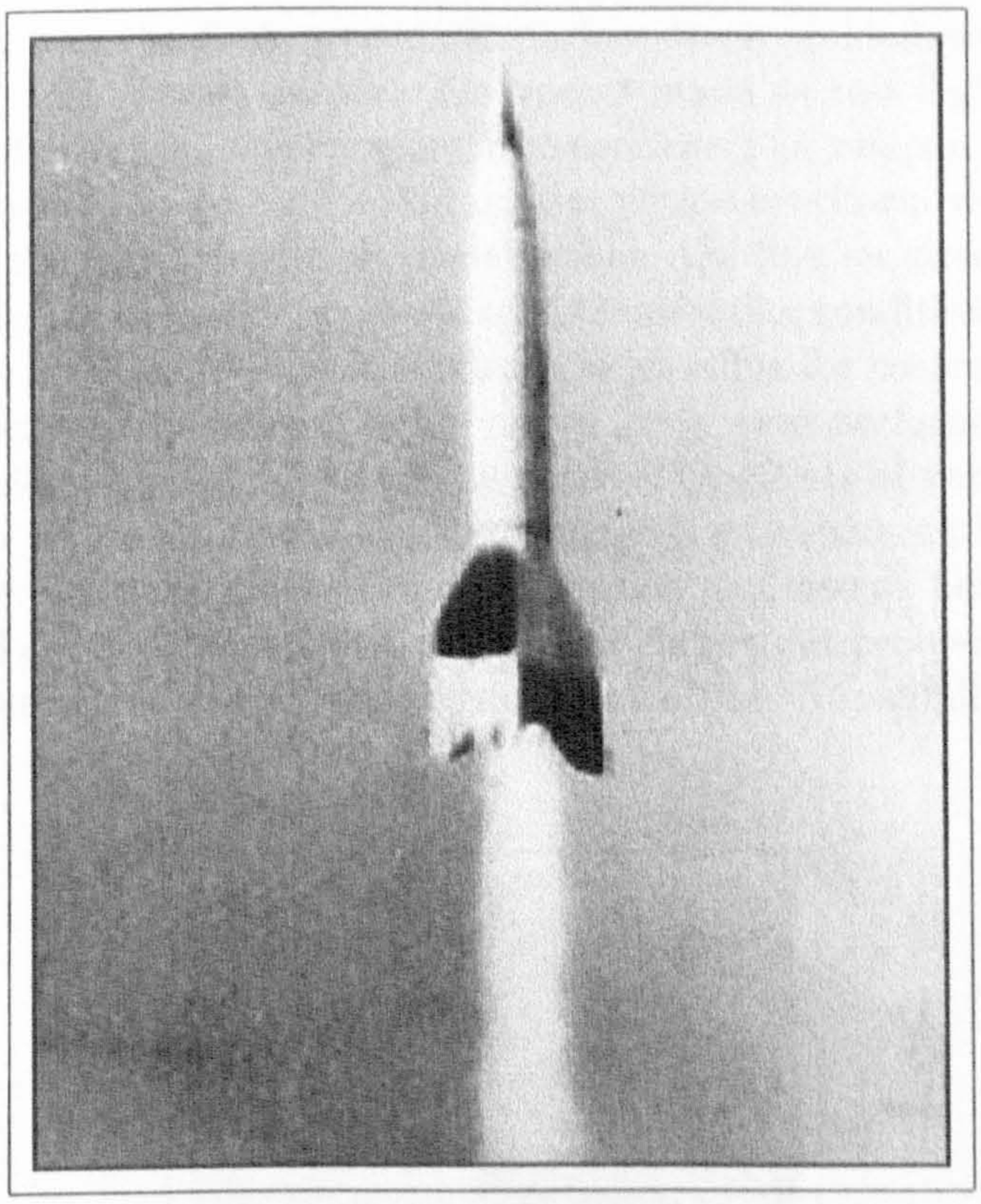

Figure A.1: *The German V-2 (A-4) Ballistic Missile*

The six years of World War II saw tremendous advances in military technology and, in particular, the advent of the jet engine, long range rockets and the atomic bomb. Germans and Americans used Panzerfaust and Bazooka anti-tank rockets. The Russians developed a 130mm lorry mounted multiple rocket system called the Katyusha, while the Western Allies used a 3 inch anti-aircraft rocket and air-ground rockets fired from aircraft to destroy ground targets. Von Braun's A-4 rocket was mass produced, designated the V-2 "Vengeance Weapon", it was first launched against London on 7th September 1944. While Von Braun's Army team were busy developing their rockets, their Luftwaffe colleagues were developing a winged subsonic cruise missile. Catapult launched, it was powered by an air breathing pulse jet engine and controlled using inertial guidance. This missile, designated the V-1, was design to fly towards its target, when, after it had reached its programmed range, after a certain time interval, the engine would shut off and the missile would stall, effectively becoming a bomb. The first German guided missile - the rocket powered, radio controlled gliding bomb designated HS-293, was launched on 23rd August 1943 against allied shipping in the Bay of Biscay. The following year the Luftwaffe launched a similar but unpowered device against Plymouth harbour, called FRITZ (FX-1400).

Probably the most complex, and revolutionary weapon to emerge from

Peenemunde was the first supersonic surface-to-air guided weapon - the "Wasserfall" anti-aircraft missile. The rocket made 44 test flights, but fortunately for the Allies, it never went into service. The weapon consisted of a slender forebody based on the A-4 design, with a cruciform wing arrangement and a similar arrangement of deflectable tail fins required to provide the manouevering capability at the Mach 2-3 operating conditions. Graphite rudders were fitted on the base to deflect the jet efflux for control during the launch phase. Comprehensive wind tunnel tests were performed on many different configurations and control systems. The effects of vortex interference at high incidence, the flight dynamic characteristics with movement in the centre of gravity due to fuel consumption, supersonic heating, target tracking and control systems and many more important problems were first addressed during the design and development of the Wasserfall.

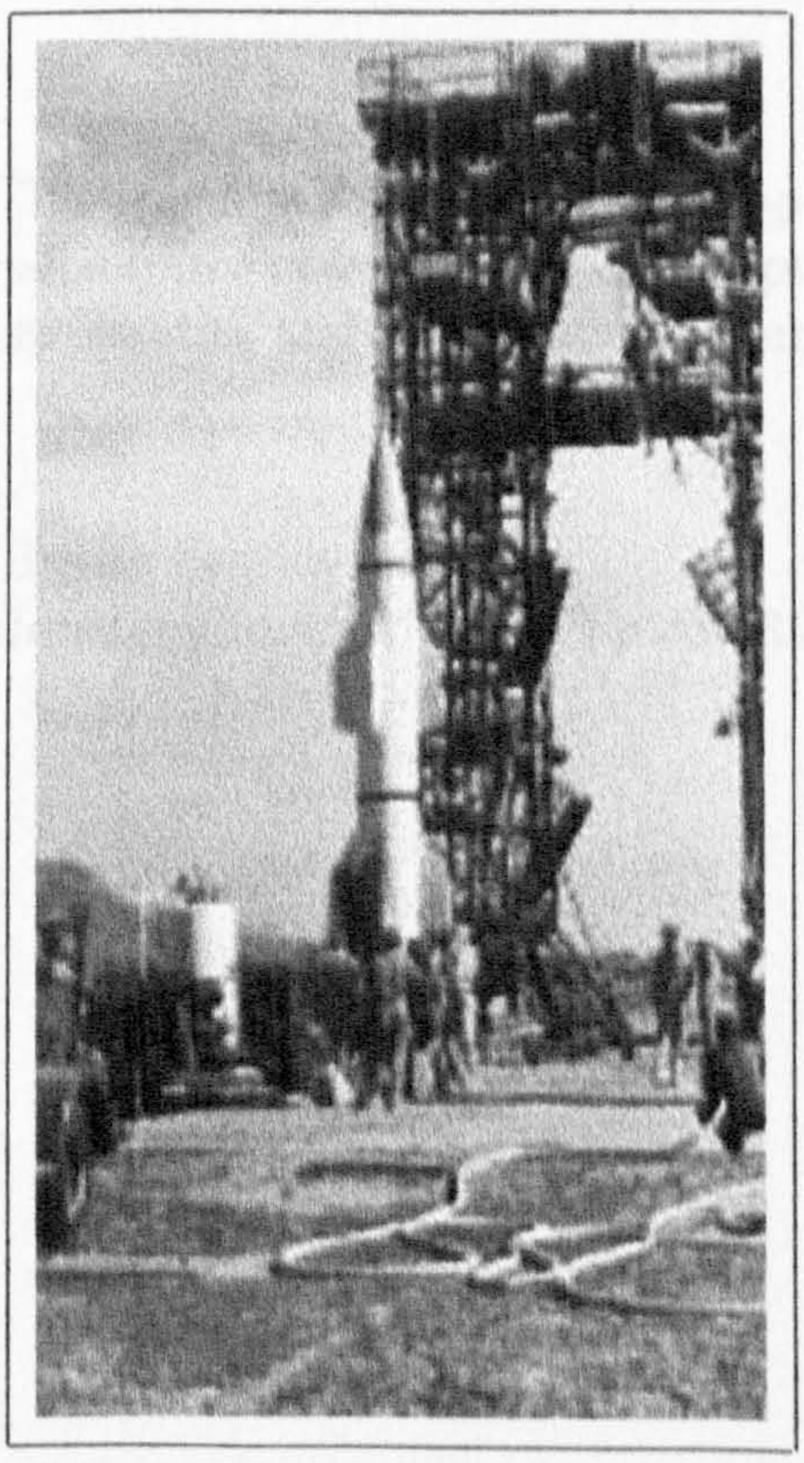

Figure A.2: *The German Wasserfall Anti-Aircraft Missile Prepared for Test Flight*

The pioneering work performed in advanced aerodynamics, by German weapon scientists and engineers during the 1930's and 40's, laid the basis for all modern aerial weapon technology. Since the Second World War ma-

jor advancements have been made in sensor technology, in micro-electronic control systems and in the understanding of radar visibility. Modern missile configuration designs, however, are still based essentially on those developed over fifty years ago in the research centres of Nazi Germany.

From this introductory history on air flight weapons, up until the end of World War II, it can clearly be seen that the historical trend which has led from the rock to the guided missile has been to deliver a weapon more accurately against an enemy target. Pin point accuracy is now a necessary requirement in the development of aerial weapons. The problem which confronts the modern weapon designer is that the enemy target is becoming faster and ever more agile and stealthy.

REFERENCES

Spearman, L.
Historical Review of Tactical Missile Airframe Developments
TacticalMissileAerodynamics : *GeneralTopics* Chapter 1,
AIAA Progress in Astronautics and Aeronautics, Volume 141, 1991.

Franklin, Carl. E.
The Hale Rocket in British Service (Part 1)
JournaloftheInterplanetarySociety Vol 51, pp 337-358, 1998.

Appendix B

Calculation of δ^* and Local Streamwise Pressure Gradient Used in Surface Pressure Measurement Error Estimation

This section outlines the methods used for the calculation of both the displacement thickness and the local streamwise pressure gradient at the surface obtained from the viscous flow solutions of CRANS3D. These properties are used in the estimation of the maximum error in the measurement of surface static pressure due to the flow disturbance from a pressure tapping (see Section 4.2). The aim of the analysis was to obtain error bars for the experimental measurements of the circumferential surface pressure distribution.

The boundary layer displacement thickness δ^*, for a compressible flow is defined as:

$$\delta^* = \int_0^{y_1} \left(1 - \frac{\rho V}{\rho_e V_e}\right) dy \tag{B.1}$$

where $\delta < y_1 < \infty$. The circumferential distribution of displacement thickness at a given axial station was evaluated by first calculating the boundary layer thickness, defined where the total velocity ($V = \sqrt{u^2 + v^2 + w^2}$) at a given J station becomes 99.5% of the total velocity at the next J station. The corresponding values of the density and total velocity at the edge of the boundary layer, ρ_e and V_e respectively, can then be taken and the appropriate radial summnation carried out between $y = 0 \rightarrow \delta$ will yield the displacement thickness. The circumferential distribution of δ^* is obtained by performing this radial calculation for each K station.

Consider the schematic of the method used to calculate the local streamwise surface pressure gradient shown in Figure B.1. The local streamwise pressure gradient at the surface is the gradient in pressure taken in the direction, **n**, of the first total velocity vector **V** above the surface (ie: at $J=2$). The velocity components, tangential to the surface, acting in the longitudinal, ξ, and circumferential, ζ, directions can then be evaluated using either the velocity and area vector components, or simple trigonometric relations involving the surface slope.

The pressure gradients at $(i, 1, k)$ in the ξ and ζ directions were treated using central differencing as shown in Figure B.1. Since the clustering in the circumferential direction was uniform for all the slender body cases, the incremental angle $d\phi$ (subtended by successive K=constant lines on the x-axis (XX) in the given x=constant plane) will be the same for each cell.

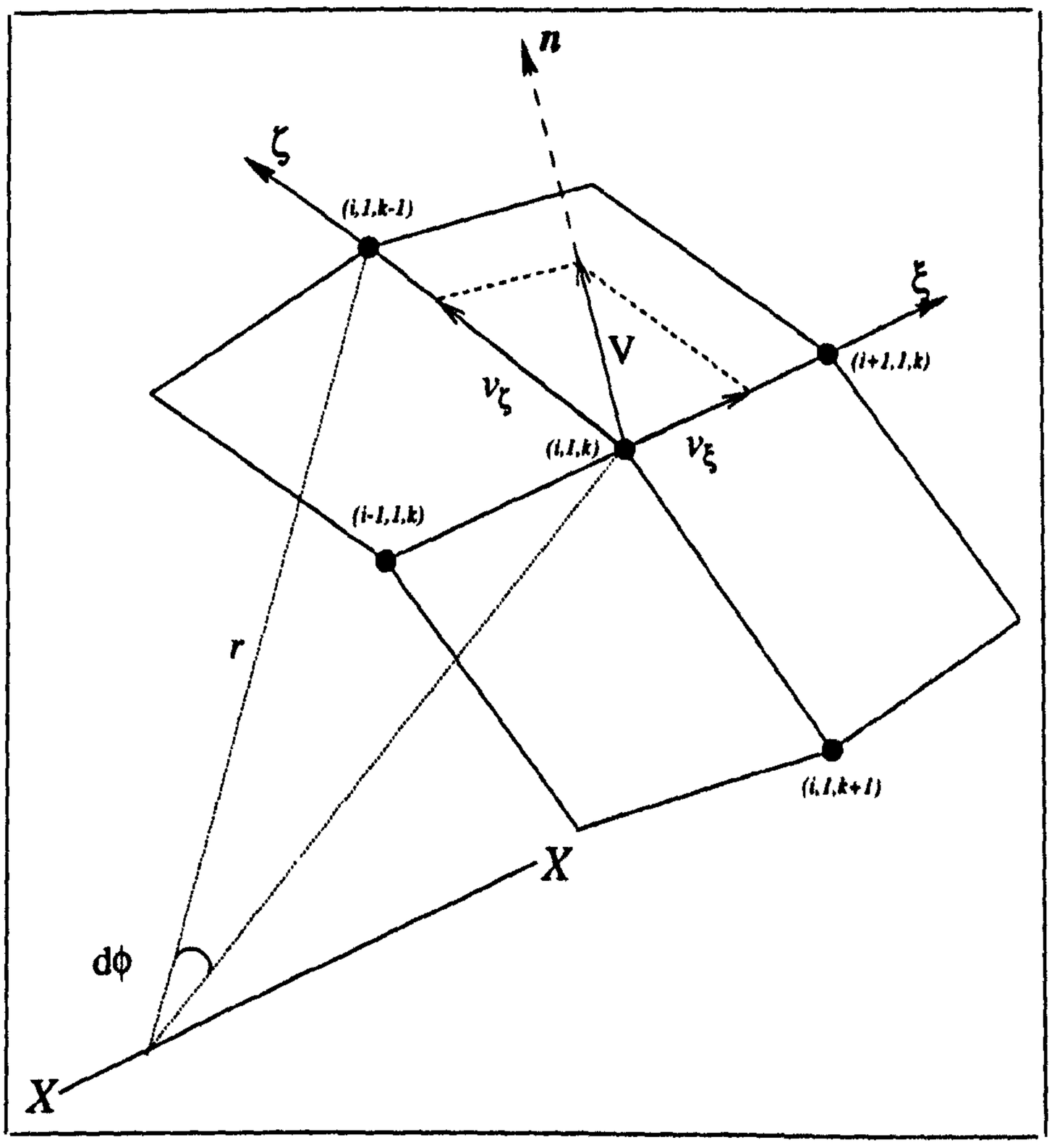

Figure B.1: *Calculation of Local Streamwise Pressure Gradient*

The pressure gradients in the ξ and ζ directions can therefore be evaluated for each cell in the circumferential direction as follows:

$$\frac{\partial p}{\partial \xi} = \frac{p_{i+1,1,k} - p_{i-1,1,k}}{\left((x_{i+1,1,k} - x_{i-1,1,k})^2 + (y_{i+1,1,k} - y_{i-1,1,k})^2\right)^{\frac{1}{2}}} \tag{B.2}$$

$$\frac{\partial p}{\partial \zeta} = \frac{p_{i,1,k+1} - p_{i,1,k-1}}{2r d\phi} \tag{B.3}$$

The required local streamwise pressure gradient on the surface can then be evaluated:

$$\frac{dp}{dn} = \frac{v_\xi}{V}\frac{\partial p}{\partial \xi} + \frac{v_\zeta}{V}\frac{\partial p}{\partial \zeta} \tag{B.4}$$

The circumferential distributions of δ^* and dp/dn can then be used in the calculation for estimating the experimental error associated with the measured circumferential surface pressure distributions.

Appendix C

Prediction of the Occurrence of the Embedded Crossflow Shock

For 2D subsonic flow past a circular object:

$$C_p = 1 - 4sin^2\theta \tag{C.1}$$

Giving a minimum C_p at $\phi = 90°$ of -3. The value of the minimum C_p, corrected for the effects of compressibility, can be obtained by application of the Prandtl-Glauert factor:

$$C_p = \frac{-3}{\sqrt{1 - M^2}} \tag{C.2}$$

At a given Mach number, the critical value of the minimum C_p, when the local flow will reach sonic conditions is given by:

$$C_{p_{Cr}} = \frac{2}{\gamma M^2}\left(\left[\left(\frac{2}{\gamma+1}\right)\left(1+\frac{\gamma-1}{2}M^2\right)\right]^{\frac{\gamma}{\gamma-1}} - 1\right) \tag{C.3}$$

Figure C.1 presents the variation of the critical value of the minimum C_p against the crossflow Mach number given by equation (C.3) together with the curve relating the minimum C_p on the circular body and the Mach number. The crossflow Mach number at which the two curves cross is that for which sonic conditions will occur in the invisced flow at $\phi = 90°$.

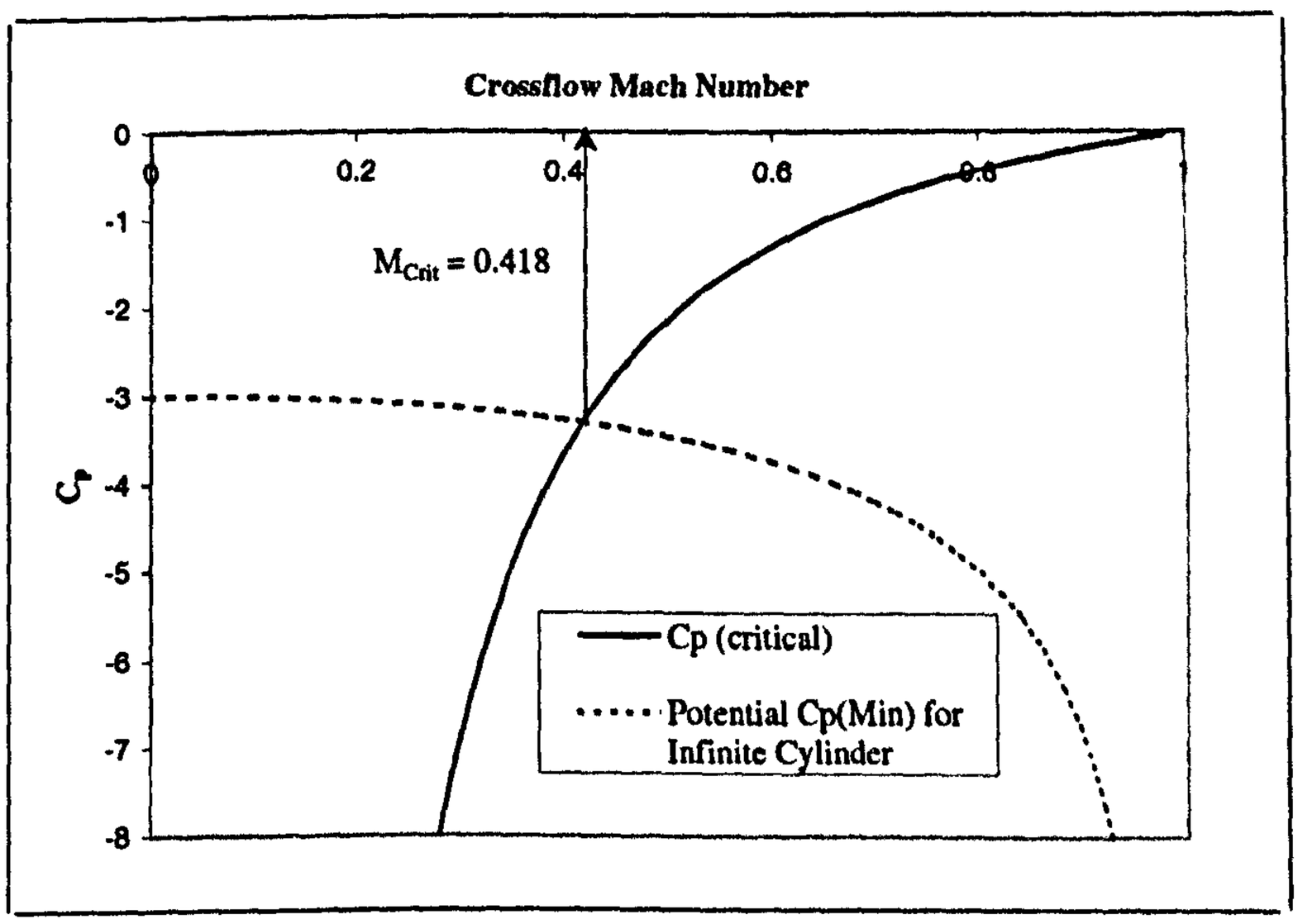

Figure C.1: *Calculation of Critical Conditions*